Measurements of the E Polarization Observable for $\gamma d \to \pi^- p(p_s)$, $\gamma d \to K^0 \Lambda(p_s)$, and $\gamma d \to \pi^+ \pi^- d(0)$ using CLAS g14 data at Jefferson Lab

by

Dao H. Ho

Submitted in partial fulfillment of the
requirements for the degree of
Doctor of Philosophy
at
Carnegie Mellon University
Department of Physics
Pittsburgh, Pennsylvania

Advised by Professor Reinhard A. Schumacher

August 21, 2015

Abstract

Photoproduction of mesons from the nucleon has a long and ongoing tradition for exploring nucleon excitations and the baryon-baryon interaction. Polarization observables which play a role in the photoproduction mechanism are, therefore, essential in addition to the differential cross section. The CLAS collaboration at Jefferson Lab, has been active in measuring these observables, but until now only on a proton targets. However, a comprehensive picture of the pseudoscalar meson photoproduction requires neutron data as well. That is, paired measurements of observables in γp and γn reactions are necessary to disentangle the photoproduction mechanism on the basis of isospin $I = 0$, and $I = 1$ photo-coupling transition amplitudes. The g14 experiment with "HDIce," a longitudinally polarized solid target of molecular hydrogen-deuteride with low background contamination from other nuclear species, provided an unique opportunity to measure several polarization observables—for the first time—on the neutron for different channels. In particular, we present our measurements of the E beam-target polarization observable, which requires circularly polarized beam and a longitudinally polarized target, for $p\pi^-$, $K^0\Lambda$, and $K^0\Sigma^0$ channels in the energy range of $1.5 \leq W \leq 2.3$ GeV. In addition, we also utilized the g14 dataset to investigate the intrinsic spin of a *possible* dibaryonic $N\Delta$ bound state by measuring the E (beam-target) observable on the $d\pi_d^{\pm}$ channel of the reaction $\gamma d \to \pi^+\pi^- d(0)$. Finally, this thesis also discusses a highly efficient multivariate analysis method called Boosted Decision Trees, which we employed extensively for this work and which has not been used before in CLAS data analysis.

Acknowledgments

First and foremost I sincerely thank my family who have supported me through the six challenging but memorable years I spent in Pittsburgh and Carnegie Mellon University. My parents were always there for me when I needed emotional support—thanks mom, dad. I thank also my sister Anh, and her husband, Minh, for being my family in the U.S.—spending time with you guys was the thing I needed after each long stressful semester.

I would like to give special thanks to my adviser, Professor Reinhard Schumacher, who was always supportive and caring. This thesis would not have been possible without your broad knowledge, patience and eye for detail. Many thanks to Professors Curtis Meyer, Gregg Franklin, Brian Quinn and Franz Klein for serving on my thesis committee and providing many helpful suggestions. My sincere gratitude goes to members of the CLAS collaboration and staff at JLab, especially the g14 working group, which provided the data and framework for this thesis. In particular, I would like to thank Andy Sandorfi, Xiangdong Wei, Mike Lowry, Tsuneo Kageya, and Annalisa D'Angelo for teaching me almost everything about the HDIce target and being supportive when I was at JLab during the g14 experiment. I am also grateful for the time I spent with my g14 colleagues Irene Zonta, Charles Hanretty, Peng Peng, and Natalie Walford sharing the joy and pain of graduate school. The last six years would not have been as interesting without my office-mates Haiyun Lu and Vahe Mamyan. Many discussions with them helped broaden my knowledge of physics and provided me with some insight about life in general.

I am indebted to Professor Manfred Paulini for being my academic adviser—providing support and understanding, especially during my first two years in graduate school. Last but not least, I would like to thank my friends Feng Yu, Robert Haussman, Ying Zhang, William Levine, Udom Sae-Ueng, Zhen Tang, Yutaro Iiyama, and You-Cyuan Jhang for hanging out with me over the years—providing much needed distractions from my work. And finally, there are many other people that I have not mentioned but nonetheless have helped me during the ups and downs of the last six years. Thanks go to all of you.

Contents

List of Tables

List of Figures

Chapter 1

Introduction

Quantum Chromodynamics, or QCD, is the standard theory to describe the strong interaction. Specifically, the theory dictates the binding of u, d, and s quarks and gluons into light mesons and nucleons. At the energy scale around 1 GeV, QCD becomes highly non-linear which does not allow for simple analytical solutions. Nevertheless, models that provide approximations to the full theory are available. Unfortunately, they predict the existence of many more excited nucleon states than experimentally observed. This interesting puzzle is referred to as the missing baryon problem and is the primary motivation for this work: helping the scientific efforts of constructing a full spectrum of nucleons.

In order to construct the full spectrum an additional degree of freedom in spin angular momentum is necessary. The spin degree of freedom manifests into polarization observables. Consequently, there are many experiments carried out to measure polarization observables. In particular, the CLAS g14 experiment at Jefferson Laboratory was designed to measure the polarization observables on a polarized bound neutron target. In this thesis we present analyses of several reactions using g14 data to obtain the E observable—referred to as the beam-target helicity asymmetry. Particularly, in this chapter we will give a brief overview of QCD and the formalism of polarization observables, and provide motivation for our study on polarized bound neutron data. Lastly, theoretical models will also be discussed.

1.1 Overview of Quantum Chromodynamics (QCD)

With the discovery of the Higgs boson [1, 2], the Standard Model is considered complete, see Figure 1.1 for a list of fundamental particles. It is the best theory to describe three fundamental forces in nature: electromagnetic, weak and strong. QCD is part of the Standard Model and describes the strong interaction. It has many parallels to quantum electrodynamics, QED, which is the theory of the electromagnetic force. In both theories, spin-1 particles mediate the forces—photons for QED and gluons for QCD—between spin-$1/2$ particles that carry charges. The two theories both satisfy

internal gauge symmetries [3]. Nevertheless, there are differences between QCD and QED. Particularly, QCD has three types of charge, colorfully termed as red (r), green (g), and blue (b). All physical particles occurring in nature must be color singlets, i.e., only color neutral combinations like $g\overline{g}$ or rgb can exist in nature. The solution to this mystery is yet to be discovered. In addition, while QED obeys $U(1)$ group gauge symmetry which does not allow its force carriers, the photons, to interact with other photons (i.e., they are neutral), QCD force carriers, the gluons, carry charge themselves, and, therefore, can interact with other gluons. In particular, exotic states made only from gluons may be possible—making the theory much more complex.

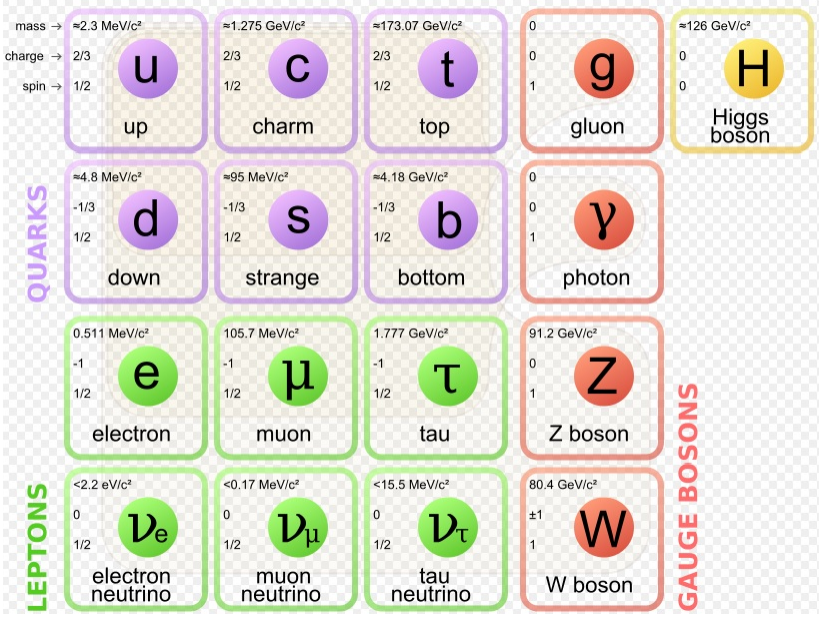

Figure 1.1: The Standard Model of elementary particles, with the three generations of matter, gauge bosons in the fourth column, and the Higgs boson in the fifth column. Image was taken from [4].

QCD obeys $SU(3)$ group gauge symmetry. The quarks carrying color charges can transform among themselves according to symmetric transformation laws. i.e., a "rotation" in the symmetry space. The rotation is carried out by the gauge field (the gluons). Mathematically, the most general gauge invariant Lagrangian density is

$$\mathcal{L} = -\overline{\Psi}\left(\gamma^{\mu} D_{\mu} + m\right)\Psi - \frac{1}{4} F^{\alpha}_{\mu\nu} F^{\mu\nu}_{\alpha}, \tag{1.1}$$

where γ^{μ} are the Dirac matrices, Ψ are the matter fields (the quarks) with mass m and D is the gauge-covariant derivative (defined for both QED and QCD):

$$D_{\mu}\Psi = \left(\partial_{\mu} - igA^{\alpha}_{\mu} t_{\alpha}\right)\Psi. \tag{1.2}$$

The gauge fields A^{α}_{μ} are massless spin-1 particles carrying the charge indexed by α. For QCD, there are eight gauge fields (eight types of gluons). The t_{α} are generators of the gauge transformation for a given representation of the matter fields, and g is a generalized charge representing the strength of the interaction. The last term in the Lagrangian density is defined as follows:

$$F^{\alpha}_{\mu\nu} = [D_{\mu}, D_{\nu}]^{\alpha} = \partial_{\mu}A^{\alpha}_{\nu} - \partial_{\nu}A^{\alpha}_{\mu} - gf^{\alpha\beta\gamma}A^{\beta}_{\mu}A^{\alpha}_{\nu}, \tag{1.3}$$

where $f^{\alpha\beta\gamma}$ are structure constants of the Lie algebra in the commutators $\left[t^{\beta}, t^{\alpha}\right] = if^{\alpha\beta\gamma}t^{\alpha}$. The last term in the Eq. 1.3 is zero for QED but non-zero for QCD. As a result, unlike QED, QCD allows both 3− and 4−gluon vertices implying gluon-gluon interactions. Another new property is asymptotic freedom, discovered by David Gross, Frank Wilczek, and David Politzer in 1973 [5, 6]. Asymptotic freedom suggests an energy dependence of the strong coupling constant α_{QCD} (in contrast $\alpha_{QED} \simeq \frac{1}{137}$ is a constant—the famous fine structure constant). Figure 1.2 shows the energy dependence of the strong coupling constant α_{QCD} as a function of the momentum transfer Q. At high Q, α_{QCD} is small and pertubative calculations are possible, while at low Q, α_{QCD} approaches unity, and calculations become non-pertubative. These two new properties result in a highly complex and non-linear theory at low energy scale. Nevertheless, there is a plethora of phenomena observed at the low energy scale. Studying these phenomena is the mission of Jefferson Laboratory and its scientists.

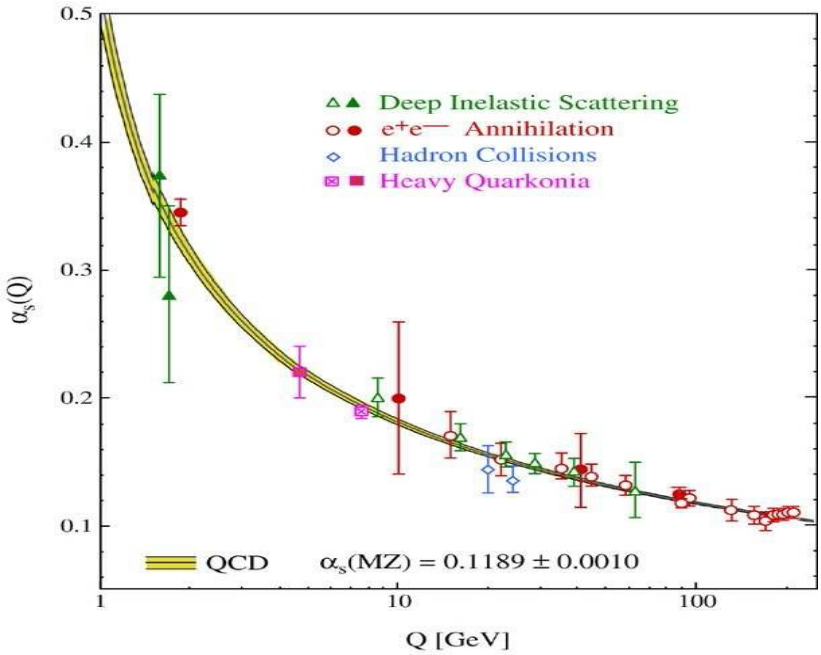

Figure 1.2: The strong coupling constant, α_{QCD}, as function of momentum transfer Q. Near 1 GeV the value of α_{QCD} is high—entering the non-pertubative regime where QCD becomes highly non-linear. Image was taken from [7].

1.2 QCD and Baryon Spectroscopy

Spectroscopy is the study of the excited states of a system. It is an extensively used method to study the properties of composite objects. In particular, atomic spectroscopy played a prominent role in understanding the internal structure of atoms which, in turn, helped develop the theory of quantum mechanics. Historically, in the late 19^{th} century, classical physicists were puzzled for decades when they observed only a discrete subset of wavelengths (energy states) rather than a continuous spectrum—in the gaseous atomic emission spectra. In 1913, Niels Bohr introduced the Bohr model of the Hydrogen atom—a breakthrough from classical physics—postulating that electrons could only have a discrete set of orbital angular momenta; when an electron jumps (falls) from one orbit to another, only a single quantum of light, a photon, is absorbed (emitted). The Bohr model explained the Hydrogen spectrum well and led the development of quantum mechanics. In 1925, Wolfgang Pauli formulated the Pauli exclusion principle—also by studying atomic spectra—which states that no two electrons can occupy the same quantum state at the same time. Consequently, it led to the concept of spin angular momentum, which is another important component in quantum mechanics in general and quantum field theory in particular.

Similarly, we study the spectrum of the nucleon—a composite system made of u and d quarks—to develop an understanding of the internal structure of the nucleon; but for a slightly different reason: quantum chromodynamics (or QCD) is the fundamental theory which governs the strong interaction—interactions between the quarks and gluons inside nucleons, but it can not be solved analytically (it can be solved numerically in Lattice QCD approach, however). As a result, we can only construct QCD-"inspired" effective theory models and check their predictions with experiments. A complete spectrum of the nucleon is an important component to verify these theories experimentally.

1.2.1 Baryon Spectroscopy

A baryon is a composite object made of three quarks, while a meson comprises of a quark-antiquark pair. Collectively, they are referred to as hadrons—particles that "feel" the strong force. Baryon spectroscopy involves injecting energy into the ground state nucleons thus exciting them into excited states (also called "resonances"). Eventually, these excited states decay back to the ground state via many different paths (or "channels"), emitting a wide variety of particles; the angular and energy distributions of these particles reveal characteristics of the nucleon spectrum.

Baryon spectroscopy is much more difficult to study than atomic spectroscopy due to the size of the nucleon (i.e., 10^{-5} time smaller than the size of a Hydrogen atom)—a large particle accelerator and a complex detector system are needed. Moreover, the collected data is also difficult to interpret; the uncertainty in their energies

(or, equivalently, their masses) are large (i.e., $\triangle E \sim 100$ MeV); broadening their energy/mass distributions causes the states to overlap. Note that according to the Heisenberg Uncertainty Principle the energy of any unstable quantum state is spread out over the range:

$$\triangle E \approx \hbar/\tau,$$

where τ is the mean lifetime of the state, and since $\triangle E \sim 100$ MeV, τ is typically about 10^{-23} seconds—i.e., these resonances are short-lived compared to weak or electromagnetic decays.

1.2.2 Constituent Quark Model, Diquark Model and the Missing Baryons Problem

In 1964, Murray Gell-Mann proposed a simple model of the baryon—the Constituent Quark Model (CQM)—where the relevant degrees of freedom are *only* in the valence quarks, and gluonic degree of freedom are not excited (see a summary by Dalitz in [8]). In particular, the model considers only the three lightest u, d, and s quarks (SU(6) spin-flavor symmetry group) interacting via a harmonic oscillator potential force with radial O(3) rotational symmetry [9]. Consequently, the baryon spectrum emerges as the supermultiplets of the full SU(6)×O(3) symmetry group. Unfortunately, the number of states predicted by the model is much higher than the number of excited states observed in πN scattering experiments. This over-abundance of predicted states is referred to as the *missing baryon resonance problem.*

Isgur and Koniuk [10] in 1980 added aspects of QCD into the basic CQM model, and, in 1992, Capstick and Roberts [11, 12] included relativistic effects into the model. Incidentally, even though the improved model *still* predicted more states than experimentally observed, its new features suggested that all the experimentally known states had strong coupling to the πN channels implying that the CQM might still be *right* and the missing resonances might only couple to non πN channels [13, 14].

Alternatively, Lichtenberg *et al.* [15] proposed reducing the baryon effective degrees of freedom in the CQM by clustering two of the three valence quarks together to decrease the number of predicted states. Many of the states absent in the model are not observed experimentally [16]; however, there is only some direct experimental evidence to support the existence of any diquark clustering inside the baryon [17].

1.2.3 Lattice QCD Predictions

Lattice QCD is a computing-based framework that tries to solve the full non-pertubative QCD numerically on a discretized space-time "lattice." The usual Minkowskian metric is converted to a 4-dimensional Euclidian metric by translating the real time dimension t into the imaginary time it dimension. Moreover, quarks are sitting on the lattice sites and local gauge symmetry is maintained to preserve QCD properties. Also, discretization naturally provides an ultraviolet cutoff of the order of the

inverse of the lattice spacing, which regularizes the theory. Lattice QCD computation is daunting but in recent years it has made tremendous progress; the full baryon spectrum upto $J^P = \frac{7}{2}^{\pm}$ has been calculated on the lattice [18]. Interestingly, these results lend support to the CQM model over the diquark model. This provides a futher impetus to search for the missing states.

1.3 Polarization Observables in Pseudoscalar Meson Photoproduction

We mentioned previously that it is essential to obtain a complete spectrum of excited nucleon states to understand the internal structure of the nucleon. To directly isolate these excited states—by studying the total cross sections of pseudoscalar meson photoproduction—is extremely difficult because these resonances are mostly broad and overlapping. Moreover, the presence of an s-channel resonance guarantees presence of a corresponding u-channel non-resonance background that significantly interferes with other resonances; thus, directly extracting the properties of these resonances is improbable. As a result, the most suitable approach is to analyze these processes at an amplitude level—the so-called Partial Wave Analysis (PWA) approach. Cross sections alone are not enough to constrain PWA models of meson production amplitudes; the spin degree of freedom in meson photoproduction as manifested in polarization observables is required. Necessarily, in the next section, we will formally discuss the polarization observables.

1.3.1 Theory and Formalism

For single pseudoscalar meson photoproduction where the initial photon, spin-$\frac{1}{2}$ target and spin-$\frac{1}{2}$ recoiling baryon can all be polarized, the most general description of the production comprises of $2 \times 2 \times 2 = 8$ complex amplitudes; but parity and rotational invariance reduce the number of independent amplitudes to four—they are commonly constructed as the Chew-Goldberger-Low-Nambu (CGLN) [19] amplitudes. Even though in their original paper Chew, Goldberger, Low, and Nambu expressed the CGLN amplitudes in a Cartesian (F_i) representation, helicity (H_i) and transversity (b_i) representations are widely used as well. However, we adopt the Cartesian (F_i) representation which has the simplest decomposition into angle-integrated electric and magnetic multipoles.

In single-pseudoscalar meson photoproduction there are sixteen possible observables, which are classified into an unpolarized differential cross section, three single-polarization asymmetries (i.e., either beam, target, or recoil is polarized), and three sets of four double-polarization asymmetries (i.e., two polarizations of either beam-target (BT), beam-recoil (BR), or target-recoil (TR)) as in [20]). These observables completely describe the single-pseudoscalar meson photoproduction and can be ex-

pressed in terms of the CGLN (F_i) amplitudes, which we will illustrate. In addition, ideally, only at most eight carefully chosen observables for both proton and neutron targets are required [21] to completely determine the amplitudes (the so-called Fierz identities). In reality, to mitigate the effects of systematic uncertainties and the limited statistical power of actual measurements in PWA a larger number of different observables is desirable.

We now briefly discuss the relation between the CGLN amplitudes and the general cross section as well as the expression of the general cross section in terms of the polarization observables. The discussion follows closely A. M. Sandorfi *et al.* [22]. We will use the case of $\gamma n \to K\Lambda$ as an example. In Figure 1.3 we defined polarization angles used in the following derivation. In detail, the $\langle \hat{x} - \hat{z} \rangle$plane is the reaction plane in the center-of-mass (c.m.) frame, $\vec{P_L^{\gamma}}$ is the polarization vector for the case of linearly polarized initial photons, $\vec{P^T}$ represents the target polarization vector, and $\vec{P^R}$ is the recoil polarization vector. Moreover, for the case of circularly polarized photons we used the helicity designations, i.e., $\mid \vec{P_C^{\gamma}} \mid = +1(-1)$ when 100% of the photon spins are parallel (anti-parallel) to the photon momentum vector.

Let us assume for now that the target and recoil polarizations are unity (i.e., $|\vec{P^T}| = |\vec{P^R}| = 1$) and pointing along $\hat{z}$—the direction of the photon beam; we also assume the photon polarization is unity $\mid \vec{P^{\gamma}} \mid = 1$. We then obtain the differential cross section as in [19]:

$$\frac{d\sigma}{d\Omega_{CM}}(\hat{\boldsymbol{P}}^{\gamma}, m_{s_N}, m_{s_\Lambda}) = \frac{|\vec{k}|}{|\vec{q}|} \left| \langle m_{s_\Lambda} | F_{CGLN} | m_{s_N} \rangle \right|^2 , \tag{1.4}$$

where $\hat{\boldsymbol{P}}^{\gamma}$ is the unit vector of $\vec{P^{\gamma}}$, $\vec{q}$ and $\vec{k}$ are the momenta of the initial state and final state particles in the overall center of mass frame, respectively. Furthermore, m_{s_Λ} and m_{s_N} are the spin substate quantum numbers of the Λ and the nucleon N along the z-direction, respectively. The F_{CGLN} are the Chew-Goldberger-Low-Nambu (CGLN) amplitudes [19] defined as follows:

$$\begin{aligned} F_{CGLN}(\theta_K) = & -i\vec{\sigma} \cdot \hat{\boldsymbol{P}}^{\gamma} F_1 - \left[\vec{\sigma} \cdot \hat{\boldsymbol{k}}\right] \left[\vec{\sigma} \cdot \left(\hat{\boldsymbol{q}} \times \hat{\boldsymbol{P}}^{\gamma}\right)\right] F_2 \\ & - i\left[\vec{\sigma} \cdot \hat{\boldsymbol{q}}\right] \left[\hat{\boldsymbol{k}} \cdot \hat{\boldsymbol{P}}^{\gamma}\right] F_3 - i\left[\vec{\sigma} \cdot \hat{\boldsymbol{k}}\right] \left[\hat{\boldsymbol{k}} \cdot \hat{\boldsymbol{P}}^{\gamma}\right] F_4, \end{aligned} \tag{1.5}$$

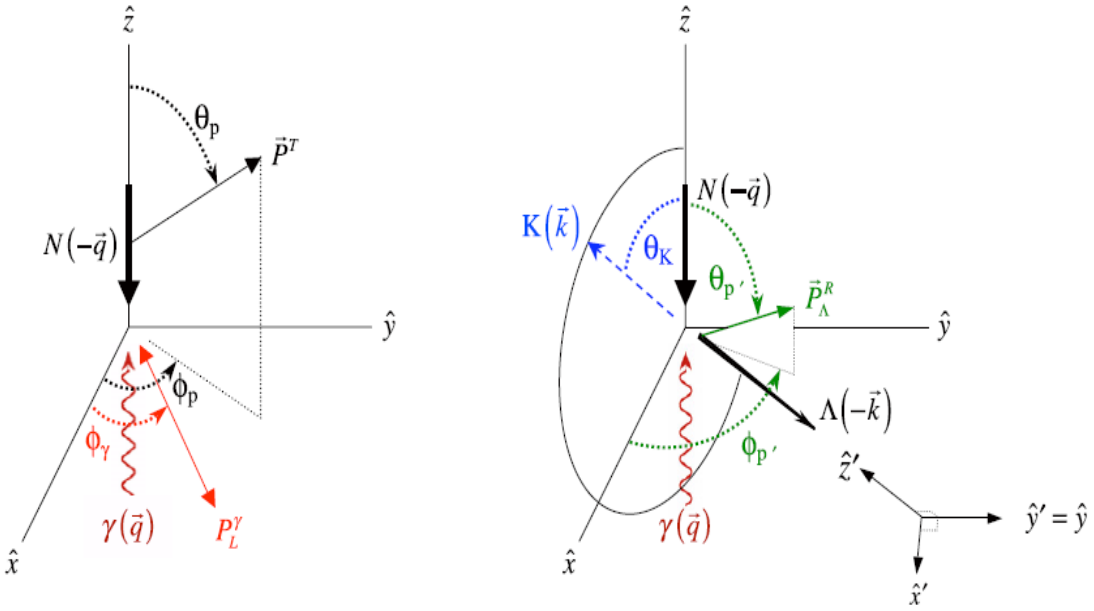

Figure 1.3: The center-of-mass (c.m.) coordinate system and angles used to specified polarizations in the reaction $\gamma(\vec{q}, \vec{P^\gamma}) + N(-\vec{q}, \vec{P^T}) \to K(\vec{k}) + \Lambda(-\vec{k}, \vec{P^R})$. The left (right) side is for the initial γN (final $K\Lambda$) state; $\hat{z}$ is along the photon beam direction; $\hat{y}$ is perpendicular to the $\langle \hat{x} - \hat{z} \rangle$ reaction plane in the $\vec{q} \times \vec{k}$ direction; $\hat{z}'$ is along the meson momentum in the c.m. frame, and $\hat{x}'$ is in the $\langle \hat{x} - \hat{z} \rangle$ reaction plane, rotated down from $\hat{z}'$ by $\theta_K + \pi/2$. Image was taken from [22].

$$F_1 = \sum_{l=0}^{l_{max}} \left(P'_{l+1}(x)E_{l+} + P'_{l-1}(x)E_{l-} + lP'_{l+1}(x)M_{l+} + (l+1)P'_{l-1}(x)M_{l-} \right), \quad (1.6)$$

$$F_2 = \sum_{l=0}^{l_{max}} \left((l+1)P'_l(x)M_{l+} + lP'_l(x)M_{l-} \right), \quad (1.7)$$

$$F_3 = \sum_{l=0}^{l_{max}} \left(P''_{l+1}(x)E_{l+} + P''_{l-1}(x)E_{l-} - P''_{l+1}(x)M_{l+} + P''_{l-1}(x)M_{l-} \right), \quad (1.8)$$

$$F_4 = \sum_{l=0}^{l_{max}} \left(-P''_l(x)E_{l+} - P''_l(x)E_{l-} + P''_l(x)M_{l+} - P''_l(x)M_{l-} \right), \quad (1.9)$$

where $\hat{\boldsymbol{k}}$ and $\hat{\boldsymbol{q}}$ are the unit vectors of $\vec{k}$ and $\vec{q}$, respectively, and $P'_l(x)$, $P''_l(x)$ are the first and second derivative of the Legendre function $P_l(x)$ with respect to $x = \hat{\boldsymbol{k}} \cdot \hat{\boldsymbol{q}} = \cos\theta_K$. $E_{l\pm}$, $M_{l\pm}$ are the electric and magnetic multipoles that are responsible

for transiting the initial state into the final states of orbital angular momentum l and total angular momentum $l \pm \frac{1}{2}$ (note that the sums have a limiting value of l_{max} depending on the input energy). And $\overrightarrow{\sigma}$ are the Pauli matrices:

$$\sigma_x = \begin{pmatrix} 0 & 1 \\ 1 & 0 \end{pmatrix}, \quad \sigma_y = \begin{pmatrix} 0 & -i \\ i & 0 \end{pmatrix}, \quad \sigma_z = \begin{pmatrix} 1 & 0 \\ 0 & -1 \end{pmatrix}.$$

We now generalize to allow arbitrary target and recoil polarization directions. However, as before, the linear photon polarization must still be in the $\langle \hat{x} - \hat{z} \rangle$plane, and the circular photon polarization must be aligned with $\hat{z}$. The corresponding cross section is:

$$\frac{d\sigma}{d\Omega_{CM}}(\hat{\boldsymbol{P}}^{\gamma}, \hat{\boldsymbol{P}}^{T}, \hat{\boldsymbol{P}}^{R}) = \frac{|\overrightarrow{k}|}{|\overrightarrow{q}|} \left| \left\langle \hat{\boldsymbol{P}}^{R} \left| F_{CGLN} \right| \hat{\boldsymbol{P}}^{T} \right\rangle \right|^2, \tag{1.10}$$

where $\left|\hat{\boldsymbol{P}}^{T}\right\rangle$ and $\left|\hat{\boldsymbol{P}}^{R}\right\rangle$ are the initial and final states spin-1/2 baryon with the spin pointing in the $\hat{\boldsymbol{P}}^{T}$, and $\hat{\boldsymbol{P}}^{R}$ directions respectively (i.e., they remain the usual helicity states along their respective polarization directions). Now consider a spin state $|\hat{s}\rangle$ that is quantized in an arbitrary direction $\hat{s} = (1, \hat{\theta}, \hat{\phi})$, the relation between $|\hat{s}\rangle$and the usual eigenstate of z-axis quantization is:

$$|\hat{s}\rangle = \sum_{m=\pm\frac{1}{2}} D^{(\frac{1}{2})}_{m,+\frac{1}{2}}(\theta, \Phi) \, |m\rangle \, , \tag{1.11}$$

where $|m\rangle$ is defined by $S_z \left|\pm\frac{1}{2}\right\rangle = \left(\pm\frac{1}{2}\right) \left|\pm\frac{1}{2}\right\rangle$, the eigenstates of the S_z spin operator, and $D^{(\frac{1}{2})}_{m,\lambda}(\theta, \phi) = \exp\left[-i(m-\lambda)\phi\right] d^{(\frac{1}{2})}_{m,\lambda}(\theta)$, the Wigner D matrix. Following the phase convention of Brink and Satchler [23], the definitions of $d^{(\frac{1}{2})}_{m,\lambda}(\theta)$ are:

$$d^{(\frac{1}{2})}_{+\frac{1}{2},+\frac{1}{2}}(\theta) = d^{(\frac{1}{2})}_{-\frac{1}{2},-\frac{1}{2}}(\theta) = \cos\frac{\theta}{2},$$

$$d^{(\frac{1}{2})}_{-\frac{1}{2},+\frac{1}{2}}(\theta) = -d^{(\frac{1}{2})}_{+\frac{1}{2},-\frac{1}{2}}(\theta) = \sin\frac{\theta}{2}.$$

Moreover, from Figure 1.3, we can express the momenta and the polarization vectors as:

$$\overrightarrow{q} = |\overrightarrow{q}|(0,0,1) \quad , \quad \overrightarrow{k} = |\overrightarrow{k}|(\sin\theta_K, 0, \cos\theta_K), \tag{1.12}$$

$$\hat{\boldsymbol{P}}^{\gamma}_{L} = (\cos\Phi_{\gamma}, \sin\Phi_{\gamma}, 0) \quad , \quad \left(\hat{\boldsymbol{P}}^{\gamma}_{C}\right)_{\pm 1} = \mp\frac{1}{\sqrt{2}}(\hat{x} \pm i\hat{y}), \tag{1.13}$$

$$\hat{\boldsymbol{P}^T} = (1, \theta_p, \Phi_p) \quad , \quad \hat{\boldsymbol{P}^R} = (1, \theta'_p, \Phi'_p). \tag{1.14}$$

Note that, for simplicity, we used the spherical variables for the target and recoil polarizations. By using equations 1.12-1.14 we derive the photoproduction matrix elements as:

$$\left\langle \hat{\boldsymbol{P}^R} \left| F_{CGLN} \right| \hat{\boldsymbol{P}^T} \right\rangle = \sum_{n=0}^{3} \left[\sum_{i=1}^{4} F_i(\theta_K) C_{i,n}(\theta_K, \Phi_\gamma) \right] \left\langle \hat{\boldsymbol{P}^R} \left| \sigma_n \right| \hat{\boldsymbol{P}^T} \right\rangle, \tag{1.15}$$

where $\sigma_0 = \mathbf{1}$, and $\sigma_1 = \sigma_x$, $\sigma_2 = \sigma_y$, $\sigma_3 = \sigma_z$. The explicit form of $C_{i,n}(\theta_K, \Phi_\gamma)$ is given in Table 1.1, and

$$\left\langle \hat{\boldsymbol{P}^R} \left| \sigma_n \right| \hat{\boldsymbol{P}^T} \right\rangle = \sum_{m_{s_\Lambda}, m_{s_N} = \pm\frac{1}{2}} D^{(\frac{1}{2})*}_{m_{s_\Lambda}, +\frac{1}{2}}(\theta_{p'}, \Phi_{p'}) D^{(\frac{1}{2})}_{m_{s_N}, +\frac{1}{2}}(\theta_p, \Phi_p) \left\langle m_{s_\Lambda} \left| \sigma_n \right| m_{s_N} \right\rangle, \tag{1.16}$$

where $\left| m_{s_{\Lambda(N)}} \right\rangle$ is defined by $S_z^{\Lambda(N)} \left| \pm\frac{1}{2} \right\rangle = \left(\pm\frac{1}{2} \right) \left| \pm\frac{1}{2} \right\rangle$, the eigenstates of the $S_z^{\Lambda(N)}$ spin operator in the z'-axis quantization direction.

	$n=0$	$n=1$	$n=2$	$n=3$
$i=1$	0	$-i\cos\Phi_\gamma$	$-i\sin\Phi_\gamma$	0
$i=2$	$\sin\theta_K \sin\Phi_\gamma$	$i\cos\theta_K \cos\Phi_\gamma$	$i\cos\theta_K \sin\Phi_\gamma$	$-i\sin\theta_K \cos\Phi_\gamma$
$i=3$	0	0	0	$-i\sin\theta_K \cos\Phi_\gamma$
$i=4$	0	$-i\sin^2\theta_K \cos\Phi_\gamma$	0	$-i\sin\theta_K \cos\theta_K \cos\Phi_\gamma$

Table 1.1: Explicit form of $C_{i,n}(\theta_K, \Phi_\gamma)$ in Eq. 1.15.

Furthermore, with non-unit polarization vectors, the general cross section can be expressed as:

$$\frac{d\sigma}{d\Omega_{CM}}(\vec{P^\gamma}, \vec{P^T}, \vec{P^R}) = \sum_{\hat{\boldsymbol{P}^\gamma} = \{\hat{\boldsymbol{P}}_1^\gamma, \hat{\boldsymbol{P}}_2^\gamma\}} \sum_{\hat{\boldsymbol{P}^T} = \pm\hat{\boldsymbol{P}^T}} \sum_{\hat{\boldsymbol{P}^R} = \pm\hat{\boldsymbol{P}}^R} \rho_{\hat{\boldsymbol{P}^\gamma}} \rho_{\hat{\boldsymbol{P}^T}} \rho_{\hat{\boldsymbol{P}^R}} \frac{d\sigma}{d\Omega_{CM}}(\hat{\boldsymbol{P}^\gamma}, \hat{\boldsymbol{P}^T}, \hat{\boldsymbol{P}^R}), \tag{1.17}$$

where $\vec{P^X}$ specifies the magnitude and direction of the polarization of particle $X = \gamma, T, R$. For the target (T) and recoil (R), this is just $\vec{P^X} = \left(\rho_{+\hat{\boldsymbol{P}^X}} - \rho_{-\hat{\boldsymbol{P}^X}} \right) \hat{\boldsymbol{P}^X}$ with $\rho_{\pm\hat{\boldsymbol{P}^X}}$ is the probability of observing X with its spin vector pointing in the $\pm\hat{\boldsymbol{P}^X}$ direction. For the photons (γ), $\rho_{\hat{\boldsymbol{P}}_1^\gamma}(\rho_{\hat{\boldsymbol{P}}_2^\gamma})$ is the probability of observing photons with

their polarization vector pointing in the $\hat{\boldsymbol{P}}_1^\gamma(\hat{\boldsymbol{P}}_2^\gamma)$ direction—for linearly polarized photons $\hat{\boldsymbol{P}}_1^\gamma$ and $\hat{\boldsymbol{P}}_2^\gamma$ are orthogonal polarization, while for circularly polarized photons $\hat{\boldsymbol{P}}_1^\gamma$ and $\hat{\boldsymbol{P}}_2^\gamma$ are the opposite helicity states.

In order to "link" the general cross section expression to polarization observables, we follow the formalism of the spin density matrix described by Fasano, Tabakin, and Saghai (FTS) [24] and rewrite Eq. 1.17 as (Einstein summation notation implied):

$$\frac{d\sigma}{d\Omega_{CM}}(\vec{P^\gamma},\vec{P^T},\vec{P^R}) = \varrho_0(\varrho^R)_{kn}(F_\mu)_{nm}(\varrho^T)_{ml}(F_\lambda^\dagger)_{lk}(\varrho^\gamma)_{\mu\lambda}, \tag{1.18}$$

where $\varrho_0 = \frac{|\vec{k}|}{|\vec{q}|}$, and $(F_\mu)_{m_{S_\Lambda} m_{S_N}} = \langle m_{s_\Lambda} | F^\mu_{CGLN} | m_{s_N} \rangle$, in which the spin states of the initial and final baryons are quantized in the z- and z'-directions, respectively. Note that for $(F_\mu)_{m_{S_\Lambda} m_{S_N}}$ $\mu \in \{1,2\}$ and $m_S \in \{-\frac{1}{2},+\frac{1}{2}\}$. The 2×2 spin density matrices [24] are defined below:

$$\varrho^\gamma = \frac{1}{2}\left[\mathbf{1} + \vec{P^\gamma}\cdot\vec{\sigma}\right] = \frac{1}{2}\left[\mathbf{1} + \sum_b^3 (\vec{P^\gamma})^b \cdot \sigma^b\right], \tag{1.19}$$

$$\varrho^T = \frac{1}{2}\left[\mathbf{1} + \vec{P^T}\cdot\vec{\sigma}\right] = \frac{1}{2}\left[\mathbf{1} + \sum_a^3 (\vec{P^T})^a \cdot \sigma^a\right], \tag{1.20}$$

$$\varrho^R = \frac{1}{2}\left[\mathbf{1} + \vec{P^R}\cdot\vec{\sigma}\right] = \frac{1}{2}\left[\mathbf{1} + \sum_{a'}^3 (\vec{P^R})^{a'} \cdot \sigma^{a'}\right], \tag{1.21}$$

where a, and b reference the unprimed x, y, z coordinates of Figure 1.3, but a' references the primed x', y', z' coordinates in Figure 1.3 with the meson momentum along the $+\hat{z}'$. In addition, note that the unpolarized differential cross section is $\frac{d\sigma_0}{d\Omega_{CM}} = (\varrho_0/4)\mathcal{N}$ where $\mathcal{N} = (F_\lambda)_{lk}(F_\lambda)^\dagger_{lk}$. As a result, we can now expand Eq. 1.18 as:

$$
\begin{aligned}
\frac{d\sigma}{d\Omega_{CM}}(\vec{P^\gamma},\vec{P^T},\vec{P^R}) =& \frac{1}{2}\frac{d\sigma_0}{d\Omega_{CM}}\left\{1+\left(\vec{P^\gamma}\right)_b\frac{(F_\mu)_{kn}(F_\lambda^\dagger)_{nk}\sigma^b_{\mu\lambda}}{\mathcal{N}}+\left(\vec{P^T}\right)_a\frac{(F_\lambda)_{kn}\sigma^a_{nm}(F_\lambda^\dagger)_{mk}}{\mathcal{N}}\right.\\
&+\left(\vec{P^R}\right)_{a'}\frac{\sigma^{a'}_{kn}(F_\lambda)_{nm}(F_\lambda^\dagger)_{mk}}{\mathcal{N}}+\left(\vec{P^T}\right)_a\left(\vec{P^\gamma}\right)_b\frac{(F_\mu)_{km}\sigma^a_{ml}(F_\lambda^\dagger)_{lk}\sigma^b_{\mu\lambda}}{\mathcal{N}}\\
&+\left(\vec{P^R}\right)_{a'}\left(\vec{P^\gamma}\right)^b\frac{\sigma^{a'}_{kn}(F_\mu)_{nl}(F_\lambda^\dagger)_{lk}\sigma^b_{\mu\lambda}}{\mathcal{N}}\\
&+\left(\vec{P^R}\right)_{a'}\left(\vec{P^T}\right)_a\frac{\sigma^{a'}_{kn}(F_\lambda)_{nm}\sigma^a_{ml}(F_\lambda^\dagger)_{lk}}{\mathcal{N}}\\
&\left.+\left(\vec{P^R}\right)_{a'}\left(\vec{P^T}\right)_a\left(\vec{P^\gamma}\right)_b\frac{\sigma^{a'}_{kn}(F_\mu)_{nm}\sigma^a_{ml}(F_\lambda^\dagger)_{lk}\sigma^b_{\mu\lambda}}{\mathcal{N}}\right\}\\
=&\frac{1}{2}\frac{d\sigma_0}{d\Omega_{CM}}\left\{1+\left(\vec{P^\gamma}\right)_b\Sigma^b+\left(\vec{P^T}\right)_a T^a+\left(\vec{P^R}\right)_{a'}P^{a'}\right.\\
&+\left(\vec{P^T}\right)_a\left(\vec{P^\gamma}\right)_b C^{BT}_{ab}+\left(\vec{P^R}\right)_{a'}\left(\vec{P^\gamma}\right)_b C^{BR}_{a'b}+\left(\vec{P^R}\right)_{a'}\left(\vec{P^T}\right)_a C^{TR}_{a'a}\\
&\left.+\left(\vec{P^R}\right)_{a'}\left(\vec{P^T}\right)_a\left(\vec{P^\gamma}\right)_b C^{TRB}_{a'ab}\right\},
\end{aligned}
\tag{1.22}
$$

where we have introduced:

$$\Sigma^b = \frac{(F_\mu)_{kn}(F_\lambda^\dagger)_{nk}\sigma^b_{\mu\lambda}}{\mathcal{N}}, \tag{1.23}$$

$$T^a = \frac{(F_\lambda)_{kn}\sigma^a_{nm}(F_\lambda^\dagger)_{mk}}{\mathcal{N}}, \tag{1.24}$$

$$P^{a'} = \frac{\sigma^{a'}_{kn}(F_\lambda)_{nm}(F_\lambda^\dagger)_{mk}}{\mathcal{N}}, \tag{1.25}$$

$$C^{BT}_{ab} = \frac{(F_\mu)_{km}\sigma^a_{ml}(F_\lambda^\dagger)_{lk}\sigma^b_{\mu\lambda}}{\mathcal{N}}, \tag{1.26}$$

$$C^{BR}_{a'b} = \frac{\sigma^{a'}_{kn}(F_\mu)_{nm}(F_\lambda^\dagger)_{mk}\sigma^b_{\mu\lambda}}{\mathcal{N}}, \tag{1.27}$$

$$C^{TR}_{a'a} = \frac{\sigma^{a'}_{kn}(F_\lambda)_{nm}\sigma^a_{ml}(F_\lambda^\dagger)_{lk}}{\mathcal{N}}, \tag{1.28}$$

$$C^{TRB}_{a'ab} = \frac{\sigma^{a'}_{kn}(F_\mu)_{nm}\sigma^a_{ml}(F_\lambda^\dagger)_{lk}\sigma^b_{\mu\lambda}}{\mathcal{N}}. \tag{1.29}$$

Note that equations 1.23, 1.24, and 1.25 (1.26, 1.27, and 1.28) present the single-polarization (double-polarization) observables, while equation 1.29 presents the triple-

polarization observable. In addtion, σ^i_{mn} represents the m^{th} row and n^{th} column component of the i^{th} Pauli matrix. Since the a, b, and a' represent three coordinates, Eq. 1.22 consists of 64 terms. However, Artru *et al.* [25] showed that due to requirements of parity and rotational invariance, there remain only 32 non-vanishing terms. Moreover, there are, in fact, only 16 distinct observables since each observable occurs twice in the expansion given by Eq. 1.22. We show below how equations 1.23-1.29 relate to the 16 observables defined in FTS [24] (i.e., the most common naming convention for polarization observables in psedoscalar meson photoproduction):

$$\Sigma^{x_B} = \Sigma, \quad T^{y_T} = T, \quad P^{y'_R} = P, \tag{1.30}$$

$$\begin{aligned} C^{BT}_{z_T z_B} &= -E, \quad C^{BT}_{z_T y_B} = -G, \quad C^{BT}_{x_T z_B} = F, \\ C^{BT}_{x_T y_B} &= -H, \quad C^{BT}_{y_T x_B} = P, \end{aligned} \tag{1.31}$$

$$\begin{aligned} C^{BR}_{z'_R z_B} &= C_{z'}, \quad C^{BR}_{z'_R y_B} = -O_{z'} \quad C^{BR}_{x'_R z_B} = C_{x'}, \\ C^{BR}_{x'_R y_B} &= -O_{x'}, \quad C^{BR}_{y'_R x_B} = T, \end{aligned} \tag{1.32}$$

$$\begin{aligned} C^{TR}_{z'_R z_T} &= L_{z'}, \quad C^{TR}_{z'_R x_T} = T_{z'}, \quad C^{TR}_{x'_R z_T} = L_{x'}, \\ C^{TR}_{x'_R x_T} &= T_{x'}, \quad C^{TR}_{y'_R y_T} = \Sigma, \end{aligned} \tag{1.33}$$

$$\begin{aligned} C^{TRB}_{y'_R x_T y_B} &= -E, \quad C^{TRB}_{y'_R x_T z_B} = G, \quad C^{TRB}_{y'_R z_T y_B} = -F, \\ C^{TRB}_{y'_R z_T z_B} &= -H, \quad C^{TRB}_{x'_R y_T y_B} = -C_{z'}, \quad C^{TRB}_{x'_R y_T z_B} = -O_{z'} \\ C^{TRB}_{z'_R y_T y_B} &= C_{x'}, \quad C^{TRB}_{z'_R y_T z_B} = O_{x'}, \quad C^{TRB}_{x'_R x_T x_B} = L_{z'}, \\ C^{TRB}_{x'_R z_T x_B} &= -T_{z'}, \quad C^{TRB}_{z'_R x_T x_B} = -L_{x'}, \quad C^{TRB}_{z'_R z_T x_B} = T_{x'}, \\ C^{TRB}_{y'_R y_T x_B} &= 1. \end{aligned} \tag{1.34}$$

We also introduce the pairs of measurements needed to construct each of the 15 observables that we defined earlier (excluding $C^{BTR}_{y'_R y_T x_B} = 1$) [22]. For simplicity, we assume 100% polarizations for the beam (B), target (T), and recoil (R). Note that we follow the notation $\sigma(\vec{P^\gamma}, \vec{P^T}, \vec{P^R}) = \frac{d\sigma}{d\Omega_{CM}}(\vec{P^\gamma}, \vec{P^T}, \vec{P^R})$, where the photon beam is characterized either by its helicity (± 1) for circular polarization, or by ϕ^L_γ for linear polarization.

$$\Sigma = \frac{\sigma(+\pi/2,0,0) - \sigma(+2\pi,0,0)}{\sigma(+\pi/2,0,0) + \sigma(+2\pi,0,0)}, \tag{1.35}$$

$$T = \frac{\sigma(0,+y,0) - \sigma(0,-y,0)}{\sigma(0,+y,0) + \sigma(0,-y,0)}, \tag{1.36}$$

$$P = \frac{\sigma(0,0,+y') - \sigma(0,0,-y')}{\sigma(0,0,+y') + \sigma(0,0,-y')}, \tag{1.37}$$

$$E = \frac{\sigma(+1,-z,0) - \sigma(+1,+z,0)}{\sigma(+1,-z,0) + \sigma(+1,+z,0)} \quad , \quad E = \frac{\sigma(+1,-z,0) - \sigma(-1,-z,0)}{\sigma(+1,-z,0) + \sigma(-1,-z,0)}, \tag{1.38}$$

$$G = \frac{\sigma(+\pi/4,+z,0) - \sigma(+\pi/4,-z,0)}{\sigma(+\pi/4,+z,0) + \sigma(+\pi/4,-z,0)} \quad , \quad G = \frac{\sigma(+\pi/4,+z,0) - \sigma(-\pi/4,+z,0)}{\sigma(+\pi/4,+z,0) + \sigma(-\pi/4,+z,0)}, \tag{1.39}$$

$$F = \frac{\sigma(+1,+x,0) - \sigma(-1,+x,0)}{\sigma(+1,+x,0) + \sigma(-1,+x,0)} \quad , \quad F = \frac{\sigma(+1,+x,0) - \sigma(+1,-x,0)}{\sigma(+1,+x,0) + \sigma(+1,-x,0)}, \tag{1.40}$$

$$H = \frac{\sigma(+\pi/4,+x,0) - \sigma(-\pi/4,+x,0)}{\sigma(+\pi/4,+x,0) + \sigma(-\pi/4,+x,0)} \quad , \quad H = \frac{\sigma(+\pi/4,+x,0) - \sigma(+\pi/4,-x,0)}{\sigma(+\pi/4,+x,0) + \sigma(+\pi/4,-x,0)}, \tag{1.41}$$

$$C_{x'} = \frac{\sigma(+1,0,+x') - \sigma(-1,0,+x')}{\sigma(+1,0,+x') + \sigma(-1,0,+x')} \quad , \quad C_{x'} = \frac{\sigma(+1,0,+x') - \sigma(+1,0,-x')}{\sigma(+1,0,+x') + \sigma(+1,0,-x')}, \tag{1.42}$$

$$C_{z'} = \frac{\sigma(+1,0,+z') - \sigma(-1,0,+z')}{\sigma(+1,0,+z') + \sigma(-1,0,+z')} \quad , \quad C_{x'} = \frac{\sigma(+1,0,+z') - \sigma(+1,0,-z')}{\sigma(+1,0,+z') + \sigma(+1,0,-z')}, \tag{1.43}$$

$$O_{x'} = \frac{\sigma(+\pi/4,0,+x') - \sigma(-\pi/4,0,+x')}{\sigma(+\pi/4,0,+x') + \sigma(-\pi/4,0,+x')} \quad , \quad O_{x'} = \frac{\sigma(+\pi/4,0,+x') - \sigma(+\pi/4,0,-x')}{\sigma(+\pi/4,0,+x') + \sigma(+\pi/4,0,-x')}, \tag{1.44}$$

$$O_{z'} = \frac{\sigma(+\pi/4,0,+z') - \sigma(-\pi/4,0,+z')}{\sigma(+\pi/4,0,+z') + \sigma(-\pi/4,0,+z')} \quad , \quad O_{z'} = \frac{\sigma(+\pi/4,0,+z') - \sigma(+\pi/4,0,-z')}{\sigma(+\pi/4,0,z') + \sigma(+\pi/4,0,-z')}, \tag{1.45}$$

$$L_{x'} = \frac{\sigma(0,+z,+x') - \sigma(0,-z,+x')}{\sigma(0,+z,+x') + \sigma(0,-z,+x')} \quad , \quad L_{x'} = \frac{\sigma(0,+z,+x') - \sigma(0,+z,-x')}{\sigma(0,+z,+x') + \sigma(0,+z,-x')}, \tag{1.46}$$

$$L_{z'} = \frac{\sigma(0,+z,+z') - \sigma(0,-z,+z')}{\sigma(0,+z,+z') + \sigma(0,-z,+z')} \quad , \quad L_{z'} = \frac{\sigma(0,+z,+z') - \sigma(0,+z,-z')}{\sigma(0,+z,+z') + \sigma(0,+z,-z')}, \tag{1.47}$$

$$T_{x'} = \frac{\sigma(0,+x,+x') - \sigma(0,-x,+x')}{\sigma(0,+x,+x') + \sigma(0,-x,+x')} \quad , \quad T_{x'} = \frac{\sigma(0,+x,+x') - \sigma(0,+x,-x')}{\sigma(0,+x,+x') + \sigma(0,+x,-x')}, \tag{1.48}$$

$$T_{z'} = \frac{\sigma(0,+x,+z') - \sigma(0,-x,+z')}{\sigma(0,+x,+z') + \sigma(0,-x,+z')} \quad , \quad T_{x'} = \frac{\sigma(0,+x,+z') - \sigma(0,+x,-z')}{\sigma(0,+x,+z') + \sigma(0,+x,-z')}, \tag{1.49}$$

Finally, notice that in xyz coordinates $\vec{P^{\gamma}} = \left(-P_L^{\gamma}\cos 2\Phi_{\gamma}^{L}, -P_L^{\gamma}\sin 2\Phi_{\gamma}^{L}, P_C^{\gamma}\right)$, we can express the general cross section (Eq. 1.22) in term of the polarization observables defined previously as:

$$\begin{aligned}
\frac{d\sigma}{d\Omega_{CM}}(\vec{P^{\gamma}}, \vec{P^{T}}, \vec{P^{R}}) =& \frac{1}{2}\frac{d\sigma_0}{d\Omega_{CM}} \times \\
& \left[\left(1 - P_L^{\gamma}P_y^T P_{y'}^R \cos 2\Phi_{\gamma}^{L}\right) + \Sigma\left(-P_L^{\gamma}\cos 2\Phi_{\gamma}^{L} + P_y^T P_{y'}^R\right)\right. \\
& + T\left(P_y^T - P_L^{\gamma}P_{y'}^R \cos 2\Phi_{\gamma}^{L}\right) + P\left(P_{y'}^R - P_L^{\gamma}P_y^T \cos 2\Phi_{\gamma}^{L}\right) \\
& + E\left(-P_C^{\gamma}P_z^T + P_L^{\gamma}P_x^T P_{y'}^R \sin 2\Phi_{\gamma}^{L}\right) + G\left(P_L^{\gamma}P_x^T \sin 2\Phi_{\gamma}^{L} + P_C^{\gamma}P_x^T P_{y'}^R\right) \\
& + F\left(P_C^{\gamma}P_x^T + P_L^{\gamma}P_z^T P_{y'}^R \sin 2\Phi_{\gamma}^{L}\right) + H\left(P_L^{\gamma}P_x^T \sin 2\Phi_{\gamma}^{L} - P_C^{\gamma}P_z^T P_{y'}^R\right) \\
& + C_{x'}\left(P_C^{\gamma}P_{x'}^R - P_L^{\gamma}P_y^T P_{z'}^R \sin 2\Phi_{\gamma}^{L}\right) + C_{z'}\left(P_C^{\gamma}P_{z'}^R + P_L^{\gamma}P_y^T P_{x'}^R \sin 2\Phi_{\gamma}^{L}\right) \\
& + O_{x'}\left(P_L^{\gamma}P_{x'}^R \sin 2\Phi_{\gamma}^{L} + P_C^{\gamma}P_y^T P_{z'}^R\right) + O_{z'}\left(P_L^{\gamma}P_{z'}^R \sin 2\Phi_{\gamma}^{L} - P_C^{\gamma}P_y^T P_{x'}^R\right) \\
& + L_{x'}\left(P_z^T P_{x'}^R + P_L^{\gamma}P_x^T P_{z'}^R \cos 2\Phi_{\gamma}^{L}\right) + L_{z'}\left(P_z^T P_{z'}^R - P_L^{\gamma}P_x^T P_{x'}^R \cos 2\Phi_{\gamma}^{L}\right) \\
& \left. + T_{x'}\left(P_x^T P_{x'}^R - P_L^{\gamma}P_z^T P_{z'}^R \cos 2\Phi_{\gamma}^{L}\right) + T_{z'}\left(P_x^T P_{z'}^R + P_L^{\gamma}P_z^T P_{x'}^R \cos 2\Phi_{\gamma}^{L}\right)\right] .
\end{aligned} \tag{1.50}$$

In particular, if *only* the beam and the target are circularly and longitudinally polarized, respectively, then the general cross section is reduced to:

$$\frac{d\sigma}{d\Omega_{CM}}(\vec{P^{\gamma}}, \vec{P^{T}}, 0) = \frac{1}{2}\frac{d\sigma_0}{d\Omega_{CM}}\left[1 - \left(P_C^{\gamma}P_z^T\right)E\right] . \tag{1.51}$$

1.3.2 Why is a polarized neutron target necessary?

In the last section, we established the formalism necessary in order to obtain the polarization observables to define a partial-wave analysis of pseudoscalar meson photoproduction. However, there is one important complication to be dealt with: since the photon field exhibits both isoscalar and isovector coupling (i.e., photon isospin $|I, I_3\rangle = |0,0\rangle, |1,0\rangle$), there are three independent isospin amplitudes. Any amplitude A can be decomposed into amplitudes for isoscalar and isovector transitions to an $I = \frac{1}{2}$ final state, $A^{(0)}_{I=1/2}$, $A^{(1)}_{I=1/2}$, and for an isovector transition to an $I = \frac{3}{2}$ final state, $A^{(1)}_{I=3/2}$ [26, 27]. For example, the amplitudes for single pseudoscalar meson photoproduction reactions can be decomposed as in [27]:

$$
\begin{aligned}
A_{\gamma p\to\pi^0 p,\, K^+\Sigma^0} &= -\frac{1}{\sqrt{3}}A^{(0)}_{I=1/2}+\frac{1}{3}A^{(1)}_{I=1/2}+\frac{2}{3}A^{(1)}_{I=3/2},\\
A_{\gamma n\to\pi^0 n,\, K^0\Sigma^0} &= +\frac{1}{\sqrt{3}}A^{(0)}_{I=1/2}+\frac{1}{3}A^{(1)}_{I=1/2}+\frac{2}{3}A^{(1)}_{I=3/2},
\end{aligned}
\tag{1.52}
$$

$$
\begin{aligned}
A_{\gamma p\to\pi^+ n,\, K^0\Sigma^+} &= +\frac{\sqrt{2}}{\sqrt{3}}A^{(0)}_{I=1/2}-\frac{\sqrt{2}}{3}A^{(1)}_{I=1/2}+\frac{\sqrt{2}}{3}A^{(1)}_{I=3/2},\\
A_{\gamma n\to\pi^- p,\, K^+\Sigma^-} &= -\frac{\sqrt{2}}{\sqrt{3}}A^{(0)}_{I=1/2}-\frac{\sqrt{2}}{3}A^{(1)}_{I=1/2}+\frac{\sqrt{2}}{3}A^{(1)}_{I=3/2},
\end{aligned}
\tag{1.53}
$$

$$
\begin{aligned}
A_{\gamma p\to\eta p,\, K^+\Lambda} &= +A^{(0)}_{I=1/2}-\frac{1}{\sqrt{3}}A^{(1)}_{I=1/2},\\
A_{\gamma n\to\eta n,\, K^0\Lambda} &= +A^{(0)}_{I=1/2}+\frac{1}{\sqrt{3}}A^{(1)}_{I=1/2}.
\end{aligned}
\tag{1.54}
$$

The coefficients are simply the Clebsch-Gordon coefficients; for example, for the reaction $\gamma p\to\pi^+ n$:

- The isospin expression for the initial state (γp): $[\alpha\,|0,0\rangle+\beta\,|1,0\rangle]_\gamma\left|\frac{1}{2},\frac{1}{2}\right\rangle_p=\alpha\left|\frac{1}{2},\frac{1}{2}\right\rangle_{initial}+\beta\left(-\frac{1}{\sqrt{3}}\left|\frac{1}{2},\frac{1}{2}\right\rangle_{initial}+\sqrt{\frac{2}{3}}\left|\frac{3}{2},\frac{1}{2}\right\rangle_{initial}\right)$,
- The isospin expression for the final state ($\pi^+ n$): $|1,1\rangle_\pi\left|\frac{1}{2},-\frac{1}{2}\right\rangle_n=\sqrt{\frac{2}{3}}\left|\frac{1}{2},\frac{1}{2}\right\rangle_{final}+\frac{1}{\sqrt{3}}\left|\frac{3}{2},\frac{1}{2}\right\rangle_{final}$,
- The total amplitude is:

$$
\begin{aligned}
&\left[\langle 1,1|_\pi\left\langle\frac{1}{2},-\frac{1}{2}\right|_n\right]\left(\hat{A}_{I=1/2}+\hat{A}_{I=3/2}\right)\left[[\alpha\,|0,0\rangle+\beta\,|1,0\rangle]_\gamma\left|\frac{1}{2},\frac{1}{2}\right\rangle_p\right]\\
=&\alpha\sqrt{\frac{2}{3}}_{final}\left\langle\frac{1}{2},\frac{1}{2}\right|\hat{A}_{I=1/2}\left|\frac{1}{2},\frac{1}{2}\right\rangle_{initial}+\beta\left(-\frac{1}{\sqrt{3}}\right)\sqrt{\frac{2}{3}}_{final}\left\langle\frac{1}{2},\frac{1}{2}\right|\hat{A}_{I=1/2}\left|\frac{1}{2},\frac{1}{2}\right\rangle_{initial}\\
&+\beta\left(\sqrt{\frac{2}{3}}\right)\frac{1}{\sqrt{3}}_{final}\left\langle\frac{3}{2},\frac{1}{2}\right|\hat{A}_{I=3/2}\left|\frac{3}{2},\frac{1}{2}\right\rangle_{initial}\\
=&\frac{\sqrt{2}}{\sqrt{3}}A^{(0)}_{I=1/2}-\frac{\sqrt{2}}{3}A^{(1)}_{I=1/2}+\frac{\sqrt{2}}{3}A^{(1)}_{I=3/2}.
\end{aligned}
$$

Notice that, for example, the reactions in Eq. 1.54 have the same corresponding coefficients for the two $I=1/2$ amplitudes but with different signs for the $A^{(1)}_{I=1/2}$;

the other equations also exhibit similar property. Consequently, the differences in the signs can help disentangle the two $I = 1/2$ amplitudes. This is a necessary requirement due to fact that the coupling strength to N^* states depends on these two amplitudes [27]. Therefore, to constrain theoretical models of the N^* resonances ($I = 1/2$) it is essential to have both proton and neutron data. Fortunately, with g14 experiment we have a low-background bound longitudinally polarized neutron target to extract polarization observables from the neutron which will promise significant breakthroughs in answering the missing baryon problem in the near future.

1.3.3 Theoretical Models

As mentioned previously, QCD can not be solved analytically to provide the complete internal structure of the nucleon. The current approach for deciphering the question of what is happening inside the nucleon is to theorize QCD-"inspired" effective models. These models use effective hardonic degrees of freedom instead of the fundamental quark and gluon degrees of freedom. In this section, we will briefly introduce such theoretical models. We do this since the results presented in this thesis will be compared to predictions made by these models.

1.3.3.1 Isobar-Based MAID and KaonMAID Models [1]

The isobar-based models generally employ an *effective* interaction Lagrangian with built-in symmetry properties, conservation laws, and restriction on complicated transition dynamics (i.e., no higher-order loops). In particular, the models restrict the dynamics to tree-level amplitudes, consisting of *only* two interaction vertices and one propagator—and to account for the finite size of the nucleons, form factors are included. For example, Figure 1.4 shows the Feynman diagrams for kaon photoproduction (i.e., KaonMAID model) on the nucleon in the s-channel (exchanging non-strange baryons), u-channel (exchanging hyperons), and the t-channel (exchanging the strange meson), respectively. s, u, and t are the invariant Mandelstam variables.

The kinematics of photoproduction allows intermediate states N, N^*, Δ, and Δ^* in the s-channel to be on the mass shell (i.e., resonance channel) while the u-channel, and t-channel propagators are off mass shell (i.e., background channels). Importantly, most of the coupling constants are not fixed by fundamental relations but must be determined from fitting to existing data (KaonMAID was not fitted to experimental data, however). Another limitation of the KaonMAID and MAID models are that, because of its dynamical restriction, requirements from unitary and gauge invariance arise as complications to consider [32]—for example, the inclusion of right most "contact" diagram in Figure 1.4.

[1] MAID is a theoretical calculative model that is maintained by the Institut für Kernphysik at the University of Mainz, Germany [28].

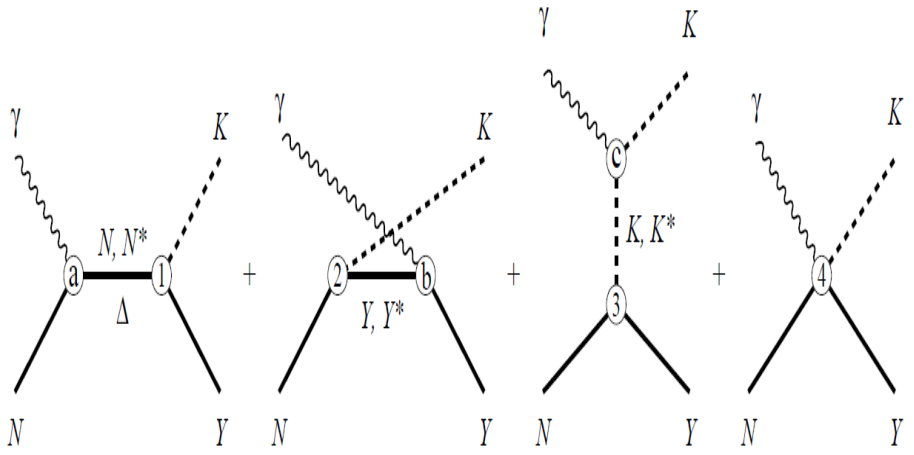

Figure 1.4: Feynman diagrams for kaon photoproduction on the nucleon. Electromagnetic vertices are denoted by (a), (b), and (c), hadronic vertices (with hadronic form factors) by (1), (2), and (3). The first diagram is the resonance s-channel, the middle two diagrams are the background u-channel, and t-channel, respectively. The last diagram (4) is required in order to restore gauge invariance after introducing hadronic form factors. Image was taken from [31]

Despite their shortcomings, the KaonMAID and MAID models successfully describe the forward peaking and simultaneous decrease of the meson photoproduction cross section above 2 GeV. They also provide predictions for all polarization observables. Moreover, the MAID model has been extended to reactions on light nuclei [31, 33] which helps to establish the sensitivity of polarization observables to relativistic and/or final-state interaction effects.

1.3.3.2 PWA-Based SAID[2] and Bonn-Gatchina[3] (BoGa) Models

An alternative to the isobar models is to employ the partial-wave analysis method to extract resonance couplings and decay widths. For resonances with strong couplings to several decay channels, the K-matrix formalism is used. The use of partial waves is, in general, more accurate but it is also more difficult because many partial waves—particularly, the presence of non-resonant backgrounds result in a large number of strongly contributing partial waves—can contribute in certain kinematic regions and interfere strongly. Nevertheless, as more world data on polarization observables is forthcoming, the situation will improve.

[2]SAID is a theoretical calculative model that is maintained by the Institute for Nuclear Studies at the George Washington University, USA [29].

[3]BoGa is a theoretical calculative model that is maintained by Helmholtz-Institut fur Strahlen und Kernphysik at the University of Bonn, Germany, and the Petersburg Nuclear Physics Institute in Gatchina, Russia [30].

In addition, there are several differences in the PWA approaches between the SAID and BoGa models. BoGa is a coupled-channel model where many decay channels are considered in a single framework. Resonances are introduced as Breit-Wigner functions and added in as needed to fit (or explain) new experimental data. On the other hand, the SAID model considers and fits only one decay channel at a time. In particular, for each decay channel data are first fitted to a model, which includes resonant and non-resonant production, to get single-energy solution; then the solutions from the decay channels are combined using K-matrix formalism to extract background and resonance paramters. Moreover, the number of resonances in the SAID model remains fixed (i.e., it assumes that there are no new resonances beside all the observed resonances in pion production data). This choice of phenomenology forces the SAID model to include an additive energy-dependent term to help fit new experimental data.

1.3.3.3 Model Comparision

Both types of theoretical models mentioned above require experimental data as model inputs. For example, the isobar models (e.g. MAID) acquire the coupling constants from fitting existing experimental data using constraints from fundemental symmetries. Since the neutron data are very spare, the predictions of neutron amplitudes have large uncertainties. In other words, there are significant differences from the theoretical models' predictions. Illustratively, Figure 1.5 shows clear disagreements in predictions from the SAID and MAID groups for Σ (the linearly-polarized beam asymmetry), E, and G (the beam-target double-polarization asymmetries for circularly and linearly polarized beam, respectively) for reaction $\gamma n \to \pi^- p$. Similarly, Figure 1.6 shows the differences between predictions from KaonMAID and SAID for the E asymmetry of reactions $\gamma n \to K^0 \Lambda$ and $\gamma n \to K^0 \Sigma^0$.

In addition, it is also necessary to compare predictions for neutron and proton targets from same reaction for completeness; unfortunately, because of the lack of neutron data, SAID and KaonMAID predictions also disagree significantly. In particular, while SAID predicts *insignificant* difference between neutron and proton data for the E asymmetry of reactions $\gamma n \to K^0 \Lambda$, KaonMAID predicts the difference to be very *large* (see Figure 1.7 for the KaonMAID predictions on proton and neutron target types).

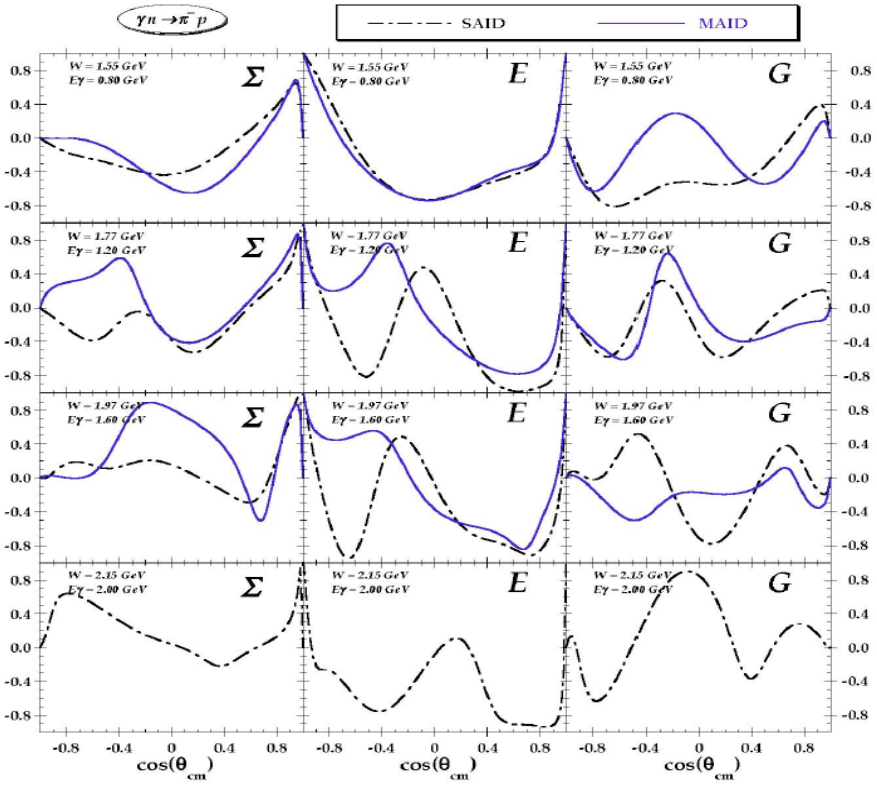

Figure 1.5: Polarization observables Σ(left), E (center), and G (right) for the $\gamma n \to \pi^- p$ reaction as predicted by the SAID and MAID groups. Image was taken from [27].

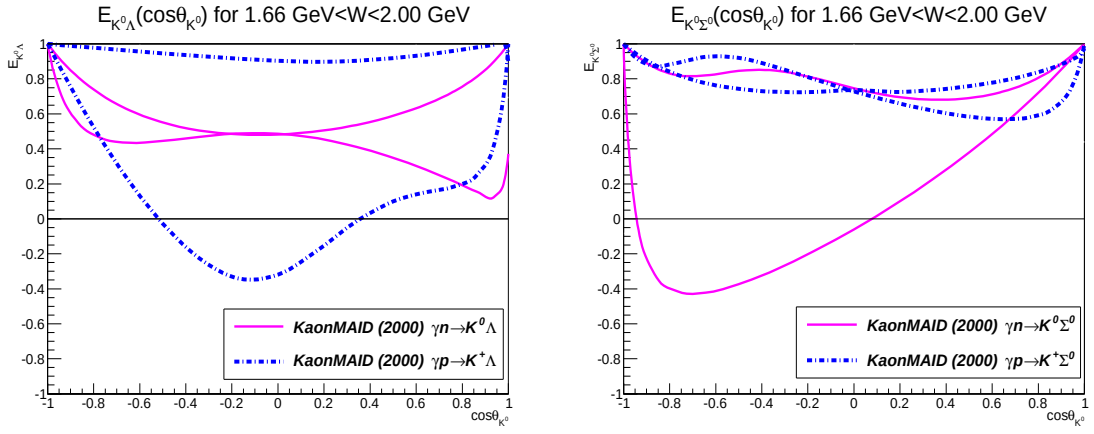

Figure 1.7: KaonMAID predictions for polarization observable E for reactions $\gamma \begin{pmatrix} n \\ p \end{pmatrix} \to \begin{pmatrix} K^0 \\ K^+ \end{pmatrix} \Lambda$ (left) and $\gamma \begin{pmatrix} n \\ p \end{pmatrix} \to \begin{pmatrix} K^0 \\ K^+ \end{pmatrix} \Sigma^0$ (right). Each model has two curves indicating the two limits of the energy range W. On the other hand, *the SAID predictions (not shown here) for proton and neutron data are almost identical.*

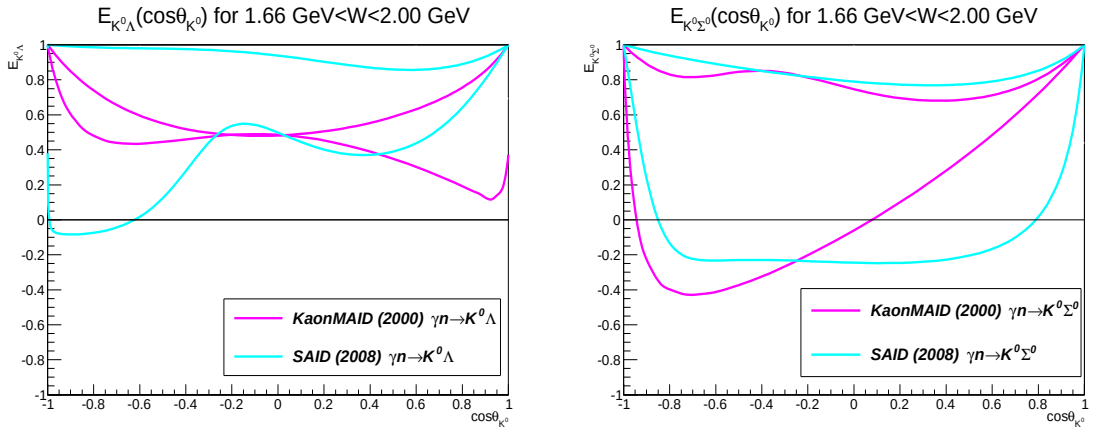

Figure 1.6: Predictions from KaonMAID and SAID models for polarization observable E for reactions $\gamma n \to K^0\Lambda$ (left) and $\gamma n \to K^0\Sigma^0$ (right). Each model has two curves indicating the two limits of the energy range W. Significant differences between the models are due to the lack of neutron data to constrain the models.

1.4 Summary and Structure of this Thesis

In this introductory chapter, we briefly introduced baryon spectroscopy as a viable approach to study the internal structure of the nucleon, and mentioned the difficulty of obtaining a complete excited spectrum of the nucleon directly. Alternatively, the task can only be accomplished through partial-wave analysis. Polarization observables provide constraints for partial wave analysis, hence, they are important and of great interest to the nuclear physics community. The g14 experimental arrangement using a longitudinally polarized bound neutron target allows for extracting many polarization observables for the neutron—many observables will be measured *for the first time*. In particular, this thesis focuses on obtaining, *for the first time,* the E asymmetry—i.e., the beam-target double-polarization asymmetries—for three reactions $\gamma d \to \pi^- p(p_S)$ (Chapter 4), $\gamma d \to K^0\Lambda(p_S)$, and $\gamma d \to K^0\Sigma^0(p_S)$ (Chapter 5). Note that p_S in the three reaction stands for *spectator proton*. Finally, we investigate the spin structure of a *possible* $N\Delta$ dibaryonic structure in reaction $\gamma d \to d\pi^+\pi^-$ (Chapter 6).

Chapter 2

Jefferson Lab, CEBAF, CLAS detector and HDIce Target

The data used in our analyses was taken as part of the g14 run period—of experiment E06-101, *N^* Resonances in Pseudoscalar-meson Photoproduction from Polarized Neutron in $\overrightarrow{H} \cdot \overrightarrow{D}$ and a Complete Determination of the $\gamma n \to K^0 \Lambda$ Amplitude*—between November 2011 to May 2012 at the Thomas Jefferson National Accelerator Facility (TJNAF), or JLab, in Newport News, Virginia. JLab consists of four experimental halls, denoted as A, B, C, and D (newly built), along with the CEBAF electron accelerator, a free-electron laser, and other research and manufacturing facilities. Figure 2.1 shows an aerial view of the lab. The experiment was conducted in Hall B with a goal of measuring polarization observables in reactions on bound polarized neutrons. The run conditions comprised of circularly and linearly polarized photon beam incident on a polarized solid HD target. Producing a photon beam required use of both CEBAF accelerator and the Hall-B photon tagging system toghether with a thin gold foil (a diamond) radiator for producing circularly (linearly) polarized photon beam located. The HD targets were kept polarized in a specifically designed in-beam cryostat.

The CEBAF Large Acceptance Spectrometer, or CLAS, which is housed in Hall B was the detector used in g14 experiment. CLAS, with its almost-4π coverage, is optimal for the detection of multi-particle final states. During its lifetime (from 1998 to May 2012) together with the continuous CEBAF electron beam and the high quality of the Hall B data acquisition system (capable of recording over 1 TB of data each day), CLAS produced many large high statistics multi-particle datasets. In this chapter, we will briefly introduce the CEBAF accelerator, the CLAS detector, and several other hardware devices, in addition to the HDIce targets which played key roles during g14 data taking. Detailed discussions of these devices will also be provided as references.

Figure 2.1: An aerial view of the Thomas Jefferson National Accelerator Facility (TJNAF), also referred to as JLab. Image was taken from [34].

2.1 CEBAF

All the experimental halls (A, B, C, and D) receive electron beams from the Continuous Electron Beam Accelerator Facility (CEBAF). CEBAF was one of the first accelerator facilities to employ superconducting radio frequency (RF) cavities to provide the acceleration gradient. Superconducting cavities are non-resistive, in contrast to traditional copper RF cavities which are resistive—resistivity of copper causes the tradition RF cavities to heat up during use and, therefore, the cavities require time to cool down. Without the need of time to cool down, the RF superconducting cavities can obtain a 100% duty factor. The continuous delivery of electrons permits quick acquisition of high statistics datasets even at low current. In Figure 2.2 we show a schematic diagram of all the major components of CEBAF.

The electron beam starts at the injector site. Electrons are produced by illuminating a strained GaAs/GaP photocathode with pulsed polarized laser light resulting in polarized electrons being produced in bunches approximately every 0.667 ns (but Hall B receives electrons in bunches every 2 ns). The electrons are then sent to CEBAF's recirculating linear accelerators (Linacs), see Figure 2.2. Each of the Linac consists of 84 superconducting Niobium RF cavities. For illustration, we show in Figure 2.3 a picture of two RF cavities assembled together. To achieve superconductivity, the cavities are immersed in liquid Helium to cool down to -271°C (or 2.15 K). The acceleration gradient to accelerate the electrons is provided by setting up radio frequency standing waves in the cavities in a fashion such that the waves are in phase with the electron bunches producing a continuous push on the electrons (see Figure 2.4)—i.e.,

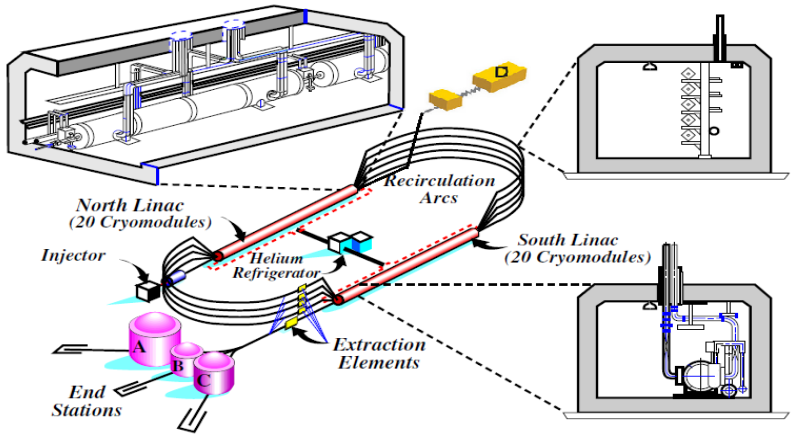

Figure 2.2: Schematic diagram of the Continuous Electron Beam Accelerator Facility (CEBAF). Image was taken from [34].

positive electric force—along the *straight sections* of the 7/8 mile *racetrack* course. During the g14 run, or before CLAS 12 upgrade, each Linac was capable of providing 600 MeV of acceleration; the upgraded Linacs will have twice the old capacity. The north and south Linacs are connected together via nine recirculation arcs, allowing the beam to make up to five passes through each Linac and, hence, obtaining up to a maximum energy of ∼6 GeV (after the upgrade the maximum energy will be ∼12 GeV). However, each hall can choose to extract the beam after any number of passes (but not exceeding the maximum number of five for Halls A, B, C, and a maximum of six passes for Hall D), giving the halls the control over their desired energies. Finally, beam extraction into the halls is performed using RF separating cavities (or usually called "RF seperators").

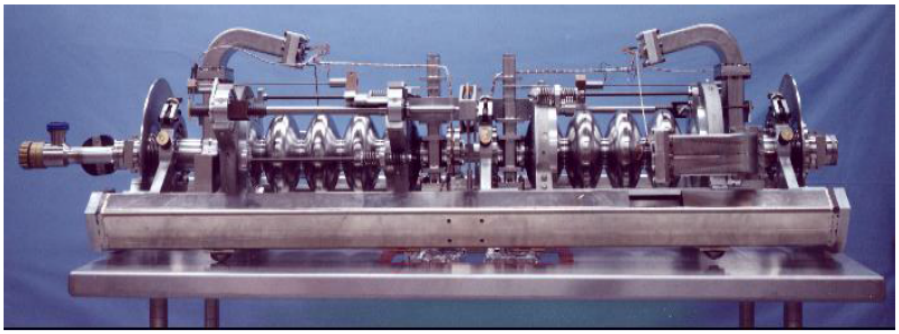

Figure 2.3: A pair of CEBAF's superconducting Niobium RF cavities, shown here with supported hardware and beam pipe. Image was taken from [34].

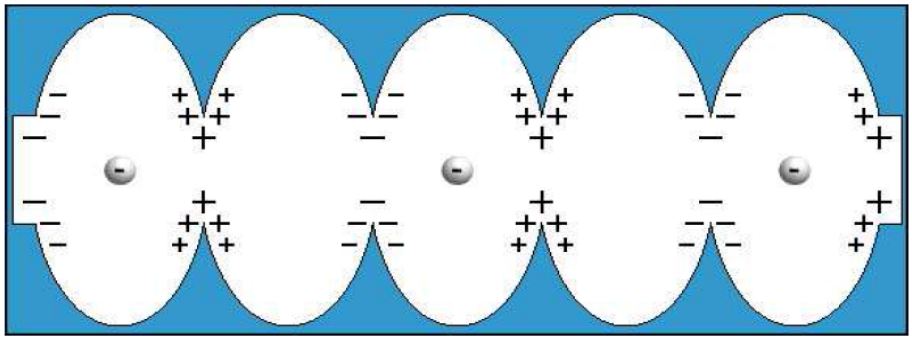

Figure 2.4: The *tuned* standing waves provide acceleration gradient to *continuously* push (via positive electric force) the propaging electrons. Image was taken from [35].

2.2 The Photon Tagger

For experiments that require photon beams, such as g14, converting the CEBAF electron beam into a photon beam is done by the photon tagging system of Hall B via a process called *bremsstrahlung* (or "braking" radiation in the German language). In particular, an electron is decelerated when it interacts with an atomic nucleus in a radiator and emits a photon. The timing and energy of the recoiling electrons are measured by a magnetic spectrometer from which the timing and energy of the photons are inferred. The other component of the tagger system is a series of collimators to remove wide-angle low-energy photons. A schematic diagram of the Hall B tagging system is shown in Figure 2.5.

2.2.1 Radiators

The g14 experiment ran with gold and diamond radiators. A gold radiator (of thickness 10^{-4} radiation lengths) was used to produce circularly polarized photons. Gold was used because it has a high atomic number, which reduces the background from electron-electron scattering in production of photons via bremsstrahlung radiation. The photons get their circular polarization by helicity transfer from the longitudinally polarized electrons. A diamond radiator (of thickness 50 microns) was used during the linearly polarized run period. In order to produce linearly polarized photons, the orientation of the diamond was chosen such that the diamond lattice was aligned relative to the electron beam direction so that the bremsstrahlung energy spectrum exhibits a desired coherent peak structure—ie., a sharp, highly linearly polarized peak at an energy that corresponds to the crystal lattice orientation. This was accomplished by mounting the diamond radiator in a goniometer, a device which can move the diamond in the horizontal and vertical direction and rotate it around all three axes with high precision.

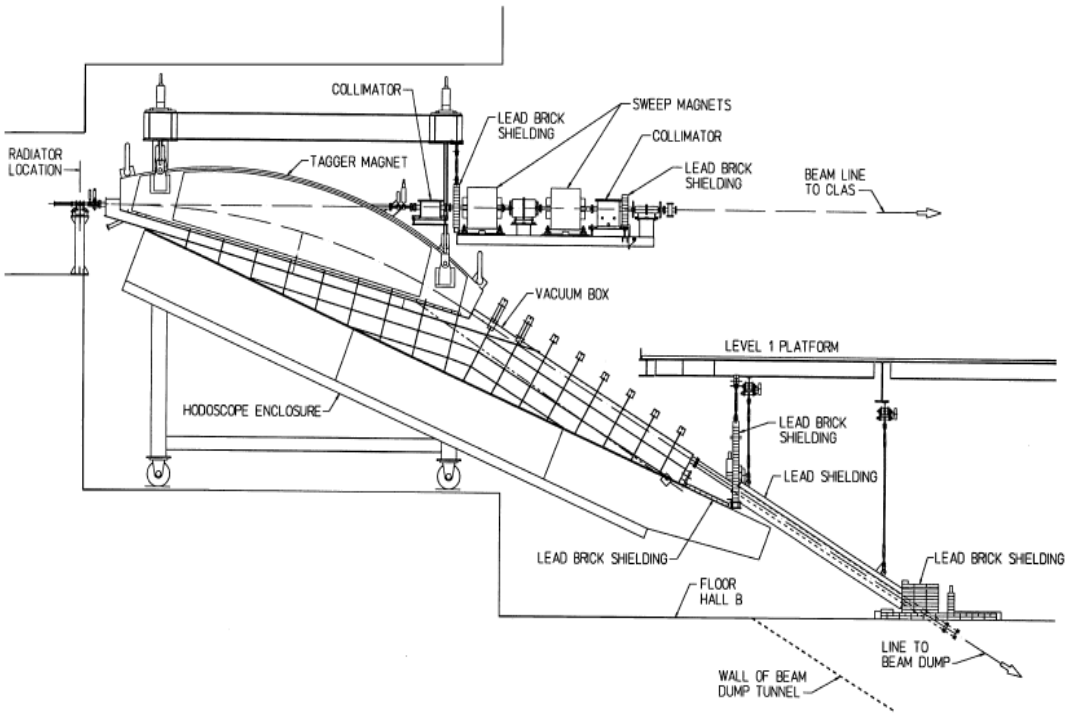

Figure 2.5: Schematic of Hall B photon tagging system. The system comprises of the radiator, magnetic spectrometer and collimators. Image was taken from [36].

2.2.2 Collimators

In order to reduce the photon beam halo, a 9.8 mm collimator was placed downstream of the tagger magnet. For the circularly polarized run period, an additional collimator (with size of 2.6 mm) was employed; in between the collimators there were sweeping magnets to remove charged particles created by photons interacting with the first collimator's material. The 2.6 mm collimator was constructed out of stacked nickel discs with a small hole in the centers. It was stacked inside a cylindrical sheath of stainless steel with four scintillators in between to measure the rate of off-centered photons hitting the front face of the collimator.

2.2.3 Magnetic Spectrometer

A mixture of non-interacting electrons, recoiling electrons and photons, resulted from the incident electron beam passing through the radiator, proceeded through the tagger magnet. The dipole magnetic field then separated the electron out of the beam while allowing the photons to continue toward the CLAS target. Since the bremsstrahlung energy spectrum is continuous, a single photon's energy is not known a prior. Since the energy transferred to the heavy nucleus (during bremsstrahlung) is negligible, the photon energy could be determined by measuring E_0 the electron beam energy, and

E_r the energy of recoiling electron, as $E_\gamma = E_0 - E_r$. Determining the energy of the recoiling electrons was accomplished by the magnetic spectrometer of the tagging system.

The tagger magnetic field bent the recoiling electrons toward two hodoscope planes, each made of overlapping arrays of scintillators and referred to as the E-plane and the T-plane. The magnetic field was tuned so that the non-interacting electrons were directed into a shielded beam-dump. The E-plane consists of 384 scintillator paddles, or E-counters, that are 20 cm long and 4 mm thick and 6-8 mm in width, arranged in an overlapping fashion to give an effective 767 logical paddles. Its main function is to measure the position of the recoiling electrons, and due to the precisely mapped field, their momenta (and, hence, their energies) are known with a designed resolution of about $10^{-3}E_0$. The second scintillator plane, or the T-plane, is used to make accurate timing measurements of the recoiling electrons. The T-plane comprises of 61 scintillator paddles (T-counters) with a thickness of 2 cm and varying widths from 9 to 20 cm, so that each paddle has a comparable counting-rate because of the $1/E_\gamma$ dependence of the bremsstrahlung cross section. The design is to achieve a timing resolution of better than 300 ps—to correctly associate a tagged electron with the corresponding 2 ns beam bucket provided by the accelerator. Figure 2.6 shows a schematic diagram of the tagger spectrometer.

In Figure 2.7 we show a schematic diagram of original setup of the front-end electronics of the tagging system. Specifically, the signals from the scintillator paddles are read out using photomultiplier tubes (PMTs). The T-counter PMT signals are passed through fast (200 MHz, Philips 715) discriminators before being "fed" to the "Master OR" (MOR) and an array of FASTBUS TDCs. The TDC array is employed to extract the timing information from all 61 T-counters and also to count the total number of hits registered in the tagger for use during normalization calculations. Since multiple photons per event may be written to tape during readout, this timing information is useful in correctly associating photons with events in the CLAS detector. Moreover, the signals from the E-counter PMTs are also sent through a discriminator and then to a multi-hit TDC. The timing signals from both the E- and T-counters are then written into the data stream for offline analysis. Recalling that the tagger's resolution is high enough to correctly identify which RF beam bucket each photon is associated with; as a result, the *event vertex time*, the time at which all the final-state particles produced in the interaction were at the same point in space, can be most accurately calculated by determining the RF time from the radiator to the event interaction vertex. Reference [36] provides more information about the tagger system.

2.3 The CLAS Detector

The CEBAF Large Acceptance Spectrometer (CLAS) is located in Hall B, and is used to detect particles produced by interactions of the photon (or electron) beam with the

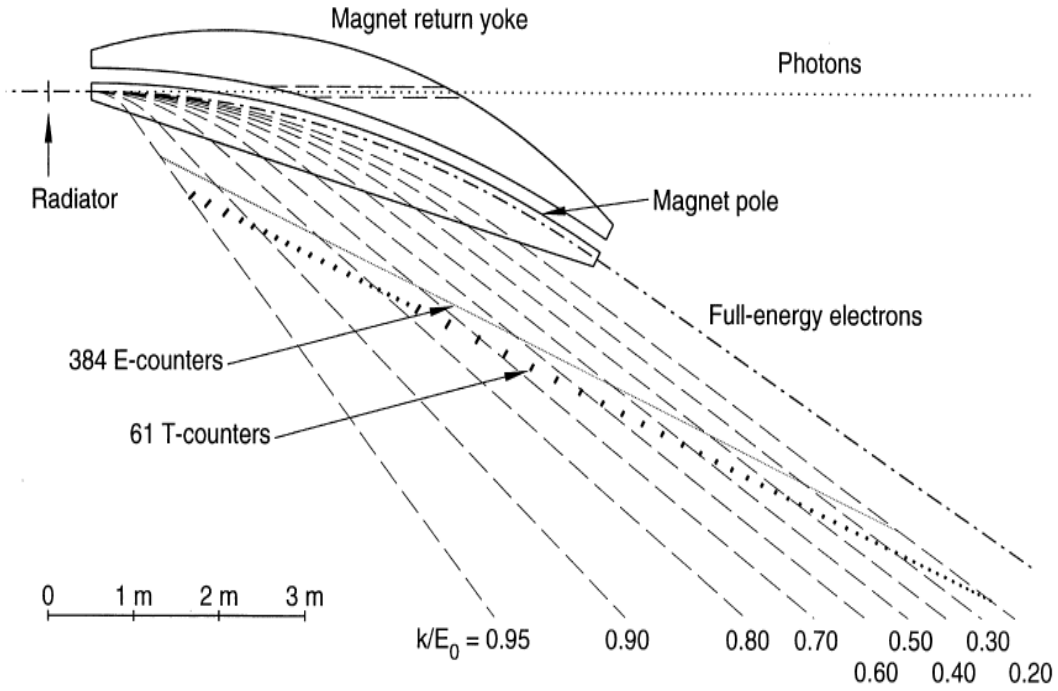

Figure 2.6: Schematic diagram of the tagger spectrometer. The dashed lines show the trajectories of the recoiling electrons corresponding to various fractional energies transferred to the outgoing photon. The E- and T-planes are shown in relation to the trajectories of electrons of various fractional momeda in units of beam energy E_0. Image was taken from [36].

target located near the center of the CLAS detector. A photograph and schematic drawing of CLAS are shown in Figure 2.8 and 2.9, respectively. CLAS comprises several subsystems like the start counter, drift chambers, time-of-flight scintillators, Cerenkov counters, and electromagnetic calorimeters (more detailed discussion about the CLAS detector system can be found in [37]). Our analyses did not use the last two detector elements, thus they will not be discussed here. The start counter was used in the g14 trigger. The drift chambers were used to track charged particles, which were bent by a superconducting toroidal magnet, as they traveled through the detector. By reconstructing a particle's flight path, the particle's momentum is determined. The time-of-flight scintillator walls, which measure the flight time of particles from the target, are used for particle identification purposes—by combining with the momentum measurements from the drift chambers. In this section we will discuss the detector subsystems, which played vital roles in our analyses.

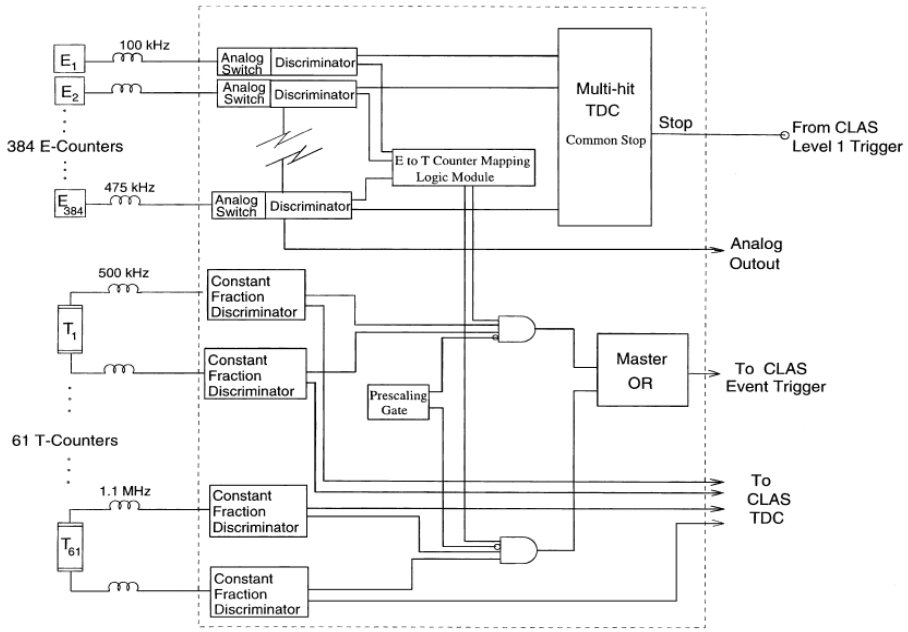

Figure 2.7: Schematic diagram of the readout electronics of the tagger system in Hall B. Image was taken from [36].

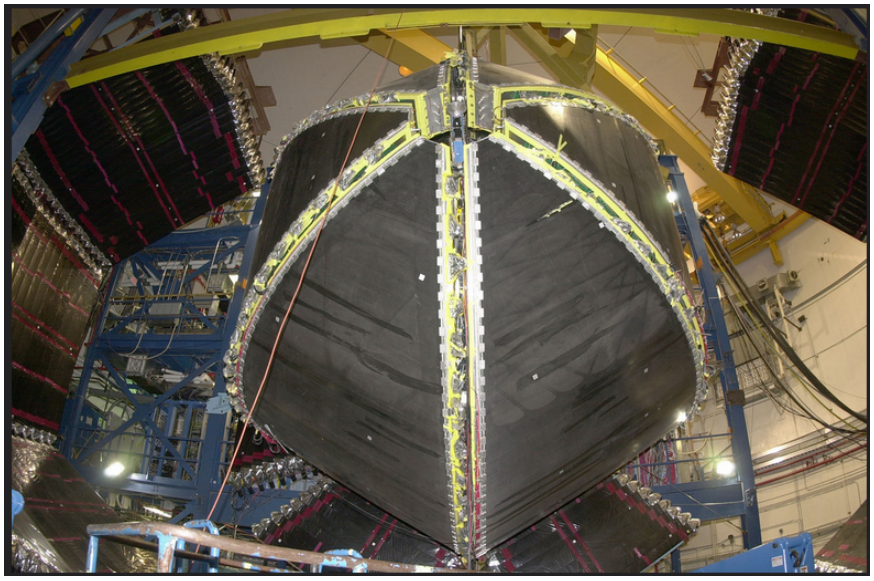

Figure 2.8: Photograph of the CLAS detector taken during a maintenance period for which the time-of-flight scintillator walls, forward region Cerenkov counters and electromagnetic calorimeters were pulled away from the interior detector elements. Image was taken from [34].

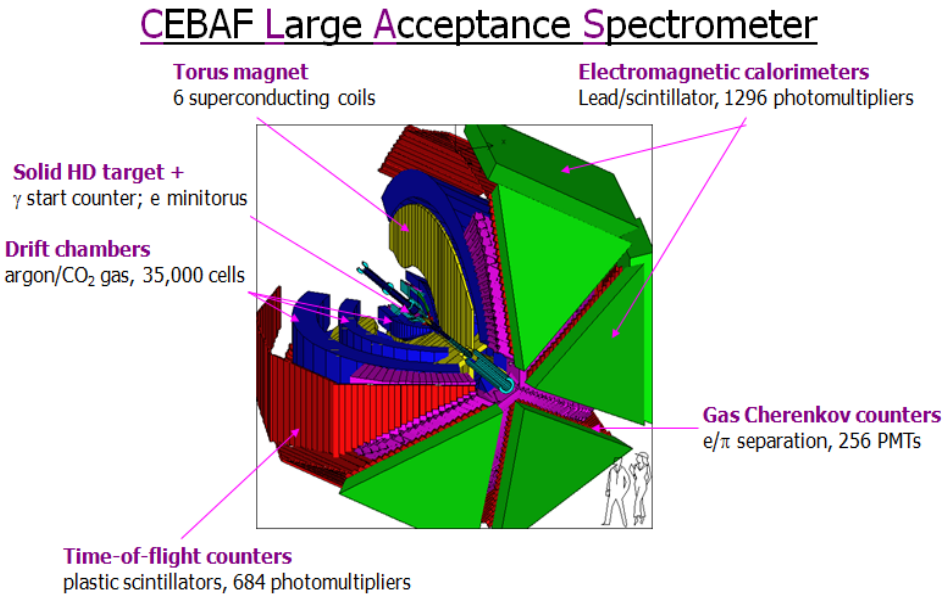

Figure 2.9: Schematic of the CLAS detector showing all of the major subsystems. The detector, which is approximately 8 m in diameter, was housed in experimental Hall B at Jefferson Lab. Image was taken from [38].

2.3.1 Start Counter

The start counter is a system of thin counters surrounding the target region to provide information to determine the correct RF beam bucket associated with a particle track. Its timing resolution is ∼400 ps. Like the CLAS detector itself, the start counter is divided into six sectors each with four scintillator paddles (see Figure 2.10). To accommodate the g14 experiment, the length of the light guides of the start counter was increased to keep the PMTs further away from the strong magnetic field from the in-beam crystat that holds the g14 targets. Though we did not incorporate the timing information obtained from the start counter in our analyses, it was included in the Level 1 trigger during g14. More information on this detector element, including details on its construction, can be found in [39].

2.3.2 Time-of-Flight Scintillators

The time-of-flight (TOF) counters enclose the CLAS detector covering the polar angular range between 8° and 142° and the entire active range in azimuthal angle Φ. It consists of six segmented scintillator walls, one for each sector, located approximately four meters from the target. The scintillator wall in each sector has four panels and a total of 57 TOF-counters of varying lengths and widths (see Figure 2.11). Each TOF-counter has a thickness of 2 inches to provide 100% detection efficiency of minimum

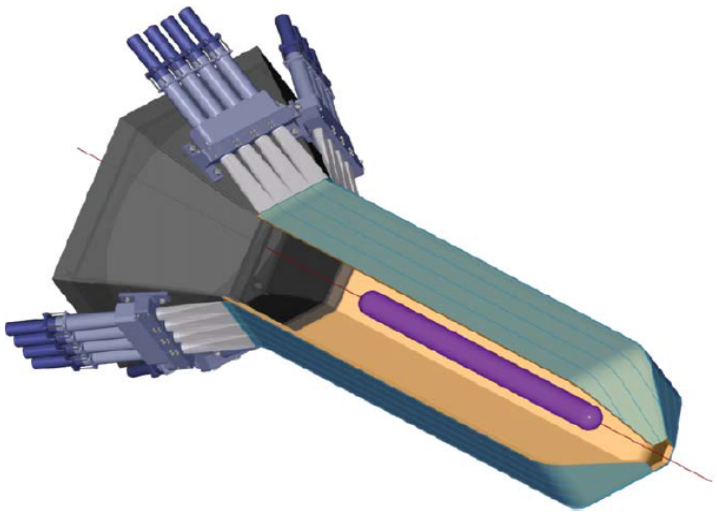

Figure 2.10: Schematic diagram of the CLAS start counter. Image was taken from [39].

ionizing particles. At each end of a TOF counter a photo-multiplier tube (PMT) was mounted to collect signals from the scintillator. The timing resolution which depends on the length of the counter—longer counters have worse resolution—is between 110 and 200 ps. The time-of-flight scintillator walls were used, with the start counters, in the Level 1 trigger and also in our analyses for performing particle identification (more detail in later analysis chapters). More details about of the TOF system, construction and performance, is given in [40].

2.3.3 Superconducting Toroidal Magnet

The magnetic field, that is necessary for bending charged particles—together with the tracking system—to determine with accuracy the particles' momenta, is generated by a six *superconducting* coils arranged in a toroidal geometry around the beam-line. Figure 2.12 shows the bare cryostats of the torus during construction of the CLAS detector and Figure 2.13 illustrates the magnetic field strength and direction of the magnet. The kidney-shaped superconducting coils were designed and tested by Oxford Instrument Ltd. The coils are separated by 60° in the azimuthal direction about the beam-line. For the first ten days, g14 ran under the *normal field* configuration in which negatively charged particles are bent toward the beam-line and positively charged particles away from the beam-line. For the remainder of the experiment, the field was reversed. The change was to increase the acceptance for forward-going negative tracks (i.e., bending into the fiducial region of the detector, not towards the beam dump). The magnet can support a peak current of 3861 A—resulting a

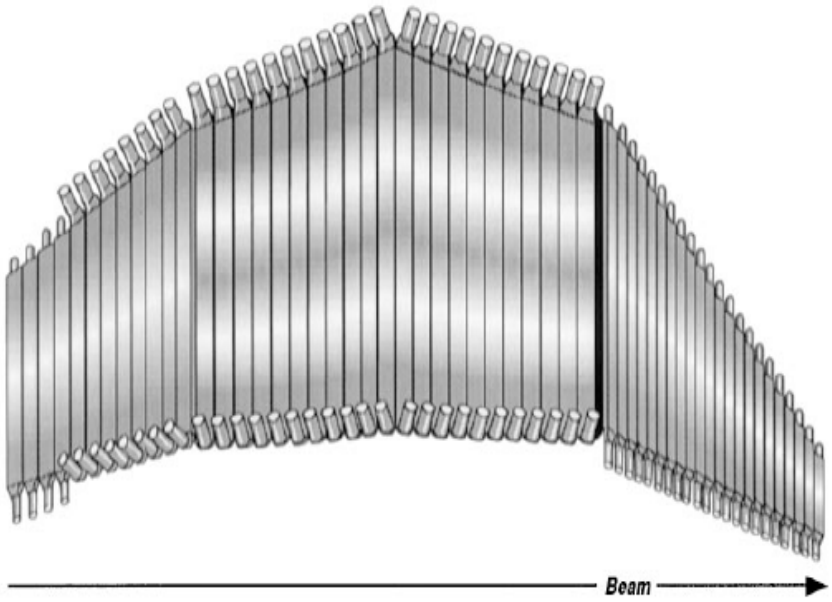

Figure 2.11: TOF counters in one sector of CLAS. There are 57 paddles grouped into four panels. Image was taken from [39].

peak integral magnetic field of 2.5 T·m, but the current for g14 was limited to +1920 (for the first 10 days) and then to −1500 A. Note that running at higher positive (negative) currents provides better momentum resolution but further decreases the acceptance for negatively (positively) charged particles. During operation, the magnet was cooled down to 4.4 K using liquid helium obtained from the central helium liquifier [41].

2.3.4 Drift Chambers

Previously, we mentioned that the momenta of charged particles are measured by tracking the particles as they travel through the magnetic field generated by the toroidal magnet. Illustratively, Figure 2.14 shows a cut-away diagram of the CLAS detector in which the three drift chamber regions are visible on the diagram. The charged particles were tracked using three separated drift chambers. Region 1 is located "inside" the torus coils, thus it experiences a very weak magnetic field. Region 2 is mounted directly to the magnet's cryostat occupying the space where the field is the strongest. Region 3 is positioned outside the torus coils, hence this region also possesses a weak magnetic field.

To optimize the track-reconstruction process, each of the drift chamber regions is further divided into two *superlayers*, one with axially oriented wires (relative to the magnetic field direction) and one with wires oriented at a 6^o stereo angle (for az-

Figure 2.12: Photograph of the CLAS toroidal magnet. Image was taken from [34].

imuthal information). Furthermore, each superlayer comprises of six layers of hexagonal drift cells arranged such that neighboring layers were offset by half a cell width. Each cell has a 20 μm gold-plated tungsten sense wire located at its center surrounded by six 140 μm gold-plated aluminum alloy field wires. The sense (field) wire(s) are kept at a positive (negative) potential. Signals from the sense wires are passed to preamplifier, then to amplifier discriminator boards (ADBs) and finally to TDCs to obtain the timing information. The drift gas mixture was chosen to be a non-flammable mix of 90% Argon and 10% CO_2. More information pertaining to the CLAS drift chambers is given in [42, 43, 44, 45].

2.4 Beamline Devices

Several beamline devices were employed during g14. Devices including beam position monitors (BPMs), harp scanners, and a Møller Polarimeter were placed upstream from the CLAS detector to monitor the quality of the beam. In particular, the BPMs monitored and controlled the beam position during data taking; harp scanners measured the profile of the beam; the Møller Polarimeter measured the electron beam polarization (later chapters include a formula to compute the photon beam polarization from the electron beam polarization). In addition, downstream devices, such as the total absorption shower counter (TASC), and pair counters (PC), were used to measure the photon flux—important for total cross section analysis but not for this analysis so they will not be discussed here.

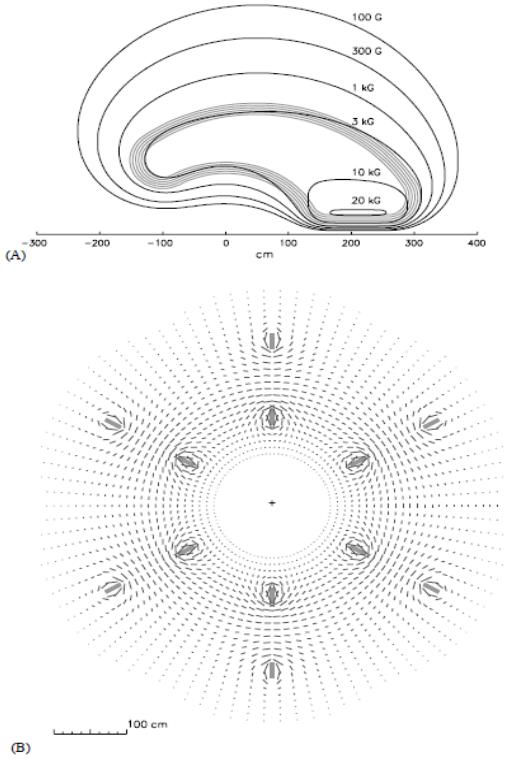

Figure 2.13: The magnetic field strength and direction of the CLAS toroidal magnet. Top: Contours of constant magnetic field strength. The magnetic field is strongest in the forward region. Bottom: Magnetic field vectors in a plane transverse to the beam direction, centered at the g14 target. The length of each line segment is proportional to the field strength at that point. Image was taken from [41].

2.5 Trigger and Data Acquisition

To prevent unwanted signals from irrelevant sources—for example, cosmic radiation passing through a detector element—to be recorded as physics events, it is necessary to have a *trigger* to determine which sets of signals constitutes a physics event. Once the decision is made, the data acquisition system (DAQ) collects the signals and writes them to magnetic tape for future offline analysis. In more detail, the trigger settings implemented in g14 were both Level 1 and 2 trigger. For Level 1 trigger, it first requires, for an individual sector, signals from any of the 4 start counter paddles and any of the 57 TOF within a coincidence window of 150 ns, and also that, at least two CLAS sectors satisfy the first condition. With a 20 nA electron beam, the total Level 1 trigger rate for the g14 run was about 2.4 kHz. Level 2 trigger requires signals from at least four segments in drift chamber superlayers within a sector and signals from any of the 4 start counter paddles and any of the 57 TOF within a coincidence

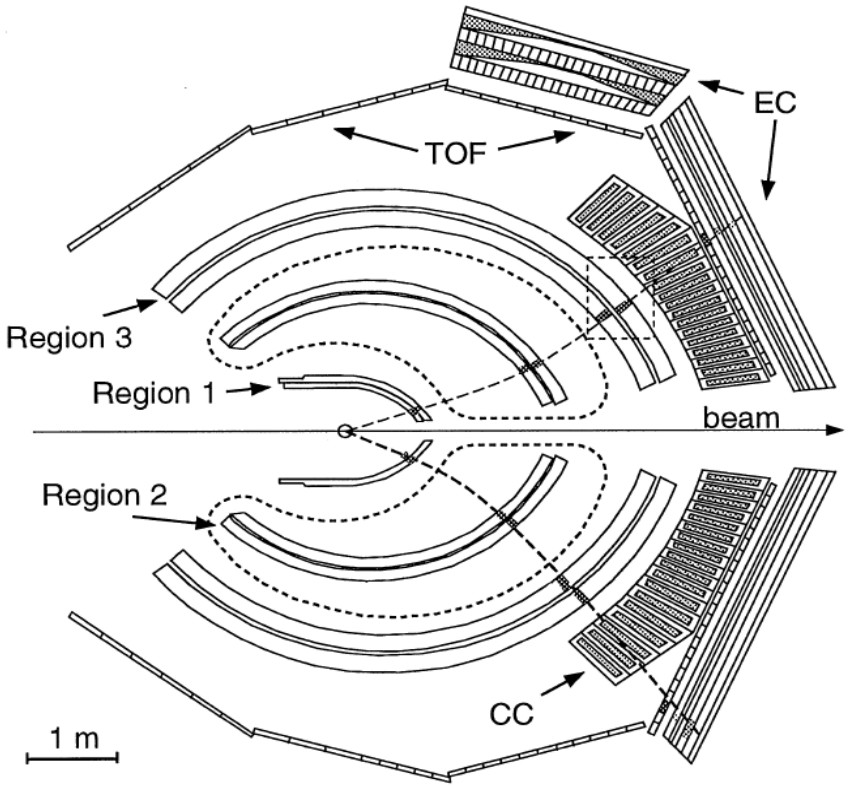

Figure 2.14: Schematic diagram of CLAS showing the relative position of the detector subsystems. The kidney shaped dashed lines outline the location of the toroidal magnetic coils. Image was taken from [42].

window of 150 ns in any two sectors.

2.6 g14 HD-Ice target

The Hydrogen and Deuterium ICE (or HDIce) target used in this experiment is a solid hydrogen-deuterium target. By design, it is able to achieve high polarization (about 25-30%) for both *free* protons and deuterons (i.e., *bound* neutrons) with a long relaxation time, i.e., spins are frozen, hence the word ICE. The lowest magnetic field to sustain the target polarization is about 1 Tesla. It is worth to mentioning that there are other types of polarized bound neutron targets. However, these types of polarized targets have several disadvantages that the HDIce target does not have. In particular, pure deuterium targets can not be polarized at magnetic fields and temperatures that are practical for doing nuclear physics experiments, ammonia and butanol targets contain other unpolarized nucleons in other atoms (e.g., carbon and oxygen for butanol, or nitrogen for ammonia) while HDIce target has no contamination. In

this section, we provide a brief overview of the physics of the HDIce target that was used in the G14 experiment as well as the process used to prepare the targets.

2.6.1 HDIce Target Physics

H_2 and D_2 molecules can be polarized at high magnetic field and low temperature but with short relaxation times. More accurately, polarization and depolarization depends mainly on the spin-lattice coupling through molecular rotations. In other words, molecules in an angular momentum state $L = 0$ are very difficult to polarize (because the s-wavefunction has no referred direction) and hence have long relaxation time, while molecules in an angular momentum state $L = 1$ are easy to polarize (because the p-wavefunction has a referred direction) and have short relaxation time. Ground-state *Ortho*-H_2 with parallel spins—and therefore $L = 1$—is readily polarized at high magnetic field and low temperature, while ground-state *para*-H_2 with anti-parallel spins, or $L = 0$, can not be polarized. Similarly, ground-state *para*-D_2 with $L = 1$ can be polarized while ground-state *ortho*-D_2 can not. At low temperature ortho-H_2 decays to para-H_2 with a $1/e$ decay time of about 6.5 days, and para-D_2 decays to ortho-D_2 with a $1/e$ decay time of about 18 days. Hence, they can not reach a polarized frozen-spin state.

An HD molecule, in its lowest energy state (at energy-equivalence temperature around 0.5 mK), is in a $L = 0$ state which makes HD a potentially ideal frozen-spin target—but also implies that direct polarization requires a very long time. Nevertheless, indirect polarization is achievable by introducing a small concentration of $L = 1$ ortho-H_2 and para-D_2 (on the order of 10^{-4}); the small contamination of polarizable H_2 and D_2 is readily polarized and their polarization can be transferred to the HD molecule via a spin-spin coupling (e.g., between an H in H_2 and an H in HD), see Figure 2.15. After a number of half-lives, most of the $L = 1$ H_2 and D_2 would decay to respective *non-polarizable* $L = 0$ H_2 and D_2 *leaving the HD molecules in a frozen-spin state*. Quantitatively, the degree of polarization for H or D is given by the Brillouin function:

$$P(x, J) = \frac{2J+1}{2J} \coth\left(\frac{2J+1}{2J}x\right) - \frac{1}{2J}\coth\left(\frac{x}{2J}\right), \tag{2.1}$$

where J is the nuclear spin, $x = \frac{\mu B}{k_B T}$, and μ, B, k_B, T are the nuclear magnetic moment, the external magnetic field, the Boltzmann's constant, and the temperature, respectively. According to Eq. 2.1, since the magnetic moment of the deuteron is smaller than that of the hydrogen ($\mu_D/\mu_H \sim 1/3$), the degree of D polarization is significantly less than the maximum H polarization.

If it is desired to have the highest possible D polarization, such as in the g14 experiment, the D polarization can be further increased by transferring polarization from H to D through the *adiabatic fast-passage* method. In particular, when the HD molecules are frozen in and H_2 and D_2 impurities have decayed sufficiently, the

population of the $m_D = +1$ substates and $m_H = +1/2$ substates are greater than the $m_D = -1$ substates and $m_H = -1/2$. Then, the *forbidden* RF transition indicated by the red dashed lines in Figure 2.16, driven at the difference of the H and D Larmor frequencies ($\nu(H-D) = 36.0416$ MHz/Tesla [27]) transfers occupancy from the initially more populous states with $|m_H = +1/2, m_D = -1, 0\rangle$ to the $|m_H = -1/2, m_D = 0, +1\rangle$ states. Recalling that the H polarization is much larger than the D polarization thus $|m_H = +1/2, m_D = -1\rangle$ state is more populous than $|m_H = -1/2, m_D = +1\rangle$. In summary, the application of a RF power source "moves" polarization from an H in one molecule to a D in a *neighboring* molecule. The g14 target group employed this method and was able to achieve up to 30% in D vector polarization, which is the population difference between the states $|m_D = +1\rangle$ and $|m_D = -1\rangle$, while Eq 2.1 sets a limit at around 15% at about 25 mK and 15 Tesla.

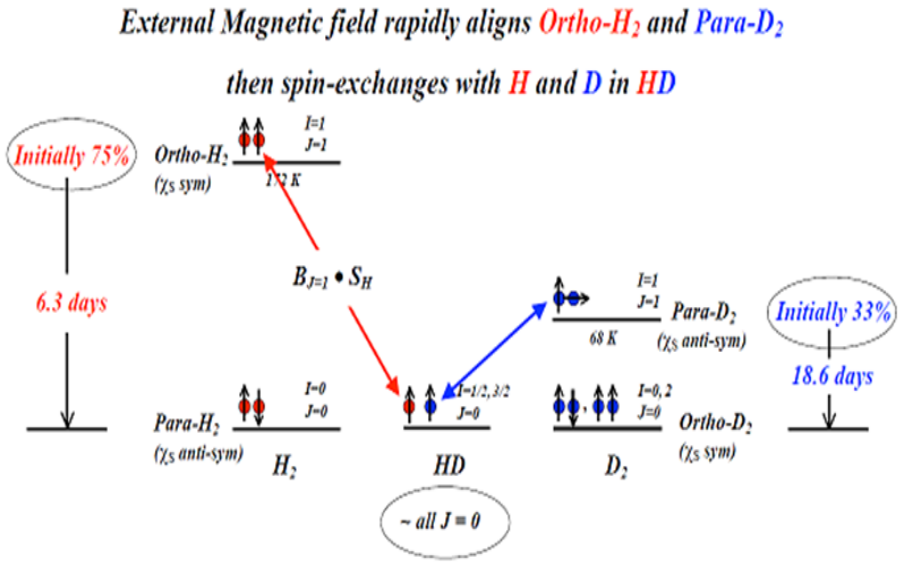

Figure 2.15: Schematic diagram showing the polarization of HD with the "help" of *ortho*-H_2 and *para*-D_2. Image was taken from [27]

2.6.2 Target Production

In this section, we introduce the components of a typical target cell, then the various Dewars used to produce, to polarize, and to store HD target. We also outline the protocol that the g14 target group implements to polarize and transfer HD targets.

2.6.2.1 Target Cell

The target cell consists of a copper ring that holds the target cell and screws into various Dewars, and inner and outer caps that contain the HD and hold the aluminum

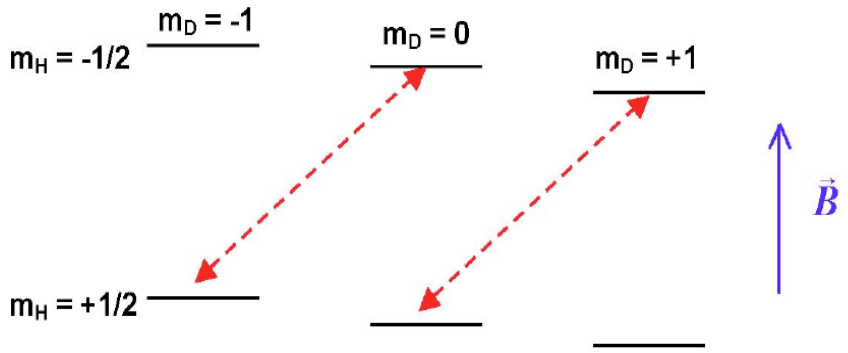

Figure 2.16: Zeeman levels in solid HD molecules. The red dasked lines indicate the forbidden RF transitions. Image was taken from [27]

cooling wires, see Figure 2.17 for an exploded view. In more detail, the copper ring has right-hand threads along its outer surface fitting the target into "cold fingers" of several cryostats—and maintaining thermal contact with the dewars. Its left-hand threads along its inner bore is to engage with the transfer cyrostat, which is essentially a giant screw driver used in the process of moving the target between Dewars. The downstream face of the copper ring has 60 holes; each hole is soldered with a bundle of aluminum cooling wires—they are necessary because the decays of ortho-H_2 and para-D_2 impurities generate heat and solid HD has poor thermal conductivity. The cell walls are made from CTFE (Chlorotrifluoroethylene), C_2ClF_3, a hydrogen-free polymer that eliminates NMR background [27] (will be referred to as "KelF" cell walls hereafter). The short inner and longer outer cell walls hold the HD away from the copper cooling ring so that particles emerging at back angles exit the cell without hitting the copper ring. Table 2.1 presents the mass fractions of material in a standard target cell, and Table 2.1 presents the measured values of the amount of aluminum in the three targets used during the experiment.

Material	Mass Fraction
HD	77%
Al	16%
KelF	7%

Table 2.1: Composition of a standard target cell. Numerical values were taken from [27].

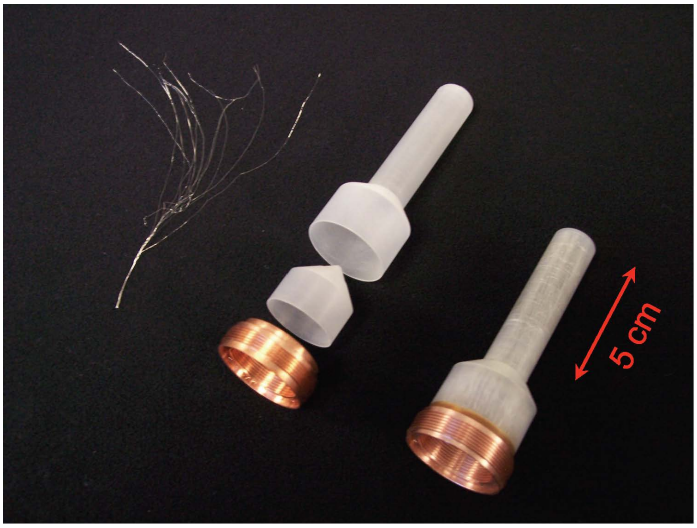

Figure 2.17: A typical target cell (left) and individual components separated (right). Image was taken from [27]

Cell	ρ(gm/cm^2)	ρ relative to 21a
21a	0.028	1.00
19b	0.020	0.70
22b	0.027	0.96

Table 2.2: Measured values of the amount of aluminum in the three targets used during the experiment. Numerical values were taken from [48].

2.6.2.2 Preparation of HD Targets and Target Transfers

The HD gas for target production is required to be of high purity—for reasons described earlier, a small contamination of H_2 and D_2 is also necessary. HD becomes solid at around 16.6 K but to achieve high polarization, temperatures of 15 mK or less are needed. A production Dewar with minimum temperature of 1.5 K is employed for crystallizing the HD molecules. It also provides a place for NMR calibration since it has a 2 Tesla magnet with high field uniformity. Next, a 2 K-and-0.12 Tesla transfer cryostat is used to extract the solid HD target from the production Dewar and load it into a dilution refrigerator where under low temperature of about 15 to 25 mK and high magnetic field (15 Tesla) the target will become polarized. After about two months the HD target has reached the frozen spin state; the target is then transferred by the transfer cryostat into the production dewar again for NMR measurement. Then a transfer is made from the production Dewar into a storage Dewar, which optimally operates at 1.6 K and 8 Tesla. When a HD target is needed in the experimental hall (Hall B), the target group moves the storage Dewar into the hall and proceeds to transfer the polarized HD target into the in-beam cryostat (IBC).

We provide a schematic of an HD target inside the IBC's "nose" and the consequent vertex distribution in Figure 2.18. The IBC is a small dilution refrigerator that fits neatly inside the CLAS detector; it operates at 250 mK and at a nominal holding magnetic field of 1 Tesla. In addition, its internal NMR system provides a continuous measure of polarization during the g14 experiment.

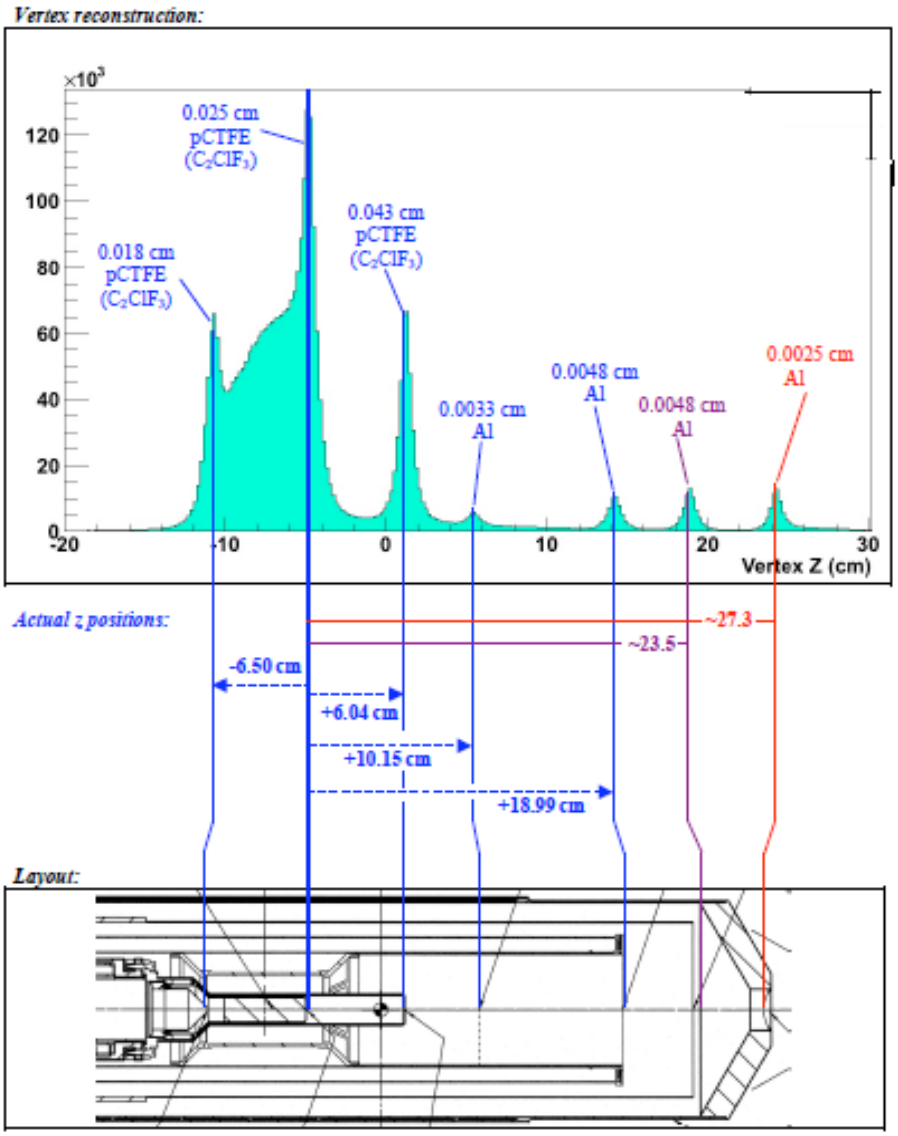

Figure 2.18: Bottom: Schematic diagram of the IBC's nose. Top: Distribution of the z component of the reconstructed interaction vertex of g14 target cell, KelF and aluminum foils for flux normalization (see Chapter 4 for details).

2.7 Summary

In this chapter, we outlined various components needed to run the g14 experiment. The introduction includes the CEBAF accelerator, the photon tagger, the CLAS detector, and the trigger and data acquisition system. At this stage, we had just digital signals which are stored on magnetic tape. In the next few chapters, we will provide details the process of converting this raw information into physics variables such as momentum, energy, time-of-flight, etc..

Chapter 3

Data Calibration and Optimization

The g14 dataset consists of about 14.8 billion event triggers (11.0 billion events with circularly-polarized photons and 3.8 billion events using linearly-polarized photons) and around 50 TB of data collected at CLAS between 12/01/2011 and 05/17/2012. The data are divided into smaller sets called "periods" due to differences in experimental settings such as different electron beam energies, and different target polarization directions, etc. In addition, these *planned* (proposed) periods were further divided into *unplanned* periods due to unfortunate losses of target polarization.

The data underwent a process known as "cooking" to convert raw electronic signals from various detector subsystems into relevant physics information (particles' time-of-flight, momenta, charges) suitable for physics analysis. Each detector subsystem was calibrated by the g14 working group to reduce systematic shifts of the measured quantities from various detector subsystems. Necessarily, for each iterations, the data was checked for improvement. The "chef" for g14 data, who was responsible for oversighting the calibration was Professor Franz Klein at Catholic University of America (CUA). The graduate students/postdocs who were responsible for the calibration were Natalie Waford (Tagger), Haiyun Lu (TOF), Jamie Fleming (Start Counter), Dao Ho (Drift Chamber), and Irene Zonta (Electromagnetic Calorimeter). After twelve iterations, Professor Franz Klein performed the drift chamber alignment check and the data was ready for analysis.

3.1 Overview of g14 experimental data

As mentioned above, the g14 data set is divided into several smaller subsets. Table 3.1 and 3.2 show different subsets for circularly polarized photon beam, and linearly polarized photon beam, respectively. For more detail, one can visit the g14 wiki page [46]. The primary reason for having different *planned* run configurations is to reduce systematic uncertainty in measuring asymmetry observables. For example, g14 had two different longitudinal directions of target polarization. Unfortunately, there were several incidents that resulted in reductions in target polarization in Target

21a—hence the *unplanned* subdivision of Silver 3, 4, and 5 periods which all had the same *planned* setting. After Silver 5b, there was another accident which resulted in a complete loss of target polarization; it was then decided to record a period in which the HD material was extracted out called the empty run period; this period was to be utilized to study the target-material background (aluminum cooling wires and KelF target cell walls). The target group, then, used Target 20b, but it was unfortunately premature and it could not retain its polarization. After about a month, Target 19b, with good polarization, was used for the experiment. This target was a successful one, and provided plenty of highly-polarized-HD-target data (hence the name Gold). The last target, or Target 22b, was utilized to run under linearly polarized photon beam with several *planned* configurations. Only one incident occurred which resulted in a 31% reduction in target polarization.

3.2 Overview of Calibration

One main goal of calibration for all detector components is to align their respective timing measurements with the beam radio frequency (RF or accelerator time). In more detail, the T-counters of the CLAS tagging system measured the scattered electron's travel time from the T-counters to the radiator. Next, the photon corresponding to the time of the scattered electron is identified and an event in the target at the center of the CLAS spectrometer is triggered. The identified photon's RF vertex time—i.e., the travel time of a photon from the radiator to the event vertex—is calculated. Furthermore, the Start Counter, the TOF scintillators and the Electromagnetic Calorimeter of the CLAS spectrometer have their distinct vertex times which are synchronized against the photon's RF vertex time. These distinct timings measured in all the components of the CLAS spectrometer are aligned together—timing alignment is thus the main subject of timing calibration. Additionally, the calibration for the drift chamber system is to improve the charged track reconstruction. In summary, the outlined tasks of calibration for each detector system are provided below (for more information, see g14 Wiki page [46])

- Tagger: Aligning T-counter and E-counter timing against the RF beam signal
- Time-of-flight (TOF): Optimizing the time and hit position reconstruction and aligning timing of the fifty seven paddles with each other and within the CLAS detection timing scheme for individual sector
- Drift Chambers (DC): Optimizing charged track reconstruction
- Electromagnetic Calorimeter (EC): Optimizing the time and energy reconstruction of neutral particles
- Start-Counter (ST): Aligning the timing of ST paddles reconstructed within the CLAS detection timing.

Period	Beam Energy (GeV)	e Beam Pol. (%)[a]	Run Range	Date Range	Events (10^6)	Torrus current (A)	Target Cell	Target Pol. (%)[b]
Silver 1	2.281	81.5±1.4±3.3	68021-68092	12/01-12/06	830	+1920	21a	+25.6±0.7±1.5
Silver 2	2.281	81.5±1.4±3.3	68094-68176	12/06-12/11	1170	+1920	21a	+23.2±0.7±1.4
Silver 3	2.281	76.2±1.4±3.1	68188-68230	12/12-12/16	250	-1500	21a	+21.2±0.8±1.3
Silver 4	2.281	88.8±1.5±3.6	68232-68305	12/16-01/04	820	-1500	21a	-6.4±0.4[c]±0.4
Silver 5	2.258	88.8±1.5±3.6	68335-68769	01/04-02/05	5210	-1500	21a	-5.9±0.2[d]±0.4
empty	3.356	88.2±1.5±3.6	68995-69037	03/08-03/09	640	-1500	21a	0.0
Gold 2	2.542	83.4±1.5±3.3	69227-69364	04/10-04/18	2100	-1500	19b	+26.8±1.0±1.6
Gold 3	2.542	83.4±1.5±3.3	69365-69369	04/19-04/19	90	-1500	19b	+15.8±0.2±1.0

Table 3.1: Summary of g14 circular beam polarization runs. We only provide the deuteron polarization (for the hydrogen polarization, see g14 wiki page [46]).

[a]Private conversation with g14 colleagues Andy Sandorfi and Franz Klein

[b]Private conversations with g14 colleagues Andy Sandorfi and Peng Peng

[c]In Chapter 4 we provide a procedure to estimate the polarization indirectly.

[d]In Chapter 4 we provide a procedure to estimate the polarization indirectly.

Period	Coherent Edge (GeV)	Run Range	Date Range	Perp. Events (Millions)	Para. Events (Millions)	Amorphous (Millions)	Target Cell	Target Pol. (%)[a]
Gold 1	2.200	69194 - 69225	04/06 - 04/09	220.5	181.1	109.3	19b	+26.8±1.0±1.6
Gold 4	2.200	69370 - 69372	04/21- 04/21	20.0	20.0	0.0	19b	+15.9±0.2±1.0
Last target 1	2.200	69375 - 69397	04/25 - 04/27	110.2	93.6	54.7	22b	+24.0±0.8±1.4
Last target 2	2.000	69398 - 69474	04/27 - 05/03	461.3	464.9	106.7	22b	+24.0±1.0±1.4
Last target 3	1.800	69476 - 69543	05/03 - 05/09	506.6	483.0	86.0	22b	+24.0±1.6±1.4
Last target 4	1.800	69544 - 69578	05/09 - 05/12	307.6	304.2	52.4	22b	−16.7±1.1±1.0
Last target 5	2.000	69583 - 69616	05/12 - 05/15	184.7	208.8	40.8	22b	−16.7±1.1±1.0
Last target 6	2.200	69618 - 69636	05/16 - 05/17	93.6	148.3	10.2	22b	−16.7±1.1±1.0

Table 3.2: Summary of g14 linear beam polarization runs. We only provide the deuteron polarization (for the hydrogen polarization, see g14 wiki page [46]).

[a]Private conversations with g14 colleagues Andy Sandorfi and Peng Peng

The procedure of calibration utilizes CLAS software packages to read in raw or reconstructed data (in BOS format) and to output calibration constants to be stored in the CLAS database. In particular, the constants obtained from the timing calibration are to reduce the systematic offset within each timing detector system. Calibration is an iterative process, i.e., when the calibration of one component is improved, it allows further improvement in another component; hence in the next iteration measurements from the detectors can be further improved. Due to this iterative nature, the calibration of certain detector components must start only after other calibrations are finished for that iteration. The order of the calibration is usually Tagger, TOF, ST, DC[1] and EC.

3.2.1 Drift Chamber (DC) Calibration[2]

The DC was designed to track the trajectories of charged particles. The CLAS toroidal magnet bends the charged particles' tracks. The track curvature is dependent on the momentum of the particle. The DC consists of small hexagonal cells filled with a mixture of 90% argon and 10% CO_2, as shown in the left plot of Figure 3.1. At the center of the cell is a sense wire (anode) surrounded by six field wires (cathodes), as shown in the right plot of Figure 3.1.

A traversing charged particle ionizes the gas inside these cells; because of the electrical potential difference between the field and sense wires, the electrons are accelerated toward the sense wire and cause further ionization until an electron "cloud" reaches the sense wire and causes a pulse, the time of which is recorded by the readout electronics. Identifying the cells that are "firing" determines the track of the charged particles in a least-squares fit (i.e., hit-based track reconstruction). To further improve the track reconstruction resolution, a "time-based" track reconstruction which is based on the measured drift time is used. The drift time refers to the time required for electrons to drift to the nearest sense wire from the place where a charged particle has crossed, as shown in the right plot of Figure 3.1.

A standard CLAS software package named "dc3" [49] is used to calibrate the CLAS drift chamber (DC). The software package uses two terms to describe the distance of a charged particle track from a sense wire: DOCA and DIST; DOCA (distance of closest approach) is the distance from the fitted track to the sense wire (i.e. fits that include all layers), and DIST is the distance from the sense wire to the track calculated from the drift time. The "dc3" software package obtains the parameters for the analytical drift velocity function—i.e., *time-to-distance* relation—for every superlayer in every sector by fitting DOCA against drift time. The calculated DIST is then obtained from the relation of the drift velocity function and the drift time. Next, it computes the time residual defined as the difference between the values of

[1]Actually, DC calibration does not have to follow this order, since the drift chamber system is semi-independent with the other systems that measure time.

[2]I was responsible for the DC calibration for g14 experiment.

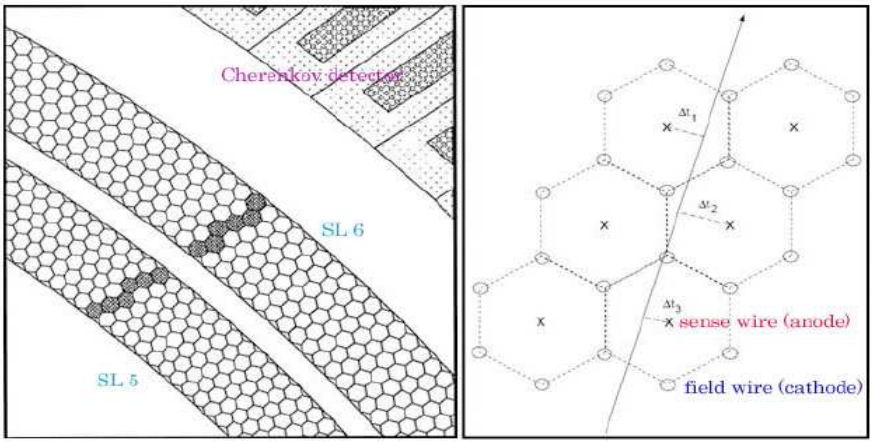

Figure 3.1: Left: Portion of a Region 3 sector showing the layout of its two superlayers filled with gas. Highlighted ("firing") drift cells indiacate the path of a charged particle. Right: Schematic diagrams showing a charged reconstructed track using "time-based" tracking. The dashed lines identifies the perimeters of the hexagonal drift cells. Image was taken from [47]

fitted DOCA and calculated DIST. The time residual is caused by systematic time shift in drift time measurements. Ultimately, the goal in DC calibration is to reduce the systematic time shift such that the value of the residual in each superlayer become approximately zero, as shown in Figure 3.2. In addition, in Figure 3.3 we show the effect of the DC calibration in reducing and "stabilizing" the time residual.

3.3 Energy Loss Correction

Detected charged particles lose energy through ionization when they travel through material in CLAS. As a result, the reconstructed momenta of charged particles are smaller and needed to be corrected. Primary sources of energy loss are the target material and cell walls, the beam pipe, the start counter and the air gap located between the start counter and the Region 1 drift chambers. Eugene Pasyuk wrote an *eloss* software package which takes into account the material presented inside CLAS to recover the average energy loss [50].

3.4 Momentum Correction

In this section, we present a brief overview of a reliable method to improve the data resolution: kinematic fitting. The method, in general, is a *least squares* fitting of kinematic variables (such as particles' momenta, tracking angles) with a set of constraint equations (for example, conservation of energy and/or momentum). To perform least

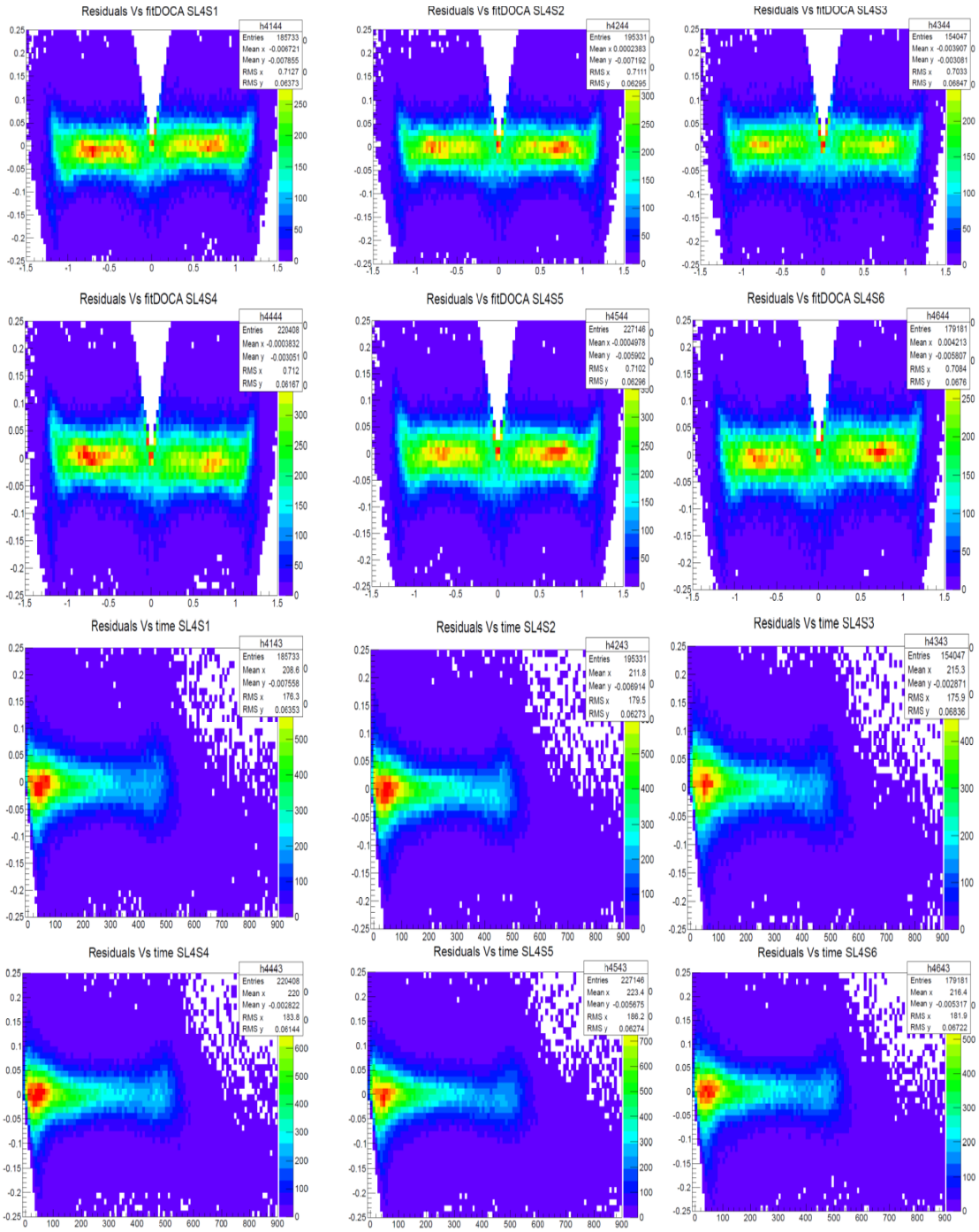

Figure 3.2: DC residue ($DOCA - DIST$) as a function of DOCA (top 6 histograms) and as a function of drift time (bottom 6 histograms) for superlayer 4. The temporal unit is ns, the spatial unit is mm.

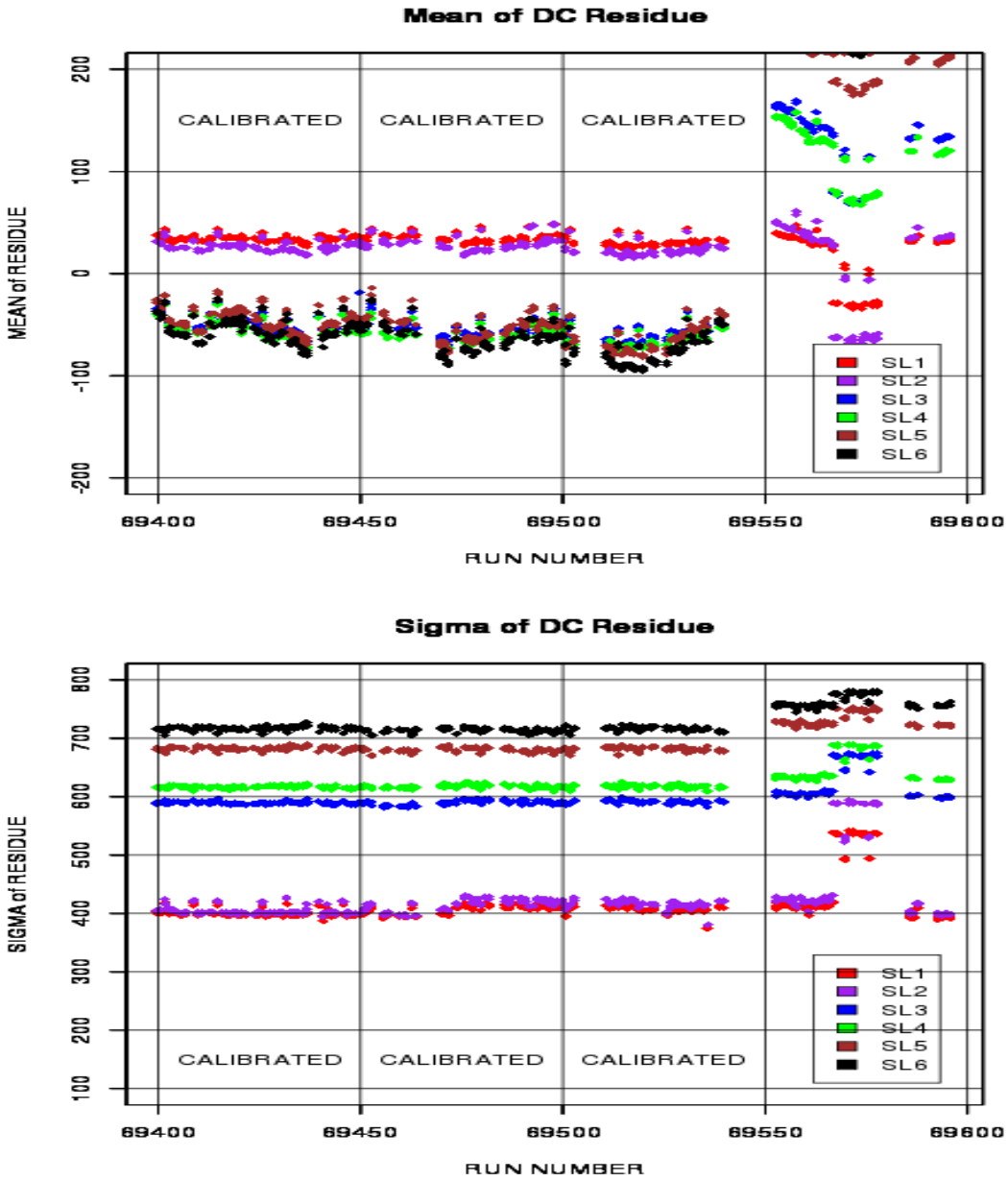

Figure 3.3: Top: Mean of the DC residue ($DOCA - DIST$) vs. Run Number. Bottom: Standard deviation of DC residue vs. Run Number. Runs after the run 69550 were *not* calibrated at the time these plots were produced. The vertical unit are μm.

squares fit with constraint equations, an usual approach is to use Lagrange multipliers; this is the approach that Mike Williams, a former CMU graduate student, chose to implement the fitting algorithm [51, 52] for the CLAS g11 dataset. We employed

his kinematic fitting algorithm to derive tagger energy and CLAS track momentum corrections to globally improve the measured momentum of detected particles. To derive the corrections, we applied kinematic fitting on the reaction $\gamma p \rightarrow p\pi^+\pi^-$. First we did tagger energy correction using "uncorrected" CLAS momenta, then we corrected the momentum with the improved tagger values. This process completed one iteration, and we repeated the whole process again several times. After each iteration we checked the improvement of momentum resolution. We stopped when the improvement is negligibly small.

3.4.1 Kinematic Fitting[3]

Usually, we have a set of n measured quantities, denoted by the n-vector $\overrightarrow{\eta}$. These are the tracking parameters for a given event, such as momentum, azimuthal and polar angles in a sector-based coordinate. Each measurement has an unknown deviation from its true value, denoted by the n-vector $\overrightarrow{\varepsilon}$. Therefore, if we denote the true values of the measured quantities as $\overrightarrow{y}$, we arrive at the following relation:

$$\overrightarrow{\eta} = \overrightarrow{y} + \overrightarrow{\varepsilon}. \tag{3.1}$$

The idea of kinematic fitting is to estimate $\overrightarrow{y}$ from $\overrightarrow{\eta}$ using a set of kinematic constraints—i.e., conservation of energy and/or momentum. In particular, if we have an exclusive reaction where all particles were detected, then every component of the total missing 4-momenta must be zero (i.e., one conservation of energy constraint, and three conservation of momentum constraints). On the other hand, for reaction that has one undetected particle, the number of constraint equations reduces to one—i.e., the total missing mass constraint. Next, consider the following n-vector $\overrightarrow{\delta}$:

$$\overrightarrow{\delta_i} = \overrightarrow{y_f} - \overrightarrow{y_i}, \tag{3.2}$$

where $\overrightarrow{y_f}$ is the final fit result, $\overrightarrow{y_i}$ is the improved measurements at the i^{th} iteration step and the n-vector $\overrightarrow{\eta}$ is assigned as the starting $\overrightarrow{y_0}$. Now if we denote the covariance matrix for the measured quantities C_η, then the least-squares quantity that needs to be minimized is $\overrightarrow{\delta}^T C_\eta^{-1} \overrightarrow{\delta}$. In addition, because of the aforementioned constraint equations, the minimization can be done by employing the procedure of Langrange multtipliers.

3.4.2 Confidence Levels and Pull Distributions

The *goodness of fit* from the kinematic fitting is measured by the confidence level. If we assume that the errors $\overrightarrow{\epsilon} = \overrightarrow{\eta} - \overrightarrow{y_f}$ are normally distributed then $\overrightarrow{\epsilon}^T C_\eta^{-1} \overrightarrow{\epsilon}$

[3]For a detailed introduction to the algorithm, and specifc implementation for CLAS, see Mike Williams's thesis [51].

follows a χ^2 distribution with $d = n - m$ degrees of freedom, where n is the number of fit parameters (and measured quantities) and m is the number of constraints[4]. Then the confidence level is computed as:

$$CL = Pr(x > \chi^2) = \int_{\chi^2}^{\infty} f(x, d)dx, \tag{3.3}$$

where $f(x, d)$ is the χ^2 probability density function with d degrees of freedom. Given the actual values $\overrightarrow{y}$ and the measurment errors $\overrightarrow{\varepsilon}$ for a particular event the confidence level is an indication how likely the measured quantities $\overrightarrow{\eta}$ occur just by random chance under the fit hyphothesis. For a group of events that satisfy the fit hyphothesis with normally distributed errors, the confidence level is flat on $(0, 1]$ interval. On the other hand, background events that do not satisfy the fit hyphothesis have small confidence levels.

The assumption of normally distributed errors needs to be verified. This can be accomplished by examining the *pull* distributions for each measured quantity. For the j^{th} fit quantity, its pull distribution is defined as:

$$z_j = \frac{\epsilon_j}{\sigma(\epsilon_j)} = \frac{\eta_j - (\overrightarrow{y_f})_j}{\sqrt{\sigma^2(\eta_j) - \sigma^2((\overrightarrow{y_f})_j)}}, \tag{3.4}$$

where the error $\sigma((\overrightarrow{y_f})_j)$ is computed by the standard error propagation techniques from C_η. The z_j's should be normally distributed about zero with $\sigma = 1$. A systematic error in the measured quantity η_j can be seen as an overall shift away from zero in the distribution. Additionally, if the error of η_j has been consistently overestimated (underestimated), then the corresponding pull distribution will be two narrow (broad). Importantly, Mike Williams mentioned in his thesis that the covariance matrix C_η obtained from CLAS track reconstruction software is underestimated, thus he had to "correct" the covariance matrix C_η (for detail see Ref. [51]). We followed his procedure to obtain better accuracy for the tracking covariance matrix C_η for g14 data.

Finally, we show the pull distributions and confidence level from the kinematic fit for the reaction $\gamma p \to p\pi^+\pi^-$ (details about event selection are provided in Section 3.4.3.1). The confidence level is shown in Figure 3.4. Note that the distribution is not flat, but as will be shown later, the momentum corrections obtained from kinematic fitting the reaction $\gamma p \to p\pi^+\pi^-$ result obvious improvements in particle momentum measurements. The reason for the confidence level slightly sloped is that there are remaining bound proton events from the reaction $\gamma d \to p\pi^+\pi^-(n_s)$. The pull distributions are shown in Figure 3.5 with the values of their means and widths presented in Table 3.3. The extracted values are in decent agreement with the ideal values of zero mean and unity width.

[4]For a more general case consisting of n measured quantities and k unknown (fitting) parameters related by m constraint functions, the degree of freedom is $d = k - m$.

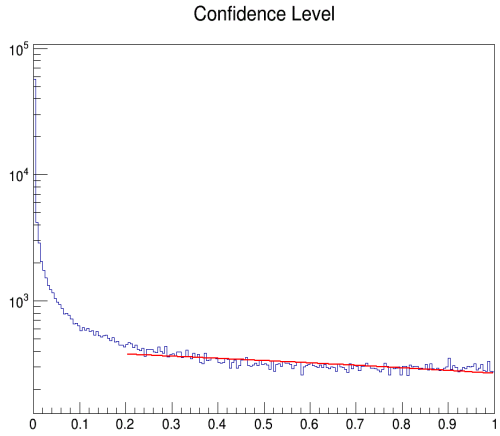

Figure 3.4: The confidence level pull distribution for the reaction $\gamma p \rightarrow p\pi^+\pi^-$ for events from the Gold 2 data set. The plot is in a logarithmic scale.

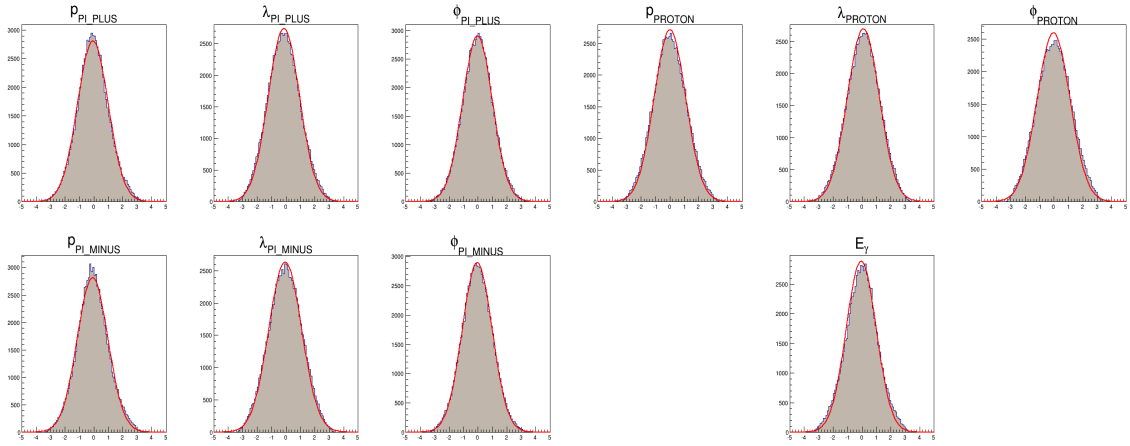

Figure 3.5: The pull distributions for the reaction $\gamma p \rightarrow p\pi^+\pi^-$ for events from the Gold 2 data set. The variables shown here are defined for the CLAS tracking covariance matrix C_η

3.4.3 Procedures to Obtain Tagger and Momentum Corrections

The tagger and momentum corrections ultilize the reaction $\gamma p \rightarrow p\pi^+\pi^-(0)$ to improve the data. This reaction has complete kinematics, and includes both positively and negatively charged particles. We selected events which had particle ID identified by the standard CLAS particle identification scheme. We did not include any addtional PID cut. To do tagger correction, we ignored the tagged photon, and used kinematic fitting to derive the photon energy. The difference between the derived photon energy and the measured photon energy determines the correction. Similarly,

Variable	Mean	Width
E_γ	-0.013	1.078
$\|p\|_p$	0.012	1.095
λ_p	0.112	1.111
ϕ_p	-0.017	1.146
$\|p\|_{\pi^+}$	-0.059	1.067
λ_{π^+}	-0.120	1.088
ϕ_{π^+}	-0.017	1.035
$\|p\|_{\pi^-}$	-0.081	1.064
λ_{π^-}	-0.038	1.137
ϕ_{π^-}	-0.037	1.038

Table 3.3: Numerical values for Gaussian means and widths for the pull distributions for the reaction $\gamma p \to p\pi^+\pi^-$. The variables shown here are defined for the CLAS tracking covariance matrix C_η.

to obtain the correction for the *vector* momentum of negatively charged particle, we ignored the measured π^- vector momentum, and used kinematic fitting to derive the momentum, then we determined the correction from the measured and derived values of the π^-momentum.

3.4.3.1 Event Selection for the reaction $\gamma p \to p\pi^+\pi^-(0)$

In g14 data, the reaction of $\gamma p \to p\pi^+\pi^-$ can happen by three different processes. The proton from the initial state can be from the hydrogen atom, or from the deuteron, or from the nucleus of the aluminum wires or target cell walls (KelF). Only the first type has complete kinematics for the kinematic fitting procedure. Thus we needed to select only events coming from the specific reaction $\gamma p \to p\pi^+\pi^-(0)$ (i.e., we tried to select only events originated from the free proton target). We realized that events coming from this reaction ideally must have zero missing momentum and zero missing energy if we assigned the target mass as the proton mass. Other events with different kinematics would not have these two properties. We could use these properties to effectively select events from the reaction $\gamma p \to p\pi^+\pi^-(0)$. Due to finite momentum resolution, we could not have very tight cuts. We decided to make the following selection cuts: $|MM^2(p\pi^+\pi^-)| < 0.03$ GeV^2 and the Missing Momentum< 0.12 GeV. Figure 3.6 shows selected events after the selection cuts.

The two cuts we used cleanly seperate $\gamma p \to p\pi^+\pi^-(0)$ from $\gamma d \to p\pi^+\pi^-(n_s)$, where the second reaction happens on the deuteron. Next we apply a cut on the z component of event's vertex, see Figure 3.7. This cut selects events inside the target region and rejects some non-HD background events. Most of the remaining non-HD background events (from alumnimum cooling wires) and background events with misidentified PID would be rejected by a cut at 0.1 on the confidence level (i.e.,

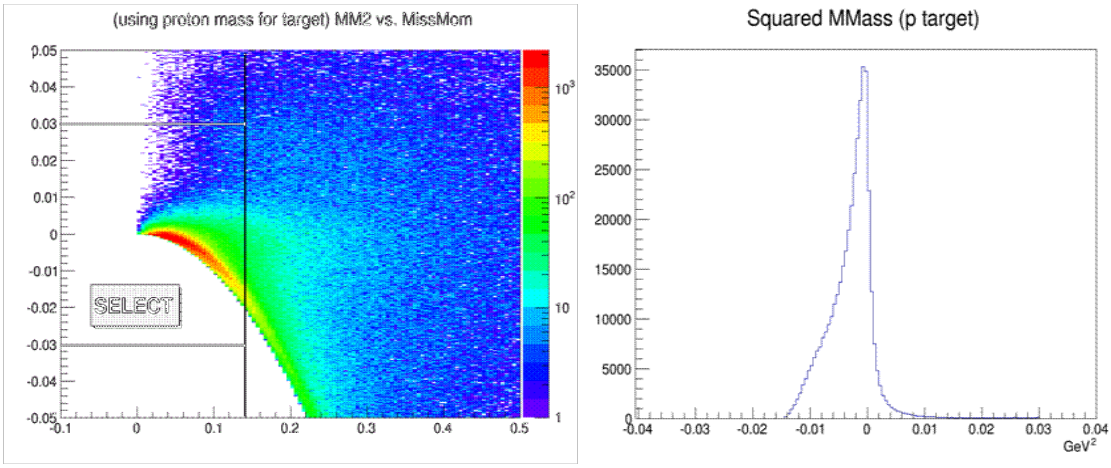

Figure 3.6: Each event consists of detected p, π^+, and π^-. We assign proton mass as target mass for these events, and then we apply the squared missing mass and missing momentum cuts. The plot on the left shows squred missing mass (in GeV^2 unit) vs. missing momentum (in GeV/c unit). The plot on the right shows the squared missing mass distribution (in GeV^2 unit) of selected events after the cuts.

rejecting events with confidence level less than 0.1). The final selected events were ultilized to obtain tagger and momentum corrections.

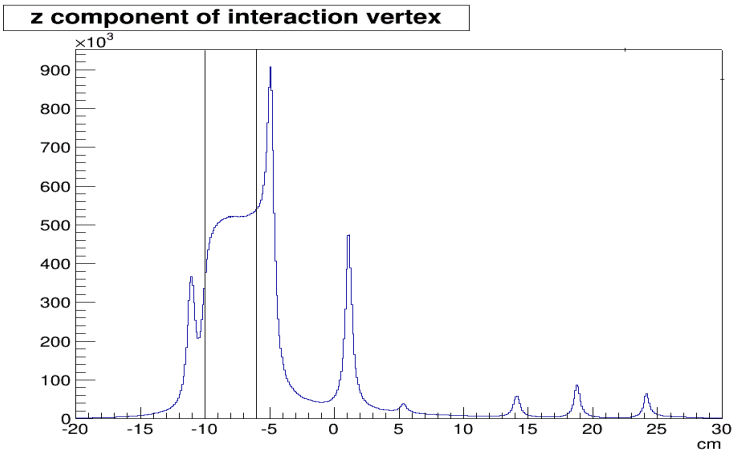

Figure 3.7: z-component of the interaction vertex for the reaction $\gamma p \to p\pi^+\pi^-(0)$. The two vertical lines indicate the z-vertex cuts.

3.4.3.2 Tagger Correction

Alignment issues in the photon tagger's focal plane were observed in several experiments before g14 (for detail, see Ref. [51])—caused by tagger sagging due to the

weight of the scintilator paddles. Corrections had been obtained for those experiments. During the cooking of g14 data similar tagger correction had been applied, thus the issue was not seen in g14 data. However, the tagger might still have a global offset with different electron beam energies. For g14 experiment, there were five different electron beam settings; the energies of the electron beam were 2.281, 2.258, 2.541, 3.356, and 5.552 GeV. We, therefore, have five different *small* tagger corrections for each beam setting.

We now describe the procedure for tagger energy correction. After selecting events from the reaction $\gamma p \to p\pi^+\pi^-(0)$, we applied energy-loss corrections and previous iteration of tagger and momentum corrections. Then we kinematically fit to the hypothesis $(\gamma)p \to p\pi^+\pi^-(0)$, igrnoring the measured photon beam energy. We only selected events with confidence level greater than 10% (cut on the confidence level value as mentioned previously) to determine the correction. Particularly, for each electron beam setting, we computed the following correcton factor C_{tag}:

$$C_{tag} = {}^{(E_\gamma^{kfit} - E_\gamma^{meas})}/_{E_{beam}}, \tag{3.5}$$

where E_γ^{kfit}, E_γ^{meas} are the photon energy values from the kinematic fitting and photon tagger system, respectively, and E_{beam} is the energy of the electron beam. Next, we plotted the C_{tag} against tagger E-counters and from each tagger E-counter, we extracted the Gaussian mean (see Figure 3.8). These Gaussian means are then stored in a look-up table—since we had five different beam settings, there are five look-up tables. When we need to apply tagger correction for a particular event, we look up its electron beam setting, its E-counter tagger ID, then find the appropriate look-up table to get the correction factor.

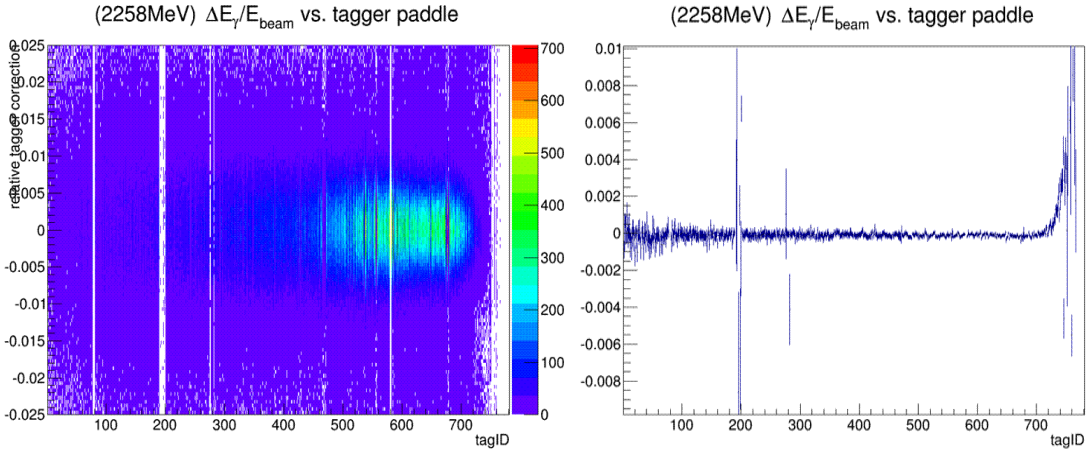

Figure 3.8: Tagger correction for one of the electron beam setting (2.258 GeV). The left plot shows relative tagger correction C_{tag} vs. E-counter tagger ID. The right plot shows the extracted Gaussian means for each E-counter tagger ID.

3.4.3.3 Momentum Correction

In this section we describe a procedure to obtain the momentum correction for inaccuracies in the reconstructed momenta. One of the reasons for the inaccuracies is due to the discrepancies in the toroidal magnetic "ideal" field map from survey information and the "actual" field during the experiment. Misalignment and sagging in various parts of the drift chamber can lead to inaccuracies as well. In order to obtain the momentum correction, we applied the energy correction and the most recent tagger correction. Then we performed three kinematic fitting procedures by treating one of the detected particles as "missing": $\gamma p \to (p)\pi^+\pi^-$, $\gamma p \to p(\pi^+)\pi^-$, and $\gamma p \to p\pi^+(\pi^-)$. For each hyphothesis, the measured momentum of the "missing" particle was compared with the missing momentum obtained from the kinematic fit. The kinematic fit estimates for the corrections for the momenta are then:

$$\triangle|p|_x = |p|_x^{kfit} - |p|_x^{meas}, \tag{3.6}$$

$$\triangle\lambda_x = \lambda_x^{kfit} - \lambda_x^{meas}, \tag{3.7}$$

$$\triangle\phi_x = \phi_x^{kfit} - \phi_x^{meas}, \tag{3.8}$$

where $x = \{p, \pi^+, \pi^-\}$ is the "missing" particle. For example, $\triangle|p|_p$ was obtained from the hypothesis $\gamma p \to (p)\pi^+\pi^-$. To obtain the correction factors for *each charged* particle type, we first divided the data into 6×180 angular subsets (i.e., 180 subsets for each sector). For *each charged* particle type, the polar angle θ is divided into nine 5^o sets for $\theta \in [5^o, 50^o)$, four 10^o sets for $\theta \in [50^o, 90^o)$, and two 25^o sets for $\theta \in [90^o, 140^o)$. The azimuthal angle ϕ is divided into twelve 5^o sets for each θ subset. Second, for each angular subset we plotted the histograms of $\triangle X_q$ vs. $|p|_q$ where $X = \{|p|, \lambda, \phi\}$ and $q = \{+, -\}$ and for each momentum bin we fitted a Gaussian on the $\triangle X_q$ quantity to obtained the mean and width. Next, we applied a polynomial fit (second or third order) on the obtained Gaussian means and widths to obtain a continous momentum correction as a function of the particle momentum. Figure 3.9 shows $\triangle|p|_+$ vs. $|p|_+$ on the left and the polynomial fit to the Gaussian means on the right.

3.4.3.4 Effectiveness

To check the effectiveness of these corrections, we studied $\gamma d \to p\pi^-(p_S)$ reaction; this reaction consists of both positive and negative charged particles and a well-defined missing particle (the spectator proton). Details of event selections are provided in Chapter 4. We first illustrate the energy loss correction in Figure 3.10. As shown in the right histogram, the correction is on the order of 5 MeV. It also appears that the energy loss correction overcompensates as the centroid of the mass spectrum after the correction is about 5 MeV lighter than the mass of the proton of about 938 MeV

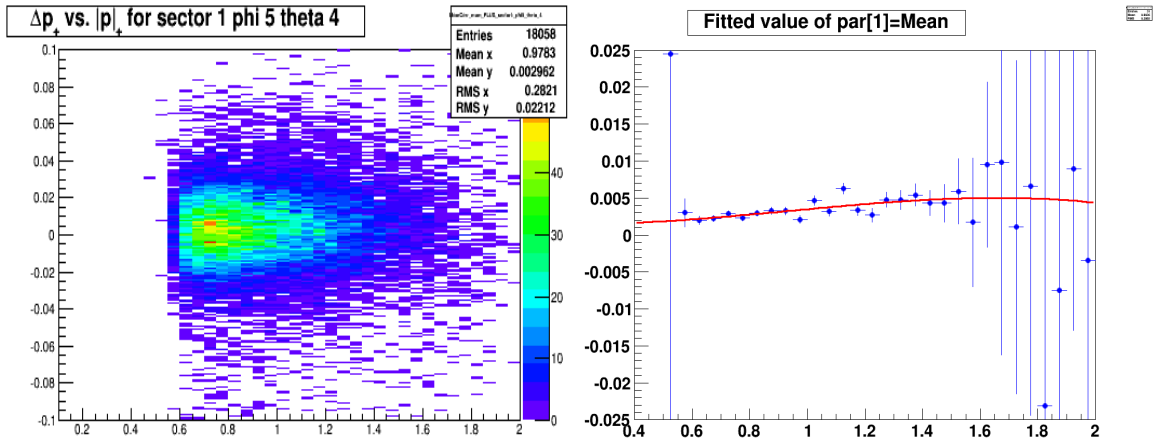

Figure 3.9: Correction for $|p|$ of positively charged particles. The left plot shows $\triangle|p|_+$ vs. $|p|_+$. The right plot shows the extracted Gaussian means for each mometum bin and a polynomial fit (the red curve).

(see the left histogram). We will show that by applying the momentum and tagger correction, the mass centroid will be closer to 938 MeV, the rest mass of the proton.

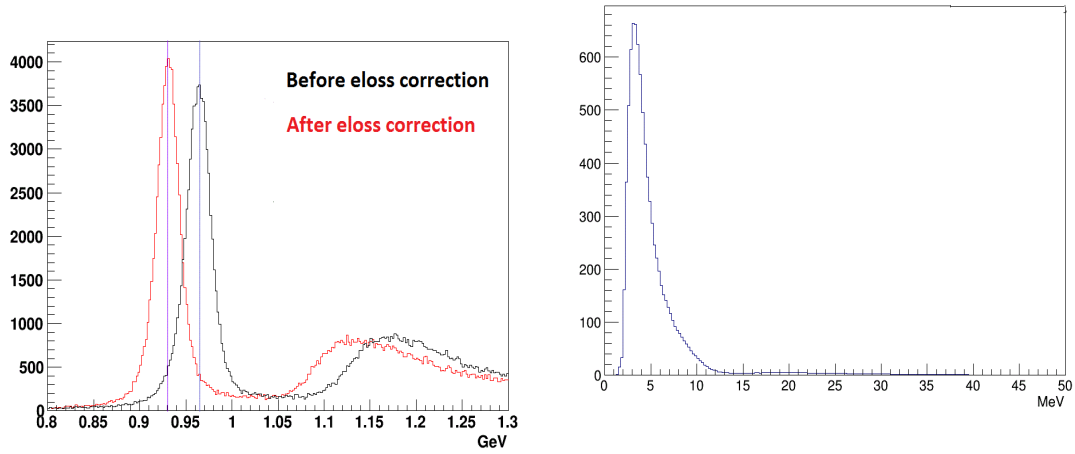

Figure 3.10: Left: Missing Mass off $(p\pi^-)$ before (black) and after (red) applying eloss correction. Right: distribution of energy correction magnitude. The data used to obtain the plots were the Gold 2 data.

In Figure 3.11 we show effect after the tagger and momentum corrections. Note that the centroid of the missing mass after the correction is closer to the mass of the proton. In addition, the three bottom histograms in Figure 3.11 illustrate clearly improvement in the momentum measurments which lead to better resolution for the spectator proton mass distribution (i.e., the mass centroid as a function of the measured $|p|_{\pi^-}$, θ_{π^-}, ϕ_{π^-} is much straighter).

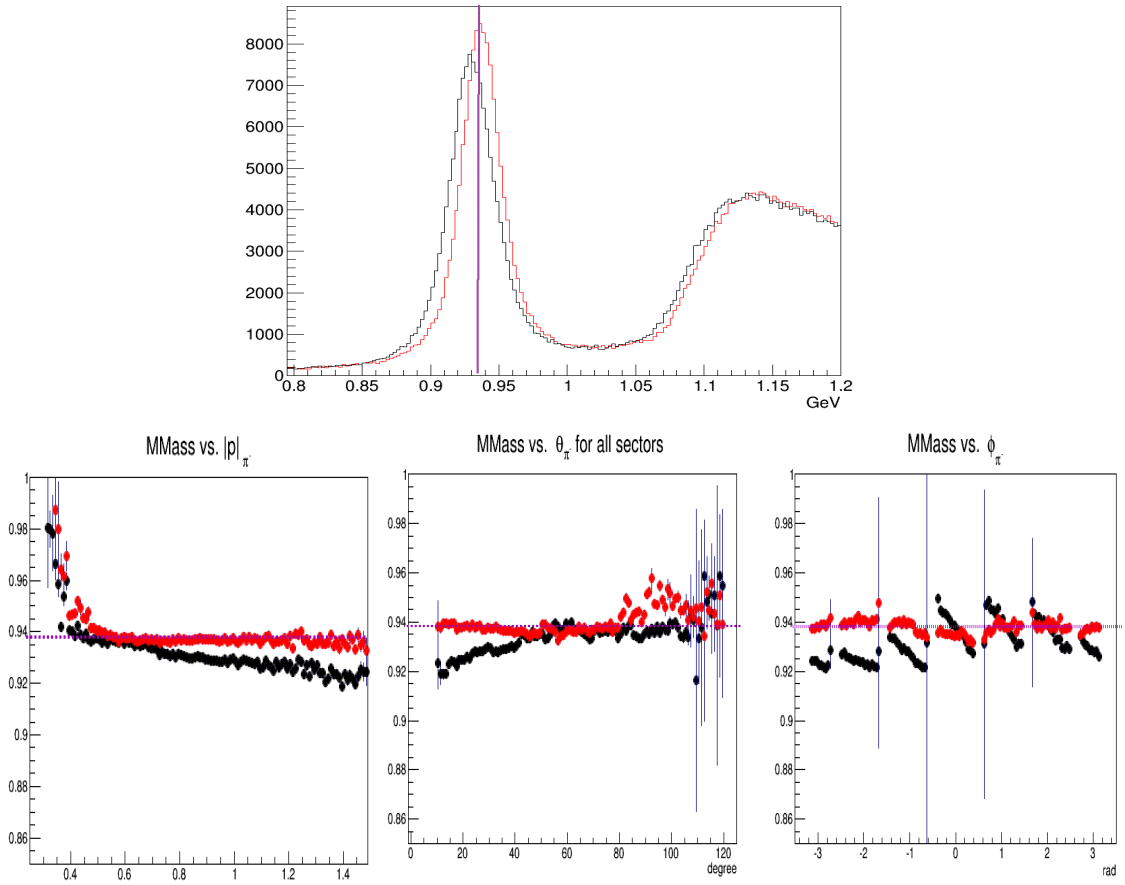

Figure 3.11: Top: Total Missing Mass off ($p\pi^-$) before (black) and after (red) momentum correction. The mass centroid is closer to 938 MeV—the mass of the proton. Bottom: missing mass centroid as a function of the measured $|p|_{\pi^-}$, θ_{π^-}, ϕ_{π^-}. The color code is the same as in the top plot. Obviously, the corrections lead to better resolution in the missing mass distribution. The data used to obtain the plots were the Gold 2 data.

3.5 Overview of Simulation of g14 data

The CLAS collaboration had developed software packages that allow one to process Monte Carlo (MC) data to see the response of the CLAS detector for a given set of events. We now give a brief overview of the software packages. The first component is a Monte Carlo event generator for photoproduction experiments called "mc-generator". It was written and maintained by Professor Reinhard Schumacher at Carnegie Mellon University (CMU). It can generate any number of MC events with a given initial state and subsequent selectable decay chain. The initial state that is of interest for the analyses in this thesis is a photon beam on a free deuteron tar-

get (the final states will be introduced more specifically in future analysis chapters). Next, the generated data was processed by the GSIM software package [53]. It is the standard CLAS detector simulation system that is based on the GEANT simulation code developed at CERN. It would propagate particles through a simulation of the CLAS detectors—to simulate the detector response: energy loss, pulse height, pulse timing, *etc.*. In Table 3.4a (left) we present a set of input parameters that is necessary to specify the g14 run conditions (for example, torus magnetic field setting, electron beam energy, *etc.*). After the GSIM stage, the generated events were then processed by the GSIM Post Processor program, or GPP for short. It smears the momentum and timing of the signal so that the resolution of the generated events matches the real data closely. Table 3.4b (right) shows a set of input parameters we specified for the g14 run period. To illustrate that we have a good matching of resolutions, we show in Figure 3.12 the Gaussian widths of the spectator protons of the reaction $\gamma d \to p\pi^-(p_S)$ as a function of the z-vertex for both simulation and real data. The plot includes twelve histograms representing twelve different W energy windows (covering the whole energy range of which we measure the E asymmetry for the reaction $\gamma d \to p\pi^-(p_S)$); the matching between the simulation and real data are good except for the last energy window—it is possible that energy and momentum corrections are not as good for that energy window, hence the resolution is larger than compared to others' resolutions (on the other hand, the resolution for the simulation data is relatively stable across the twelve energy windows). In addition, the mismatch near $z \sim -4$ cm was due to the fact that there was just a few bound neutron events and hence the extracted fitted-Gaussian widths were larger reflecting a larger statistical fluctuation. After GPP, in the next stage, individual tracks are constructed. This was done by USERANA—the CLAS standard program for reconstructing particle tracks. USERANA also saves the simulation data in the same format as the real data to faciliate comparisions between simulation and real data.

3.6 Summary

In this chapter, we provided an overview of g14 run conditions which includes the naming convention that we will used extensively in later chapters (for example, Gold 2 period refers to runs 69227-69364 with target 19b). An outline of procedures—detector calibration, energy and momentum corrections—to improve g14 data quality was also introduced. Lastly, we discussed required steps to simulate MC data with g14 run conditions as well as illustrated good agreement in resolution between real and simulation data. In later chapters, we will be more specific about the final state that we would like to generate.

Input parameters for *ffread* card

AUTO	1
KINE	1
MAGTYPE	2
MAGSCALE	-1495
TMGIFIELD	5
MGPOS	0.0 0.0 -7.5
FIELD	2
GEOM	“ALL” “ST”
NOGEOM	“SQL” “IC” “FOIL” “MINI” “PTG”
NOMCDATA	“ALL”
NOSEC	“OTHE”
TARGET	13
TGMATE	“HD”
TGPOS	0.0 0.0 -7.5
STZOFF	1.0
STTYPE	1
TGCUTS	0.01 0.01 0.01 0.01 0.01
CUTS	5.e-3 5.e-3 5.e-3 5.e-3 5.e-3
DCCUTS	1.e-4 1.e-4 1.e-4 1.e-4 1.e-4
ECCUTS	1.e-4 1.e-4 1.e-4 1.e-4 1.e-4
SCCUTS	1.e-4 1.e-4 1.e-4 1.e-4 1.e-4
STCUTS	5.e-5 5.e-5 5.e-5 5.e-5 5.e-5
SAVE	“ALL” “LEVL” 10 “HARD” 0.001
NSTEPMAX	50,000
TIME	2,000,000 2,000,000 2,000,000
RUNG	1
BEAM	2.541
POSBEAM	0.0 0.0

Input parameters for GPP

P	0x1f
R	69300
Y	
f	1.0
a	2.0
b	2.0
c	2.0

Table 3.4: Input parameters given to the GSIM (left) and GPP (right) simulation software.

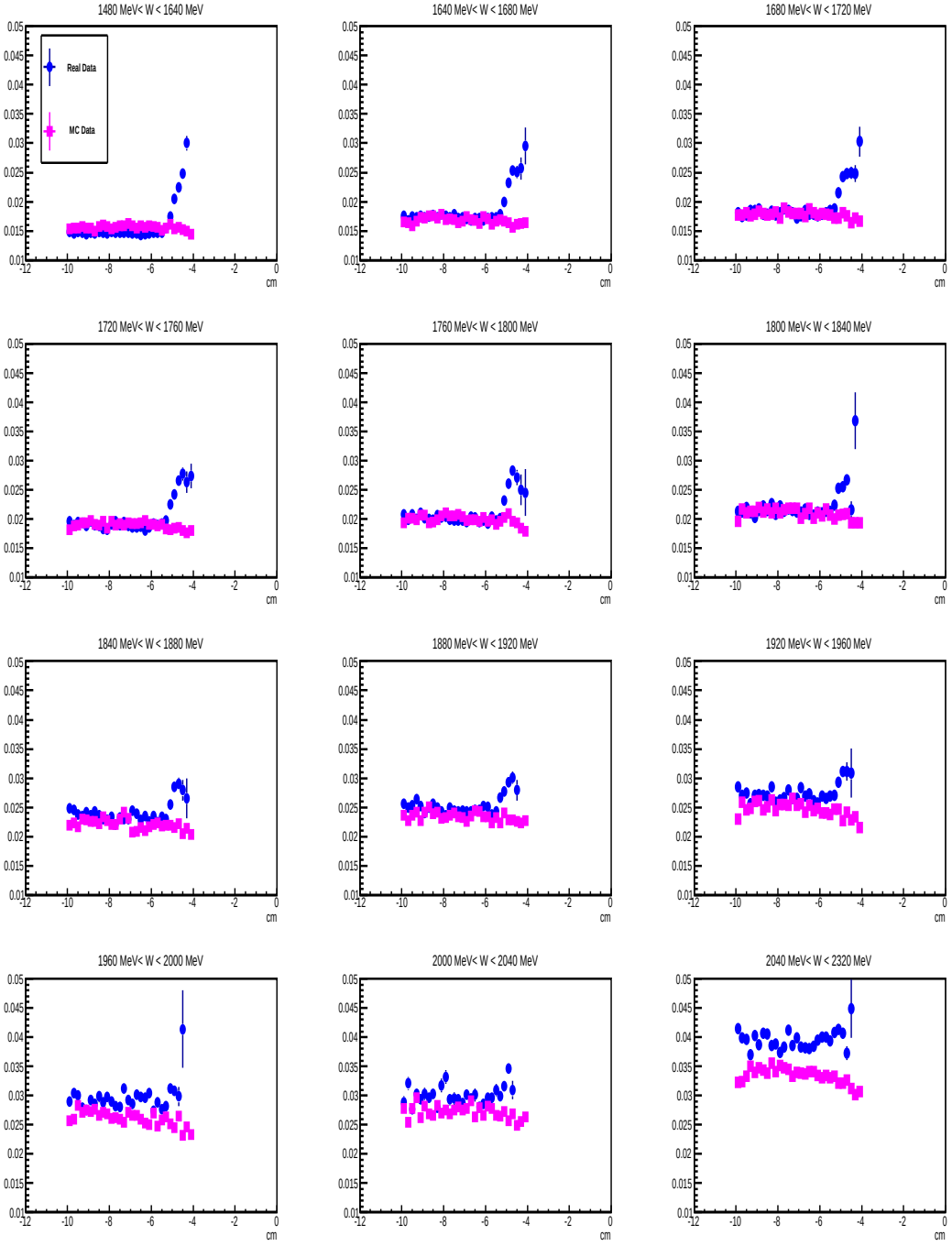

Figure 3.12: Comparing the Gaussian widths of spectator protons for simulation (magenta) and the Gold2 real data (blue) as a function of the z-vertex, see text for explainations of the observed mismatches. The vertical unit is GeV, the horizontal unit is cm.

Chapter 4

Results for the E Observable for Reaction $\gamma d \to \pi^- p(p_s)$

We present the first set of measurements of the helicity asymmetry E for the reaction $\gamma d \to \pi^- p(p_s)$ using the CLAS g14 data. Our analysis consisted of several sequential stages. First, we identified $p\pi^-$ events using a set of well-calibrated cuts. The second step was to select events that were from bound neutrons and rejected events from target material (aluminum wires and KelF cell walls), and background from other reactions with the same detected particles. Two methods for doing event selection will be introduced. The first method is referred to as 1D-cut background suppression and subtraction; it consists of a set of cuts to remove the background and utilizes the empty target data to "subtract" away remaining target background. The second method is based on machine learning and utilizing the Boosted Decision Trees (BDT) algorithm; it is a multivariate data analysis tool (algorithm) developed in 1996 [54] and well-known in the HEP community [55, 56]. The algorithm "learns" how to separate the background and signal through supplied *training* data. We will show that the E measurements from the BDT method are consistent with the 1D-cut background suppression and subtraction method, but the BDT event selection procedure has higher efficiency (we provide useful insights about the BDT algorithm in Appendix A). Thirdly, after selecting the bound neutron events, the E measurements were obtained for all circularly-polarized-photon run periods (Silver 1, 2, 3, 4, 5, and Gold 2, for more detail about the run periods see Chapter 3). In addition, before combining the results from all periods, we obtained estimations for the target polarizations of the Silver 4 and 5 periods using the E measurements from Silver 1&2 (the term Silver 1&2 implies a combined data from Silver 1 and 2 data sets) periods. The final stage was systematic uncertainty studies which are reported in section 4.4.

4.1 $\pi^- p$ Event Selection for the Reaction

We began the analysis with the task of selecting "$p : \pi^-$" events. In particular, using the measured momentum, the path length and the *time-of-flight* of each detected particle, a measured mass was obtained. Next, if a positively charged particle has a measured mass within 0.8 GeV to 1.2 GeV, it is assigned a proton "ID". Similarly, if a negatively charged particle has a measured mass within 0.0 GeV to 0.3 GeV, it is assigned a π^- "ID". We plot the measured masses of the selected "$p : \pi^-$" events in Figure 4.1, and in Figure 4.2 we plot the total missing mass, $MM(p\pi^-)$.

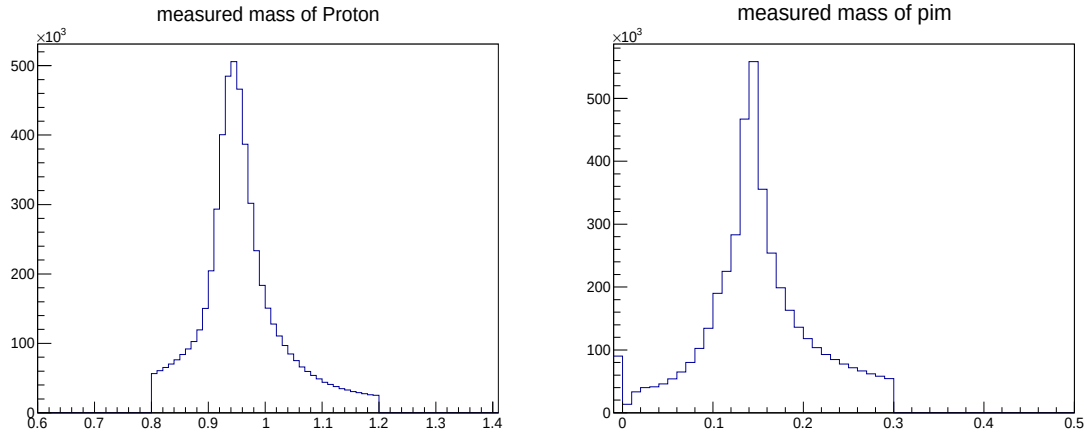

Figure 4.1: Left: Measured mass of particle identifieded as proton. Right: Measured masses of particle identified as π^-. A set of cuts will be applied next to clean up the mass distributions. The data used to plot was Gold 2 period. The masses are in GeV.

4.1.1 Particle Identification: ΔTOF Cuts

To reduce further the background due to particle misidentification, we applied ΔTOF cuts. An explanation of the cut follows. For every detected particle, the CLAS detector reconstruction algorithm records its momentum, its path length from the target vertex to the TOF counter, and its *time-of-flight* ($TOF_{measured}$). For a given particle with an assumed mass, one can also compute a $TOF_{calculated}$ from the momentum and the path length of the particle. The difference between the $TOF_{calculated}$ and the $TOF_{measured}$ is ΔTOF:

$$\Delta TOF = TOF_{measured} - TOF_{calculated}, \tag{4.1}$$

where $TOF_{measured}$ is the measured *time-of-flight*. This is the time difference between event vertex time and time at which the particle hit the TOF scintillator walls—encircling the CLAS drift chamber. The $TOF_{calculated}$ is computed as:

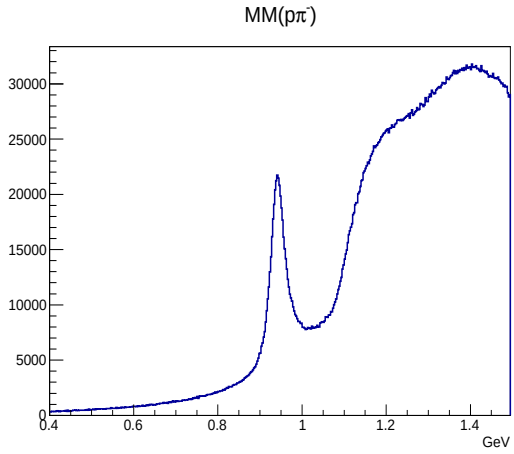

Figure 4.2: Total missing mass, $MM(\pi^- p)$. A set of cuts will be applied next to clean up the missing mass distribution. The data used to plot was Gold 2 period.

$$TOF_{calculated} = \frac{L}{c}\sqrt{1 + \left(\frac{m}{p}\right)^2}, \tag{4.2}$$

where L is the measured pathlength from the target to the TOF scintillator, c is the speed of light, m is the hypothesized mass and p is the magnitude of the measured 3-momentum. In detail, if the particles were correctly identified, then in a plot of particles' ΔTOF against their momenta, a straight horizontal band around zero should be observed. Figure 4.3 plots the protons' ΔTOF (on the left) and the π^-s' ΔTOF (on the right). Cuts at $-1 \leq \Delta TOF_{\pi^-} \leq 1$ ns were applied, but there were no ΔTOF cuts on the proton since if the negative charged particle is the π^-, then the positive charged particle must be the proton. The right plot of Figure 4.4 shows a cleaner set of events than the left plot—misidentified e^- and μ^- events were mostly rejected, and lastly, Figure 4.5 illustrates the effect of the ΔTOF cuts on the distribution of the total missing mass.

4.1.2 Detector Performance: Fiducial Cuts

It is crucial to have good simulations that represent closely the real data to "train" the BDT (more detail later); and for this reason, understanding the CLAS detectors, and simulating correctly their performances is important. However, there are some regions or elements of the detectors that are hard to simulate. To allow a reliable comparison between real data and simulation data, these regions have to be removed from both real and MC data; this section addresses this type of cuts. Primarily, we only applied cuts on the drift chamber detector (since we did not perform a cross section analysis but rather a target-beam asymmetry, simulating the *exact* CLAS acceptance is not necessary).

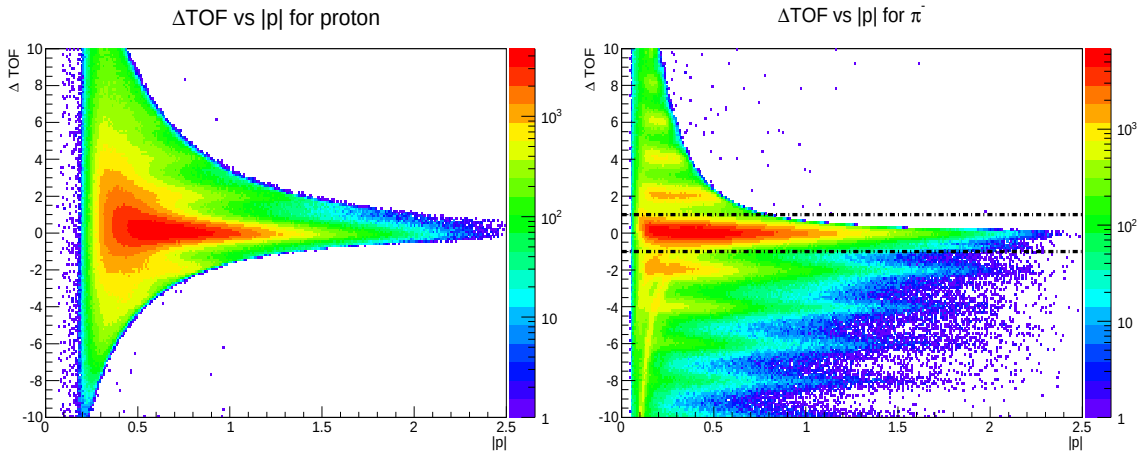

Figure 4.3: Left: Proton ΔTOF vs. $|p|$. Right: π^- ΔTOF vs. $|p|$. The horizontal band at zero corresponds to correct PID. The horizontal lines at ± 1 ns indicate the ΔTOF cuts. The horizontal bands at different times (± 2, ± 4, etc.) correspond to events with "wrong" initial photons (so they are also background events). The data used to plot was Gold 2 period. The plots are on a logarithmic scale. Time is in ns. Momentum is in GeV/c.

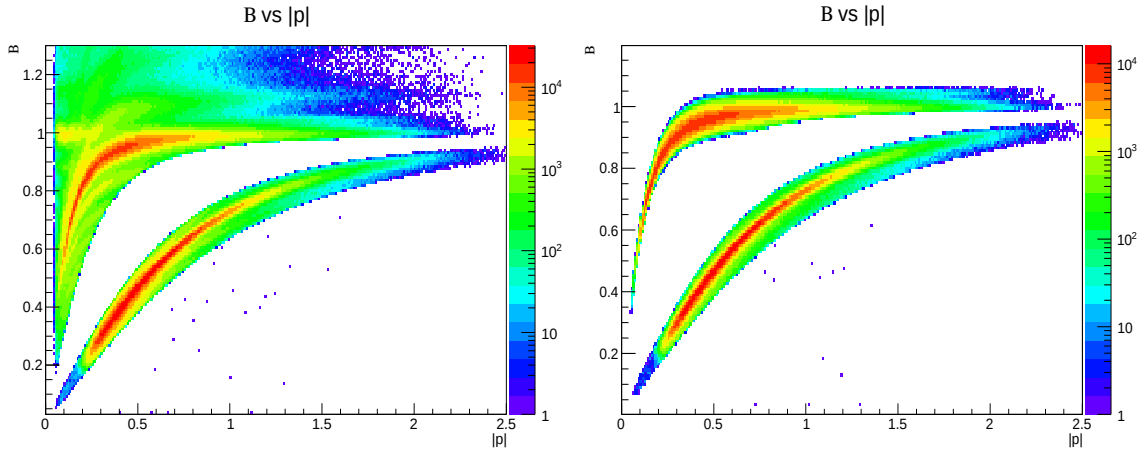

Figure 4.4: β vs. $|p|$ for selected proton and π^- before (left) and after (right) the π^- ΔTOF cuts. The data used to plot was Gold 2 period. The plots are on a logarithmic scale. Momentum is in GeV/c.

Previous studies such as the G11 works [51] advised removing events with tracks going near the superconducting torus coils where the magnetic field varies too rapidly to be properly modeled (by GSIM). We thus removed events which have *at least* one track going into these regions. Particularly, in the forward direction where the coils occupy a great amount of space, we placed a hard cut for tracks with $\cos(\Theta_{lab}) > 0.985$. In addition, we placed cuts at 0.4 rad on the angle Φ_{sector} (measured in the

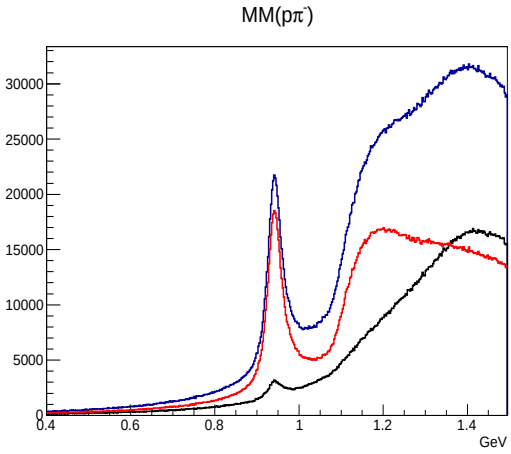

Figure 4.5: Total missing mass, $MM(\pi^- p)$ after the ΔTOF cuts is the red histogram. Events in the black histogram were rejected by the cuts. The data used to plot was Gold 2 period.

sector coordinate), consistent with g11 Φ_{sector} cuts. In other words, accepted particles had their measured $|\Phi_{sector}| < 0.4\,\text{rad}$. The Φ cuts were to remove the edges of the CLAS drift chambers (there are total six sectors cover 360^0), which are hard to simulate.

In addition, we also made cuts in the backward direction (Θ cuts). These cuts were employed to remove the target-material background events—not the same goal as the previously discussed cuts. The cut on the proton was at $\Theta_p < 90^0$, and the cut on the π^- was at $\Theta_{\pi^-} < 120^0$. These cuts are loose—when we studied the simulation data, we learned that these cuts reject only a small number of bound neutron events (see Figure 4.6). For real data, Figure 4.7 shows the angular distribution of the protons before (left) and after (right) the fiducial cuts, while Figure 4.8 shows the angular distribution of of the π^-s before (left) and after (right) the fiducial cuts. Finally, we show the total missing mass after the fiducial cuts in Figure 4.9.

4.1.3 Proton and π^- Momentum and Angular Cuts

As shown in the red histogram of Figure 4.9, the depth of the "valley" on the right side of the spectator proton mass (near 1.0 to 1.1 GeV) is modestly high. This is a strong indication that the background "leaking" in under the proton peak is still significant. The two methods for selecting the bound neutrons, which will be discussed in the next two sections, could not completely remove these events. Nevertheless, these background events should be removed because they might effect the E measurements. Hence, we applied cuts on the scattered (detected) protons and π^- to reject a portion of this background. The applied cuts were motivated by studying the joint distributions of the total missing mass and the measured momentum of the

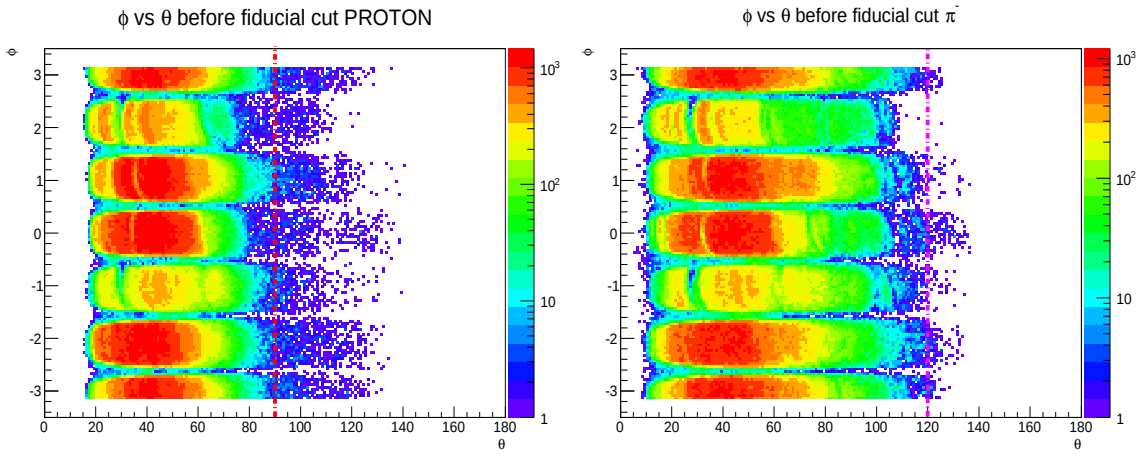

Figure 4.6: Left: proton angular distribution: ϕ vs. Θ before the fiducial cuts. Right: π^- angular distribution: ϕ vs. Θ before the fiducial cuts. The vertical lines indicate the extra cuts on the proton and π^- to reject target-material background events. ϕ is in rad, while Θ is in degree. The data used to plot was simulation data of the signal channel. The plots are on a logarithmic scale.

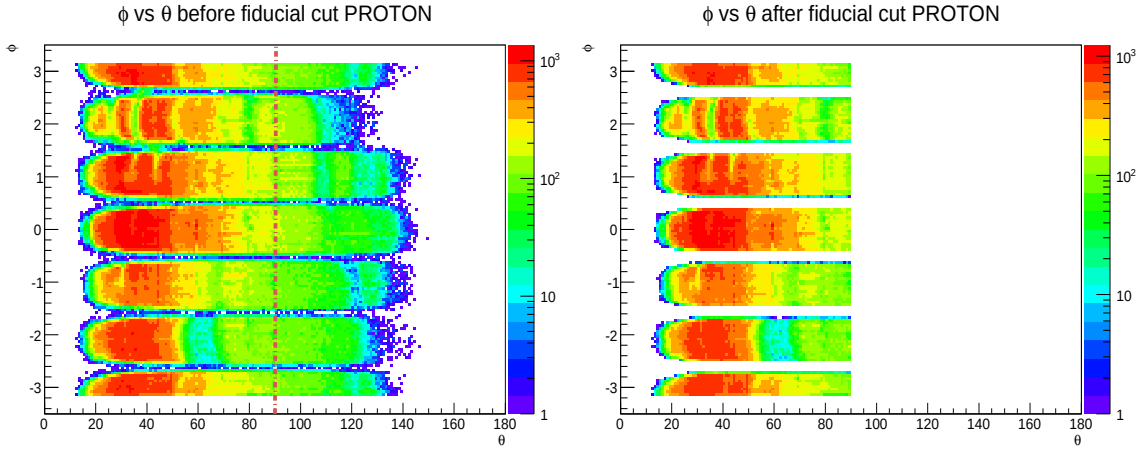

Figure 4.7: On the left (right) proton angular distribution: ϕ vs. Θ before (after) the fiducial cuts. ϕ is in rad, while Θ is in degree. The data used to plot was Gold 2 period. The plots are on a logarithmic scale.

scattered (detected) protons and π^-, see Figure 4.10, 4.11. Furthermore, we had different cut values—the cuts for Gold 2 on the π^- would be too tight for the Silver periods; the values of these cuts are presented in Table 4.1 (the differences in the joint distributions for the Gold 2 and Silver periods possibly come from the electron energy: about 2.5 GeV for the Gold 2 period and about 2.2 GeV for the Silver periods). As shown in Figure 4.12 the background was modestly reduced. These cuts concluded our procedure of selecting events from the reaction $\gamma d \to \pi^- p(p_s)$.

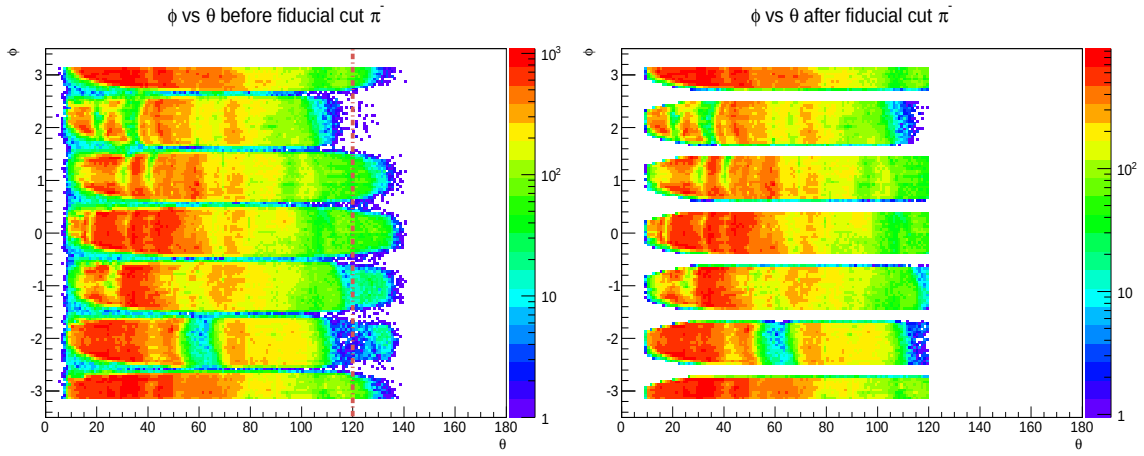

Figure 4.8: On the left (right) π^- angular distribution: ϕ vs. Θ before (after) the fiducial cuts. ϕ is in rad, while Θ is in degree. The data used to plot was Gold 2 period. The plots are on a logarithmic scale.

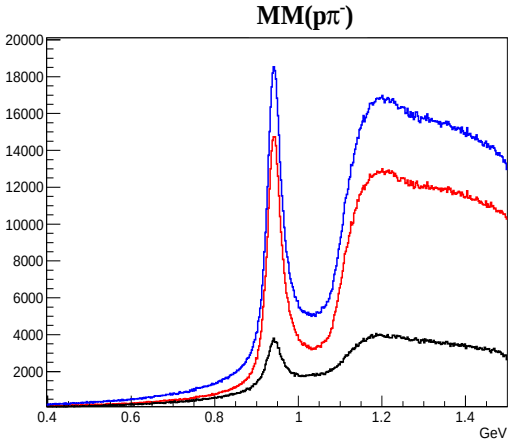

Figure 4.9: Total missing mass, $MM(\pi^- p)$ after the ΔTOF cuts is the blue histogram, and the red histogram is after the fiducial cuts. Events in the black histogram were rejected by the fiducial cuts. The data used to plot was Gold 2 period.

Cut	Gold 2 period	Silver periods
$\|p\|_p$	$\geq$0.40 GeV	$\geq$0.40 GeV
$\|p\|_{\pi-}$	$\geq$0.40 GeV	$\geq$0.27 GeV

Table 4.1: Cut values on the scattered protons and π^-s for Gold 2 period and Silver periods, respectively.

4.2 Selection of $\gamma d \to \pi^- p(p_s)$ Events

The next task was to select events originating from the bound neutrons. Consequently, there are two types of background to be removed: from target material (aluminum

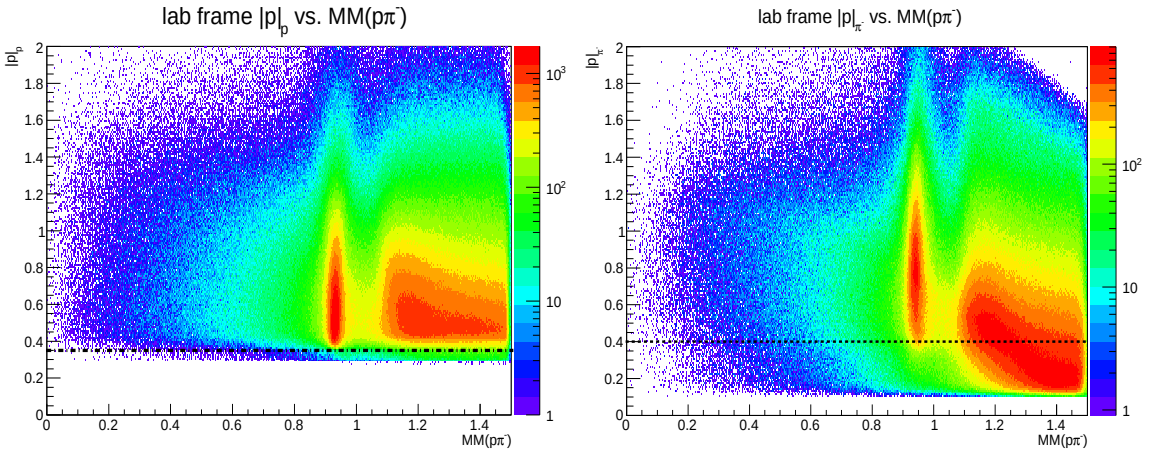

Figure 4.10: Left: Proton momentum $|p|$ vs. $MM(\pi^- p)$. Right: π^- momentum $|p|$ vs. $MM(\pi^- p)$. The data used to plot was the Gold 2 period. The plots are on a logarithmic scale. The horizontal lines indicate the cuts. The $MM(\pi^- p)$ is in GeV, while $|p|$ is in GeV/c.

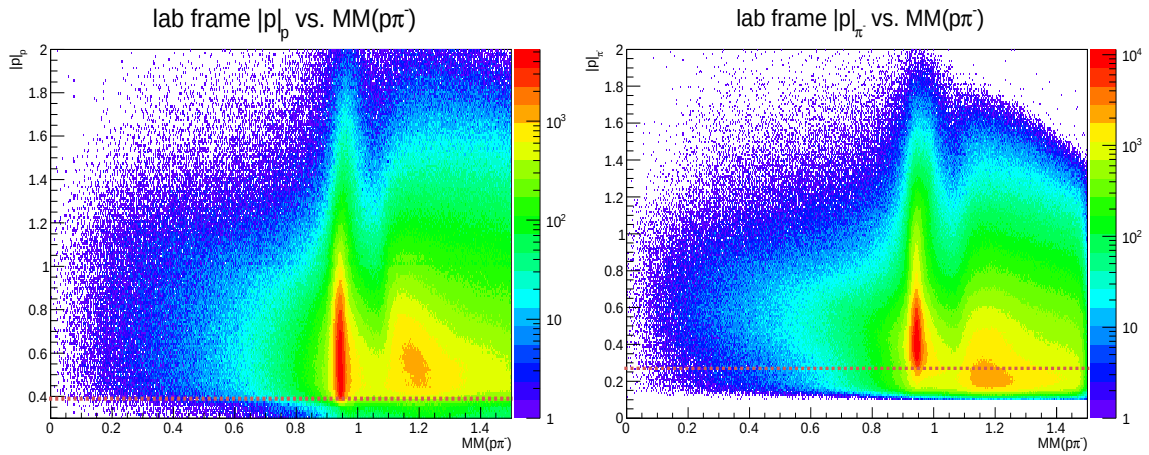

Figure 4.11: Left: Proton momentum $|p|$ vs. $MM(\pi^- p)$. Right: π^- momentum $|p|$ vs. $MM(\pi^- p)$. The data used to plot was the Silver 1 period. The plots are on a logarithmic scale. The horizontal lines indicate the cuts. The $MM(\pi^- p)$ is in GeV, while $|p|$ is in GeV/c.

wires and KelF cell caps) and from the Δ and/or multi-pion reactions. The Δ reaction background consists of events with an extra missing pion (i.e., $\gamma d \rightarrow \pi^- \Delta(p_s) \rightarrow \pi^- p(\pi p_s)$).

Since the target background has zero E asymmetry—will be shown in Section 4.3, it will dilute the final E measurements if not fully removed. The Δ and/or multi-pion backgrounds are not the reactions of interest, and should be rejected as well. In the next two sub sections, we will introduce two methods for the bound neutron

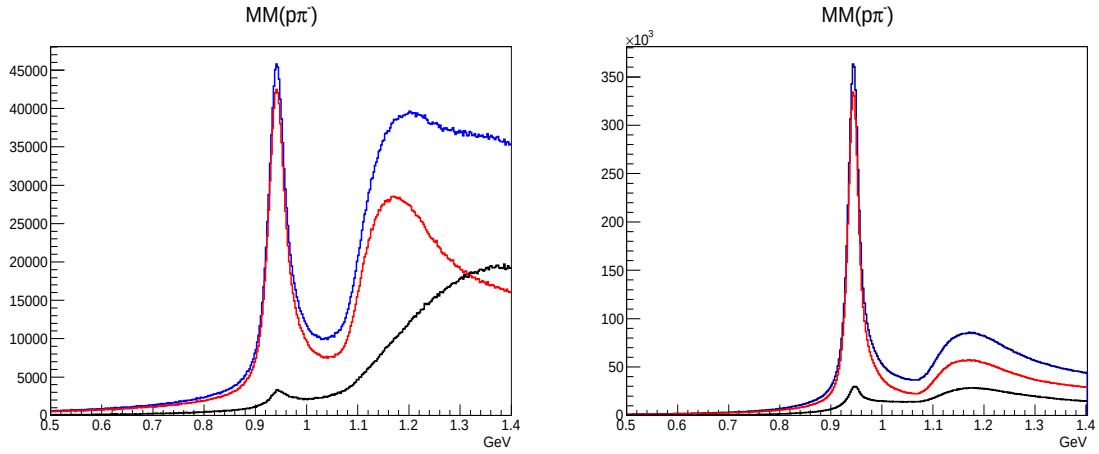

Figure 4.12: Left: $MM(\pi^- p)$ from the Gold 2 run period. Right: $MM(\pi^- p)$ from the Silver 1 run period. For both plots, the blue histograms are before the momentum cuts, the red histograms are after the cuts, and the black histograms represent events that were rejected by the cuts .

event selection. The first method is referred to as 1D-cut background suppression and subtraction which includes a set of cuts to remove the mentioned background especially the Δ and multi-pion backgrounds; any remaining target background is accounted for by utilizing the empty target run data for "subtraction" hence the name background subtraction. The second method employs a Boosted Decision Trees algorithm (BDT) to efficiently separate the signal and background (we will verify later that the BDT has better performance than the 1D-cut background suppression and subtraction method). In brief, the BDT is a "forest" of decision trees build by "learning" from training data—which has distributional representations of the signal and background real data (more detail later). The algorithm performs efficiently because it can "view" the multivariate data in a high dimensional space (while we humans can only view the data at most in three dimensions simultaneously) in which the signal and background data have better "separation."

4.2.1 1D-Cut Background Suppression and Subtraction Method

As mentioned above, the 1D-cut background suppression and subtraction method comprised of several cuts to remove the background. To determine the values for the cuts, we studied the simulated data for $\gamma n(p_s) \rightarrow \pi^- p(p_s)$. Each simulated event consisted of an incident photon from a bremsstrahlung distribution, while the detected p and π^-were generated from a two-body phase space distribution, and lastly, an *independent* spectator proton p_s with its momentum distribution followed the Hulthen potential [57] (there are two other models for the deuteron potential [58, 59] which are considered more accurate, but for our purpose the Hulthen potential

is sufficient). The formula used for the Hulthen wavefunction is:

$$\Phi(p) = \left[\frac{1}{p^2 + (\alpha\hbar)^2} - \frac{1}{p^2 + (\beta\hbar)^2}\right]^2, \tag{4.3}$$

where $\alpha = 0.2316\ (fm)^{-1}$, and $\beta = 1.385\ (fm)^{-1}$ from [60]. Figure 4.13 shows the simulated distributions of three variables that we placed the cuts on, and in Table 4.2 we provide numerical values of the cuts. The missing mass cut was to reject mostly events with an extra missing pion (see Figure 4.12). Coplanarity angle helped to reject events where the missing momentum is high. Of course, the two cuts also rejected a significant number of events from the target background as shown in Figure 4.14—plotting the empty-target run data. We show the cuts on similar histograms for Gold 2 data in Figure 4.15. On the missing momentum plot of Figure 4.15 we also include a (scaled) histogram from the simulation data for comparison. Obviously, the missing momentum cut at 0.11 GeV/c (see Table 4.2) seems tighter than suggested by the simulation data, but this is the maximum value such that there would be a few Δ and/or multi-pion background events. We will discuss why and how we determined this value in the next sub section after introducing the "subtraction" part of the method.

Variable Name	Description	Cut Value
Missing Mass	Total Missing Mass, $MM(\pi^- p)$	$\leq$1.05 GeV
Missing Momentum	Total Missing Momentum	$\leq$0.11 GeV/c
Coplanarity Angle	$\arccos\left(\hat{p}_p \times \hat{p}_\gamma\right) . \left(\hat{p}_{\pi^-} \times \hat{p}_\gamma\right)$	$\leq 20^0$

Table 4.2: List of variables used in 1D-cut background suppression and subtraction for the task of selecting the bound neutron events.

Previously, we claimed (and will verify) that after the three cuts, there would be an insignificant number of events which are not $\gamma d \to \pi^- p(p_s)$, however, there was still some remaining target background events. Below we provide a procedure to estimate the remaining target background (which will be used extensively in later sections):

1. Plot the z component of the interaction vertex for both empty target runs and full target runs, and,

2. Scale the histogram from the empty target so that the outside of the target region ($z > -1.0\,\text{cm}$) of both histograms matched, see Figure 4.16. This is to account for different incident beams from different run periods.

3. Record the value of the scaling, denote as ε. Note that since Gold 2 target has less aluminum material, ε is scaled down by a factor of 0.7 (see Table 2.2).

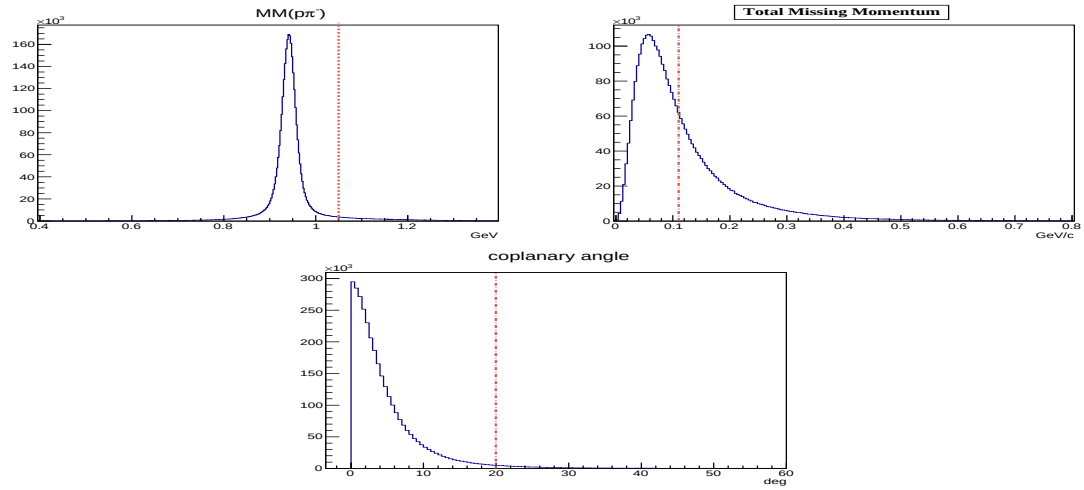

Figure 4.13: Top left: Total missing mass, $MM(\pi^- p)$. Top right: Total missing momentum. Bottom: coplanarity angle (see explaination in Table 4.2). The vertical lines are the adopted cuts for the real data. These histograms were obtained from the signal simulation data.

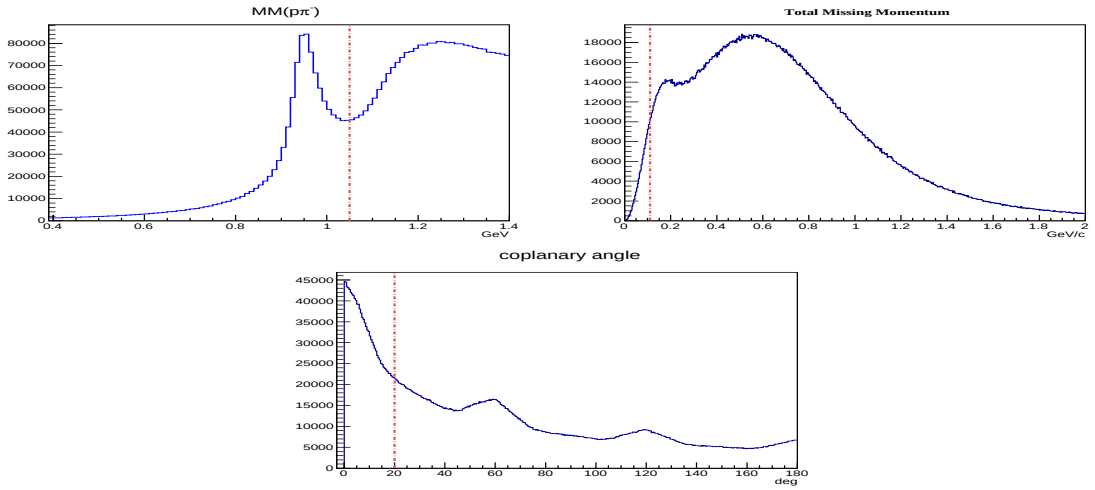

Figure 4.14: Top left: Total missing mass, $MM(\pi^- p)$. Top right: Total missing momentum. Bottom: coplanarity angle (see explaination in Table 4.2). These were obtained from the empty-target data.

4.2.1.1 Determination of a Cut Value on the Total Missing Momentum

Here we address the decision to place a cut on the total missing momentum at 0.11 GeV/c. In general, one way to check for an effect of the missing momentum cut is to vary it and observe how the E asymmetry evolves as the mentioned cut varies (detail of how to obtain the E asymmetry and target-material background subtraction will be

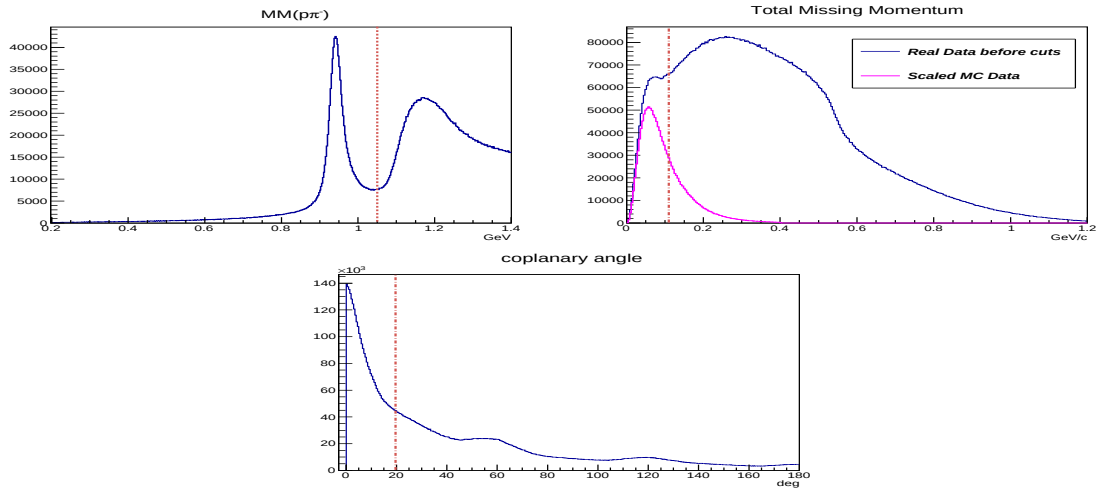

Figure 4.15: Top left: Total missing mass $MM(\pi^- p)$. Top right: Total missing momentum (the magenta histogram is from the simulation data). Bottom: coplanarity angle (see explaination in Table 4.2). These plots were obtained from the Gold 2 data.

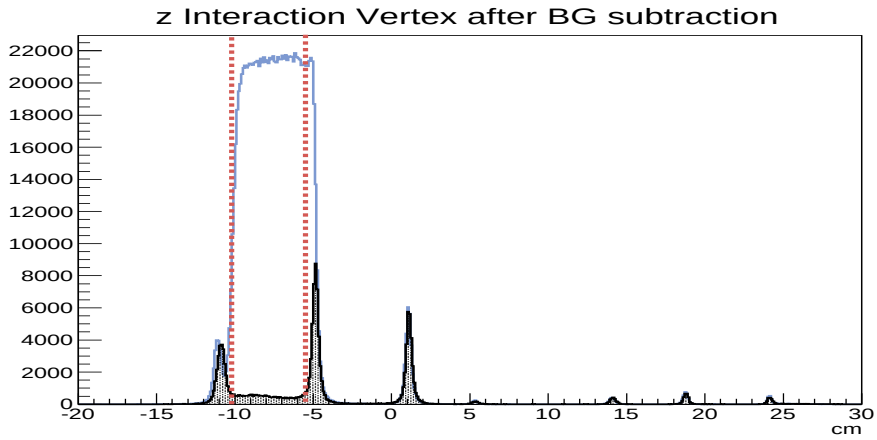

Figure 4.16: z-vertex plots from Gold 2 (blue), and scaled empty run (black). The region $-10\,\text{cm} < z < -5.5\,\text{cm}$ of Gold 2 has less aluminum material (down by a factor of 0.7).

presented later). Figure 4.17 shows comparisons of the E values between cuts at 300, 200, 150, 75 MeV/c and the cut at 110 MeV/c (all plots were after target-material background subtraction). Clear evidence of a "shifting" effect on the E values for cuts larger than 110 MeV/c is seen. Comparison of the E values between 110 MeV/c and 75 MeV/c shows statistical consistency. Because the empty target background had been "subtracted" away in these plots, a possible explanation for the obseved effect is that there was still remaining Δ and/or multi-pion backgrounds, which might have

positive E asymmetry that led to upward shifting for the E asymmetry of the reaction $\gamma d \to \pi^- p(p_s)$. To verify that, we "combined" the simulation data—scaled appropriately, and the scaled—using the procedure discussed previously—empty data; then compare the combined distribution with the distribution from the full target data (Gold 2 data in particular). As shown in Figure 4.18 the histogram from "combined" data only *matches* the histogram from the full data if the missing momentum is less than 110 MeV/c—supporting our estimation. As a result, we decided to place a cut on the total missing momentum at 110 MeV/c.

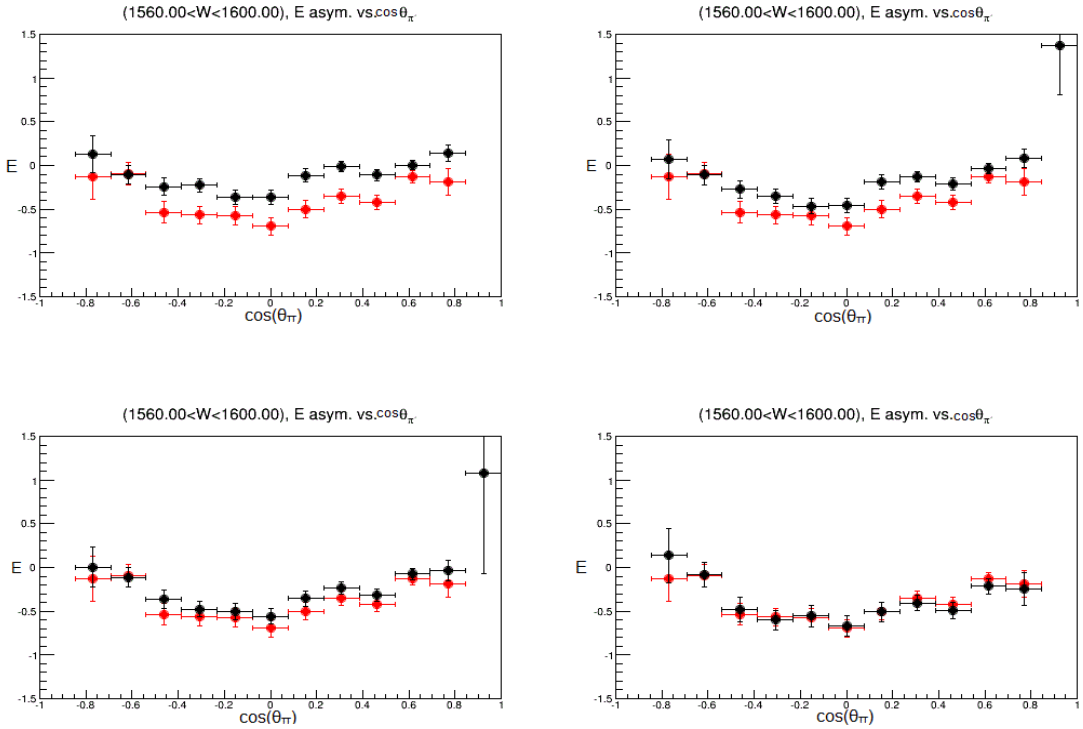

Figure 4.17: Top left: Comparing E asymmetry values for missing momentum cut at 300 MeV/c (black) and at 110 MeV/c (red). Top right: comparing between 200 MeV/c (black) and at 110 MeV/c (red). Bottom left: comparing between 150 MeV/c (black) and at 110 MeV/c (red). Bottom right: Top right: comparing between 75 MeV/c (black) and at 110 MeV/c (red). The evolutions of the E values suggest the unaccounted Δ and/or multi-pion backgrounds for missing momentum larger than 110 MeV/c.

4.2.2 Boosted Decision Trees Method

The set of cuts for the 1D-cut background suppression and subtraction method (see Table 4.2) is well-calibrated to reject most of the background. However, cuts, in general, are not the most efficient method to remove background. Firstly, cuts may

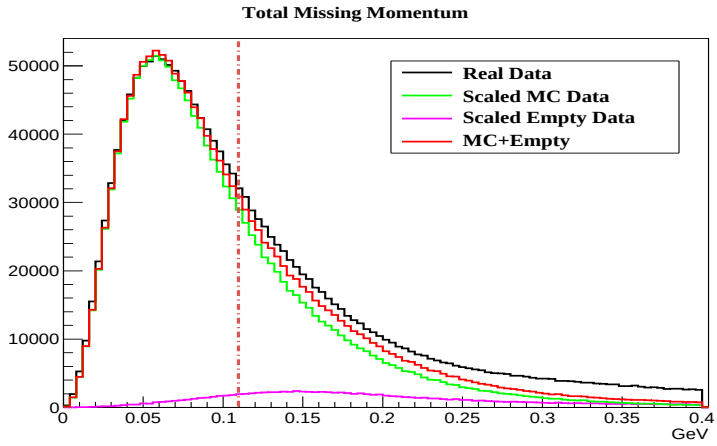

Figure 4.18: Missing Momentum distribution; "combined" data (red) from scaled empty and simulation underestimates the full-target real data (black) for momentum greater than 110 MeV/c.

ignore a significant portion of the interesting phase space. For example, a *signal* event that failed the missing momentum cut would not be reconsidered even though it might pass the others (the cut on the missing momentum is very tight). Second, since the cuts were applied sequentially, the data were "viewed" only in one dimension at a time—yet it is highly multidimensional (characterized by many independent kinematic variables). In many situations, "viewing" multivariate data in highly multidimensional space—i.e., plotting the data simultaneously in many coordinates—reveals more structure of the data. Or equivalently, projecting the data into lower dimensional space reduces available (possibly useful) information. In conclusion, those two reasons are inherent limitations for the 1D-cut-background-suppression-and-subtraction method. Consequently, in this section, we introduce a *multivariate* analysis tool called Boosted Decision Trees (BDT) as a more optimal method to do the event selection. In particular, it is more efficient because it consists of features to overcome the mentioned limitations that prevent the 1D-cut background suppression and subtraction method achieving optimal performance (or efficiency).

The Boosted Decision Trees (BDT) tool is an algorithm for building a "forest" of *distinct decision trees* that are linked together by a *boosting* mechanism. Each decision tree constitutes a *disjunction* of logical conjunctions (i.e., a graphical representation of a set of *if-else* rules). Thus, the whole phasespace is considered by every decision tree. Moreover, the decision trees are designed to "view" any multivariate data in highly multidimensional space; hence they utilize available structural information from the data more optimally. Necessarily, it is important to know that the "forest" of distinct and *boosted* decision trees has better performance than any individual decision tree in the "forest." Informatively, the BDT algorithm has been used in particle physics data analyses, for example, the BABAR collaboration employs

the BDT for Muon and Kaon particle identifications [61], and the GlueX collaboration at Jefferson Laboratory is planning to use the BDT algorithm for Kaon particle identification. We also provide pedagogic details about the BDT algorithm in Appendix A (in particular, we explain how the trees are distinct, and what the boosting mechanism is).

The cuts in Table 4.2 for the 1D-cut background suppression and subtraction method are particular to the desired task of separating the bound neutron events from the background (we will use "separation" and "classification" interchangeably). They were based on the distributional characteristics of the signal and background events. The BDT algorithm is similar in that we needed to provide "training" data so that the algorithm could infer the distributional difference between the signal and background data. Importantly, training data must have the same distributional characteristics as the real data but with only one additional feature: the category (signal or background) of each training event is known. Usually the training data is generated from simulation. For our case, we only simulated training *signal* data. The simulation consisted of incident photon from a bremsstralung distribution, a two-body phase space distribution for the scattered p and π^-, and an *independent* spectator p_s with its momentum distribution generated from the Hulthen potential [57] (see equation 4.3). The MC data was processed by GSIM, GPP, and USERANA to simulate the CLAS detector efficiency (see section 3.5 for more detail). We used the empty target run data as the training *background* data. Implicitly, we had assumed the empty target background could also represent the physics background (the Δ and other multi-pion backgrounds); it is a valid assumption because that same physics reaction occurs for the empty target run data as well.

We employed a ROOT based analysis package called TMVA to execute the BDT algorithm [56] (see Appendix A for more detail about the package). The package implementation facilitates the classification task. Particularly, each event after being processed by the BDT acquires a single real number (referred to as BDT output) between -1 and $+1$—the more positive the BDT output is, the more likely it is signal, and vice versa. Thus we needed only to make a cut on this BDT output variable to separate (or classify) the signal and background events. Furthermore, each event (both signal and background) consisted of ten continuous variables (for example, one of the variables is the total missing momentum), and—*in the case of training data*—one two-value discrete variable to indicate whether the event is signal or background. Table 4.3 provides definitions of the input continuous variables. The last three variables are the Dirac light-cone coordinate variables [62]. Note that only variables from the missing particles (in the case of signal events, the missing particle is the spectator proton) were used. This was to reduce the requirement for generating simulation data that must exactly match the real data. Ideally, if the reaction are really *quasi-free*, then the spectator protons needed to be the "isolated" partners and their kinematic variables should then have low dependencies on other variables such as the incident photon energy, the measured momentum of the detected π^-,

etc. In other words, modeling the bound neutron events ($\gamma d \rightarrow \pi^{-} p(p_s)$) should not be concerned about other distributions beside the kinematic distributions of the spectator proton—i.e., must only model correctly the Hulthen's wave function for the spectator proton [57]. Once the simulation signal data was ready to use, we supplied the training data and executed the TMVA ROOT program to build (or "train") the decision trees. Histograms of input variables are illustrated in Figures 4.19, and 4.20; blue histograms show signal training data, and red histograms show background training data.

Variable Name	Description
$CoplanarityAngle$	$(\hat{p}_p \times \hat{p}_\gamma) \,.\, (\hat{p}_{\pi^-} \times \hat{p}_\gamma)$
$MissingMomentum$	Total missing momentum
$MissingEnergy$	Total missing energy
$MissingTheta$	Θ of missing momentum
$MissingPhi$	Φ of missing momentum
$MissingBeta$	β
$MissingGamma$	γ
$MissingPlus$	$E^{missing} - c\lvert p_z^{missing}\rvert$
$MissingMinus$	$E^{missing} + c\lvert p_z^{missing}\rvert$
$MissingPerp$	$\lvert p_{transverse}^{missing}\rvert$

Table 4.3: List of variables used to construct the BDT for the task of selecting the bound neutron events. The last three variables are the so-called Dirac light-cone coordinate variables [62]. In addition, note that we only used kinematic variables from the missing particle for the reason mentioned previously (see text).

Since the desired task for the BDT was to separate signal and background events in the real data where we do not know the true identity of each event, it is required that the BDT has consistent performance (or classification efficiency) on both the training data and the real data. Formally, this is referred to as no *overtraining* (or *overfitting*); i.e., the BDT must generalize well for some other independent but similar—to the training data—data sets. To check for overtraining the ROOT TMVA program divided the signal and background training data randomly into four subsets: signal and background training data, and signal and background testing data. The program ran the BDT and evaluated the BDT's performances on the four data sets by employing the Kolmogorov–Smirnov test—to verify whether the BDT output distributions from the training and testing data are statistically the same (note that the test is applied separately on signal data and background data). *High* probabilities from the Kolmogorov-Smirnov test as shown in Figure 4.21 suggest consistent performances on training and independent test data sets—or equivalently, *no* evidence of *overtraining* observed because according to the Kolmogorov-Smirnov test the distributions of the BDT output from the training data sets and the test data sets are statistically similar

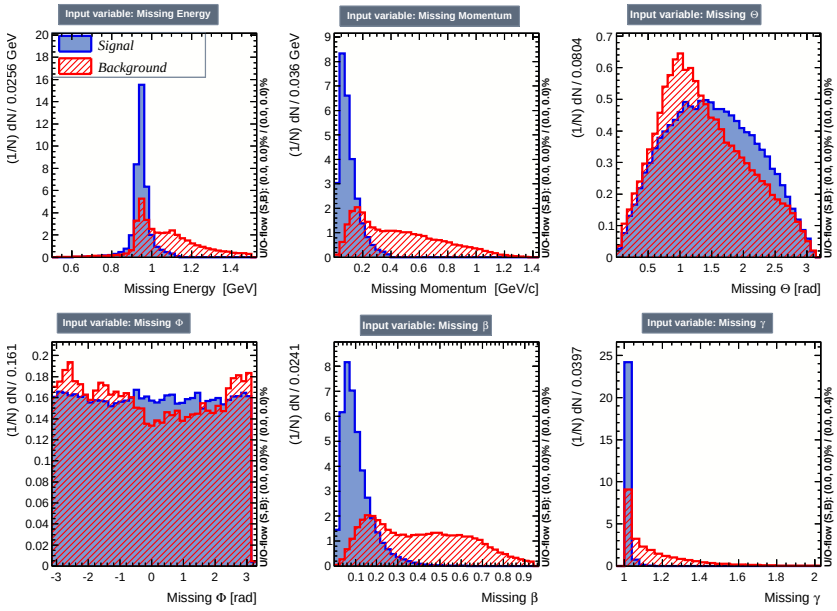

Figure 4.19: Histograms of input variables used to construct both BDT during training phase. The red histograms are from background (empty target run period), and the blue histograms are from the signal simulation data.

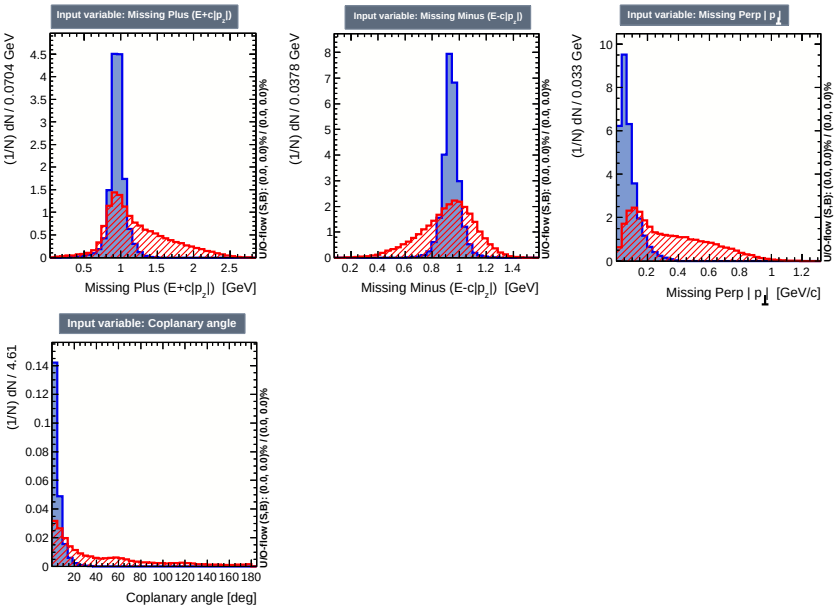

Figure 4.20: More histograms of some of the input variables used to construct both BDT during training phase. The red histograms are from background (empty target run period), and the blue histograms are from the signal simulation data.

(see Appendix A for how to "fix" an overtrained BDT). Figure 4.22 shows cut efficiencies and an optimal cut value. i.e., the efficiencies of selecting and rejecting signal and background data, respectively, as a function of the BDT output (recall that for every event after being processed through the BDT, each event is a value between -1 and $+1$). An optimal cut at 0.03 that maximizes the $S/\sqrt{S+B}$ ratio, which statistically means minimizing the misclassification cost, will be used—to obtain this number we must provide the *initial* signal (S) to background (B) ratio which we estimated to be roughly one to two. In particular, from Figure 4.23 we could estimate the numbers of signal and background events (the *one-to-two* ratio is roughly accurate for all the events with the missing momentum less than 400 MeV/c—only these events were processed by the BDT). Nevertheless, when studying systematic uncertainties, we will vary this cut to study its effect. Furthermore, in Figure 4.24, we plot background rejection efficiency vs. signal efficiency; in other words, it is a plot of the background rejection efficiency as a function of the signal efficiency. Lastly, we include Table 4.4 for a qualitative assessment on how often each variable was used in building the BDT, and for illustration, Figure 4.25 shows the first constructed decision tree.

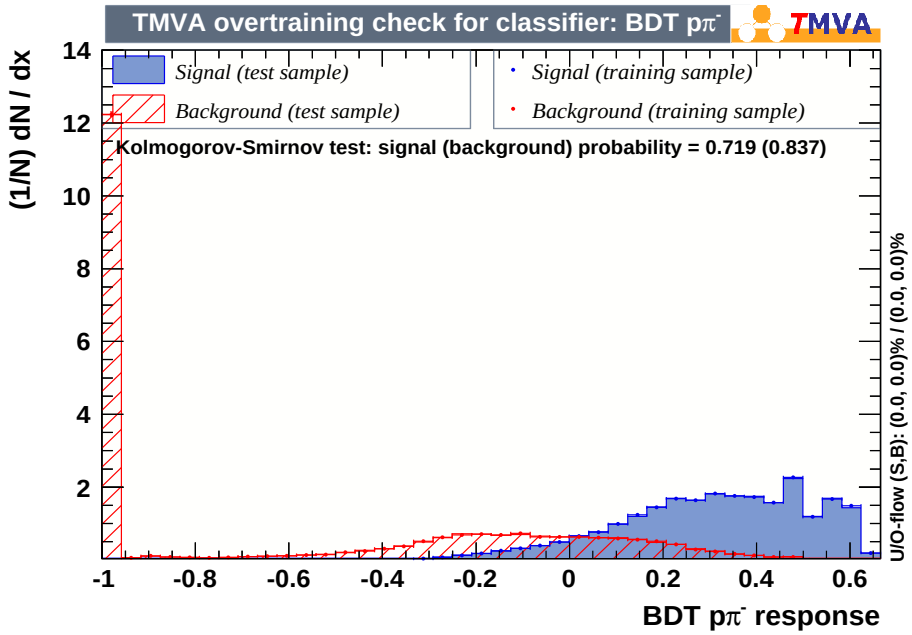

Figure 4.21: Overtraining check, *high* Kolmogorov-Smirnov probabilities for both signal and background suggest *no overtraining* because the performance (distributions) of the BDT is consistent with independent training and testing data sets.

In Figure 4.26, on the left for simulation signal data we show the total missing mass before ("blue" histogram) and after the BDT cut (i.e., selected events in "red" and rejected events in "black"), and the total missing momentum before and after the cut on the right. Similarly, in Figure 4.27 for the empty target run period the

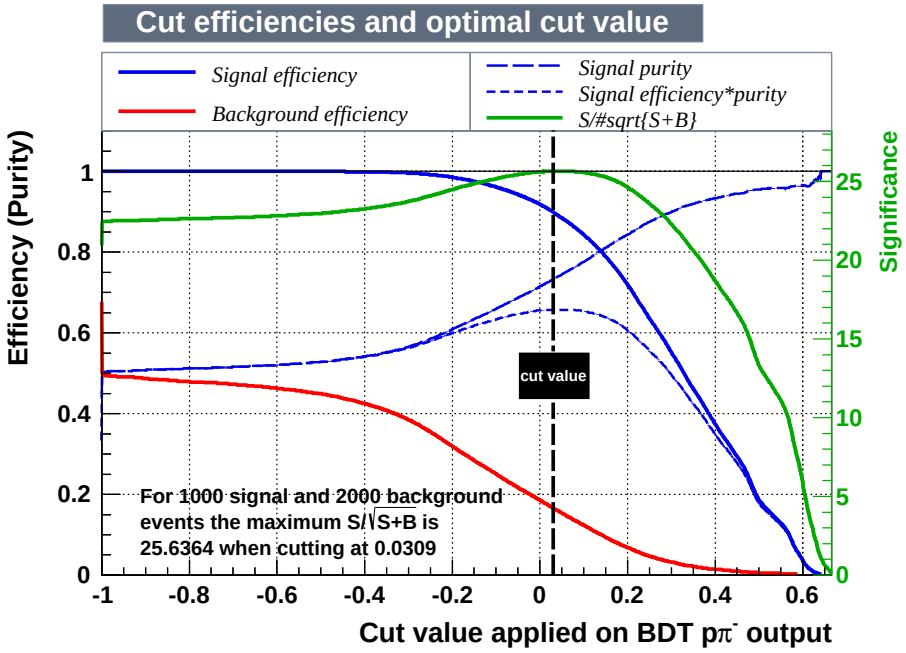

Figure 4.22: Plot of cut efficiencies show the efficiencies as a function of cut value, and an optimal cut value at 0.03 assuming the *initial* signal-to-background ratio is one-to-two (roughly accurate for all the events with the missing momentum less than 400 MeV/c).

Variable Name	Relative Ranking
$MissingMomentum$	1.00
$coplanarityAngle$	0.37
$MissingMinus$	0.25
$MissingEnergy$	0.23
$MissingPerp$	0.07
$MissingTheta$	0.06
$MissingPlus$	0.05
$MissingGamma$	0.05
$MissingBeta$	0.04
$MissingPhi$	0.02

Table 4.4: Table of relative variable ranking. The higher the ranking the more the variable was used to construct the trees. All the rankings were normalized to the absolute ranking of the missing momentum variable.

missing mass and the missing momentum before ("blue" histogram) and after the cut (i.e., *wrongly* selected events in "red" and *correctly* rejected events in "black") are shown on the left and right plots, respectively. Additionally, for empty data, we also

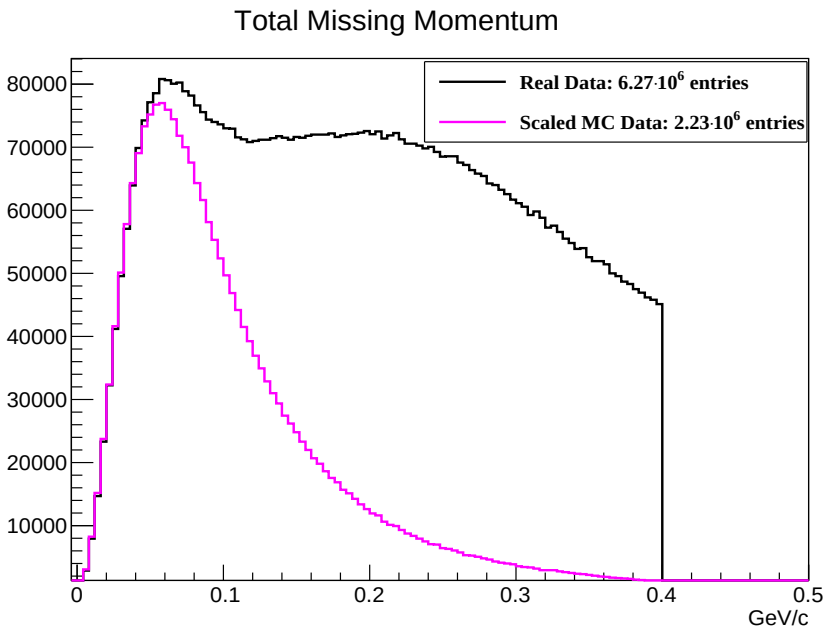

Figure 4.23: Total missing momentum; the black histogram is from Gold 2 data, and the magenta histogram is from the simulation data. From these histograms we estimated the signal-to-background ratio to be one-to-two.

plot the z-component of the interaction vertex in Figure 4.28. From the three figures, we concluded that the signal selection and the background rejection efficiencies of the BDT are outstanding.

In conclusion, we introduced the BDT algorithm as a—yet to be proven—better alternative to the 1D-cut background suppression and subtraction method and we presented the procedure to "train" the BDT as well as verified that the BDT had consistent performances on both training and testing data (no overtraining). Furthermore, we decided to place a 0.03 cut on the BDT output variable to optimally separate (classify) the signal and background events—the cut minimizes misclassification cost. We will employ the constructed BDT on the real data (the Gold 2 and Silver data sets) to select the bound neutron events in the next section.

4.3 Obtaining the E Observable Measurements

In this section we describe procedures to obtain measurements of the E observable for the reaction $\gamma d \to \pi^- p(p_s)$ where each event consists of detected proton and π^- with a missing spectator proton. We discussed previously the two methods that we employed to reject the main backgrounds for this particular reaction. We will show that the BDT method provides consistent results with the typical method of 1D-cut background suppression and subtraction and, additionally, illustrate that the BDT

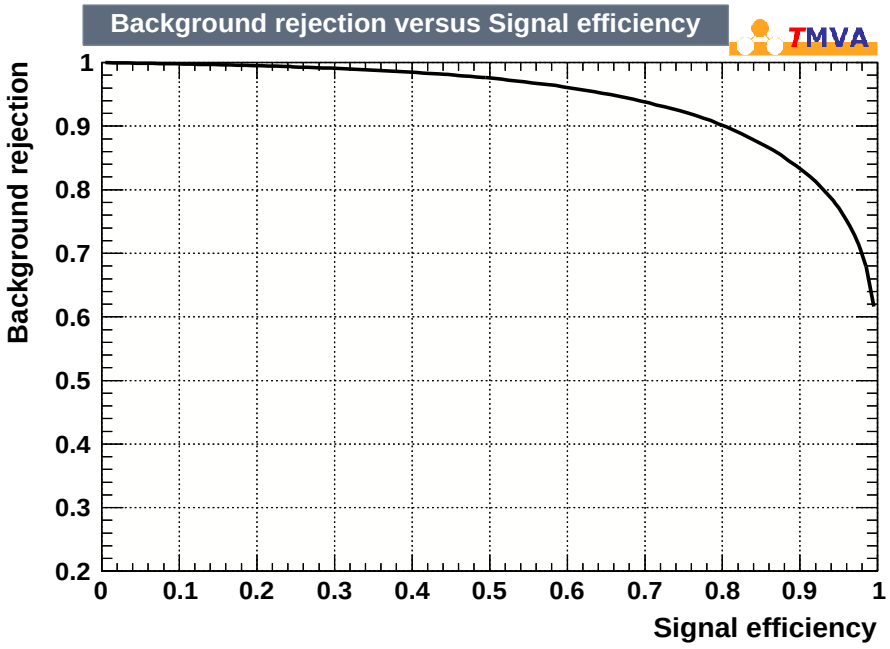

Figure 4.24: Background rejection vs. Signal efficiency of the constructed BDT for training (signal and background) data.

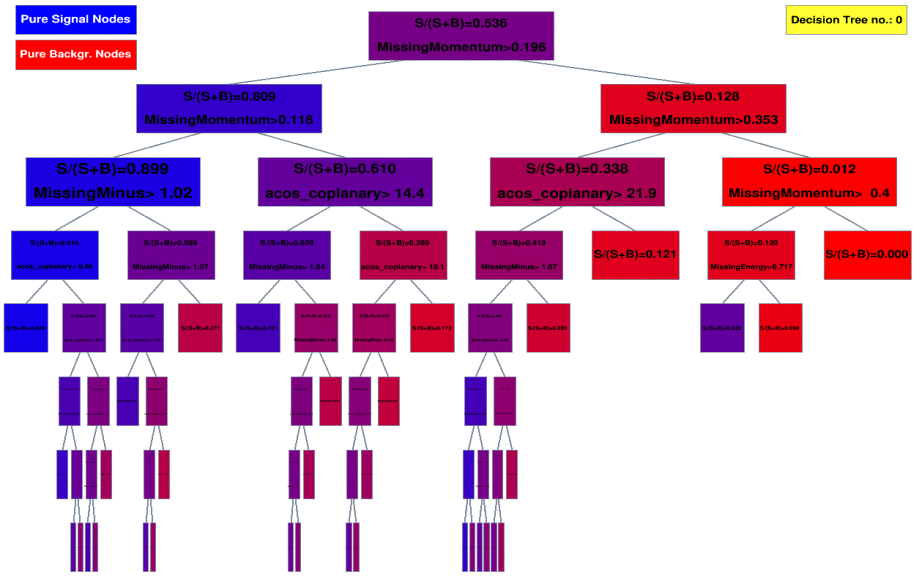

Figure 4.25: The first constructed decision tree, for illustration (see Appendix A for more detail). Note that all variables can be used multiple times.

method is more efficient than the other method, i.e., the event sample from the BDT method is larger than the event sample from the 1D-cut background suppression and subtraction method. Moreover, we will introduce a procedure to estimate the target

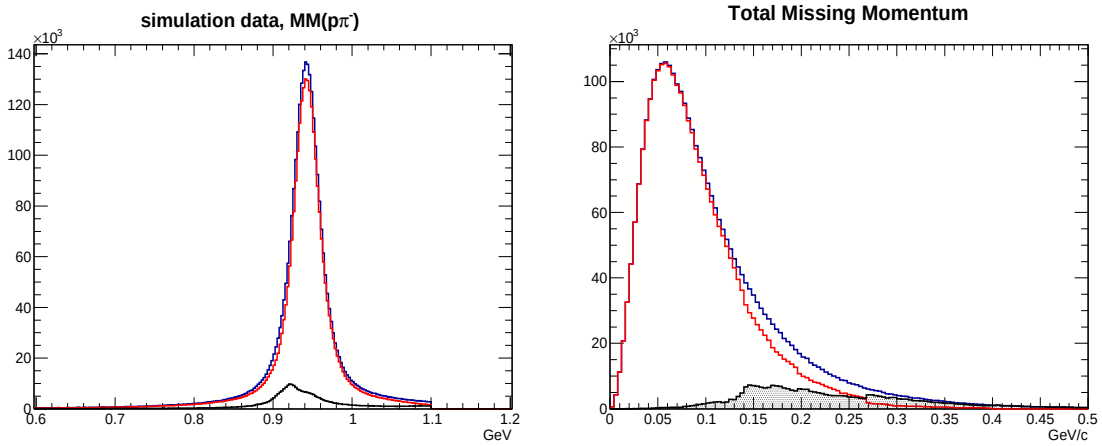

Figure 4.26: Left: Total missing mass, $MM(\pi^- p)$ before ("blue") and after the BDT cut (selected events in "red" and rejected events in "black"). Right: Missing momentum before ("blue"), and after the BDT cut (selected events in "red" and rejected events in "black"). The plots were constructed from the MC data. The *selection* efficiency is outstanding.

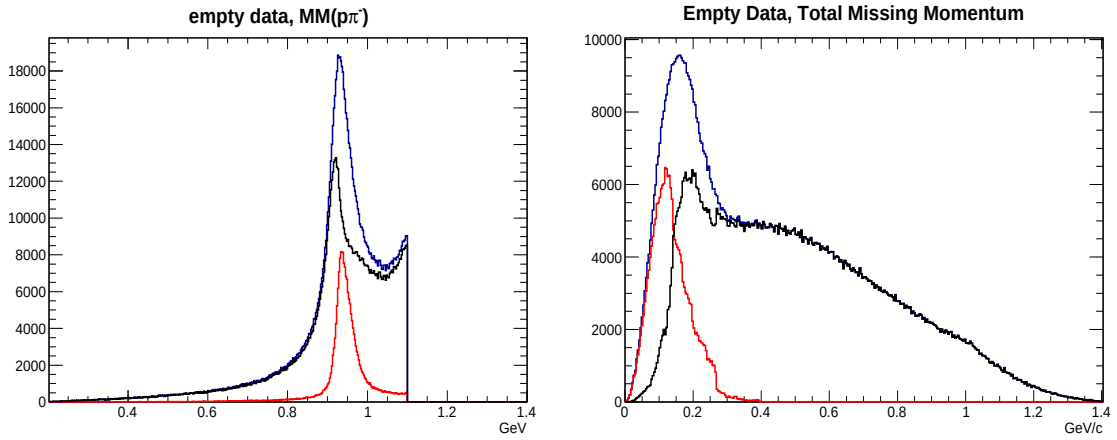

Figure 4.27: Left: Total missing mass, $MM(\pi^- p)$ before ("blue") and after the BDT cut (*wrongly* selected events in "red" and *correctly* rejected events in "black"). Right: Missing momentum before ("blue"), and after the BDT cut (*wrongly* selected events in "red" and *correctly* rejected events in "black"). The plots were constructed from the data of the empty target runs. The *rejection* efficiency is high.

polarization for Silver 4 and Silver 5 run periods using the Silver 1&2 run periods. And finally, we will plot the combined E asymmetry results from all the run periods.

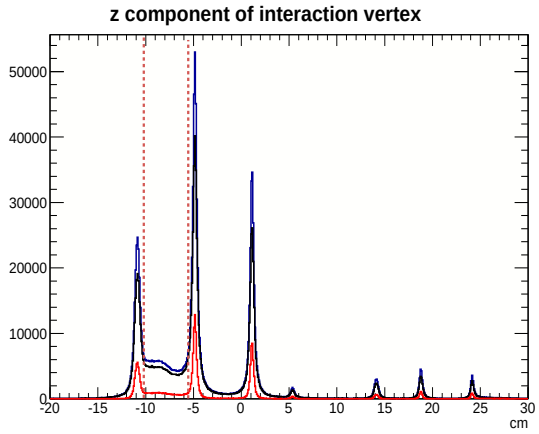

Figure 4.28: z-component of interaction vertex before ("blue"), and after the BDT cut (*wrongly* selected events in "red" and *correctly* rejected events in "black"). The plots were constructed from the data of the empty target runs. The *rejection* efficiency is high.

4.3.1 The E Asymmetry Observable

The measurements of the E observable requires the incoming photon and the target to be circularly and longitudinally polarized, respectively. The g14 experiment had these conditions. Formally, the formula to calculate the E observable for each W_i energy window is:

$$E_{ij}(x_j) = \frac{1}{\overline{{}_iP_\gamma}} \frac{1}{P_{target}} \frac{{}_iY(x_j)^{\downarrow\uparrow} - {}_i\,Y(x_j)^{\uparrow\uparrow}}{{}_iY(x_j)^{\downarrow\uparrow} + {}_i\,Y(x_j)^{\uparrow\uparrow}}, \tag{4.4}$$

where x_j is the j^{th} measuring bin of either the missing momentum, or the missing mass, or the z-vertex, or $\cos(\theta_{\pi^-})$ variable (measuring the E asymmetry against the variable $\cos(\theta_{\pi^-})$ is the main motivation for this analysis thus the variable requires a detailed definition: θ_{π^-} is the angle between the vector momentum of the scattered π^- and the beam line in the center of mass frame of the incoming photon and target neutron where the neutron is assumed *at-rest*). ${}_iY(x_j)^{\downarrow\uparrow}$ is the number of events when the helicity of the photon and the direction of the target polarization vectors are anti-parallel for events in the energy window W_i and the measuring bin x_j, and, similarly, ${}_iY(x_j)^{\uparrow\uparrow}$ is the number of events with the two polarization vectors parallel. P_{target} is the target polarization magnitude, and $\overline{{}_iP_\gamma}$ is the weighted average of the photon polarizations P_γ for energy window W_i (formula is provided below). The uncertainty on the $E(x)$ (a shorthand notation for $E_{ij}(x_j)$) can be calculated as follows:

$$\frac{\sigma_{E(x)}}{E(x)} = \frac{1}{\overline{{}_iP_\gamma}} \frac{1}{P_{target}} \frac{2\sqrt{[Y^{\downarrow\uparrow}]\,[Y^{\uparrow\uparrow}]}}{\sqrt{[Y^{\downarrow\uparrow} + Y^{\uparrow\uparrow}]\,[Y^{\downarrow\uparrow} - Y^{\uparrow\uparrow}]}}, \tag{4.5}$$

note that the target and beam polarization uncertainties were not included in the above equation because they are more appropriately categorized as systematic uncertainty. The derivation of σ_E^2 (ignoring the constants $\overline{{}_iP_\gamma}$ and P_{target}) is as follow:

$$\sigma_E^2 = \left(\frac{\partial E}{\partial\left[Y^{\downarrow\uparrow}\right]}\right)^2 \sigma^2_{\left[Y^{\downarrow\uparrow}\right]} + \left(\frac{\partial E}{\partial\left[Y^{\uparrow\uparrow}\right]}\right)^2 \sigma^2_{\left[Y^{\uparrow\uparrow}\right]} + \left(\frac{\partial E}{\partial\left[Y^{\downarrow\uparrow}\right]}\right)\left(\frac{\partial E}{\partial\left[Y^{\uparrow\uparrow}\right]}\right) cov\left(Y^{\downarrow\uparrow}, Y^{\downarrow\uparrow}\right),$$

where

$$\left(\frac{\partial E}{\partial\left[Y^{\downarrow\uparrow}\right]}\right) = \frac{1}{\overline{{}_iP_\gamma}}\frac{1}{P_{target}}\frac{2Y^{\uparrow\uparrow}}{\left[Y^{\downarrow\uparrow}+Y^{\uparrow\uparrow}\right]^2} \quad , \quad \left(\frac{\partial E}{\partial\left[Y^{\uparrow\uparrow}\right]}\right) = \frac{1}{\overline{{}_iP_\gamma}}\frac{1}{P_{target}}\frac{-2Y^{\downarrow\uparrow}}{\left[Y^{\downarrow\uparrow}+Y^{\uparrow\uparrow}\right]^2},$$

and

$$\sigma^2_{\left[Y^{\uparrow\uparrow}\right]} = Y^{\uparrow\uparrow}, \quad \sigma^2_{\left[Y^{\downarrow\uparrow}\right]} = Y^{\downarrow\uparrow}, \quad cov\left(Y^{\downarrow\uparrow}, Y^{\downarrow\uparrow}\right) = 0,$$

since the $Y^{\downarrow\uparrow}$, and $Y^{\uparrow\uparrow}$ are governed by counting statistics, and independent measurements. The result of Eq. 4.5 is now readily obtained. Next, we introduce the formula to compute the photon polarizations P_γ which is referred to as the Maximon and Olson formula [63]. It shows that the photon polarization for "each" event depends on the electron beam polarization, the electron beam energy and the energy of the incoming photon of that particular event:

$$P_\gamma = \frac{\left(4\epsilon - \epsilon^2\right)P_e}{4 - 4\epsilon + 3\epsilon^2}, \tag{4.6}$$

where P_e is the incident electron beam's polarization, ϵ is the ratio of the resultant photon energy to the incident electron beam's energy, $\epsilon = E_\gamma / E_{electron}$. Note that the P_γ in Eq. 4.6 was computed for *each* event while the $\overline{{}_iP_\gamma}$ in Eq. 4.4 is the weighted *average* of all events in the energy window W_i.

Eq. 4.4 can not be applied directly in the presence of background, thus it must be modified. And as previously mentioned, some background events came from the target material. In particular, g14 targets contain aluminum wires for cooling purposes, and KelF target cell caps (see Chapter 2 for more detail). The target background events are not polarized (E observable was measured to be zero, see Figure 4.29) which would dilute the measurements of the E observable; the background must be removed from the data set (using BDT or 1D cuts). The second type of background came from the Δ and/or multi-pion reactions, and are not the interactions of interest. In the next two subsections, we discuss how the background-subtraction and the BDT methods were employed to reject the mentioned backgrounds. In addition, effects from remaining background will be investigated in detail.

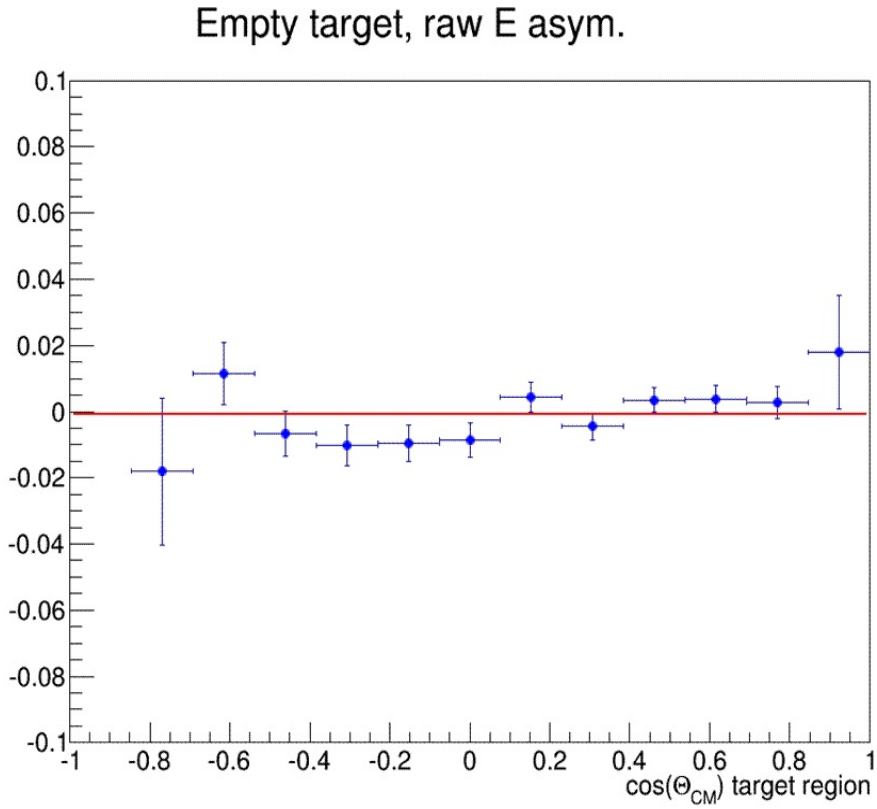

Figure 4.29: The raw E asymmetry vs. $\cos(\theta_{\pi^-})$ for the empty-target data. The result is consistent with zero asymmetry because target material was not polarized.

4.3.1.1 Determination of Cut Values on the z Component of the Reconstructed Interaction Vertex

As shown in Figure 4.16 the majority of the remaining target background events within the target region (i.e., $z \leq$6.0 cm) came from the two KelF caps (at around -11.0 and -6.0 cm), thus before plotting the E asymmetry as a function of $\cos(\theta_{\pi^-})$ or W, we needed to study where to place cuts on the z component of the interaction vertex (z vertex for short). In particular, we studied the E asymmetry as a function of the z vertex using the BDT selected sample (see Section 4.3.1.3 below for detail about the BDT selection), and learned that making selection from -10.2 cm to -5.5 cm was optimal to have a small and "controllable" target background. Figure 4.30 shows that the E values are statistically flat across $-10.2\,\text{cm} \leq z \leq -5.5\,\text{cm}$.

4.3.1.2 Measuring E Using the 1D-Cut Background Suppression and Subtraction Method

We provide detail of the 1D-cut background suppression and subtraction method in this section. The set of cuts discussed in Table 4.2 were employed to remove both

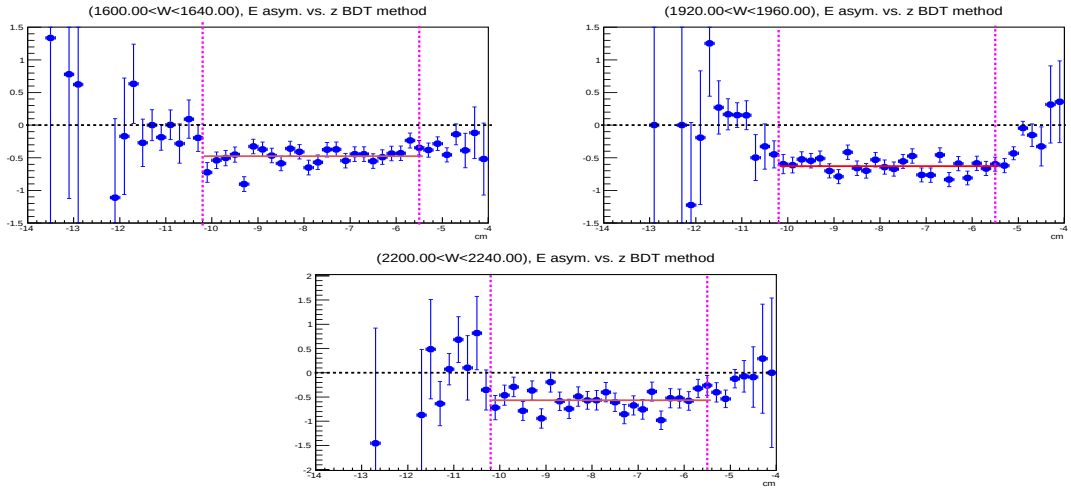

Figure 4.30: The E asymmetry vs. the z vertex (the x-axis is in cm and from -14 to -4 cm) for three different energy bins (W). The region of $-10.2\,\text{cm} \leq z \leq -5.5$ cm has "constant" (flat) E values. The horizontal lines below the zero lines are the 0^{th} polynomial fits.

the physics and target background, see Figure 4.31. Previously, in section 4.2.1.1, we argued that the remaining physics background would be insignificant after the missing momentum cut (see Figure 4.18). Therefore, the dominating background is the target background; and this section mainly discusses a procedure to account for the remaining target background. In particular, we used the empty target data to do background "subtraction."

We utilized the empty-target run data to both estimate and subtract the remaining target background. In Figure 4.32 the z-vertex distribution of the empty run data was scaled up to match the Gold 2 run data distribution for region of $-1.0\,\text{cm} \leq z \leq +30\,\text{cm}$. The obtained scaling, denoted as ε (or more accurately ε_j for energy window W_j), were used to estimate the target background (note that for Gold 2 period data, the scaling is smaller by a factor of 0.7 because there is less aluminum material in the Gold 2 target than in the empty (or Silver) target). To do subtraction, we implemented the following procedure:

- For the energy window W_j, subtract the target background to obtain the yields for the signal data (events from the HD material):

$$ {}_jY^{\uparrow\uparrow}_{HD} = {}_j\,Y^{\uparrow\uparrow}_{full} - \frac{\epsilon_j}{2} Y^j_{empty} \quad , \quad {}_jY^{\downarrow\uparrow}_{HD} = {}_j\,Y^{\downarrow\uparrow}_{full} - \frac{\epsilon_j}{2} Y^j_{empty}, $$

where ${}_jY^{\downarrow\uparrow}_{full}$ is the yield when the helicity of the photon and the direction of the target polarization vector are antiparallel, ${}_jY^{\uparrow\uparrow}_{full}$ is the yield when the two vectors are parallel for events in the energy window W_j. Y^j_{empty} is the yield from the empty target

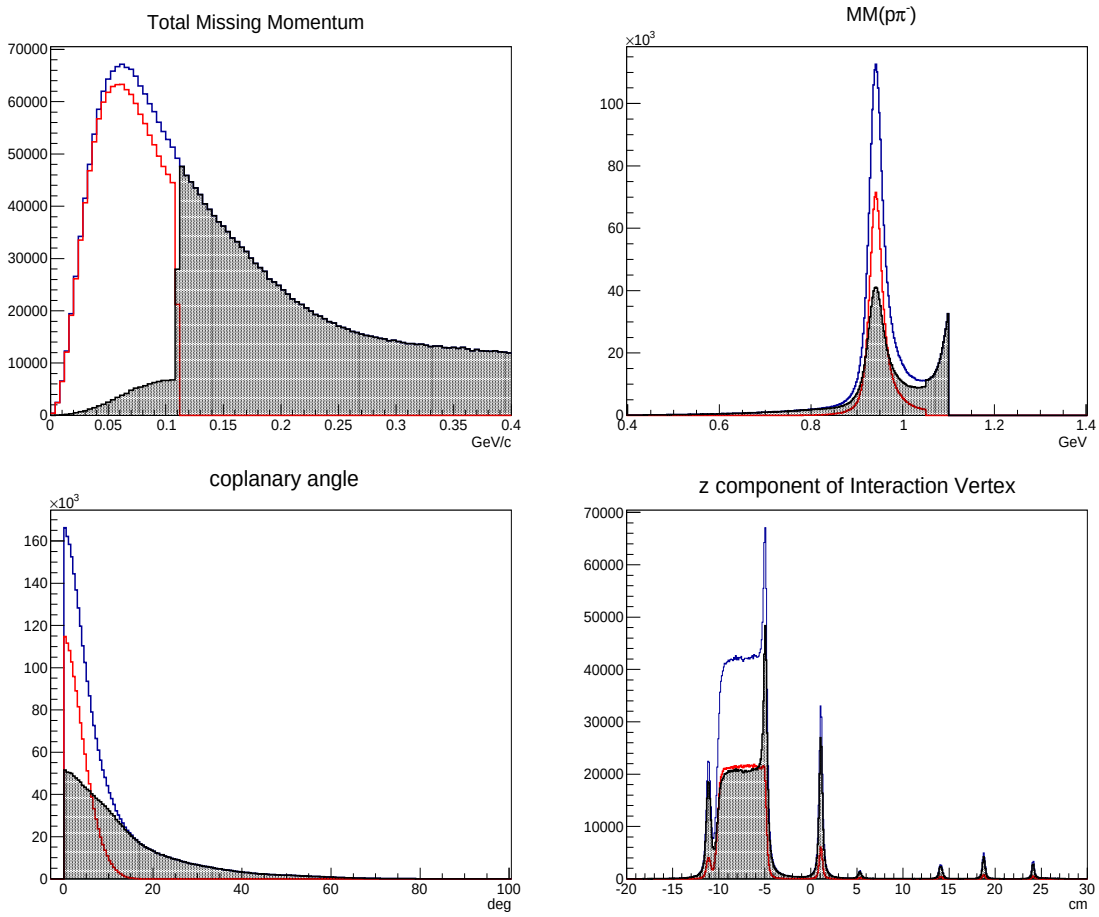

Figure 4.31: Top left: Missing momentum before ("blue"), and after the cuts given in Table 4.2 (selected events in "red", rejected events in "black"). Top right: Total missing mass, $MM(\pi^- p)$ before ("blue") and after the cuts (selected events in "red", rejected events in "black"). Bottom left: coplanarity angle before ("blue") and after the cuts (selected events in "red", rejected events in "black"). Bottom right: the z-component of the interaction vertex before ("blue"), and after the cuts (selected events in "red", rejected events in "black"). The plots were constructed using the Gold 2 period data.

data, and ε_j is the scaling factor in the energy window W_j, see Table 4.5 for Gold 2 and Silver 1&2 values of the ε_j. The factor of a half is because we implicitly assume the E asymmetry of the target material is zero (see Figure 4.29) and therefore did not divide the empty data into two smaller disjoint subsets. Importantly, for each energy window W_j this step is carried out bin by bin because values of Y^j_{empty} might be different for different measuring bins, but the scaling ε_j is assumed to be constant within the energy window W_j. Note that the statistical uncertainties on ${}_jY^{\uparrow\uparrow}_{HD}$, and ${}_jY^{\uparrow\uparrow}_{HD}$ include the contribution from the statistical uncertainty of the appropriate ε_j

(i.e., errors on the ε_j values were propagated into the ${}_jY^{\uparrow\uparrow}_{HD}$, and ${}_jY^{\uparrow\uparrow}_{HD}$).

- Compute Equation 4.4 bin by bin (x_l) for each energy window W_j:

$$ {}_jE_{HD}(x_l) = \frac{1}{{}_j\overline{P_\gamma}} \frac{1}{P_{target}} \frac{{}_jY^{\downarrow\uparrow}_{HD}(x_l) -_j Y^{\uparrow\uparrow}_{HD}(x_l)}{{}_jY^{\downarrow\uparrow}_{HD}(x_l) + {}_jY^{\uparrow\uparrow}_{HD}(x_l)}, $$

- Apply a correction of (1+0.036) to account for a dillution effect due to the fact that the neutron is *bound* inside the deuteron, see discussion in Section 4.3.4.1 for detail:

$$ {}_jE_{HD}(x_l) = (1 + 0.036) \frac{1}{{}_j\overline{P_\gamma}} \frac{1}{P_{target}} \frac{{}_jY^{\downarrow\uparrow}_{HD}(x_l) -_j Y^{\uparrow\uparrow}_{HD}(x_l)}{{}_jY^{\downarrow\uparrow}_{HD}(x_l) + {}_jY^{\uparrow\uparrow}_{HD}(x_l)}. $$

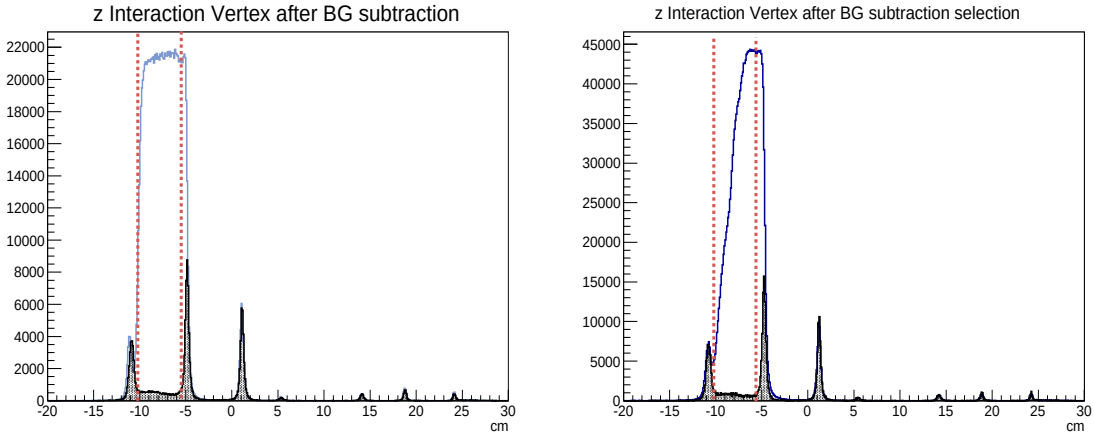

Figure 4.32: Left: Distributions of the z-component of the interaction vertex from Gold 2 (blue) and scaled empty (black) data. Right: Distributions of the z-component of the interaction vertex from Silver 1&2 (blue) and scaled empty (black) data. The vertical lines indicate the z vetex cuts.

4.3.1.3 Measuring E using the Boosted Decision Tree Method

In section 4.2.2 we discussed the steps to train and evaluate the BDT algorithm. In this section, the constructed BDT is employed on the real data to select bound neutron events. In preparation, we placed two loose cuts (MM($p\pi^-$)<1.1 GeV and Missing Momentum< 400 MeV/c) to reject unambiguous background events. After the two cuts, all remaining events were evaluated by the BDT; i.e., each event acquired a BDT output value, which was a real number between -1.0 and $+1.0$. We then selected only events with the BDT output greater than 0.03—the cut on the BDT

W (MeV)	ε^{gold2}	$\varepsilon^{silver1\&2}$
1500	1.18±0.01	24.32±3.21
1540	1.13±0.01	15.97±1.82
1580	1.00±0.02	18.61±2.90
1620	1.38±0.04	12.77±2.16
1660	1.18±0.03	10.81±2.04
1700	1.37±0.04	9.83±1.86
1740	1.38±0.04	10.41±2.23
1780	1.31±0.04	10.05±2.30
1820	1.31±005	8.60±2.14
1860	1.35±0.06	10.22±3.00
1900	1.29±0.06	10.21±3.43

W (MeV)	ε^{gold2}	$\varepsilon^{silver1\&2}$
1940	1.65±0.09	9.78±3.48
1980	1.25±0.07	8.37±3.10
2020	1.59±0.11	11.51±5.32
2060	1.42±0.10	8.03±4.12
2100	1.56±0.14	9.94±5.25
2140	0.92±0.09	10.60±6.71
2180	1.38±0.14	5.14±2.76
2220	1.59±0.19	6.25±4.44
2260	1.66±0.26	NA
2300	1.40±0.27	NA

Table 4.5: Table of scaling constants ε_j for the Gold 2 and Silver 1&2 run periods. Note that the empty-target data used for Silver 1&2 subtraction (positive torrus field, see Section 3.1) is about 1/6 smaller in statistics compared to the empty-target data used for Gold 2 subtraction (negative torrus field). The scaling constants are modestly self-consistent except for a few energy bins with low statistics (i.e., W=2260 and 2300 MeV for Gold 2 data, and W=2180, and 2220 MeV for Silver 1&2 data).

output chosen to maximize the $S/\sqrt{S+B}$ ratio, which statistically means minimizing the misclassification cost (see discussion in section 4.2.2). Figure 4.33 shows the distributions of the total missing momentum, the total missing mass and the z vertex before and after the BDT selection cut.

To estimate the remaining target background after the BDt cut we also used the empty run data. In Figure 4.34 the z-vertex distribution of the empty run data was scaled up to match the the Gold 2 period data distribution for region of $-1.0\,\mathrm{cm} \leq z \leq 30\,\mathrm{cm}$. The obtained scaling was then used to estimate the number of target background and true HD events within the region of $-10.2\,\mathrm{cm} \leq z \leq -5.5\,\mathrm{cm}$. (note that for Gold 2 data, the scaling is smaller by a factor of 0.7 because there is less aluminum material in the Gold 2 target than in the empty target). Next, we obtained the *target-background-to-true-HD* ratio for all run periods, see Table 4.6. Since the numbers of HD events are on the order of a few hundred thousand and the ratios are typically a few percent, the statistical uncertainties on these ratios are insignificant (see Table 4.6); thus we did not "propagate" the uncertainties of the ratios into the measured values of the E. The ratios which are reported in Table 4.6 were used as overall scaling factors to account for the dilution effects from *non-polarized* target background on the E asymmetry measurements; see below:

$$E_{full} = \frac{1}{\overline{P_\gamma}} \frac{1}{P_t} \frac{\left[Y_{HD}^{\downarrow\uparrow} - Y_{HD}^{\uparrow\uparrow}\right] + \left[Y_{target}^{\downarrow\uparrow} - Y_{target}^{\uparrow\uparrow}\right]}{\left[Y_{HD}^{\downarrow\uparrow} + Y_{HD}^{\uparrow\uparrow}\right] + \left[Y_{target}^{\downarrow\uparrow} + Y_{target}^{\uparrow\uparrow}\right]} = \frac{1}{\overline{P_\gamma}} \frac{1}{P_t} \frac{\left[Y_{HD}^{\downarrow\uparrow} - Y_{HD}^{\uparrow\uparrow}\right] + 0}{\left[Y_{HD} + Y_{target}\right]}, \quad (4.7)$$

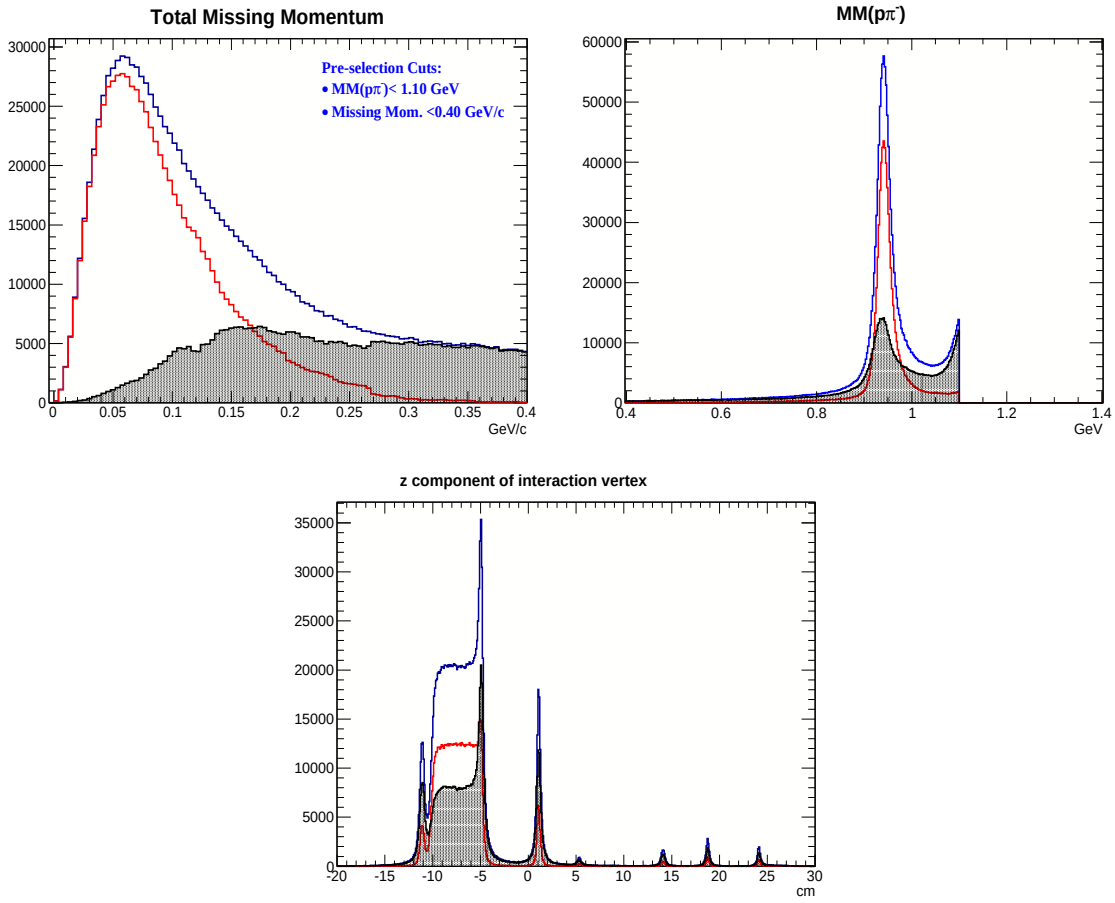

Figure 4.33: Top left: Missing momentum before ("blue"), and after the BDT cut (selected events in "red", rejected events in "black"). Top right: Total missing mass, $MM(\pi^- p)$ before ("blue") and after the BDT cut (selected events in "red", rejected events in "black"). Bottom: z-component of interaction vertex before ("blue"), and after the BDT cut (selected events in "red", rejected events in "black"). The plots were constructed using the Gold 2 period data.

$$\Leftrightarrow E_{full} = \frac{1}{\overline{P_\gamma}} \frac{1}{P_t} \frac{1}{\left[1 + \frac{Y_{target}}{Y_{HD}}\right]} \frac{\left[Y_{HD}^{\downarrow\uparrow} - Y_{HD}^{\uparrow\uparrow}\right]}{[Y_{HD}]} = \frac{1}{\left[1 + \frac{Y_{target}}{Y_{HD}}\right]} E_{HD}, \tag{4.8}$$

$$\Longrightarrow E_{HD} = \left[1 + \frac{Y_{target}}{Y_{HD}}\right] E_{full}, \tag{4.9}$$

where E_{full}, and E_{HD} are the E asymmetries computed from full target (target background included) and from *only* HD events, respectively. $Y^{\downarrow\uparrow}$ is the yield when the helicity of the photon and the direction of the target polarization vectors are anti-

parallel, and $Y^{\uparrow\uparrow}$ is the yield when the two polarization vectors are parallel. Y_{target} and Y_{HD} are the total yield for target background events and HD events, respectively. P_t is the target polarization magnitude, and $\overline{P_\gamma}$ is the weighted average of the photon polarizations P_γ (see Equation 4.6). Note that the scaling $\left[1+\frac{Y_{target}}{Y_{HD}}\right]$ is assumed to be constant across *all* measuring bins and *all* energy windows W. This is distinctly different from the 1D-cut background suppression and subtraction method where the subtraction was applied bin by bin. In addition, we also applied a correction of (1+0.086) to account for the dillution effect "caused" by the spectator proton, see discussion in Section 4.3.4.1 for detail:

$$E_{HD} = (1+0.086)\left[1+\frac{Y_{target}}{Y_{HD}}\right]E_{full}, \tag{4.10}$$

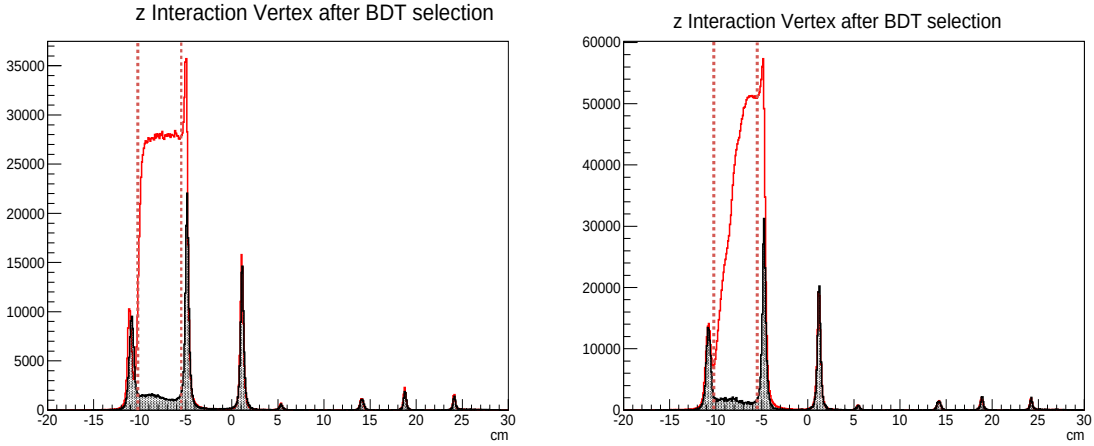

Figure 4.34: Left: Distributions of the z-component of the interaction vertex from Gold 2 (red) after the BDT cut and scaled empty (black) data. Right: Distributions of the z-component of the interaction vertex from silver1 &2 (red) after the BDT cut and scaled empty (black) data. The vertical lines indicate the z vetex cuts

Run period	*Background-to-HD* ratio, Y_{target}/Y_{HD}
Gold 2	0.0310±0.0007
Silver1&2	0.0443±0.0005
Silver3	0.0536±0.0001
Silver4	0.0539±0.0005
Silver5	0.0552±0.0008

Table 4.6: Table of target background to HD signal ratios.

The previous procedure described the only correction we made on the E measurements. It is justified only if the target background is small so that its dilution effect

does not vary noticeably across energy and angular bins; this condition seems to be valid because the background is only a few percent of the signal events. In addition, in Table 4.7 we provide the *Background-to-HD* ratios' values for different energy (W) bins showing that the ratios are relatively constant across the energy range we considered, thus it is reasonable to apply only *one* correction factor for all energy (W) bins. Secondly, the Δ and/or multi-pion backgrounds must be "completely" removed. The BDT selection procedure should reject most of the Δ background—but not all. Studying Figure 4.35 we decided to apply tighter cuts on the missing mass and missing momentum from initial cut conditions $MM(p\pi^-) < 1.1$ GeV and missing momentum$<$ 400 MeV/c applied before the BDT cut. In particular, all selected events must have missing momentum less than 200 MeV/c, and missing mass less than 1.03 GeV.

W (MeV)	Y_{target}/Y_{HD}
1500	0.025±0.003
1540	0.031±0.003
1580	0.036±0.002
1620	0.037±0.002
1660	0.032±0.001
1700	0.032±0.001
1740	0.034±0.002
1780	0.030±0.003
1820	0.033±0.003
1860	0.032±0.003
1900	0.030±0.003

W (MeV)	Y_{target}/Y_{HD}
1940	0.032±0.002
1980	0.033±0.002
2020	0.033±0.003
2060	0.033±0.003
2100	0.031±0.003
2140	0.032±0.004
2180	0.028±0.004
2220	0.029±0.005
2260	0.030±0.007
2300	0.027±0.008

Table 4.7: Table of *Background-to-HD* ratios for the Gold 2 run period. The ratios are consistent with the ratio's value for the Gold 2 period in Table 4.6.

Recall from section 4.2.1.1 (see Figure 4.18) that we set the missing momentum cut for the 1D-cut background suppression and subtraction method at 110 MeV/c to reject "all" the Δ and/or multi-pion background. If this assertion is true then plotting the E asymmetry against the total missing mass variable would indicate no mass-dependent dilution effect; i.e., the E asymmetry distribution should be statistically flat across the missing mass spectrum. Similarly, we expected to observe the same phenomena for the data sample selected by the BDT method—because we expect that the physics background was only insignificantly present. Figure 4.36 plots the E asymmetry, integrated over all angles, against the total missing mass from both methods. The plot suggests no mass-dependent dilution effect—zeroth order polynomial fits (for the BDT method) have χ^2/dof close to *one*, and a good agreement between the methods (note that the remaining target background corrections was applied for both methods). In conclusion, we showed that we had a clean data sample from the BDT selection procedure with a small portion of background

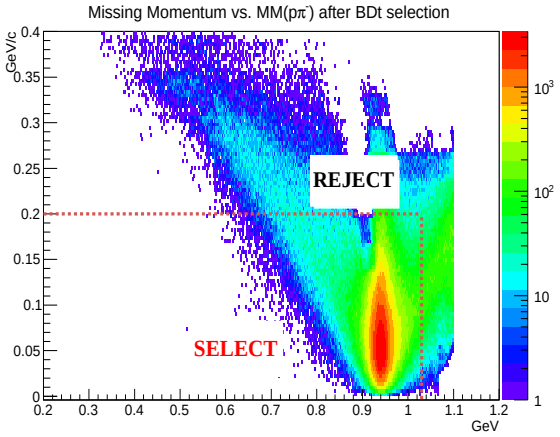

Figure 4.35: Missing Momentum vs. Total Missing Mass, $MM(\pi^- p)$ from the Gold 2 period data after the BDT selection.

remain*ing*—but mostly accounted for.

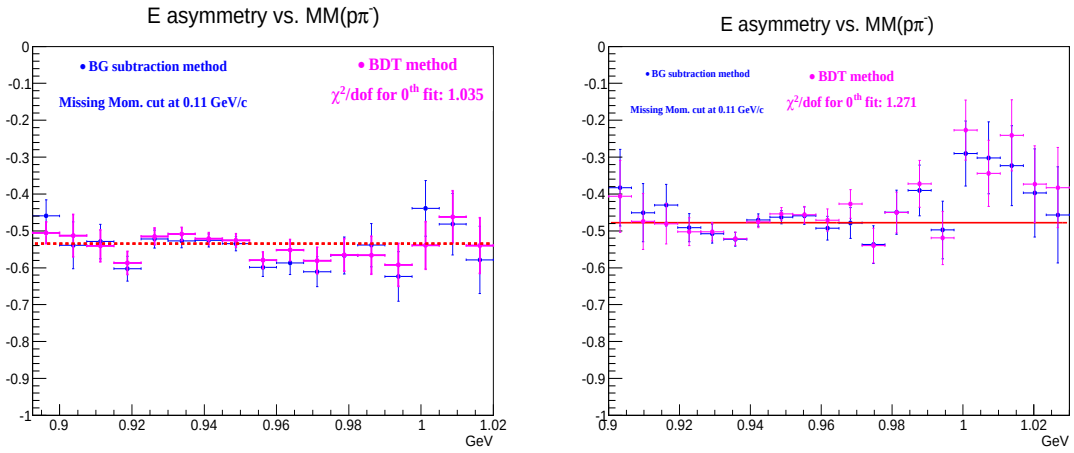

Figure 4.36: Easymmetry vs. Total missing mass, $MM(\pi^- p)$ after the BDT selection from Gold 2 run data (left) and Silver 1&2 run data (right).

4.3.2 Comparing Boosted Decision Trees (BDT) and 1D-Cut Background Suppression and Subtraction Methods

We discussed above in detail about the two event selection methods. In this section we compare the E asymmetry measurements obtained by the two methods. Particularly, a procedure to quantify the systematic difference between the two methods will be discussed. Recall that when we introduced the BDT method with built-in features that

overcome some inherent inefficiencies from the standard 1D-cut background suppression and subtraction method, an implicit assumption that the BDT would perform better was made. Now, we can provide evidence to support our previous assumption.

Equation 4.4 shows how to calculate the E asymmetry as a function of a variable x. To quantify the systematic difference of the two methods, we can pick x such that E is statistically constant across the domain of x. Consequently, we chose to study the E asymmetry as a function of the z component of interaction vertex (z vertex for short); because the spatial distribution of the E asymmetry should be a constant (ideally, the target polarization should be uniform along the beam line, or the z axis). The value of the constant can be estimated; any fluctuation around this constant is mainly statistical, and is assumed to follow a normal distribution (assumption of Gaussian distribution makes what we discuss below possible). Considering the following procedure:

1. Compute the E asymmetry as a function of the z vertex, $\widehat{E(z)}$, using the 1D-cut background suppression and subtraction method,

2. Compute the E asymmetry as a function of the z vertex, $\widetilde{E(z)}$, using the BDT method,

3. For each z vertex bin j, and energy bin i, compute $\Delta_{ij} = \widetilde{E_i(z_j)} - \widehat{E_i(z_j)}$,

4. Fit the Δ_{ij} with a Gaussian distribution and obtain the mean (μ_Δ) and width (σ_Δ) from the fitted Gaussian.

It remains to interpret the mean and the width of the fitted Gaussian. Let us consider two scenarios. The first scenario consists of a hypothetical infinitely large data set; now execute both step 1 and step 2 from the above procedure on this very large data set. For either method, statistical uncertainties would be very small; in other words, if fitted using a Gaussian distribution, the fitted Gaussian would be a delta function with the centroid at the weighted average of all data points. As a result, after executing step 1 and 2 we would have two delta functions with possibly different centers. The difference between the two centroids is obviously the systematic difference between the two methods. Note that in this scenario all the values of the Δ_{ij} are constant (and equal to the difference between the two centroids). Now if we reduce the statistics of the data set gradually, the values of the Δ_{ij} would fluctuate around the difference between the two previous centroids (the two delta functions become wider as the statistics decreases). Consequently, the centroid of the fitted Gaussian using the Δ_{ij} values is the best estimate of the systematic difference between the two methods. Next, we discuss about the second scenario; it consists of a hypothetical finite data set (referred to as data set A), and a subset of A (referred to as data set S). We applied *only* step 1 (or 2) on both data sets A and S, then fitted a Gaussian on both results. Apparently, since the data set A is larger, the width of the fitted Gaussian

on A is smaller than the fitted Gaussian on S. It is known that the difference of two Gaussian distributed random variables is also a Gaussian random variable, thus when fitting $\Delta'_{ij} = E_i^S(z_j) - E_i^A(z_j)$ to a Gaussian then:

$$\mu_{\Delta'} \approx 0, \tag{4.11}$$

$$\sigma^2_{\Delta'} \approx \sigma^2_{E_S} - 2\rho\sigma_{E_S}\sigma_{E_A} + \sigma^2_{E_A}, \tag{4.12}$$

where $\mu_{\Delta'}$ and $\sigma_{\Delta'}$ are the mean and the width of the fitted Gaussian, respectively. the mean $\mu_{\Delta'}$ and the width $\sigma_{\Delta'}$ are the best estimations of the right sides of equations 4.11 and 4.12, respectively. Concluding from the second scenario study, the width of the fitted Gaussian using the values of Δ_{ij} in step 4 is the measure of the *statistical similarity* between the data sets selected by the two methods; the degree of similarity between data sets A and S is measured by the correlation coefficient ρ. In other words, ρ is 1 if A and S are identical, and 0 if the data set S is not a subset (but independent) of the data set A. Note that ρ is generally unknown and very difficult to estimate directly. Thus, while the σ_{E_S} and σ_{E_A} can be estimated directly (from the statistical uncertainties of $E_i^A(z_j)$ and $E_i^S(z_j)$), $\sigma_{\Delta'}$ can not be obained directly without the knowledge of ρ. But, by using the Gaussian fit approach we can indirectly obtain the $\sigma_{\Delta'}$. Note that the width can be employed to estimate the *uncertainty* of the systematic difference, i.e., $\sigma_{\mu_\Delta} = \sigma_\Delta/\sqrt{N}$ where N is the total number of bins, thus using the Gaussian fit approach not only we can obtain the best estimate of the systematic difference between two methods (regardless of the correlation between the two data sets A and S), but we can also obtain the uncertainty on our estimation. More importanly, estimating the systematic difference by fitting a Gaussian is more robust compared to a simple average ($\overline{\Delta} = \frac{1}{N}\sum \Delta_{ij}$) because the simple average is very sensitive to outliers (bins with extremely unreasonable values)[1]. For example, the centroid of the fitted Gaussian for Silver 1&2 is 0.07 (see Figure 4.42 below) while the weighted mean using all bins is 0.10.

In summary, note that the first senario comprised of two methods applying only on one data set, while the second senario comprised of only one method applying on two related data sets. Analyzing both senarios revealed the nature of the mean (μ_Δ) and width (σ_Δ) of the fitted distribution in step 4 (distribution of Δ_{ij}). In later sections, particularly in Section 4.4 where we study systematic uncertainties, we will implement this procedure as described here to quantify the systematic uncertainty assignment.

[1]The Gaussian fit was obtained by applying the least-square fitting algorithm (thus the fitted Gaussian centroid would be close to the mode of the histogram of values of Δ_{ij}). Note that if the maximum likelihood method were used, the centroid of the fitted Gaussian would be the same as the simple average ($\overline{\Delta} = \frac{1}{N}\sum \Delta_{ij}$).

4.3.2.1 The Gold 2 Target Run Period Comparison

Previously, we discussed the procedure to estimate the systematic difference between the 1D-cut background suppression and subtraction method and the BDT method. In this section we will show the result for the Gold 2 run period. Figure 4.37 shows the distribution of the $\Delta_{ij} = \widetilde{E_i(z_j)} - \widehat{E_i(z_j)}$ (see the previously discussed procedure) and the fitted Gaussian. The mean of the Gaussian is positive indicating that, on average, the values of the E measurements obtained by the BDT method is *more negative* than the E values obtained by the 1D-cut background suppression and subtraction (there are possibly still remaining Δ and/or multi-pion background events, see Section 4.2.1.1 for detailed discussion). Since we only use the 1D-cut background suppression and subtraction method to validate the BDT method, we will not investigate this further. Moreover, a closer inspection of Figures 4.38, and 4.39, which show the E asymmetry as a function of the z vertex for 21 energy windows (each spans 40 MeV) covering 1480 MeV$<W<$2320 MeV from the BDT (red) and the 1D-cut background suppression and subtraction (black) methods, revealed that the systematic difference is on the order of the statistical uncertainties of E measurements obtained by the BDT method. Thus we concluded that the results from two methods are statistically consistent.

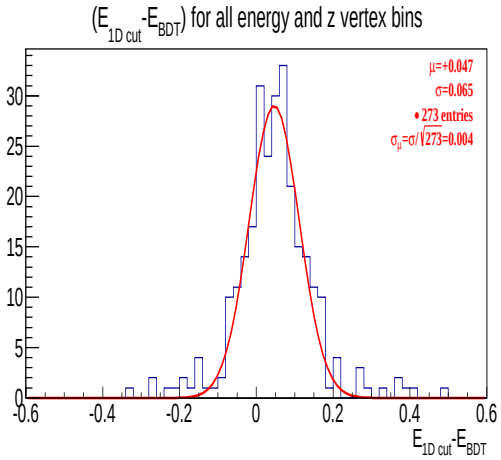

Figure 4.37: Distribution of $\Delta_{ij} = \widetilde{E_i(z_j)} - \widehat{E_i(z_j)}$ (blue histogram) and a fitted Gaussian (red). Small mean (μ=+0.047±0.004) indicates good consistency between the BDT and the 1D-cut background suppression and subtraction methods for Gold 2 run period.

In addition, to illustrate that the BDT selected data sample is generally larger than the 1D-cut background suppression and subtraction method, we plot $[\sigma_{BGsub} - \sigma_{BDT}]/\sigma_{BDT}$ for each energy bin, and z vertex bin (σ_{BGsub}, and σ_{BDT} are the statistical uncertainty of E measured by the 1D-cut background suppression and subtraction , the BDT methods, respectively) in Figures 4.40, 4.41. Note that positive values for

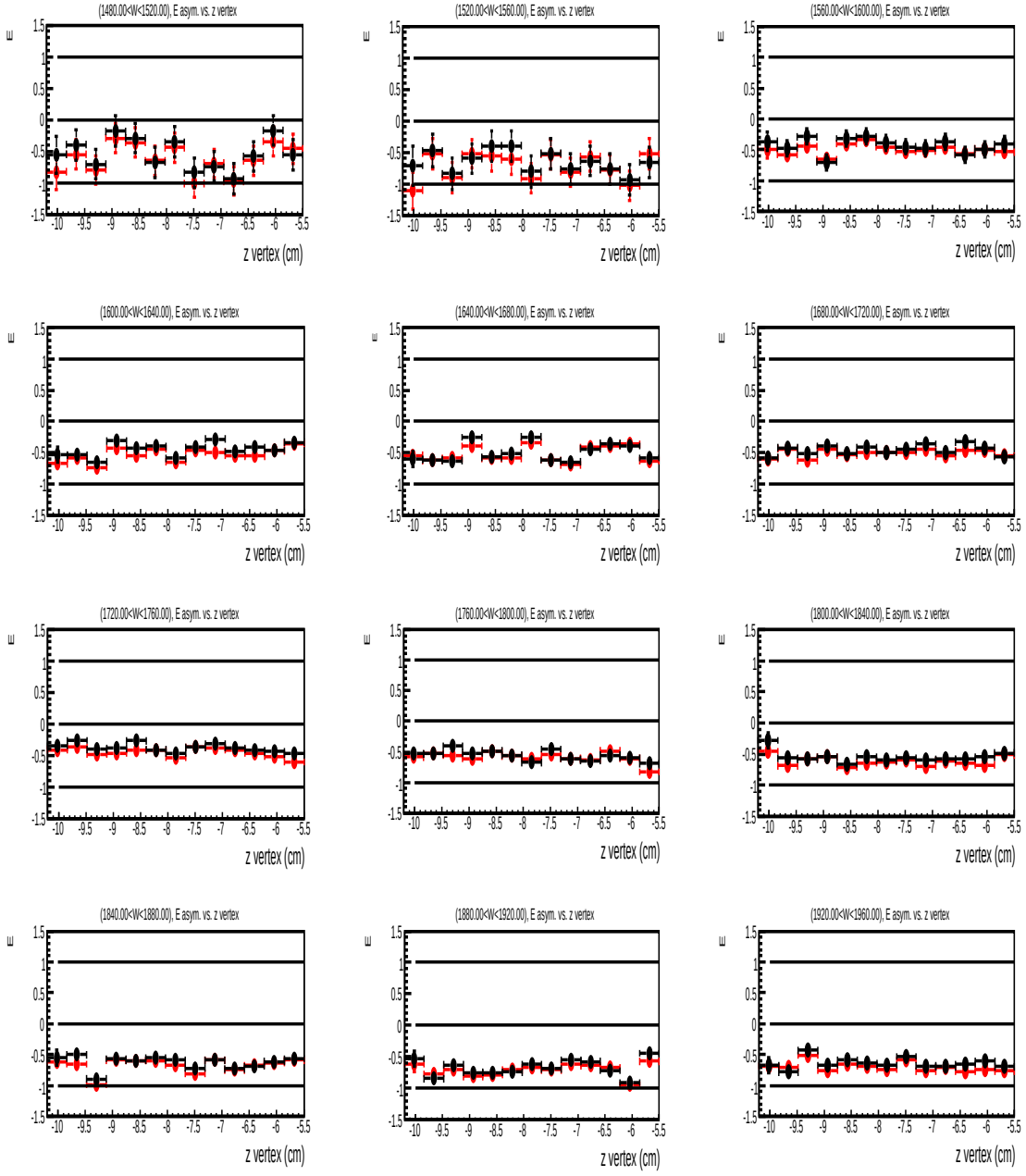

Figure 4.38: E vs. the z-component of the interaction vertex for the first 12 energy windows 1480 MeV$<W<$1960 MeV for the Gold 2 period. The black points are from the 1D-cut background suppression and subtraction and the red points are from the BDT method. There is a small systematic difference between the two methods (see discussion in Section 4.3.2.1). The horizontal lines are at 1.0, 0.0, and -1.0. The horizontal axis is in cm and from $-10.2\,\text{cm} \leq z \leq -5.5\,\text{cm}$.

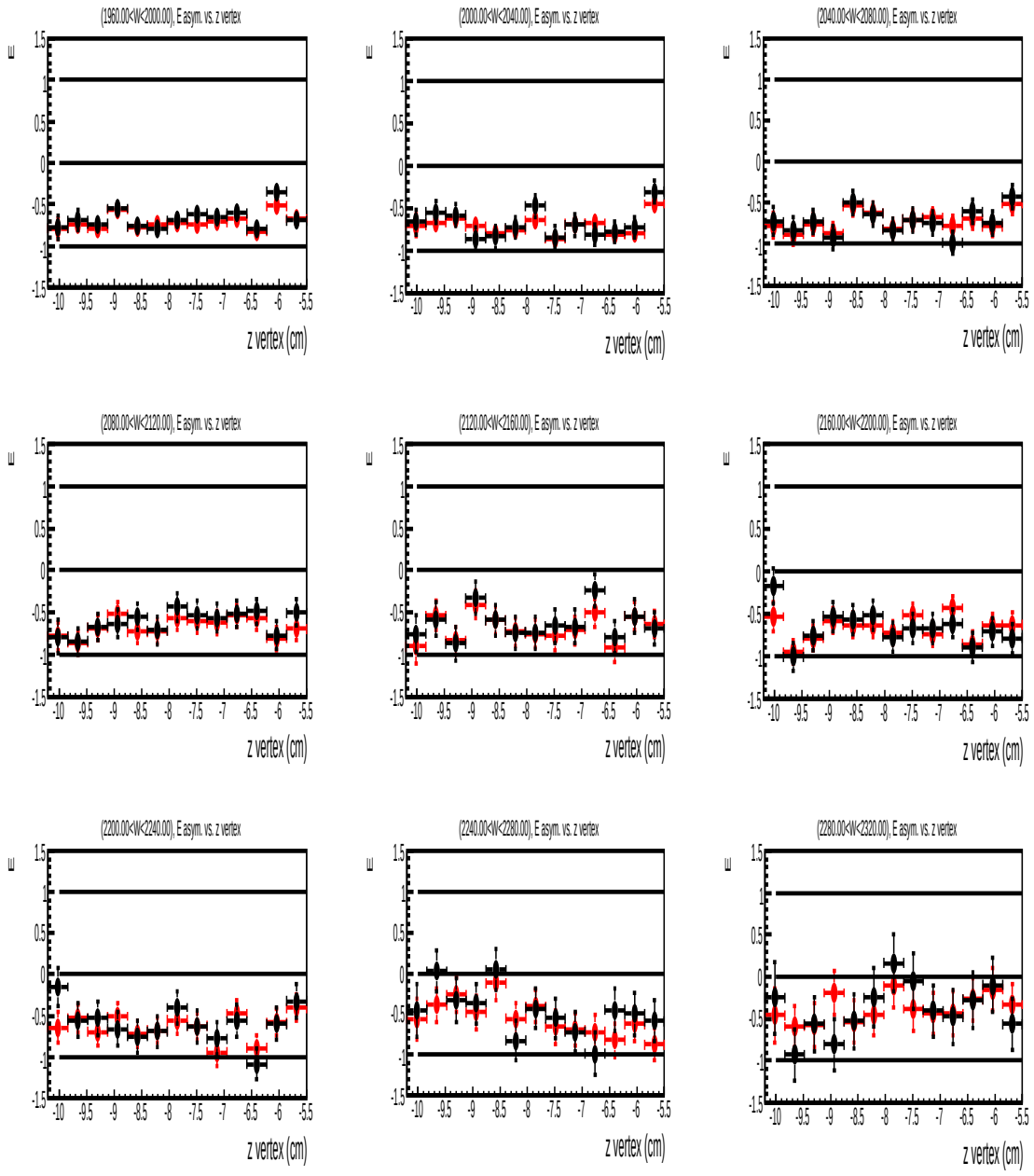

Figure 4.39: E vs. the z-component of the interaction vertex for last 9 energy windows from 1960 MeV$<W<$2320 MeV for the Gold 2 period. The black points are from the 1D-cut background suppression and subtraction and the red points are from the BDT method. There is a small systematic difference between the two methods (see discussion in Section 4.3.2.1). The horizontal lines are at 1.0, 0.0, and -1.0. The horizontal axis is in cm and from $-10.2\,\text{cm} \leq z \leq -5.5\,\text{cm}$.

$[\sigma_{BGsub} - \sigma_{BDT}]\,/\sigma_{BDT}$ imply larger data set (smaller error) for the BDT — i.e., higher efficiency.

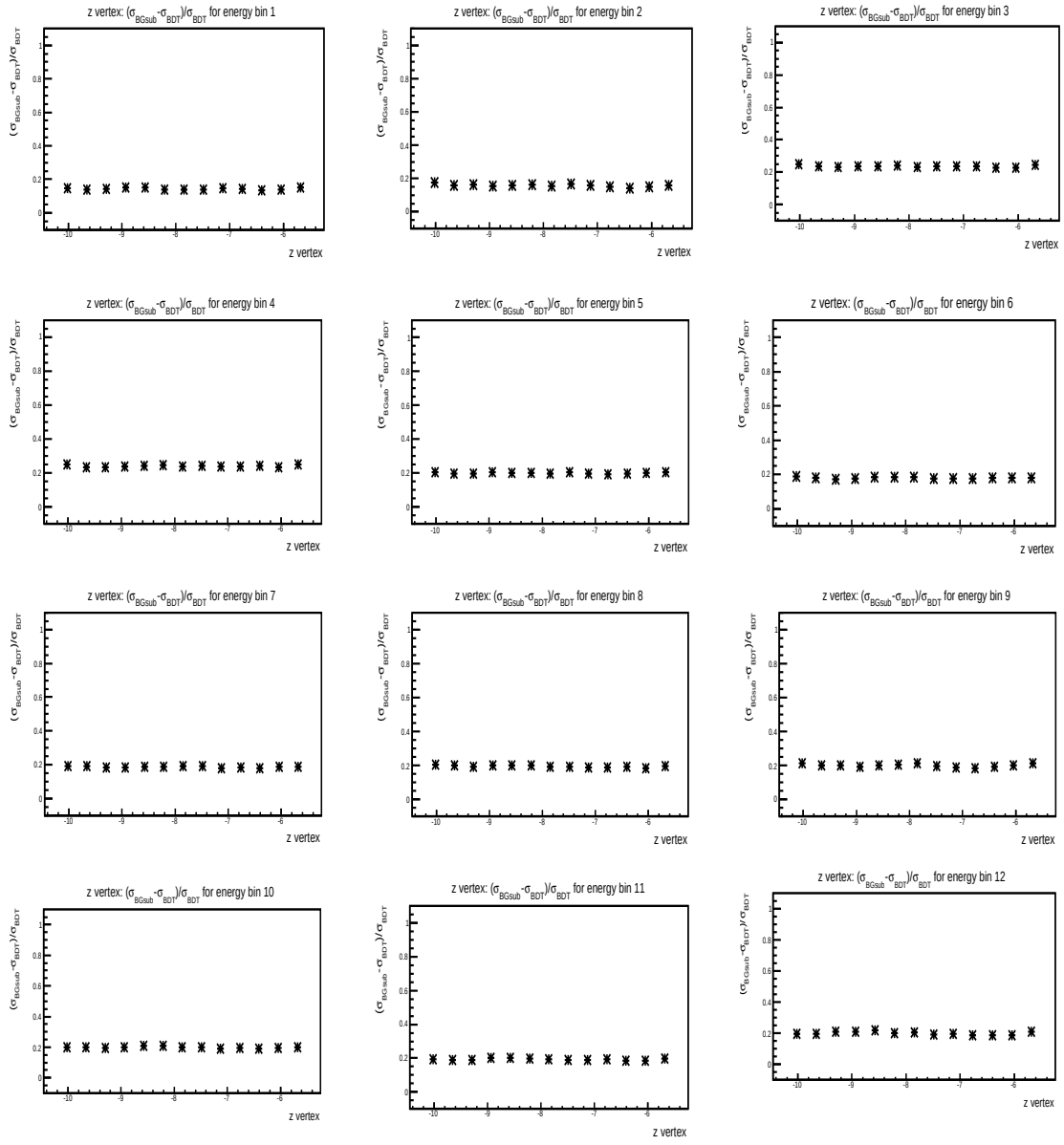

Figure 4.40: $[\sigma_{BGsub} - \sigma_{BDT}]\,/\sigma_{BDT}$ vs. the z-component of the interaction vertex for the first 12 energy windows from 1480 MeV$<W<$1960 MeV for the Gold 2 period. All the points are positive indicating σ_{BDT} is everywhere smaller than σ_{BGsub}. The horizontal axis is in cm and from $-10.2\,\text{cm} \leq z \leq -5.5\,\text{cm}$.

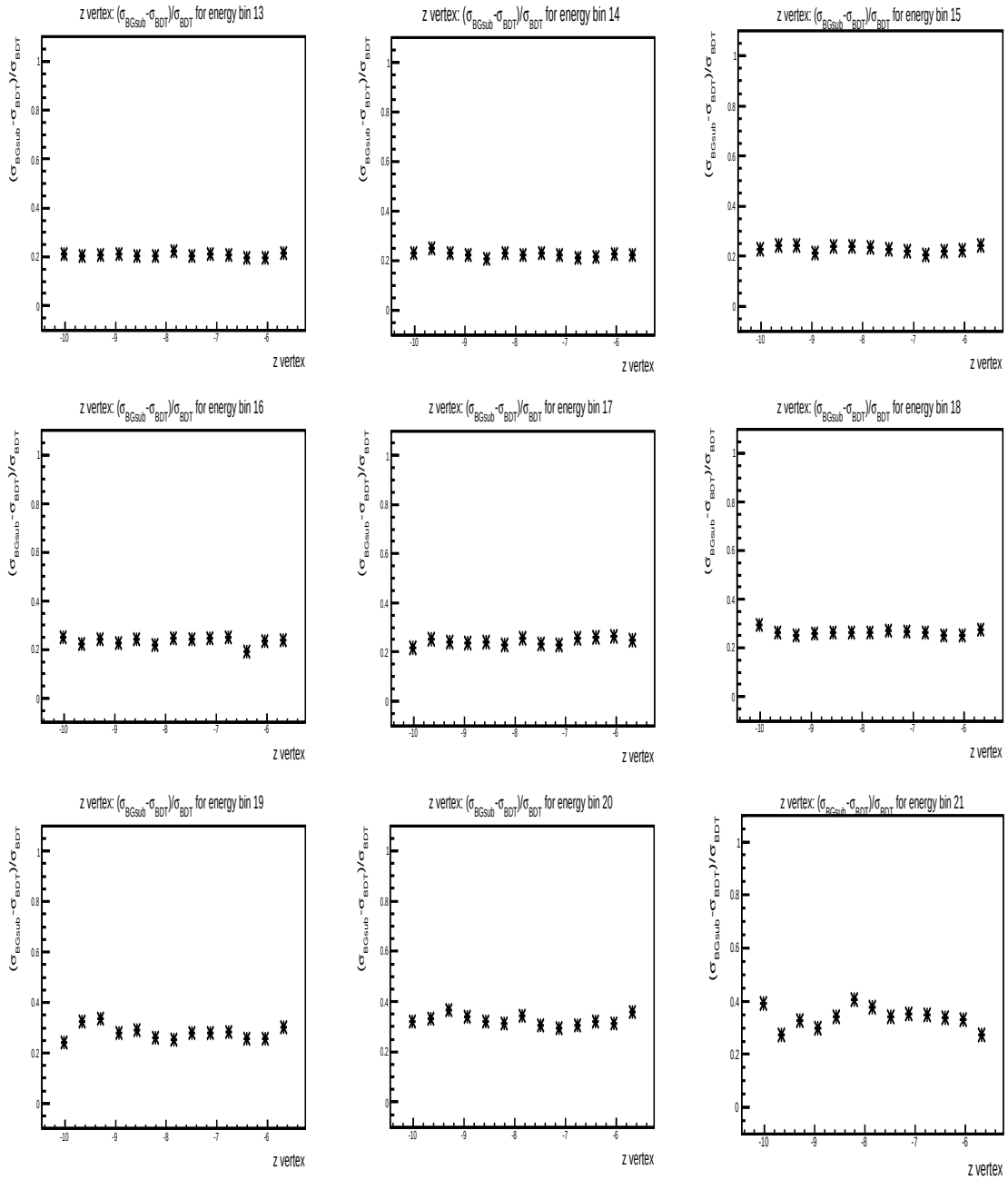

Figure 4.41: $[\sigma_{BGsub} - \sigma_{BDT}]/\sigma_{BDT}$ vs. the z-component of the interaction vertex for the last 9 energy windows from 1960 MeV$<W<$2320 MeV for the Gold 2 period. All the points are positive indicating σ_{BDT} is everywhere smaller than σ_{BGsub}. The horizontal axis is in cm and from $-10.2\,\text{cm} \leq z \leq -5.5\,\text{cm}$.

4.3.2.2 Silver 1&2 Target Run Period Comparison

In this section we show the result for Silver 1&2 run periods (combined). Particularly, Figure 4.42 shows the distribution of the Δ_{ij} (see previously discussed procedure) and the fitted Gaussian; a larger mean compared to the Gold 2 data indicates worsen agreement. However, a closer inspection of Figures 4.43, and 4.44 reveals that the difference in E values for the two methods are most significant in the region of $z < -8.5$ cm, where there is not many events to select (see the right plot of Figure 4.34). The two methods are in decent agreement in the region of $z > -8.5$ cm.

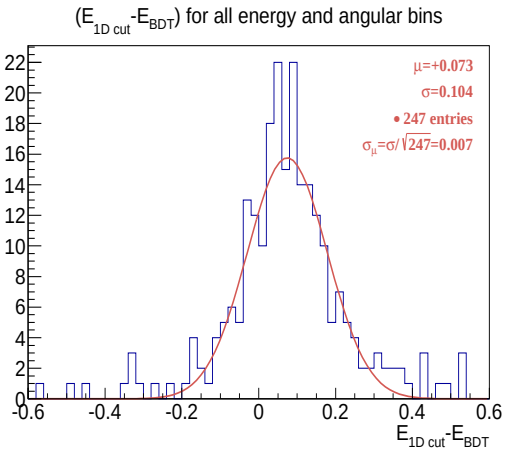

Figure 4.42: Distribution of Δ_{ij} (blue histogram) and a fitted Gaussian (red). The fitted Gaussian centroid (μ=+0.073±0.007) indicates decent agreement between the BDT and the 1D-cut background suppression and subtraction methods for Silver 1 & 2 run periods.

As before, to illustrate that the BDT selected data sample is generally larger than the 1D-cut background suppression and subtraction method, we plot $[\sigma_{BGsub} - \sigma_{BDT}]/\sigma_{BDT}$ for each energy bin, and z vertex bin. Positive values for $[\sigma_{BGsub} - \sigma_{BDT}]/\sigma_{BDT}$ were again observed suggesting higher efficiency for the BDT method in Figures 4.45, 4.46.

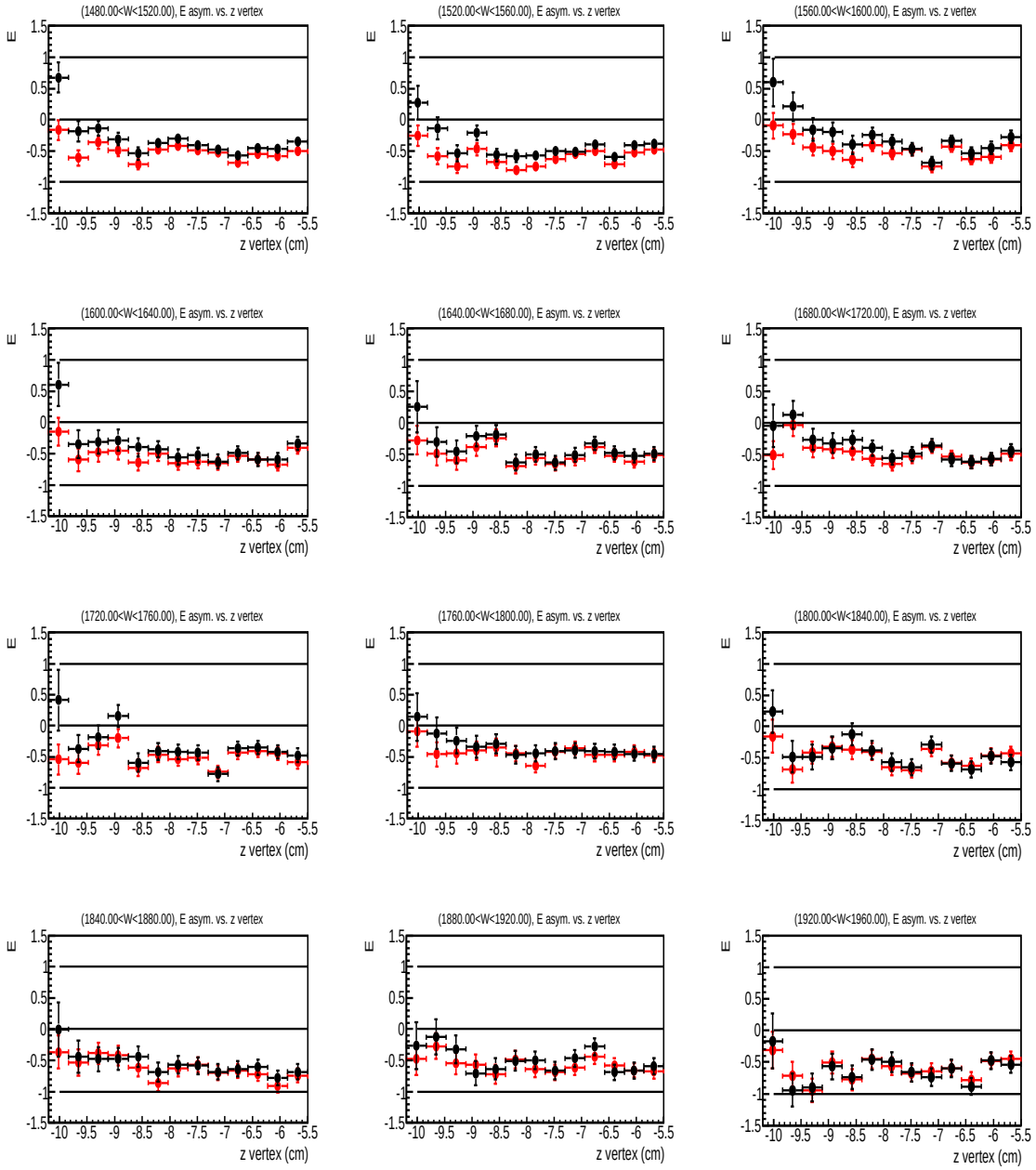

Figure 4.43: E vs. the z-component of the interaction vertex for the first 12 energy windows from 1480 MeV$<W<$1960 MeV for the Silver 1&2 periods. The black points are from the 1D-cut background suppression and subtraction and the red points are from the BDT method. The agreement between the two methods is decent. As shown in the third histograms (the right plot on the first row), the 1D-cut background suppression and subtraction method has some issues for $z < -8.5$ cm (but we did not investigate further). The horizontal lines are at 1.0, 0.0, and -1.0. The horizontal axis is in cm and from $-10.2\,\text{cm} \leq z \leq -5.5\,\text{cm}$.

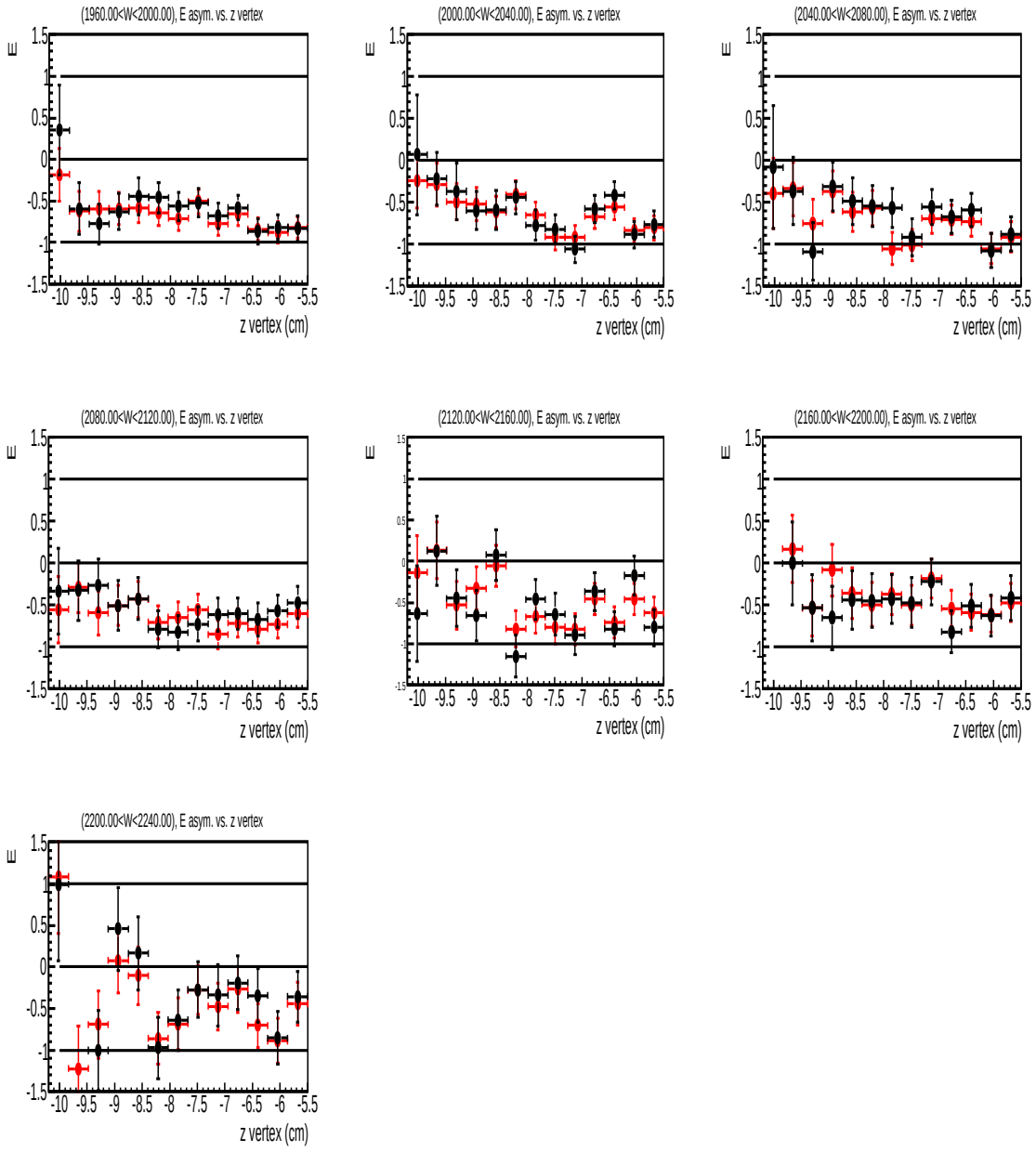

Figure 4.44: E vs. the z-component of the interaction vertex for the last 7 energy windows from 1960 MeV$<W<$2240 MeV for the Silver 1&2 periods. The black points are from the 1D-cut background suppression and subtraction and the red points are from the BDT method. The agreement between the two methods is decent. The horizontal lines are at 1.0, 0.0, and -1.0. The horizontal axis is in cm and from $-10.2\,\text{cm} \leq z \leq -5.5\,\text{cm}$.

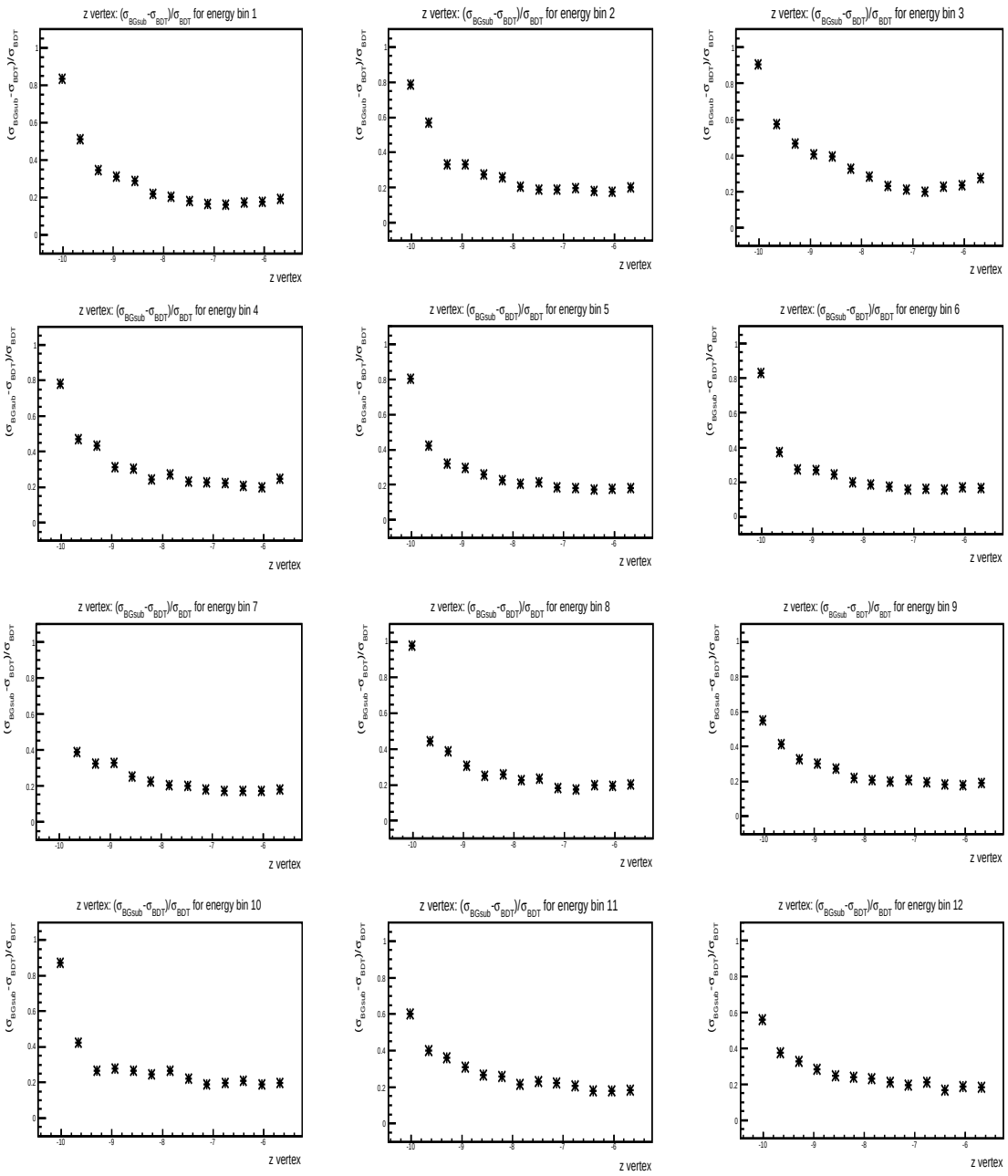

Figure 4.45: $[\sigma_{BGsub} - \sigma_{BDT}]/\sigma_{BDT}$ vs. the z-component of the interaction vertex for first 12 energy windows from 1480 MeV$<W<$1960 MeV for the Silver 1&2 periods. All the points are positive indicating σ_{BDT} is everywhere smaller than σ_{BGsub}. The unit of the horizontal axis is cm and from $-10.2\,\text{cm} \leq z \leq -5.5\,\text{cm}$.

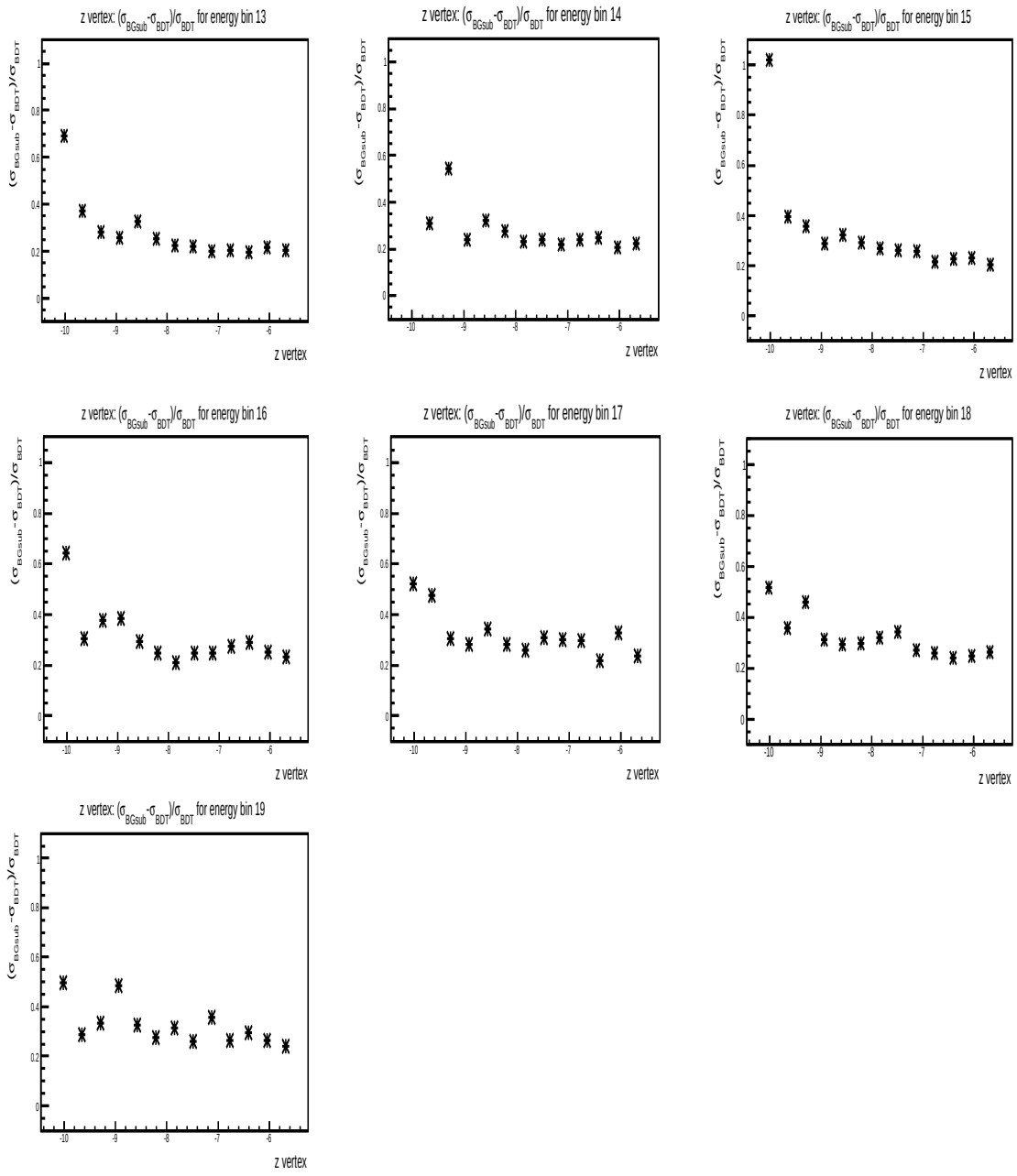

Figure 4.46: $[\sigma_{BGsub} - \sigma_{BDT}]/\sigma_{BDT}$ vs. z-component of the interaction vertex for the last 7 energy windows from 1960 MeV$<W<$2240 MeV for the Silver 1&2 periods. All the points are positive indicating σ_{BDT} is everywhere smaller than σ_{BGsub}. The unit of the horizontal axis is cm and from $-10.2\,\text{cm} \leq z \leq -5.5\,\text{cm}$.

4.3.2.3 Conclusion

Previous sections show an statistical consistency (small systematic difference) between the BDT method and the 1D-cut background suppression and subtraction method, even though the two methods have different approaches in the event selections and the treatments of the remaining background. Furthermore, we showed that the BDT selection data sample is larger than the data sample from the 1D-cut background suppression and subtraction method. Hence, in later sections we will use only the BDT method for event selection. We also plot the E asymmetry as a function of $\cos(\theta_{\pi^-})$ for both methods in Figures 4.47, and 4.48 (for Gold 2 data), and 4.49, and 4.50 (for Silver 1&2 data) to illustrate the decent agreement between the two methods (small positive systematic difference indicates that there remained background events that the 1D-cut background suppression and subtraction method could not completely remove and/or subtract).

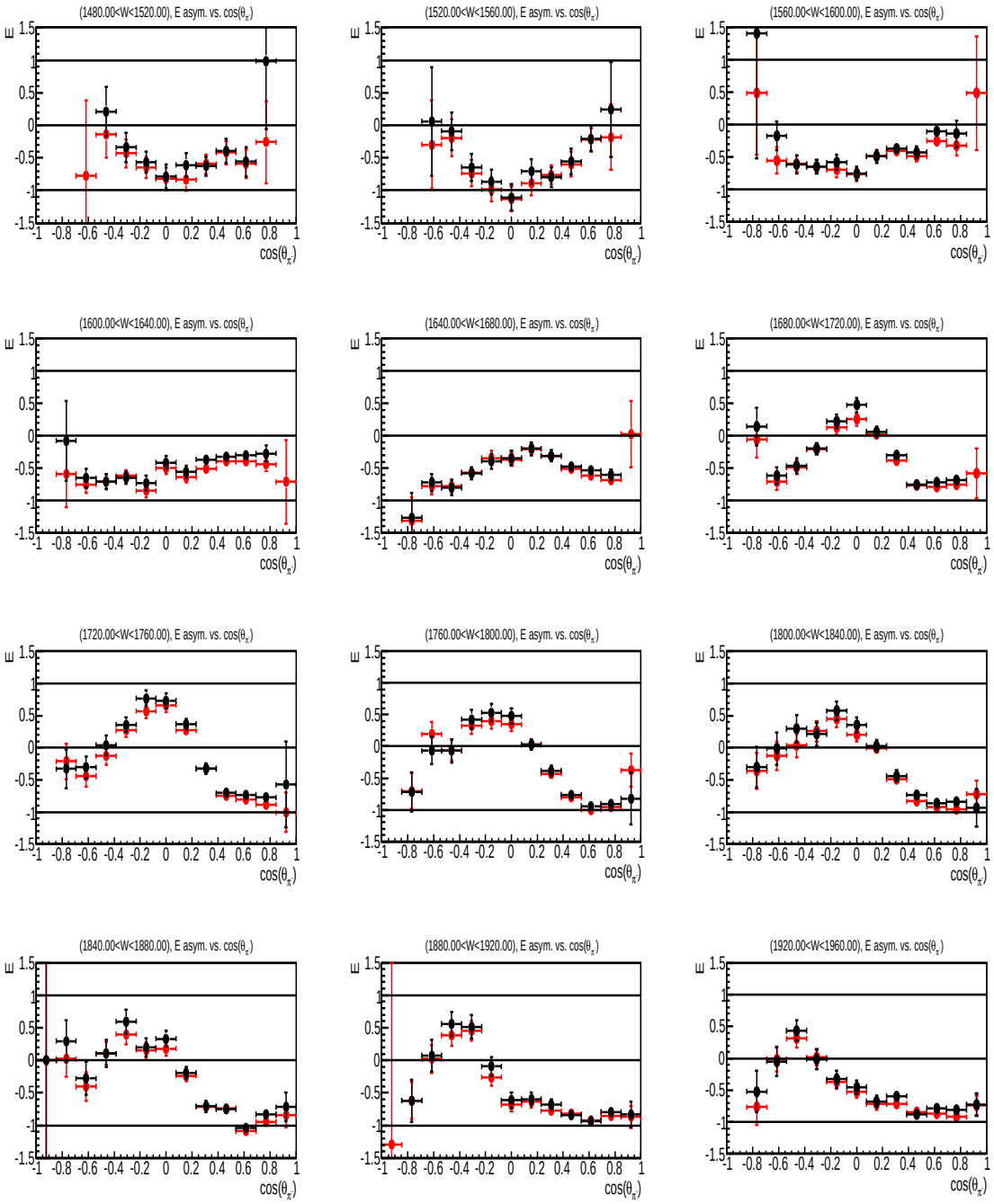

Figure 4.47: E vs. $\cos(\theta_{\pi^-})$ for the first 12 energy windows from 1480 MeV$<W<$1960 MeV for the Gold 2 period. The black points are from the 1D-cut background suppression and subtraction method and the red points are from the BDT method. The agreement between the two methods is good.

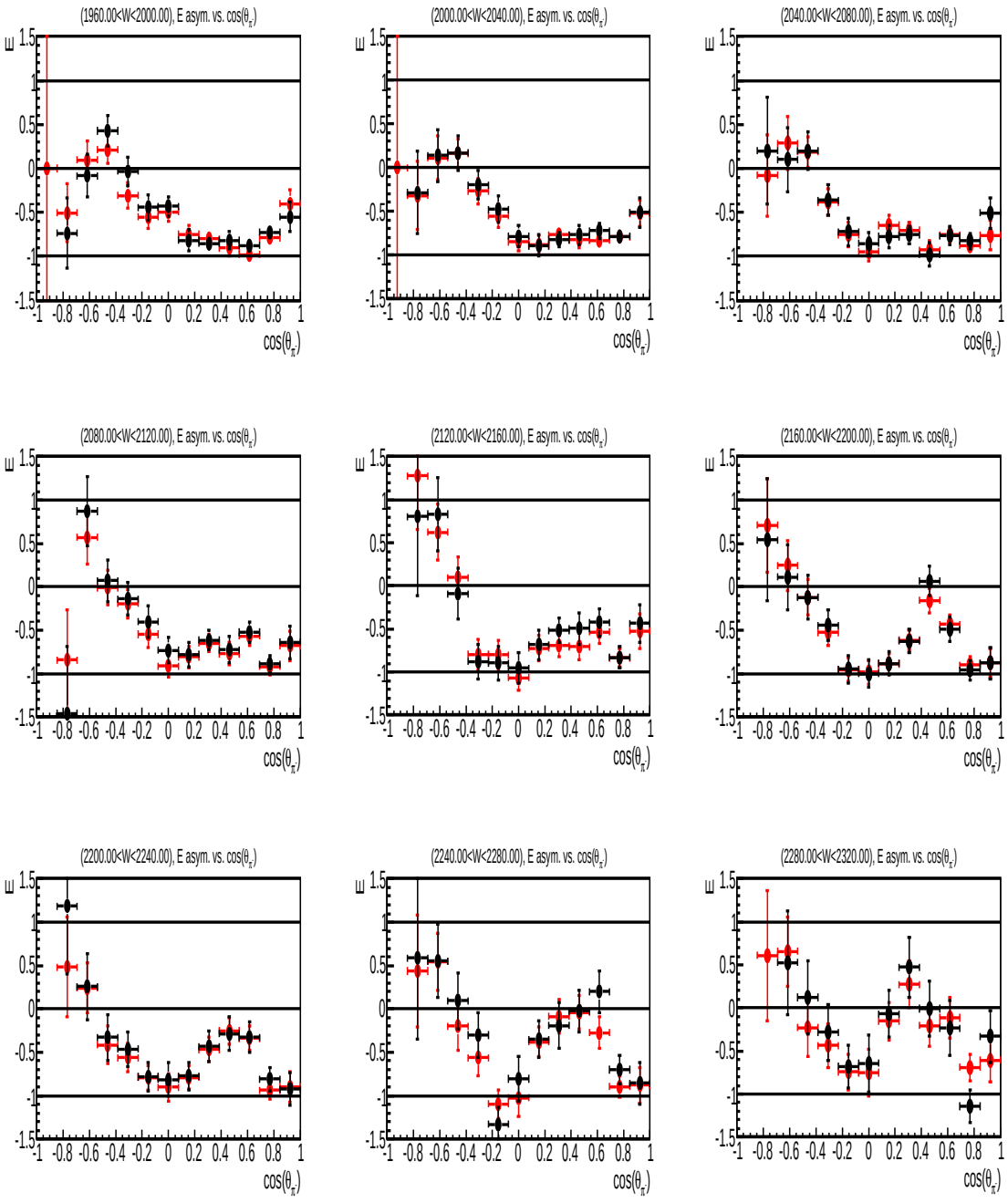

Figure 4.48: E vs. $\cos(\theta_{\pi^-})$ for the last 9 energy windows from 1960 MeV$<W<$2320 MeV for the Gold 2 period. The black points are from the 1D-cut background suppression and subtraction method and the red points are from the BDT method. The agreement between the two methods is good.

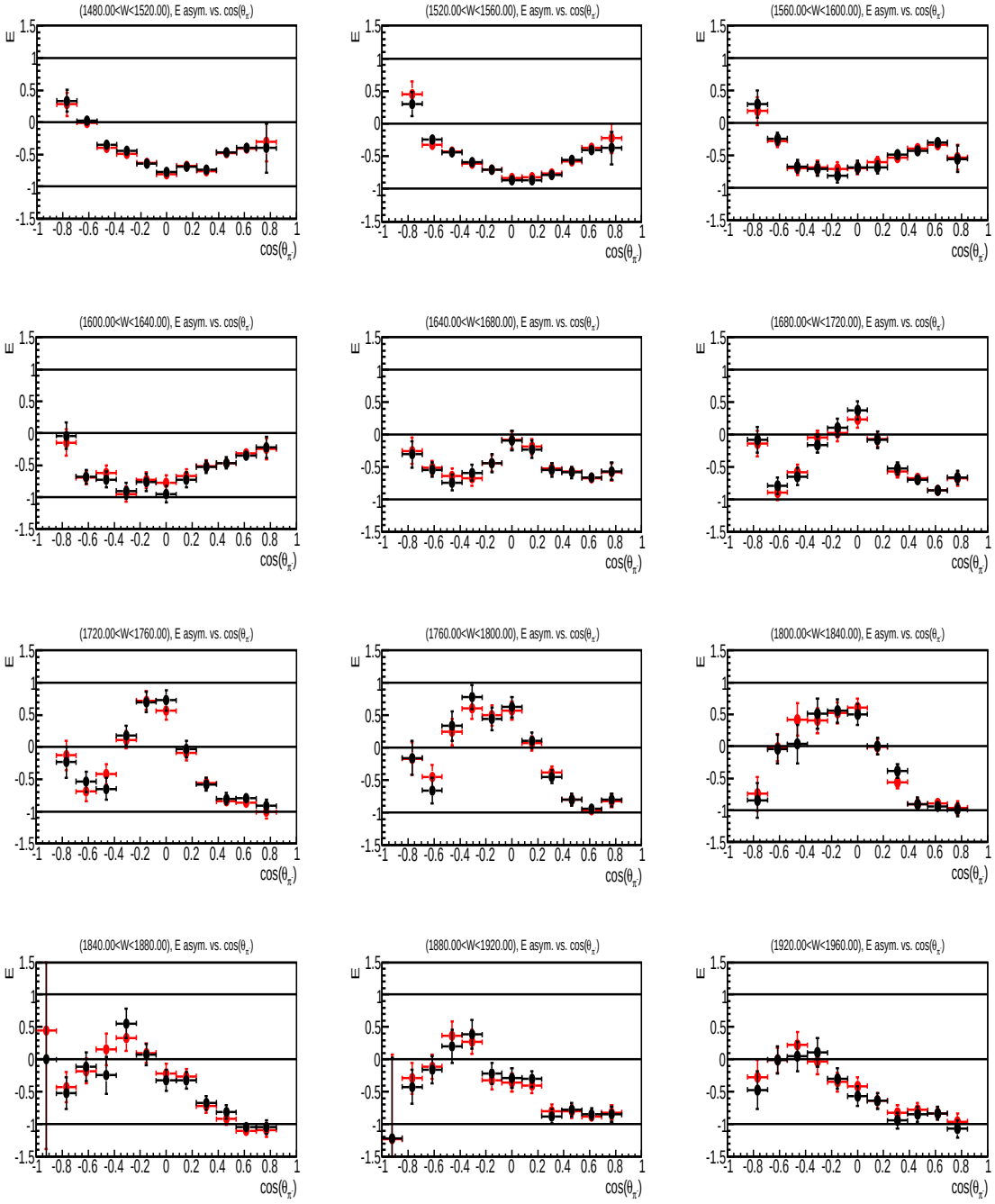

Figure 4.49: E vs.cos($\theta_{\pi-}$) for the first 12 energy windows from 1480 MeV$<W<$1960 MeV for the Silver 1&2 periods. The black points are from the 1D-cut background suppression and subtraction method and the red points are from the BDT method. The agreement between the two methods is good.

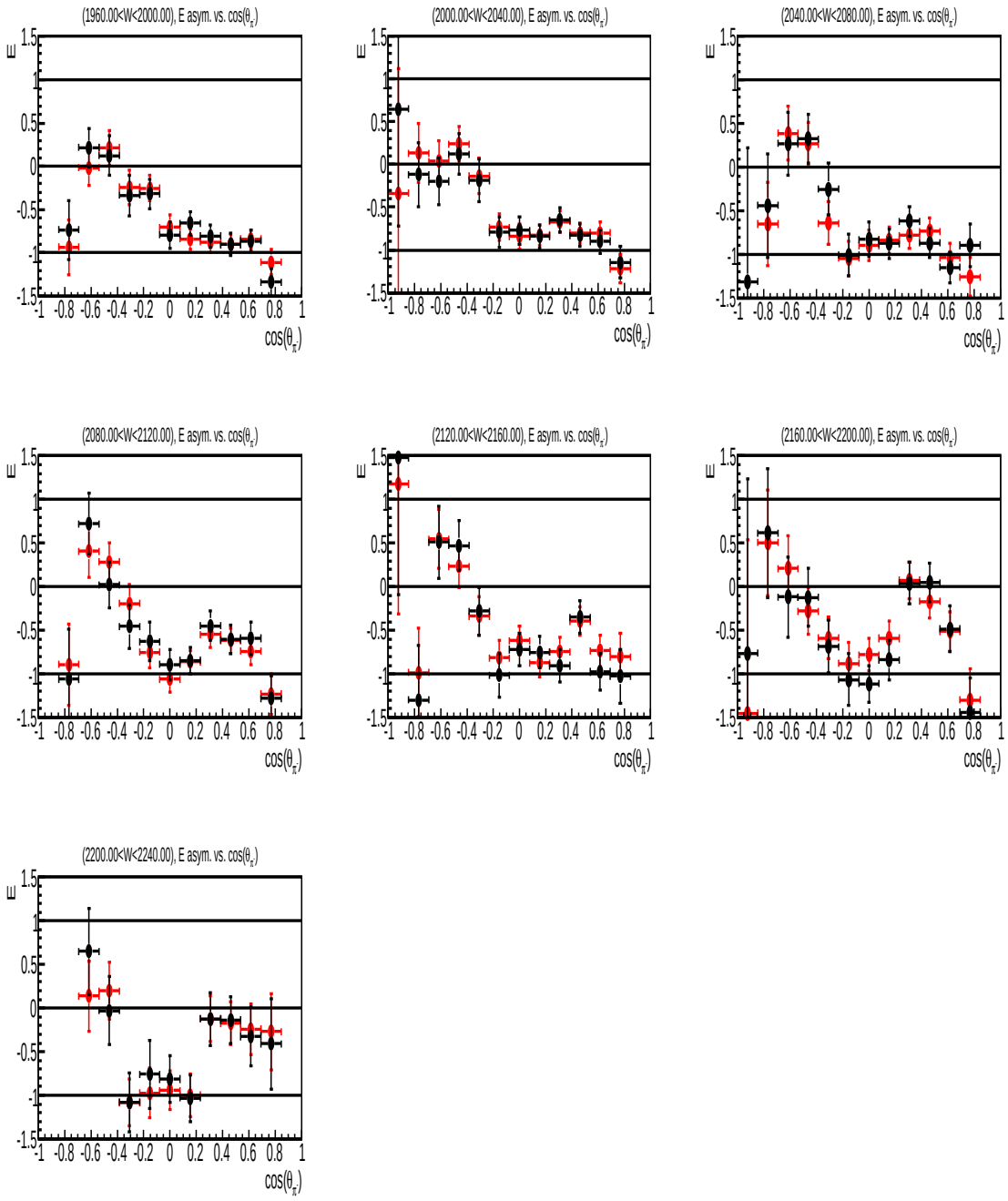

Figure 4.50: E vs. $\cos(\theta_{\pi-})$ for the last 7 energy windows from 1960 MeV$<W<$2240 MeV for the Silver 1&2 periods. The black points are from the 1D-cut background suppression and subtraction method and the red points are from the BDT method. The agreement between the two methods is good.

4.3.3 Estimating the Target Polarizations of Silver 4 and 5 Periods

In section 3.1, we mentioned that the target porlarizations of Silver 4 and 5 were not measured correctly. In particular, the magnitude of the E asymmetry obtained using the measured polarizations was smaller when comparing to the Silver 1, 2, and Gold 2 periods. This indicates the true values of Silver 4 and 5 target polarizations must be smaller than initially measured. Necessarily, in this section, we will implement a procedure to obtain the correct polarizations indirectly by using Silver 1&2 data. The procedure is based on the well-known χ^2 test:

- Compute the E asymmetry as a function of the z vertex from Silver 1&2 data, denote as $E_{s12}(z_i)$ where i indicates the i^{th} bin,
- Iterate over a set of possible values for Silver 4 (or 5) target polarization,

1. For each polarization value P, compute the E asymmetry as a function of the z vertex, denote as $E_{s4}(z_i, P)$ (i indicates the i^{th} bin),
2. Compute χ^2 statistic for this particular value P:

$$\chi^2(P) = \sum_i \frac{\left(E_{s4}(z_i, P) - E_{s12}(z_i)\right)^2}{\sigma^2_{s4}(z_i, P) + \sigma^2_{s12}(z_i)},$$

note that $\chi^2(P)$ is defined as a weighted least square estimator, and the weights are proportional to $\left(\sigma^2_{s4}(z_i, P) + \sigma^2_{s12}(z_i)\right)^{-1}$ (i.e., a smaller weight for a larger statistical uncertainty); the best estimate of the polarization P^* is such that $\chi^2(P^*) = \min_P \chi^2(P)$. Moreover, if we also assume P is normally distributed with a centroid μ_P, and a width σ_P, then

$$\chi^2(P) = \frac{\left(P - \mu_P\right)^2}{\sigma^2_P} + constant,$$

note that $\chi^2(P^*) = \min_P \chi^2(P)$ when $P^* = \mu_P$, and $\chi^2(P^* \pm \sigma_P) = \chi^2(P^*) + 1$. The next two steps are apparent:

- Fit a 2^{nd} order polynomial ($f(P)$) using all previously obtained values of $\chi^2(P)$,
- The best estimate of the polarization is P^* such that $f(P^*) = \min_P f(P)$, and its statistical uncertainty σ_P is such that $f(P^* \pm \sigma_P) = \chi^2(P^*) + 1$.

In Figure 4.51 we plot the fitted 2^{nd} polynomial functions on the set of $\chi^2(P)$ values for the Silver 4 and Silver 5 data sets. It is straightforward to obtain P^* and σ_P for both run periods from the fits. Importantly, because we utilized Silver 1&2 data to

estimate the polarizations of Silver 4 and 5, we consequently introduced correletions between the Silver 1&2 and Silver 4, and 5 data sets. Necessarily, we computed the empirical covariances (from the data) using the following definition of the covariance:

$$\sigma_{s12,s4} = \frac{1}{N}\sum_i \left(E_{s12}(z_i) - \overline{E_{s12}}\right)\left(E_{s4}(z_i, P^*) - \overline{E_{s4}}\right),$$

where N is the total number of bins, $\overline{E_{s12}}$,and $\overline{E_{s4}}$ are the averages of the E asymmetry (as a function of z vertex) for Silver 1&2, and Silver 4, respectively. Correlation between Silver 1&2 and Silver 5 was computed similarly. We present all the results in Table 4.8.

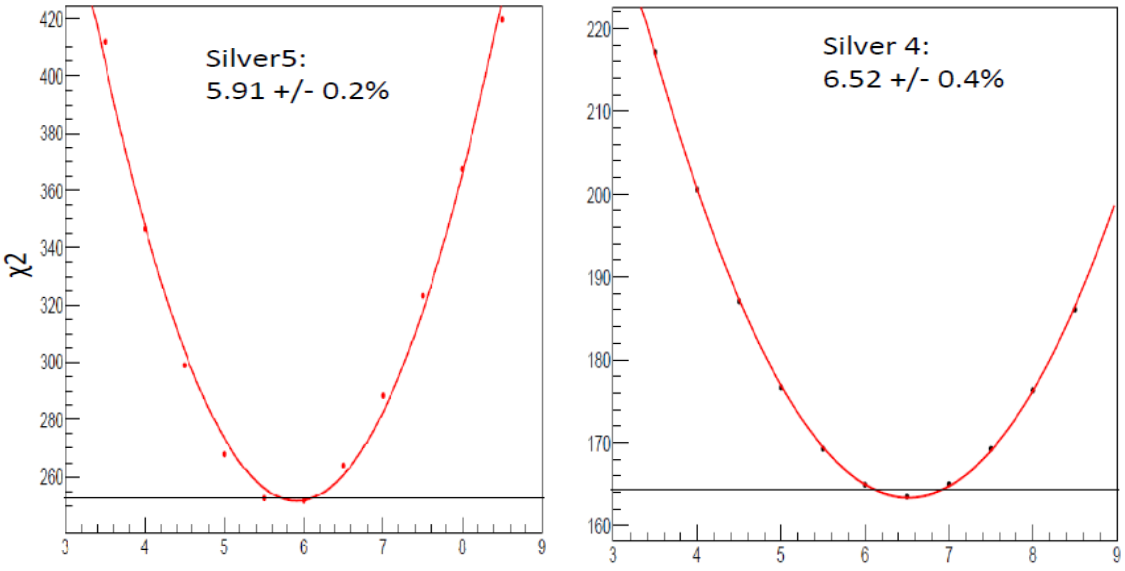

Figure 4.51: χ^2 as a function of possible values of P. The left plot was obtained for Silver 5 data, and the right plot was obtained for Silver 4 data. The unit for P is percentage (%).

Run period	Estimated Polarization	Induced Covariance in E
Silver4	6.52 ± 0.40 %	0.0072
Silver5	5.91 ± 0.20 %	0.0117

Table 4.8: Estimated values of the target polarizations for Silver 4 and 5 periods.

4.3.4 Combining Results from All Run Periods with Circular Beam Polarization

In this section, we combine the E measurments from the Gold 2 and all the Silver run periods into one set of measurements. If all measurements were independent, the following formulas would give the weighted mean, and its uncertainty; the weights are inversely proportional to the squared statisitical uncertainties of the individual measurements—i.e., the most precise measurements has the highest weight:

$$\overline{E} = \frac{\sum\limits_{t} \left(1/\sigma_t^2\right) E_t}{\sum\limits_{t} 1/\sigma_t^2}, \quad \frac{1}{\sigma_{\overline{E}}^2} = \sum_{t} \frac{1}{\sigma_t^2}, \tag{4.13}$$

where t is the indicator for each individual run period (it represents all Silver periods and Gold 2 period); E_t, and σ_t are the E measurement and its statistical uncertainty, respectively, for the t^{th} run period, and $\overline{E}$ is the combined value (weighted average) of all measurements. When the measurments are not independent, the above formula is rewriten more generally as follows:

$$\begin{aligned} \overline{E} &= \sum_t w_t E_t, \qquad & \sigma_{\overline{E}}^2 &= \sum_t w_t^2 \sigma_t^2 + 2 \sum_{t \neq t'} w_t w_{t'} \sigma_{t,t'}, \\ w_t &\approx \frac{1/\sigma_t^2}{\sum\limits_t 1/\sigma_t^2} + f(\sigma_t, \sigma_{t'}, \sigma_{t,t'}) \end{aligned} \tag{4.14}$$

where $\sigma_{t,t'}$ is the covariance of E_t and $E_{t'}$, and $f(\sigma_t, \sigma_{t'}, \sigma_{t,t'})$ is an extra term which depends on both σ_t, $\sigma_{t'}$, and $\sigma_{t,t'}$. We had estimated, in section 4.3.3, that the covariance between Silver 4 (Silver 5) with Silver 1&2 is 0.0072 (0.0117); the other covariances are zero because of their statistical independence. Importantly, when calculating the weights for Silver 4 and 5 data, we could safely ignore the term $f(\sigma_t, \sigma_{t'}, \sigma_{t,t'})$ because the Silver 4 and 5 data have small weights (see next paragraph for explaination).

In section 4.3.2.3, we showed the E asymmetry for both Gold 2 and Silver 1&2 run periods. We now present the E asymmetry obtained from the Silver 3, 4, and 5 run periods in Figures 4.52, 4.53, and 4.54 for completeness. Notice that the statistical uncertainties for the three periods are much larger than for the Silver 1&2 and Gold 2 periods. This is because the Silver 3 period has effectively a tenth of Gold 2 statistics while the target polarizations of the Silver 4 and 5 are about a fifth of the target polarization of the Gold 2 period. We will show the combined results in the next three sections.

4.3.4.1 The E asymmetry as a Function of $|\mathbf{p}|_{\mathbf{missing}}$

In Figure 4.55 we illustrate the relation between the E asymmetry and the missing (recoil) momentum. It is very interesting to observe that the absolute value of the magnitude of the E asymmetry decreases as the magnitude of the recoil momentum increases. Since the remaining background is insignificant (and had been accounted

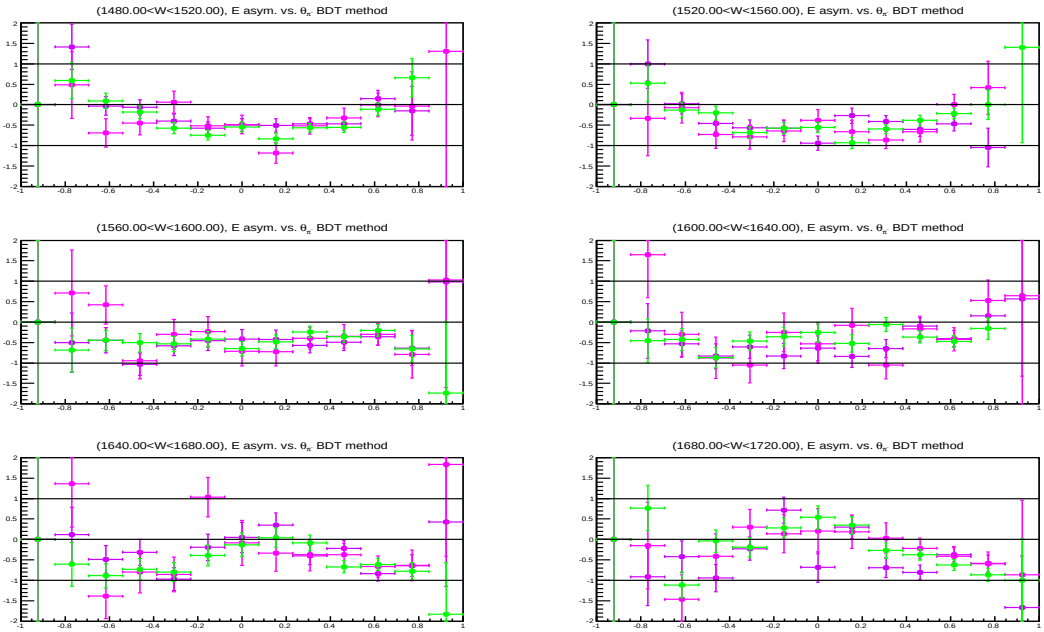

Figure 4.52: E vs. $\cos(\theta_{\pi-})$ for the first 6 energy windows from 1480 MeV$<W<$1720 MeV. The violet, magenta, and green points are from the Silver 3, 4, and 5 data, respectively.

for appropriately), the pronounced phenomona must be *real* physics; i.e., we suspect this is due to interaction between the neutron and the proton inside the deuteron (initial state interaction) and/or the interaction between the spectator proton and the scattered particles (final state interaction).

Since the BDT method can keep events with missing momentum up to 200 MeV/c, it is necessary to "correct" for the dilution effect as shown in Figure 4.55 (i.e., the magnitude of the E asymmetry gets smaller for larger recoil momentum). We implemented the following procedure:

- Compute the weighted average of missing momentum bins within 20 MeV/c to 70 MeV/c (this is a small momentum—and relatively flat—inteval, thus, the dilution effect is small, but this interval is with high statistics, thus, the estimation is very precise); this is our estimate of the E asymmetry for when the missing momentum is "zero," referring to as E_{pure}^{AVE}.

- Apply a third order polynomial fit, see Figure 4.55 to extrapolate the value of the E asymmetry for when the missing momentum is "zero," referring to as E_{pure}^{FIT}.

- Compute the weighted average of the E in all the bins (i.e., up to 200 MeV/c);

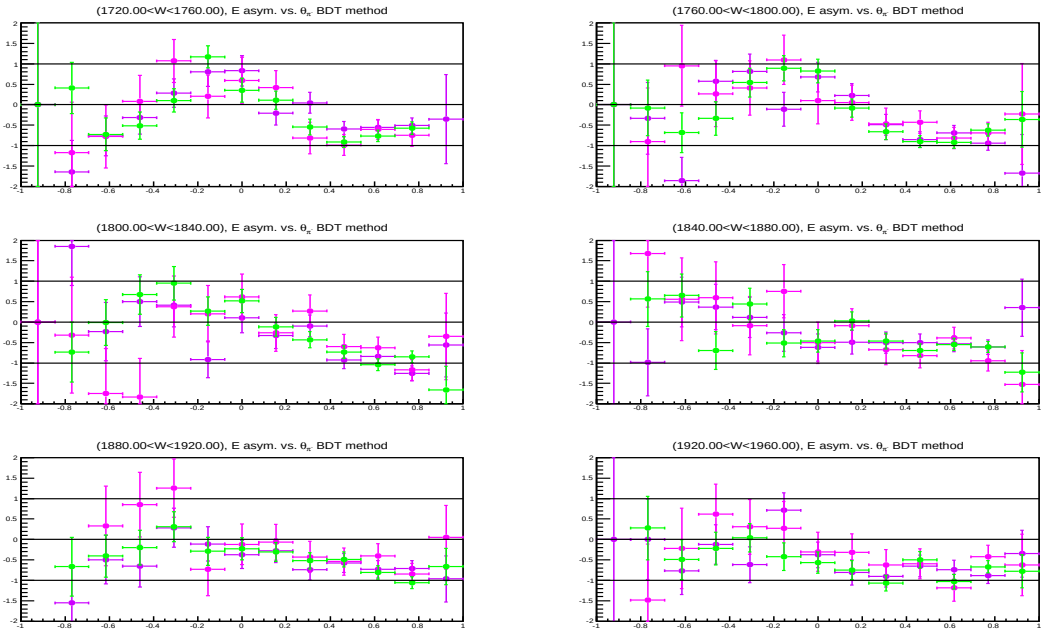

Figure 4.53: E vs. $\cos(\theta_{\pi^-})$ for the middle 6 energy windows from 1720 MeV<W<1960 MeV . The violet, magenta, and green points are from the Silver 3, 4, and 5 data, respectively.

this is our estimate of the average diluted E asymmetry for the BDT method, referring to as $E^{BDT}_{diluted}$.

- Compute the weighted average of the measuring bins with Missing Momentum≤110 MeV/c; this is our estimate of the average diluted E asymmetry for the background-subtraction method, referring to as $E^{BGsub}_{diluted}$.

- Obtain the correction factors for the BDT method (Missing Momentum<200 MeV/c), and the background-subtraction method (Missing Momentum<110 MeV/c):

$$1 + c_{method} = \frac{E^{AVE}_{pure}}{E^{method}_{diluted}},$$

$$\sigma^2_{c_{method}} = \left(\frac{E^{AVE}_{pure}}{E^{method}_{diluted}}\right)^2 \left[\frac{\sigma^2_{E^{AVE}_{pure}}}{\left(E^{AVE}_{pure}\right)^2} + \frac{\sigma^2_{E^{method}_{diluted}}}{\left(E^{method}_{diluted}\right)^2} - 2\frac{cov(E^{AVE}_{pure}, E^{method}_{diluted})}{E^{AVE}_{pure} \cdot E^{method}_{diluted}}\right],$$

where, for example,

$$cov(E^{AVE}_{pure}, E^{BDT}_{diluted}) = cov\left(\sum_{i=3}^{7} w_i E_i, \sum_{j=1}^{20} W_j E_j\right) = \sum_{i=3}^{7} w_i W_i \sigma^2_{E_i},$$

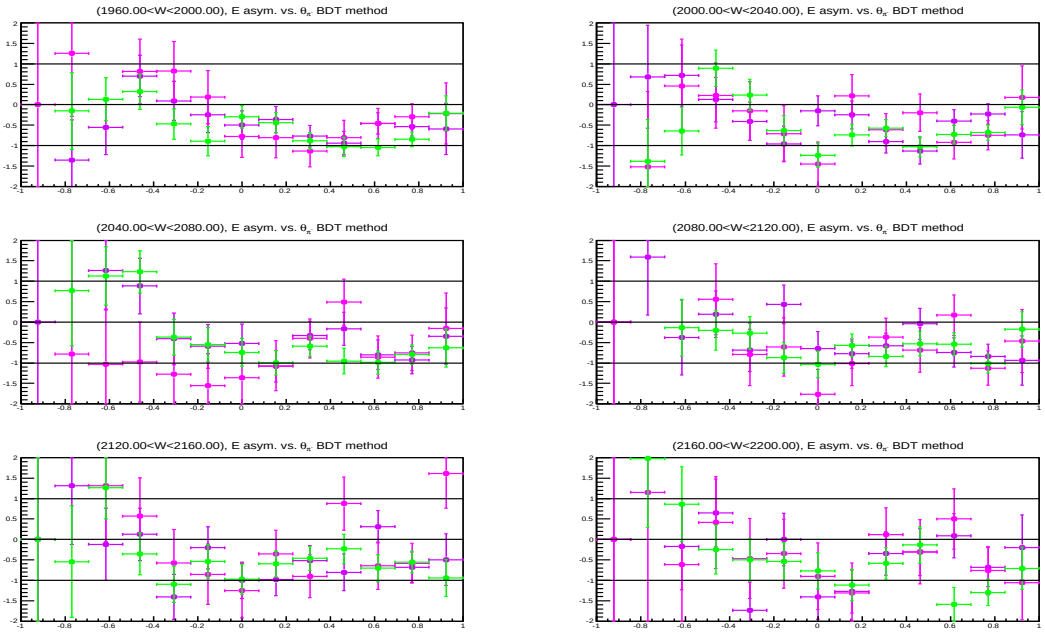

Figure 4.54: E vs. $\cos(\theta_{\pi^-})$ for the last 6 energy windows from 1960 MeV$<W<$2200 MeV. The violet, magenta, and green points are from the Silver 3, 4, and 5 data, respectively.

where w_i, and W_j are the weights to compute the E^{AVE}_{pure}, and the $E^{BDT}_{diluted}$, respectively. Note that we computed the E^{AVE}_{pure} using only the third to the seventh missing momentum bins, while to compute the $E^{BGsub}_{diluted}$ we used the first 11 bins, and to compute the $E^{BDT}_{diluted}$ we used all the bins. It is clear that the decision to select only bins with missing momentum within 20 MeV/c to 70 MeV/c to obtain the E^{AVE}_{pure} was rather arbitrary. Therefore, the E^{FIT}_{pure} is considered a more optimal estimation since it is obtained using all the measured bins (the third order polynomial fit on twenty missing momentum bins). However, we also learned that the difference between E^{AVE}_{pure} and E^{FIT}_{pure} is small, see Table 4.9. Hence, we will compute the correction factor by using the E^{FIT}_{pure}, but estimate the covariance using the E^{AVE}_{pure}; it is straightforward to compute the covariance using the above formula.

The correction is assumed to be a global scaling constant, i.e., independence of energy W bins , and angular $\cos(\theta_{\pi^-})$ bins. To verify whether this assumption is valid, we divided the data by placing cuts on the W and the $\cos(\theta_{\pi^-})$. In particular, we obtained the correction factors for the two disjoint subsets with W$<$1900 MeV, and W$\geq$1900 MeV. Next, we selected a smaller subset for which $\cos(\theta_{\pi^-})\geq$0.0, and computed the correction factors (we did not consider the case of $\cos(\theta_{\pi^-})<$0.0 because, firstly, the E asymmetry values change from negative to positive quite often, and, secondly, the statistics are low). We present the obtained values of the correc-

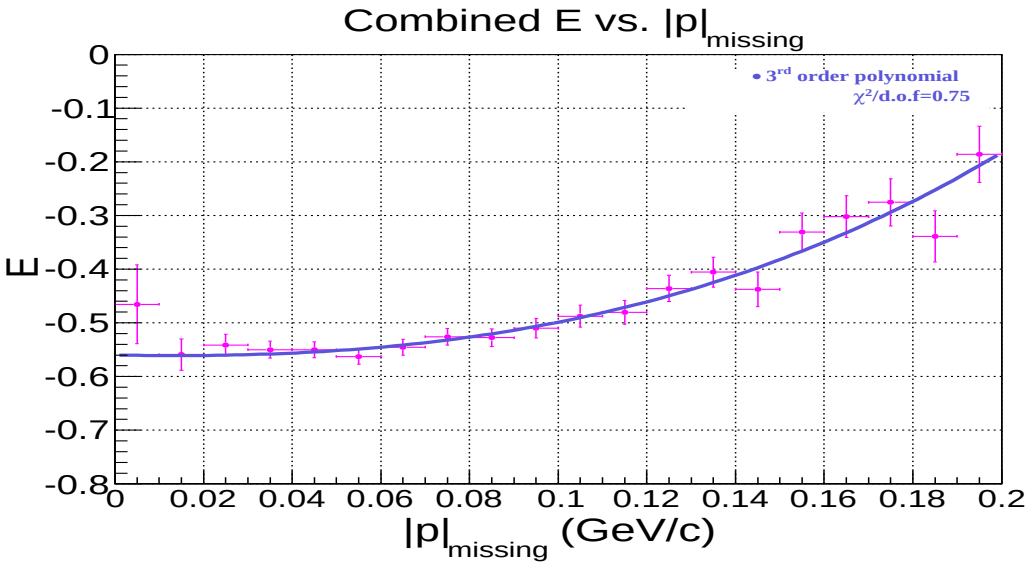

Figure 4.55: Combined E vs. $|p|_{missing}$ for 1480 MeV$<W<$2320 MeV, with $MM(p\pi^-) < 1.03$ GeV, and without any angular cuts. The third order polynomial fit is the blue curve (it is not a theoretical suggestion).

tion factor in Table 4.9; the values of the correction factors are statistically consistent with each other. Hence, the assumption that the correction for the final state (and/or the initial state) interaction(s) can be treated as a global correction is valid, and use the values in the last row of Table 4.9 because they were obtained with all available statistics. In addition, we also plot the E asymmetry vs. the missing momentum for the three mentioned data sets in Figure 4.56; the plots look consistent with Figure 4.55. Note that this global correction can easily be replaced (by rescaling the E values by a single reported constant) by more elaborate energy-and-angular-dependent corrections.

We have assumed that the neutron polarization is equal to the deuteron polarization, but this is not true. The neutron polarization is always smaller than the deuteron polarization. It is because the deuteron wavefunction has, in addition to an S-wave component, a D-wave component in which the spin of the neutron is anti aligned to the deuteron's spin. In particular, according to the paper by Ramachandran *et. al.* [64], the neutron polarization can be approximately computed as $P_n = P_d(1 - \frac{3}{2}P_D)$, where P_n and P_d are neutron and deuteron polarizations, respectively, and P_D denotes the deuteron D-state probability. Note that the D-state contribution increases as the Fermi motion of the neutron (or proton) gets larger, thus the neutron's polarization decreases; this effect partially explains why in Figure 4.55 the magnitude of the E asymmetry decreases as the missing (recoil) momentum increases. At low recoil mo-

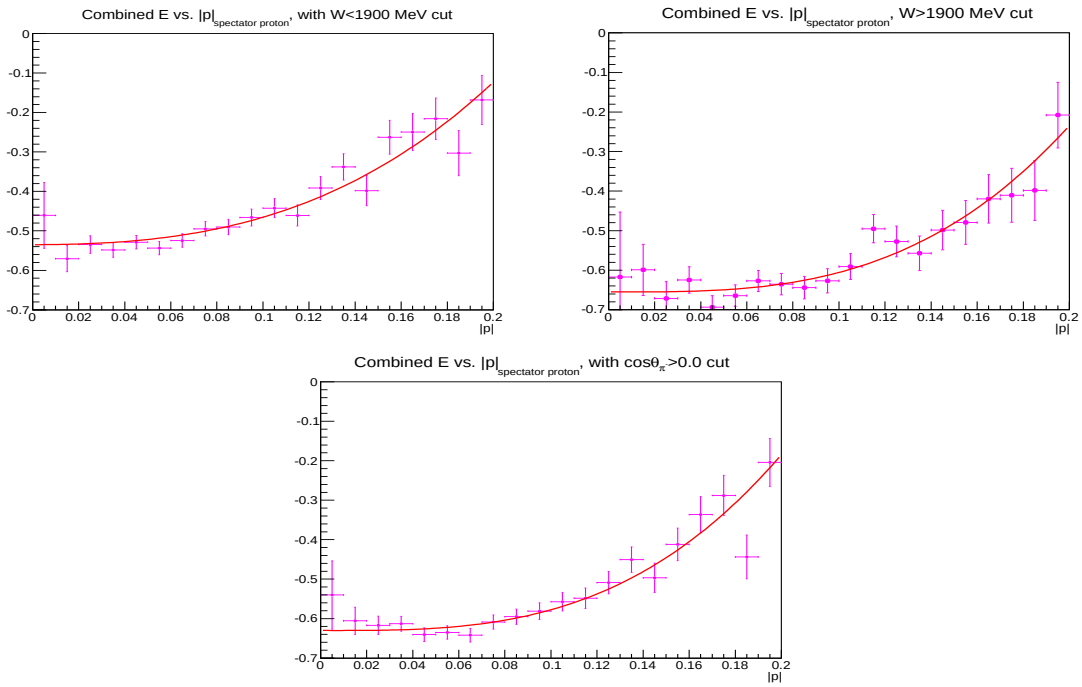

Figure 4.56: Combined E vs. $|p|_{missing}$ for W<1900 MeV (top left), with $W\geq$1900 MeV (top right), and with $\cos(\theta_{\pi-})\geq$0.0 (bottom). The third order polynomial fits (red curves) are to help guide the eyes, not a theoretical suggestion.

Selection	E_{pure}^{AVE}	E_{pure}^{FIT}	$E_{diluted}^{BDT}$	$E_{diluted}^{BGsub}$
W<1900MeV/c	-0.530±0.008	-0.535±0.006	-0.485±0.006	-0.512±0.006
W≥1900MeV/c	-0.650±0.013	-0.655±0.011	-0.601±0.009	-0.631±0.010
$\cos(\theta_{\pi-})\geq$0.0	-0.627±0.008	-0.630±0.007	-0.583±0.006	-0.611±0.006
NO CUT	-0.552±0.007	-0.554±0.006	-0.510±0.005	-0.535±0.005

Selection	BDT correction	Background-subtraction correction
W<1900MeV/c	0.103±0.013	0.045±0.010
W≥1900MeV/c	0.090±0.013	0.038±0.011
$\cos(\theta_{\pi-})\geq$0.0	0.080±0.009	0.031±0.006
NO CUT	0.086±0.008	0.036±0.005

Table 4.9: Correction factors for dilution effect caused by the spectator proton. Note that the correction factors were obtained using the values of E_{pure}^{FIT} (not E_{pure}^{AVE}), and the corrections would be applied multiplicatively as (1+0.086) for the BDT method and (1+0.036) for the 1D cut background supression and subtraction method.

mentum the D-state contribution is on the order of 5%[2] which implies the neutron polarization is only 92.5% of the deuteron polarization. Notice that this is consistent

[2]Private conversation with g14 colleague Andy Sandorfi.

with the correction factor (8.6%) in Table 4.9. In other words, another approach to correct for the dilution effect is to scale down our reported target polarizations in Tables 3.1 and 3.2 to 92.5% of their reported values. In a recent theoretical calculation, accounting for energy-and-angular dependence, Harry Lee found that for signal events with missing momentum less than 100 MeV/c the dilution effect from the D-state component on the E asymmetry for this $p\pi^-$ channel is negligible[3]. Consequently, we are confident that the 8.6% correction is optimal to correct for the dilution effect shown in Figure 4.55. Notice that we did not use the other approach—i.e., reducing the target polarization to 92.5%—because we think the 8.6% correction accounts for also the final-state interaction and is more appropriate because it was obtained based on the data where the E asymmetry was measured. Nevertheless, for low statistics data for which a similar study like in this section may not be possible, reducing the target polarization to 92.5% to be used as neutron polarization in computing the E asymmetry is the best approach.

4.3.4.2 The E asymmetry as a Function of $\cos\left(\mathbf{\Theta}_{\pi^-}^{\mathbf{CM}}\right)$, and W

The angle $\Theta_{\pi^-}^{CM}$ is defined as the angle between the incident photon and the scattered π^- in the overall center-of-mass frame—the target neutrons were assumed to be *at-rest*, ignoring any effects of Fermi motion. We selected this center-of-mass frame because the direction of the incident photon is unchanged; thus the angles between the photon helicity and the target polarization vector remain either 0^0 or 180^0 as in the lab frame. The alternative would be to select the proton-and-pion rest frame (this frame "includes" the effects of the Fermi motion, but requires more corrections for the E measurements because of the effect of Wigner rotation on the polarization vectors). Nevertheless, we examined the results in this alternative frame and found only modest differences. Hence, we decided to use the overall center-of-mass frame. Next, we plot the E asymmetry as a function of the $\cos\left(\mathbf{\Theta}_{\pi^-}^{\mathbf{CM}}\right)$ in Figures 4.57, and 4.58. Additionally, in Figures 4.59 and 4.60, we present the plots of the E asymmetry vs. W. These plots are the complements of the plots in Figure 4.57 and 4.58. They show the energy dependence of the E asymmetry, and are of theoretical interest as well. The plots are after the correction discussed in Section 4.3.4.1.

[3]Private conversation with Harry Lee.

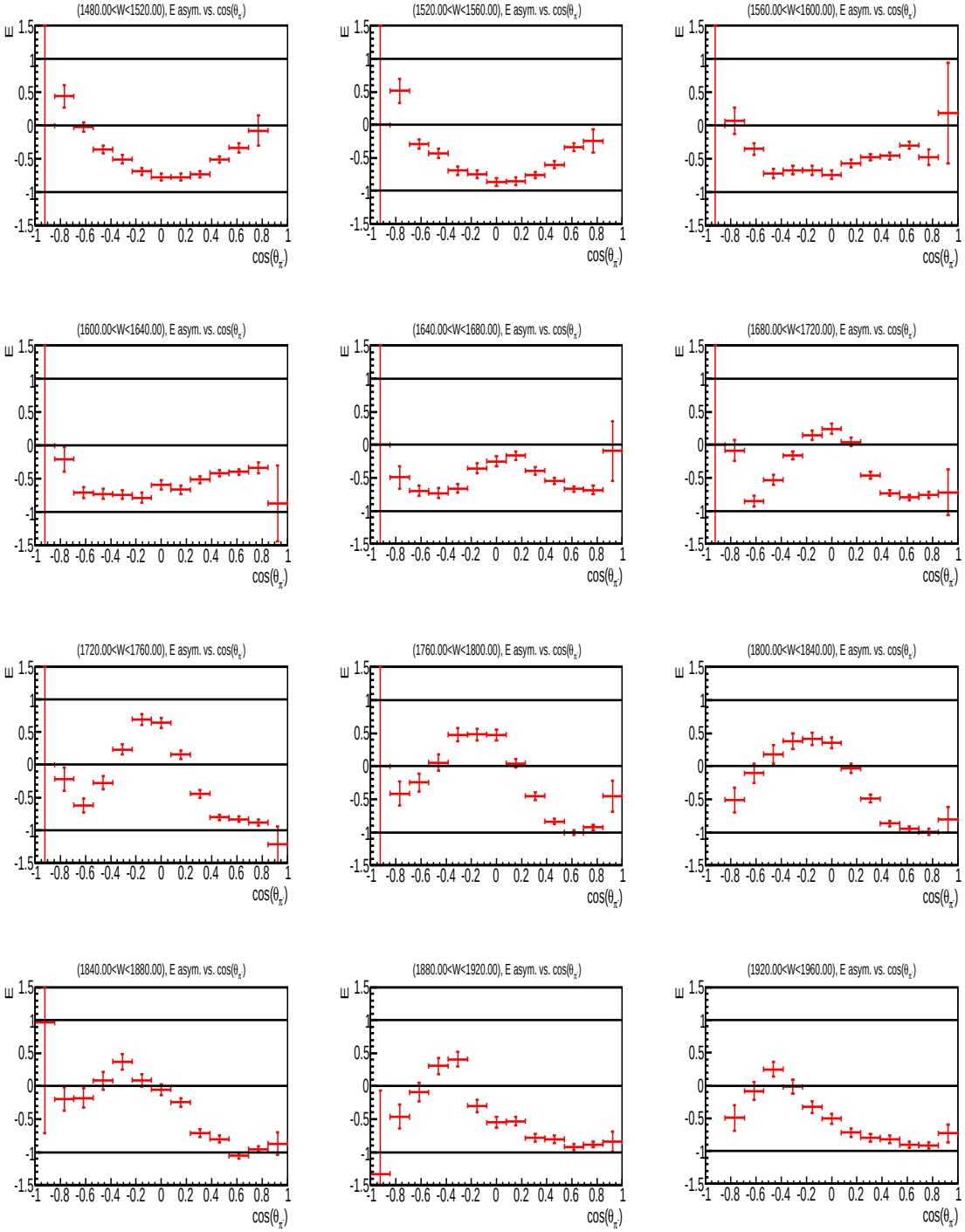

Figure 4.57: Combined E asymmetry vs. $\cos(\theta_{\pi^-})$ for the energy windows from 1480 MeV$<W<$1960 MeV.

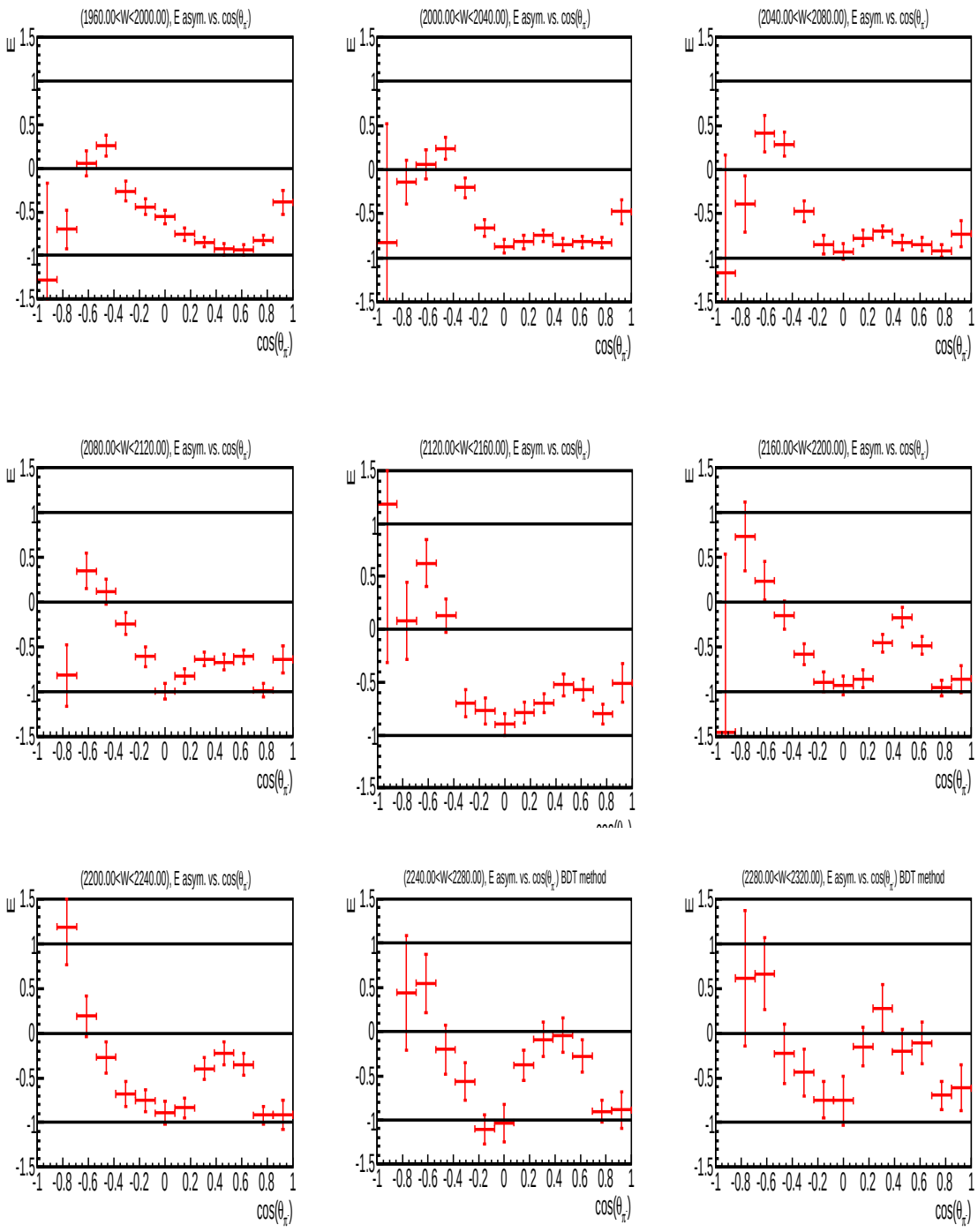

Figure 4.58: Combined E asymmetry vs. $\cos(\theta_{\pi^-})$ for the energy windows from 1960 MeV$<W<$2320 MeV.

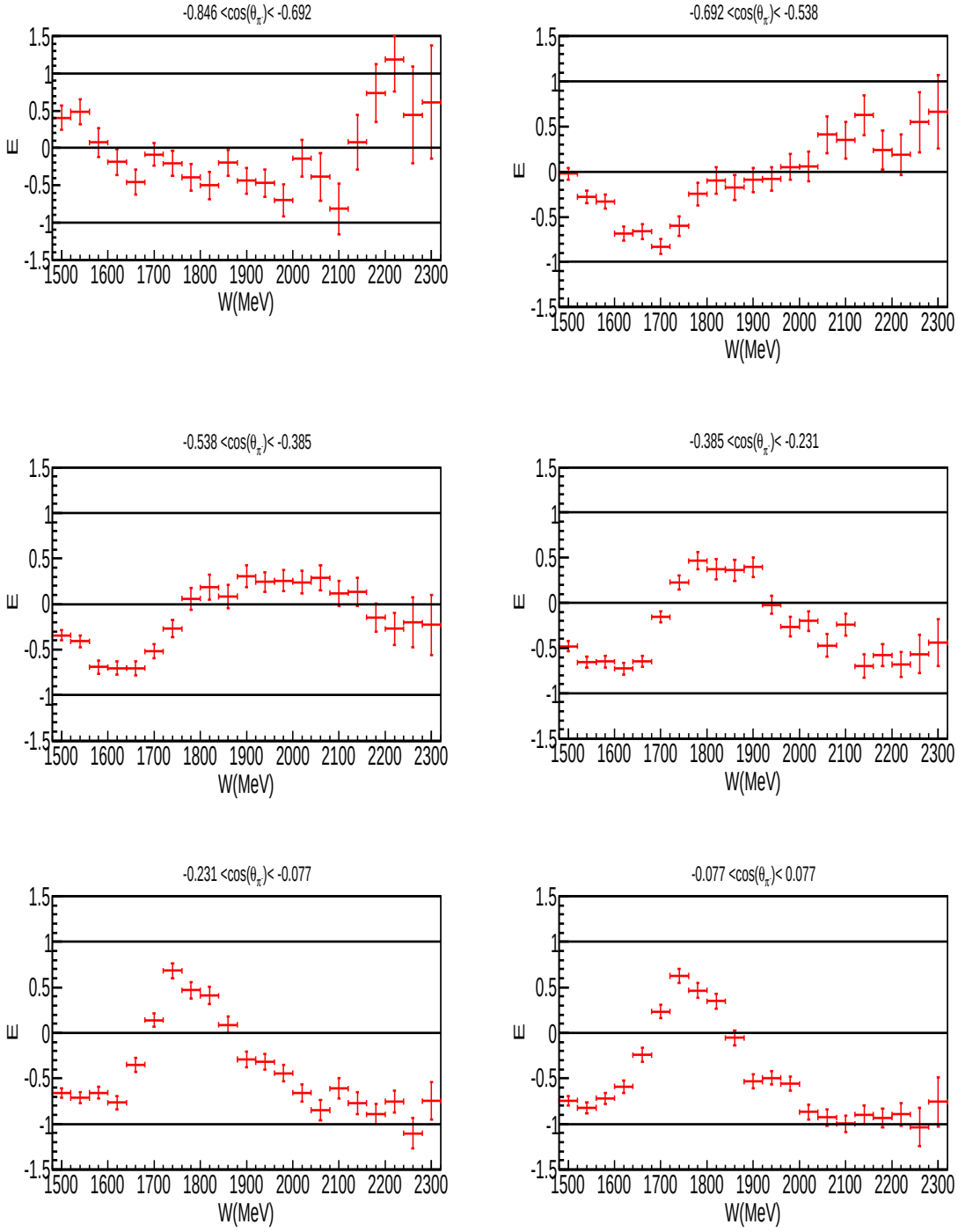

Figure 4.59: Combined E vs. W for the $\cos\left(\Theta_{\pi^-}^{\mathbf{CM}}\right)$ windows from -0.846 to 0.077.

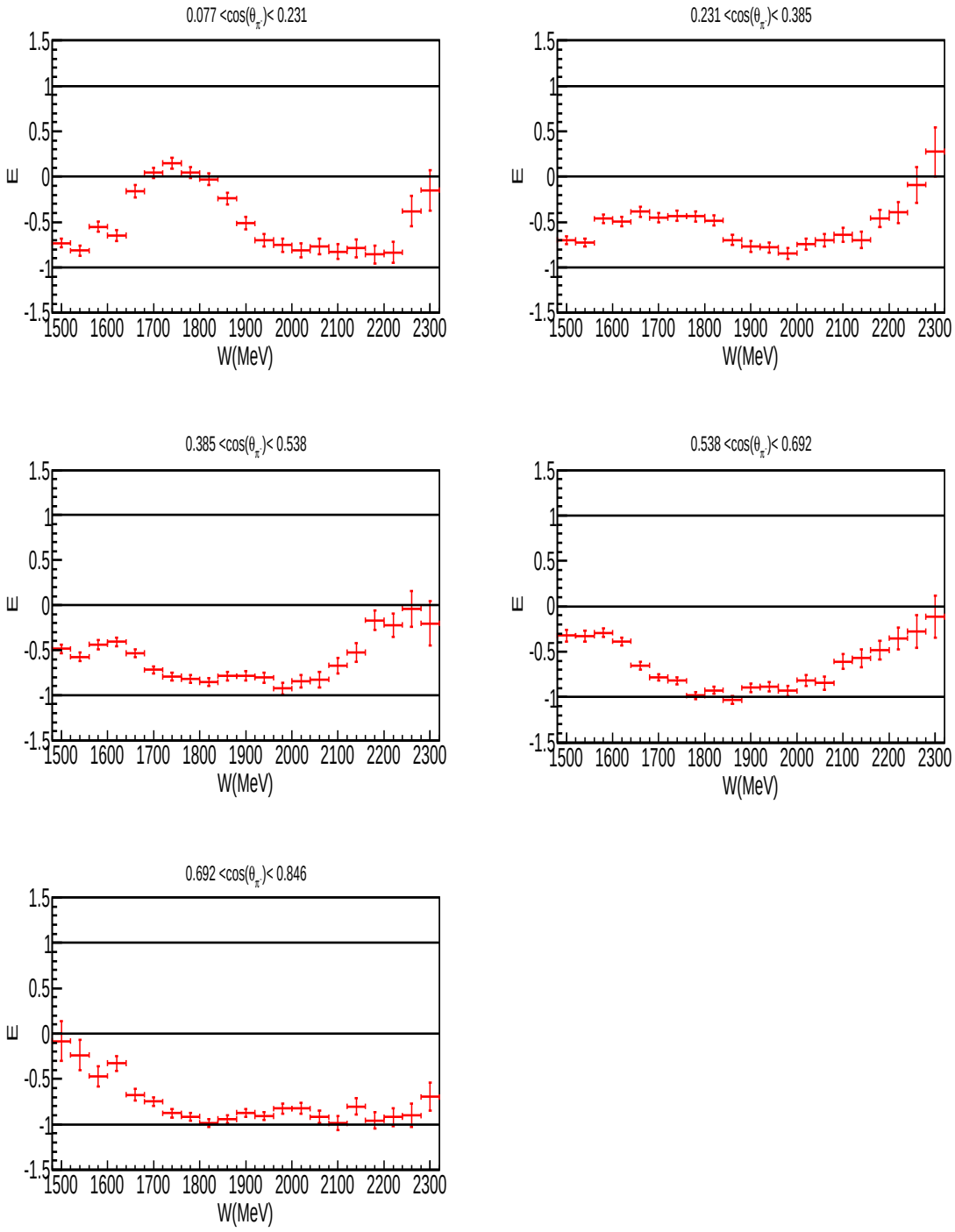

Figure 4.60: Combined E vs. W for the $\cos\left(\mathbf{\Theta}_{\pi^-}^{\mathbf{CM}}\right)$ windows from 0.077 to 0.692.

4.4 Systematics Studies

In this section, we employ various systematics studies to quantify the robustness of the BDT method in selecting the bound neutron events. Note that each systematics test results in a slightly different selection event sample with a different number of remaining background events. Consequently, for each test, we obtain a different dilution factor $\frac{Y_{Target}}{Y_{HD}}$. In section 4.3.4 we asserted that the more precise the measurement (smaller statistical uncertainty), the larger weight it contributes to the combined (weighted average) measurement. Consequently, on average, the difference of the E measurements between the combined and Gold 2 (or Silver 1&2) values is much smaller than the other run periods (because the statistics of the Silver 3 is small while the target polarizations of the Silver 4 and 5 are low, thus, they have larger statistical uncertainties). In Figures 4.61, we plot the difference between the combined E and the individual E (obtained solely from the Silver 1&2, Gold 2, Silver 3, and Silver 4, respectively); as expected, on average, the values of the combined E are closer to the values from the Gold 2 (or the Silver 1&2) periods than from the Silver 3, and 5 periods (this statement is also true for the Silver 4 as well). Therefore, systematic uncertainties for the combined E measurements are affected mostly by the systematic uncertainties of Gold 2 and Silver 1&2 periods. Hence, we only focused on the systematic uncertainties from Gold 2 and Silver 1&2 data. We employed the following procedure to estimate the systematics uncertainty for *each* systematics test:

- Execute the following steps for both the Silver 1&2 and Gold 2 periods:

1. Compute the E asymmetry as a function of the z vertex, $\widehat{E(z)}$, using the BDT method,
2. Vary appropriate parameter(s) for each systematics test and compute the E asymmetry as a function of the z vertex, $\widetilde{E(z)}$,
3. For each z vertex bin j, and energy bin i, compute $\delta_{ij} = \widetilde{E_i(z_j)} - \widehat{E_i(z_j)}$,
4. Fit the δ_{ij} with a Gaussian distribution and obtain the mean (μ_δ) and width (σ_δ) from the fitted Gaussian (see 4.3.2 for how to interpret for the two fitted parameters),
5. Obtain σ_μ, the uncertainty on the mean μ_δ by computing $\sigma_\mu = \sigma_\delta/\sqrt{N}$, where N is the total number of z bins.
6. Compute the overall systematic uncertainty by *combining* the Gold 2 and Silver 1&2 systematic uncertainties (taking a weighted quadratic mean):

$$\sigma_{systematic} = \frac{\sqrt{\frac{1}{\sigma^2_{\mu_{Gold2}}}\mu^2_{Gold2} + \frac{1}{\sigma^2_{\mu_{Silver1\&2}}}\mu^2_{Silver1\&2}}}{\sqrt{\frac{1}{\sigma^2_{\mu_{Gold2}}} + \frac{1}{\sigma^2_{\mu_{Silver1\&2}}}}}, \tag{4.15}$$

Note that since the values of $\widehat{E(z)}$, and $\widetilde{E(z)}$ are negative (see Figures 4.39, and 4.44) if μ_δ is positive then the magnitude of $\widehat{E(z)}$ is larger). We implemented nine systematic tests and will present more detail in the following sections. For each test, we computed the $\sigma_{systematic}$. To estimate the total systematic uncertainty, we computed the square root of the quadratic sum of all individual systematic test's $\sigma_{systematic}$ (i.e., $\sigma^{total}_{systematic} = \sqrt{\sum_i \left[\sigma^i_{systematic}\right]^2}$). Note that this procedure estimates only an overall (average) systematic uncertainty—i.e., it is the same for all measuring bins. This is a reasonable approach if the statistical uncertainties, on average, are larger than the systematic uncertainties (small systematic difference between the BDT and the 1D-cut background suppression and subtraction methods suggests this assumption is valid).

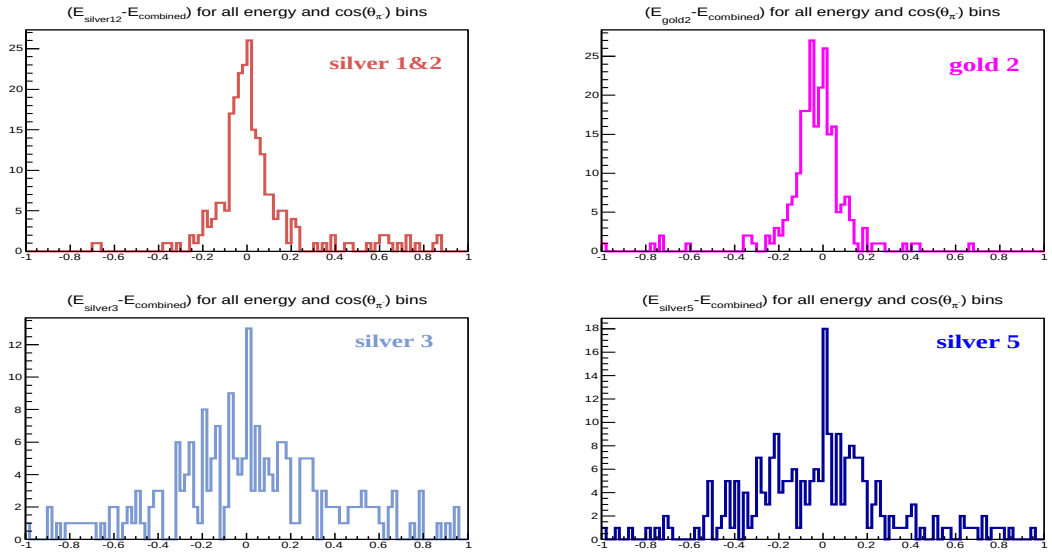

Figure 4.61: Difference between the combined E and individual E (obtained individually from the Silver 1&2, Gold 2, Silver 3, and Silver 5 periods, respectively) as $E_{Period} - E_{Combined}$.

4.4.1 Systematic Effects from Tightening the Z Vertex Cuts

In section 4.3 we placed cuts on the z vertex to reject a majority of remaining target background (selecting only events within $-10.2\,\text{cm} \leq z \leq -5.5\,\text{cm}$), we then estimated the remaining target background and applied an overall scaling factor (see Eq. 4.9). We now applied tighter cuts (selecting only events within $-9.6\,\text{cm} \leq z \leq -6.0\,\text{cm}$)—inevitably sacrificing some signal events, and obtained the E measurements. Note that for this test the E measurements were computed as a function of $\cos\left(\Theta^{\mathbf{CM}}_{\pi^-}\right)$. Next we

compared the $E(\cos\left(\mathbf{\Theta}^{\mathbf{CM}}_{\pi^-}\right))$ measurements from the old ($-10.2\,\mathrm{cm} \leq z \leq -5.5\,\mathrm{cm}$) and the tighter ($-9.6\,\mathrm{cm} \leq z \leq -6.0\,\mathrm{cm}$) cuts. In detail, Figure 4.62 shows the Gaussian fits to the bin-by-bin difference histogram for the Gold 2 and Silver 1&2 data, and Table 4.10 lists the numerical results. The fitted means are small implying a small systematic uncertainty. Unfortunately, since the E measurement's statistical uncertainties are not constant across the domain of $\cos\left(\mathbf{\Theta}^{\mathbf{CM}}_{\pi^-}\right)$, our procedure might overestimate the correct standard deviation (or fluctuation) of the differences $(E_{BDT} - E_{TEST})$ resulting a possibly larger Gaussian widths in Figure 4.62. On the other hand, since the E distribution is expected to be statistically flat across the domain of z, the estimations would be more accurate (thus the remaining tests were carried out with using the variable z vertex).

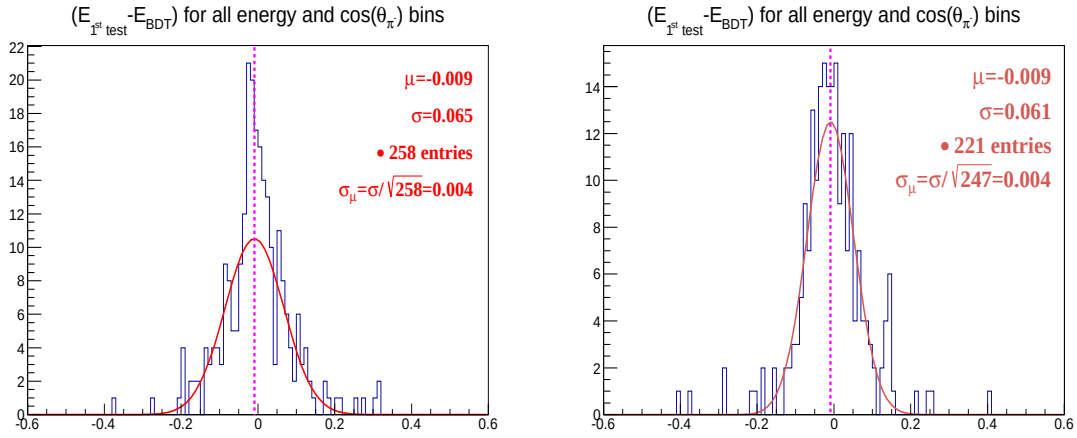

Figure 4.62: Distributions of δ_{ij} fitted with Gaussians for Gold 2 (left plot) and Silver 1&2 (right plot) for the first test (tightening the z vertex cuts).

Run period	$\frac{Y_{Target}}{Y_{HD}}$	Systematic difference $(E_{BDT} - E_{TEST})$	$\sigma_{systematic}$
Gold 2	2.81%	-0.009 ± 0.004	0.009
Silver 1&2	4.09%	-0.009 ± 0.004	

Table 4.10: Estimated $\sigma_{systematic}$ for the first test: tightening the z-vertex cuts.

4.4.2 Systematic Effects from Removing the Missing Mass and Missing Momentum Cuts

In section 4.3.1.2, we introduced the cuts on the missing mass and missing momentum (see Figure 4.35) to reject a small remaining physics background. Note that we did not make any correction after the cuts (correction was only for the target background). For the second test, we relaxed the cuts and studied the new E values.

We compared the two sets of measurements (with and without the missing mass and missing momentum cuts) and estimated the systematic difference. Table 4.11 lists the numerical results, and Figure 4.63 shows the Gaussian fits for the Gold 2 and Silver 1&2 data. As expected, relaxing the cuts results in a slightly diluted E asymmetry (the Gaussian centroids are positive).

Run period	$\frac{Y_{Target}}{Y_{HD}}$	Systematic difference ($E_{BDT} - E_{TEST}$)	$\sigma_{systematic}$
Gold 2	3.65%	$+0.030 \pm 0.002$	0.026
Silver 1&2	5.16%	$+0.021 \pm 0.002$	

Table 4.11: Estimated $\sigma_{systematic}$ for the second test: relaxing the missing mass and missing momentum cuts.

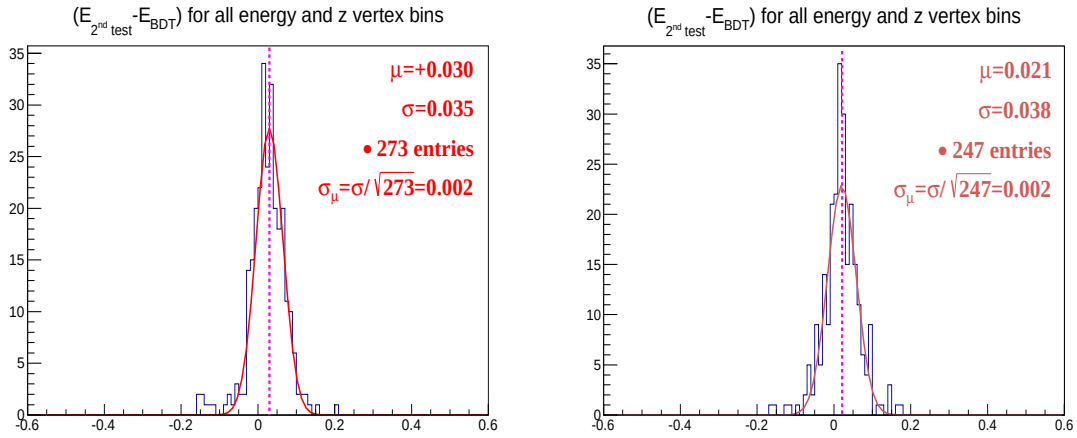

Figure 4.63: Distributions of δ_{ij} fitted with Gaussians for Gold 2 (left plot) and Silver 1&2 (right plot) for the second test (relaxing the missing mass and missing momentum cuts).

4.4.3 Systematic Effects from Varying the BDT Output Cut

This systematic study consits of three smaller tests. Recall that we place a cut at 0.03 on the BDT output to minimize the misclassification cost. Here we set the cut at 0.00, 0.06, and 0.09, respectively. Apparently, the cut at 0.0 allows more background, while the other two values reject more background (reject more signal as well). Figures 4.64, 4.65, and 4.66 show the Gaussian fits for the Gold 2 and Silver 1&2 data for different tests on the BDT cut values. Table 4.12 presents results: the BDT cut at 0.00 results in a very slightly diluted E asysmetry, while the magnitude of the asymmetry is higher when tightening the BDT cut.

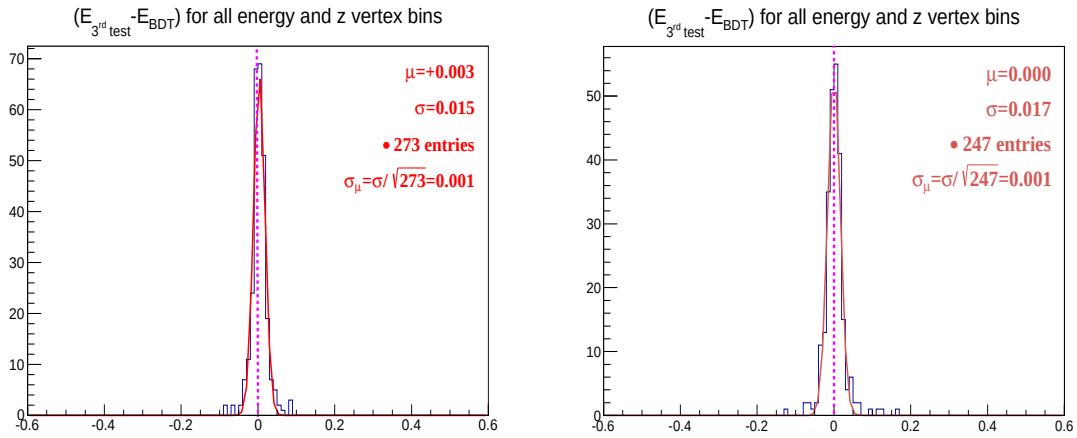

Figure 4.64: Distributions of δ_{ij} fitted with Gaussians for Gold 2 (left plot) and Silver 1&2 (right plot) for the third test (loosening the BDT cut to 0.00).

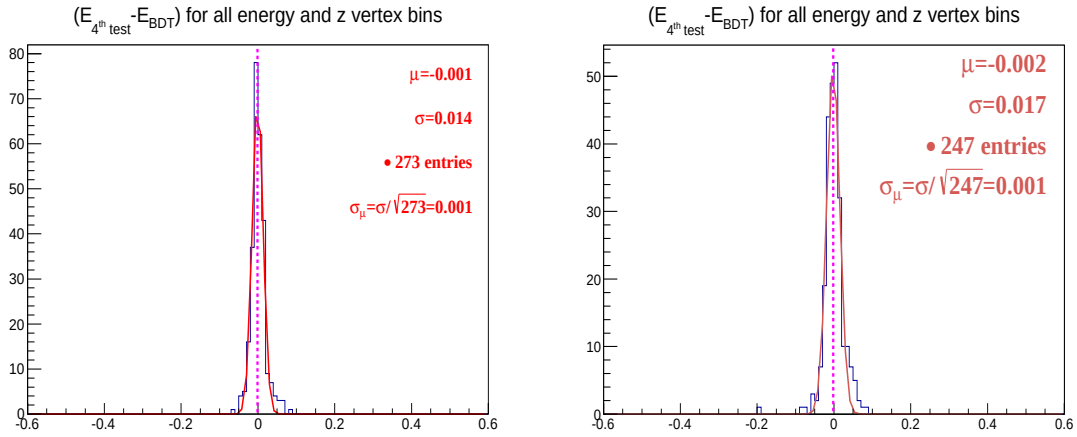

Figure 4.65: Distributions of δ_{ij} fitted with Gaussians for Gold 2 (left plot) and Silver 1&2 (right plot) for the forth test (tightening the BDT cut to 0.06).

BDT cut	Run period	$\frac{Y_{Target}}{Y_{HD}}$	Systematic difference ($E_{BDT} - E_{TEST}$)	$\sigma_{systematic}$
0.00	Gold 2	3.23%	+0.003 ± 0.001	0.002
	Silver 1&2	4.60%	0.000 ± 0.001	
0.06	Gold 2	2.90%	-0.001 ± 0.001	0.002
	Silver 1&2	4.28%	-0.002 ± 0.001	
0.09	Gold 2	2.80%	-0.003 ± 0.002	0.003
	Silver 1&2	4.10%	-0.002 ± 0.002	

Table 4.12: Estimated $\sigma_{systematic}$ for the test of varying the BDT output cut.

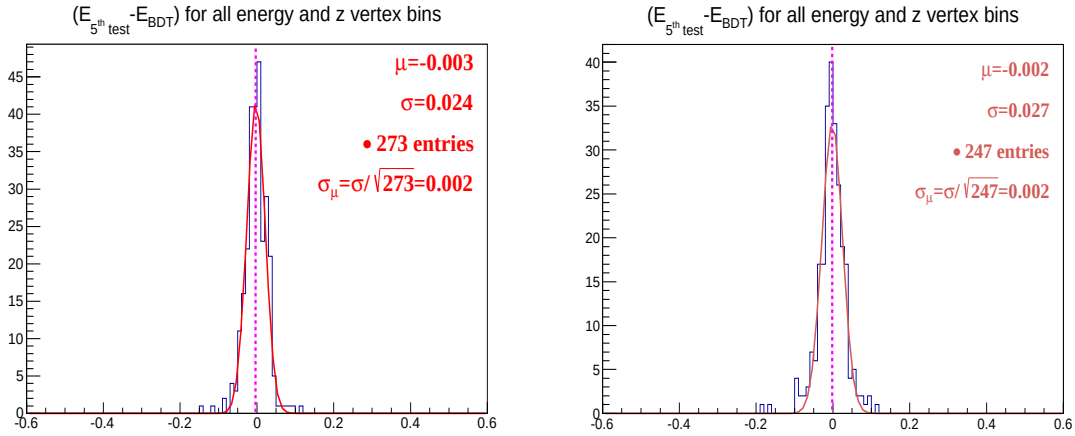

Figure 4.66: Distributions of δ_{ij} fitted with Gaussians for Gold 2 (left plot) and Silver 1&2 (right plot) for the fifth test (tightening the BDT cut to 0.09).

4.4.4 Systematic Effects from Employing a Differently Constructed BDT

In this study we trained (constructed) a new BDT using a different training signal simulation data. In particular, since the BDT algorithm relies on the training data to learn the distributional characteristics of the real data, distributionally different training data will result in a differently constructed BDT. To obtain a distributionally different training data, we purposely improved the momentum resolutions (about twice the correct resolution) of the scattered proton and π^-, which propagated into different missing momentum and missing mass distributions, see Figure 4.67. In particularly, it was the drift chamber resolution that was improved. The reason for this test is to quantify the sensitivity of the BDT classification performance. Fortunately, the BDT method is insensitive to the improved training signal data as verified by a small systematic difference shown in Table 4.13 and Figure 4.68.

Run period	$\frac{Y_{Target}}{Y_{HD}}$	Systematic difference ($E_{BDT} - E_{TEST}$)	$\sigma_{systematic}$
Gold 2	2.98%	-0.001 ± 0.002	0.002
Silver 1&2	4.27%	-0.002 ± 0.002	

Table 4.13: Estimated $\sigma_{systematic}$ for the sixth test: employing a differently constructed BDT.

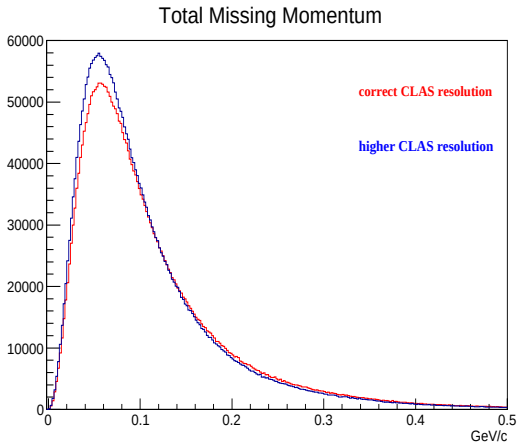

Figure 4.67: Missing Momentum distributions from signal simulation data; red histogram has correct momentum resolution (for detected p, and π^-), and blue histogram has higher momentum resolution than CLAS drift chamber momentum resolution.

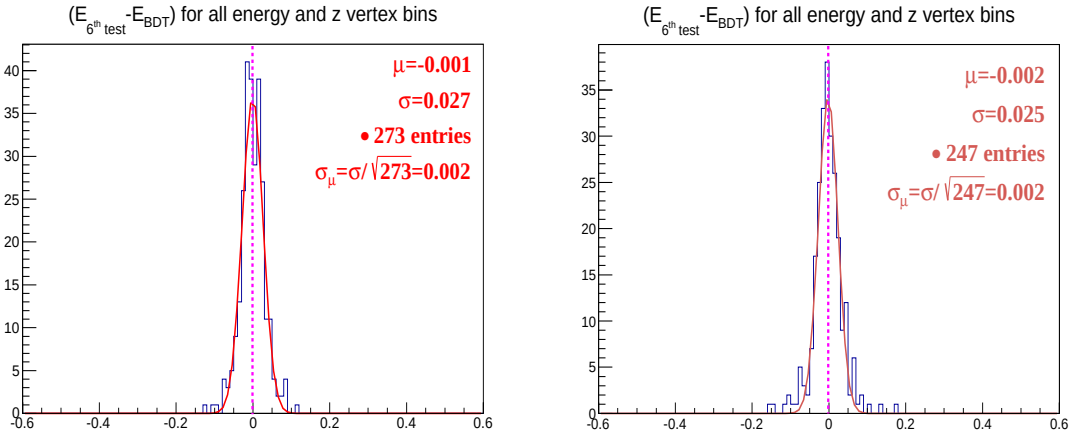

Figure 4.68: Distributions of δ_{ij} fitted with Gaussians for Gold 2 (left plot) and Silver 1&2 (right plot) for the sixth test (employing a differently constructed BDT).

4.4.5 Systematic Effects from Tighening the Missing Momentum Cut

In section 4.3.4.3, we observed that the magnitude of E asymmetry decreases as the magnitude of the missing momentum increases. Although, we considered this phenomena as a *real* physics effect—possibly the evidences of both final state and initial state interactions, we implemented a simple procedure to correct it. In particular, if we only selected events with the missing momentum less than 110 MeV/c, then the multiplicative correction factor is only about 3%, while the multiplicative correction factor is about 8% if we make a wider missing momentum selection (i.e., less than 200

MeV/c). It is still possible that after the *global* corrections, there might still remain some residue systematic difference. In particular, for this test, we placed a tighter cut at 110 MeV/c on the missing momentum and obtained a new set of E measurements. Then carrying the same procedure as in other tests to derive the systematic difference, see Table 4.14 and Figure 4.69 (note that the correction factor of 1.036 was applied for this testing set of E values). As expected, the tighter cut increased the magnitude of the E asymmetry (negative systematic difference). Note that the systematic difference is small.

Run period	$\frac{Y_{Target}}{Y_{HD}}$	Systematic difference ($E_{BDT} - E_{TEST}$)	$\sigma_{systematic}$
Gold 2	1.40%	-0.001 ± 0.004	0.009
Silver 1&2	2.10%	-0.013 ± 0.004	

Table 4.14: Estimated $\sigma_{systematic}$ for the seventh test: tightening the missing momentum cut (to 110 MeV/c).

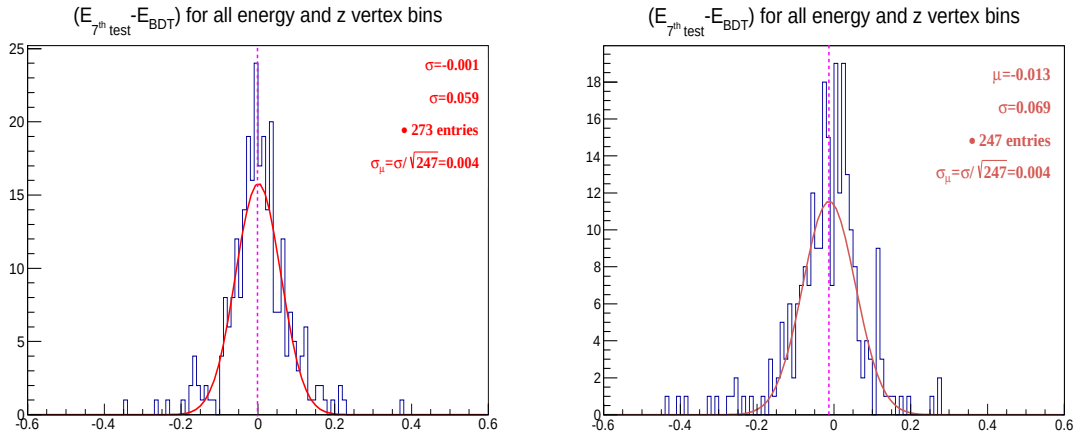

Figure 4.69: Distributions of δ_{ij} fitted with Gaussians for Gold 2 (left plot) and Silver 1&2 (right plot) for the seventh test (tightening the missing momentum cut to 110 MeV/c).

4.4.6 Systematic Effects from Polarization Uncertanties

In this section, we provide results from our systematic test on the uncertainties of the beam and target polarizations—the numerical values for the statistical uncertainties were reported in Table 3.1. To quantify the systematic effect we computed the E asymmetry but with reduced beam and target polarizations; i.e., *both* quantities were reduced by one standard deviation of their respective total uncertainties (statistical and systematic). The effect on the E asymmetry is shown in Figure 4.70. As a

sanity check, we also reduced both polarizations (beam and target) for the Gold 2 run by *two* standard deviation of their respective total uncertainties. As expected, the systematic shift is proportionally larger. In particular, while applying one standard deviation reduction, we obtained $\mu_{Gold2} = -0.049$ (see left plot of Figure 4.70), we obtained $\mu_{Gold2} = -0.104$ for two standard deviation reduction. Table 4.15 presents the numerical values of the systematic uncertainty study. Also, note that the dilution factor $\frac{Y_{Target}}{Y_{HD}}$ is the same as in Table 4.6.

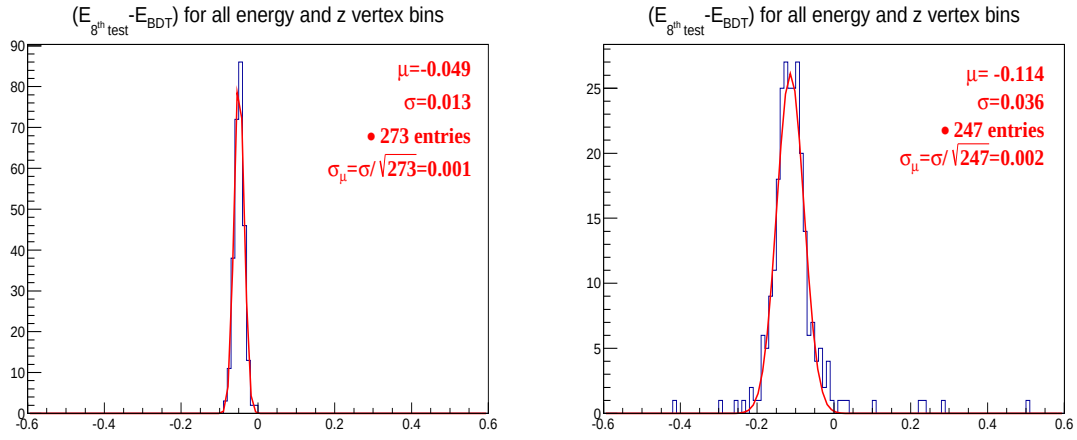

Figure 4.70: Distributions of δ_{ij} fitted with Gaussians for Gold 2 (left plot) and Silver 1&2 (right plot) for the eighth test (reducing the beam and target polarizations).

Run period	Systematic difference ($E_{BDT} - E_{TEST}$)	$\sigma_{systematic}$
Gold 2	-0.049 ± 0.001	0.062
Silver 1&2	-0.114 ± 0.002	

Table 4.15: Estimated $\sigma_{systematic}$ for the eighth test: reducing the beam and target polarizations.

4.4.7 Sytematic Uncertainty Assignment for the BDT Method

Previously, we described several studies to test the robustness of the BDT method. For each test, the systematic differences were estimated separately for the Gold 2 and Silver 1&2 data, and the combined systematic was obtained next by computing the weighted quadratic mean. In addition to these tests, the study in section 4.3.2 where the BDT was compared with the 1D-cut background suppression and subtraction method is also qualified as a proper systematic test. Therefore, we included the systematic estimate from section 4.3.2 into the final list of the systematic tests in Table 4.16. The overall systematic uncertainty was derived as a

square root of the quadratic sum of the individual $\sigma_{systematic}$. The numerical value for the overall systematic uncertainty is presented in Table 4.16 as well. This result ($\sigma_{overall}$ =0.088) is the total systematic uncertainty for the average value of the E asymmetry, which is estimated to be -0.570 ± 0.005 (see Figure 4.71). Equivalently, the systematic uncertainty can be expressed as the fraction of the average value of the E asymmetry (i.e., $^{0.088}/_{0.570} = 15.4\%$); this alternative is more appropriate when reporting the systematic uncertainties of $E\left(\cos\left(\Theta_{\pi^-}^{CM}\right)\right)$, and/or $E(W)$ values—i.e., $\sigma_{systematic} = 0.154 \times E\left(\cos\left(\Theta_{\pi^-}^{CM}\right)\right)$.

	$\sigma_{systematic}$	$\sigma^2_{systematic}$
1^{st} test (Table 4.10)	0.009	$8.10{\cdot}10^{-5}$
2^{nd} test (Table 4.11)	0.026	$6.76{\cdot}10^{-4}$
3^{rd} test (Table 4.12)	0.002	$4.00{\cdot}10^{-6}$
4^{th} test (Table 4.12)	0.002	$4.00{\cdot}10^{-6}$
5^{th} test (Table 4.12)	0.003	$9.00{\cdot}10^{-6}$
6^{th} test (Table 4.13)	0.002	$4.00{\cdot}10^{-6}$
7^{th} test (Table 4.14)	0.009	$8.10{\cdot}10^{-5}$
8^{th} test (Table 4.15)	0.062	$3.84{\cdot}10^{-3}$
9^{th} test	0.055	$3.03{\cdot}10^{-3}$
$\sigma^2_{overall}$		$7.73{\cdot}10^{-3}$
$\sigma_{overall}$		0.088

Table 4.16: List of estimated $\sigma_{systematic}$ for all the systematic tests (including the test of consistency between BDT and 1D-cut background suppression and subtraction method (referred to as the 9^{th} test)), see text for test enumeration. The last row reports the overall systematic uncertainty.

4.5 Summary

This chapter presented the first set of the E asymmetry measurements for the reaction $\gamma d \to \pi^- p(p_s)$ (for 1480 MeV$\leq W \leq$2320 MeV). We described in detail the cuts to select a clean sample of $\pi^- p$. We then introduced the 1D-cut background suppression and subtraction and the boosted decision trees (BDT) methods to select bound neutrons events. The E asymmetry was obtained by both methods; but comparing the results suggests the BDT is consistent with the 1D-cut background suppression and subtraction method. It is more efficient (smaller statistical uncertainties), however. Therefore, the final measurements were obtained using only the BDT method. We then combined results from the Silver (1, 2, 3, 4, and 5) and Gold 2 periods. Furthermore, we plotted the combined E asymmetry as a function of $\cos\left(\mathbf{\Theta}_{\pi^-}^{\mathbf{CM}}\right)$, W, and the recoil momentum $|p|_{missing}$. While the relation between the E asymmetry and $\cos\left(\mathbf{\Theta}_{\pi^-}^{\mathbf{CM}}\right)$ (or W) is an important input (or constraint) for the partial wave

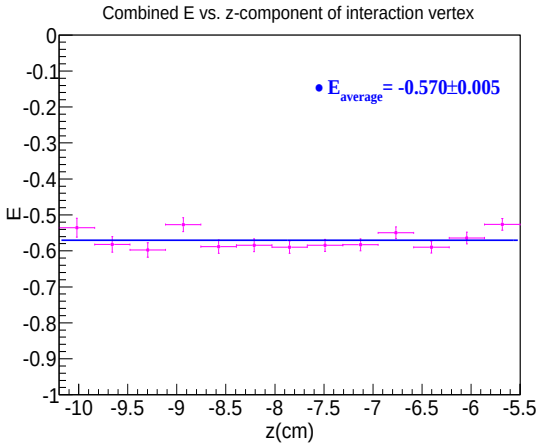

Figure 4.71: Combined E vs. the z component of the interaction vertex, for all energy windows and angular bins.

analysis to study the N^* spectrum (see Chapter 7 for a comparision of the E asymmetry measurements with partial wave analysis models), the relation between E and $|p|_{missing}$ might reveal interesting interactions between the neutron and the proton inside the deuteron (and/or the final state interactions). Next, we implemented several systematics tests to estimate the overall systematic uncertainty which is 15.4% (i.e., $\sigma_{systematic} = 0.154 \times E$). Lastly, the numerical values of the measured E asymmetry are reported in Appendix B.

Chapter 5

Results for the E Observable for Reaction $\gamma d \to K^0 Y(p_s)$

We present the first set of measurements for the helicity asymmetry E for the reaction $\gamma d \to K^0 Y(p_s)$, where Y is either Λ or Σ^0, using the CLAS g14 data. Our analysis includes several sequential steps. The first step was to identify $p\pi^+\pi^-\pi^-$ final-state events using a set of well-calibrated cuts. The second step was to select events that were from bound neutrons and to reject target-material-background (i.e., events from aluminum wires and KelF cell walls). The next step was to remove the phasespace background $p\pi^+\pi^-\pi^-$. This was followed by separating the $K^0\Lambda$, and $K^0\Sigma^0$ events. It is worth noting that the number of good signal events—$K^0\Lambda$, and $K^0\Sigma^0$ events that were originated from the bound neutrons—is significantly smaller than compared to the dominating $p\pi^+\pi^-\pi^-$ non-resonant background and/or target-material backgrounds. Therefore, we employed *only* the Boosted Decision Trees (BDT) analysis tool for the tasks of rejecting the target-material and phasespace ($p\pi^+\pi^-\pi^-$) backgrounds as well as seperating the $K^0\Lambda$, and $K^0\Sigma^0$ events. This is because the BDT algorithm—as shown in Chapter 4— is highly efficient compared to a simple "cut" method in both rejecting background and keeping signal events. In particular, we provide details about our well-calibrated cuts to select the $\pi^+\pi^- p\pi^-$events in Section 5.2. After that a BDT algorithm was employed to select the bound neutron in a deuteron. A second BDT algorithm was utilized to remove the $p\pi^+\pi^-\pi^-$ non-resonant background events, and finally, we "trained" the third BDT algorithm to separate the $K^0\Lambda$, and $K^0\Sigma^0$ events. We report the E measurements in Section 5.4, and systematic uncertainty studies are presented in Section 5.5.

5.1 Initial Skim

We began by selecting "$+:+:-:-$" events; i.e., each event included two positively and two negatively charged particles. Event with multiple initial photons was treated as a set of independent events. Using the measured momentum, measured *time-of-*

flight, and path length, a measured mass was determined for each particle. The left and the right plots in Figure 5.1 show the measured mass distributions of positive particles ("plus" vs. "plus") and negative particles ("minus" vs. "minus"), respectively. The squared missing mass was calculated given the hypothesis "$p : \pi^+ : \pi^- : \pi^-$" (i.e.,computing the $MM^2(p\pi^+\pi^-\pi^-)$ of reaction $\gamma d \rightarrow p\pi^+\pi^-\pi^-(X)$) and is shown in Figure 5.2; i.e., for every event the *first* positive particle—for particles with the same charge, the particle with higher momentum is usually recorded first—was given a proton ID. At this stage, we did not place any cut on the squared missing mass.

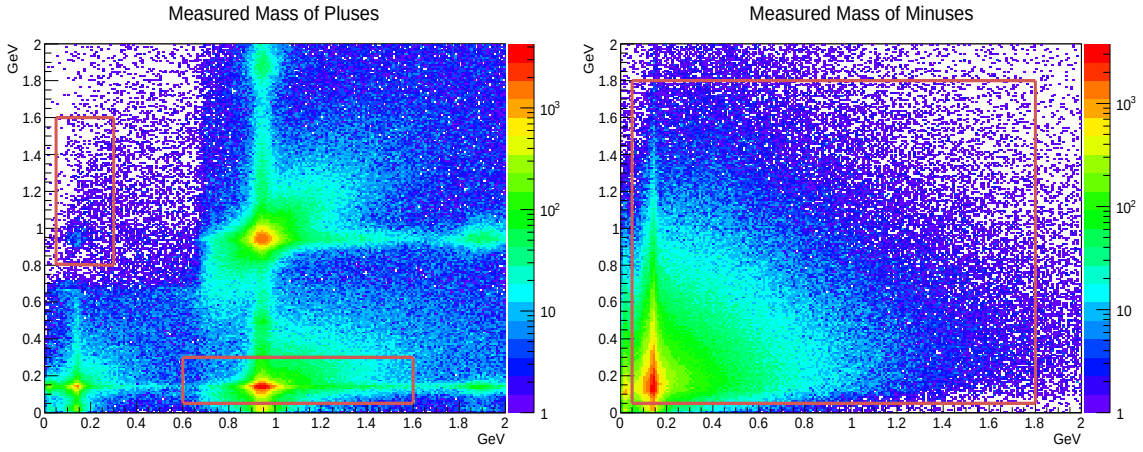

Figure 5.1: Left: Measured mass of 1^{st} "plus" vs. 2^{nd} "plus". Two red rectangles indicate where we placed our mass cuts to select good "$p\pi^+\pi^-\pi^-$" events (see Section 5.2.1). Events inside the bottom rectangle represents "$p\pi^+\pi^-\pi^-$" hypothesis while events in the top left rectangle represents "$\pi^+p\pi^-\pi^-$" hypothesis. Right: Measured mass of 1^{st} "minus" vs. 2^{nd} "minus". Note that for particles with the same charge, the particle with higher momentum is usually recorded first, so the plots do not look symmetric. The plots were obtained from the Gold 2 period data, and they are on a logarithmic scale.

5.2 $\pi^+\pi^-p\pi^-$ Event Selection

5.2.1 Particle Identification: Measured Mass Cuts

We selected "$+ : + : - : -$" events which statisfy the "$p : \pi^+ : \pi^- : \pi^-$" or "$\pi^+ : p : \pi^- : \pi^-$" hypothesis. Therefore, we selected region I (bottom rectangle in the left plot of Figure 5.1) and region II (top left rectangle in the left plot of Figure 5.1) because they have the required tracks. For every event in region I the first positive particle was assigned the proton ID and the second positive was assigned the π^+ ID. For every event in region II a reverse order was assigned. Moreover, the red

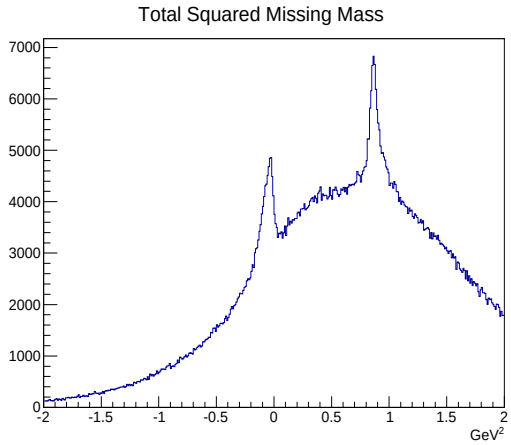

Figure 5.2: Total squared missing mass, $MM^2(p\pi^+\pi^-\pi^-)$, calculated with hypothesis "$p:\pi^+:\pi^-:\pi^-$", i.e., the *first* positive particle was assigned a proton ID. The peak near 1 GeV^2 is of interest for this analysis. We did not investigate the peak near 0 GeV^2. The plot was obtained from the Gold 2 period data.

rectangles in Figure 5.1 represent our mass cuts (see below)—these selection cuts are looser than the CLAS PID cuts to save events, but tight enough to not select many events with K^+ or d final-state particles:

- Region I: $0.6 < mass_p < 1.6$ and $0.05 < mass_{\pi^+} < 0.3$ GeV
- Region II: $0.8 < mass_p < 1.6$ and $mass_{\pi^+} < 0.3$ GeV
- For minuses: $mass_{\pi^-} > 0.05$ GeV

Note that we only placed a lower limit mass cut (at 0.05 GeV) on the minuses to simply remove electron background events. Figure 5.3 shows the measured mass distributions after our mass cuts—*after assigning the particle identification for each charged track*; the right plot suggests an upper limit mass cut on the minuses is unnecessary given no clear presence of other negative charged particles (or the presence of these particles is insignificant). In Figure 5.4 squared missing mass distribution after the mass cuts (the red histogram) was much cleaner than before the cuts (the blue histogram). In addition, we placed a loose cut on the squared missing mass at zero. Note that events in the left tail (the lower mass side) of the squared missing mass distribution are most likely from the target-material background—these events were removed later by a BDT algorithm.

5.2.2 Particle Identification: ΔTOF Cuts

To further reduce the background due to particle misidentification, we applied ΔTOF cuts. An explanation of this technique follows: For every detected charged particle

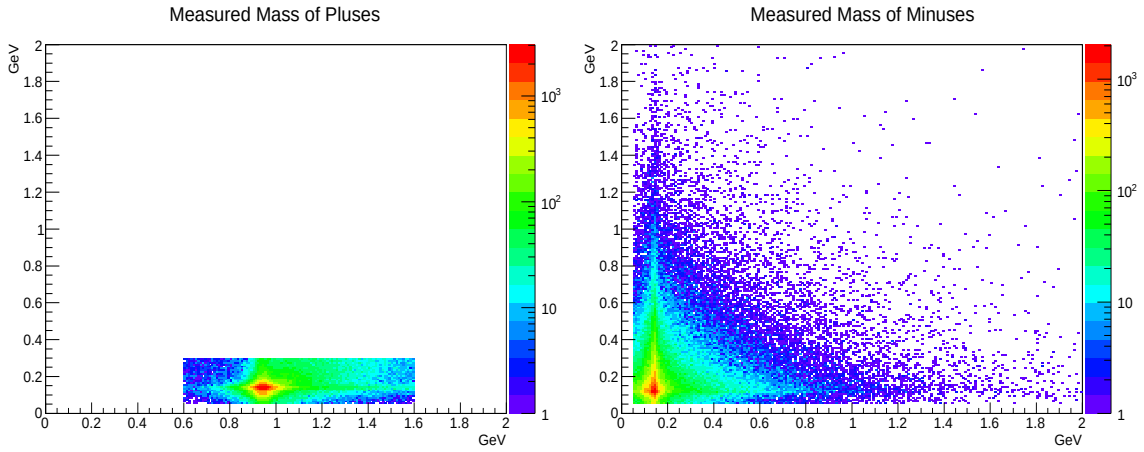

Figure 5.3: Left: Measured masses of *assigned* protons vs. *assigned* π^+s, i.e., the plot is *after assigning the particle identification for each charged track*. Right: Measured masses of 1^{st} π^- vs. 2^{nd} π^-. The plots were obtained from the Gold 2 period data, and they are on a logarithmic scale.

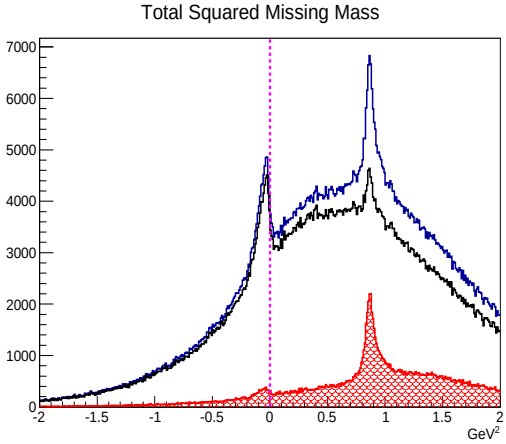

Figure 5.4: Total squared missing mass, $MM^2(p\pi^+\pi^-\pi^-)$, of reaction $\gamma d \rightarrow p\pi^+\pi^-\pi^-(X)$. The blue histogram is before the measured-mass particle selection cuts. Events in the red histogram were selected and events in the black histogram were rejected by the mass cuts. The plot was obtained from the Gold 2 period data.

track, the CLAS track reconstruction algorithm records its momentum, its path length from target vertex to TOF counter, and its *time-of-flight* ($TOF_{measured}$). For a given particle with an assumed mass, one can compute $TOF_{calculated}$ from the momentum and the path length of the particle. The difference between the $TOF_{calculated}$ and the $TOF_{measured}$ is ΔTOF:

$$\Delta TOF = TOF_{measured} - TOF_{calculated}, \tag{5.1}$$

where $TOF_{measured}$ is the measured *time-of-flight*. This is the time difference between event vertex time and time at which the particle hit the TOF scintillator walls—encircling the CLAS drift chamber system. The $TOF_{calculated}$ is computed as

$$TOF_{calculated} = \frac{L}{c}\sqrt{1 + \left(\frac{m}{p}\right)^2}, \tag{5.2}$$

where L is the measured pathlength from the target to the TOF scintillator, c is the speed of light, m is the hypothesized mass and p is the magnitude of the measured 3-momentum. Moreover, if the particle was correctly identified, then in a plot of particles' ΔTOF against their momenta a straight horizontal band around zero should be observed. If the particles' type was assigned incorrectly, then the same plot results in a curved band that flattens out at high momentum. Illustratively, Figure 5.5 plots the protons' ΔTOF (on the left) and the second π^-s' ΔTOF (on the right) where the two visible curved bands are from e^- and μ^- tracks which were misidentified as the π^-.

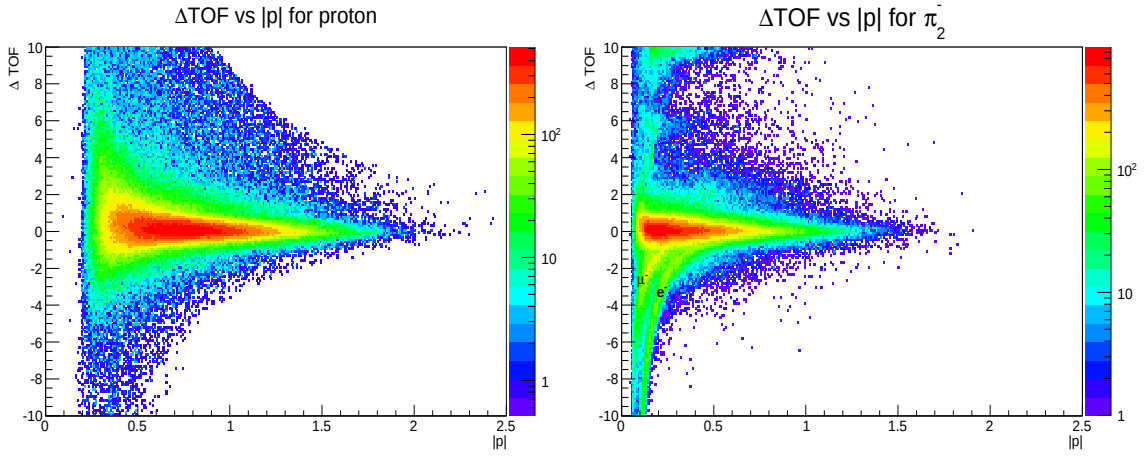

Figure 5.5: Left: Proton ΔTOF vs. $|p|$. Right: 2^{nd} π^- ΔTOF vs. $|p|$. The horizontal band at zero corresponds to correct PID, two curved bands corresponses to e^- and μ^-. The plots were obtained from the Gold 2 period data. The plots are on a logarithmic scale.

As illustrated in Figure 5.6 showing the plots of the ΔTOF_p vs. ΔTOF_{π^+} (on the left), and ΔTOF_{π^-} vs. ΔTOF_{π^-} (on the right), there are visible clusters, that are 2.00 ns apart. Events in these clusters have corrected particle identification but belongs to a different RF beam "bucket" (the photons are delivered in pulses that are 2.00 ns apart). The ΔTOF cuts we applied were to remove these events which have wrong *track-and-photon-timing* combinations. The cuts resemble an "iron cross," our moniker for these cuts, see Figure 5.7. In effect, Figure 5.8 suggests a small amount of signal being rejected, while the cuts were able to remove a significant number of

background events. Note that the "iron cross" cut was meant to be very loose. Any remaining background would be rejected by later cuts.

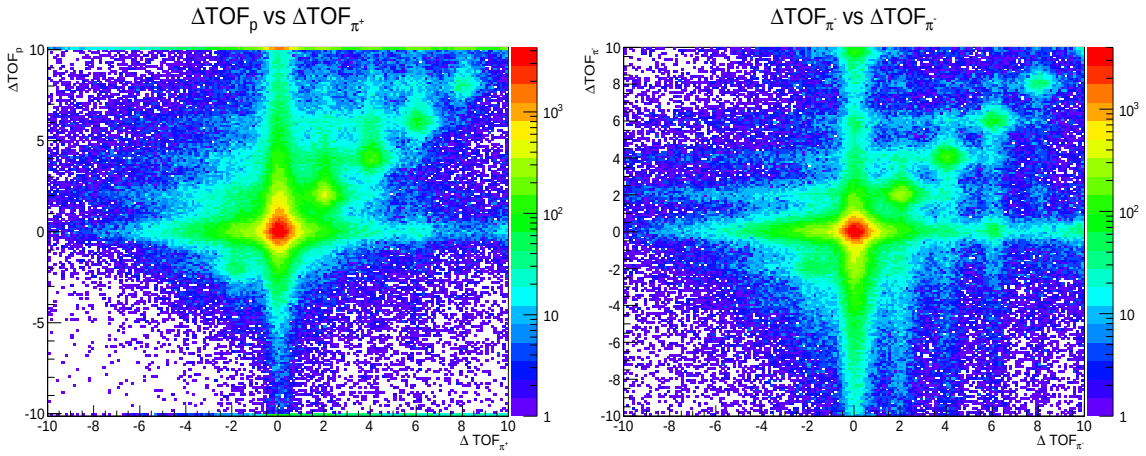

Figure 5.6: Left: the ΔTOF_p vs. ΔTOF_{π^+}. Right: ΔTOF_{π^-} vs. ΔTOF_{π^-}. Visible clusters are at 2 ns interval, $(\pm 2, \pm 2)$, $(\pm 4, \pm 4)$, etc. The data used to plot was the Gold 2 period data. The plots are on a logarithmic scale.

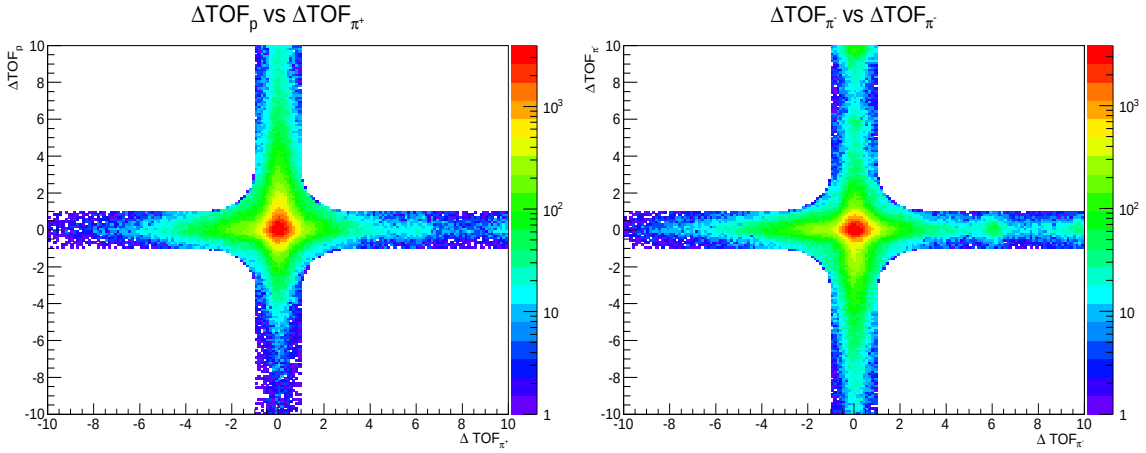

Figure 5.7: Left: the ΔTOF_p vs. ΔTOF_{π^+}. Right: ΔTOF_{π^-} vs. ΔTOF_{π^-}. The ΔTOF cuts were employed primarily to remove events with wrong *track-and-photon-timing* combination. The data used to obtain the plots was the Gold 2 period data. The plots are on a logarithmic scale.

5.2.3 Detector Performance: Fiducial Cuts

As mentioned before, we relied on the BDT algorithm to reject most of the difficult-to-seperate backgrounds. To optimize the BDT's performance, it is necessary to have

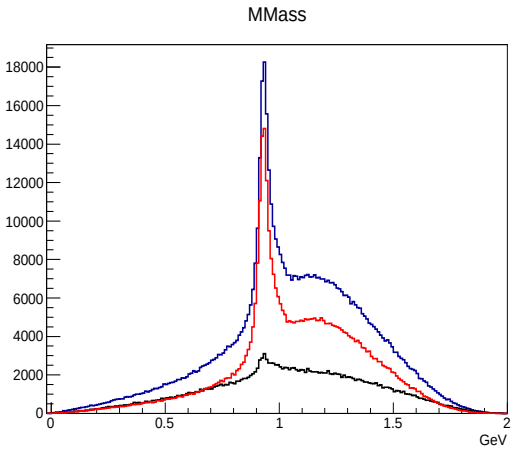

Figure 5.8: Total missing mass $MM(p\pi^+\pi^-\pi^-)$ of reaction $\gamma d \to p\pi^+\pi^-\pi^-(X)$ after ΔTOF cuts is the red histogram. Events in the black histogram were rejected by the cuts. The plot was obtained from the Gold 2 period data.

good simulations that represent closely the real data to "train" the BDT (more detail later); for this reason, understanding the CLAS detectors, and simulating correctly their performances is important. In particular, because there are some regions or elements of the detectors that were not well understood or hard to simulate, to allow a reliable comparison between the real data and simulation data, these regions have to be removed from both real and MC data; this section discusses these types of cuts. Primarily, we only applied cuts on the drift chamber detectors (since we did not perform a cross section analysis, but rather a target-beam asymmety, simulating the *exact* CLAS acceptance is not necessary).

Previous studies for the g11 data set [51] advised removing events with tracks going near the superconducting torus coils where the magnetic field varies too rapidly to be properly modeled (by GSIM). We thus removed events which have *at least* one track going into these regions. Particularly, in the forward direction where the coils occupy up to $\sim 80\%$ of space, we placed a hard cut in the forward direction for tracks with $cos\Theta_{lab} > 0.985$. In addition, we placed cuts at 0.5 rad (note that g11 fiducial cuts are at 0.4 rad [51]; we loosened the cut to preserve statistics) on the angle Φ_{sector} measured in the sector coordinate system. In other words, accepted particles had their measured $|\Phi_{sector}| < 0.5$ rad. These Φ cuts were to remove the edges of each of the CLAS drift chambers which are difficult to simulate. Finally, Figure 5.9 shows the angular distribution of protons before (left) and after (right) our fiducial cuts, while Figure 5.10 shows the angular distribution of π^- before (left) and after (right) our fiducial cuts (the angular plots for π^+ are similar). Finally, we show the total missing mass, $MM(p\pi^+\pi^-\pi^-)$, after the fiducial cuts in Figure 5.11.

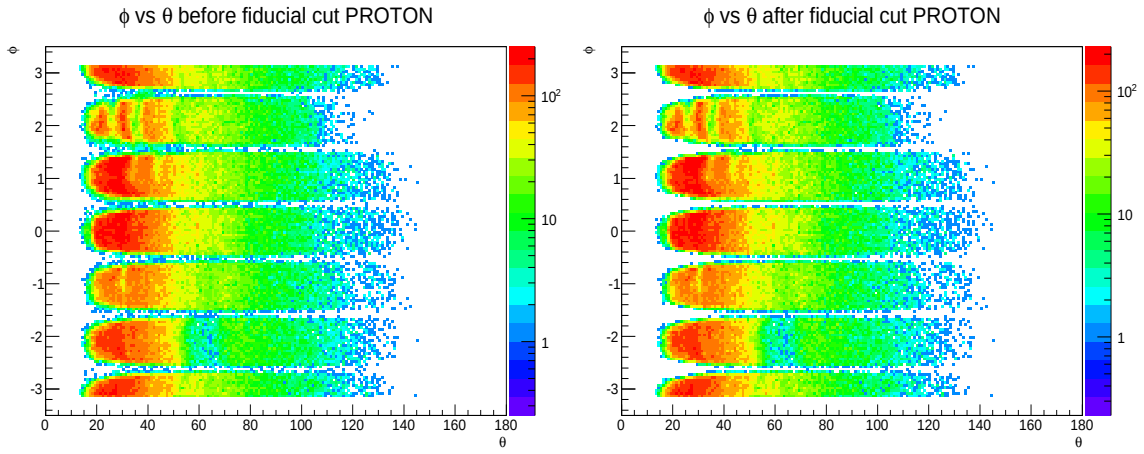

Figure 5.9: Left: Proton angular distribution: Φ vs. Θ before the fiducial cuts. Right: Proton angular distribution: Φ vs. Θ after the fiducial cuts. The unit of Φ is radian, while the unit of Θ is degree. The plots were obtained from the Gold 2 period data. The plots are on a logarithmic scale.

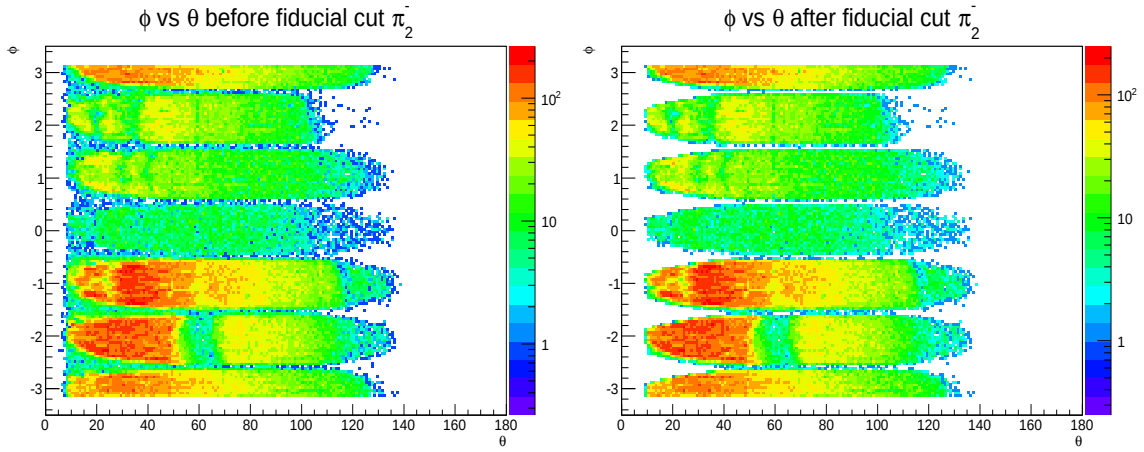

Figure 5.10: Left: π^- angular distribution: Φ vs. Θ before the fiducial cuts. Right: π^- angular distribution: Φ vs. Θ after the fiducial cuts. The unit of Φ is radian, while the unit of Θ is degree. The plots were obtained from the Gold 2 period data. The plots are on a logarithmic scale.

5.2.4 Squared Missing Mass Cut

In this section we discuss a cut to reject some target-material background events. The remaining target-material background—that survived this cut—would be rejected by employing the BDT algorithm (more detail later). However, by rejecting some background events at this stage, we "force" the BDT to "focus" on the more difficult-to-remove background events (i.e., events that are nearly indistinguishable from the

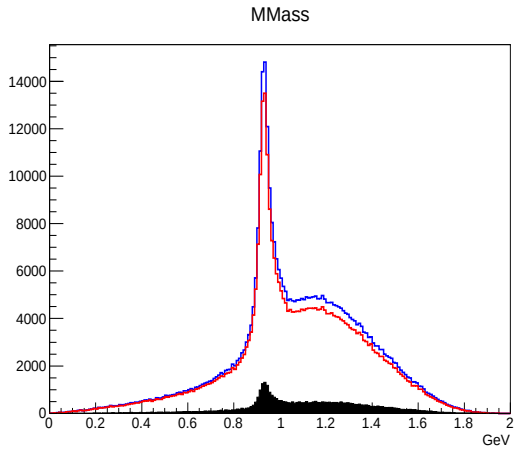

Figure 5.11: Total missing mass $MM(p\pi^+\pi^-\pi^-)$ before and after the the fiducial cuts are the blue and red histograms, respectively. Events in the black histogram were rejected by the fiducial cuts. The plot was obtained from the Gold 2 period data.

bound signal events). To implement the cut, for every event we assigned the *neutron* mass as the target mass and computed the total squared missing mass; then we placed a cut at -0.2 GeV^2. Effectively, the squared missing mass distribution "amplifies" the difference between the *quasi-free* signal and the target-material background events. In particular, as shown in Figure 5.12 the cut is very effective in rejecting a majority of target-material background (the right plot which was obtained from the empty-target-period data), while it is very loose for the *quasi-free* signal simulation data (the left plot which was obtained from the signal simulation data). Moreover, we show the effect of the cut on the Gold 2 data in Figure 5.13. Note that both the missing mass and missing momentum distributions were computed using the *deuteron* mass as the target mass. Moreover, the cut rejected *correctly* events with large missing momenta (the right plot), even though they might have missing mass values close to 938 MeV—the mass of the proton. Lastly, two loose selection cuts were implemented to remove unambiguous target-material background events:

- Total Missing Mass (reaction $\gamma d \to p\pi^+\pi^-\pi^-(X)$) larger than 1.4 GeV, and
- Total Missing Momentum (reaction $\gamma d \to p\pi^+\pi^-\pi^-(X)$) larger than 0.6 GeV/c.

Note that each $K^0\Sigma^0$ event has an extra undetected photon (i.e.,$\gamma n(p_s) \to K^0\Sigma^0(p_s) \to K^0\Lambda(\gamma p_s)$), hence the missing mass and missing momentum are larger because of the inclusion of this undetected photon—it is the main reason for us to place the loose selection cuts as described above to preserve these $K^0\Sigma^0$ events.

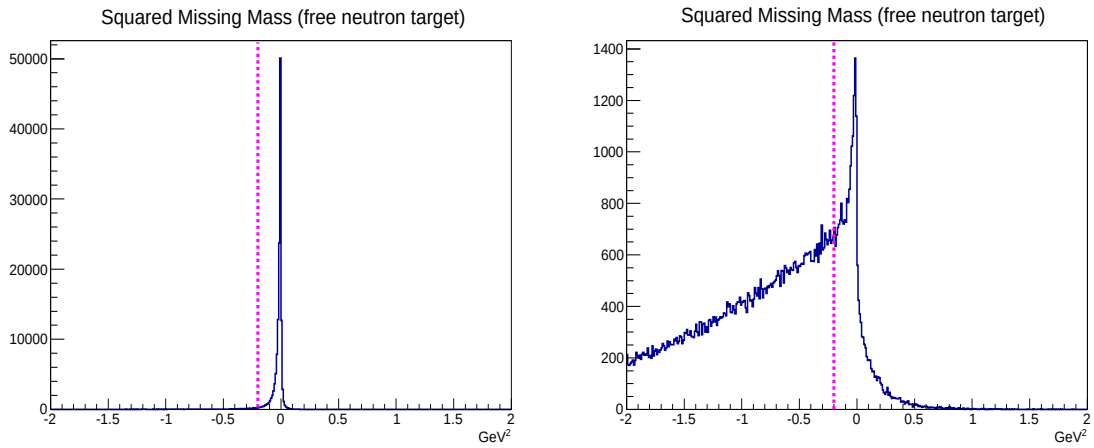

Figure 5.12: Left: Total squared missing mass, $MM^2(p\pi^+\pi^-\pi^-)$, of reaction $\gamma n \rightarrow p\pi^+\pi^-\pi^-(X)$ from simulation data. Right: Total squared missing mass, $MM^2(p\pi^+\pi^-\pi^-)$, from the empty-target-run-period data. The magenta lines indicate the cut to reject background events originating from the target material (i.e., rejecting events with $MM^2(p\pi^+\pi^-\pi^-) < -0.2$ GeV^2).

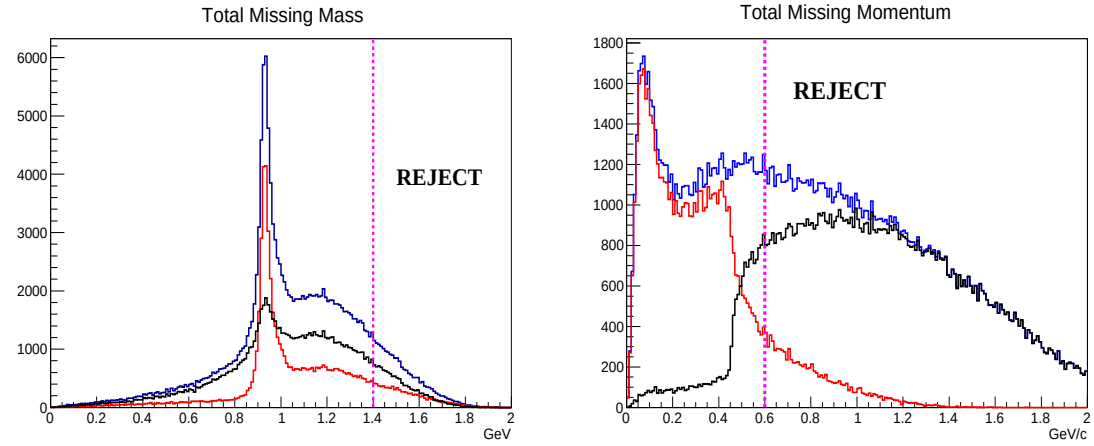

Figure 5.13: Left: Total missing mass, $MM(p\pi^+\pi^-\pi^-)$, of reaction $\gamma d \rightarrow p\pi^+\pi^-\pi^-(X)$ before (blue) and after the squared missing mass cuts (selection in "red" and rejection in "black"). Right: Total missing momentum before (blue) and after the squared missing mass cut (selection in "red" and rejection in "black"). The magenta lines indicate additional cuts on the missing mass and missing momentum to reject unambiguous background events. The plots were obtained from the Gold 2 period data.

5.2.5 K^0Y Loose Selection Cuts

The last section concluded our $\pi^+\pi^-p\pi^-$ event selection. We proceed into the next step: K^0Y event selection. Note that we referred $K^0\Lambda$ and $K^0\Sigma^0$ events collectively

as K^0Y events. Figure 5.14 plots invariance mass of $(p\pi_2^-)$ versus invariance mass of $(p\pi_1^-)$, $IM(p\pi_2^-)$ vs. $IM(p\pi_1^-)$, obtained from the Gold 2 data showing that both the π^- are equally likely to form a pair with the proton (or the π^+). Consequently, a naive assignment such as always combining the proton (or π^+) with the first π^- and the second π^- with the other positive would not be efficient. We will present a better procedure.

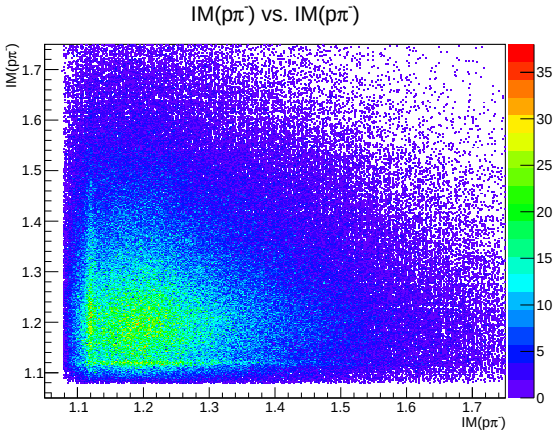

Figure 5.14: $IM(p\pi_2^-)$ vs. $IM(p\pi_1^-)$. Two bands that represent the Λ particle bound have equal strength suggesting both the π^-s are equally likely form a pair with the proton. The units are in GeV. The data used to plot was the Gold 2 period data.

It is worth studying again the K^0Y signal simulation data to decide the best model (or fit) for the K^0 and Λ invariance mass distributions. Particularly, the left plot in Figure 5.15 shows $IM(p\pi_1^-)$ vs. $IM(p\pi_2^-)$. It is obvious, that for the events with $IM(p\pi_2^-)$ >1.2 GeV, the first π^- is the decay product of the Λ. Furthermore, the right plot in Figure 5.15 shows the $IM(p\pi_1^-)$ for events with $IM(p\pi_2^-)$ >1.2 GeV with a fitted Gaussian. Understandably, the fit is not good, because the momentum resolution for the scattered p and π^- are energy-dependent (i.e., the higher the momentum, the worse the resolution)—a single Gaussian distribution represents an energy-independent resolution. To improve the fit, we could fit two Gaussians with different widths to the histogram as shown in the left plot of Figure 5.16—clearly the alternative fit is much better. Moreover, we could fit the histogram with a Breit-Wigner distribution as shown in the right plot of Figure 5.16. The qualities of the two fits in Figure 5.16 are about the same, but the Breit-Wigner fit has fewer parameters. Therefore, we modeled the K^0 and Λ invariance mass distributions with the Breit-Wigner distribution. We introduce a procedure to "pair" the particles next.

First, it is apparent that for *true* $K^0\Lambda$ events, there are only two possible combinations: either $(p\pi_1^-)$ and $(\pi^+\pi_2^-)$, or $(p\pi_2^-)$ and $(\pi^+\pi_1^-)$. Furthermore, let us assume that the $(p\pi_1^-)$ and $(\pi^+\pi_2^-)$ combination is the correct one, then $IM(p\pi_1^-)$ and $IM(\pi^+\pi_2^-)$ should be closer to the Λ and the K^0 mass centroids than the other

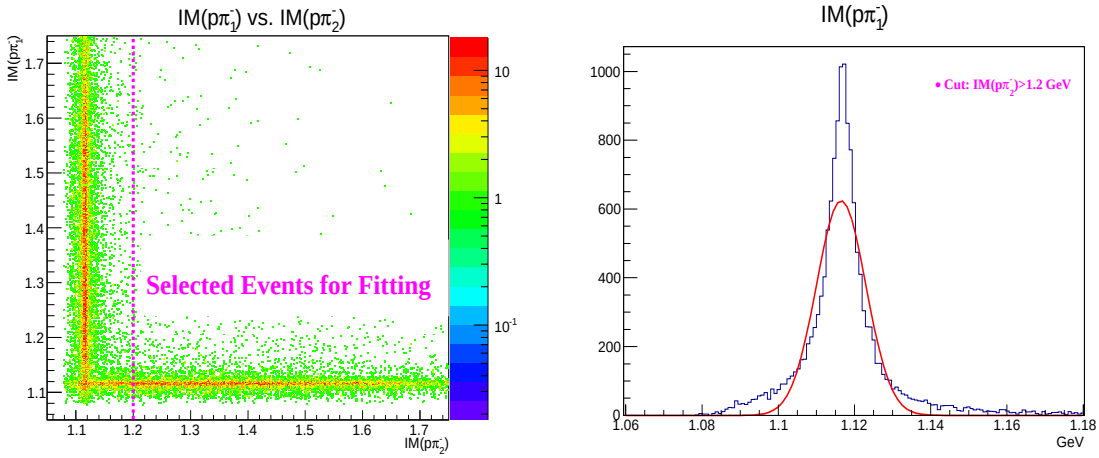

Figure 5.15: Left: $IM(p\pi_1^-)$ vs. $IM(p\pi_2^-)$. The two bands represent the Λ particle. The unit is in GeV. Right: $IM(p\pi_1^-)$ for events with $IM(p\pi_2^-)$ >1.2 GeV (thus the first π^- is surely the decay product of the Λ). The data used to plot was the signal simulation data.

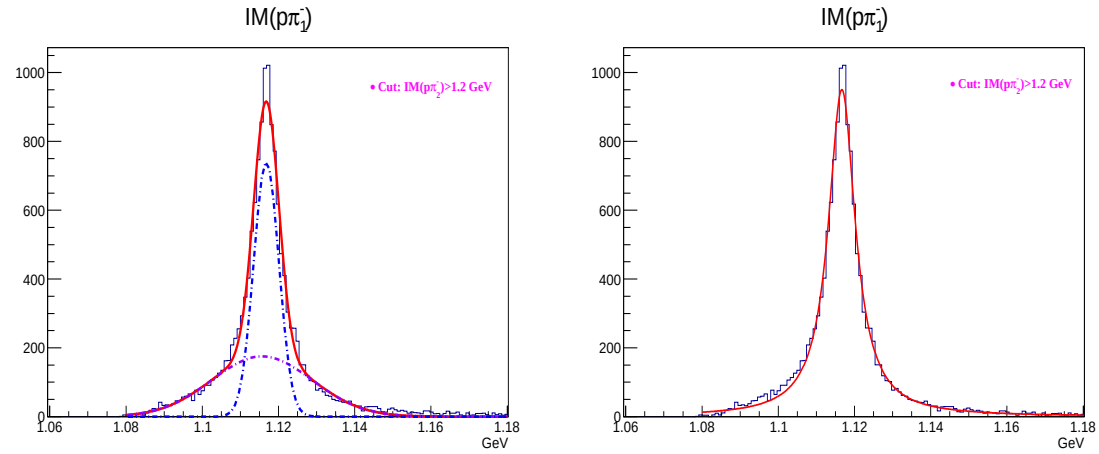

Figure 5.16: $IM(p\pi_1^-)$ for events with $IM(p\pi_2^-)$ >1.2 GeV (thus the first π^- is surely the decay product of the Λ). The left plot was fitted with double Gaussians, and the right plot was fitted with a Breit-Wigner distribution. The data used to plot was the signal simulation data.

combination. In other words, we *should* observe the followings for *true* $K^0\Lambda$ events:

$$|IM(p\pi_1^-) - m_\Lambda| \leq |IM(p\pi_2^-) - m_\Lambda|, \quad and \tag{5.3}$$

$$|IM(\pi^+\pi_2^-) - m_{K^0}| \leq |IM(\pi^+\pi_1^-) - m_{K^0}|, \tag{5.4}$$

where m_Λ, and m_{K^0} are the mass centroids of the Λ and the K^0, respectively. As discussed previously, the Λ and K^0 invariance mass distributions can be modeled by the Breit-Wigner distribution. With these two loose assumptions, we could now obtain a very effective procedure to ID the π^-:

1. Compute $IM(p\pi_1^-)$, $IM(p\pi_2^-)$, $IM(\pi^+\pi_1^-)$, and $IM(\pi^+\pi_2^-)$,
2. Compute the product of $f_{BW}(IM(p\pi_1^-), m_\Lambda, \Gamma_\Lambda) \times f_{BW}(IM(\pi^+\pi_2^-), m_{K^0}, \Gamma_{K^0})$, where $f_{BW}(m, m_0, \Gamma) = \frac{\Gamma}{2\pi[(m-m_0)^2+(\Gamma/2)^2]}$ is the probability distribution function of the Breit-Wigner distribution with parameter m_0 being the centroid of the distribution, and Γ being the full width at half maximum (FWHM); these variables were obtained from fits, see Table 5.1, and
3. Compute the product of $f_{BW}(IM(p\pi_2^-), m_\Lambda, \Gamma_\Lambda) \times f_{BW}(IM(\pi^+\pi_1^-), m_{K^0}, \Gamma_{K^0})$,
4. Compare results of Step 2 and Step 3. If the product in Step 2 is greater, then pairing π_1^- with p, and π_2^- with π^+; otherwise, reversing the assignment.

	Simulation	Gold 2	Silver 1&2
Λ	$m_0 = 1,117.16 \pm 0.09$	$m_0 = 1,119.58 \pm 0.14$	$m_0 = 1,119.76 \pm 0.24$
	$\Gamma = 9.06 \pm 0.20$	$\Gamma = 9.54 \pm 0.52$	$\Gamma = 9.42 \pm 0.54$
K^0	$m_0 = 501.75 \pm 0.17$	$m_0 = 506.88 \pm 0.42$	$m_0 = 505.81 \pm 0.95$
	$\Gamma = 21.96 \pm 0.34$	$\Gamma = 27.16 \pm 0.86$	$\Gamma = 24.26 \pm 1.88$

Table 5.1: Parameters for the Breit-Wigner distributions obtained from fittings.

Statistically speaking, for a true K^0Y signal Step 2 and Step 3 calculate the event likelihoods of kinematically being K^0Y (we only used the invariant mass information). It should be clear now that the correct combination should have higher likelihood. To test the effectiveness of the above procedure, we applied it on our $\gamma n(p_s) \to K^0\Lambda(p_s)$ simulation data, Figure 5.17 shows on the left the $IM(\pi^+\pi_{K^0}^-)$ vs. $IM(p\pi_\Lambda^-)$—assignments preferred by the procedure, and on the right the $IM(\pi^+\pi_\Lambda^-)$ vs. $IM(p\pi_{K^0}^-)$—assignment against the "suggestion". It is obvious that the procedure works very well for $K^0\Lambda$ signal simulation events. Unfortunately, the procedure introduces bias when applied on $p\pi^+\pi^-\pi^-$ phase space background. Figure 5.18 points out the lack of events surrounding the mass region of the $K^0\Lambda$ for the right plot, which means there were more events in the mass region of the K^0Y for the left plot—like before the left plot shows suggested "right" combination by the procedure. It turns out that the observed bias is due to the way we assigned combinations using *just invariance mass information*. i.e., the combination that is "closer" to the K^0Y region is the right combination. For K^0Y signal events the "closer" combination is always the correct combination, but for $p\pi^+\pi^-\pi^-$phase space background events the "closer" combination can be either "correct" or not (both combinations should be wrong for

background, but we need to identify one combination for later usage). In particular, ideally, for this symmetric phase space background, the "closer" combination should be assigned as K^0Y combination only 50% of the time. The procedure does not include a feature to make random assignment for phase space background events, hence the observed bias. The only consequence of this imperfection is that there are more background events under the K^0Y region than there should have been, which only means any background rejection method needs to be better than it needs it to be otherwise. Finally, Figure 5.19 shows on the left the $IM(\pi^+\pi^-_{K^0})$ vs. $IM(p\pi^-_{\Lambda})$, and on the right the $IM(\pi^+\pi^-_{\Lambda})$ vs. $IM(p\pi^-_{K^0})$ for the Gold 2 data.

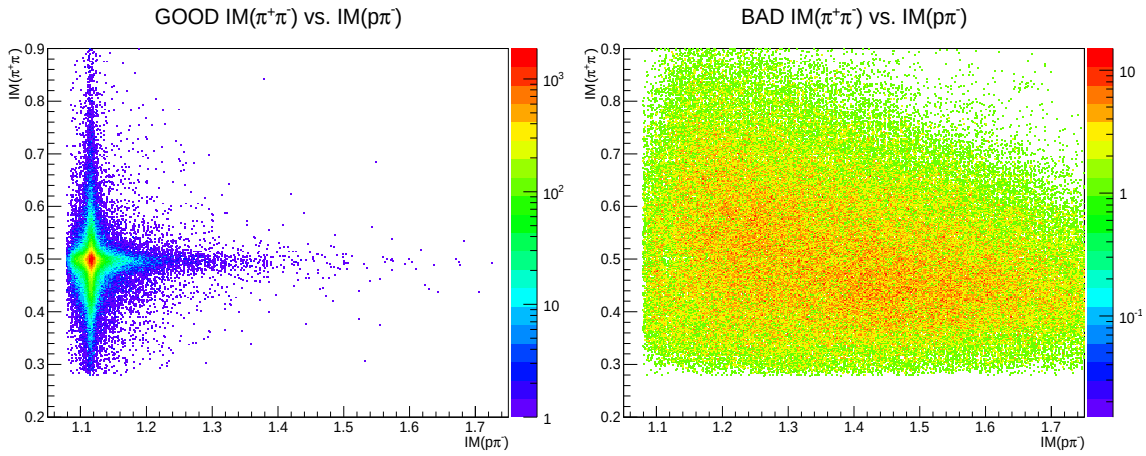

Figure 5.17: Left: $IM(\pi^+\pi^-_{K^0})$ vs. $IM(p\pi^-_{\Lambda})$ of the preferred combination for $(p\pi^-)$ and $(\pi^+\pi^-)$ by the discussed procedure. Right: the $IM(\pi^+\pi^-_{\Lambda})$ vs. $IM(p\pi^-_{K^0})$ for the other "wrong" combination. The procedure works very well in this case. The data used to plot was the *simulation data of the signal reaction* $\gamma n(p_s) \to K^0\Lambda(p_s)$. The units are in GeV. The plots are on a logarithmic scale.

We then applied loose selection cuts to remove unambiguous phase space background events as followed:

- Cut on Λ invariance mass: $IM(p\pi^-_{\Lambda})$ <1.2 GeV,
- Cut on K^0 invariance mass: 0.4 GeV< $IM(\pi^+\pi^-_{K^0})$ <0.6 GeV.

Finally, we show in Figure 5.20 the distributions of $IM(p\pi^-_{\Lambda})$ (on the left) and $IM(\pi^+\pi^-_{K^0})$ (on the right) from the Gold 2 period data, the the Λ and K^0 invariance mass distributions were fitted with the Breit-Wigner lineshape and the phase space background was fitted by 3^{rd} order polynomial.

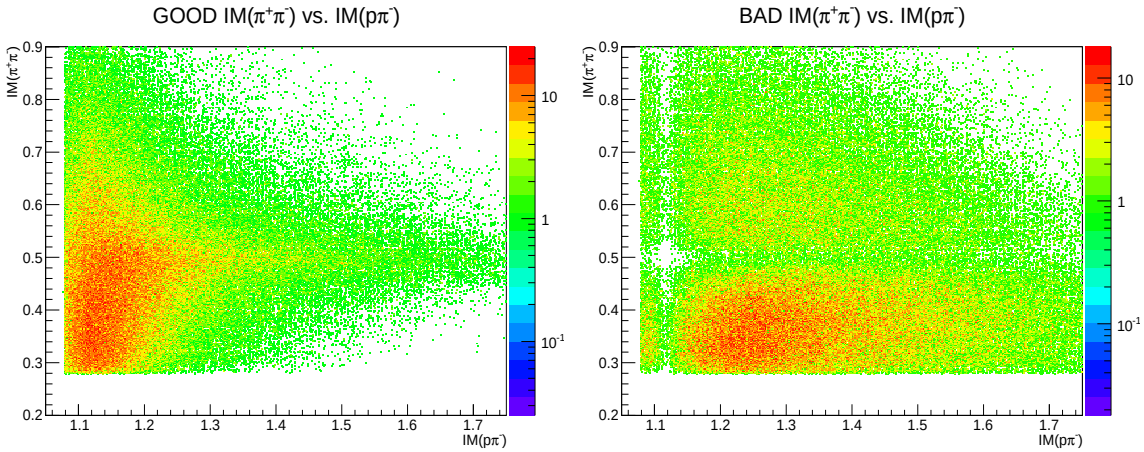

Figure 5.18: Left: $IM(\pi^+\pi^-_{K^0})$ vs. $IM(p\pi^-_{\Lambda})$ of the preferred combination for $(p\pi^-)$ and $(\pi^+\pi^-)$ by the discussed procedure. Right: the $IM(\pi^+\pi^-_{\Lambda})$ vs. $IM(p\pi^-_{K^0})$ for the "wrong" combination. The procedure introduces bias in this case. The data used to plot was the *simulation data of the 4-body phase space background reaction* $\gamma n(p_s) \to \pi^+\pi^- p\pi^-(p_s)$. The units are in GeV. The plots are on a logarithmic scale.

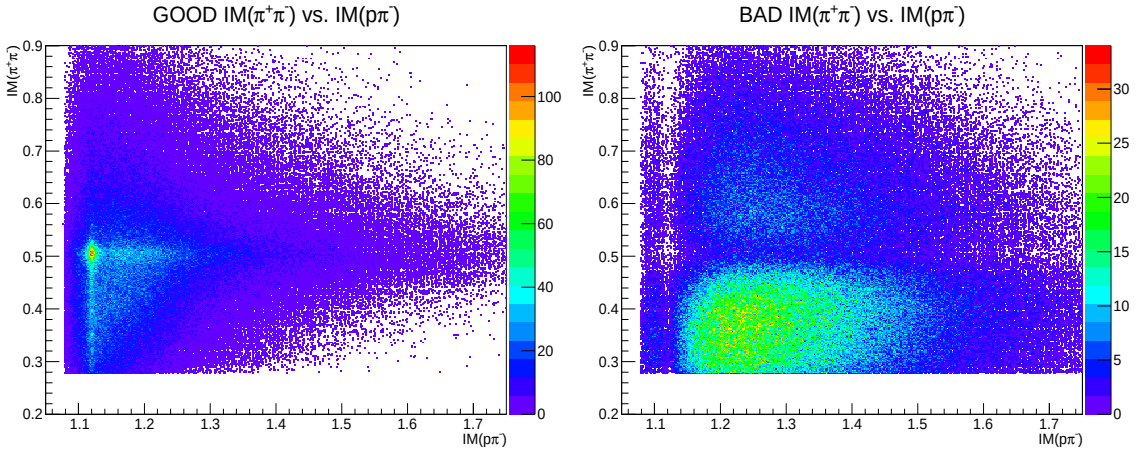

Figure 5.19: Left: $IM(\pi^+\pi^-_{K^0})$ vs. $IM(p\pi^-_{\Lambda})$ of the preferred combination for $(p\pi^-)$ and $(\pi^+\pi^-)$ by the discussed procedure. Right: the $IM(\pi^+\pi^-_{\Lambda})$ vs. $IM(p\pi^-_{K^0})$ for the "wrong" combination. The units are in GeV. The data used to plot was *the Gold 2 period data*. The plots are on a linear scale.

5.3 Bound *Neutron* K^0Y Event Selection using Boosted Decision Trees

This section provides details about the three tasks required to select the signal events that would be utilized to obtain the E asymmetry measurements. First, note that

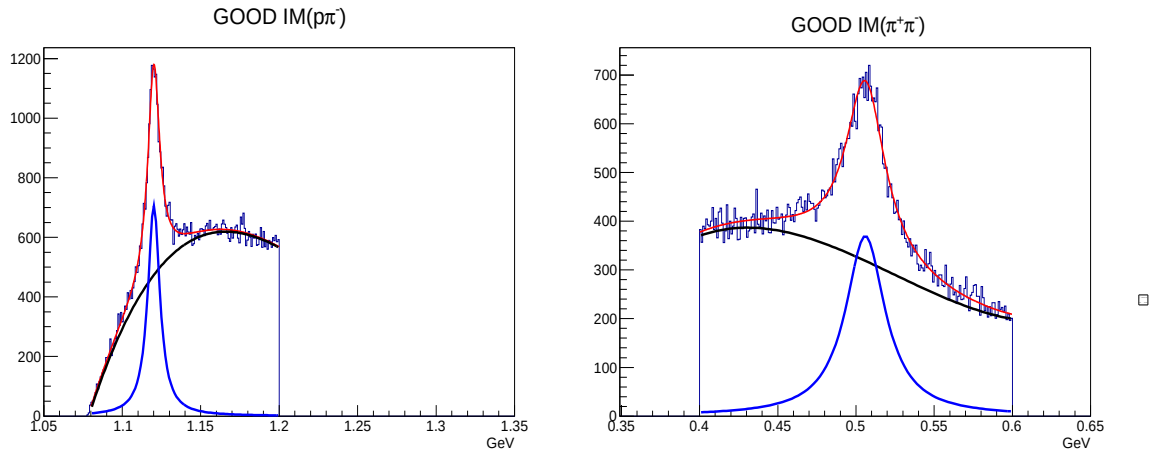

Figure 5.20: Left: $IM(p\pi^-_\Lambda)$ after all the cuts introduced previously, a fit of a sum of a Breit-Wigner lineshape and a 3^{rd} order polynomial is shown. Right: $IM(\pi^+\pi^-_{K^0})$ after all the cuts introduced previously, a fit of a sum of a Breit-Wigner lineshape and a 3^{rd} order polynomial is shown. The plots were obtained from the Gold 2 period data.

every event must originate from either the bound neutrons or the target-material (KelF cell walls and/or aluminum "cooling" wires) background. Second, the same event must be either a K^0Y or a non-resonant background ($p\pi^+\pi^-\pi^-(\gamma)$) event. In other words, the data is naturally partitioned into four *disjoint* subsets—of which every event must belong to only *one* of them (see Table 5.2(a)). The first two tasks are, therefore, to select *bound neutron* K^0Y events. Furthermore, in Table 5.2(b) we introduce the last task: separating K^0Y events into $K^0\Lambda$ and $K^0\Sigma^0$. In summary, to obtain the E asymmetry measurements we selected K^0Y signal events that originate from the bound neutrons, then separated Y into Λ or Σ^0.

One way to achieve the three required tasks is to partition the whole data set at once, but this approach may not robust due to its complexity. The other approach, which is more robust and less complex, is to partition the data sequentially. Particularly, firstly, we selected the bound neutron events (equivalently, rejected the target-material background). Secondly, we selected the K^0Y events from the *selected bound neutron events* by removing the non-resonant background background events. And thirdly, we separated the *bound neutron* K^0Y signal events into $K^0\Lambda$ and $K^0\Sigma^0$ events. At every stage, we could check the background rejection/signal selection performances, and estimated the remaining background, which would not be straightforward to implement if we had followed the other approach. We "trained" (constructed) three distinct Boosted Decision Trees (BDT) algorithms to execute the outlined tasks.

In Chapter 4 (and in Appendix A), we discussed in detail the BDT algorithm. We

repeat briefly here that the BDT is a "forest" of decision trees; the trees "view" the data in a high dimensional space (each input variable represents a dimension in that space) and "sculpt" the signal subset out of the signal-and-background "mixture". Note that it is important to pick a good set of input variables that has a large separation between the signal and background subsets in the multidimensional space. In addition, before it can be used, the BDT algorithm needs to "learn" the distributional structure of the signal and background events from training data. We generated simulation data to be used as training data with the exception of the target-material background data, for which we have the empty-target-period real data.

	K^0Y	Non-Strange Non-Resonant Background
Bound Neutrons	*SELECT*	REJECT
Target-Material Background	REJECT	REJECT

(a) The description of all disjoint subsets that every event should belong to *at most one of them*. The subset of interest for this analysis is the intersection of the first row and the first column.

	K^0Y	
Bound Neutrons (SELECT)	$K^0\Lambda$	$K^0\Sigma^0$
Target-Material Background (REJECT)	$K^0\Lambda$	$K^0\Sigma^0$

(b) Another possible classification the K^0Y set (first column in the previous table). After selecting the bound neutron K^0Y events, we then seperate Y into $\Lambda(\Sigma^0)$.

Table 5.2: Classification tasks required for this analysis.

The first BDT algorithm was "trained" for the task of efficiently removing the target-material background. This task is the same as the one in Chapter 4. Recall from Chapter 4 that the constructed BDT was able to optimally select the signal bound neutron events. An indirect implication is that the simulation data models the bound neutrons inside the deuteron well (i.e., momentum of the spectator proton follows the Hulthen momentum distribution [57]). We, hence, used the same model for simulation for this current task (as before the simulation data were passed through GSIM, GPP, and USERANA to simulate the CLAS detector efficiency). Nevertheless, there is one important difference. For the bound neutron events in the reaction $\gamma d \to \pi^- p(p_s)$, the missing momentum (momentum of the spectator protons) is small (mostly less than 200 MeV/c), which helped the BDT algorithm achieved high efficiency in classifying bound neutron signal and target-material background events (recall that the target-material background typically has *high* missing momentum—larger than 200 MeV/c—on average). The missing momentum distribution of the bound neutron events for the reaction $\gamma d \to K^0Y(p_s)$ is on average wider and peaks at a higher value of momentum—implying less *distributional* "separation" between the bound neutron signal and target-material background. This is because of the presence of an extra photon from the decay product of $\Sigma^0 \to \Lambda\gamma$, or from

a 5-body non-resonant background reaction $\gamma d \to \pi^+\pi^- p\pi^-(\gamma p_s)$. Therefore, since only the four charged particles were detected, the missing mometum might consist of the momentum of the spectator proton and an additional photon. This is illustrated in Figure 5.21, which shows the missing momentum distributions from simulated $\gamma n(p_s) \to K^0\Lambda(p_s)$ events (on the left plot) and from simulated $\gamma n(p_s) \to K^0\Sigma^0(p_s)$ events (on the right plot). Fortunately, we will introduce a slightly different BDT algorithm that can still achieve a high efficiency for separating these event catergories.

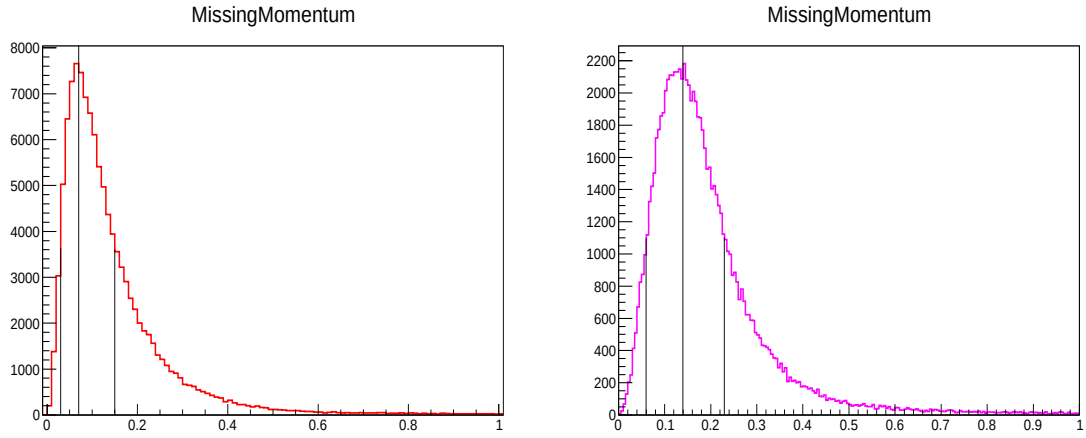

Figure 5.21: Left: Missing momentum for the simulated reaction $\gamma n(p_s) \to K^0\Lambda(p_s)$, the centroid of the distribution is at around 70 MeV/c, and the full width at half max is about 120 MeV/c. Right: Missing momentum for the simulated reaction $\gamma n(p_s) \to K^0\Sigma^0(p_s)$ (this reaction has an extra undetected photon), the centroid of the distribution is at around 140 MeV/c, the and full width at half max is about 170 MeV/c. Clearly the combined distribution from the two reactions (combining distributions for both plots) would be wider and peak at high value than the distribution on the left plot. The plots were constructed from the processed simulation data. The units are in GeV/c.

We learned that the $\gamma d \to K^0 Y(p_s)$ reaction of interest has very low statistics, and there are several factors to explain that. Firstly, $K^0\Lambda$ has a small total cross section of about $2\mu b$ [65] (so does $K^0\Sigma^0$). Secondly, only charged decay of both K^0 and Λ were selected which effectively reduced the amount of collectable data by about a half. These two factors help explain a low signal to background ratio (of about 1 : 4, see Figure 5.20). Thirdly, the CLAS drift chamber system has poor acceptance for this reaction since we required, for each event, four detected charged tracks; given a rough estimate of an acceptance of 0.7 for one charged track, then for four uncorrelated tracks we have an acceptance of about $0.7^4 \approx 0.24$. Furthermore, due to technical reasons, the g14 targets were shorter than typical targets used in previous CLAS experiments. Consequently, the number of $K^0\Lambda$ (or $K^0\Sigma^0$) signal events is modest. As a result, we needed a highly efficient procedure to remove most

of the $p\pi^+\pi^-\pi^-$ non-resonant background—the effect from the background is greater when the signal data is small—while only removing a small portion of signal events. Hence, we relied on the BDT algorithm to complete the difficult task.

The last task of separating $K^0\Lambda$ and $K^0\Sigma^0$ is equally difficult. If the target bound neutrons were at rest, computing the missing mass off K^0 would easily separate the two reactions. However, when we computed the missing mass off K^0 by *assuming the target neutrons being at-rest while they are, in fact, moving* (i.e., Fermi motion), then the missing mass off K^0 distributions of the two reactions ($K^0\Lambda$ and $K^0\Sigma^0$) are blurred. Hence, the two distributions become strongly overlapping, see Figure 5.22. Consequently, we employed another BDT algorithm to separate $K^0\Lambda$ and $K^0\Sigma^0$.

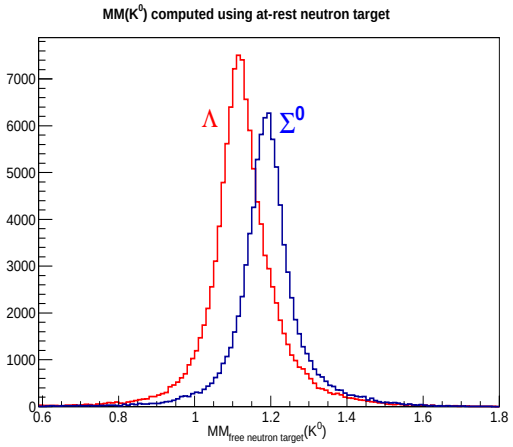

Figure 5.22: Missing mass off K^0 distributions computed by assuming *at-rest* target neutrons. Red histogram is obtained from the $K^0\Lambda$ simulation data, and blue histogram is obtained from the $K^0\Sigma^0$ simulation data. Strong overlapping is obvious, thus a simple mass cut on the missing mass off K^0 variable would not cleanly seperate the two types of signal. Note that both simulation data sets included Fermi motion of the target neutrons. The unit is in GeV.

In summary, we will present the procedures for selecting the signal events of interest ($K^0\Lambda$ and/or $K^0\Sigma^0$ originated from the bound target neutrons) using only the BDT algorithm. Necessarily, we estimated the remaining target-material and non-resonant background to implement corrections for dilution effect on the E asymmetry. The final sets of selected events (from the Gold 2 and the Silver run periods) were employed to measure the E helicity asymmetry in Section 5.4.

5.3.1 Bound Neutron Event Selection

The task of removing target-material background is the similar to the task in Chapter 4 where we first introduced the BDT algorithm. The same set of variables, therefore, are used for training the BDT for bound neutron event selection. In detail, Table

5.3 lists the variables, and the histograms of the variables are illustrated in Figure 5.23 (blue histograms were obtained from bound neutron simulation of signal data, and red histograms show the background which were obtained from the empty-target data.

Variable Name	Description
$MissingEnergy$	Total missing energy
$MissingMomentum$	Total missing momentum
$MissingTheta$	Θ of missing momentum
$MissingBeta$	β
$MissingGamma$	γ
$CoplanarityAngle$	$\left(\hat{p}_{(p\pi^-_\Lambda)} \times \hat{p}_\gamma\right) . \left(\hat{p}_{(\pi^+\pi^-_{K0})} \times \hat{p}_\gamma\right)$
$MissingPlus$	$E^{missing} + c\lvert p_z^{missing}\rvert$
$MissingMinus$	$E^{missing} - c\lvert p_z^{missing}\rvert$
$MissingPerp$	$\lvert p_{transverse}^{missing}\rvert$

Table 5.3: List of variables used in the first BDT—for selecting the bound neutron events. The last three variables are the so-called Dirac light-cone coordinate variables [62].

As discussed previously in Chapter 4, only variables related to the missing particles (of the reaction $\gamma d \to p\pi^+\pi^-\pi^-(X)$) are utilized. This was to reduce the requirement for generating simulation data that must be exactly matched to the real data. Ideally, if the neutrons are really bound, then the spectator protons needed to be the "isolated" partners and their kinematic variables should then have litle dependency on other variables such as the incident photon energy, the measured momentum of the detected π^-, etc. In other words, modeling the bound neutron events should not be concerned about other distributions beside the kinematic distributions of the spectator proton—i.e., must only model correctly the Hulthen mmentum distribution [57] for the spectator proton. Moreover, to model the reaction $\gamma d \to K^0\Sigma^0(p_s)$—these events have extra undetected photons from the decay $\Sigma^0 \to \Lambda\gamma$, we simply generated the reaction $\gamma n(p_s) \to K^0\Sigma^0(p_s)$ with the Hulthen wave function for the spectator protons and allowed the Σ^0 to decay. Note that we did not generate the 5-body non-resonant background reaction $\gamma n(p_s) \to \pi^+\pi^- p\pi^-(\gamma p_s)$ because it is not necessary for training the BDT. In addition, the bound neutron simulation data were processed through GSIM, GPP, and USERANA to simulate the detector performance (for more detail see Section 3.5). For training data of target-material background the empty-target-period data was employed.

As mentioned earlier, with the presence of the extra photons from the electromagnetic decay of the Σ^0, the missing momentum distribution peaks at a higher value and is broader; consequently, it is more difficult to seperate the signal and background events, thus potentially reducing the performance of the BDT algorithm. As

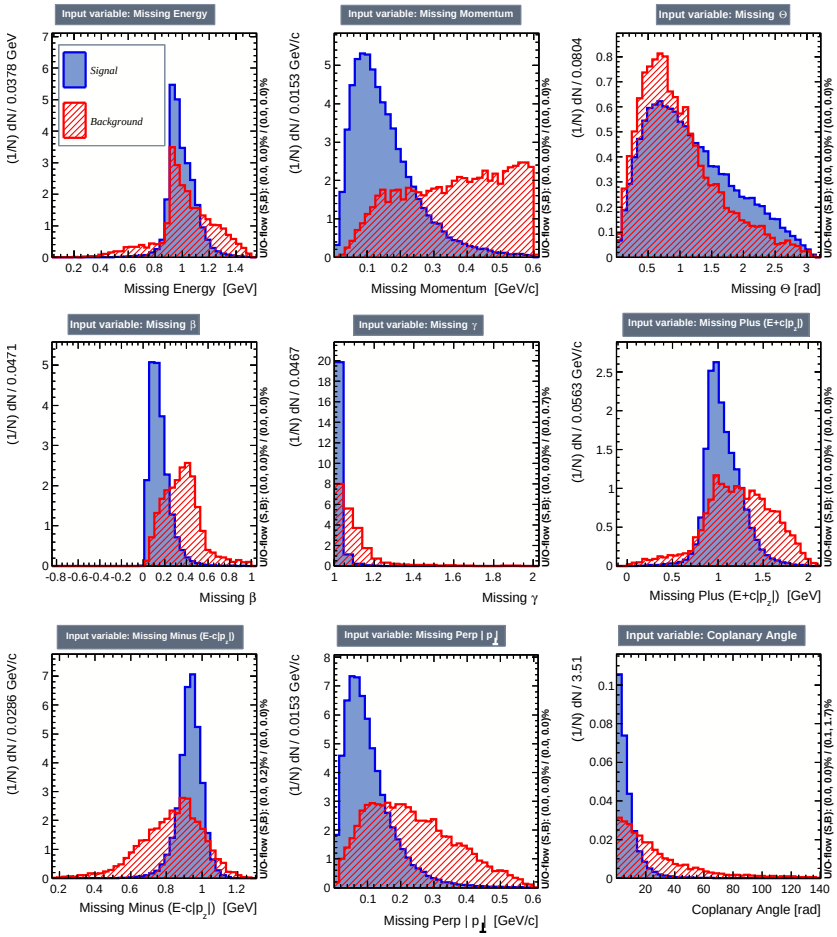

Figure 5.23: Histograms of variables used in the first BDT. The red histograms are from training background (empty-target-period), and the blue histograms are from the training signal simulation data.

a result, we implemented a more optimal BDT algorithm—which is referred to as a *categorical* BDT. We now briefly introduce this algorithm. Firstly, *a categorical variable which separates the training data into two disjoint subsets was chosen.* In particular, we selected the variable z-component of the interaction vertex to divide the training data into aluminum-dominated-region and KelF-dominated-region subsets—every signal/background event can only belong to *one* subset. Secondly, for each disjoint subset, the signal and background training data—belonging to that disjoint subset—were used to construct a BDT. After the training phase, there were two independently-built and *distinct* BDT algorithms, one for each subset. In summary, instead of using only *one* BDT (or one "forest" of decision trees) for the whole data set, we partitioned the data into *two disjoint* subsets and employed two *different* BDT (two "forests").

In some cases, paritioning the data into disjoint subsets can reduce the correla-

tions between the training variables within each subset, sometimes significantly; thus the performance of each BDT algorithm might be improved. Another significant consequence of partitioning the data is that, on average, the constructed decision trees could grow more without being overtrained (i.e., the average depth is higher than the simple BDT algorithm)—in Appendix A we disscuss why the BDT classification ability is increasing if the decision trees grow bigger as long as the BDT is not overtrained. One possible explanation is that when we partitioned the data, signal (background) events in each disjoint subset become more similar; in other words the data is less "noisy" (in Appendix A we mentioned that the overtraining problem occurs because of statistical "noise" in the data). To summarize, partitioning and training a different BDT on each data subset *might improve* the combined performance because it allows each BDT to be more specialized.

Figure 5.24 which plots *background rejection efficiency vs. signal efficiency*—ie., given a percentage of *rejected* background the curve quantifies the percentage of *remaining* signal—shows an optimal performance for the categorical BDT (black) compared to the simple BDT (red) algorithms. It is obvious to choose the categorical BDT over the simple BDT algorithms, thus only the categorical BDT is referred to hereafter. No evidence of overtraining is observed for the categorical BDT as shown in the left plot of Figure 5.25; high probabilities from the Kolmogorov-Smirnov tests suggest consistent performances on training data and independent test data. The right plot Figure 5.25 shows cut efficiencies and an optimal cut value. i.e., the efficiencies of selecting and rejecting signal and background data, respectively, as a function of the BDT output—the output value from the BDT between -1 and $+1$ to indicate how likely the event is a signal or background event. A recommended cut at 0.036 that minimizes the misclassifcation cost will be used—to obtain this number we must provide the *initial* signal to background ratio which we estimated to be roughly 3.35/1. In particular, from Figure 5.26 we could estimate the numbers of signal and background events (the *three-to-one* ratio is roughly accurate for all the events of interest within the target region). Nevertheless, when studying systematic uncertainties, we will vary this cut to study its effect. Lastly, we include Table 5.4 for a qualitative assessment on how often each variable was used in building the BDT, and for illustration, Figure 5.27 shows the first constructed decision tree.

We present the estimated efficiency of rejecting the target-material background by placing the recommend cut on the categorical BDT output at 0.036. In Figure 5.28 we plot the empty-target-period-data distribution of the z-component of the interaction vertex (blue histogram is before the cut, events in red (black) histogram were selected (rejected) by the cut). We also placed an additional cut on the z-vertex at -2.0 cm. Finally, Figure 5.29 show the missing mass and the missing momentum distributions (blue histograms are before the BDT and the z-vertex cuts, events in red (black) histograms were selected (rejected) by the cuts) on the left and right plots, respectively. We also estimated the survival fraction—i.e., percentage of remaining target-material background survived the BDT and z-vertex cuts—by calculating $p =$

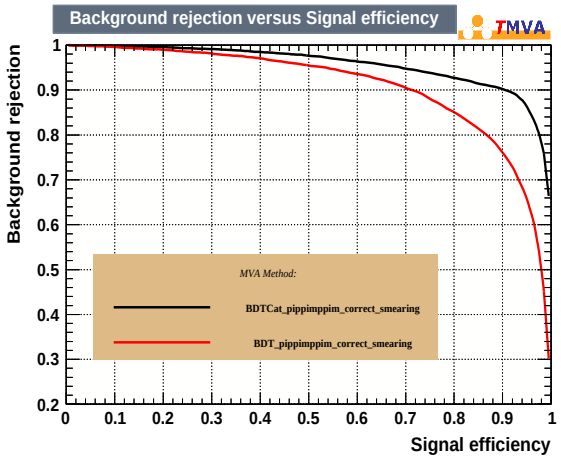

Figure 5.24: Background rejection vs. Signal efficiency (ie., given a percentage of *rejected* background the curve quantifies the percentage of *remained* signal) from training data for the simple BDT (red) and the categorical BDT (black).

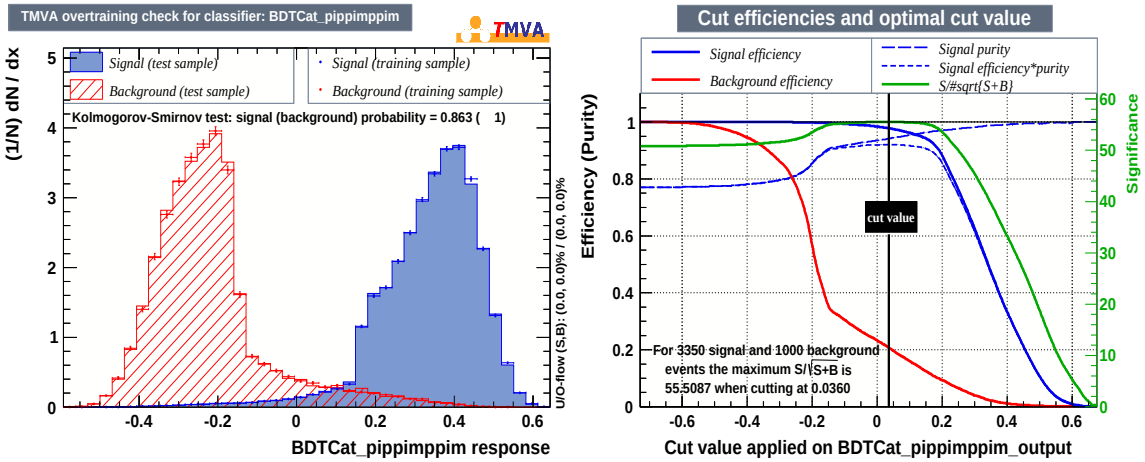

Figure 5.25: Left: Overtraining check, high Kolmogorov-Smirnov probabilities for both signal and background suggest no overtraining because the performance (distributions) of the categorical BDT is consistent with independent training and testing data sets. Right: Plots of cut efficiencies show the efficiencies as a function of cut value-and optimal cut value.

$S/(S+R)$ and $\sigma_p = \sqrt{p(1-p)}/\sqrt{S+R}$, where p is the estimated survival fraction, S (R) is the number of events selected (rejected) by the BDT cut; the numerical value of the estimated survival fraction is shown in Table 5.5. For illustration, we plot the simulated missing mass and missing momentum distributions before and after the BDT cut in Figure 5.30.

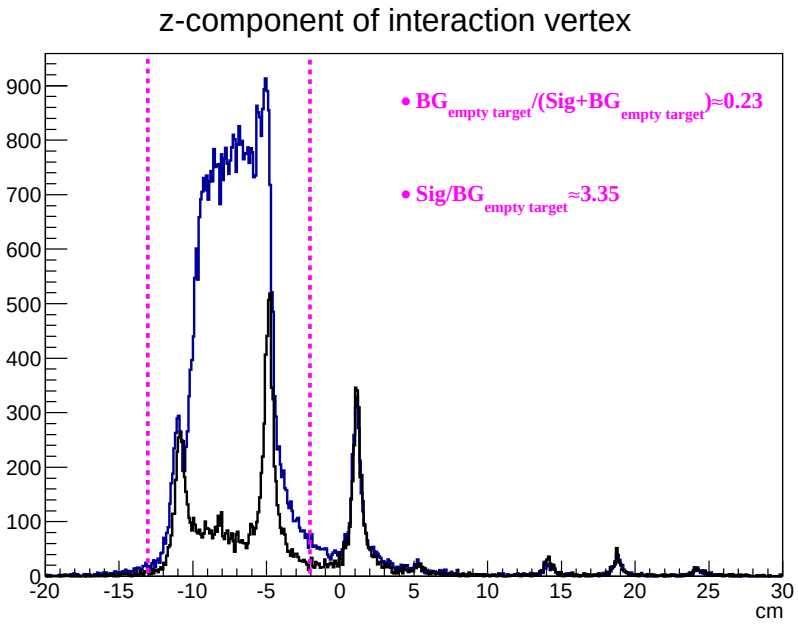

Figure 5.26: z-component of the interaction vertex; the blue histogram is from the Gold 2 data, and the black histogram are from the empty-target-period data. From these histograms we estimated the signal-to-background ratio to be 3.35 : 1 for events within the target region (inside the magenta lines).

Variable Name	Relative Ranking
$MissingMomentum$	1.00
$CoplanarityAngle$	0.84
$MissingPerp$	0.54
$MissingEnergy$	0.46
$MissingMinus$	0.43
$MissingPlus$	0.41
$MissingTheta$	0.36
$MissingGamma$	0.33
$MissingBeta$	0.21

Table 5.4: Table of relative variable ranking. The higher the ranking the more the variable was used to construct the decision trees. All the rankings were normalized to the absolute ranking of the missing momentum variable.

5.3.2 K^0Y Event Selection

In this section, we present our procedure to remove the $\pi^+\pi^- p\pi^-(\gamma)$ non-resonant backgrounds (i.e., both the 4- and 5-body non-resonant background types). For several reasons, it is not optimal to do event selection for this reaction by applying a

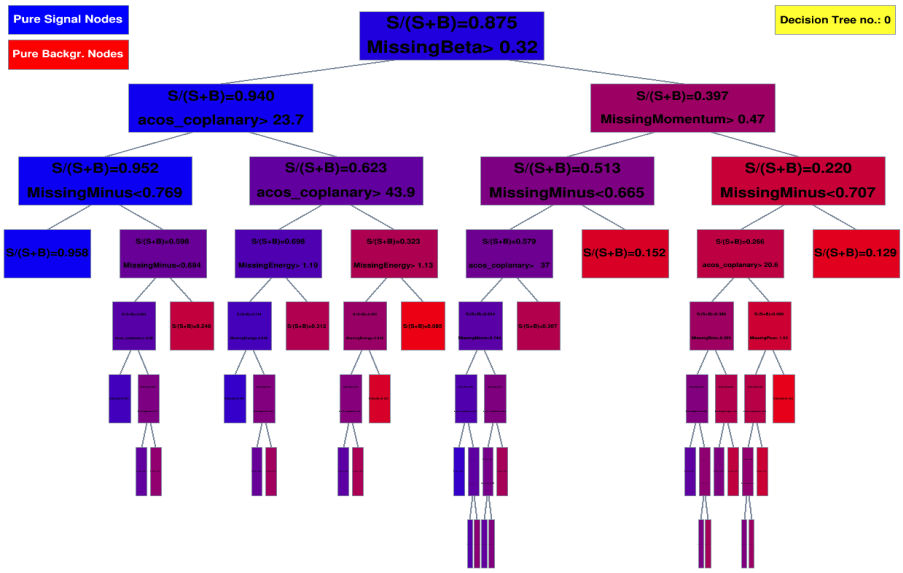

Figure 5.27: The first constructed decision tree, for illustration. Note that all variables can be used multiple times.

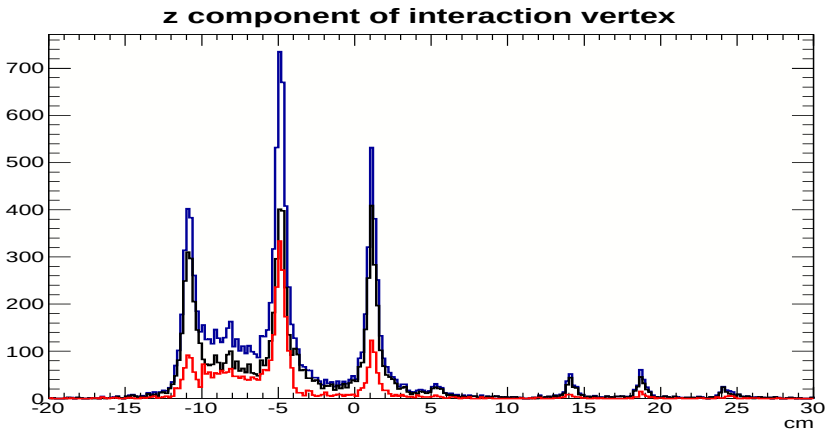

Figure 5.28: z-component of interaction vertex before (blue), and after the BDT cut (selected events are shown in red, and rejected events are in black). The plots were constructed from the empty-target-run-period data.

	Total Events	Surviving Events	Survival Fraction
Target-material BG	12,622	3,172	$\frac{3{,}172}{12{,}622} = 0.250 \pm 0.004$

Table 5.5: Estimated survival fraction for the empty-target-period background data after the BDT cut.

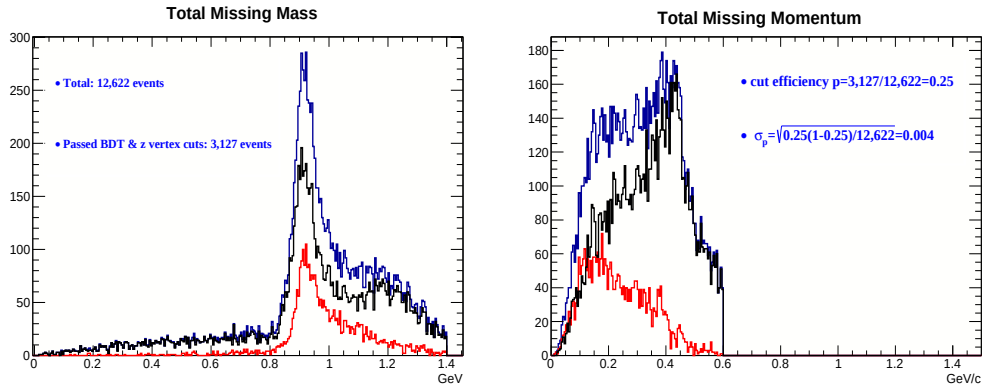

Figure 5.29: Left: Missing mass, $MM(p\pi^+\pi^-\pi^-)$, before (blue) and after the BDT cut (selected events are shown in red, and rejected events are in black). Right: Missing momentum before (blue), and after the BDT cut (selected events are shown in red, and rejected events are in black). The plots were constructed from the empty-target-run-period data.

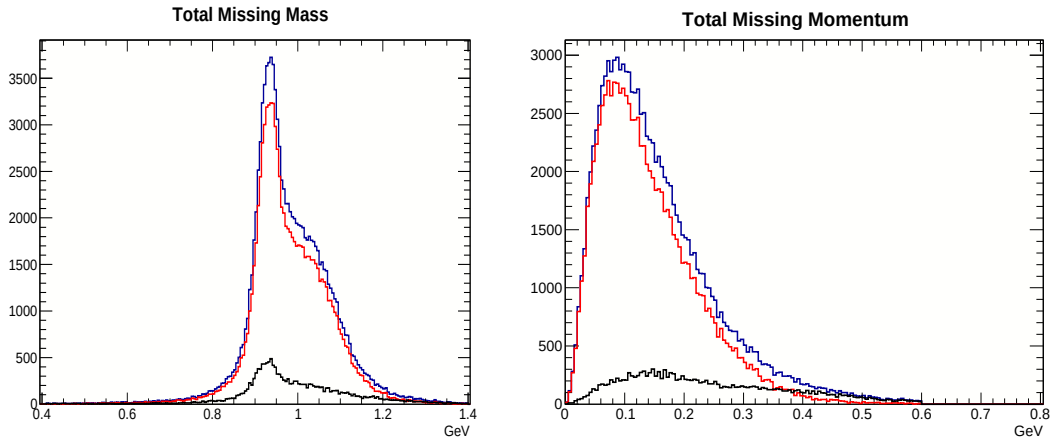

Figure 5.30: Left: Missing mass, $MM(p\pi^+\pi^-\pi^-)$, before (blue) and after (red) BDT and z-vertex cuts. Right: Missing momentum before (blue), and after (red) the cuts. The plots were constructed from signal simulation data.

simple cut method. In particular, Figure 5.31 shows the $IM(\pi^+\pi^-_{K^0})$ vs. the $IM(p\pi^-_{\Lambda})$ for the *simulated* K^0Y signal data (where Y is either Λ or Σ^0), and Figure 5.32 shows the same invariance mass distributions but for the Gold 2 *real* data. It is obvious that a simple circular mass cut as shown on both figures would probably be too tight for signal events and would not be effective in removing background events under the the K^0 and Λ masses. Hence, we employed the BDT algorithm to obtain a more optimal signal-selection-and-background-rejection performance than the simple circular mass cut could do. To train the BDT, we generated two simulation data sets: $K^0\Lambda$ signal

and non-strange phase space $\pi^+\pi^-p\pi^-$ background—background simulation data was generated from a uniform 4-body symmetric phase space kinematics. Necessarily, all the simulation data sets were proccessed through GSIM, GPP, and USERANA to simulate the CLAS detector efficiencies (for more detail see Section 3.5).

Addtionally, we show in Figure 5.33 the distributions of $IM(p\pi^-_\Lambda)$ (on the left) and $IM(\pi^+\pi^-_{K^0})$ (on the right) from the Gold 2 data, the Λ and K^0 invariance mass distributions were fitted with the Breit-Wigner lineshape and the non-resonant background was fitted with 3^{rd} order polynomial; integrating the fit functions, we can estimated the *background-to-signal* ratio. The uncertainty for the *background-to-signal* ratio can be obtained by propagating the uncertainties of the integrations (the ratio is to be used to estimate the remaining non-resonant background):

$$\sigma^2_{Sig+BG} = \sigma^2_{Sig} + \sigma^2_{BG} + 2\sigma_{Sig,BG}, \tag{5.5}$$

$$\Rightarrow \sigma_{Sig,BG} = \frac{1}{2}\left[\sigma^2_{Sig+BG} - \sigma^2_{Sig} - \sigma^2_{BG}\right], \tag{5.6}$$

$$\sigma^2_{BG/Sig} = \left(\frac{BG}{Sig}\right)^2 \left[\frac{\sigma^2_{Sig}}{Sig^2} + \frac{\sigma^2_{BG}}{BG^2} - 2\frac{\sigma_{Sig,BG}}{Sig \times BG}\right], \tag{5.7}$$

where Sig, and σ_{Sig} are the value and its uncertainty of the signal integral, respectively, and BG, and σ_{BG} are the value and its uncertainty of the background integral, respectively. σ_{Sig+BG} is the uncertainty on the integral of *total* signal and background fit, and $\sigma_{Sig,BG}$ is the covariance between the integrals of signal and background fits. Furthermore, the $\sigma_{BG/Sig}$ is the uncertainty of the *background-to-signal* ratio. Since there are two *background-to-signal* ratios, obtained from fitting the $IM(p\pi^-_\Lambda)$ and $IM(\pi^+\pi^-_{K^0})$ distributions seperately, we can compute the weighted average of the *background-to-signal* ratios (see Eq. 5.8 and Eq. 5.9). Note that since we did not have an accurate parametric fitting function to "describe" correctly the background (3^{rd} order polynomial is very general), the estimated values of signal and background in the two fits would likely *not* be the same (but the sums of signal and background from the two fit should be within an allowed statistical fluctuation). Therefore, it is better to take the average of the two ratios from the fits. Table 5.6 presents the numerical values for the obtained ratios.

$$r_{avg} = \left[\frac{1}{\sigma^2_{r_{K^0}}} r_{K^0} + \frac{1}{\sigma^2_{r_\Lambda}} r_\Lambda\right] \left[\frac{1}{\sigma^2_{r_{K^0}}} + \frac{1}{\sigma^2_{r_\Lambda}}\right]^{-1}, \tag{5.8}$$

$$\frac{1}{\sigma^2_{avg}} = \frac{1}{\sigma^2_{r_{K^0}}} + \frac{1}{\sigma^2_{r_\Lambda}}, \tag{5.9}$$

As shown in Table 5.1, the invariance mass distributions of the Λ and the K^0 from the signal simulation data does not perfectly match the same distributions from the

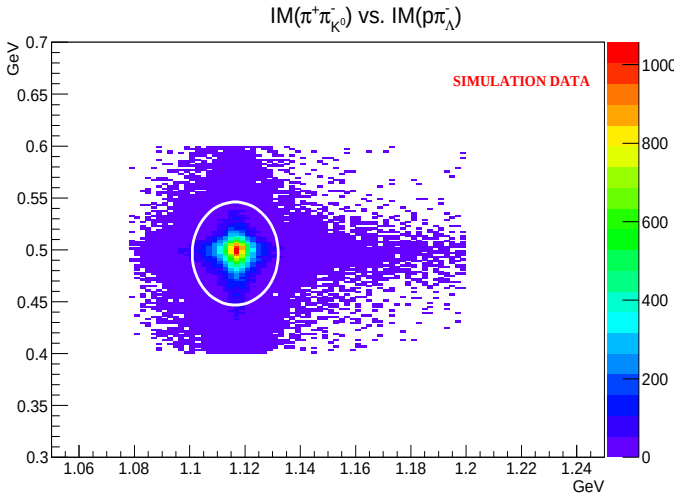

Figure 5.31: $IM(\pi^+\pi^-_{K0})$ vs. $IM(p\pi^-_\Lambda)$ for $K^0\Lambda$ signal simulation data, thus all events shown are good. A tight cut like the illustrative circle might not be efficient.

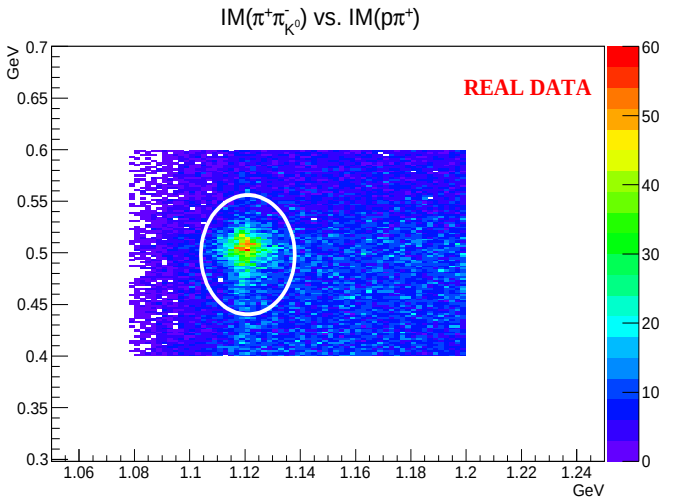

Figure 5.32: $IM(\pi^+\pi^-_{K0})$ vs. $IM(p\pi^-_\Lambda)$ for the Gold 2 real data. The non-resonant background is included in the plot; obviously, the illustrative circular cut can not remove background under the K^0 and Λ mass peaks.

real data (ie., the Breit-Wigner centroids and widths for the simulation and the real data are different). Therefore, to reduce *possible* performance issues, we did not use the $IM(\pi^+\pi^-_{K0})$, and the $IM(p\pi^-_\Lambda)$ as input variables for the BDT. Nevertheless, a transformation of these two variables was implemented so that we could still "exploit" their useful information. The new variable is defined as followed:

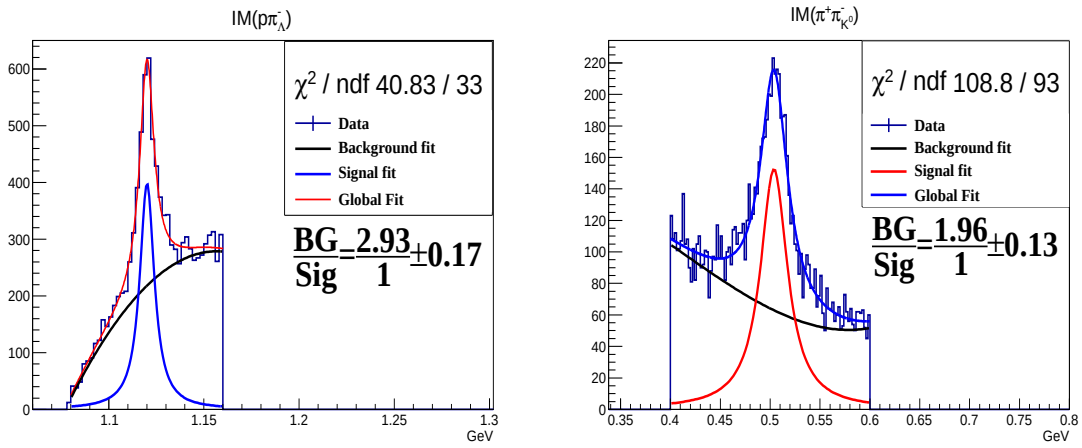

Figure 5.33: Left: $IM(p\pi^-_\Lambda)$ after the first BDT cut (to remove the target material background). Right: $IM(\pi^+\pi^-_{K^0})$ after the first BDT cut. For each plot, a fit of a sum of a Breit-Wigner lineshape and a 3^{rd} order polynomial is shown. The plots were obtained from the Gold 2 data. By integrating both fits for both plots, we estimated the average ratio of background to signal is about 2.3/1.0, see Table 5.6 (the signal and background training data sets for the second BDT would have the exact cuts).

	Signal	Background	Total	BG/Sig	Avg BG/Sig
$IM(p\pi^-_\Lambda)$	5.33 ± 0.24	15.60 ± 0.26	20.93 ± 0.20	$2.93/1 \pm 0.17$	$2.32/1 \pm 0.10 \pm 0.61$
$IM(\pi^+\pi^-_{K0})$	7.04 ± 0.30	13.77 ± 0.33	20.81 ± 0.20	$1.96/1 \pm 0.13$	

Table 5.6: Numerical values of the integrations on the fits shown in Figure 5.33, and the obtained *background-to-signal* ratios with statistical and systematic uncertainty; the statistical uncertainty is 0.10, the systematic uncertainty is 0.61 (i.e., 2.93-2.32=0.61).

$$\mathcal{L} \equiv \ln\left[f_{BW}(IM(p\pi^-_\Lambda), m_\Lambda, \Gamma_\Lambda) \times f_{BW}(IM(\pi^+\pi^-_{K^0}), m_{K^0}, \Gamma_{K^0})\right], \tag{5.10}$$

where $f_{BW}(m, m_0, \Gamma)$ is the Breit-Wigner probability distribution function with parameters m_0 (the centroid of the distribution), and Γ (the full width at half maximum (FWHM)), which was defined previously. The values for these parameters were taken from Table 5.1. For true signal events this is the statistical likelihood of being $K^0\Lambda(\Sigma^0)$, hence we named the variable likelihood. Note that, the variable is *normalized*, thus if the simulation and real data have a slight difference in the Λ and the K^0 mass distributions, the performance of the BDT on simulation and real data would remain consistent.

In Tables 5.7 and 5.8 we list a set of variables used in the second BDT. The variables listed in Table 5.7 are modestly correlated to the $\mathcal{L}$ variable (because they

are kinematically related), thus background events that are underneath the $K^0\Lambda(\Sigma^0)$ mass region can still be difficult to remove. In order to improve the BDT classification power for these events, we added several spacial variables, see Table 5.8 and Figure 5.34. In detail, we exploited the weak-decay natures of the Λ and the K^0 to obtain the additional set of spacial variables which exhibit small correlations to the kinematic variables. Even though the resolution of reconstructed vertices in CLAS is modest, the introduction of these variables provides a noticeable improvement. Next, we plot the distributions of all input variables for the signal and background training data—that BDT algorithm would be trained on—in Figures 5.35, and 5.36.

Variable Name	Description
$\mathcal{L}$ (ln(likelihood))	see Eq. (6.10)
Energy of Λ	Energy of the $(p\pi^-_\Lambda)$ system
Energy of K^0	Energy of the $(\pi^+\pi^-_{K^0})$ system
$\lvert P\rvert_\Lambda$	Magnitude of the 3-momentum of the $(p\pi^-_\Lambda)$ system
$\lvert P\rvert_{K^0}$	Magnitude of the 3-momentum of the $(\pi^+\pi^-_{K^0})$ system
$\cos\theta_\Lambda$	cosΘ of the 3-momentum of the $(p\pi^-_\Lambda)$ system in lab coordinate
$\cos\theta_{K^0}$	cosΘ of the 3-momentum of the $(\pi^+\pi^-_{K^0})$ system in lab coordinate
$\cos\theta_{p\&\pi^-_\Lambda}$	cosΘ between p and π^-_Λ
$\cos\theta_{\pi^+\&\pi^-_{K0}}$	cosΘ between (π^+) and $\pi^-_{K^0}$
$\cos\theta_{K^0\&\Lambda}$	cosΘ between $(p\pi^-_\Lambda)$ and $(\pi^+\pi^-_{K^0})$ systems
$\beta_{\pi^-_{K^0}}$	Beta of $\pi^-_{K^0}$ in the lab frame
$\beta_{\pi^-_\Lambda}$	Beta of π^-_Λ in the lab frame
β_p	Beta of π^-_p in the lab frame
β_{π^+}	Beta of π^+ in the lab frame
$\beta_{(\pi^+\pi^-_{K^0})}$	Beta of the $(\pi^+\pi^-_{K^0})$ system in the lab frame
$\beta_{(p\pi^-_\Lambda)}$	Beta of the $(p\pi^-_\Lambda)$ system in the lab frame

Table 5.7: List of variables used in the second BDT—to remove the non-strange non-resonant background. For spatial variables' definitions see Figure 5.34.

Simple BDT and categorical BDT algorithms were "trained" by the $K^0\Lambda(\Sigma^0)$ signal and non-strange 4-body non-resonant background simulation training data using the set of variables listed in Table 5.8. The categorical variable chosen for the categorical BDT is the first variable on the list—in detail, for the categorical BDT algorithm we divided the training data into two disjoint subsets, one is with $\mathcal{L} < -7$, and the other is with $\mathcal{L} \geq -7$ (see Figure 5.35). Note that for the categorical BDT

Variable Name	Description
$(\pi^+\pi^-_{K^0})$ decay distance	distance between interaction vertex and $(\pi^+\pi^-_{K^0})$ vertex (or OA) in the $(\pi^+\pi^-_{K^0})$ rest frame
$(p\pi^-_{\Lambda})$ decay distance	distance between interaction vertex and $(p\pi^-_{\Lambda})$ vertex (or OB) in the $(p\pi^-_{\Lambda})$ rest frame
$(\pi^+\pi^-_{\Lambda})$ decay distance	distance between interaction vertex and $(\pi^+\pi^-_{\Lambda})$ vertex (or OA') in the $(\pi^+\pi^-_{\Lambda})$ rest frame
$(p\pi^-_{K^0})$ decay distance	distance between interaction vertex and $(p\pi^-_{K^0})$ vertex (or OB') in the $(p\pi^-_{K^0})$ rest frame
π^+ and π^-_{Λ} DOCA	distance of closest approach between π^+ and π^-_{Λ} momenta (or CE)
p and $\pi^-_{K^0}$ DOCA	distance of closest approach between p and $\pi^-_{K^0}$ momenta (or DF)
K^0 and Λ DOCA	distance of closest approach between $(p\pi^-_{\Lambda})$ and $(\pi^+\pi^-_{K^0})$ momenta (or AB)

Table 5.8: List of spatial variables used in the second BDT—to remove the non-strange non-resonant background. For the variables' definitions see Figure 5.34.

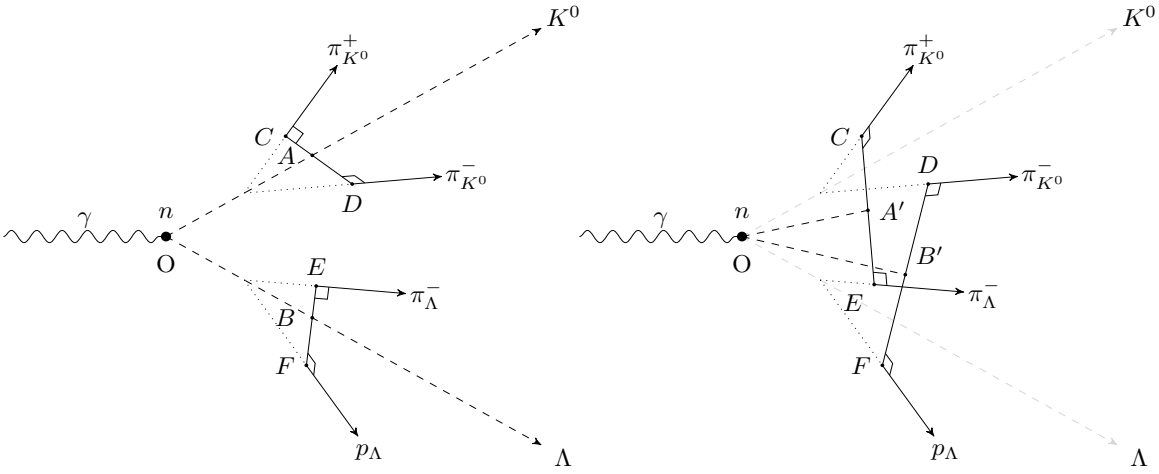

Figure 5.34: 3-D sketch of the reaction $\gamma n \to K^0\Lambda \to \pi^+\pi^-_{K^0}p\pi^-_{\Lambda}$ in the lab frame with *at-rest* target neutrons. The spacial variables described in Table 5.7 include OA, OB, OA', OB', CE, DF, and AB distances.

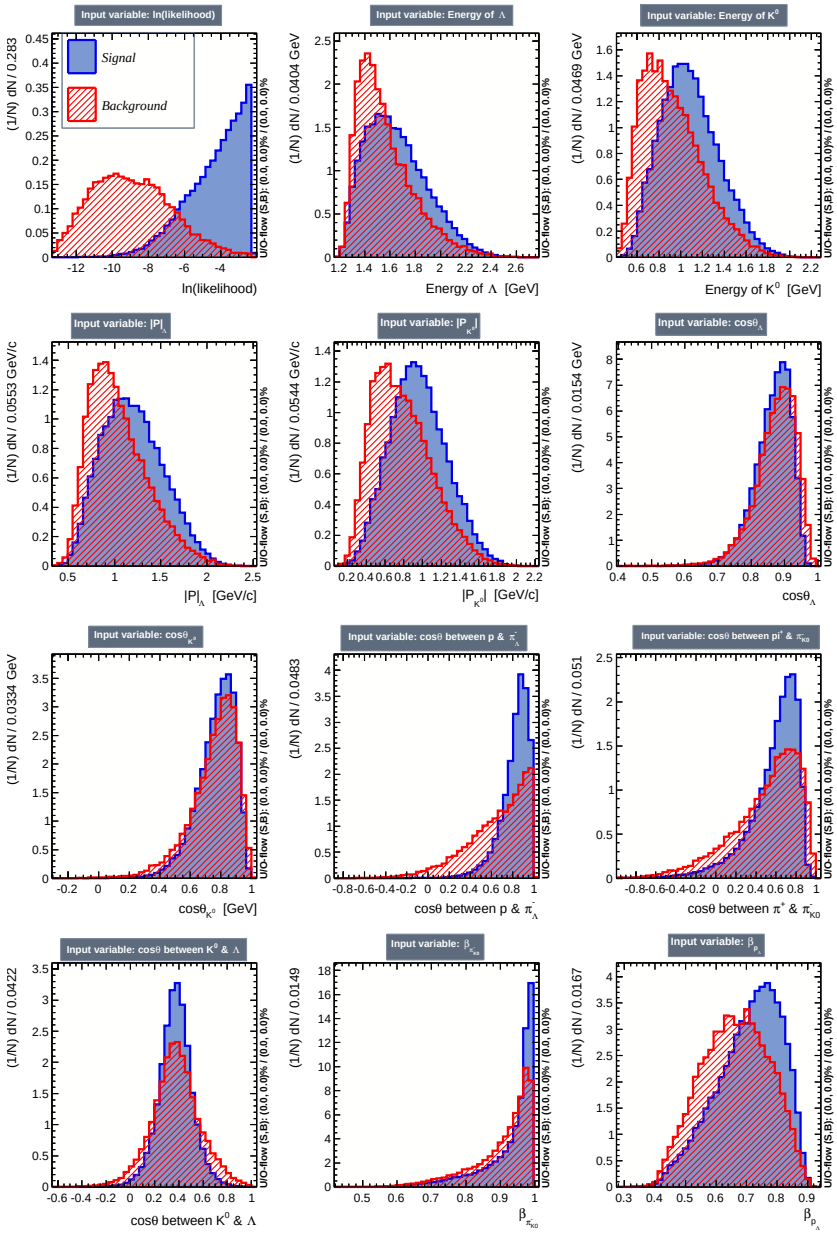

Figure 5.35: Histograms of variables used in the second BDT. The red histograms are from non-strange non-resonant background MC data, and the blue histograms are from the signal MC data.

algorithm, after the training phase, there would be two distinct and independently-built "forests" of decision trees. Next, as shown in Figure 5.37 the performance of the categorical BDT (black) is more optimal than the performance of simple BDT (red), see previous section for discussion about this. Later, we employed only the newly-built categorical BDT algorithm for the task of selecting the $K^0\Lambda(\Sigma^0)$ signal

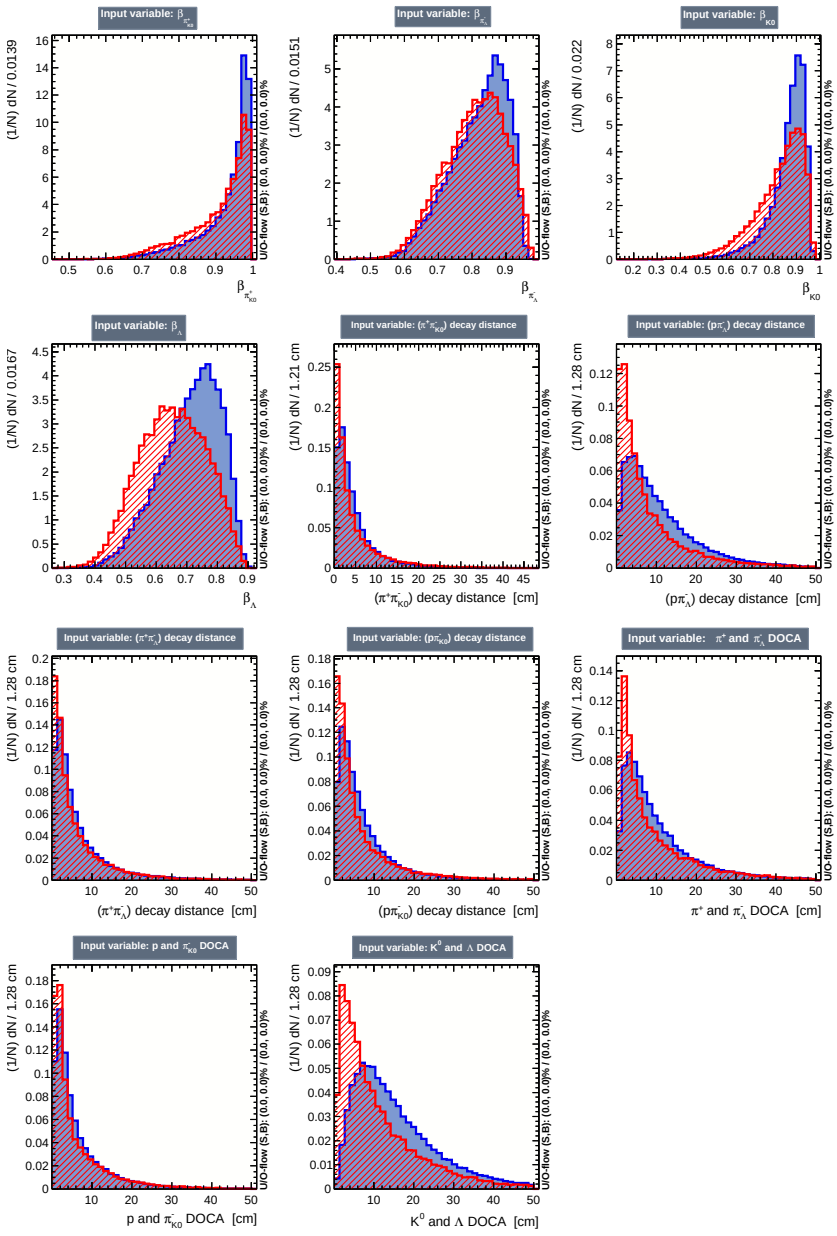

Figure 5.36: More histograms of variables used in the second BDT. The red histograms are from non-strange non-resonant background MC data, and the blue histograms are from the signal MC data.

events. In addition, Figure 5.38 shows no evidence of overtraining for the categorical BDT algorithm—Kolmogorov-Smirnov tests result in high probabilities indicating consistency between independent training and testing data sets for both signal and background reactions. Furthermore, we include Table 5.9 for a quantitative assessment on how often each variable was used in building the BDT, and for illustration,

Figure 5.39 shows the first constructed decision tree.

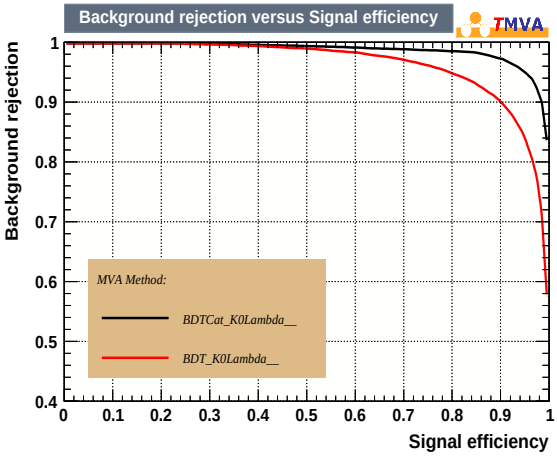

Figure 5.37: Background rejection vs. Signal efficiency from training data for the simple BDT (red) and the categorical BDT (black).

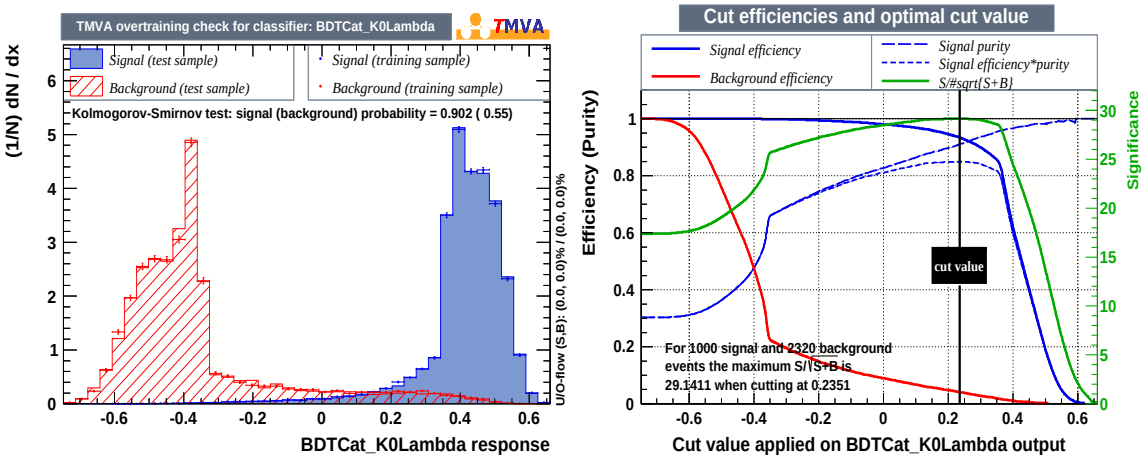

Figure 5.38: Left: Overtraining check, high Kolmogorov-Smirnov probabilities for both signal and background suggest no overtraining because the performance (distributions) of the categorical BDT is consistent with independent training and testing data sets. Right: Plots of cut efficiencies show the efficiencies as a function of cut value-and optimal cut value.

Previously, we estimated the *background-to-signal* ratio to be 2.32/1.00 for the Gold 2 data, see Table 5.6. Consequently, a recommended cut at 0.24 on the BDT output was obtained. In the systematic study section, we will vary this cut to test its robustness. And lastly, we applied the newly-constructed categorical BDT algorithm to the simulation data, see Figures 5.40, 5.41. We also estimated the survival

Variable Name	Ranking	Variable Name	Ranking
$\mathcal{L}$ (or ln(likelihood))	1.0	$\cos\theta_{K^0}$	0.14
$\cos\theta_{\pi^+\&\pi^-_{K0}}$	0.27	$\lvert P\rvert_{K^0}$	0.13
$(p\pi^-_{K^0})$ decay distance	0.25	p and $\pi^-_{K^0}$ DOCA	0.13
$\cos\theta_{K^0\&\Lambda}$	0.20	$(\pi^+\pi^-_\Lambda)$ decay distance	0.13
$\beta_{\pi^-_\Lambda}$	0.20	$(\pi^+\pi^-_{K^0})$ decay distance	0.12
$\cos\theta_\Lambda$	0.19	$\beta_{(\pi^+\pi^-_{K^0})}$	0.12
π^+ and π^-_Λ DOCA	0.17	Energy of K^0	0.12
$(p\pi^-_\Lambda)$ decay distance	0.17	$\beta_{(p\pi^-_\Lambda)}$	0.11
$\cos\theta_{p\&\pi^-_\Lambda}$	0.16	β_{π^+}	0.11
β_p	0.16	$\lvert P\rvert_\Lambda$	0.11
K^0 and Λ DOCA	0.15	Energy of Λ	0.10
$\beta_{\pi^-_{K^0}}$	0.14		

Table 5.9: Table of relative variable ranking. The higher the ranking the more the variable was used to construct the decision trees. All the rankings were normalized to the absolute ranking of the $\mathcal{L}$ (ln(likelihood)) variable.

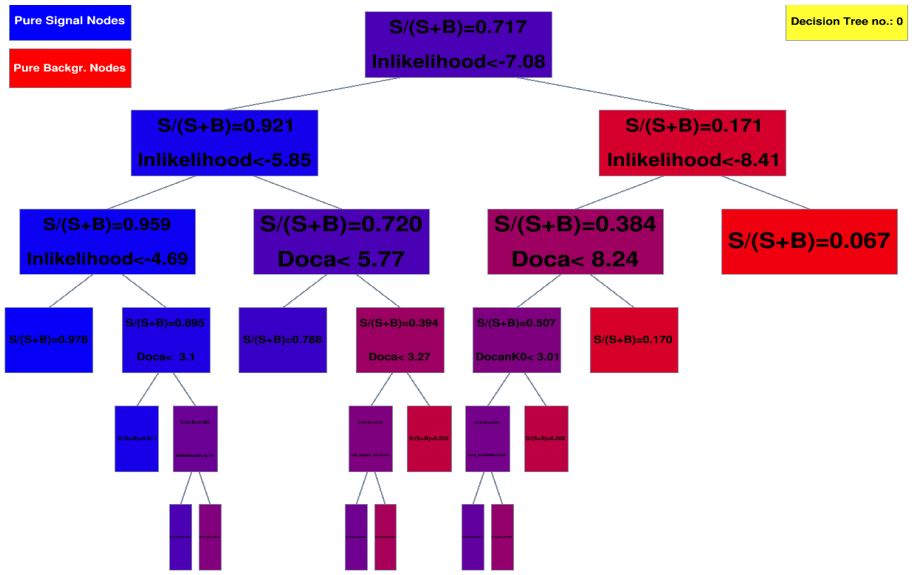

Figure 5.39: The first constructed decision tree from the second BDT, for illustration. Note that all variables can be used multiple times.

fraction—i.e., percentage of remaining non-resonant background survived the BDT cut—by calculating $p = {}^{S}/_{(S+R)}$ and $\sigma_p = \sqrt{p(1-p)}/\sqrt{S+R}$, where p is the estimated survival fraction, S (R) is number of events selected (rejected) by the BDT cut; the numerical value of the estimated survival fraction is shown in 5.10.

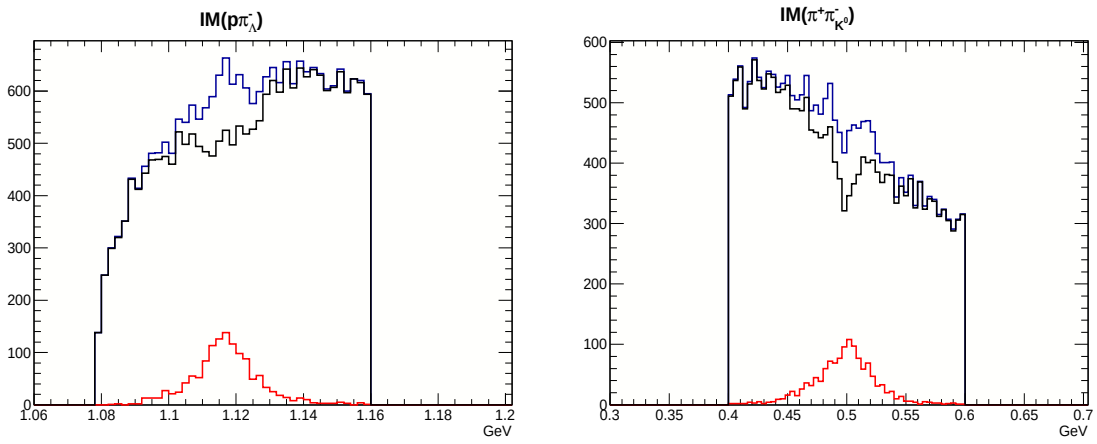

Figure 5.40: Left: $IM(p\pi^-_\Lambda)$ before (blue), rejected (black), and *wrongly* selected (red) by the BDT cut. Right: $IM(\pi^+\pi^-_{K0})$ before (blue), rejected (black), and *wrongly* selected (red) by the BDT cut. The plots were constructed from the non-strange phase space MC data. The units are in GeV.

	Total Events	Survived Events	Survival Fraction
Phase space BG	$22,312$	$1,282$	0.057 ± 0.002

Table 5.10: Estimated survival fraction for the non-strange phase space background MC data after the BDT cut.

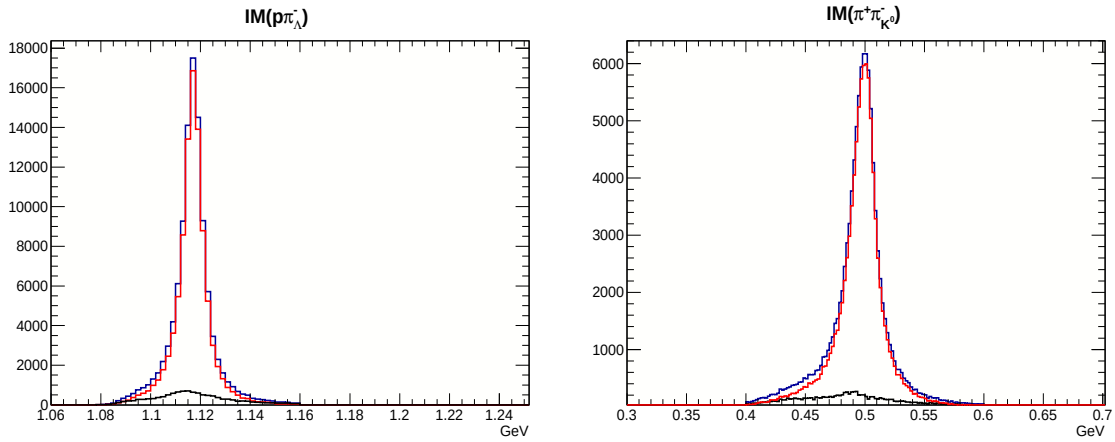

Figure 5.41: Left: $IM(p\pi^-_\Lambda)$ before (blue), rejected (black), and selected (red) by the BDT cut. Right: $IM(\pi^+\pi^-_{K0})$ before (blue), rejected (black), and selected (red) by the BDT cut. The plots were constructed from signal MC data. The units are in GeV.

5.3.3 Separating $K^0\Lambda$, $K^0\Sigma^0$ Events

We continue with the last task for this analysis: seperating $K^0\Lambda$, $K^0\Sigma^0$ events. As previously mentioned, this task would have been straightforward if the target neutrons were *at-rest*—by computing the missing mass off K^0—since, then, the Λ, and Σ^0 mass spectra would be well seperated. In reality, the target neutrons are in Fermi motion; therefore computing the missing-mass-off-K^0 spectrum by *assuming the target neutrons being at-rest* results in broadened and strongly overlapped Λ, and Σ^0 mass spectra, see Figure 5.22. Hence it was clear that we needed to build another BDT algorithm to optimally separate the two reactions. In detail, Table 5.11 introduces a list of input variables for "training" the BDT. Note that these variables exploit the fact that the $K^0\Sigma^0$ events have an extra photon, which is the decay product of $\Sigma^0 \to \Lambda\gamma$, undetected, while the missing particles for the $K^0\Lambda$ channel are just the spectator protons. Next, for illustration, we plot the distributions of the input variables for the $K^0\Lambda$ and the $K^0\Sigma^0$ events in Figure 5.42. In those histograms, $K^0\Lambda$ events are in blue (and called *"signal"* events), while $K^0\Sigma^0$ events are in red (and called *"background"* events). The histograms were obtained from the simulation data which was used to train the BDT.

Variable Name	Description
Missing Mass	Total missing mass (deuteron target)
Missing Energy	Total missing energy (deuteron target)
Missing Momentum	Total missing momentum (deuteron target)
Missing Theta	Θ of the missing momentum in lab coordinate (deuteron target)
Missing Beta	$\beta_{missing}$ (deuteron target)
Missing Gamma	$\gamma_{missing}$ (deuteron target)
Missing Plus	$E^{missing} - c\lvert p_z^{missing}\rvert$ (deuteron target)
Missing Minus	$E^{missing} + c\lvert p_z^{missing}\rvert$ (deuteron target)
Missing Perp	$\lvert p_{transverse}^{missing}\rvert$ (deuteron target)
Coplanarity Angle	$\left(\hat{p}_{(p\pi^-_\Lambda)} \times \hat{p}_\gamma\right) . \left(\hat{p}_{(\pi^+\pi^-_{K0})} \times \hat{p}_\gamma\right)$ (deuteron target)
Missing Mass off K^0	$MM(\pi^+\pi^-_{K0})$ (*at-rest* neutron target)
$\theta_{K^0\&\Lambda}$	angle between $(\pi^+\pi^-_{K0})$ and $(p\pi^-_\Lambda)$ in $(\gamma n_{\text{at-rest}})$ rest frame

Table 5.11: List of input variables used in the third BDT for the task of seperating $K^0\Lambda$, $K^0\Sigma^0$ events.

We trained two different BDT algorithms; the first one is just the simple BDT, and the second one is the categorical BDT. The categorical variable is the Total Missing Mass variable. Note that it is computed with the deuteron mass as the

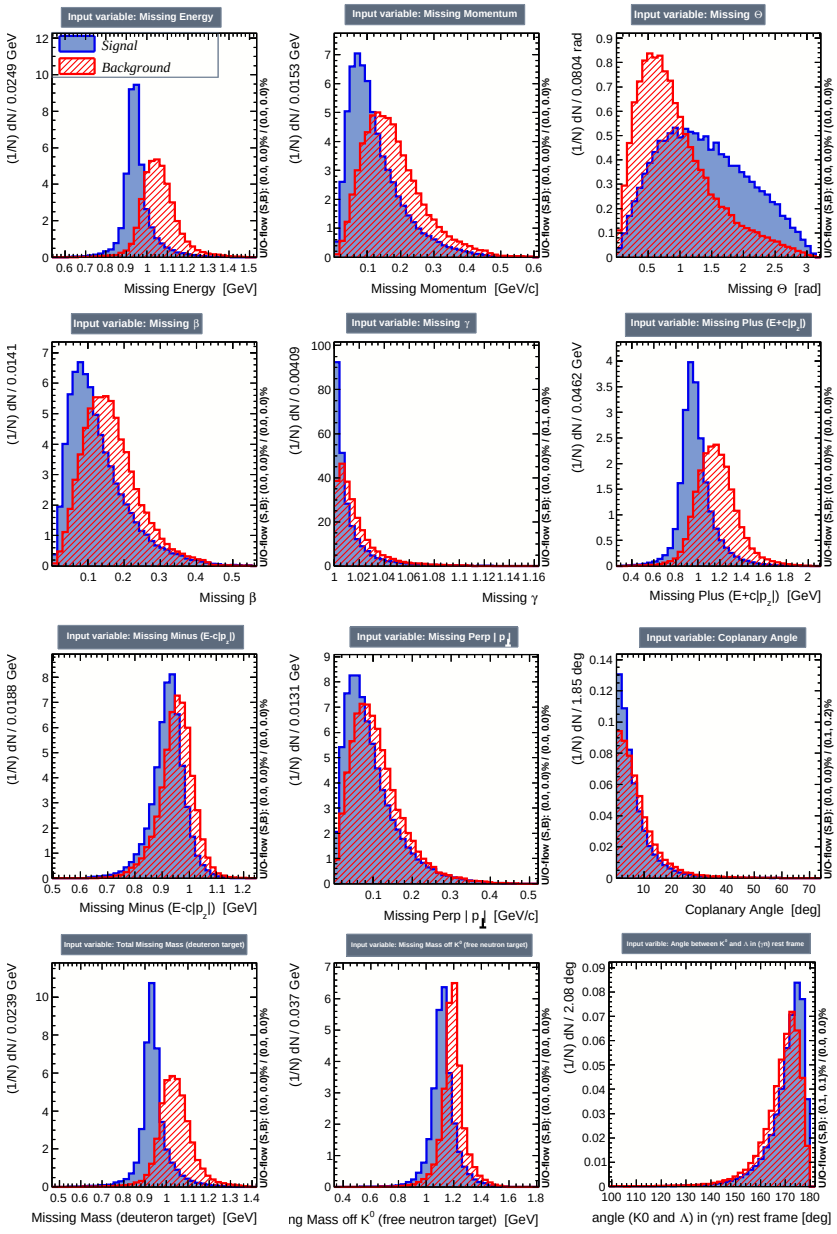

Figure 5.42: Histograms of variables used in the third BDT. The red histograms are from $K^0\Sigma^0$ simulation data (referred to as background), and the blue histograms are from the $K^0\Lambda$ simulation data (referred to as signal).

target mass. The training data was divided into two disjoint subsets, one is with $MM(p\pi^+\pi^-\pi^-) < 0.99$ GeV, and the other is with $MM(p\pi^+\pi^-\pi^-) \geq 0.99$ GeV (note that this is only applied for the categorical BDT). In addition, even though we referred to the $K^0\Lambda$ events as signal events, and to the $K^0\Sigma^0$ as background, the $K^0\Sigma^0$ events would not be discarded. In fact, we intended to measure the E asymmetries

for both reactions. Next, for illustration, we plot in Figure 5.43 the performances of the categorical BDT (black) and the simple BDT (red). It is apparent that we should use the categorical BDT algorithm. Also, we show in the left plot of Figure 5.44 that there is no evidence of overtraining for the categorical BDT algorithm—Kolmogorov-Smirnov tests result in high probabilities for both signal and background data, and, in the right plot of Figure 5.44 we show the signal-acceptance and background-rejection efficiencies as a function of the BDT output; a recommended cut on the BDT output at 0.03 was obtained by assuming the initial signal to background (Λ to Σ^0) ratio to be $1:1$. Since we would not discard any events, this ratio does not need to be very precise—but we expect the $1:1$ ratio is close to the true value. Nevertheless, for systematic studies we varied this cut value. Furthermore, variable ranking is presented in Table 5.12, and in Figure 5.45 the first decision tree of the BDT is shown.

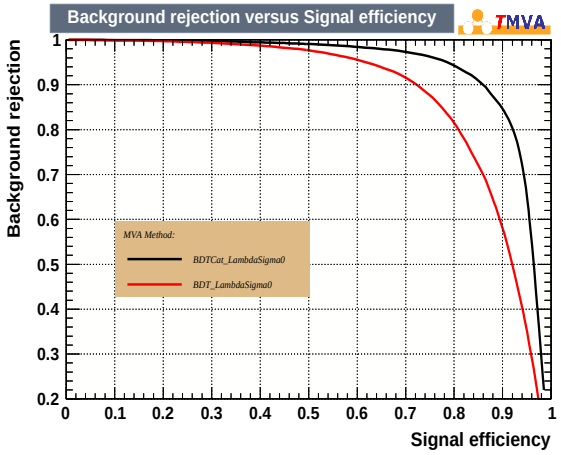

Figure 5.43: Background rejection vs. Signal efficiency from training data for the simple BDT (red) and the categorical BDT (black).

Variable Name	Ranking	Variable Name	Ranking
Missing Energy	1.00	Missing Theta	0.22
Missing Mass	0.72	Missing Gamma	0.19
Missing Mass off K^0	0.70	$\theta_{K^0\&\Lambda}$	0.19
Missing Momentum	0.56	Missing Beta	0.15
Missing Minus	0.28	Missing Plus	0.08
Missing Perp	0.26	Coplanarity Angle	0.05

Table 5.12: Table of relative variable ranking. The higher the ranking the more the variable was used to construct the decision trees. All the rankings were normalized to the absolute ranking of the missing energy variable.

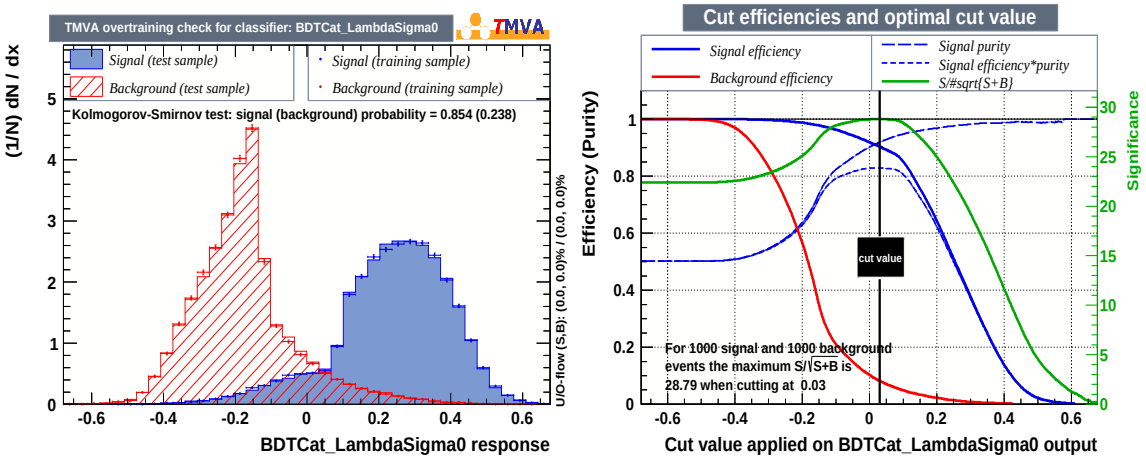

Figure 5.44: Left: Overtraining check, high Kolmogorov-Smirnov probabilities for both signal and background suggest no overtraining because the performances (distributions) of the categorical BDT are consistent with independent training and testing data sets. Right: Plot of cut efficiencies show the signal-acceptance and background-rejection efficiencies as a function of the BDT output and an optimal cut value (of 0.02).

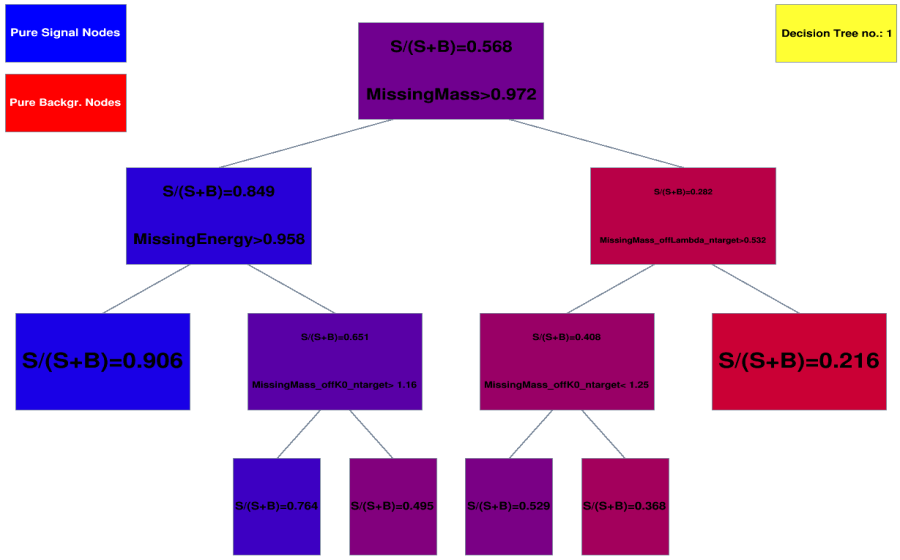

Figure 5.45: The first constructed decision tree from the third BDT, for illustration. Note that all variables can be used multiple times.

In Figures 5.46, and 5.47 we illustrate the high performances of the categorical BDT (we obtained the plots from simulation data). For example, the number of $K^0\Lambda$ events that were correctly identified is much higher than the number of events that were *incorrectly identified as* $K^0\Sigma^0$ (similar observation can be seen for the $K^0\Sigma^0$

data). Importantly, note that an event is "identified" as $K^0\Sigma^0$ if it has its BDT output value less than 0.02, otherwise, it is "identified" as $K^0\Lambda$. Finally, Table 5.13 presents the numerical values of the BDT performances for both $K^0\Lambda$ and $K^0\Sigma^0$. We now introduce several notations to faciliate future discussions in later sections:

- N_Λ^{true} ($N_{\Sigma^0}^{true}$) is the total number of $K^0\Lambda$ ($K^0\Sigma^0$) events in the real data (such as Gold 2 data),
- N_Λ^{BDT} ($N_{\Sigma^0}^{BDT}$) is the number of events that have the BDT output larger (smaller) than 0.02,
- ω_Λ (ω_{Σ^0}) is the BDT efficiency for the $K^0\Lambda$ ($K^0\Sigma^0$) events (i.e., percentage of number of simulated events that are correctly "identified" by the 3^{rd} BDT),

$$N_\Lambda^{BDT} = \omega_\Lambda N_\Lambda^{true} + (1-\omega_{\Sigma^0}) N_{\Sigma^0}^{true}, \tag{5.11}$$

$$N_{\Sigma^0}^{BDT} = (1-\omega_\Lambda) N_\Lambda^{true} + \omega_{\Sigma^0} N_{\Sigma^0}^{true}, \tag{5.12}$$

combining these, we get:

$$N_\Lambda^{BDT} - \frac{(1-\omega_{\Sigma^0})}{\omega_{\Sigma^0}} N_{\Sigma^0}^{BDT} = \left[\omega_\Lambda - \frac{(1-\omega_{\Sigma^0})}{\omega_{\Sigma^0}}(1-\omega_\Lambda)\right] N_\Lambda^{true}. \tag{5.13}$$

Therefore, by utilizing the obtained BDT efficiency for the $K^0\Lambda$ ($K^0\Sigma^0$) events, we could "subtract" the remaining misidentified events for each reaction.

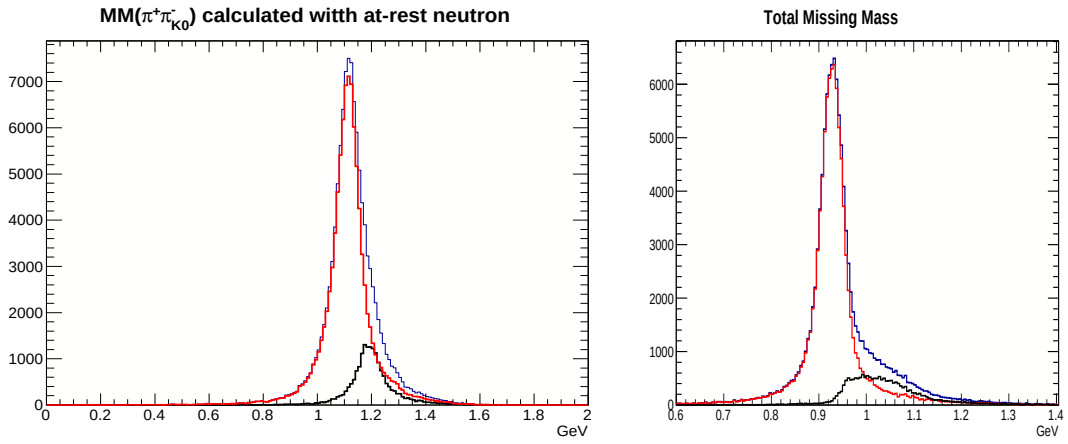

Figure 5.46: Left: $MM(\pi^+\pi^-_{K^0})$. Right: the total missing mass distribution. The histograms were obtained from the $K^0\Lambda$ simulation data. Blue histograms are before the BDT cut, black histograms are *wrongly* "identified" as $K^0\Sigma^0$ events (because they were rejected by the cut), and red histograms are *correctly* "identified" as $K^0\Lambda$ events (because they were selected by the cut).

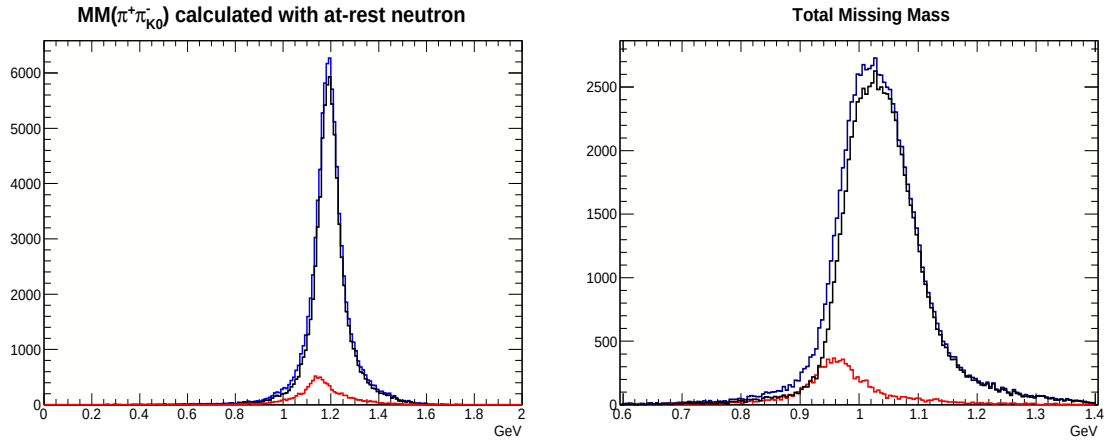

Figure 5.47: On the left $MM(\pi^+\pi^-_{K^0})$, and on the right the total missing mass distribution. The histograms were obtained from the $K^0\Sigma^0$ simulation data. Blue histograms are before the BDT cut, red histograms are *wrongly* "identified" as $K^0\Lambda$ events (because they were selected by the cut), and black histograms are *correctly* "identified" as $K^0\Sigma^0$ events (because they were rejected by the cut).

	Total	Correct Identification	Estimated Efficiency
$K^0\Lambda$ signal	$123,172$	$107,248$	$\omega_\Lambda = 0.871 \pm 0.001$
$K^0\Sigma^0$ signal	$90,058$	$82,054$	$\omega_{\Sigma^0} = 0.911 \pm 0.001$

Table 5.13: Estimated performance efficiencies for K^0Y signal simulation data.

5.3.4 Estimate Remaining Backgrounds after the BDT Cuts for the Real Data

It is crucial to estimate the remaining backgrounds—target-material and non-resonant background—for the Gold 2 and all the Silver data. Since the target material (Aluminum wires and KelF cell walls) was unpolarized, the measured E asymmetry values would be diluted. In addition, the non-resonant background was not the reaction of interest, and have zero E asymmetry (see Section 5.4). As a result, the E asymmetry measurements must be "corrected" for the dilution effect from the remaining background. To obtain the estimated number of remaining target-material background events, we multiplied the estimated *initial* number of target-material background events by the survival fraction after the first BDT cut (the value for the survival fraction is 0.25, see Table 5.5). The *initial* number of target-material background events is obtained by the following procedure:

1. Plot the histograms of the z-component of the interaction vertex of both full-target (Silver 1&2, for example) data and empty-target data

2. Scale the empty histogram such that the yields $Y_{empty} = Y_{full}$ for $0 < z < 30$

cm (this region is outside the target, thus remains the same during the whole experiment),

3. Scale the yield of empty data Y_{empty} for $-15 < z < -2$ cm using the scaling number obtained in step 2 (note that events with $z > -2$ cm were never utilized to get the estimated survival fraction),

4. Get the number of scaled yield from the empty-target data (this is the best estimate of the *initial* number of target-material background events).

Similarly, to obtain the estimated number of remaining non-strange non-resonant background events, we multiplied the estimated *initial* number of non-resonant background events by the survival fraction after the second BDT cut (the value for the survival fraction is 0.057, see Table 5.10). The *initial* number of non-resonant background events is obtained by the following procedure:

1. Plot the $IM(p\pi^-_\Lambda)$, and $IM(\pi^+\pi^-_{K^0})$ distributions for the full-target (Silver 1&2, for example) data, and record the the total initial number of events,

2. Fit each invariance mass distribution with a sum of a Breit-Wigner distribution (signal fit) and a 3^{rd} order polynomial function (background fit),

3. Integrate the signal and background fits (for both $IM(p\pi^-_\Lambda)$, and $IM(\pi^+\pi^-_{K^0})$ distributions),

4. For each invariance mass distribution, compute the signal-to-background ratio from the obtained integrations (in Section 5.3.2 we showed the steps to correctly compute the uncertainty on the ratio),

5. Compute the weighted average of the two signal-to-background ratios (in Section 5.3.2 we showed the steps to compute the weights for the $IM(p\pi^-_\Lambda)$, and $IM(\pi^+\pi^-_{K^0})$ ratios),

6. Compute the *initial* number of non-resonant background events by ultilizing the obtained weighted-average ratio and the total initial number of events.

In the next sub section, we will present in detail the two above procedures applying on the Gold 2 data, and for the Silver data (Silver 1&2, 4, and 5) we just report the final numerical values.

5.3.4.1 Event Selection for the Gold 2 Data

We first present the result of estimating the remaining target-material background. As discussed previously, we scaled the empty-target data to "match" the Gold 2 data, see Figure 5.48. The *initial* number of target-material background events was then estimated from the scaling factor and the yield from the empty-target data.

However, for the Gold 2 data a slight modification is needed. In particular, the amount of aluminum material inside the Gold 2 target (19b) is only about 70% compared to the empty target (21a), see Table 2.2. Hence for region $-10.0 < z < -6.0$ cm—target-material background is mostly originated from the aluminum wires for this region—the scaling factor is reduced by 0.7.

$$N_{Gold2}^{background} = Scaling \times \left(0.7 \times N_{empty}^{Al-region} + N_{empty}^{KelF-regions}\right) = 1,548 + 5,651 = 7,199, \tag{5.14}$$

$$N_{Gold2}^{remaining} = p_{survive} \times N_{Gold2}^{background} = 0.25 \times 7,199 = 1,800, \tag{5.15}$$

where *Scaling* was obtained by matching empty-target and Gold 2 data for the region outside the target (its numerical value is 1.23 ± 0.09), $N_{empty}^{Al-region}$ is the yield from empty target run data for the region $-10.0 < z < -6.0$ cm, and $N_{empty}^{KelF-regions}$ is the yield from regions outside the aluminum region, $p_{survive}$ is the survival fraction of target-material after the first BDT cut (see Table 5.5). $N_{Gold2}^{background}$, and $N_{Gold2}^{remaining}$ are the estimated number of target-material background events before and after (remaining) the first BDT cut, respectively. *The statistical uncertainty for* $N_{Gold2}^{remaining}$ *after proper error propagation is 136* events.

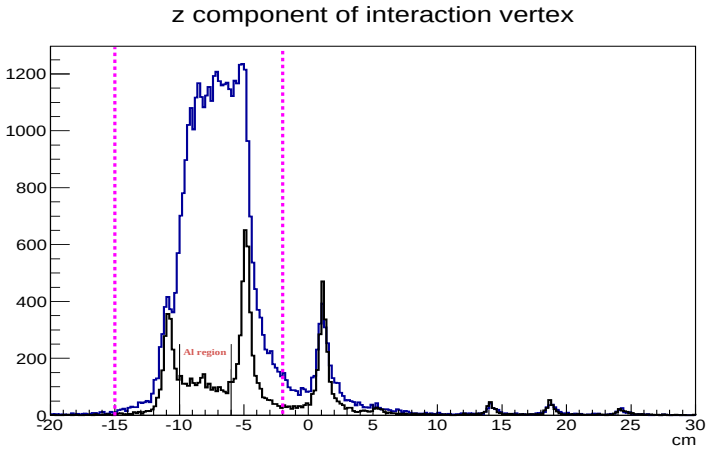

Figure 5.48: z-vertex plots from Gold 2 (blue), and scaled empty run (black). Region $-10.0 < z < -6.0$ cm (denoted as Al region in the plot) has lower aluminum material. The two magenta lines indicate the z-vertex cuts.

In Figure 5.49 we illustrate the effect of the first BDT cut on the Gold 2 data, and in Figure 5.50 we show the data before and after the BDT and z-vertex ($z < -2$ cm) cuts. We then computed the number of bound neutron events that passed the BDT and z-vertex cuts:

$$N_{Gold2}^{HD} = N_{Gold2}^{Passed} - N_{Gold2}^{remaining} = 22,490 - 1,800 = 20,690, \tag{5.16}$$

$$\sigma_{N^{HD}_{Gold2}} = \sqrt{\sigma^2_{N^{Passed}_{Gold2}} + \sigma^2_{N^{remaining}_{Gold2}}}, \tag{5.17}$$

$$\sigma_{N^{HD}_{Gold2}} = \sqrt{\left(\sqrt{22,490}\right)^2 + 136^2} = 202, \tag{5.18}$$

$$R^{targetBG}_{Gold2} \equiv \frac{N^{remaining}_{Gold2}}{N^{HD}_{Gold2}} = \frac{1,800}{20,690} = 0.087, \tag{5.19}$$

$$\sigma_{R^{targetBG}_{Gold2}} = \frac{N^{remaining}_{Gold2}}{N^{HD}_{Gold2}} \sqrt{\left(\frac{\sigma_{N^{HD}_{Gold2}}}{N^{HD}_{Gold2}}\right)^2 + \left(\frac{\sigma_{N^{remaining}_{Gold2}}}{N^{remaining}_{Gold2}}\right)^2 - 2\frac{(-1)\sigma_{N^{HD}_{Gold2}}\sigma_{N^{remaining}_{Gold2}}}{N^{HD}_{Gold2}N^{remaining}_{Gold2}}}, \tag{5.20}$$

$$\sigma_{R^{targetBG}_{Gold2}} = 0.087\sqrt{\left(\frac{202}{20,690}\right)^2 + \left(\frac{136}{1,800}\right)^2 + 2\frac{202 \cdot 136}{20,690 \cdot 1,800}} = 0.007, \tag{5.21}$$

where N^{Passed}_{Gold2} is the number of events that passed the BDT and z-vertex cuts, and N^{HD}_{Gold2} is the number of bound neutron events passed the cuts. *Note that we assigned* -1 *for the correlation between* N^{HD}_{Gold2} *and* $N^{remaining}_{Gold2}$ *in computing* $\sigma_{R^{targetBG}_{Gold2}}$ *in Eq. 5.20 and 5.2*1. The $R^{targetBG}_{Gold2}$ was used to make correction for the dilution effect from the remaining target-material background (more detail in the next section). Before applying the second BDT cut, we tightened the $IM(p\pi^-_\Lambda)$ from 1.20 GeV to 1.16 GeV to remove unambiguous non-resonant background. Note that by not placing this cut earlier we had saved good bound neutron events to obtain better estimation for the $R^{targetBG}$ ratio.

In Figure 5.33 we plotted the invariance mass distributions ($IM(p\pi^-_\Lambda)$ and $IM(\pi^+\pi^-_{K^0})$). We fitted each histogram with a sum of Breit-Wigner distribution (signal fit) and a 3^{rd} order polynomial function (background fit). We, next, integrated the fits of both histograms. Using the numerical values of the integrations, for each histogram we obtained an estimation of the non-resonant *background-to-signal* ratio; we obtained the average of the two ratios next (see Section 5.32, and Table 5.6). Quantitatively, Table 5.6 presents the numerical values of the ratios, and their average. Since we knew the number of total events (after the first BDT and z-vertex cuts), we could estimate the *initial* and the remaining (after the second BDT cut) number of non-resonant background events:

$$Y^{background}_{Gold2} = Y^{total}_{Gold2} \times \frac{r_{avg}}{1 + r_{avg}} = 10,512 \times \frac{2.31}{1 + 2.31} = 7,336, \tag{5.22}$$

$$\sigma_f \equiv \sigma_{\frac{r_{avg}}{1+r_{avg}}} = \frac{\sigma_{avg}}{1 + r_{avg}} = \frac{0.62}{1 + 2.31} = 0.27, \tag{5.23}$$

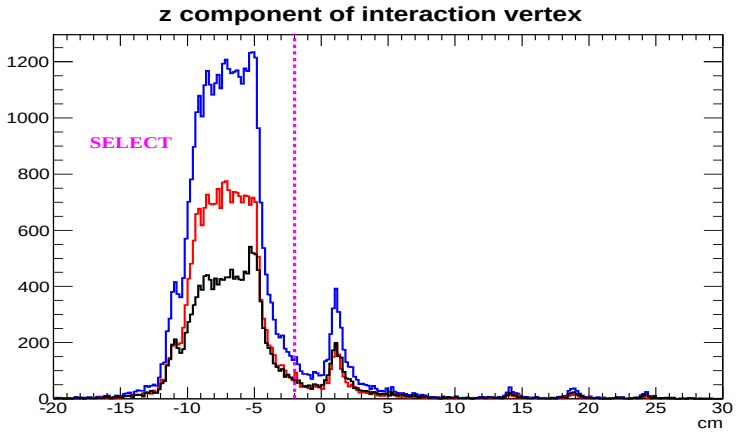

Figure 5.49: z-vertex plots from the Gold 2 data, before (blue), rejected (black), and selected (red) by the *first* BDT cut.

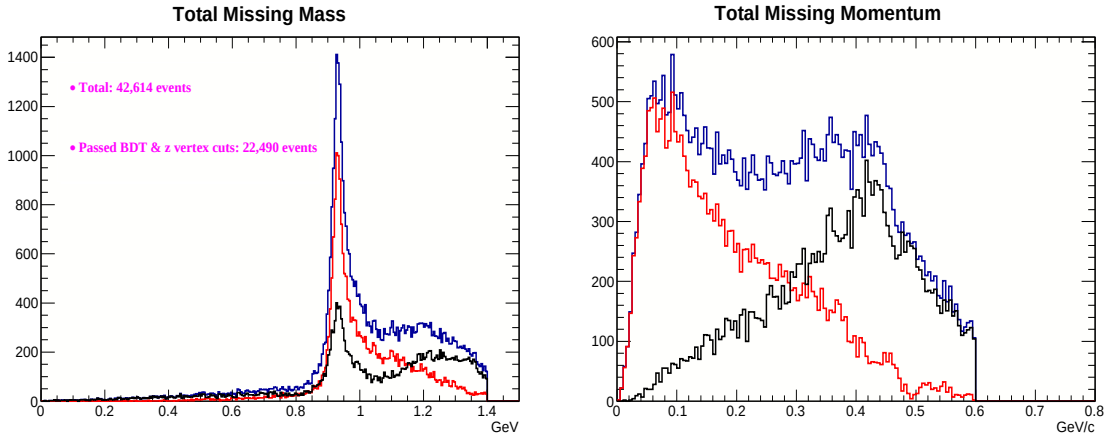

Figure 5.50: Left: Missing mass before (blue), rejected (black), and selected (red) by the first BDT and the z-vertex (cut at $z < -2$ cm) cuts. Right: Missing momentum before (blue), rejected (black), and after (red) the cuts. The plots were constructed from Gold 2 data.

$$\sigma_{Y_{Gold2}^{background}} = Y_{Gold2}^{background} \sqrt{\left(\frac{\sigma_{Y_{Gold2}^{total}}}{Y_{Gold2}^{total}}\right)^2 + \left(\frac{\sigma_f}{\frac{r_{avg}}{1+r_{avg}}}\right)^2}, \tag{5.24}$$

$$\sigma_{Y_{Gold2}^{background}} = 7,336 \sqrt{\left(\frac{\sqrt{10,512}}{10,512}\right)^2 + \left(\frac{0.27}{\frac{2.31}{1+2.31}}\right)^2} = 2,839, \tag{5.25}$$

$$Y_{Gold2}^{remaining} = q_{survive} \times Y_{Gold2}^{background} = 0.057 \times 7,336 = 418, \tag{5.26}$$

$$\sigma_{Y_{Gold2}^{remaining}} = Y_{Gold2}^{remaining}\sqrt{\left(\frac{\sigma_{Y_{Gold2}^{background}}}{Y_{Gold2}^{background}}\right)^2 + \left(\frac{\sigma_{q_{survive}}}{q_{survive}}\right)^2}, \tag{5.27}$$

$$\sigma_{Y_{Gold2}^{remaining}} = 418\sqrt{\left(\frac{2839}{7,336}\right)^2 + \left(\frac{0.002}{0.057}\right)^2} = 162, \tag{5.28}$$

where $Y_{Gold2}^{background}$, and $Y_{Gold2}^{remaining}$ are the estimated number of non-resonant background before and after (remaining) the second BDT cut, respectively, and $p_{survive}$ is the survival fraction of non-resonant background after the second BDT cut (see Table 5.10). In Figure 5.51 we illustrate the effect of the second BDT cut on the Gold 2 data. We then estimated the number of K^0Y signal events passed the BDT cut:

$$Y_{Gold2}^{K^0Y} = Y_{Gold2}^{Passed} - Y_{Gold2}^{remaining} = 2,882 - 418 = 2,464, \tag{5.29}$$

$$\sigma_{Y_{Gold2}^{K^0Y}} = \sqrt{\sigma^2_{Y_{Gold2}^{Passed}} + \sigma^2_{Y_{Gold2}^{remaining}}}, \tag{5.30}$$

$$\sigma_{Y_{Gold2}^{K^0Y}} = \sqrt{\left(\sqrt{2,882}\right)^2 + 162^2} = 170, \tag{5.31}$$

$$R_{Gold2}^{non-resonantBG} \equiv \frac{Y_{Gold2}^{remaining}}{Y_{Gold2}^{K^0Y}} = \frac{418}{2,464} = 0.170, \tag{5.32}$$

$$\sigma_{R_{Gold2}^{non-resonantBG}} = \frac{Y_{Gold2}^{remaining}}{Y_{Gold2}^{K^0Y}}\sqrt{\left(\frac{\sigma_{Y_{Gold2}^{K^0Y}}}{Y_{Gold2}^{K^0Y}}\right)^2 + \left(\frac{\sigma_{Y_{Gold2}^{remaining}}}{Y_{Gold2}^{remaining}}\right)^2 - 2\frac{(-1)\sigma_{Y_{Gold2}^{K^0Y}}\sigma_{Y_{Gold2}^{remaining}}}{Y_{Gold2}^{K^0Y}Y_{Gold2}^{remaining}}}, \tag{5.33}$$

$$\sigma_{R_{Gold2}^{non-resonantBG}} = 0.17\sqrt{\left(\frac{170}{2,464}\right)^2 + \left(\frac{162}{418}\right)^2 + 2\frac{170\cdot 162}{2,464\cdot 418}} = 0.078. \tag{5.34}$$

where Y_{Gold2}^{Passed} is the number of events that passed the second BDT cut, and $Y_{Gold2}^{K^0Y}$ is the number of K^0Y *signal events* that passed the cut. *Note that we assigned* -1 *for the correlation between* $Y_{Gold2}^{K^0Y}$ *and* $Y_{Gold2}^{remaining}$ *in computing* $\sigma_{R_{Gold2}^{non-resonantBG}}$ *in Eq. 5.33 and 5.*34. The $R_{Gold2}^{non-resonantBG}$ was used to make correction for the dilution effect from the remaining target-material background (more detail in the next section).

For illustration, we also show the result after the 3^{rd} BDT cut for the Gold 2 data in Figure 5.52. In particular, the figure plots $MM(\pi^+\pi^-_{K0})$ assuming *at-rest* target neutrons; the blue histogram represents events that passed the first and second BDT

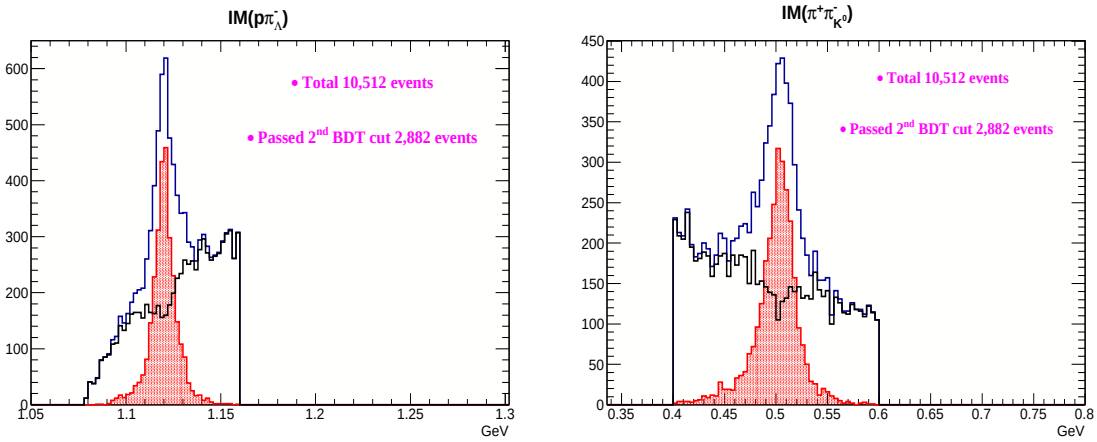

Figure 5.51: Left: $IM(p\pi^-_\Lambda)$, blue histogram is before the 2^{nd} BDT cut, red (black) histogram is selected (rejected) by the cut. Right: $IM(\pi^+\pi^-_{K^0})$, blue is before the 2^{nd} BDT cut, red (black) histogram is selected (rejected) by the cut. Note that there are remaining non-strange non-resonant background after the 2^{nd} BDT selection cut, hence there are "dips" in the rejected (black) distributions. The data used to plot was the Gold 2 period.

cuts (and the z-vertex cut), the red histogram is from events that were assigned $K^0\Lambda$ identity, while the purple histogram is from events that were assigned $K^0\Sigma^0$ identity. It is worth repeating that the red histogram contains a few $K^0\Sigma^0$ events, and the purple histogram contains a few $K^0\Lambda$ events. We would need to subtract these misidentified events to obtain the correct E asymmetry measurements for both reactions. Implementation detail will be provided in Section 5.4.

In summary, we presented, in detail, the procedures to obtain the best sample of bound neutron K^0Y events using the first and second BDT cuts for the Gold 2 data; remaining backgrounds were estimated and quantified in term of $R^{targetBG}_{Gold2}$, and $R^{non-resonantBG}_{Gold2}$. In Section 5.4, we will discuss how to ultilize these two ratios. Furthermore, the third BDT algorithm was employed to seperate the signal K^0Y events into two, albeit not perfectly pure, subsets—$K^0\Lambda$ and $K^0\Sigma^0$ sets. Section 5.4 provides a procedure to correct for this. Next, we applied the same procedures for the Silver data sets (see next section). Finally, *for illustration purpose only* we also plot $MM(\pi^+\pi^-_{K^0})$ for events that only passed the second BDT (i.e., target-material background has not been rejected) in Figure 5.53—in other words, this histogram includes K^0Y events from nuclei other than the deuteron. Note that the histogram from simulation data in Figure 5.22 resembles the histogram in Figure 5.53, which suggests that our simulation data are decently matched the real data.

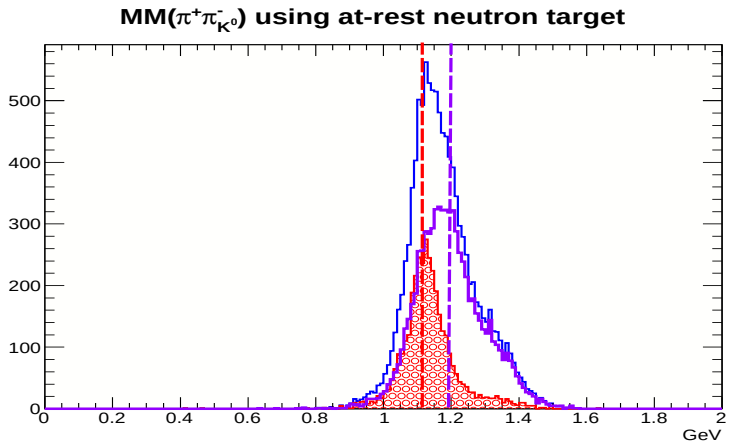

Figure 5.52: $MM(\pi^+\pi^-_{K^0})$, asumming the target neutrons being *at-rest*. Blue histogram is before the 3^{rd} BDT cut, red histogram represents events identified as $K^0\Lambda$, purple histogram represents events identified as $K^0\Sigma^0$. The two colored vertical lines indicate the mass centroids of Λ and Σ^0, respectively. These events were from the Silver 5 period (it is the highest statistics data set so that we can illustrate clearly the effect of the 3^{rd} BDT classification.

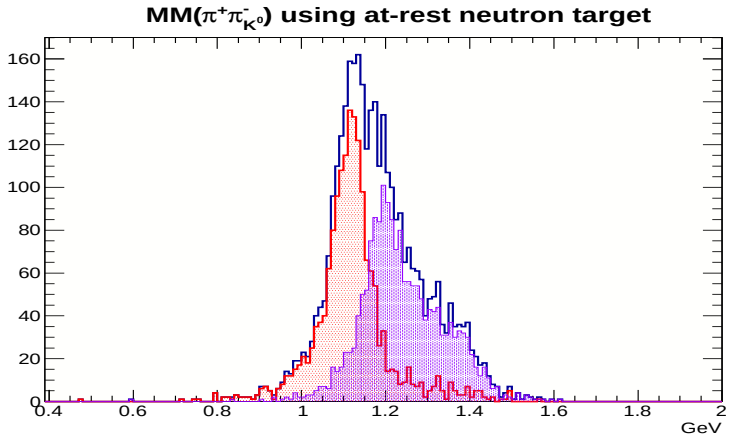

Figure 5.53: $MM(\pi^+\pi^-_{K^0})$, asumming the target neutrons being *at-rest*. Blue histogram is before the 3^{rd} BDT cut, red histogram represents events identified as $K^0\Lambda$, purple histogram represents events identified as $K^0\Sigma^0$. These events were from the Gold 2 period and after the 2^{nd} BDT cut but no the 1^{st} BDT.

5.3.4.2 Summary of Event Selection for the Gold 2 and the Silver Data

Previously, we presented in detail procedures to obtain the ratios $R^{targetBG}$ and $R^{non-resonantBG}$ for the Gold 2 data. Next, we applied the same procedures to Silver 1&2, 4 and 5 data. Table 5.14 presents the numerical values for the ratio $R^{targetBG}$,

and Table 5.15 presents the numerical values for the ratio $R^{non-resonantBG}$. Comparing the first and third columns of Table 5.15 with the second and third columns of Table 5.16, respectively, suggests that our estimations of non-resonant background using *non-resonant-background-to-K^0Y-signal* ratios (for all run periods) are reliable. Also note that after the 2^{nd} BDT cut, there are signal events that were rejected, and background events that were selected. Lastly, Table 5.17 shows the values of *non-resonant-background-to-K^0Y-signal* ratios for all run periods.

	Initial target-material BG	Remaining target-material BG	bound neutrons signal	$R^{targetBG}$
Gold 2	7,199±535	1,800±136	20,690±202	0.087 ± 0.007
Silver 1&2	2,218±255	555±59	5,071±95	0.110 ± 0.012
Silver 4	4,711±385	1,778±98	9,019±143	0.197 ± 0.011
Silver 5	16,018±1035	4,005±267	31,000±326	0.129 ± 0.009

Table 5.14: Numerical values for target-material background correction factors for all the data sets.

	Initial non-resonant BG	Remaining non-resonant BG	K^0Y signal	$R^{non-resonantBG}$
Gold 2	7,336±2,839	418±162	2,464±170	0.170 ± 0.078
Silver 1&2	1,961±386	112±22	670±36	0.167 ± 0.042
Silver 4	5,012±466	286±28	2,127±56	0.135 ± 0.017
Silver 5	16,784±507	957±44	6,604±97	0.145 ± 0.008

Table 5.15: Numerical values for non-strange non-resonant background correction factors for all data sets.

	Before 2^{nd} BDT cut	Rejected	Selected
Gold 2	10,512±102	7,630±87	2,882±54
Silver 1&2	2,956±54	2,174±46	782±28
Silver 4	7,706±88	5,293±73	2,413±49
Silver 5	24,777±157	17,216±131	7,561±87

Table 5.16: Effect from the 2^{nd} BDT cut on all data sets. Note that there are signal events that were rejected, and background events that were selected.

		$^{BG}/_{Sig}$	Avg $^{BG}/_{Sig}$
Gold 2	$IM(p\pi^-_\Lambda)$	$^{2.93}/_{1} \pm 0.17$	$^{2.31}/_{1} \pm 0.10 \pm 0.61$
	$IM(\pi^+\pi^-_{K0})$	$^{1.96}/_{1} \pm 0.13$	
Silver 1&2	$IM(p\pi^-_\Lambda)$	$^{1.75}/_{1} \pm 0.25$	$^{1.98}/_{1} \pm 0.19 \pm 0.33$
	$IM(\pi^+\pi^-_{K0})$	$^{2.30}/_{1} \pm 0.30$	
Silver 4	$IM(p\pi^-_\Lambda)$	$^{2.00}/_{1} \pm 0.11$	$^{1.86}/_{1} \pm 0.08 \pm 0.15$
	$IM(\pi^+\pi^-_{K0})$	$^{1.71}/_{1} \pm 0.11$	
Silver 5	$IM(p\pi^-_\Lambda)$	$^{2.09}/_{1} \pm 0.07$	$^{2.10}/_{1} \pm 0.05 \pm 0.01$
	$IM(\pi^+\pi^-_{K0})$	$^{2.10}/_{1} \pm 0.07$	

Table 5.17: Numerical values of *non-resonant-background-to-K^0Y-signal* ratios for all data sets (including statistical and systematic uncertainties).

5.4 Obtaining the E Observable Measurements

The E observable requires the incoming photon and the target to be circularly and longitudinally polarized, respectively. The g14 experiment had these conditions. Formally, the formula to calculate the E observable for each W_i energy window is:

$$E_{ij}(x_j) = \frac{1}{\overline{{}_iP_\gamma}} \frac{1}{P_{target}} \frac{{}_iY(x_j)^{\downarrow\uparrow} -_i Y(x_j)^{\uparrow\uparrow}}{{}_iY(x_j)^{\downarrow\uparrow} +_i Y(x_j)^{\uparrow\uparrow}}, \tag{5.35}$$

where x_j is the j^{th} measuring bin of $\cos(\theta_{K^0})$ variable, in particular, θ_{K^0} is the angle between the vector momentum of the reconstructed K^0 and the photon direction in the center of mass frame of the incoming photon and target neutron where the neutron is assumed *at-rest*. ${}_iY(x_j)^{\downarrow\uparrow}$ is the yield when the helicity of the photon and the direction of the target polarization vectors are anti-parallel for events in the energy window W_i and the measuring bin x_j, and, similarly, ${}_iY(x_j)^{\uparrow\uparrow}$ is the yield when the two polarization vectors are parallel. *P_{target} is the neutron target polarization magnitude (see Section 4.3.4.1 for detail)*, and $\overline{{}_iP_\gamma}$ is the weighted average of the photon polarizations P_γ for energy window W_i (formula is provided below). The uncertainty on the $E(x)$ (a shorthand notation for $E_{ij}(x_j)$) can be calculated as follows:

$$\frac{\sigma_{E(x)}}{E(x)} = \frac{1}{\overline{{}_iP_\gamma}} \frac{1}{P_{target}} \frac{2\sqrt{[Y^{\downarrow\uparrow}]\,[Y^{\uparrow\uparrow}]}}{\sqrt{[Y^{\downarrow\uparrow} + Y^{\uparrow\uparrow}]\,[Y^{\downarrow\uparrow} - Y^{\uparrow\uparrow}]}}, \tag{5.36}$$

note that the target and beam polarization uncertainties were not included in the above equation because they are more appropriately categorized as systematic uncertainty (see Section 5.3.1 for derivation of σ^2_E). Next, we introduce the formula to compute the photon polarizations P_γ which is referred to as the Maximon and Olson formula [63]. It shows that the photon polarization for each event depends on the electron beam polarization, the electron beam energy and the energy of the incoming

photon of that particular event:

$$P_\gamma = \frac{(4\epsilon - \epsilon^2)\, P_e}{4 - 4\epsilon + 3\epsilon^2}, \tag{5.37}$$

where P_e is the incident electron beam's polarization, ϵ is the ratio of the resultant photon energy to the incident electron beam's energy, $\epsilon = E_\gamma / E_{electron}$. Importantly, the P_γ in Eq. 5.43 was computed for *each* event while the $\overline{{}_iP_\gamma}$ in Eq. 5.41 is the *average* of all events in the energy window W_i.

The Eq. 5.35 can not be applied directly in the presence of remaining backgrounds, thus it must be modified. As previously mentioned, the two dominating backgrounds are the target material and non-resonant backgrounds. To study the E asymmetry for the backgrounds, we selected empty-target period data to represent the target material background, while to *select* the non-strange non-resonant background we *rejected* events that satisfy $IM(p\pi^-_\Lambda)$ <1.2 GeV, and 0.4 GeV< $IM(\pi^+\pi^-_{K^0})$ <0.6 GeV. Figure 5.54 shows consistent-with-zero E asymmetries for both types of background, hence their presences would dilute the final measurements of the E asymmetry for the signal channels. We will discuss a procedure to correct for these dilution effects in the next section.

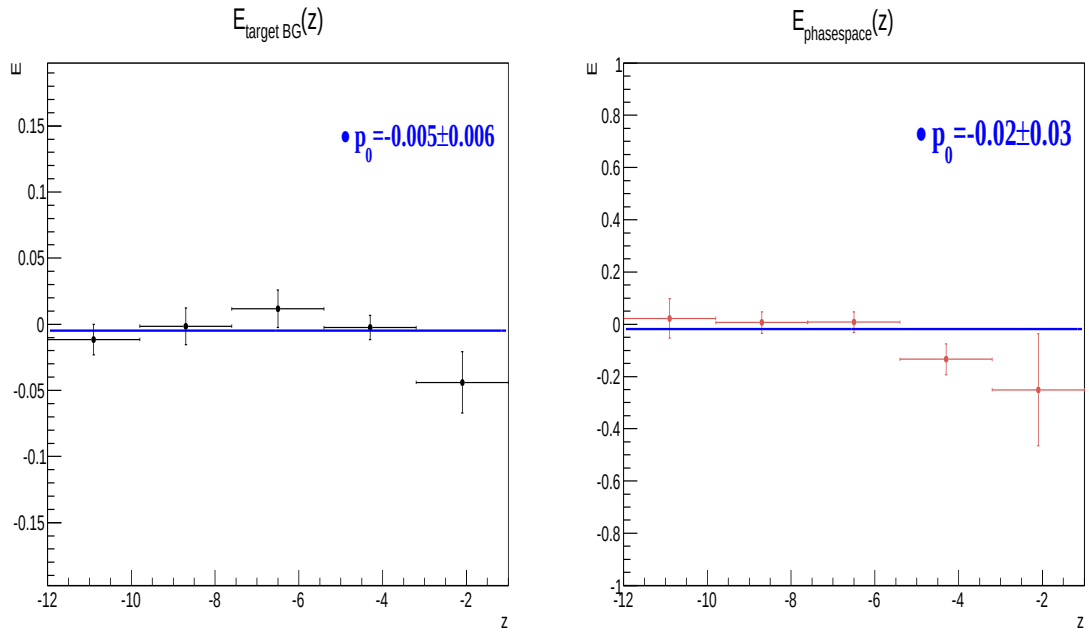

Figure 5.54: Left: The raw E asymmetry vs. z-vertex for the empty-target data. Right: The E asymmetry vs. z-vertex for the non-resonant background events (the events were from the Gold 2 data). The results are consistent with zero asymmetry.

5.4.1 Corrections for the Remaining Backgrounds

Recalling from Section 5.3.4, we estimated two ratios $R^{targetBG} = \frac{N^{remaining}}{N^{HD}}$, and $R^{non-resonantBG} = \frac{Y^{remaining}}{Y^{K^0Y}}$, where $N^{remaining}$, N^{HD} are the estimated number of remaining target-material background and true bound events after the first BDT and z-vertex cuts, respectively, and $Y^{remaining}$, Y^{K^0Y} are the estimated number of remaining non-strange non-resonant and true K^0Y events after the second BDT cut, respectively. Denote Y_{BDT} to be the number of events that passed the z-vertex and the first two BDT cuts, then Y_{BDT} can be partitioned into:

$$Y_{BDT} = Y^{K^0Y} + Y^{remaining} = \left(1 + R^{non-resonantBG}\right) Y^{K^0Y}. \tag{5.38}$$

In addition, since Y^{K^0Y} also comprises of events from the remaining target-material background and the bound signal events, Y_{BDT} can be partitioned further:

$$Y_{BDT} = \left(1 + R^{non-resonantBG}\right) \left[Y_{HD}^{K^0Y} + Y_{targetBG}^{K^0Y}\right], \tag{5.39}$$

and if we assumed $\frac{Y_{targetBG}^{K^0Y}}{Y_{HD}^{K^0Y}} = \frac{N^{remaining}}{N^{HD}} = R^{targetBG}$, then Y_{BDT} can finally be expressed as:

$$Y_{BDT} = \left(1 + R^{non-resonantBG}\right) \left(1 + R^{targetBG}\right) Y_{HD}^{K^0Y}, \tag{5.40}$$

$$\Rightarrow Y_{HD}^{K^0Y} = \left(1 + R^{non-resonantBG}\right)^{-1} \left(1 + R^{targetBG}\right)^{-1} Y_{BDT}. \tag{5.41}$$

If we further assumed that Eq. 5.41 remains valid for both $Y_{BDT}^{K^0\Lambda}$ and $Y_{BDT}^{K^0\Sigma^0}$, where $Y_{BDT}^{K^0\Lambda}$ and $Y_{BDT}^{K^0\Sigma^0}$ are the $K^0\Lambda$ and $K^0\Sigma^0$ bound neutrons signal events, respectively, then we could correct for the dilution effects on the E asymmetry as follows:

$$E_{corrected}^{K^0Y} = \left(1 + R^{non-resonantBG}\right) \left(1 + R^{targetBG}\right) E_{BDT}^{K^0Y}, \tag{5.42}$$

where $E_{BDT}^{K^0Y}$ is obtained from $Y_{BDT}^{K^0Y}$ (or, more correctly, $Y_{BDT}^{\uparrow\uparrow}$ and $Y_{BDT}^{\downarrow\uparrow}$ of the K^0Y subset).

5.4.2 "Purifying" the After-3^{rd}-BDT-Cut $K^0\Lambda$ and $K^0\Sigma^0$ Events

In this section, we introduce another correction for the final E asymmetry measurements. Recall that the third BDT cut seperates the bound neutron K^0Y events into two subsets: one is mostly $K^0\Lambda$ events, and the other is mostly $K^0\Sigma^0$. In other words, if we denote N_Λ^{BDT}, and $N_{\Sigma^0}^{BDT}$ as the number of events the third BDT identified as $K^0\Lambda$ and $K^0\Sigma^0$ events, respectively, then we have the following expressions:

$$N_\Lambda^{BDT} = \omega_\Lambda N_\Lambda^{true} + (1 - \omega_{\Sigma^0}) N_{\Sigma^0}^{true}, \tag{5.43}$$

$$N_{\Sigma^0}^{BDT} = (1-\omega_\Lambda)N_\Lambda^{true} + \omega_{\Sigma^0} N_{\Sigma^0}^{true}, \tag{5.44}$$

where ω_Λ and ω_{Σ^0} are the fractions of events correctly idenfied (see Section 5.3.3 for more detail, and Table 5.13 for the numerical values). After rearrangement, we derive the following expressions (for derivation see Section 5.3.3):

$$N_\Lambda^{true} = \left[\omega_\Lambda - \frac{(1-\omega_{\Sigma^0})}{\omega_{\Sigma^0}}(1-\omega_\Lambda)\right]^{-1}\left[N_\Lambda^{BDT} - \frac{(1-\omega_{\Sigma^0})}{\omega_{\Sigma^0}}N_{\Sigma^0}^{BDT}\right], \tag{5.45}$$

$$N_{\Sigma^0}^{true} = \left[\omega_{\Sigma^0} - \frac{(1-\omega_\Lambda)}{\omega_\Lambda}(1-\omega_{\Sigma^0})\right]^{-1}\left[N_{\Sigma^0}^{BDT} - \frac{(1-\omega_\Lambda)}{\omega_\Lambda}N_\Lambda^{BDT}\right]. \tag{5.46}$$

The final E asymmetry was obtained using the derived N_Λ^{true}, and $N_{\Sigma^0}^{true}$. In summary, we had to apply three different corrections.

5.4.3 Results for the E Asymmetry Measurements

We divided the data into two energy windows 1.7 GeV$\leq W <$2.02 GeV, and 2.02 GeV$\leq W <$2.34 GeV. For each W window, we plot the $E_{K^0\Lambda}$ (and $E_{K^0\Sigma^0}$) as a function of $\cos\theta_{K^0}$ in the overall center of mass frame where the target neutrons were assumed to be *at-rest*. Firgure 5.55 presents the final E asymmetry for the $K^0\Lambda$ channel, while Figure 5.56 presents the final E asymmetry for the $K^0\Sigma^0$ channel. Note that the final E asymmetry measurements are a combined result from the Gold 2 and Silver 1&2, 4, and 5 data sets and are after the previously discussed corrections.

5.5 Systematic Studies

In this section, we employ various systematic studies to quantify the robustness of the BDT methods and the sensitivity of our result on the three correction procedures implemented in the previous section. In particular, we implemented four studies. The first test focuses on the sensitivity of the E results on the third correction—the correction procedure that was implemented to "purify" the final selected $K^0\Sigma^0(K^0\Lambda)$ sample. The next two tests study the effect of loosening the second and the first BDT cuts, respectively. Note that it is more important to study the sensitivity when there are more remaining background events because the procedures which were employed to correct for the dilution effect from the remaining non-resonant and target-material backgrounds (see Section 5.4.1) is just an approximation—which is more accurate if there are fewer background events. In addition, tightening the BDT cuts would result in a smaller data sample—of an already small data sample, thus we think the statistical fluctations would overwhelm any systematic effect if the BDT cuts were to

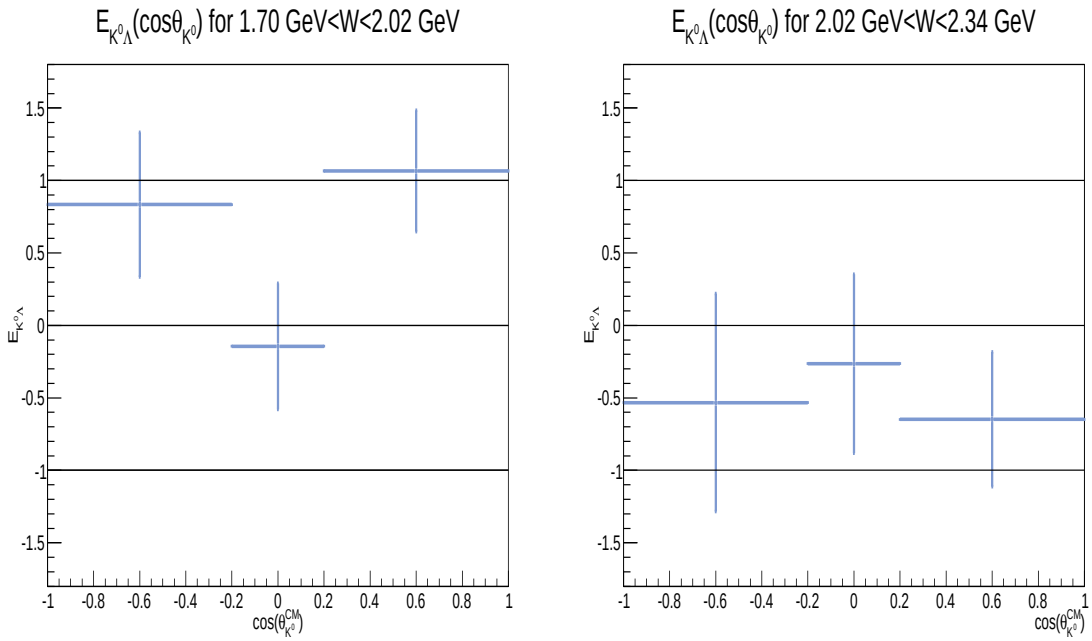

Figure 5.55: The $E_{K^0\Lambda}$ asymmetries vs. $\cos\theta_{K^0}$ for the energy windows 1.7 GeV$\leq W <$2.02 GeV (left) and 2.02 GeV$\leq W <$ 2.34 GeV (right).

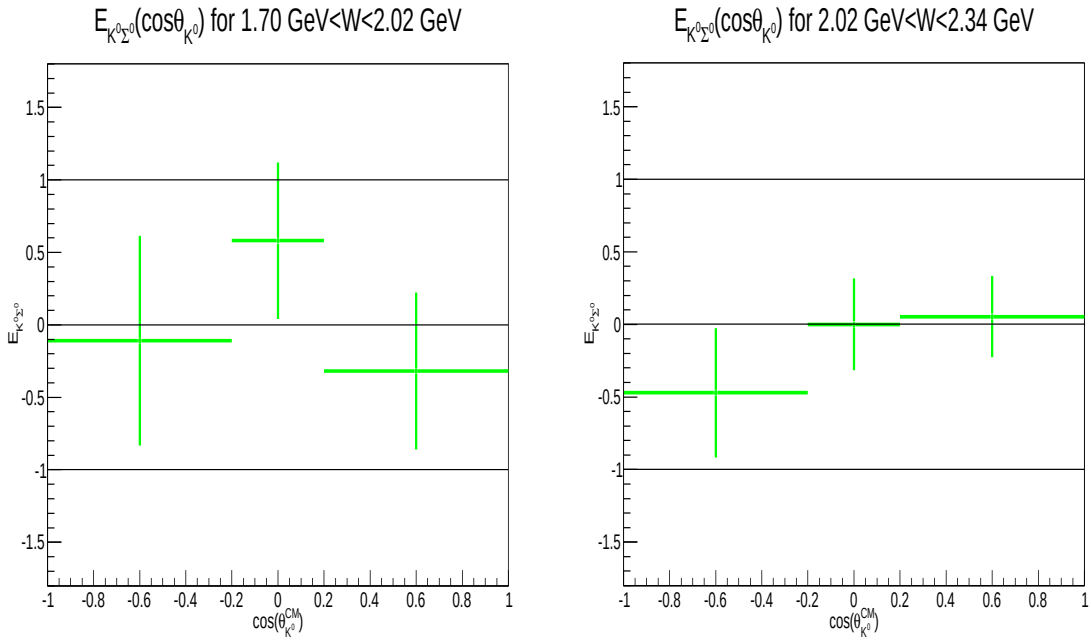

Figure 5.56: The $E_{K^0\Sigma^0}$ asymmetries vs. $\cos\theta_{K^0}$ for the energy windows 1.7 GeV$\leq W <$2.02 GeV (left) and 2.02 GeV$\leq W <$ 2.34 GeV (right).

be tightened any further. Lastly in the fourth test, we reduced the beam and target polarizations by one standard deviation of their respective statistical uncertainties to study the effect on the E results.

5.5.1 Systematic Effect from not Accounting for the Remaining $K^0\Sigma^0$ ($K^0\Lambda$) Events in the BDT-Selected $K^0\Lambda$ ($K^0\Sigma^0$) Events

As shown in Section 5.3.3, the final $K^0\Lambda(K^0\Sigma^0)$ sample selected by the third BDT has remaining $K^0\Sigma^0(K^0\Lambda)$ events. In Section 5.4.2 we introduced a simple procedure to "purify" the final samples. However, we suspected that the procedure has a modest effect on the final measured values of the E asymmetry. In this systematic test, we will quantify the effect. In particular, for this test we purposely did not apply the "purify" procedure and proceeded to obtain the E asymmetry values. In Table 5.18 we show the differences between $E_{test1} - E_{final}$, where E_{test1} values are obtained without the "purify" procedure and E_{final} values are obtained with the procedure. Notice that without the "purify" procedure, for W_1 energy window, the E asymmetries for $K^0\Lambda$ channel would be reduced because of the inclusion of the $K^0\Sigma^0$ channel (the values for the two channels have opposite sign); this fact is shown in the first row of Table 5.18.

		$\cos\theta_{K^0}$		
		-0.6	0.0	$+0.6$
$K^0\Lambda$	W_1	-0.05	0.03	-0.09
	W_2	-0.02	-0.07	-0.12
$K^0\Sigma^0$	W_1	0.20	-0.09	0.19
	W_2	0.01	0.02	0.04

Table 5.18: Differences between $E_{test1} - E_{final}$.

5.5.2 Systematic Effect from Loosening the 2^{nd} BDT Cut

For this test, we loosened the 2^{nd} BDT cut from 0.24 (see Section 5.3.2) to 0.15. Consequently, the percentage of surviving non-strange non-resonant background events after the 2^{nd} BDT cut increases from 5.7% (see Table 5.10) to 10.6%. Implementing the same procedure as described in Section 5.3.4 we estimated a new set of $R^{non-resonantBG}$ ratios which we present in Table 5.19. After obtaining the final event samples from the loosen 2^{nd} BDT cut, we computed a new set of values for the E asymmetry. Table 5.20 shows the difference $E_{test2} - E_{final}$, where E_{test2} values are obtained from the loose 2^{nd} BDT cut and E_{final} values are obtained with the optimized cut. Notice that the angular bins $\cos\theta_{K^0} = \pm 0.6$ have larger differences than the bin $\cos\theta_{K^0} = \pm 0.0$; this might be due statistical fluctuation.

	$R^{non-resonantBG}$
Gold 2	0.254 ± 0.016
Silver 1&2	0.295 ± 0.034
Silver 4	0.227 ± 0.014
Silver 5	0.242 ± 0.012

Table 5.19: Numerical values for non-resonant background correction factors for all data.

		$\cos\theta_{K^0}$		
		-0.6	0.0	$+0.6$
$K^0\Lambda$	W_1	-0.03	-0.01	-0.10
	W_2	0.25	-0.02	0.01
$K^0\Sigma^0$	W_1	-0.17	-0.03	-0.39
	W_2	0.36	0.10	0.05

Table 5.20: Differences between $E_{test2} - E_{final}$.

5.5.3 Systematic Effect from the Loosening the 1^{st} BDT Cut

We loosened the 1^{st} BDT cut from 0.036 (see Section 5.3.1) to 0.0 for this test. As a result, the percentage of survived target-material background events increases from 25% (see Table 5.5) to 29%. We then estimated a new set of $R^{targetBG}$ ratios, see Table 5.21 for numerical values (the procedure to obtain the ratios was discussed in Section 5.3.4). The new set of E values (E_{test3}) was obtained next. Quantitatively, Table 5.22 shows the differences between $E_{test3} - E_{final}$. Notice that the angular bin $\cos\theta_{K^0} = -0.6$ have larger differences than the other bins; this might be due statistical fluctuation.

	$R^{targetBG}$
Gold 2	0.092 ± 0.08
Silver 1&2	0.115 ± 0.05
Silver 4	0.200 ± 0.02
Silver 5	0.135 ± 0.01

Table 5.21: Numerical values for non-resonant background correction factors for all data.

		$\cos\theta_{K^0}$		
		-0.6	0.0	$+0.6$
$K^0\Lambda$	W_1	0.27	0.09	-0.16
	W_2	0.23	-0.07	-0.04
$K^0\Sigma^0$	W_1	-0.31	-0.10	0.15
	W_2	0.15	0.11	-0.01

Table 5.22: Differences between $E_{test3} - E_{final}$.

5.5.4 Systematic Effect from the Target and Beam Polarizations

In this section, we provide results from our systematic test on the uncertainties of the beam and target polarizations—the numerical values for the statistical uncertainties were reported in Table 3.1. To quantify the systematic effect we computed the E asymmetry but with reduced beam and target polarizations; i.e., *both* quantities were reduced by one standard deviation of their respective statistical uncertainties. The effect on the E asymmetry measurements are shown as $E_{test4} - E_{final}$, where E_{test4} values are obtained by reducing the beam and target polarizations, in Table 5.23. Notice that the values of the difference $E_{test4} - E_{final}$ in Table 5.23 are consistent with the sign and the amplitude of the E asymmetries for both channels.

		$\cos\theta_{K^0}$		
		-0.6	0.0	$+0.6$
$K^0\Lambda$	W_1	0.076	-0.020	0.098
	W_2	-0.036	-0.004	-0.050
$K^0\Sigma^0$	W_1	-0.012	0.040	-0.033
	W_2	-0.032	0.001	0.005

Table 5.23: Differences between $E_{test4} - E_{final}$.

5.5.5 Systematic Uncertainty Assignment

In this section we combine all the systematic tests into one assignment of the systematic uncertainty. For each data point (there are total 12 data points), we compute the square root of the quadratic sum of the individual test's $\sigma_{systematic}$. For example, the systematic uncertainty for the data point belongs to $K^0\Lambda$ channel, energy window W_1 and $\cos\theta_{K^0} = 0.0$ is $\sqrt{0.03^2 + 0.01^2 + 0.09^2 + 0.02^2} = 0.10$. Table 5.24 presents the systematic uncertainties for all data points.

		$\cos\theta_{K^0}$		
		-0.6	0.0	$+0.6$
$K^0\Lambda$	W_1	0.287	0.098	0.231
	W_2	0.345	0.101	0.136
$K^0\Sigma^0$	W_1	0.406	0.144	0.460
	W_2	0.391	0.150	0.065

Table 5.24: Systematic uncertainty of E asymmetry measurements for $K^0\Lambda/K^0\Sigma^0$ channels.

5.6 Summary

In this chapter, we presented the first set of the E asymmetry measurements for the reaction $\gamma d \to K^0 Y(p_s)$ (for 1,700 MeV$\leq W \leq$2,340 MeV). In particular, we described in detail the cuts to select a clean sample of $p\pi^+\pi^-\pi^-$. Three categorical BDT were constructed to firstly select the bound neutron K^0Y events and to secondly seperate $K^0\Lambda$ and $K^0\Sigma^0$ channels. We plotted the combined E asymmetry as a function of $\cos\left(\theta^{\mathbf{CM}}_{\mathbf{K^0}}\right)$ as well. Next, we implemented several systematic tests to estimate the overall systematic uncertainties for all measuring bins—they are smaller than the statistical uncertainties. The numerical values of the measured E asymmetries and their statistical and systematic uncertainties are reported in Table 5.25.

E		$\cos\theta_{K^0}$		
		-0.6	0.0	$+0.6$
$K^0\Lambda$	W_1	$0.834\pm0.499\pm0.287$	$-0.144\pm0.436\pm0.098$	$1.066\pm0.419\pm0.231$
	W_2	$-0.533\pm0.752\pm0.345$	$-0.263\pm0.618\pm0.101$	$-0.648\pm0.464\pm0.136$
$K^0\Sigma^0$	W_1	$-0.110\pm0.723\pm0.406$	$0.581\pm0.539\pm0.144$	$-0.319\pm0.541\pm0.460$
	W_2	$-0.471\pm0.446\pm0.391$	$0.0002\pm0.317\pm0.150$	$0.054\pm0.281\pm0.065$

Table 5.25: Systematic uncertainty of E asymmetry measurements for $K^0\Lambda/K^0\Sigma^0$ channels.

As mentioned before, this analysis is plagued by small statistics so that the measurements of the E asymmetry might not offer significant help to constrain PWA models (see Chapter 7 for a comparision of the E asymmetry measurements with partial wave analysis models). Nevertheless, this analysis has shown that one can efficiently select bound neutron $K^0\Lambda$ and $K^0\Sigma^0$ events using the Boosted Decision Trees algorithm; therefore, future analysis of polarization observables on the $K^0\Lambda$ and $K^0\Sigma^0$ channels for the neutron data can be of benefit by following the outlined procedures described, in detail, in this chapter.

Chapter 6

Spin Determination for *Possible* $N\Delta$ Resonance Structure in Reaction $\gamma d \to \pi^+\pi^- d(0)$

When examining the reaction $\gamma d \to d\pi^+\pi^-(0)$, we observed a pronounced physics phenomena: the final state exhibits a strong correlation between the deuteron and one of the pions, see Figure 6.1. The state is above the sum of masses of the deuteron and the pion, which is $m_d + m_\pi = 1875 + 140 = 2015\,\text{MeV}$, but it lies below the sum of masses of the N and the Δ, which is $m_N + m_\Delta = 939 + 1232 = 2171\,\text{MeV}$. Therefore, it is possible that we might be looking at an evidence of a $N\Delta$ dibaryonic object. In a paper by Mulders *et al.* [66] the $N\Delta$ dibaryon was described as a six-quark state in a bag model with a ${}^{2S+1}L_J = {}^5S_2$ configuration. Within the framework of the πNN Fadeev equations, Gal and Garcilazo [67, 68] theorized the existence of $N\Delta$ and $\Delta\Delta$ dibaryons (recently the WASA-at-COSY collaboration reported evidence for a state consistent with the $\Delta\Delta$ dibaryon [69]). Experimentally, a mass peak in the $d\pi$ system—similar to what we observed—was reported by Werner *et al.*, Denegri *et al.*, Brunt *et al.*, and Aladashvili *et al.* [70, 71, 72, 73]. Importantly, Aladashvili *et al.* studied the reaction $dp \to ppn$ and found "enhancement" *only* in the pp invariant mass but not in the pn mass spectrum; the two-proton decay mode of the $N\Delta$ resonance led them to concluded that the state has $\boldsymbol{J}^P = \mathbf{2}^+$ [73]. Unfortunately, none of the previously mentioned works provided a direct measurment for the spin of the suspected $N\Delta$ resonance.

Necessarily, to determine whether the structure (see Figure 6.1) is a resonance or just a "threshold enhancement" requires extensive studies to measure the cross section, the mass centroid, the decay width, and the parity, as well as the spin. Unfortunately, g14 data is only suitable to measure the spin but not the others (the g10 and g13 data sets are more suitable for the other studies). This chapter, thus, mainly focuses on spin analysis of the *possible* $N\Delta$ resonance. In other words, we implicitly assumed the observed structure in the $(d\pi)$ system is a dibaryonic resonance

and utilized the g14 data set to determine its spin. To provide details about this analysis, we, firstly, present the "$d : \pi^+ : \pi^-$" event selection. Secondly, a discussion of the Boosted Decision Trees algorithm used to reject target-material background follows. Thirdly, we discuss two spin hypotheses for the $N\Delta$ resonance—total spin one $\boldsymbol{J = 1}$ and total spin two $\boldsymbol{J = 2}$—and a procedure to determine the best hypothesis that matches the g14 data (the procedure consists mainly of measuring the E helicity-target asymmetry). Finally, we report our systematics study in Section 6.5.

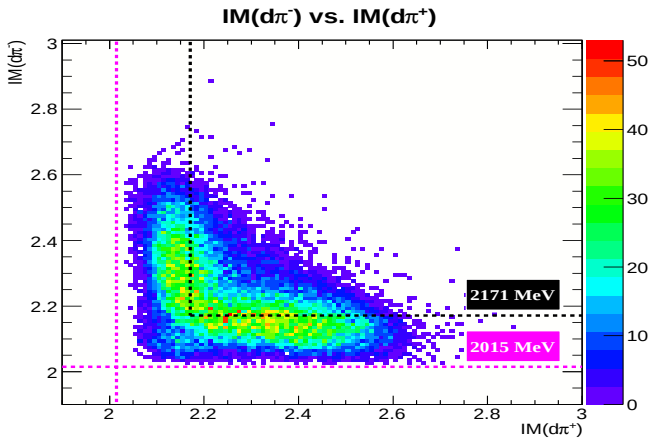

Figure 6.1: $IM(d\pi^-)$ vs. $IM(d\pi^+)$, purple lines represent $m_d + m_\pi$ mass value, and black lines represent $m_N + m_\Delta$ mass value. The units are in GeV. The data used to obtain the plot is the Silver 5 period data.

6.1 $d\pi^+\pi^-$ Event Selection

We began the analysis by selecting "$d : \pi^+ : \pi^-$" events. Particularly, by using the measured momentum, the path length and the *time-of-flight* of each detected track, we obtained a measured mass of each track. If a positively charged track has a measured mass within the range 1.8 GeV to 2.2 GeV, it is assigned a deuteron "ID". Similarly, if a negatively (positively) charged track has the measured mass within the range 0.0 GeV to 0.3 GeV, it is assigned a π^- (π^+) "ID". We plot the measured mass distributions of negative versus positive tracks in Figure 6.2. A cut at 48 MeV on the π^- mass distribution was applied to reject unambiguous e backgrounds. In addition, Figure 6.3 shows the squared total missing mass before (blue histogram) and after the cut on the π^- measured mass distribution (rejection is in black, selection is in red).

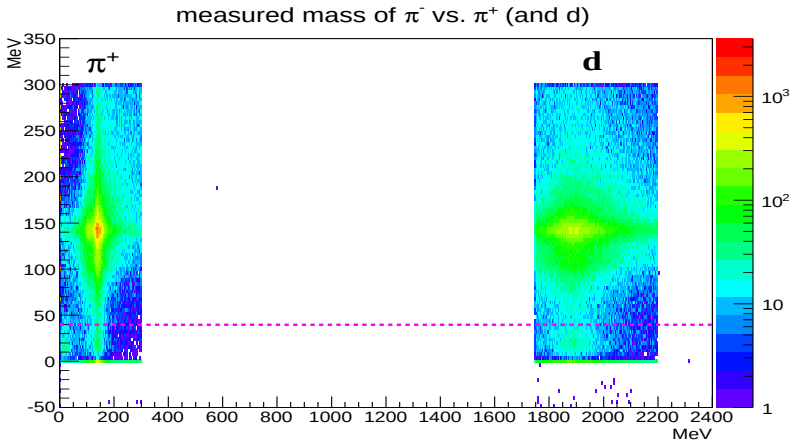

Figure 6.2: The *measured mass* of negative (π^-) vs. positive (d, π^+) particles. The magenta line indicates the cut placed on the π^- measured mass distribution. The plot is obtained from the Gold 2 data.

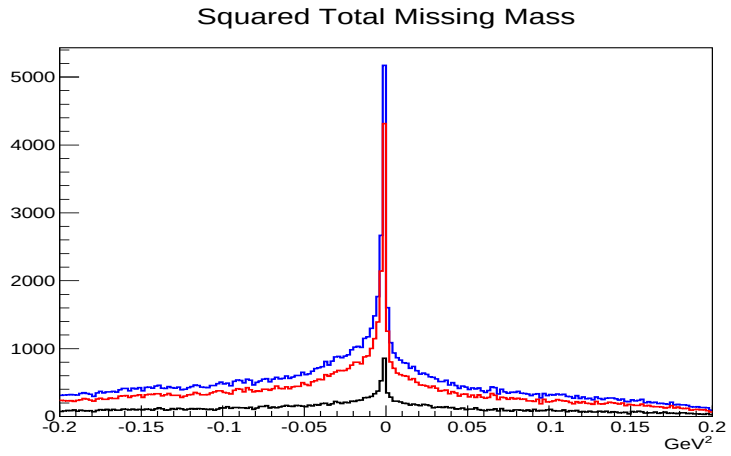

Figure 6.3: Squared total missing mass, $MM^2(d\pi^+\pi^-)$, blue histogram is before, red histogram represents events selected by the π^- measured mass cut, and black histogram represents rejected events by the cut. The data used to plot is the Gold 2 data.

6.1.1 Particle Identification: ΔTOF Cuts

To further reduce the background due to particle misidentification, we applied ΔTOF cuts. In particular, for each detected charged track, the CLAS track reconstruction algorithm records its momentum, its path length from target vertex to TOF counters, and its time of flight ($TOF_{measured}$). For a given particle with an assumed mass, one can compute $TOF_{calculated}$ from the momentum and the path length of the particle. The difference between the $TOF_{calculated}$ and the $TOF_{measured}$ is the ΔTOF:

$$\Delta TOF = TOF_{measured} - TOF_{calculated}, \tag{6.1}$$

where $TOF_{measured}$ is the measured *time-of-flight*. This is the time difference between event vertex time and time at which the particle hit the TOF scintillator walls—encircling the CLAS drift chamber. The $TOF_{calculated}$ is computed as:

$$TOF_{calculated} = \frac{L}{c}\sqrt{1 + \left(\frac{m}{p}\right)^2}, \tag{6.2}$$

where L is the pathlength from the target to the scintillator, c is the speed of light, m is the hypothesized mass and p is the magnitude of the measured 3-momentum. When plotting a particle's ΔTOF against its momentum, if the particle's identification was correctly assigned, then a straight horizontal band around zero should be observed. If the particle type was wrongly assigned, then the same plot results in a curved band that flatten out at high momentum. Figure 6.4 plots the π^+'s ΔTOF (on the top left) and the π^- 's ΔTOF (on the top right), and the d's ΔTOF (on the bottom left). Also, we learned that some misidentified protons with wrong $TOF_{measured}$ can get measured masses that are consistent with the deuteron mass; thus, to reject events with these misidentified protons, we purposely assigned the hypothesized mass m the mass of the proton (see Eq. 6.2), and plot the ΔTOF of the "fake" protons on the bottom right plot of Figure 6.4—a straight horizontal band around 20 ns contains events with the misidentified protons. We then placed cuts at 19 and 21 ns to reject these events.

In addition, in the pion ΔTOF plots of Figure 6.4, there are several horizontal bands that are 2.00 ns apart. A particle belonging to such horizontal bands has a mass equal to its assigned mass which indicates correct particle identification but it belongs to a different RF beam "bucket" (the beam is delivered in pulses that are 2.00 ns apart). For illustration, we plot ΔTOF_{π^-} vs. ΔTOF_{π^+} on the left of Figure 6.5. The plot shows visible clusters of events around $(\pm 2, \pm 2)$, $(\pm 4, \pm 4)$, etc. The next ΔTOF cuts we applied were to remove these events which have wrong *track-and-photon-timing* combinations. The cuts resemble an "iron cross," see the right plot of Figure 6.5. Finally, Figure 6.6 illustrates the effect in the total missing mass distribution of the ΔTOF cuts on the pions and the deuterons.

6.1.2 Detector Performance: Fiducial Cuts

Like the two previous analyses we relied on a BDT algorithm to reject the target-material background. Importantly, to optimize the BDT performance, it is crucial to have good simulations that represent closely the real data to "train" the BDT (more detail later); and for this reason, understanding the CLAS detectors, and simulating correctly their performances is important. However, there are some regions or elements of the detectors that are hard to simulate. To allow a reliable comparison

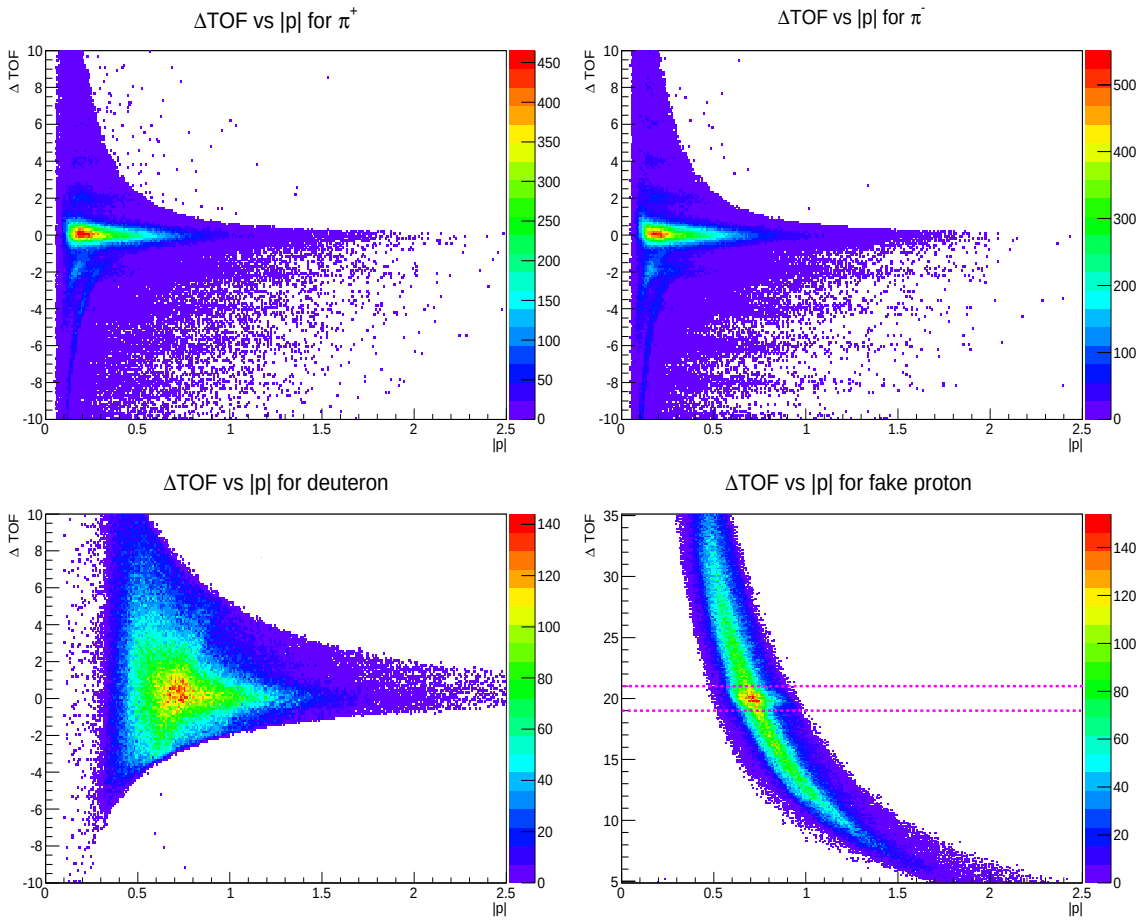

Figure 6.4: Top left: $\pi^+ \Delta TOF$ vs. $|p|$. Top right: π^- ΔTOF vs. $|p|$. Bottom left: d ΔTOF vs. $|p|$. Bottom right: "fake" proton ΔTOF vs. $|p|$—a straight horizontal band at 20 ns corresponding to misidentified protons; we placed cuts at 19 and 21 ns to reject these events. The data used to plot was Gold 2 period. The plots are on a linear scale.

between real data and simulation data, these regions have to be removed from both real and MC data; this section addresses this type of cuts. Primarily, we only applied cuts on the drift chamber detector (since we did not perform a cross section analysis but rather a target-beam asymmetry, simulating the *exact* CLAS acceptance is not necessary).

Previous studies such as those with g11 data [51] advised removing events with tracks going near the superconducting torus coils where the magnetic field varies too rapidly to be properly modeled (by GSIM). We thus removed events which have *at least* one track going into these regions. Particularly, in the forward direction where the coils occupy a great amount of space, we placed a hard cut for tracks with $\cos(\Theta_{lab}) > 0.985$. In addition, we placed cuts at 0.4 rad on the angle Φ_{sector}

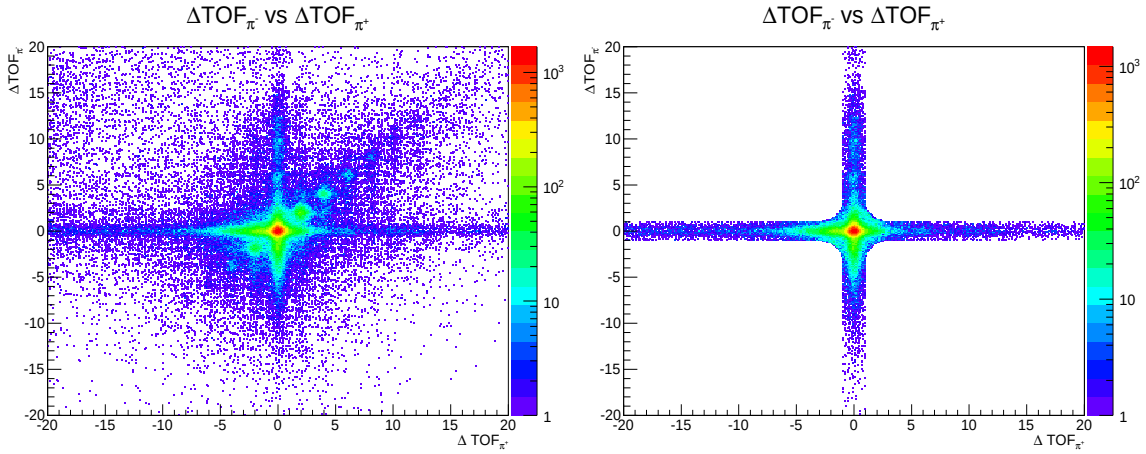

Figure 6.5: The ΔTOF_{π^-} vs. ΔTOF_{π^+} before (left), and after (right) the ΔTOF cuts. The data used to plot was the Gold 2 period data. The plots are on a logarithmic scale.

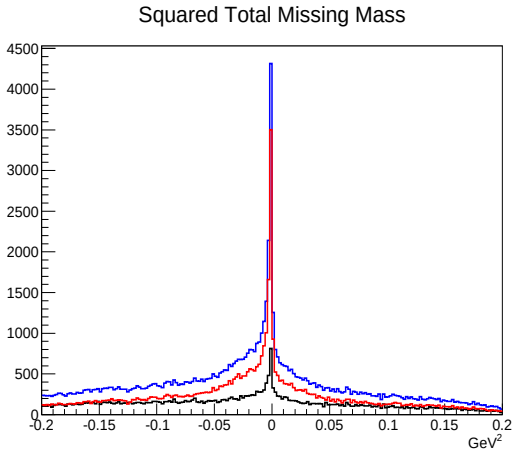

Figure 6.6: Squared total missing mass, $MM^2(d\pi^+\pi^-)$, before (blue histogram) and after the ΔTOF cuts (red histogram). Events in the black histogram were rejected by the ΔTOF cuts. The data used to plot was the Gold 2 period data.

(measured in the sector coordinate), consistent with g11 Φ_{sector} cuts (i.e., accepted particles had their measured $|\Phi_{sector}| < 0.4\,\mathrm{rad}$). The Φ cuts were to remove the edges of the CLAS drift chambers which are hard to simulate.

In addition, we also placed a cut in the backward direction (Θ cuts) for the deuterons. The cut was to remove the target-material background—not the same goal as the previously discussed cuts. The cut was at $\Theta_d < 70^0$. This cut is loose—when we studied the signal simulation data (i.e., simulating free deuterons events), we learned that it only rejects a small number of good signal events (see Figure 6.7). For the real data, Figure 6.8 shows the angular distribution of the deuterons before

(left) and after (right) the fiducial cuts (we learned that the strangely clustered group of events will be rejected by later event selections; the remaining events from these groups have insignificant effect on our final measurement), while Figures 6.9 (6.10) shows the angular distribution of the π^+s (the π^-s) before (left) and after (right) the fiducial cuts. Finally, we show the squared total missing mass after the fiducial cuts in Figure 6.11.

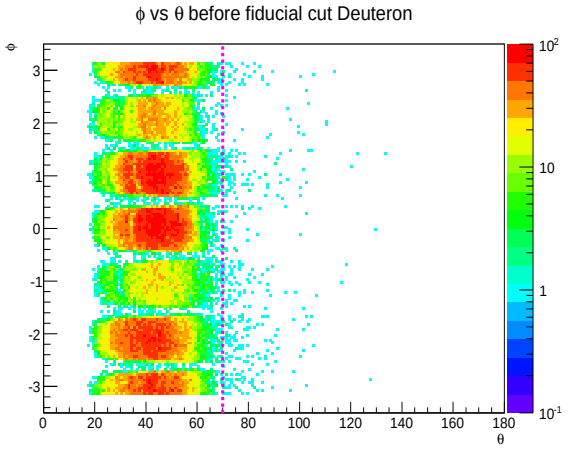

Figure 6.7: Deuteron angular distribution: Φ vs. Θ before the fiducial cuts. The vertical line indicates the extra cut on the deuteron to reject target-material background. The unit of Φ is rad, while the unit of Θ is degree. The events plotted are the signal simulation data. The plot is on a logarithmic scale.

6.2 Deuteron Event Selection Using Boosted Decision Trees

After selecting a clean sample of "$d : \pi^+ : \pi^-$" events, the next task was to select events originating from the initial-state polarized deuterons, and rejected the target-material background, which is non-polarized. In order to optimize efficiency, we employed the BDT algorithm once more. In particular, we generated signal simulation data which consists of incident photons from a bremsstralung distribution, a three-body phase space distribution for the scattered d, π^+, and π^-. The MC data was processed by GSIM, GPP, and USERANA to simulate the CLAS detector efficiency (see Section 3.5 for more detail). The simulation data was used as *signal* training data, while the empty-target-run data was used as *background* training data. Each event (both signal and background) consists of six continuous variables (for example, one of the variables is the total missing momentum), and—*only applied to training data*—one two-value discrete variable to indicate whether the event is signal or background. Table 6.1 provides definitions of the input continuous variables. Note

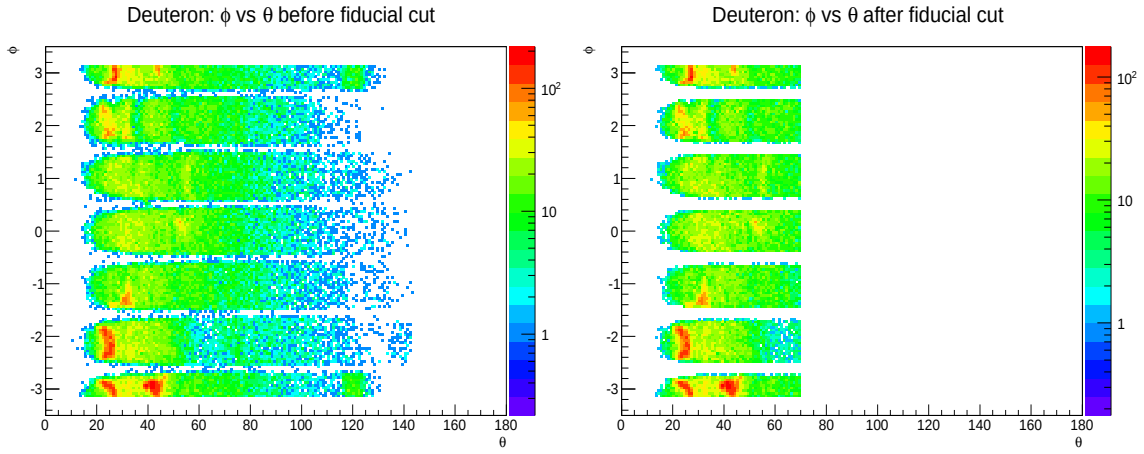

Figure 6.8: On the left (right) deuteron angular distribution: Φ vs. Θ before (after) the fiducial cuts. The unit of Φ is rad, while the unit of Θ is degree. We learned that the strangely clustered group of events will be rejected by later event selections; the remaining events from these groups have insignificant effect on our final measurement. The data used to plot was the Gold 2 period data. The plots are on a logarithmic scale.

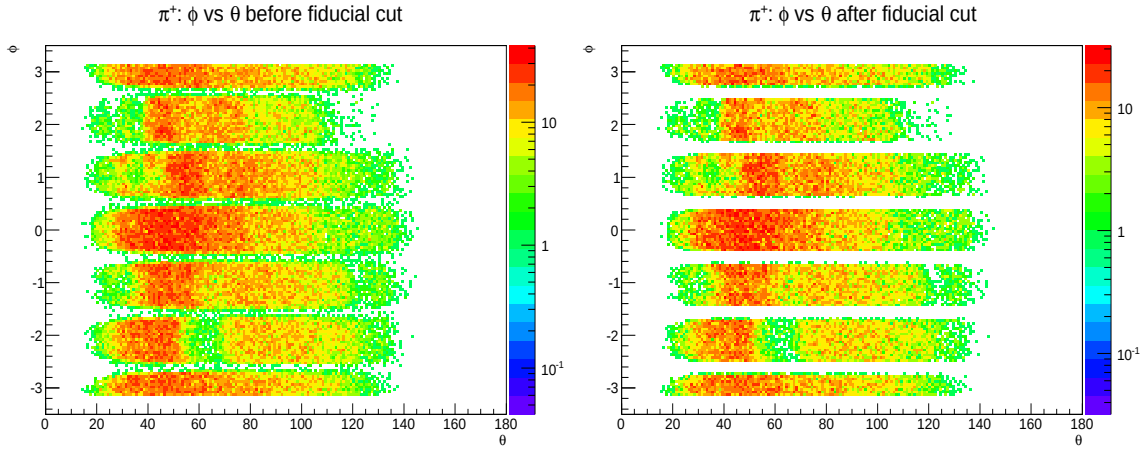

Figure 6.9: On the left (right) π^+ angular distribution: Φ vs. Θ before (after) the fiducial cuts. The unit of Φ is rad, while the unit of Θ is degree. The data used to plot was the Gold 2 period data. The plots are on a logarithmic scale.

that the set of variables in Table 6.1 is distinctly different from the ones presented in Section 4.2.2 or Section 5.3.1. This is because in those sections the spectator proton was "missing", while for this reaction *no* particle is "missing." As a result, there were no variables β and Γ in the list. Also, we replaced the coplanarity angle with an angle we will refer to as correlation angle which is the angle between two planes formed by $(d\pi^+)$ and $(d\pi^-)$ systems in the overall center of mass frame. Ideally, sig-

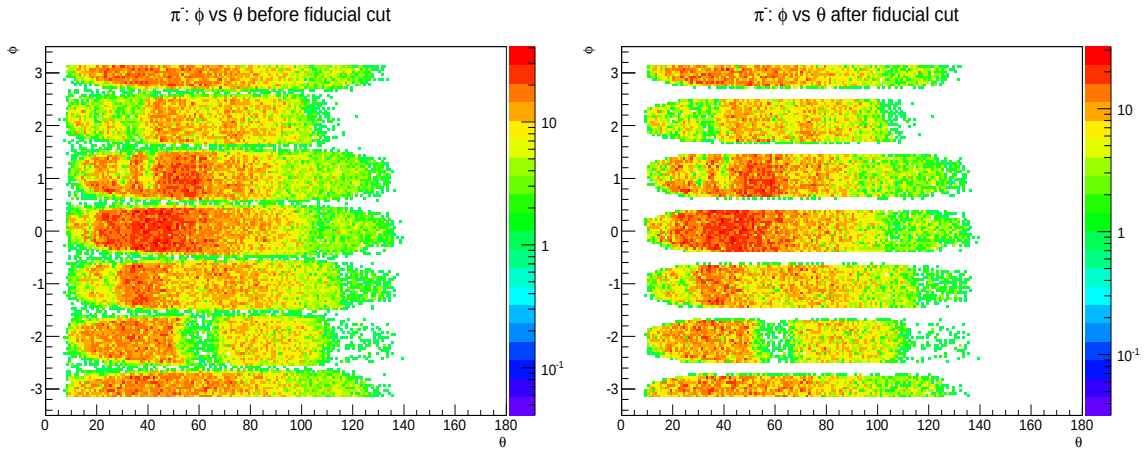

Figure 6.10: On the left (right) π^- angular distribution: Φ vs. Θ before (after) the fiducial cuts. The unit of Φ is rad, while the unit of Θ is degree. The data used to plot was the Gold 2 period data. The plots are on a logarithmic scale.

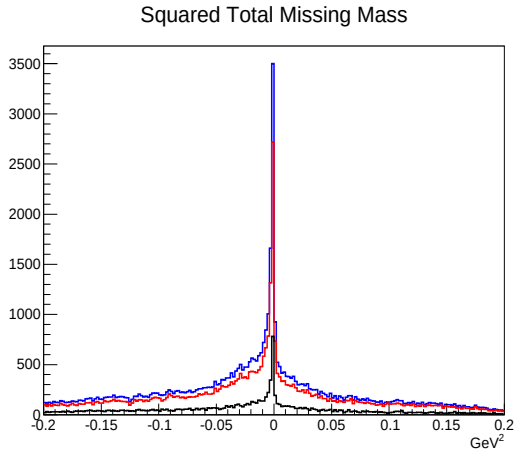

Figure 6.11: Squared total missing mass, $MM^2(d\pi^+\pi^-)$. The blue histogram is after the ΔTOF cuts, and the red histogram is after the fiducial cuts. Events in the black histogram were rejected by the fiducial cuts. The data used to plot was Gold 2 period.

nal events should have zero missing momentum, and zero missing energy—but due to a finite momentum resolution of the drift chamber detectors, the variables may contain non-zero values. Fortunately, however, the "deuterons" inside the aluminum nucleus are tightly bound than the free deuterons in the H-D molucules, thus there is still a visible kinematic distinction between the signal and target-material background events; to illustrate we plot histograms of input variables for both signal and background training data in Figures 6.12. Blue histograms show signal training data, and red histograms show background training data. The BDT algorithm was trained on these variables.

Variable Name	Description
$CosCorrelationAngle$	$\cos\left((\hat{p}_{\pi+} \times \hat{p}_d) \,.\, (\hat{p}_{\pi-} \times \hat{p}_d)\right)$
$MissingMomentum$	Total missing momentum
$MissingEnergy$	Total missing energy
$MissingTheta$	Θ of missing momentum
$MissingMomentum\_z$	$\lvert p_z^{missing} \rvert$
$MissingMomentum\_perp$	$\lvert p_{transverse}^{missing} \rvert$

Table 6.1: List of variables used to construct the BDT for the task of selecting the deuteron and rejecting the target-material background events.

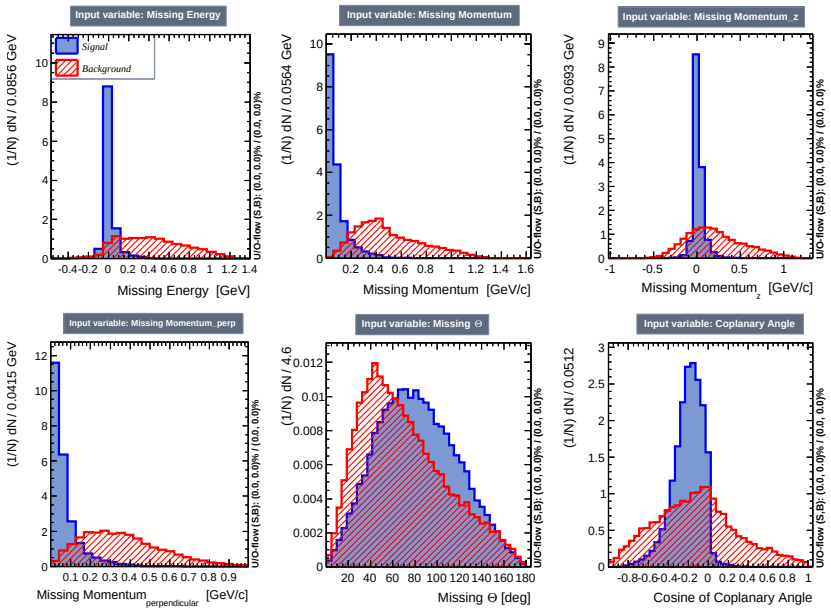

Figure 6.12: Histograms of input variables used to construct the BDT during the training phase. The red histograms are from background (empty target run period), and the blue histograms are from the signal simulation data.

As before, we checked for signs of overtraining (or overfitting) to ensure that the BDT would generalize well for some other independent but similar—to the training—data sets. To check for overtraining the ROOT TMVA program divided the signal and background training data randomly into four subsets: signal and background training data, and signal and background testing data. The program ran the BDT and evaluated the similarity between the BDT's performances on the four data sets by employing the Kolmogorov–Smirnov test—to verify whether the BDT output distributions from the training and testing data are statistically the same (note that the test is applied separately on signal data and background data). *High* probabilities from the Kolmogorov-Smirnov test, as shown in Figure 6.13, suggest consistent

performances on training and independent test data sets—or equivalently, *no* evidence of *overtraining* observed because according to the Kolmogorov-Smirnov test the distributions of the BDT output from the training data and the test data are statistically similar (see Appendix A for how to "fix" an overtrained BDT). Next, Figure 6.14 shows cut efficiencies and an optimal cut value, i.e., the efficiencies of selecting and rejecting signal and background data, respectively, as a function of the BDT output (it is the output from the BDT algorithm for every event after being processed). A recommended cut at 0.195 that maximizes the $S/\sqrt{S+B}$ ratio, which statistically means minimizing the misclassification cost, will be used—to obtain this number we must provide the *initial* signal-to-background ratio which we estimated to be roughly one to two. In particular, from Figure 6.15 we could estimate the numbers of signal and background events to be *one-to-two* ratio (for *all* events within -20 cm$\leq z \leq$30 cm—we did not place cut on the z-vertex at this stage). Note that the estimation for the Gold 2 data accounted for the fact that the aluminum material is less than in the empty target. When studying systematic uncertainties, we will vary this BDT-output cut to study its effect. For illustration, in Figure 6.16 we plot background rejection efficiency vs. signal efficiency and in Figure 6.17 we show the first constructed decision tree. Lastly, we include Table 6.2 for a qualitative assessment on how often each variable was used in building the BDT.

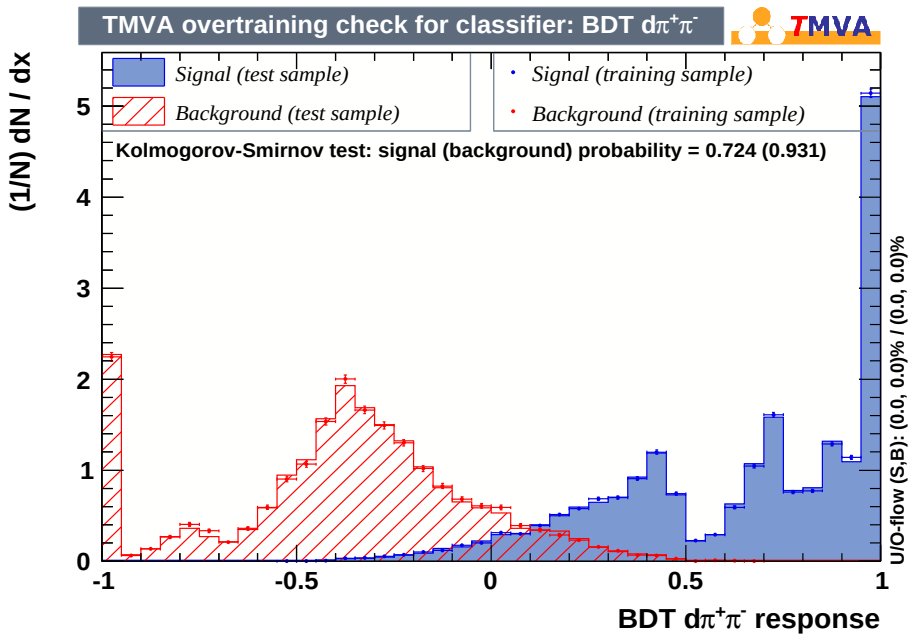

Figure 6.13: Overtraining check, *high* Kolmogorov-Smirnov probabilities for both signal and background data suggest *no overtraining* because the performances (distributions) of the BDT are consistent between independent training and testing data sets.

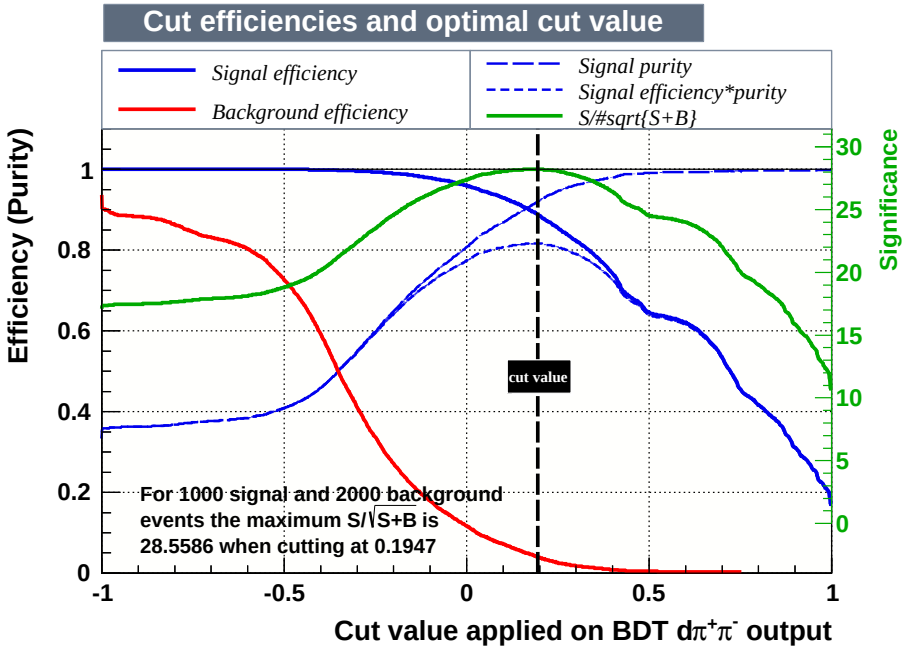

Figure 6.14: Plot of cut efficiencies show the efficiencies as a function of the BDT-output cut value, and an optimal BDT-output cut at 0.195 assuming the *initial* signal-to-background ratio is one-to-two.

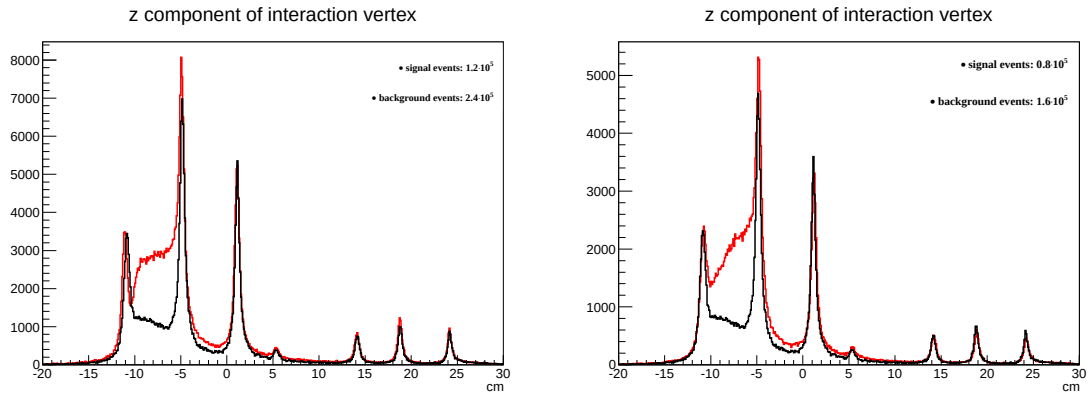

Figure 6.15: The z component of the interaction vertex; the black histograms are (scaled) from the empty-target data, the red histograms are from the Gold 2 data (left) and the Silver 1&2 data (right). From these histograms we estimated the signal-to-background ratio to be one-to-two (for the z-vertex range from -20 cm to $+30$ cm).

6.2.1 Applying the BDT Algorithm to Signal Simulation and Empty-Target Background Data

In Figure 6.18, on the left for simulation signal data we show the squared total missing mass before ("blue" histogram) and after the BDT cut (i.e., selected events in "red"

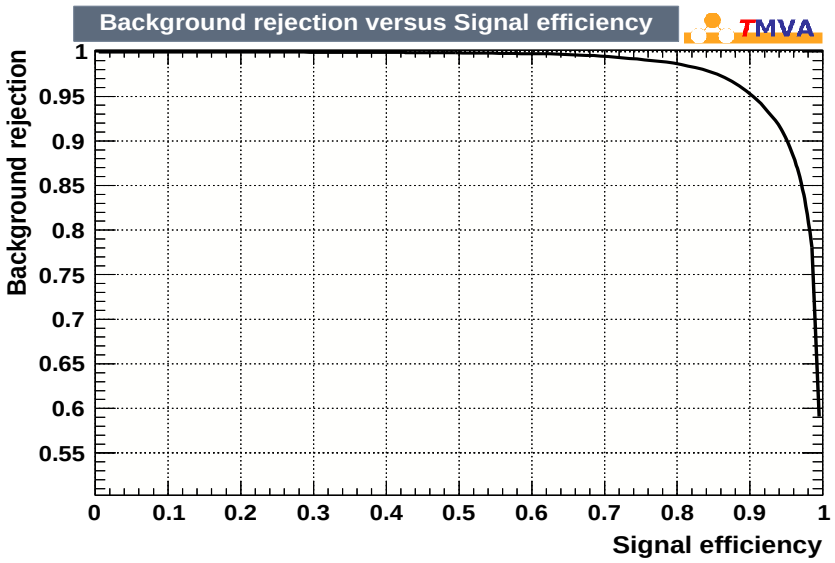

Figure 6.16: Background rejection vs. Signal efficiency of the constructed BDT for training (signal and background) data.

Variable Name	Relative Ranking
$MissingMomentum$	1.00
$MissingEnergy$	0.24
$MissingMomentum\_perp$	0.17
$MissingMomentum\_z$	0.14
$CosCorrelationAngle$	0.12
$MissingTheta$	0.10

Table 6.2: Table of relative variable ranking. The higher the ranking the more the variable was used to construct the trees. All the rankings were normalized to the absolute ranking of the missing momentum variable.

and rejected events in "black"), and the total missing momentum before and after the cut on the right. Similarly, in Figure 6.19 for the empty-target-run-period data the squared total missing mass and the missing momentum before ("blue" histogram) and after the cut (i.e., *wrongly* selected events in "red" and *correctly* rejected events in "black") are shown on the left and right plots, respectively. Additionally, for empty data, we also plot the z-component of the interaction vertex in Figure 6.20. From the three figures, we concluded that the signal selection and the background rejection efficiencies of the newly constructed BDT are outstanding. We applied the constructed BDT on the real data (the Gold 2 and Silver data sets) to select the deuteron events in the next section.

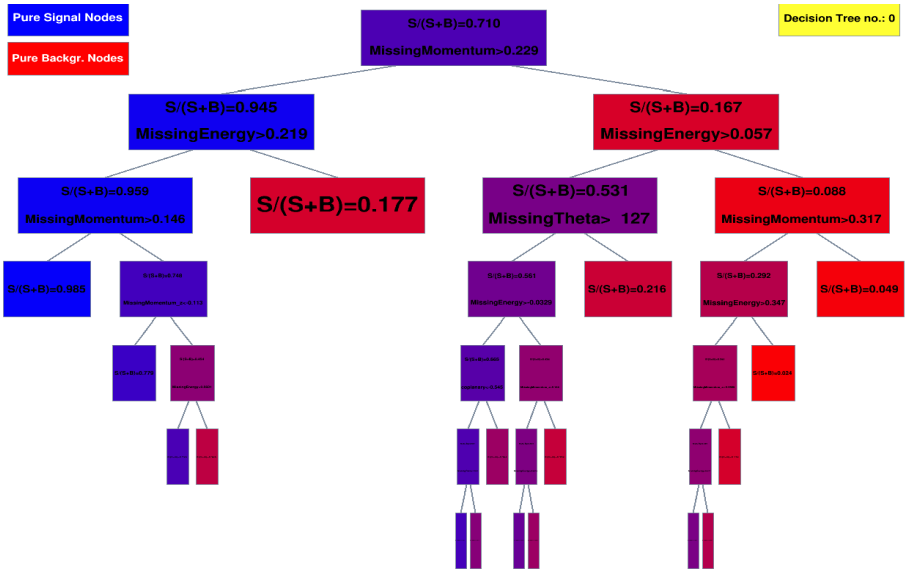

Figure 6.17: The first constructed decision tree, for illustration. Note that all variables can be used multiple times.

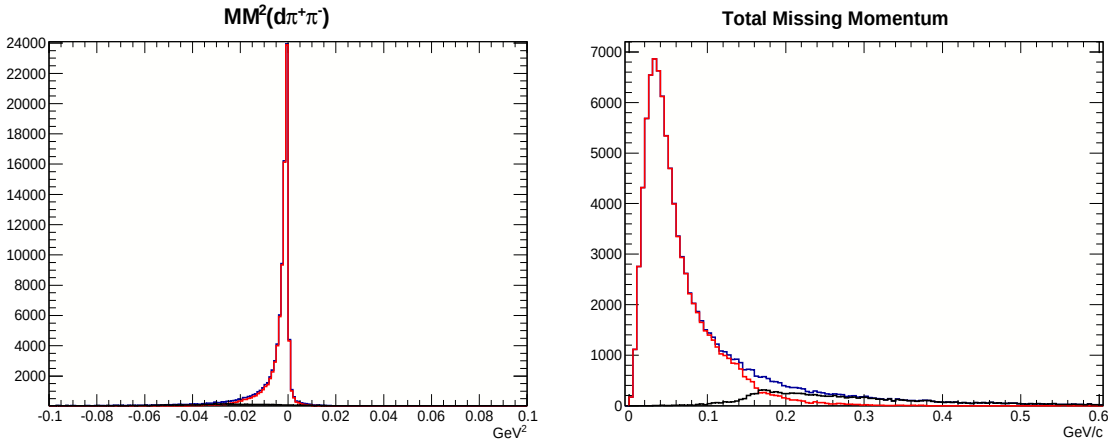

Figure 6.18: Left: Squared total missing mass, $MM^2(d\pi^+\pi^-)$, before ("blue") and after the BDT cut (selected events in "red" and rejected events in "black") . Right: Missing momentum before ("blue"), and after the BDT cut (selected events in "red" and rejected events in "black"). The plots were constructed from the MC data. The *selection* efficiency is outstanding.

6.2.2 Applying the BDT Algorithm to the Real Data

We showed previously that the BDT algorithm has a high performance on both selecting signal and rejecting background events. The next task was to employ the BDT to select the deuteron signal events for the Gold 2 and all Silver periods. In this

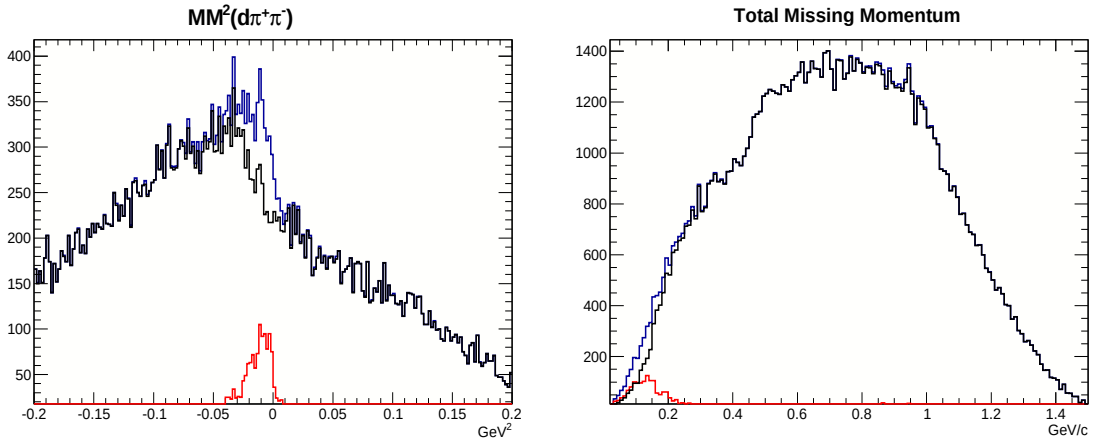

Figure 6.19: Left: Squared total missing mass, $MM^2(d\pi^+\pi^-)$, before ("blue") and after the BDT cut (*wrongly* selected events in "red" and *correctly* rejected events in "black") . Right: Missing momentum before ("blue"), and after the BDT cut (*wrongly* selected events in "red" and *correctly* rejected events in "black"). The plots were constructed from the data of the empty-target-run period. The *rejection* efficiency is outstanding.

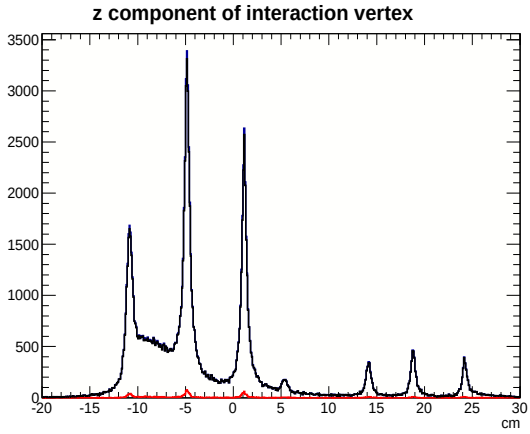

Figure 6.20: z-component of interaction vertex before ("blue"), and after (*wrongly* selected events in "red" and *correctly* rejected events in "black") the BDT cut. The plots were constructed from the data of the empty-target-run period. The *rejection* efficiency is outstanding.

section, we, however, illustrate only the results for the Gold 2 and Silver 5 data sets since they have high statistics. In particular, we plot histograms of the squared total missing mass, total missing momentum, z component of the interaction vertex before and after the BDT cut in Figures 6.21, 6.22, and 6.23. We also include the histograms of the invariance masses of the $(d\pi^-)$ system versus the $(d\pi^+)$ system before and after

the BDT cut in Figures 6.24, and 6.25. The right plots of Figures 6.24, and 6.25 show a pronounced structure of the $(d\pi^{\pm})$ systems. In addition, we also applied some loose cuts to reject remaining unambiguous (but very small) target-material background, see below:

- Select events with missing momentum less than 200 MeV/c,
- Select events with squared total missing mass from $-0.05\,\mathrm{GeV}^2$ to $+0.05\,\mathrm{GeV}^2$,
- Select events with z vertex from $-10.5\,\mathrm{cm}$ to $-5.0\,\mathrm{cm}$.

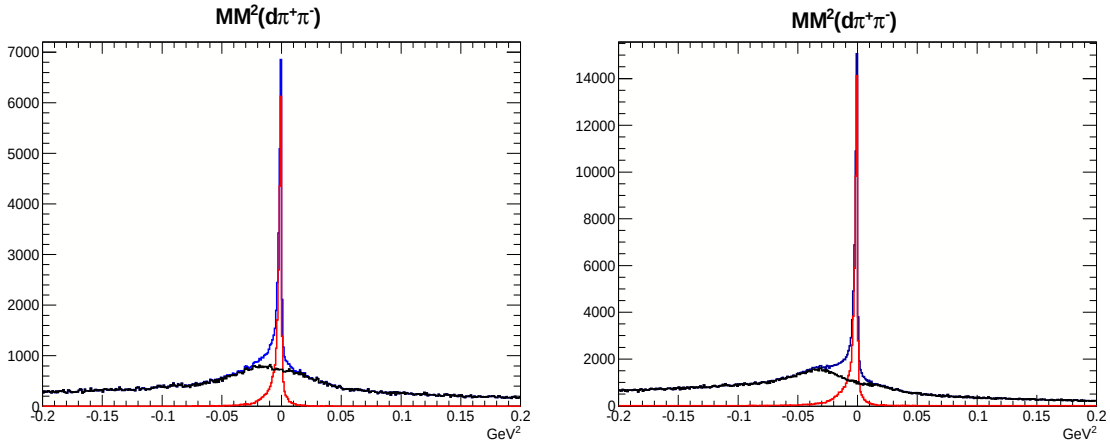

Figure 6.21: Squared total missing mass, $MM^2(d\pi^+\pi^-)$, before ("blue") and after the BDT cut (selected events in "red" and rejected events in "black"). The left plot was constructed from the Gold 2 period data, the right plot was constructed from the Silver 5 period data.

6.3 $N\Delta$ Regional Selection and ρ Background Subtraction

The last two sections introduced our procedures to select a clean sample of $d\pi^+\pi^-$ events that originated from the *polarized* deuterons (the deuterons in the H-D molecules). Then, as illustrated in Figures 6.24, and 6.25, a band-like structure in the $(d\pi^{\pm})$ systems was visible. The goal for this analysis is to determine the spin of this structure *assuming* that it is a dibaryonic $N\Delta$ resonance. Consequently, the $d\pi^+\pi^-$ non-resonant and the $d\pi^+_\rho\pi^-_\rho$ (i.e., $\rho \to \pi^+_\rho\pi^-_\rho$) backgrounds must be removed or subtracted. This section discusses a procedure to subtract *incoherently* the two remaining backgrounds—it is the best approach in the absence of a coherent amplitude-level quantum mechanical description.

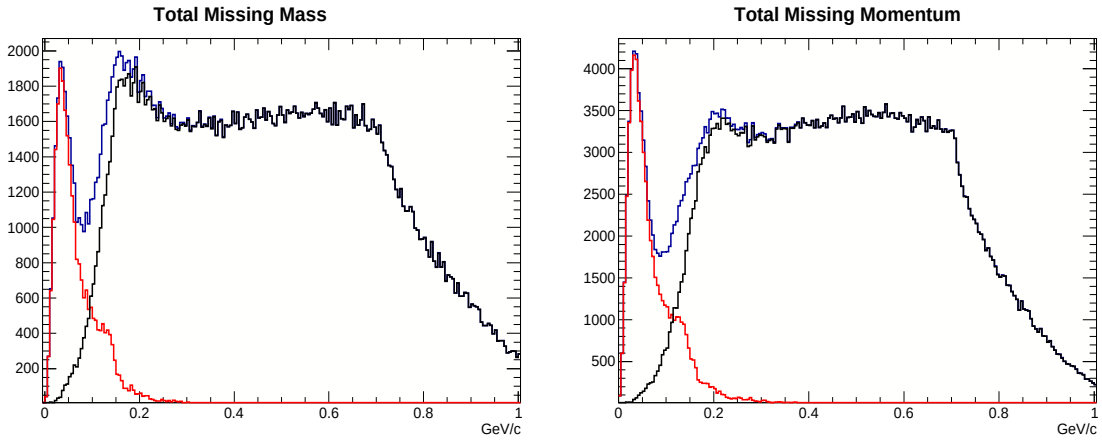

Figure 6.22: Missing momentum before ("blue") and after the BDT cut (selected events in "red" and rejected events in "black"). The left plot was constructed from the Gold 2 period data, the right plot was constructed from the Silver 5 period data.

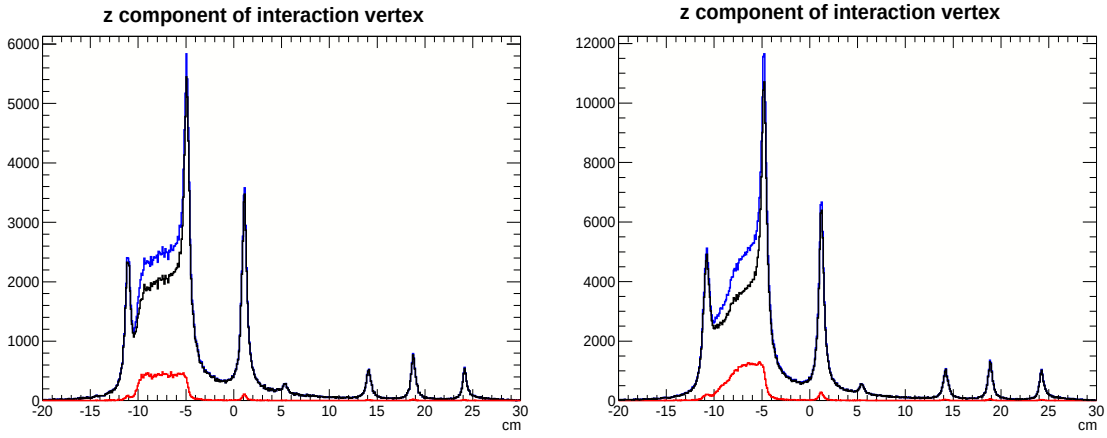

Figure 6.23: The z-component of the interaction vertex before ("blue") and after the BDT cut (selected events in "red" and rejected events in "black"). The left plot was constructed from the Gold 2 period data, the right plot was constructed from the Silver 5 period data.

6.3.1 Dibaryon $N\Delta$ Event Selection

In order to select the signal events we implemented a two-stage procedure:

1. Select $E_\gamma < 1.2\,\text{GeV}$, and $IM(\pi^+\pi^-) < 0.6\,\text{GeV}$, see Figure 6.26,

2. Select $(d\pi^+)$ system: $IM(d\pi^+) < 2.25\,\text{GeV}$ and $IM(d\pi^-) > 2.25\,\text{GeV}$; and select $(d\pi^-)$ system: $IM(d\pi^-) < 2.25\,\text{GeV}$ and $IM(d\pi^+) > 2.25\,\text{GeV}$, see the

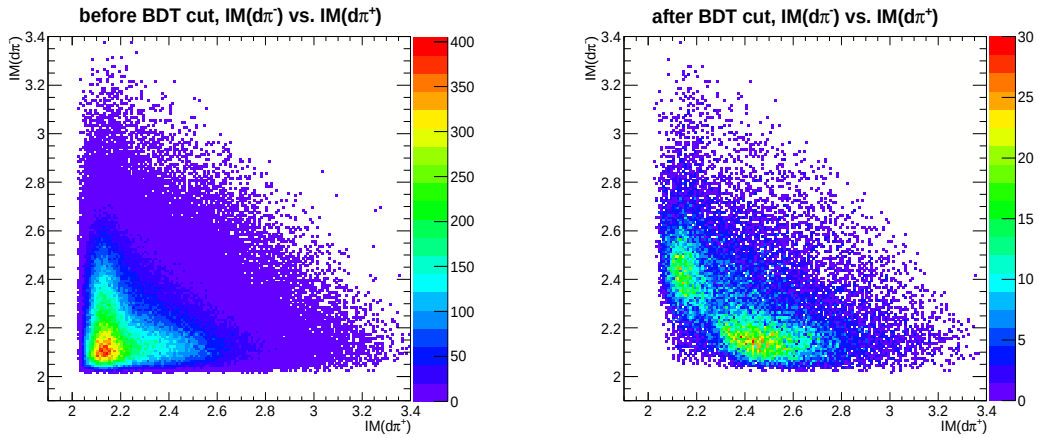

Figure 6.24: $IM(d\pi^-)$ vs. $IM(d\pi^+)$ before (left plot) and after the BDT cut (right plot). The units are in GeV. The data used to obtain the plots is the Gold 2 period data.

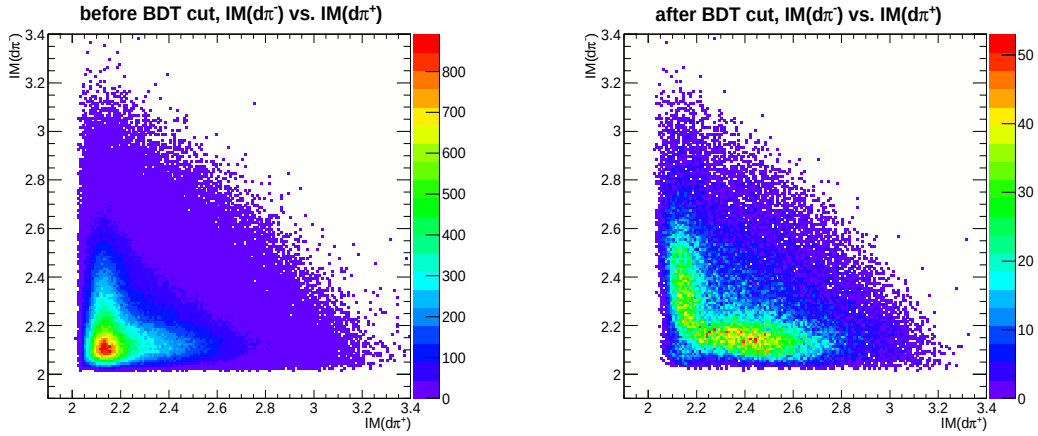

Figure 6.25: $IM(d\pi^-)$ vs. $IM(d\pi^+)$ before (left plot) and after the BDT cut (right plot). The units are in GeV. The data used to obtain the plots is the Silver 5 period data.

right plot of Figure 6.27,

where E_γ is the incident photon energy, $IM(\pi^+\pi^-)$, $IM(d\pi^-)$, and $IM(d\pi^+)$ are the invariance masses of the $(\pi^+\pi^-)$, the $(d\pi^-)$, and the $(d\pi^+)$ systems, respectively. Note that the first stage mainly removes the ρ and non-resonant backgrounds, while the second stage removes ambiguous kinematic regions where it is not clear which pion should be combined with the deuteron. Even after the cuts, it is resonable to suspect that there is still background remaining; and to study the background more carefully we looked into a smaller kinematic background region—particularly, the

region of which $E_\gamma < 1.2\,\text{GeV}$, and $IM(\pi^+\pi^-) > 0.6\,\text{GeV}$, see Figure 6.26, and the left plot of Figure 6.28.

By studying both Figures 6.27 and 6.28, we learned that in the $d\pi^\pm$ regions there are remaining background events associated with the ρ resonance. Assuming that the join distribution of $IM(d\pi^-)$ and $IM(d\pi^+)$, as shown in Figure 6.28, represents well the remaining background in Figure 6.27, then the remaining background could be "subtracted" by utilizing events in this background region (i.e., $E_\gamma < 1.2\,\text{GeV}$, and $IM(\pi^+\pi^-) > 0.6\,\text{GeV}$)—but the region must be scaled appropriately. Fortunately, we could obtain the scaling factor because of the following observation: since the triangular region in Figure 6.27 is mostly background (denoted as $BG_{SignalRegion}$), we could "fit" the triangular region in Figure 6.28 (denoted as $BG_{BackgroundRegion}$) into the $BG_{SignalRegion}$ to obtain the scaling factor. i.e., find ε such that $BG_{SignalRegion} = \varepsilon BG_{BackgroundRegion}$. We chose to fit in two dimensions (i.e., the $IM(d\pi^-)$ and $IM(d\pi^+)$ dimensions) because it provides more degrees of freedom. In addition, since the statistics for both $BG_{SignalRegion}$ and $BG_{BackgroundRegion}$ are scarce, we implemented a fitting algorithm based on Poisson distribution which is more accurate for the current situation. Details about the algorithm is provided in the next section.

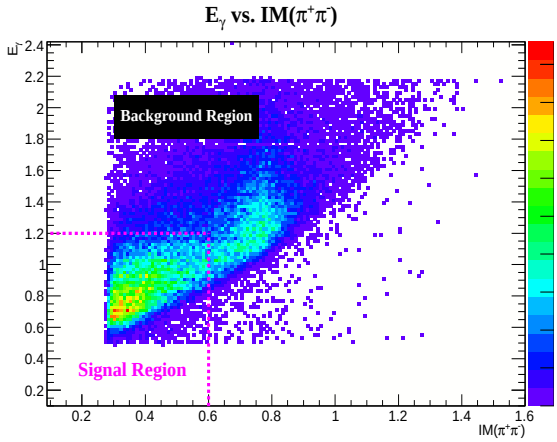

Figure 6.26: E_γ vs. $IM(\pi^+\pi^-)$, the magenta lines indicate the cuts to reject the ρ and non-resonant backgrounds. The units are in GeV. The data used to obtain the plots is the Silver 5 period data.

6.3.2 Ξ^2 Fitting Algorithm

As discussed in the last section, to implement succesfully a background subtraction procedure, it is necessary to find a kinematic region that resembles the remaining background in the signal region, and find an appropriate scaling factor ϵ that

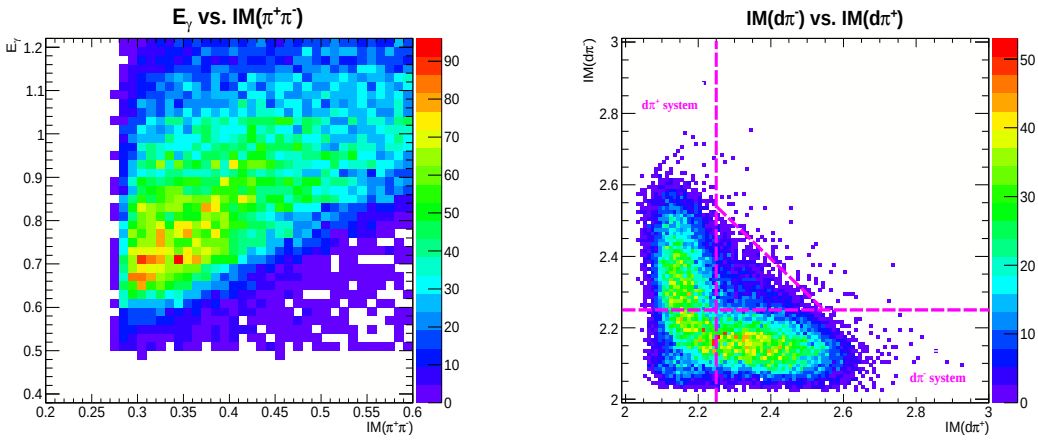

Figure 6.27: Left: E_γ vs. $IM(\pi^+\pi^-)$ in the *signal* region. Right: $IM(d\pi^-)$ vs. $IM(d\pi^+)$ distribution for events selected by the cuts $E_\gamma < 1.2\,\text{GeV}$, and $IM(\pi^+\pi^-) < 0.6\,\text{GeV}$ (i.e., events in the left plot). The triangular region inthe right plot marked by the dashed lines was used to estimate the number of remaining background (for detail see text). The units are in GeV. The data used to obtain the plot is the Silver 5 period data.

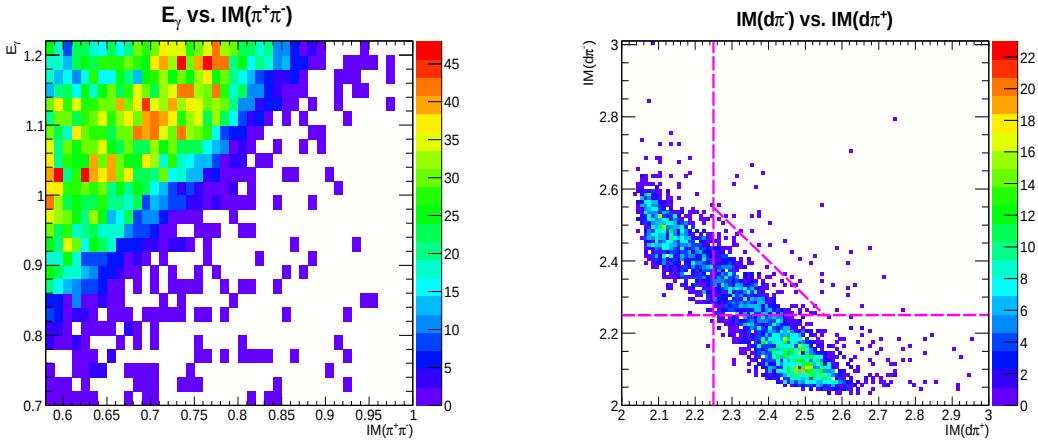

Figure 6.28: Left: E_γ vs. $IM(\pi^+\pi^-)$ in the *background* region. Right: $IM(d\pi^-)$ vs. $IM(d\pi^+)$ distribution for events selected by the cuts $E_\gamma < 1.2\,\text{GeV}$, and $IM(\pi^+\pi^-) > 0.6\,\text{GeV}$ (i.e., events in the left plot). The triangular region in the right plot was used to estimate the number of remaining background (for detail see text). The units are in GeV. The data used to obtain the plot is the Silver 5 period data.

"matches" the backgrounds. In other words, the task is to find ϵ such that:

$$BG_{SignalRegion} = \varepsilon BG_{BackgroundRegion}. \tag{6.3}$$

Note that this is a two-dimensional fit to the Dalitz-like plots, and the data has bins with low (less than 10 counts) statistics. We introduce two fitting algorithms to estimate ϵ: χ^2 fitting and Ξ^2 fitting. Both fitting procedures are derived from the maximum likelihood method. We will argue that the Ξ^2 fitting is more applicable to the present low-statistics situation—thus implementing only this algorithm, but present the χ^2 fitting algorithm as an anchor point that most people know.

For the χ^2 fitting method consider experimental data with a large number of counts per bin, it is appropriate to approximate the data statistics in each bin with a Gaussian distribution. The likelihood is then

$$L(\vec{\epsilon}) = \prod_{i=1}^{n} \frac{1}{\sqrt{2\pi N_i}} exp[-\frac{(N_i - f_i)^2}{2N_i}], \tag{6.4}$$

where N_i is the number of counts in bin i and $f_i = f(i;\vec{\epsilon}) = \sum_{k=1}^{q} \epsilon_k g_k(i)$ is the sum of q linear terms (for our case $q = 1$). f_i is a best fit if it maximizes $L(\vec{\epsilon})$ or equivalently it minimizes $-lnL(\vec{\epsilon})$. To achieve this, f_i has to be such that

$$\chi^2(\vec{\epsilon}) \equiv \sum_{i=1}^{n} \frac{(N_i - f_i)^2}{N_i}, \tag{6.5}$$

or the term that is recognized as $\chi^2(\vec{\epsilon})$ is minimized. The χ^2 fitting method has a limitation. It is not designed to handle low statistics data. Hence, by construction, it ignores zero-count channels (bins). Consequently, results of the fit will be biased in a systematic way. To overcome these limitations, we introduce the Ξ^2 fitting method.

It usually occurs in experimental physics, especially in nuclear and particle physics, that experimental data exhibits the Poisson distribution. Low-statistics data is well represented by the distribution. Zero-count channels are as important as non-zero count channels in the Poisson distribution. For large-statistics data, the Poisson and the Gaussian distributions give identical results. Realizing these features of the Poisson distribution in contrast to the Gaussian distribution, we were compelled to develop the Ξ^2 fitting method based on Poisson statistics. We obtained the likelihood for the Poisson distribution:

$$L(\vec{\epsilon}) = \prod_{i=1}^{n} \frac{f_i^{N_i} e^{-f_i}}{N_i!}, \tag{6.6}$$

where N_i and f_i are defined as before. f_i is a best fit if it maximizes $L(\vec{\epsilon})$ or, equivalently, it minimizes $-lnL(\vec{\epsilon})$. To achieve this, f_i has to be such that

$$\Xi^2(\vec{\epsilon}) \equiv \sum_{i=1}^{n} f_i - N_i - N_i ln \frac{f_i}{N_i}, \tag{6.7}$$

the term referred to as $\Xi^2(\vec{\epsilon})$, is minimized. To get this result, one needs to use Sterling's factorial approximation $lnN_i! \approx \frac{1}{2}(ln2\pi + lnN_i) + N_i lnN_i - N_i$. Also, it can

be shown that in the limit of large N_i

$$\Xi^2(\vec{\epsilon}) \approx \sum_{i=1}^{n} \frac{(N_i - f_i)^2}{N_i} = \chi^2(\vec{\epsilon}). \tag{6.8}$$

Thus, for large statistics data, the two methods are equivalent. Since $\lim_{X\to 0} X(\ln X) \to 0$, the summand above (Eq. 6.7) reduces to f_i for the channels (bins) that contain no counts. i.e. this method does not ignore zero-count channels (bins). Necessarily, the initial values for parameters of f_i for this fitting method have to be carefully assigned because of the introduction of the logarithm in the formula. In particular, $f(i;\vec{\epsilon})$ may not go all the way to zero or become negative, reflecting the physical requirement that the number of counts remains positive everywhere. In conclusion, the two fitting algorithms, χ^2-fitting and Ξ^2-fitting, are designed to find the optimal estimate of the $\vec{\epsilon}$ by minimize $\chi^2(\vec{\epsilon})$ and $\Xi^2(\vec{\epsilon})$, respectively. But the $\Xi^2(\vec{\epsilon})$ fitting algorithm is more suitable for low-statistics data such as our current situation—hence we only employed the $\Xi^2(\vec{\epsilon})$ fitting algorithm to estimate the scaling factor ϵ. Table 6.3 presents fitting results for all the run periods. Moreover, in the last column of Table 6.3, we also show the ratio of $N_{BG_{SignalRegion}}/N_{BG_{BackgroundRegion}}$ for all data periods for comparision. As shown, the two set of values of scaling factors are different. We chose the set obtained from the Ξ^2 fitting method but will vary these values in one of the systematics studies to assess how sensitive the final measurements to the values of the scaling factor ϵ.

Run Period	ϵ	Ξ^2/dof	$N_{BG_{SignalRegion}}/N_{BG_{BackgroundRegion}}$
Gold 2	0.73±0.05	1.31	0.61±0.04
Silver 1&2	0.62±0.06	1.31	0.55±0.05
Silver 3	0.60±0.10	1.70	0.55±0.12
Silver 4	0.58±0.07	1.30	0.82±0.09
Silver 5	0.80±0.05	1.34	0.70±0.04

Table 6.3: Results of the Ξ^2 fitting method for the scaling factor ϵ for all run periods compared with $N_{BG_{SignalRegion}}/N_{BG_{BackgroundRegion}}$.

6.4 Spin Determination for a *Possible* $N\Delta$ Resonance Structure

We considered the reaction $\gamma d \to \pi_f \overline{N\Delta} \to \pi_f(\pi_d d)$, where π_f is the formation pion and π_d is the pion from the decay of the $N\Delta$ dibaryon (denoted as $\overline{N\Delta}$ hereafter). We assumed that the orbital angular momentum between the formation pion, π_f, and the $\overline{N\Delta}$ state is dominantly in S-wave, and that the $\overline{N\Delta}$ resonance has positive parity (both the N and Δ baryons have positive parity). Furthermore, because the intrinsic spins of the N and Δ baryons are $1/2$, and $3/2$, respectively, the intrinsic spin

of the $\overline{N\Delta}$ dibaryon is assumed to be only 1 or 2 (i.e., $\boldsymbol{J}^P_{N\Delta} = \mathbf{1}^+$ or $\mathbf{2}^+$)—more elaborated theoretical models by Mulders *et al.* [66], and Gal and Garcilazo [67, 68] favor the $\boldsymbol{J}^P_{N\Delta} = \mathbf{2}^+$configuration. In addition, as a result of $\boldsymbol{J}_d = \mathbf{1}$, and $\boldsymbol{J}_\pi = \mathbf{0}$, to conserve angular momentum between the initial $\overline{N\Delta}$ state and the final $\pi_d d$ state, there must be contribution from orbital angular momentum between the d and the π_d ($\boldsymbol{L}_{\pi_d d}$); i.e., if $\boldsymbol{J}_{\overline{N\Delta}} = \mathbf{2}$, then $\boldsymbol{L}_{\pi_d d} = \left\{\vec{1}, \vec{3}\right\}$ (we use different notations for the values of $\boldsymbol{J}_{\overline{N\Delta}}$, and $\boldsymbol{L}_{\pi_d d}$ to distinguish them even though they are both angular momenta); note that $\boldsymbol{L}_{\pi_d d} = \vec{2}$ is not allowed because final $\pi_d d$ state would have negative parity. On the other hand, the orbital angular momentum ($\boldsymbol{L}_{\pi_d d}$) can only be *one* if $\boldsymbol{J}_{\overline{N\Delta}} = \mathbf{1}$—again, to conserve parity. Consequently, we could obtain the value for the spin of the $\overline{N\Delta}$ *indirectly* by studying the angular distribution of the $\boldsymbol{L}_{\pi_d d}$ in the rest frame of the $\pi_d d$ system.

6.4.1 The Beam-Target E Asymmetry

This analysis takes full advantage of the fact that the g14 experiment has both longitudinally polarized photons and deuterons; thus, in the overall center-of-mass frame, there are only two possible values for J_z; i.e., $J_z = 0$ ($J_z = 2$) if the polarization vectors are anti-aligned (aligned). Note that in the rest frame of the $\overline{N\Delta}$ state, the initial J_z values would still be two and zero along the same z-axis. We now discuss the formalism of the E asymmetry below.

- Consider the configuration $\boldsymbol{J}_{\overline{N\Delta}} = \mathbf{2}$, and $\boldsymbol{L}_{\pi_d d} = \vec{1}$:

$$|\boldsymbol{J} = \mathbf{2}, J_z = 2\rangle_{\overline{N\Delta}} = Y_{1,+1}(\theta, \phi)\chi^d_{+1}, \tag{6.9}$$

$$|\boldsymbol{J} = \mathbf{2}, J_z = 0\rangle_{\overline{N\Delta}} = a_+ Y_{1,-1}(\theta, \phi)\chi^d_{+1} + a_0 Y_{1,0}(\theta, \phi)\chi^d_0 + a_- Y_{1,+1}(\theta, \phi)\chi^d_{-1}, \tag{6.10}$$

where $\chi^d_{\{-1,0,+1\}}$ are the final-state deuteron spin states (e.g., $\chi^d_{+1} = |\boldsymbol{J} = \mathbf{1}, J_z = +1\rangle_d$), and $Y_{1,\{-1,0,+1\}}(\theta, \phi)$ are the spherical harmonic functions representing the orbital angular momentum $\boldsymbol{L}_{\pi_d d} = \vec{1}$. The coefficents a_-, a_0, and a_+ satisfy $a_-^2 + a_0^2 + a_+^2 = 1$. The decay intensity angular distributions, I_0 and I_2, are given by:

$$I_2(\theta) \sim_{d\pi} \langle \boldsymbol{J} = \mathbf{2}, J_z = 2 | \boldsymbol{J} = \mathbf{2}, J_z = 2\rangle_{\overline{N\Delta}} = \frac{3}{8\pi}\sin^2\theta, \tag{6.11}$$

$$I_0(\theta) \sim_{d\pi} \langle \boldsymbol{J} = \mathbf{2}, J_z = 0 | \boldsymbol{J} = \mathbf{2}, J_z = 0\rangle_{\overline{N\Delta}} = \frac{3}{8\pi}\left(\left(a_+^2 + a_-^2\right)\sin^2\theta + 2a_0^2\cos^2\theta\right), \tag{6.12}$$

since $a_+^2 + a_-^2 + a_0^2 = 1$,

$$I_0(\theta) \sim_{d\pi} \langle \boldsymbol{J}=\mathbf{2}, J_z=0|\boldsymbol{J}=\mathbf{2}, J_z=0\rangle_{\overline{N\Delta}} = \frac{3}{8\pi}\left(\left(1-a_0^2\right)\sin^2\theta + 2a_0^2\cos^2\theta\right), \tag{6.13}$$

which leads to

$$E(\cos\theta) = \frac{I_0(\theta)-I_2(\theta)}{I_0(\theta)+I_2(\theta)} = \frac{a_0^2\left(3\cos^2\theta-1\right)}{2-a_0^2+\left(3a_0^2-2\right)\cos^2\theta}. \tag{6.14}$$

where θ is the angle of the deuteron in the rest-frame of the $d\pi_d$ system. By fitting the measured E values we can estimate a_0^2.

- Consider the configuration $\boldsymbol{J}_{\overline{N\Delta}}=\mathbf{2}$, and $\boldsymbol{L}_{\pi_d d}=\vec{3}$:

$$|\boldsymbol{J}=\mathbf{2}, J_z=2\rangle_{\overline{N\Delta}} = b_+ Y_{3,+1}(\theta,\phi)\chi^d_{+1} + b_0 Y_{3,2}(\theta,\phi)\chi^d_0 + b_- Y_{3,+3}(\theta,\phi)\chi^d_{-1}, \tag{6.15}$$

$$|\boldsymbol{J}=\mathbf{2}, J_z=0\rangle_{\overline{N\Delta}} = c_+ Y_{3,-1}(\theta,\phi)\chi^d_{+1} + c_0 Y_{3,0}(\theta,\phi)\chi^d_0 + c_- Y_{3,+1}(\theta,\phi)\chi^d_{-1}, \tag{6.16}$$

where $\chi^d_{\{-1,0,+1\}}$ are the final-state deuteron spin states (e.g., $\chi^d_{+1} = |\boldsymbol{J}=\mathbf{1}, J_z=+1\rangle_d$), and $Y_{3,\{-1,0,+1,+2,+3\}}(\theta,\phi)$ are the spherical harmonic functions representing the orbital angular momentum $\boldsymbol{L}_{\pi_d d}=\vec{3}$. The coefficents b_-, b_0, and b_+ (c_-, c_0, and c_+) satisfy $b_-^2+b_0^2+b_+^2=1$ ($c_-^2+c_0^2+c_+^2=1$). The decay intensity angular distributions, I_0 and I_2, are given by:

$$I_2(\theta) \sim_{d\pi} \langle \boldsymbol{J}=\mathbf{2}, J_z=2|\boldsymbol{J}=\mathbf{2}, J_z=2\rangle_{\overline{N\Delta}}$$

$$= \frac{7}{64\pi}\left[3b_+^2\sin^2\theta\left(5\cos^2\theta-1\right)^2 + 30b_0^2\sin^4\theta\cos^2\theta + 5b_-^2\sin^6\theta\right], \tag{6.17}$$

$$= \frac{7}{64\pi}\left[3b_+^2\sin^2\theta\left(5\cos^2\theta-1\right)^2 + 30b_0^2\sin^4\theta\cos^2\theta + 5\left(1-b_0^2-b_+^2\right)\sin^6\theta\right], \tag{6.18}$$

$$I_0(\theta) \sim_{d\pi} \langle \boldsymbol{J}=\mathbf{2}, J_z=0|\boldsymbol{J}=\mathbf{2}, J_z=0\rangle_{\overline{N\Delta}}$$

$$= \frac{7}{64\pi}\left(3\left(c_+^2+c_-^2\right)\sin^2\theta\left(5\cos^2\theta-1\right)^2 + 4c_0^2\cos^2\theta\left(5\cos^2\theta-3\right)^2\right), \tag{6.19}$$

$$= \frac{7}{64\pi}\left(3\left(1-c_0^2\right)\sin^2\theta\left(5\cos^2\theta-1\right)^2 + 4c_0^2\cos^2\theta\left(5\cos^2\theta-3\right)^2\right), \tag{6.20}$$

$$\Rightarrow E(\cos\theta) = \frac{I_0(\theta) - I_2(\theta)}{I_0(\theta) + I_2(\theta)} \tag{6.21}$$

$$= -\frac{3\left(b_+^2 + c_0^2 - 1\right)\left(5\cos^2\theta - 1\right)^2 + \left(30b_0^2\sin^4\theta - 4c_0^2\left(5\cos^2\theta - 3\right)^2\right)\cot^2\theta + 5\left(1 - b_0^2 - b_+^2\right)\sin^4\theta}{3\left(b_+^2 - c_0^2 + 1\right)\left(5\cos^2\theta - 1\right)^2 + \left(30b_0^2\sin^4\theta + 4c_0^2\left(5\cos^2\theta - 3\right)^2\right)\cot^2\theta + 5\left(1 - b_0^2 - b_+^2\right)\sin^4\theta}. \tag{6.22}$$

Similarly, by fitting the measured E asymmetry we could estimate b_+^2, b_0^2, and c_0^2.

- Consider the configuration $\boldsymbol{J}_{\overline{N\Delta}} = \mathbf{1}$, and $\boldsymbol{L}_{\pi_d d} = \vec{1}$:

$$|\boldsymbol{J} = \mathbf{1}, J_z = 2\rangle_{\overline{N\Delta}} = 0, \tag{6.23}$$

therefore,

$$I_2(\theta) = 0. \tag{6.24}$$

Hence,

$$E(\cos\theta) = \frac{I_0(\theta) - I_2(\theta)}{I_0(\theta) + I_2(\theta)} = +1. \tag{6.25}$$

Therefore, *if the measured E asymmetry is statistically flat at $+1$, then the spin of the $\overline{N\Delta}$ state is one. On the other hand, if the measures E is angle-dependent then it may be possible that $\boldsymbol{J}_{\overline{N\Delta}} = \mathbf{2}$*; estimating the values of a_0^2, b_+^2, b_0^2, and c_0^2 may provide indication of the existence of the *possible* dibaryonic $\overline{N\Delta}$ state with $\boldsymbol{J}_{\overline{N\Delta}} = \mathbf{2}$. This is because the fitting coefficient(s) a_0^2, or b_+^2, b_0^2, and c_0^2 must be statistically consistent with the Clebsch-Gordan coefficients for a true resonance with a defined intrinsic spin. We will show in the next section that the fitted value for a_0^2 is statistically consistent with the Clebsch-Gordan coefficient for the configuration $\boldsymbol{J}_{\overline{N\Delta}} = \mathbf{2}$, and $\boldsymbol{L}_{\pi_d d} = \vec{1}$. We now introduce another fitting configuration where the coefficients a_0^2, b_+^2, b_0^2, and c_0^2 are fixed as the Clebsch-Gordan coefficients but the $\overline{N\Delta}$ state is allowed to be in a superposition of $\boldsymbol{L}_{\pi_d d} = \vec{1}$ and $\boldsymbol{L}_{\pi_d d} = \vec{3}$.

$$|\boldsymbol{J} = \mathbf{2}, J_z = 2\rangle_{\overline{N\Delta}} = \alpha\left|\boldsymbol{J} = \mathbf{2}, J_z = 2, \boldsymbol{L}_{\pi_d d} = \vec{1}\right\rangle_{\overline{N\Delta}} + \beta\left|\boldsymbol{J} = \mathbf{2}, J_z = 2, \boldsymbol{L}_{\pi_d d} = \vec{3}\right\rangle_{\overline{N\Delta}}, \tag{6.26}$$

$$|\boldsymbol{J} = \mathbf{2}, J_z = 2\rangle_{\overline{N\Delta}} = \alpha Y_{1,+1}(\theta,\phi)\chi_{+1}^d + \beta\left[\sqrt{\frac{1}{21}}Y_{3,+1}(\theta,\phi)\chi_{+1}^d - \sqrt{\frac{5}{21}}Y_{3,2}(\theta,\phi)\chi_0^d + \sqrt{\frac{5}{7}}Y_{3,+3}(\theta,\phi)\chi_{-1}^d\right], \tag{6.27}$$

and,

$$|\boldsymbol{J} = \mathbf{2}, J_z = 0\rangle_{\overline{N\Delta}} = \alpha\left|\boldsymbol{J} = \mathbf{2}, J_z = 0, \boldsymbol{L}_{\pi_d d} = \vec{1}\right\rangle_{\overline{N\Delta}} + \beta\left|\boldsymbol{J} = \mathbf{2}, J_z = 0, \boldsymbol{L}_{\pi_d d} = \vec{3}\right\rangle_{\overline{N\Delta}}, \tag{6.28}$$

$$|\boldsymbol{J}=\mathbf{2},J_z=0\rangle_{\overline{N\Delta}} = \alpha\left[\sqrt{\frac{1}{6}}Y_{1,-1}(\theta,\phi)\chi^d_{+1}+\sqrt{\frac{2}{3}}Y_{1,0}(\theta,\phi)\chi^d_0+\sqrt{\frac{1}{6}}Y_{1,+1}(\theta,\phi)\chi^d_{-1}\right] + \beta\left[\sqrt{\frac{2}{7}}Y_{3,-1}(\theta,\phi)\chi^d_{+1}-\sqrt{\frac{3}{7}}Y_{3,0}(\theta,\phi)\chi^d_0+\sqrt{\frac{2}{7}}Y_{3,+1}(\theta,\phi)\chi^d_{-1}\right], \quad (6.29)$$

where $|\alpha^2|$, and $|\beta^2|$ are the probabilities that the state is in $\boldsymbol{L}_{\pi_d d}=\vec{1}$ and $\boldsymbol{L}_{\pi_d d}=\vec{3}$, respectively (note that $|\alpha^2|+|\beta^2|=1$). We also assume that α and β are real (so that this fitting configuration is a one-parameter fitting). We now introduce the formalism of the E asymmetry below.

$$\begin{aligned} I_2(\theta)\sim_{d\pi}\langle\boldsymbol{J}=\mathbf{2},J_z=2|\boldsymbol{J}=\mathbf{2},J_z=2\rangle_{\overline{N\Delta}} &= \alpha^2\frac{3}{8\pi}\sin^2\theta \\ &+ \beta^2\frac{1}{64\pi}\left[\sin^2\theta\left(5\cos^2\theta-1\right)^2+50\sin^4\theta\cos^2\theta+25\sin^6\theta\right] \\ &+ \alpha\beta\frac{1}{8\pi}\sqrt{\frac{3}{2}}\sin^2\theta\left(5\cos^2\theta-1\right), \end{aligned} \quad (6.30)$$

and,

$$\begin{aligned} I_0(\theta)\sim_{d\pi}\langle\boldsymbol{J}=\mathbf{2},J_z=0|\boldsymbol{J}=\mathbf{2},J_z=0\rangle_{\overline{N\Delta}} &= \alpha^2\left[\frac{1}{8\pi}\sin^2\theta+\frac{1}{2\pi}\cos^2\theta\right] \\ &+ \beta^2\frac{3}{16\pi}\left[\sin^2\theta\left(5\cos^2\theta-1\right)^2+\cos^2\theta\left(5\cos^2\theta-3\right)^2\right] \\ &+ \alpha\beta\frac{1}{4\pi}\left[\sqrt{\frac{3}{2}}\sin^2\theta\left(5\cos^2\theta-1\right)\right] \\ &+ \alpha\beta\frac{1}{4\pi}\left[-\sqrt{6}\cos^2\theta\left(5\cos^2\theta-3\right)\right], \end{aligned} \quad (6.31)$$

and,

$$E(\cos\theta)=\frac{I_0(\theta)-I_2(\theta)}{I_0(\theta)+I_2(\theta)}. \quad (6.32)$$

6.4.2 Measuring the Beam-Target E Asymmetry

Previously we mentioned that the remaining background is the ρ and non-resonant background. Since it is difficult to separate the signal and remaining background events, the background, can only be subtracted. In section 6.3.1 we identified a background kinematic region (see Figure 6.28) that likely resembles the remaining background in the $d\pi^{\pm}$ regions (see Figure 6.27). Moreover, section 6.3.2 discussed the Ξ^2 fitting algorithm to obtain the scaling factors ε to match the background statistics of both regions. In this section, we introduce a procedure to subtract the remaining background (we applied this procedure individually for each run period since the scaling factors ε are different, see Table 6.3):

- Select events in the signal region (i.e., $E_\gamma < 1.2\,\text{GeV}$, and $IM(\pi^+\pi^-) < 0.6\,\text{GeV}$); then boost into the $(d\pi^+)$ rest frame for events with $IM(d\pi^+) < 2.25\,\text{GeV}$ and $IM(d\pi^-) > 2.25\,\text{GeV}$, and boost into the $(d\pi^-)$ rest frame for events with $IM(d\pi^-) < 2.25\,\text{GeV}$ and $IM(d\pi^+) > 2.25\,\text{GeV}$ (see Figure 6.27). Denote the total yields (signal plus remaining background) as $Y^{\uparrow\uparrow}$, and $Y^{\downarrow\uparrow}$, where $Y^{\uparrow\uparrow}$, and $Y^{\downarrow\uparrow}$ are the yields (combining events from both $d\pi^\pm$ systems) when the helicity of the photon and the direction of the target polarization vector are antiparallel and parallel, respectively.

- Select events in the background region (i.e., $E_\gamma < 1.2\,\text{GeV}$, and $IM(\pi^+\pi^-) \geq 0.6\,\text{GeV}$); then boost into the $(d\pi^+)$ rest frame for events with $IM(d\pi^+) < 2.25\,\text{GeV}$ and $IM(d\pi^-) > 2.25\,\text{GeV}$, and boost into the $(d\pi^-)$ rest frame for events with $IM(d\pi^-) < 2.25\,\text{GeV}$ and $IM(d\pi^+) > 2.25\,\text{GeV}$ (see Figure 6.27). Denote the background yields as $Y_{BG}^{\uparrow\uparrow}$, and $Y_{BG}^{\downarrow\uparrow}$, similarly, $Y_{BG}^{\uparrow\uparrow}$, and $Y_{BG}^{\downarrow\uparrow}$ are the yields (combining events from both $d\pi^\pm$ systems) when the helicity of the photon and the direction of the target polarization vector are antiparallel and parallel, respectively.

- Scale the background yields by ε to *match the remaining background in the signal region,*

- Subtract the *remaining background in the signal region* to obtain the signal yields (events from the $N\Delta$ decay):

$$Y_{N\Delta}^{\uparrow\uparrow} = Y^{\uparrow\uparrow} - \epsilon Y_{BG}^{\uparrow\uparrow} \quad , \quad Y_{N\Delta}^{\downarrow\uparrow} = Y^{\downarrow\uparrow} - \epsilon Y_{BG}^{\downarrow\uparrow}.$$

Note that this step is carried out bin by bin because values of $Y_{BG}^{\downarrow\uparrow}$ and $Y_{BG}^{\uparrow\uparrow}$ might be different for different measuring $(\cos\theta_d)$ bins, but the scaling ε is assumed to be constant. And, statistical uncertainty on ε was propagated into the $Y_{N\Delta}^{\uparrow\uparrow}$, and $Y_{N\Delta}^{\downarrow\uparrow}$).

- Compute the following equation bin by bin $(\cos\theta_d)$:

$$E(\cos\theta_d) = \frac{1}{\overline{P_\gamma}} \frac{1}{P_{target}} \frac{Y_{N\Delta}^{\uparrow\uparrow}(\cos\theta_d) - Y_{N\Delta}^{\downarrow\uparrow}(\cos\theta_d)}{Y_{N\Delta}^{\uparrow\uparrow}(\cos\theta_d) + Y_{N\Delta}^{\downarrow\uparrow}(\cos\theta_d)}, \tag{6.33}$$

where P_{target} is the target polarization magnitude, and $\overline{P_\gamma}$ is the weighted average of the photon polarizations P_γ [63]. The angle θ_d is the polar angle of the final-state deuterons in the $(d\pi^+)$ rest frame for events with $IM(d\pi^+) < 2.25\,\text{GeV}$ and $IM(d\pi^-) > 2.25\,\text{GeV}$, while it is the polar angle of the final-state deuterons in the $(d\pi^-)$ rest frame for events with $IM(d\pi^-) < 2.25\,\text{GeV}$ and $IM(d\pi^+) > 2.25\,\text{GeV}$ (see Figure 6.27).

Finally, we applied the above procedure individually for all Silver and Gold 2 period data, and then computed the weighted average (see below) of the results from all the run periods:

$$\overline{E}(\cos\theta_d) = \frac{\sum\limits_t \left(1/\sigma_t^2\right) E_t(\cos\theta_d)}{\sum\limits_t 1/\sigma_t^2} \;,\; \frac{1}{\sigma^2_{\overline{E}}} = \sum_t \frac{1}{\sigma_t^2}, \tag{6.34}$$

where the summation is taken over all the run periods (the Silver 1, 2, 3, 4, 5, and Gold 2 data sets). The combined E asymmetry values were fitted using formulas discussed previously (see Section 6.4.1). Figure 6.29 shows the combined measured E asymmetry as a function of $\cos\theta_d$. In particular, the left plot of Figure 6.29 was fitted with the configuration $\boldsymbol{J}_{\overline{N\Delta}} = \mathbf{2}$ and $\boldsymbol{L}_{d\pi_d} = \overrightarrow{1}$, while the right plot was fitted with the configuration $\boldsymbol{J}_{\overline{N\Delta}} = \mathbf{2}$ and $\boldsymbol{L}_{d\pi_d} = \overrightarrow{3}$. It is apparent that the E asymmetry values are not "flat" around +1, thus the hypothesis $\boldsymbol{J}_{\overline{N\Delta}} = \mathbf{1}$ and $\boldsymbol{L}_{d\pi_d} = \overrightarrow{1}$ should be discarded. In detail, Table 6.4 provides the fitted values of a_0^2 (for the configuration $\boldsymbol{J}_{\overline{N\Delta}} = \mathbf{2}$ and $\boldsymbol{L}_{d\pi_d} = \overrightarrow{1}$), and b_+^2, b_0^2, and c_0^2 (for the configuration $\boldsymbol{J}_{N\Delta} = \mathbf{2}$ and $\boldsymbol{L}_{d\pi_d} = \overrightarrow{3}$). Notice that the value of a_0^2 is consistent with the Clebsch–Gordan coefficient for a system with two units of angular momentum decaying into two subsystems each with one unit of angular momentum (the numerical value is $\left(\sqrt{2/3}\right)^2 \approx 0.67$), i.e.,

$$|\boldsymbol{J} = \mathbf{2}, J_z = 0\rangle_{\overline{N\Delta}} = \sqrt{\frac{1}{6}}\,|\mathbf{1}, -1, \mathbf{1}, +1\rangle + \sqrt{\frac{2}{3}}\,|\mathbf{1}, 0, \mathbf{1}, 0\rangle + \sqrt{\frac{1}{6}}\,|\mathbf{1}, +1, \mathbf{1}, -1\rangle\,. \tag{6.35}$$

We considered this as a "hint" that the $\overline{N\Delta}$ is a real state with a defined intrinsic spin. In addition, the fitting values for the three coefficients b_+^2, b_0^2, and c_0^2 of the configuration $\boldsymbol{J}_{N\Delta} = \mathbf{2}$ and $\boldsymbol{L}_{d\pi_d} = \overrightarrow{3}$ are much different from the Clebsch–Gordan coefficients. Thus, we are inclined to conclude that according to the data the configuration $\boldsymbol{J}_{N\Delta} = \mathbf{2}$ and $\boldsymbol{L}_{d\pi_d} = \overrightarrow{1}$ is more likely. Furthermore, in Figure 6.30 we show the fitting result for the third configuration, where we consider a superposition of $\boldsymbol{L}_{d\pi_d} = \overrightarrow{1}$, and $\boldsymbol{L}_{d\pi_d} = \overrightarrow{3}$; as expected, the fit suggests that $\boldsymbol{J}_{\overline{N\Delta}} = \mathbf{2}$ and $\boldsymbol{L}_{d\pi_d} = \overrightarrow{1}$ is much more probable.

$L_{d\pi_d} = \overrightarrow{1}$		$L_{d\pi_d} = \overrightarrow{3}$		
	a_0^2	b_+^2	b_0^2	c_0^2
Value	0.53±0.15	0.46±0.25	0.00±0.12	0.35±0.17
χ^2/dof	0.76	0.89		

Table 6.4: Fitted values of a_0^2 (for the configuration $\boldsymbol{J}_{\overline{N\Delta}} = \mathbf{2}$ and $\boldsymbol{L}_{d\pi_d} = \overrightarrow{1}$), and b_+^2, b_0^2, and c_0^2 (for the configuration $\boldsymbol{J}_{\overline{N\Delta}} = \mathbf{2}$ and $\boldsymbol{L}_{d\pi_d} = \overrightarrow{3}$).

Lastly, we performed two necessary studies: first, selecting events with $E_\gamma > 1.4$ GeV and $IM(\pi^+\pi^-) < 0.6$ GeV ((i.e., the region where the 3-body $d\pi\pi$ non-resonant background dominates) and second, selecting events with $E_\gamma < 1.2$ GeV

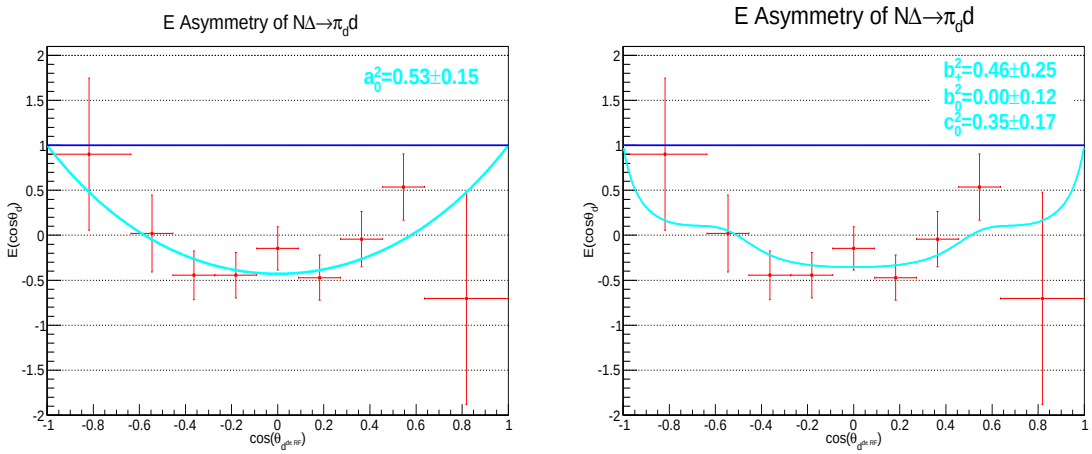

Figure 6.29: E asymmetry vs. $\cos\theta_d$. Left: The histogram is fitted with the formula for the $\boldsymbol{J}_{\overline{N\Delta}} = \mathbf{2}$ and $\boldsymbol{L}_{d\pi_d} = \overrightarrow{1}$ configuration. Right: The histogram is fitted with the formula for the $\boldsymbol{J}_{\overline{N\Delta}} = \mathbf{2}$ and $\boldsymbol{L}_{d\pi_d} = \overrightarrow{3}$ configuration. It is obvious that $E(\cos\theta_d) \neq +1$, so the $\boldsymbol{J}_{\overline{N\Delta}} = \mathbf{1}$ and $\boldsymbol{L}_{d\pi_d} = \overrightarrow{1}$ hypothesis should be discarded.

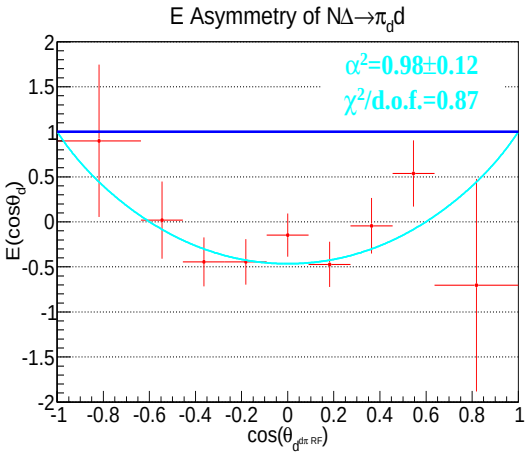

Figure 6.30: E asymmetry vs. $\cos\theta_d$. The histogram is fitted with the formula for the superposition of $\boldsymbol{L}_{d\pi_d} = \overrightarrow{1}$ and $\boldsymbol{L}_{d\pi_d} = \overrightarrow{3}$ configuration. The fit suggests the $\boldsymbol{L}_{d\pi_d} = \overrightarrow{1}$ component dominates.

and $IM(\pi^+\pi^-) > 0.6$ (i.e., the region where the ρ background dominates) and obtain the E asymmetry for both regions. Figures 6.31 and 6.32 show the result; it is apparent that these background events do not share the same physics as our signal events (both plots show a linearly decreasing E asymmetry).

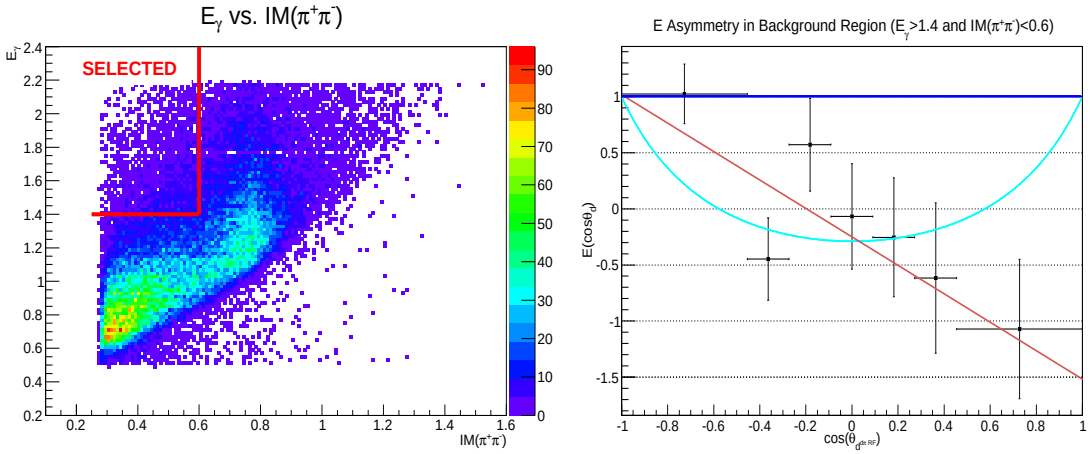

Figure 6.31: Left: E_γ vs. $IM(\pi^+\pi^-)$ showing the selected 3-body $d\pi\pi$ non-resonant background region employed to study the E asymmetry of general background events. Right: E asymmetry vs. $\cos\theta_d$ for selected *background* events showing in the left histogram.

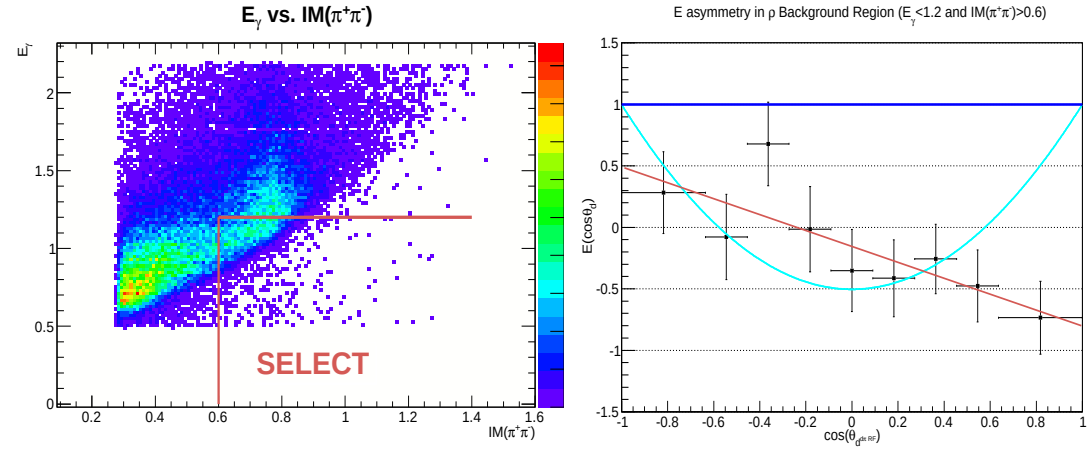

Figure 6.32: Left: E_γ vs. $IM(\pi^+\pi^-)$ showing the selected ρ background region employed to study the E asymmetry of general background events. Right: E asymmetry vs. $\cos\theta_d$ for selected *background* events showing in the left histogram.

6.5 Systematics Studies

In this section, we present various systematics studies to test the robustness of our fitting result a_0^2 for the configuration $\boldsymbol{J}_{N\Delta} = 2$ and $\boldsymbol{L}_{d\pi_d} = \overrightarrow{1}$ —since I showed that if the $\overline{N\Delta}$ exists, it is dominantly in $\boldsymbol{J}_{N\Delta} = 2$ and $\boldsymbol{L}_{d\pi_d} = \overrightarrow{1}$ state. In detail, we will vary the ρ scaling factors, loosen the E_γ cut, tighten the $IM(\pi^+\pi^-)$ cut, and lastly, loosen the BDT cut. The first test focuses on the effect on the E asymmetry from our estimation of the ρ scaling factors, while the next two test concentrate on our

$\overline{N\Delta}$ event selection (or equivalently, how well we rejected the remaining ρ and non-resonant backgrounds). The next test is to study how the target-material background would dilute the final E asymmetry measurements. And the last test is to study the effect on the E asymmetry of reducing the target and beam polarizations.

6.5.1 Systematic Effects from Varying the ρ Scaling Factors

As mentioned in Section 6.3, the ρ scaling factors ϵ were estimated (for each run period) by employing an incoherent fitting algorithm. However, the final-state interference between the ρ and the $\overline{N\Delta}$ might result in larger or smaller scaling factors. Unfortunately, we could not model the interference. Therefore, we could only quantify the effect on the final E asymmetry measurements by purposely varying the previously obtained scaling factors ϵ. We decided to add (subtract) $5\sigma_\epsilon$ and studied the efffect on the E asymmetry measurements. We presumed that $\epsilon \pm 5\sigma_\epsilon$ is a sufficient interval (to cover the values of the ratios $N_{BG_{SignalRegion}}/N_{BG_{BackgroundRegion}}$ as shown in Table 6.3). Table 6.5 presents the numerical values for the new ρ scaling factors, while Table 6.6 provides the fitted values of a_0^2 (for the configuration $\boldsymbol{J}_{\overline{N\Delta}} = \mathbf{2}$ and $\boldsymbol{L}_{d\pi_d} = \overrightarrow{1}$). In addition, Figure 6.33 (6.34) shows the fitting result using the scaling factors $\epsilon - 5\sigma_\epsilon$ ($\epsilon + 5\sigma_\epsilon$). Next, we present the numerical values of $E_{TEST} - E_{FINAL}$ for the nine angular bins in Table 6.10.

Run Period	ϵ	$\epsilon + 5\sigma_\epsilon$	$\epsilon - 5\sigma_\epsilon$
Gold 2	0.73±0.05	0.98	0.48
Silver 1&2	0.62±0.06	0.92	0.32
Silver 3	0.60±0.10	1.10	0.10
Silver 4	0.58±0.07	0.93	0.23
Silver 5	0.80±0.05	1.05	0.55

Table 6.5: The scaling factor ϵ for all run periods. The last two columns present the new scaling factors we used in the first systematic study.

$\epsilon - 5\sigma_\epsilon$	a_0^2	$\epsilon + 5\sigma_\epsilon$	a_0^2
Value	0.49±0.14	Value	0.56±0.16

Table 6.6: Fitted values of a_0^2 for configuration $\boldsymbol{J}_{\overline{N\Delta}} = \mathbf{2}$ and $\boldsymbol{L}_{d\pi_d} = \overrightarrow{1}$ for the first systematic study.

6.5.2 Systematic Effects from Loosening the E_γ Cut

As shown in Figure 6.26, a cut on the E_γ at 1.2 GeV is optimal in selecting the $\overline{N\Delta}$ signal events. For this systematic study, we loosened this cut to 1.6 GeV. A new set

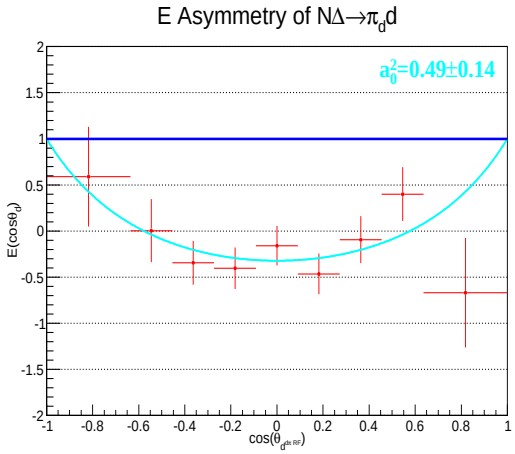

Figure 6.33: E asymmetry vs. $\cos\theta_d$. The histogram is fitted with the formula for $\boldsymbol{J}_{\overline{N\Delta}} = \mathbf{2}$ and $\boldsymbol{L}_{d\pi_d} = \overrightarrow{1}$ configuration. This is obtained using $\epsilon - 5\sigma_\epsilon$ scaling factors (this is part 1 of the first systematic study).

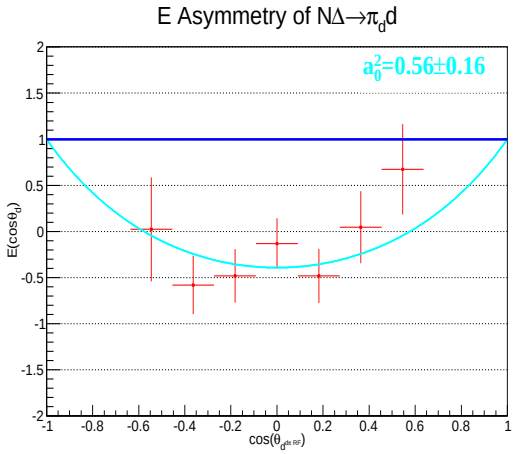

Figure 6.34: E asymmetry vs. $\cos\theta_d$. The histogram is fitted with the formula for $\boldsymbol{J}_{\overline{N\Delta}} = \mathbf{2}$ and $\boldsymbol{L}_{d\pi_d} = \overrightarrow{1}$ configuration. This is obtained using $\epsilon + 5\sigma_\epsilon$ scaling factors (this is part 2 of the first systematic study).

of scaling factors ϵ was estimated. Note that the new values of ϵ would be smaller since there are fewer additonal events—events which otherwise would be rejected by the 1.2 GeV cut—in the signal region than in the background region when the cut is loosened to 1.6 GeV (again see Figure 6.26). Table 6.8 presents the new numerical values for the ρ scaling factors, while Table 6.9 provides the fitted values of a_0^2 (for the configuration $\boldsymbol{J}_{\overline{N\Delta}} = \mathbf{2}$ and $\boldsymbol{L}_{d\pi_d} = \overrightarrow{1}$). In addition, in Figure 6.35 presents the fitting result. Finally, we present the numerical values of $E_{TEST} - E_{FINAL}$ for the nine angular bins in Table 6.10.

$\cos\theta^{d}_{d\pi\ \mathrm{RF}}$	$\lvert E_{TEST} - E_{FINAL}\rvert$	
	$\epsilon - 5\sigma_\epsilon$	$\epsilon + 5\sigma_\epsilon$
-0.818	0.310	1.957
-0.545	0.160	0.003
-0.364	0.100	0.136
-0.182	0.039	0.039
0.000	0.013	0.015
$+0.182$	0.006	0.010
$+0.364$	0.051	0.089
$+0.545$	0.137	0.138
$+0.818$	0.033	1.783

Table 6.7: Differences $|E_{TEST} - E_{FINAL}|$ (for the first systematic study).

Run Period	ϵ
Gold 2	0.45±0.02
Silver 1&2	0.43±0.03
Silver 3	0.49±0.05
Silver 4	0.40±0.03
Silver 5	0.51±0.02

Table 6.8: The scaling factor ϵ for all run periods for E_γ <1.6 GeV (for the second systematic study).

	a_0^2
Value	0.49±0.14

Table 6.9: Fitted values of a_0^2 (for the configuration $\boldsymbol{J}_{\overline{N\Delta}} = \mathbf{2}$ and $\boldsymbol{L}_{d\pi_d} = \overrightarrow{1}$) for E_γ <1.6 GeV (the second systematic study).

6.5.3 Systematic Effects from Tightening the $IM(\pi^+\pi^-)$ Cut

In this study we tighten the $IM(\pi^+\pi^-)$ cut from 0.60 GeV to 0.45 GeV (only for signal events); i.e., to select the signal events the cuts are now $E_\gamma < 1.20$ GeV, and $IM(\pi^+\pi^-) < 0.45$ GeV). Note that the cuts for the background region are still the same as before (i.e., for the background region the cuts are still $E_\gamma < 1.20$ GeV, and $IM(\pi^+\pi^-) \geq 0.60$ GeV). By tightening the $IM(\pi^+\pi^-)$ cut, the signal sample should be cleaner (fewer remaining background events) as well as smaller in statistics. As before, a new set of scaling factors ϵ was estimated, see Table 6.11. Table 6.12 provides the fitted values of a_0^2 (for configuration $\boldsymbol{J}_{\overline{N\Delta}} = \mathbf{2}$ and $\boldsymbol{L}_{d\pi_d} = \overrightarrow{1}$), and Figure 6.36

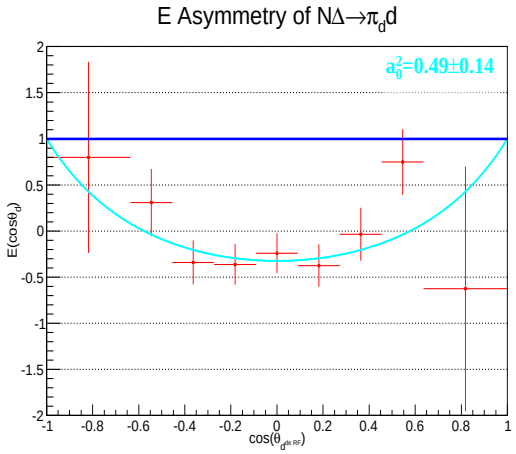

Figure 6.35: E asymmetry vs. $\cos\theta_d$. The histogram is fitted with the formula for the $\boldsymbol{J}_{\overline{N\Delta}} = \mathbf{2}$ and $\boldsymbol{L}_{d\pi_d} = \overrightarrow{1}$ configuration. This is the result for the second systematic study (loosening the E_γ cut to 1.6 GeV).

$\cos\theta^d_{d\pi\ \mathrm{RF}}$	$\lvert E_{TEST} - E_{FINAL}\rvert$
-0.818	0.102
-0.545	0.290
-0.364	0.104
-0.182	0.081
0.000	0.096
$+0.182$	0.096
$+0.364$	0.007
$+0.545$	0.212
$+0.818$	0.077

Table 6.10: Differences $|E_{TEST} - E_{FINAL}|$ (for the second systematic study).

illustrates the fitting result. In addition, Table 6.13 presents the numerical values of $E_{TEST} - E_{FINAL}$ for the nine angular bins.

Run Period	ϵ
Gold 2	0.34±0.04
Silver 1&2	0.28±0.04
Silver 3	0.40±0.12
Silver 4	0.33±0.06
Silver 5	0.43±0.03

Table 6.11: The scaling factor ϵ for all run periods for $IM(\pi^+\pi^-)$ <0.45 GeV (the third systematic study).

	a_0^2
Value	0.51±0.16

Table 6.12: Fitted values of a_0^2 (for the configuration $\boldsymbol{J}_{\overline{N\Delta}} = \mathbf{2}$ and $\boldsymbol{L}_{d\pi_d} = \overrightarrow{1}$) for $IM(\pi^+\pi^-)$ <0.45 GeV (the third systematic study).

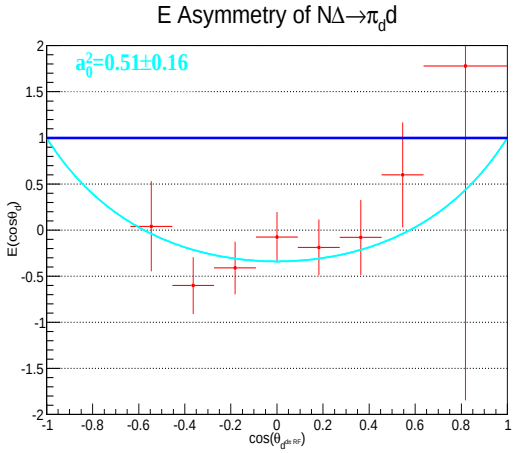

Figure 6.36: E asymmetry vs. $\cos\theta_d$. The histogram is fitted with the formula for the$\boldsymbol{J}_{\overline{N\Delta}} = \mathbf{2}$ and $\boldsymbol{L}_{d\pi_d} = \overrightarrow{1}$ configuration. This is the result for the third systematic study (tightening the $IM(\pi^+\pi^-)$ cut to 0.45 GeV).

$\cos\theta^d_{d\pi\ \mathrm{RF}}$	$\lvert E_{TEST} - E_{FINAL}\rvert$
−0.818	4.912
−0.545	0.021
−0.364	0.156
−0.182	0.032
0.000	0.069
+0.182	0.283
+0.364	0.037
+0.545	0.063
+0.818	2.482

Table 6.13: Differences $|E_{TEST} - E_{FINAL}|$ (for the third systematic study).

6.5.4 Systematic Effects from Loosening the BDT-Output Cut

This systematic test studies the dilution effect from the target-material background. Recall from Section 6.2.1 that a cut on the BDT-output variable was at 0.195. We

illustrated that the after-cut sample has an insignificant number of target-material background events (see Section 6.2), hence we did not make any correction to the final E asymmetry measurements. Nevertheless, it is informative to loosen the BDT-output cut and to study the changes in the E asymmetry measurements. Particularly, we placed the BDT-output cut at 0.0 and then obtained the E asymmetry values (note that there was no new set of scaling factors ϵ). Table 6.14 provides the fitted values of a_0^2 (for configuration $\boldsymbol{J}_{N\Delta} = \mathbf{2}$ and $\boldsymbol{L}_{d\pi_d} = \overrightarrow{1}$) and Figure 6.37 shows the fitting result. Lastly, In Table 6.15 we present the numerical values of $E_{TEST} - E_{FINAL}$ for the nine angular bins.

	a_0^2
Value	0.47±0.15

Table 6.14: Fitted values of a_0^2 (for the configuration $\boldsymbol{J}_{\overline{N\Delta}} = \mathbf{2}$ and $\boldsymbol{L}_{d\pi_d} = \overrightarrow{1}$) for BDT-output>0.0 (the fourth systematic study).

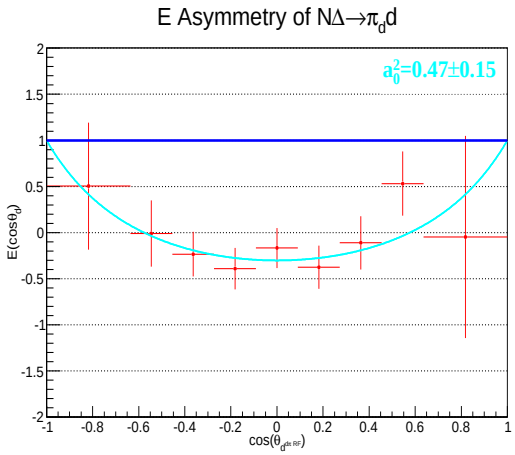

Figure 6.37: E asymmetry vs. $\cos\theta_d$. The histogram is fitted with the formula for the $\boldsymbol{J}_{N\Delta} = \mathbf{2}$ and $\boldsymbol{L}_{d\pi_d} = \overrightarrow{1}$ configuration. This is the result for the fourth systematic study (loosening the BDT-output cut to 0.0).

6.5.5 Systematic Effects from Polarization Uncertanties

In this section, we provide result from our systematic test on the uncertainties of the beam and target polarizations—the numerical values for the total uncertainties (systematic and statistical) can be obtained from Table 3.1. To quantify the systematic effect we computed the E asymmetry but with reduced beam and target polarizations; i.e., *both* quantities were reduced by one standard deviation of their respective total uncertainties. The effect on the E asymmetry, and changes on the fitting parameters

$\cos\theta^{d}_{d\pi\ \mathrm{RF}}$	$\lvert E_{TEST} - E_{FINAL}\rvert$
-0.818	0.396
-0.545	0.030
-0.364	0.211
-0.182	0.053
0.000	0.021
$+0.182$	0.097
$+0.364$	0.068
$+0.545$	0.006
$+0.818$	0.656

Table 6.15: Differences $|E_{TEST} - E_{FINAL}|$ (for the fourth systematic study).

are shown in Figure 6.38 and Table 6.16. Lastly, Table 6.17 presents the numerical values of $E_{TEST} - E_{FINAL}$ for the nine angular bins.

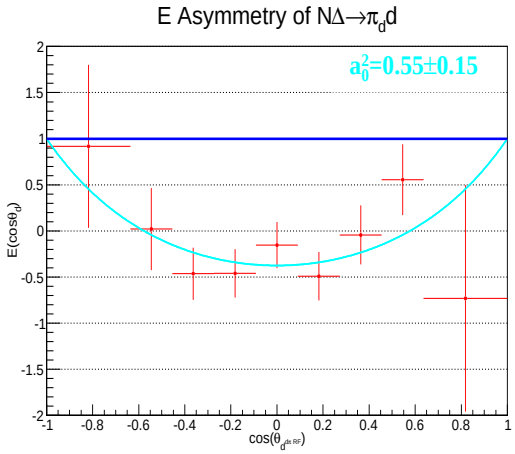

Figure 6.38: E asymmetry vs. $\cos\theta_d$. The histogram is fitted with the formula for the $\boldsymbol{J}_{\overline{N\Delta}} = \mathbf{2}$ and $\boldsymbol{L}_{d\pi_d} = \overrightarrow{1}$ configuration. This is the result for the fifth systematic study (reducing beam and target polarizations by one standard deviation of their respective total uncertainties).

	a_0^2
Value	0.56±0.16

Table 6.16: Fitted values of a_0^2 (for the configuration $\boldsymbol{J}_{\overline{N\Delta}} = \mathbf{2}$ and $\boldsymbol{L}_{d\pi_d} = \overrightarrow{1}$) for reducing beam and target polarizations by one standard deviation (the fifth systematic study).

$\cos\theta^{d}_{d\pi\ \mathrm{RF}}$	$\lvert E_{TEST} - E_{FINAL}\rvert$
-0.818	0.111
-0.545	0.013
-0.364	0.033
-0.182	0.030
0.000	0.012
$+0.182$	0.039
$+0.364$	0.014
$+0.545$	0.048
$+0.818$	0.080

Table 6.17: Differences $E_{TEST} - E_{FINAL}$ (for the fifth systematic study).

6.5.6 Sytematic Uncertainty Assignment

Previously, we described several studies to test the robustness of our fitting result a_0^2 for configuration $\boldsymbol{J}_{\overline{N\Delta}} = \mathbf{2}$ and $\boldsymbol{L}_{d\pi_d} = \overrightarrow{1}$. In this section, for each test, the systematic differences will be estimated as the differences between the final fitted values (see Table 6.4) and the fitted results obtained individually in each study. The overall systematic uncertainty is derived as a square root of the quadratic sum of the individual test's σ_{sys}. The numerical value for the overall systematic uncertainty is presented in Table 6.18 for configuration $\boldsymbol{J}_{\overline{N\Delta}} = \mathbf{2}$ and $\boldsymbol{L}_{d\pi_d} = \overrightarrow{1}$.

final-fitting result a_0^2=0.53±0.15			
	a_0^2	$\lvert\sigma_{sys}\rvert$	σ^2_{sys}
1^{st} test (part 1)	0.49	0.04	0.0016
1^{st} test (part 2)	0.56	0.03	0.0009
2^{nd} test	0.49	0.04	0.0016
3^{rd} test	0.51	0.02	0.0004
4^{th} test	0.47	0.06	0.0036
5^{th} test	0.56	0.03	0.0009
$\sigma^2_{overall}$			0.0085
$\sigma_{overall}$			0.10

Table 6.18: List of estimated σ_{sys} for all the systematic tests for a_0^2 (for the configuration $J_{\overline{N\Delta}} = \mathbf{2}$ and $L_{d\pi_d} = \overrightarrow{1}$), see text for test enumeration. The last row reports the overall systematic uncertainty.

6.6 Summary

This chapter presented the spin analysis for the *possible* $\overline{N\Delta}$ resonance structure in the reaction $\gamma d \to d\pi^+\pi^-(0)$ by measuring the E asymmetry (definition in Section 6.4.1). We described in detail the cuts to select a clean sample of $d\pi^+\pi^-$. We then introduced the Boosted Decision Trees (BDT) method to select cleanly polarized deuteron events (by rejecting target-material background). A procedure to subtract the remaining ρ and non-resonant background was implemented. The measurement of the E asymmetry is consistent with the intrinsic spin $\boldsymbol{J}_{\overline{N\Delta}} = \mathbf{2}$, which agrees with theoretical models by Mulders *et al.* [66], and Gal and Garcilazo [67, 68]. Moreover, we fitted the data seperately using two spin hypotheses ($\boldsymbol{L}_{d\pi_d} = \overrightarrow{1}$ and $\boldsymbol{L}_{d\pi_d} = \overrightarrow{3}$). We showed that the configuration $\boldsymbol{J}_{\overline{N\Delta}} = \mathbf{2}$ and $\boldsymbol{L}_{d\pi_d} = \overrightarrow{1}$ (see Figure 6.30) is more probable given the current E asymmetry measurements. We also studied several systematics tests to quantify the robustness of the final fitting result for a_0^2 of the configuration $\boldsymbol{J}_{\overline{N\Delta}} = \mathbf{2}$ and $\boldsymbol{L}_{d\pi_d} = \overrightarrow{1}$. The systematic assignment for the fitted parameters is presented in Table 6.18. Lastly, the numerical values of the measured E asymmetry are reported in Table 6.19.

$\cos\theta^d_{d\pi\ \mathrm{RF}}$	E	σ_{stat}	σ_{sys}
-0.818	$+0.900$	0.846	5.313
-0.545	$+0.019$	0.428	0.333
-0.364	-0.445	0.272	0.330
-0.182	-0.443	0.253	0.119
0.000	-0.147	0.240	0.122
$+0.182$	-0.472	0.252	0.317
$+0.364$	-0.430	0.308	0.130
$+0.545$	$+0.537$	0.369	0.298
$+0.818$	-0.703	1.180	3.128

Table 6.19: Numerical values of the measured E asymmetry with the statistical and systematic uncertainties.

Chapter 7

Final Results, Discussion, and Conclusions

In this work we presented in detail the procedures to obtain the E asymmetry measurements for $p\pi^-$, $K^0\Lambda$, and $K^0\Sigma^0$ channels. These measurements are the first-ever results for neutron data which will significantly improve PWA models to disentangle the nucleon spectrum. Moreover, the analysis on the reaction $\gamma d \to d\pi^+\pi^-(0)$ to determine the spin of a *possible* dibaryonic $\overline{N\Delta}$ state is also the first of its kind. We now review what we have learned from the three analyses.

7.1 Summary of the E Asymmetry Measurements for $p\pi^-$ Final State

Figure 7.1 plots our measurements against the SAID models of 2012 (or CM-12) and 2014 (or ST-14) for reaction $\gamma n \to p\pi^-$ (each model is represented by two curves computed at the bin end point energies). Note that the gray bands at zero indicate the systematic uncertainties, see Section 4.4 for more detail. The main difference between the two models is the inclusion of new data for reaction $\gamma n \to n\pi^+$ from S. Strauch *et al.* which was published in 2014 [74]. Qualitatively, for the first twelve energy window Ws the two models are in good agreement, and appear to explain the data well; on the other hand, for the last nine energy windows, the two models differ significantly (see Figure 7.1)—this is because at higher photon energies there is a limited experimental data to constrain the models. As shown in Figure 7.1, the older SAID 2012 model follows our data better than the newer SAID 2014 model in the backward direction, while in the forward direction the SAID 2014 is better at explaining the data than the SAID 2012 model. Note that the current situation is not a disappointment given the fact that both models were constrained by *only* proton data. Our measurements, therefore, can significantly improve the SAID model. Furthermore, we also compared our data with another theoretical model, the Bonn-Gatchina PWA or BoGa model.

This model explains the data well for the first nine energies windows, but predicts less accurately the last twelve windows (see Figure 7.2). Note that the disagreement between the BoGa and SAID 2014 models for high energies bin were mainly due to their different schemes in amplitude calculation and their different approaches to extract resonance couplings unless there are more constraints from the experimental data. Moreover, given the lack of predictive power of these models for the neutron, we are not too surprised by the lack of agreement with our new data; we expect both model approaches to be in much better aggrement with the data once these results are fitted within those calculation schemes.

7.2 Summary of the E Asymmetry Measurements for K^0Y Final State

This thesis presents the first E asymmetry measurements for the reaction $\gamma d \to K^0 Y(p_s)$ where Y can be either Λ or Σ^0. Unfortunately, the analysis was hampered by very limited statistics. Nevertheless, we have illustrated an efficient procedure for K^0Y event selection using the Boosted Decision Tree (BDT) algorithm. Chapter 5 outlines the procedure in detail. Future analyses to obtain other asymmetry observables from the K^0Y channels can follow the outlined procedure with ease. In this section we compare our measurements with the theoretical models: SAID, KaonMAID, and BoGa.

7.2.1 Summary of the E Asymmetry Measurements for $K^0\Lambda$ Final State

We first compar the data with the SAID, and KaonMAID models on a neutron target (i.e., the models for reaction $\gamma n \to K^0\Lambda$). Figure 7.3 shows our results with the curves from the two models. Note that for each energy W, each model has two curves—each was computed at the bin end point energies. For example, in the left plot the curves were computed for $W = 1.70$ and $W = 2.02$ GeV. Notice that the two models are significantly different because of the lack of model constraints, which require measurements on the neutron. For the lower energy window ($1.70 < W < 2.02$ GeV) both models are equally adequate given the data. For the second energy window ($2.02 < W < 2.34$ GeV) the SAID model appears to match the data better.

We next compare the data with the SAID, KaonMAID, and BoGa models, but for the proton target (ie., the models for reaction $\gamma p \to K^+\Lambda$). Interestingly, it appears that the KaonMAID, and BoGa models for proton data explain better the neutron data than the models for neutron data, see Figure 7.4. From this comparison, it is clear that the theoretical models for neutron data can be improved using our measurements.

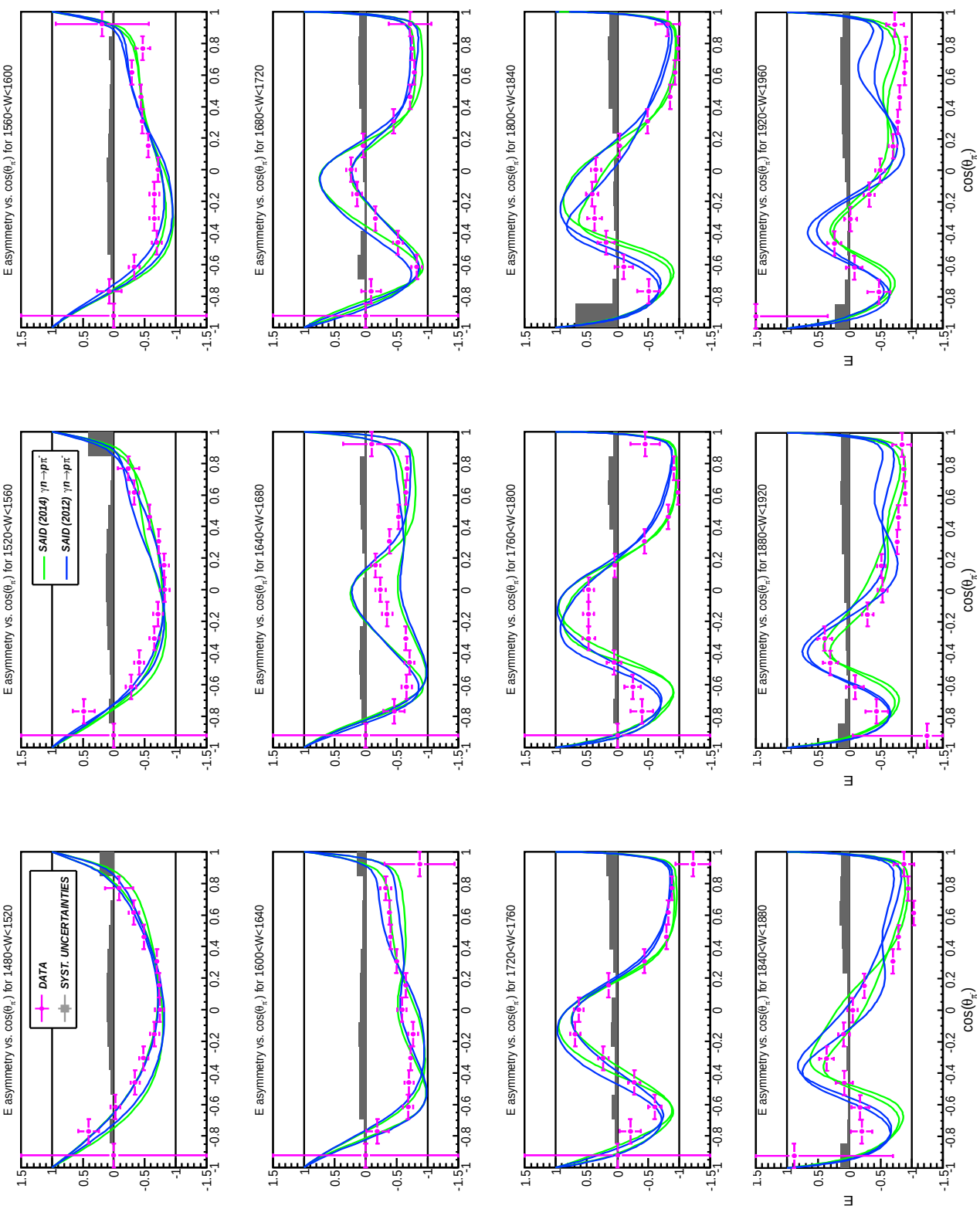
E asymmetry vs. cos(θ_π) for 1480<W<1520
DATA
SYST. UNCERTAINTIES
E asymmetry vs. cos(θ_π) for 1520<W<1560
SAID (2014) γn→pπ⁻
SAID (2012) γn→pπ⁻
E asymmetry vs. cos(θ_π) for 1560<W<1600
E asymmetry vs. cos(θ_π) for 1600<W<1640
E asymmetry vs. cos(θ_π) for 1640<W<1680
E asymmetry vs. cos(θ_π) for 1680<W<1720
E asymmetry vs. cos(θ_π) for 1720<W<1760
E asymmetry vs. cos(θ_π) for 1760<W<1800
E asymmetry vs. cos(θ_π) for 1800<W<1840
E asymmetry vs. cos(θ_π) for 1840<W<1880
E asymmetry vs. cos(θ_π) for 1880<W<1920
E asymmetry vs. cos(θ_π) for 1920<W<1960
E
cos(θ_π)

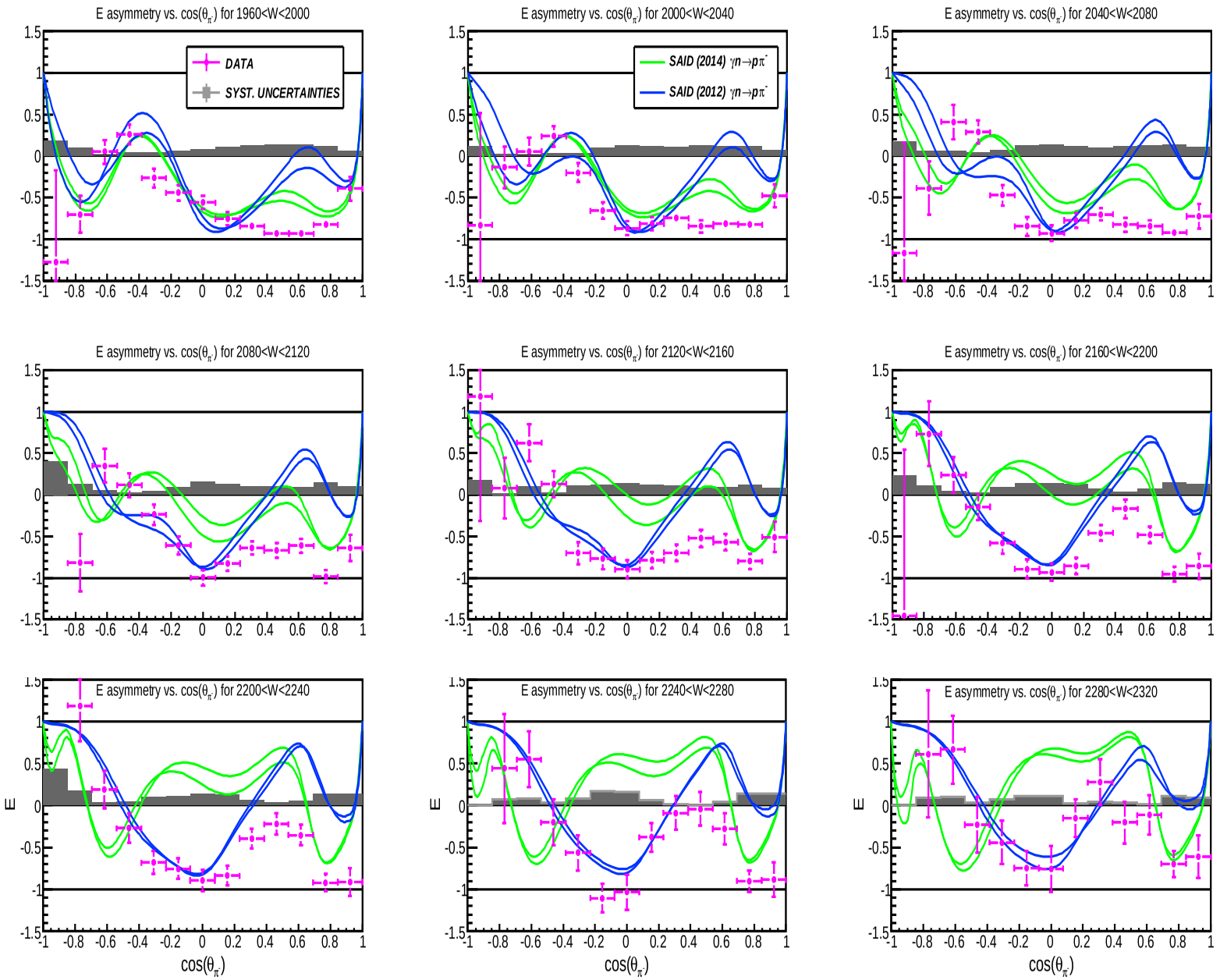

Figure 7.1: Combined E asymmetry vs. $\cos(\theta_{\pi^-})$ for the energy windows from 1480 MeV$<W<$2320 MeV. Theoretical models (CM-12 in blue and ST-14 in green) from the SAID group included. Each variant is represented by two curves indicating the energy end points of the energy window. The gray bands at zero indicate the systematic uncertaities.

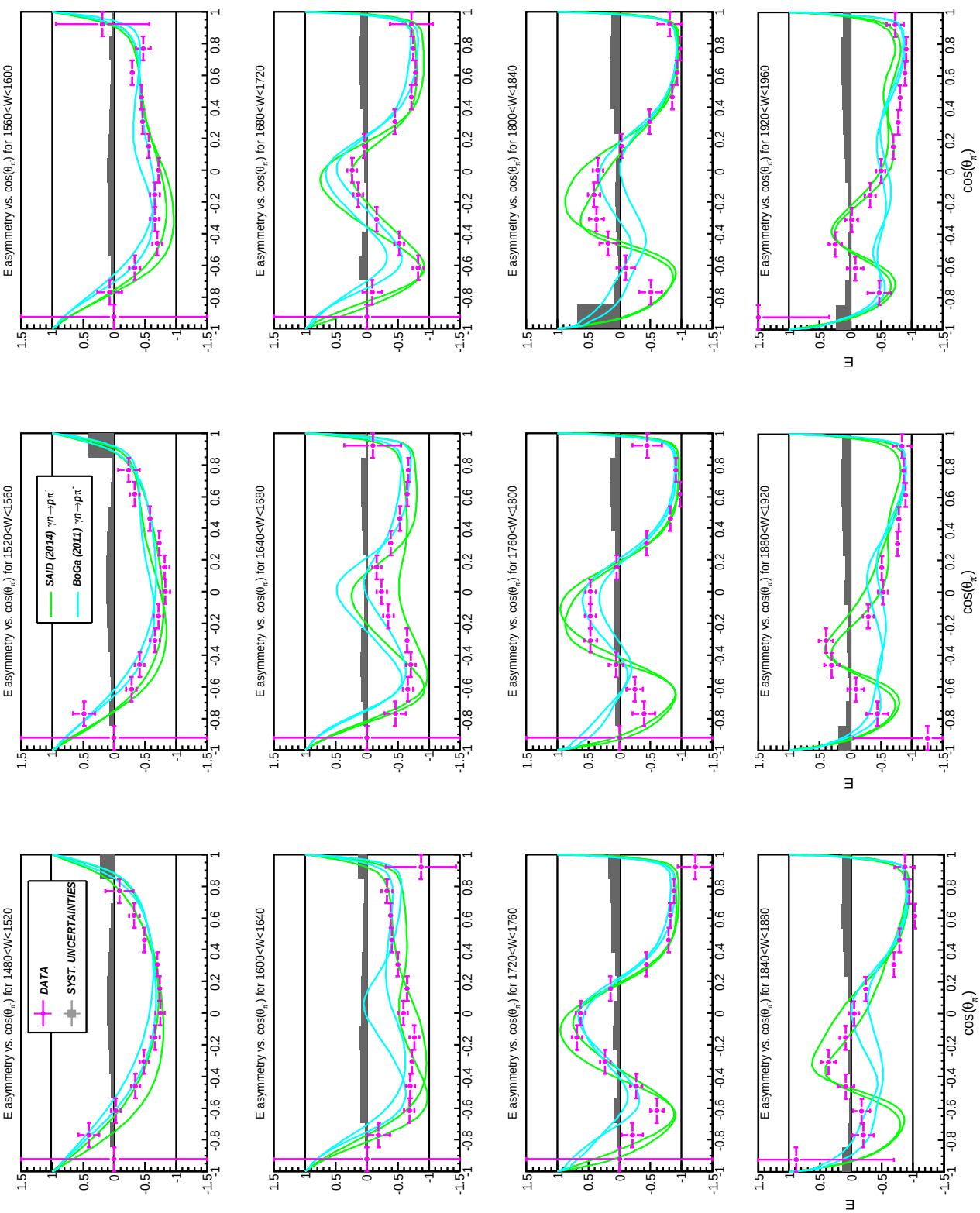
E asymmetry vs. cos(θ_π) for 1480<W<1520
E asymmetry vs. cos(θ_π) for 1520<W<1560
E asymmetry vs. cos(θ_π) for 1560<W<1600
E asymmetry vs. cos(θ_π) for 1600<W<1640
E asymmetry vs. cos(θ_π) for 1640<W<1680
E asymmetry vs. cos(θ_π) for 1680<W<1720
E asymmetry vs. cos(θ_π) for 1720<W<1760
E asymmetry vs. cos(θ_π) for 1760<W<1800
E asymmetry vs. cos(θ_π) for 1800<W<1840
E asymmetry vs. cos(θ_π) for 1840<W<1880
E asymmetry vs. cos(θ_π) for 1880<W<1920
E asymmetry vs. cos(θ_π) for 1920<W<1960
DATA
SYST. UNCERTAINTIES
SAID (2014) γn→pπ⁻
BoGa (2011) γn→pπ⁻
E
cos(θ_π)

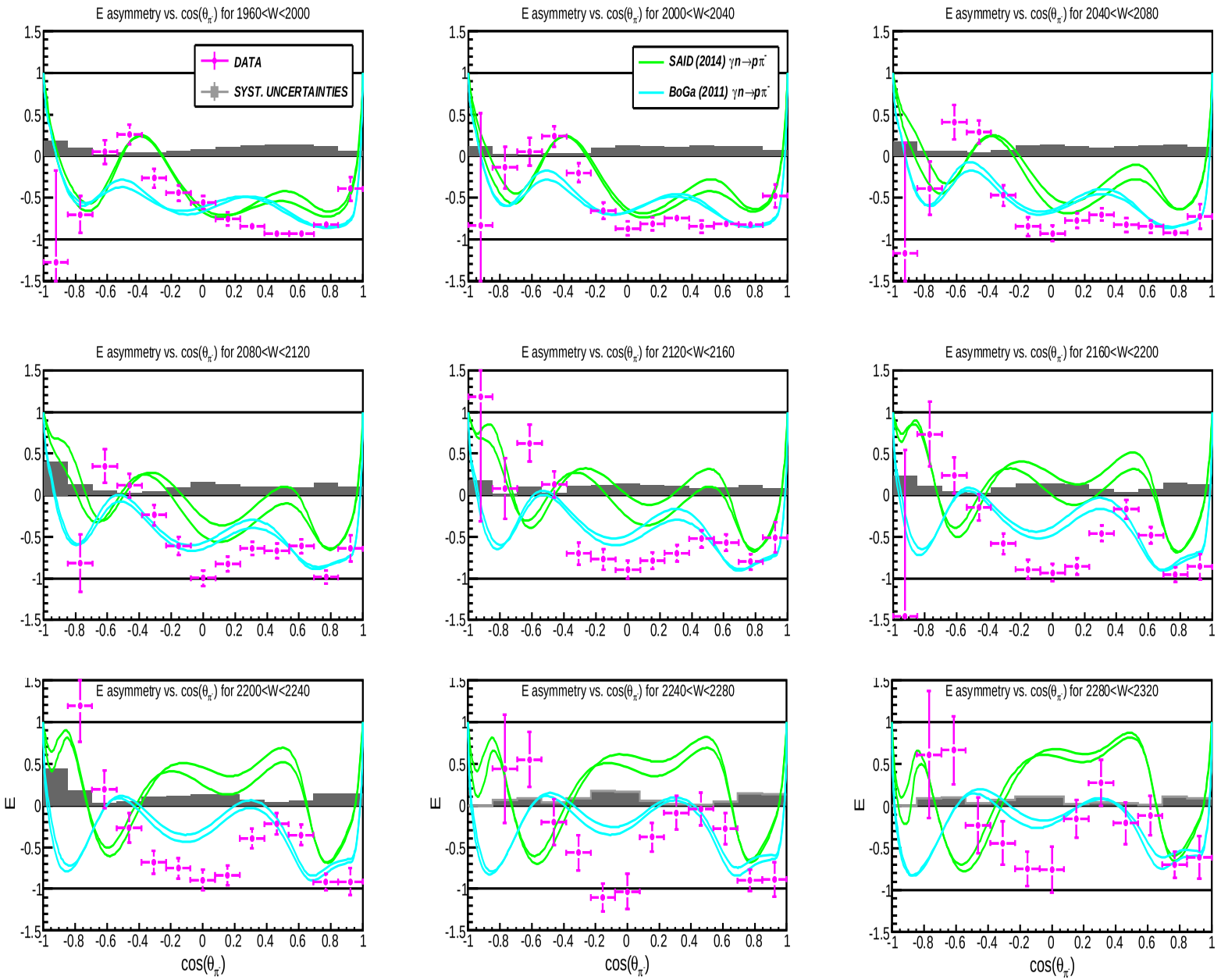

Figure 7.2: Combined E asymmetry vs. $\cos(\theta_{\pi^-})$ for the energy windows from 1480 MeV$<W<$2320 MeV. Theoretical models from the SAID (2014) and BoGa (2011) group included. Each model is represented by two curves indicating the energy end points of the energy window. The gray bands at zero indicate the systematic uncertaities.

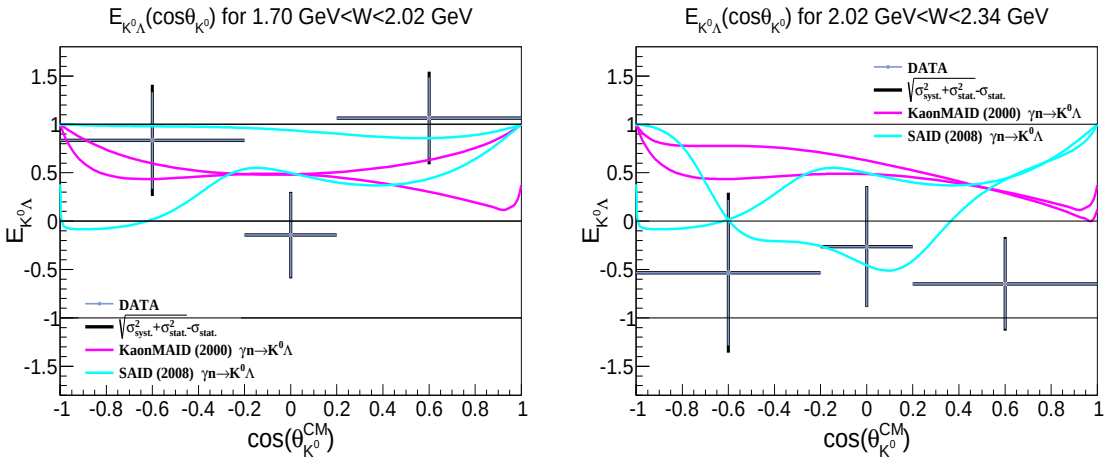

Figure 7.3: The $E_{K^0\Lambda}$ asymmetries (with systematic uncertainties included, see legends for detail) vs. $\cos\theta_{K^0}$ for the energy windows 1.7 GeV$\leq W <$2.02 GeV (left) and 2.02 GeV$\leq W <$ 2.34 GeV (right). Each model has two curves computed at the bin end point energies.

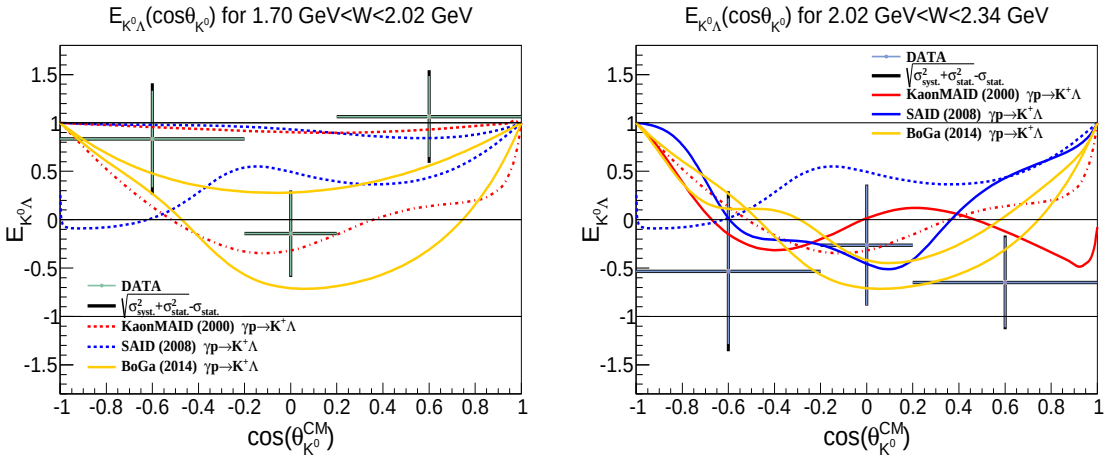

Figure 7.4: The $E_{K^0\Lambda}$ asymmetries (with systematic uncertainties included, see legends for detail) vs. $\cos\theta_{K^0}$ for the energy windows 1.7 GeV$\leq W <$2.02 GeV (left) and 2.02 GeV$\leq W <$ 2.34 GeV (right). Each model has two curves computed at the bin end point energies.

7.2.2 Summary of the E Asymmetry Measurements for $K^0\Sigma^0$ Final State

Similar comparisons were done for the $K^0\Sigma^0$ final state. In particular, we compare the data with the SAID and KaonMAID models for neutron data. The E measurements and the theoretical curves are illustrated in Figure 7.5. It appears that the SAID model follows the data better than the MAID model. Nevertheless, this is a very

qualitative statement given our low statistics situation. The comparison between our data and the models for the proton target (i.e., $\gamma p \to K^+\Sigma^0$) also indicates the KaonMAID model is less successful in explaining the data than the other models.

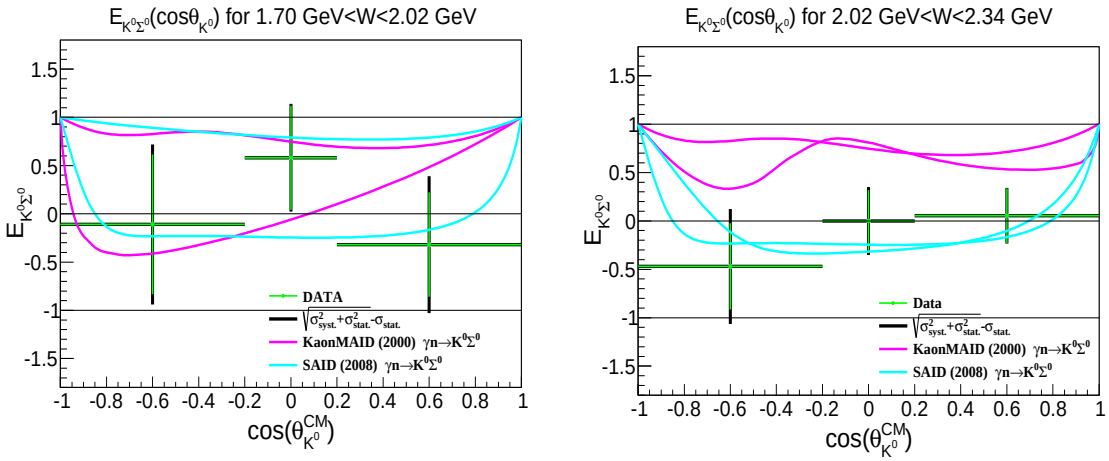

Figure 7.5: The $E_{K^0\Sigma^0}$ asymmetries (with systematic uncertainties included, see legends for detail) vs. $\cos\theta_{K^0}$ for the energy windows 1.7 GeV$\leq W <$2.02 GeV (left) and 2.02 GeV$\leq W <$ 2.34 GeV (right). Each model has two curves computed at the bin end point energies.

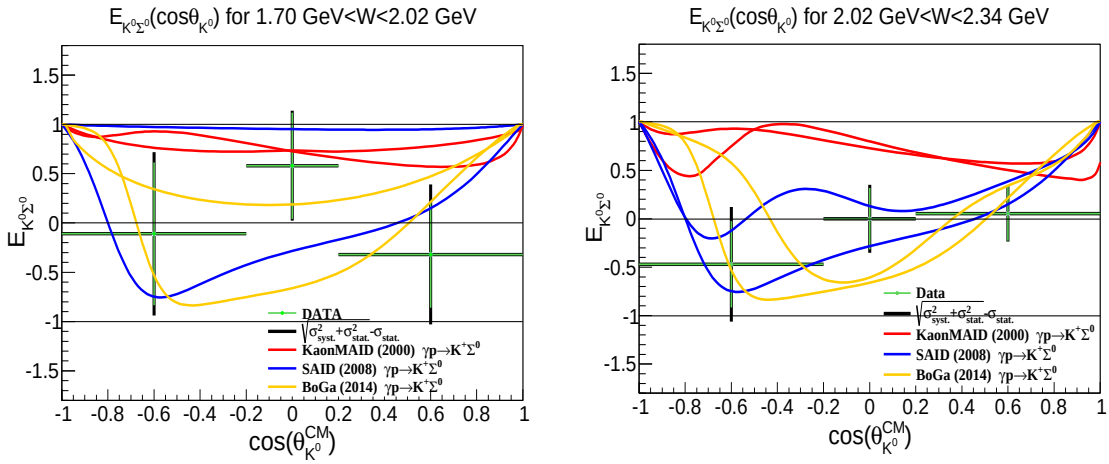

Figure 7.6: The $E_{K^0\Sigma^0}$ asymmetries (with systematic uncertainties included, see legends for detail) vs. $\cos\theta_{K^0}$ for the energy windows 1.7 GeV$\leq W <$2.02 GeV (left) and 2.02 GeV$\leq W <$ 2.34 GeV (right). Each model has two curves computed at the bin end point energies.

7.3 Summary of the E Asymmetry Measurements for $\pi_d^{\pm} d$ Final State

In Chapter 6 we presented the procedure and the result of the E asymmetry measurement for the $\pi_d^{\pm} d$ final state. Note that we must assume the $\pi_d^{\pm} d$ state is the decay product of a $\overline{N\Delta}$ bound state for this analysis result to be interpretable. We stated that the data does not support the $\boldsymbol{J}_{\overline{N\Delta}} = \mathbf{1}$ hypothesis. We then proceeded to fit the measurements of E with two other hypotheses $\boldsymbol{J}_{\overline{N\Delta}} = \mathbf{2}$ and $\boldsymbol{L}_{d\pi_d} = \{\overrightarrow{1}, \overrightarrow{3}\}$. Given the limited statistics, the simpler hypothesis $\boldsymbol{J}_{\overline{N\Delta}} = \mathbf{2}$ and $\boldsymbol{L}_{d\pi_d} = \overrightarrow{1}$ fits the data well with the fitting coefficient a_0^2 statistically consistent with the Clebsch–Gordan coefficient for a state with a defined intrinsic spin 2. In another fit where we include both $\boldsymbol{L}_{d\pi_d} = \{\overrightarrow{1}, \overrightarrow{3}\}$ components, the fit suggests that the $\overline{N\Delta}$ state is dominantly in $\boldsymbol{L}_{d\pi_d} = \overrightarrow{1}$. Moreover, we tested the $\boldsymbol{L}_{d\pi_d} = \overrightarrow{1}$ fit stability by adding and subtracting one statistical and *total*[1] standard deviation into the fit parameter and study the results as shown in Figure 7.7. In conclusion, the obtained value of the fit parameter a_0^2 of model $\boldsymbol{J}_{\overline{N\Delta}} = \mathbf{2}$ and $\boldsymbol{L}_{d\pi_d} = \overrightarrow{1}$ is reasonable and provides strong evidence to support the possible existence of the dibaryonic $\overline{N\Delta}$ state with $\boldsymbol{J}_{\overline{N\Delta}} = \mathbf{2}$.

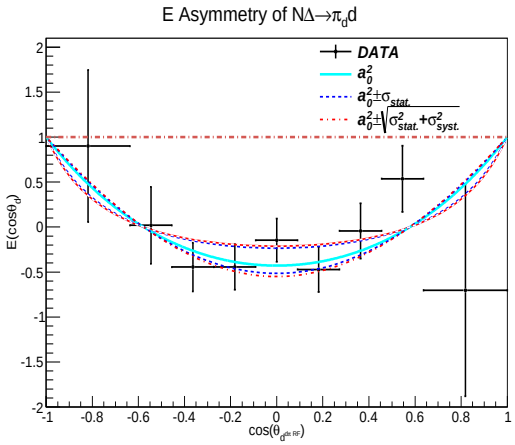

Figure 7.7: E asymmetry vs. $\cos\theta_d$. The histogram is fitted with the formula for the $\boldsymbol{J}_{\overline{N\Delta}} = \mathbf{2}$ and $\boldsymbol{L}_{d\pi_d} = \overrightarrow{1}$ configuration. The effects of including systematic and statistical uncertainties on the fitting parameters are shown.

7.4 Summary

In this chapter, we presented our final assessments when comparing our E measurement on $p\pi^-$, $K^0\Lambda$, and $K^0\Sigma^0$. Our measurement will significantly improve

[1] $\sigma_{total} = \sqrt{\sigma_{stat}^2 + \sigma_{syst}^2}$

theoretical models for pion photoproduction. The measurements on K^0Y with large statistical uncertainties will likely make a lesser impact. Nevertheless, the measurement is a successful one in terms of defining a clear procedure for future analyses to measure other observables for kaon photoproduction. Lastly, the analysis of the reaction $\gamma d \to d\pi^+\pi^-$ proved to be a constructive one as our result, that we believe, has provided strong evidence about the existence of a spin 2 dibaryonic $\overline{N\Delta}$ state.

Bibliography

[1] G. Aad *et al.*. [ATLAS Collaboration], "*Observation of a new particle in the search for the Standard Model Higgs Boson with the ATLAS Detector at the LHC,*"Phys. Lett. B **716**, 1 (2012) [arXiv:1207.7214 [hep-ex]].

[2] S. Chatrchyan *et al.* [CMS Collaboration], "*Observation of a New Boson at a Mass of 125 GeV with the CMS Experiment at the LHC,*"Phys. Lett. B **16**, 30 (2012) [arXiv:1207.7235 [hep-ex]].

[3] M. E. Peskin and D. V. Schroeder, "*An Introduction to Quantum Field Theory,*" Westview Press (1995).

[4] Wikipedia contributors. *Standard Model* [Internet]. Wikipedia, The Free Encyclopedia. Available from: https://en.wikipedia.org/wiki/Standard_Model.

[5] J. D. Gross and F. Wilczek, "*Ultraviolet Behavior of Non-Abelian Gauge Theories,*" Phys. Rev. Lett. **30**, 1343 (1973).

[6] H. D. Politzer, "*Reliable Perturbative Results for Strong Interaction?,"* Phys. Rev. Lett. **30**, 1346 (1973).

[7] H. Fritzsch, *"The History of QCD,"* CERN COURIER, Sep. 27, 2012.

[8] R.H. Dalitz, *"Les Houches Lectures,"* Gordon and Breach Science Publishers Inc. (1965).

[9] D. Faiman and A. W. Hendry, *"Harmonic-Oscillator Model for Baryons,"* Phys. Rev. **173**, 1720 (1968).

[10] R. Koniuk and N. Isgur, *"Baryon Decays in a Quark Model with Chromodynamics,"* Phys. Rev. **D** 21, 1868 (1980).

[11] S. Capstick, *"Photo- and Electroproduction of Nonstrange Baryon Resonances in the Relativistic Quark Model,"* Phys. Rev. **D** 46, 2864 (1992).

[12] S. Capstick and W. Roberts, *"$N\pi$ Decays of Baryons in a Relativised Model,"* Phys. Rev. **D** 47, 1994 (1993).

[13] S. Capstick and W. Roberts, *"Quasi-Two-Body Decays of Nonstrange Baryons,"* Phys. Rev. **D** 49, 4570 (1994).

[14] S. Capstick and W. Roberts, *"Strange Decays of Nonstrange Baryons,"* Phys. Rev. **D** 58, 074011 (1998).

[15] D. B. Lichtenberg, L. J. Keleman, *"Quark-Diquark Model of Baryons and SU(6),"* Phys. Rev. **167,** 1535 (1968).

[16] D. B. Lichtenberg, W. Namgung, E. Predazzi, and J. G. Wills, *"Baryon Masses in a Relativistic Quark-Diquark Model,"* Phys. Rev. Lett. **48**, 1653 (1982).

[17] G.D. Cates, C. W. de Jager, S. Riordan, and B. Wojtsekhowski, *"Flavor Decompossition of the Elastic Nucleon Electromagnetic Form Factors,"* Phys. Rev. Lett. **106**, 252003 (2011).

[18] R. G. Edwards, J. J. Dudek, D. G. Richards, S. J. Wallace, *"Excited State Baryon Spectroscopy from Lattice QCD,"* Phys. Rev. **D 84**, 074508 (2011).

[19] G.F. Chew, M.L. Goldberger, F.E. Low, and Y. Nambu, "*Application of Dispersion Relations to Low-Energy Meson-Nucleon Scattering*," Phys. Rev. **106,** 1345 (1957).

[20] I. S. Barker , A. Donnachie, and J. K. Storrow, "*Complete Experiments in Pseudoscalar Photoproduction*," Nucl. Phys. **B95**, 347 (1975).

[21] W. T. Chiang and F. Tabakin, "*Completeness Rules for Spin Observables in Pseudoscalar Meson Photoproduction*," Phys. Rev. **C 55**, 2054 (1997).

[22] A. M. Sandorfi *et al., "Determining Pseudoscalar Meson Photoproduction Amplitudes from Complete Experiments,"* J. Phys. G **38** 053001 (2011).

[23] D. M. Brink and G. R. Satchler, "*Angular Momentum,*" 1968 (Oxford: Oxford Univesity Press).

[24] C. G. Fasano, F. Tabakin, and B. Saghai, *"Spin Observables at Threshold for Meson Photoproduction,"* Phys. Rev. **C** 46, 2430 (1992).

[25] X. Artru, M. Elchikh, J. M. Richard, J. Soffer, and O. V. Teryaev, "*Spin Observables and Spin Structure Functions: Inequalities and Dynamics,*" Phys. Rept. 471, 1 (2009).

[26] F. J. Gilman, *"Photoproduction and Electroproduction,"* Phys. Rep. **4**, 95 (1972).

[27] A. M. Sandorfi, F. Klein *et al., "N* Resonances in Pseudoscalar-meson Photoproduction from Polarized Neutron in* $\overrightarrow{H} \cdot \overrightarrow{D}$ *and a Complete Determination of the* $\gamma n \to K^0\Lambda$ *Amplitude,"* g14 Proposal E06-101.

[28] T. Mart, C. Bennhold, H. Haberzettl, and L. Tiator, *"Kaon-MAID,"* http://www.kph.uni-mainz.de/MAID/kaon/kaonmaid.html.

[29] William J. Briscoe, Diane Schott, Igor I. Strakovsky, and Ron L. Workman, "*SAID Partial Wave Analysis*," http://gwdac.phys.gwu.edu.

[30] A. V. Anisovich, A. Sarantsev, and E. Klempt, "*Bonn-Gatchina Partial Wave Analysis*", http://pwa.hiskp.uni-bonn.de.

[31] F.X. Lee, T. Mart, C. Bennhold, H. Haberzettl, L.E. Wright, *"Quasifree Kaon Photoproduction on Nuclei,"* Nucl. Phys. **A695**, 237 (2001) .

[32] H. Haberzettl, *"Gauge-Invariant Theory of Pion Photoproduction with Dressed Hadrons,"* Phys. Rev. **C** 56, 2041 (1997).

[33] K. Miyagawa *et al., "Electromagnetic K^+ Production on the Deuteron with Hyperon Recoil Polarization,"* Nucl. Phys. **A691**, 64 (2001).

[34] The JLab Picture Exchange, http://www1.jlab.org/ul/jpix.

[35] S. Gagnon, *Jefferson Lab Site Tour*, http://education.jlab.org/sitetour/guidedtour05.1.alt.html.

[36] D. I. Sober *et al., "The Bremsstrahlung Tagged Photon Beam in Hall B at JLab,"* Nucl. Instr. Meth. **A440**, 263-284 (2000).

[37] B.A. Mecking *et al., "The CEBAF Large Acceptance Spectrometer,"* Nucl. Instr. Meth. **A503**, 513 (2003).

[38] Jefferson Lab. *Experimental Hall B*, http://www.jlab.org/Hall-B/.

[39] Y.G. Sharabian *et al., "A New Highly Segmented Start Counter for the CLAS Detector,"* Nucl. Phys. **A656**, 246 (2006).

[40] E. Smith *et al., "The time-of-flight system for CLAS,"* Nucl. Instr. Meth. **A432**, 265 (1999).

[41] Alan J. Street *et al., "Final Site Assembly and Testing of the Superconducting Toroidal Magnet for the CEBAF Large Acceptance Spectrometer (CLAS),"* IEEE Trans. Mag. **32,** No. 4, 2074 (1996).

[42] M. D. Mestayer *et al., "The CLAS Drift Chamber System,"* Nucl. Instr. Meth. **A449**, 81 (2000).

[43] D. S. Carman *et al., "The Region One Drift Chamber for the CLAS Spectrometer,"* Nucl. Instr. Meth. **A419**, 315 (1998).

[44] Y. M. Qin *et al., "Prototype Studies and Design Considerations for the CLAS Region Two Drift Chambers,"* Nucl. Instr. Meth. **A367**, 316 (1995).

[45] F. J. Barbosa *et al., "A Drift Chamber System for a Toroidal Detector,"* Nucl. Instr. Meth. **A323**, 19 (1992).

[46] g14 wiki. Available at http://clasweb.jlab.org/rungroups/g14/wiki.

[47] B.A Mecking *et al., "The CLAS Drift Chamber System,"* NIM **A503**, 513 (2003).

[48] Private conversation with A. D. Sandorfi.

[49] D. Lawrence, M. Mestayer, *"CLAS Drift Chamber Calibration: Software and Procedures,"* CLAS Internal Report: CLAS-Note 2002-016 (2002).

[50] E. Pasyuk, *"Energy Loss Corrections for Charged Particles in CLAS,"* CLAS Internal Report: CLAS-Note 2007-016 (2007).

[51] M. Williams, "*Measurement of Differential Cross Sections and Spin Density Matrix Elements along with a Partial Wave Analysis for $\gamma p \rightarrow p\omega$ using CLAS at Jefferson Lab*," Ph. D thesis, Carnegie Mellon University, (May 2007). http://www.jlab.org/Hall-B/general/thesis/williams_thesis.pdf.

[52] M. Williams and C. A. Meyer, "*Kinematic Fitting in CLAS*," CLAS Internal Report: CLAS-Note 2003-017 (2003).

[53] M. Holtrop (CLAS), "*CLAS GEANT simulation,*" https://www.physics.unh.edu/maurik/gsim_info.shtml.

[54] H. Drucker and C. Cortes, "*Boosting Decision Trees*," Adv. Neural Inform. Process. Systems, **8** (1996).

[55] B. P. Roe, H. J. Yang, J. Z., "*Boosted Decision Trees, a Powerful Event Classifier*," Proceedings of PHYSTAT05 (Statistical Problems in Particle Physics, Astrophysics and Cosmology), Oxford, UK, September 12-15, 2005.

[56] A. Hoecker, P. Speckmayer, J. Stelzer, J. Therhaag, E. von Toerne, and H. Voss, "*TMVA−Toolkit for Multivariate Data Analysis,*" PoS ACAT 040 (2007), arXiv:physics/0703039.

[57] J. Cladis, W. Hess, and B. Moyer, "*Nucleon Momentum Distributions in Deuterium and Carbon Inferred from Proton Scattering*," Phys. Rev. **87**, 425 (1952).

[58] M. Lacombe *et al., "Parametrization of the Deuteron Wavefunction of the Paris N—N Potential,"* Phys. Lett. B **101**,139 (1981).

[59] R. Machleidt, K. Holinde, C. Elster, "*The Bonn Meson-Exchange Model for the Nucleon—Nucleon Interaction*," Phys. Rep. **149**, 1 (1987).

[60] L. Lamia *et al.,* "*Influence of the d-State Component of the Deuteron Wavefunction on the Application of the Trojan Horse Method*," Phys. Rev. C **85**, 025805 (2012).

[61] C. O. Vuosalo *et al.*, "*Muon Identification Using Decision Trees*," The BABAR Collaboration, BAD 1853, (2008).

[62] Y. Kim, M. Noz, "*Dirac's Light-Cone Coordinate System*," Am. J. Phys. **50**, 721 (1982).

[63] L.C. Maximon and H.Olsen, "*Photon and Electron Polarization in High-Energy Bremsstrahlung and Pair-Production with Screening,*" Phys. Rev. **114**, 887 (1959).

[64] G. Ramachandran, R.S Keshava Murthy, and M.V.N. Murthy, "*Target Asymmetry and Effective Neutron Polarization with Polarized Deuteron Targets,*" Physics Letters. **B**87, 3 (1979).

[65] C. Taylor, "*$K_S\Lambda$ Photoproduction on the Neutron within the Resonance Region*," Ph.D. Thesis, Idaho State University (December, 2012). http://www.jlab.org/Hall-B/general/thesis/CTaylor_thesis.pdf

[66] P.J. Mulders *et al.*, "*Multi-Quark States. 3. Q**6 Dibaryon Resonances*," Phys. Rev. **D21**, 2653 (1980).

[67] A. Gal and H. Garcilazo, "*Three-Body Model Calculations of $N\Delta$ and $\Delta\Delta$ Dibaryon Resonances*," (2014), arXiv:1402.3171 [nucl-th].

[68] A. Gal and H. Garcilazo, "*Pion-Assisted $N\Delta$ and $\Delta\Delta$ Dibaryons*," (2014), arXiv:1401.3165 [nucl-th].

[69] P. Adlarson *et al.* [WASA-at-COSY Collaboration], "*Abashian-Booth-Crowe Effect in Basic Double-Pionic Fusion—Obsevation of a New Resonance?*" Phys. Rev. Lett. **106**, 242302 (2011).

[70] B. Werner *et al.,* "*Coherent Production of the $K^-\pi^+\pi^-$ System in K^--d Interaction at 5.5 GeV/c*," Phys. Rev. **188**, 2023 (1969).

[71] D. Denegri *et al.,* "*Coherent k^-d Interactions at 12.6 Gev/c*," Nucl. Phys. **B9**, 286 (1969).

[72] D.C. Brunt *et al.,* "*The Final State $pd\pi^+\pi^-$ in pd Interactions at about 2 Gev/c*," Physics Letters. **B26**, 317 (1968).

[73] B.S. Aladashvili *et al.,* "*On the Two Nucleon Mass Enhancement Associated with the High Momentum Tail of the Spectator in the Deuteron breakup*," Nucl. Phys. **A274**, 486 (1976).

[74] S. Strauch *et al.* [CLAS Collaboration], arXiv:1503.05163 [nucl-ex].

[75] T. M. Mitchell, "*Machine Learning*," McGraw-Hill Science/Engineer/Math (1997).

[76] Aarti Singh (2014), "*Decision Trees and Boosting* [PowerPoint slides]." Retrieved from https://piazza.com/cmu/fall2014/1070115781/home.

[77] Y. Freund, R. E. Schapire, "*Game Theory, on-line Prediction and Boosting*," Proceedings of the Ninth Annual Conference on Computational Learning Theory, page 325-332 (1996).

Appendix A

Boosted Decision Trees

In Chapter 5, 6 and 7, we relied mainly on the Boosted Decision Trees (BDT) algorithm to efficiently select signal events from mixtures of signal and background. We showed that the method works well and in some cases more optimally than the typical method of *cuts* (as shown in Chapter 5). Nevertheless, the algorithm is closely similar to making cuts. In this appendix we would like to review the algorithm in a more rigorous framework so that the algorithm can be understood and more importantly be employed appropriately. For interested readers, reference [54] was the first paper that introduces the BDT algorithm, while reference [55] illustrated the application of the algorithm in particle physics.

A.1 Motivation

For motivation, let us consider an oversimplified example consisting of two hundred events belonged to two distinct classes; each event is characterized by two variables. The left plot on Figure A.1 shows all the events with two colors (red and blue) representing their classes plotting only the first variable. Clearly, a cut at 0.2 would select a clean sample of "blue" events while a cut at 0.8 would be reasonable to get a clean sample of "red" events. The situation is undesirable since most of the data is within 0.2 and 0.8. Nevertheless, when viewing the data using both variables, see the right plot on Figure A.1, it is clear that a diagonal cut can separate cleanly and efficiently the two classes. Note that the diagonal cut is a combination of the two variables. Therefore, for this very simple example, in particular, it is better to seperate the classes using both variables by placing a cut on a linear combination of them. In fact, sometimes it is better to plot the data in as many dimensions as possible because the higher the dimension the more separation between each pair of event—or equivalently projecting data into lower dimensional space reduces available information. However, it is also important to realize that the more correlated the considered variables are, the less separation the data has in high dimensional space, i.e., less information is gained. Imperfectly, humans can only view data at most in *three* dimensions simulta-

neously, thus limiting our ability to do classification. Fortunately, the BDT is one of the algorithms designed to ameliorate this problem. In short, it is correct to say that the algorithm "views" the data in multidimensional space and separates any distinct classes in that high dimensional space. At the moment, it is sufficient to know that before employing the BDT, it needs to be "trained" and checked for "overtraining". We will explain these points in more detail in later sections.

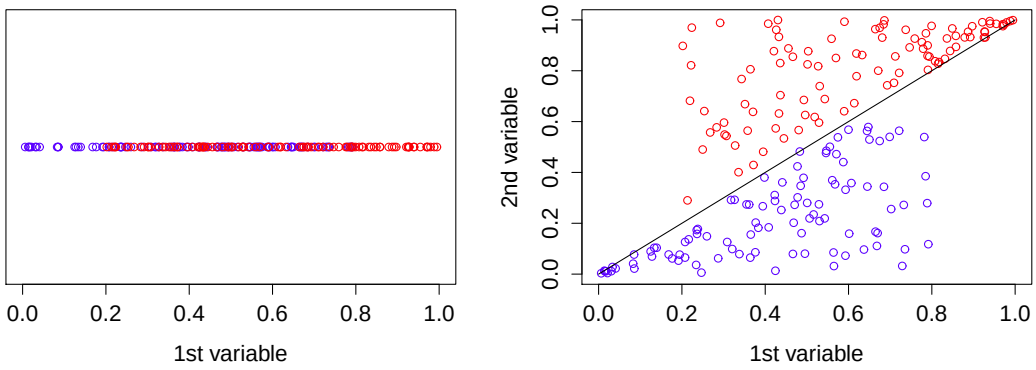

Figure A.1: Left: Data points from the simple example described above plotted using only the first variable. Right: Data points plotted using both variables. As often like this example, viewing the data in more dimensions reveals a richer structure in the data.

A.2 Introduction

We mentioned above that the BDT needs to be trained for a particular classification task. In other words, training data, which has the same distributional characteristics as the real data, is used to build the algorithm—this type of algorithm is called supervised learning. The only difference between training data and real data is that training data has *labels*. In detail, each event in the training data is a pair consisting of an input object (typically a vector of values) and a desired output value—i.e., the class label. For example, in our data, the labels are indicators of whether each training event is background or signal. The BDT algorithm then analyzes the training data and produces an inferred function, which can be used on other similar data sets. Consequently, for a supervised learning algorithm to be useful, its performance on the training data must be consistent with its performance on other similar data sets. When the performance on a test data is lower than on the training data, the algorithm is said to be "*overtrained*," i.e., it built a specialized procedure to perform optimally only on the training data and failed to generalize the training performance to other

data sets. Making sure the BDT is not overtrained is as important as optimizing its performance. Usually, there is a tradeoff between these two (it is called bias-variance tradeoff). Next we will introduce how to construct the decision tree, then the mechanism of *boosting*, and finally how *boosting* helps to combine a "forest" of decision trees to create a powerful classifier.

A.2.1 Decision Tree

A decision tree is a graphical representation of a set of if-then rules. Formally, a branch of the tree constitutes a disjunction of logical conjunctions and each leaf represents the final decision to be executed [75]. Figure A.2 shows an example of a general decision tree with one continuous variable (X_1) and one categorical variable (X_2). It is obvious from Figure A.2 that the decision tree partitions the space into smaller rectangular regions and assigns a category (referred to as a class or a label) to each region. This observation can be generalized into three or higher dimensional space. i.e., the decision tree partitions the multidimensional space into hyper rectangles. In addition, each label corresponds to a certain decision. For example, the white rectangles (assigned zero) in Figure A.2 can correspond to classifying all events within the region to be signal while the black ones are background regions. Figure A.2 shows a general tree, but only binary trees with continuous variables are considered hereafter.

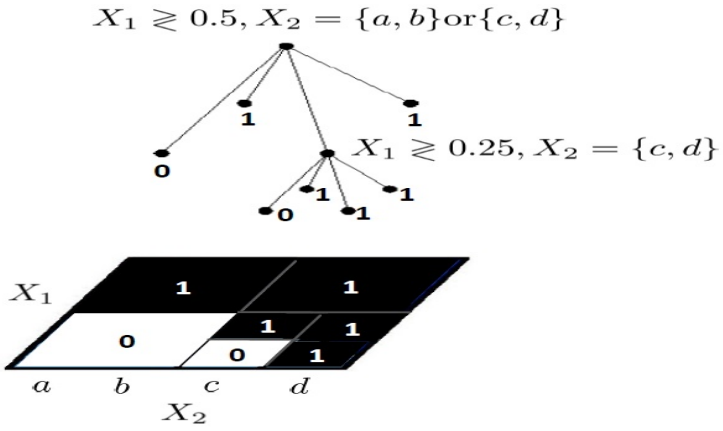

Figure A.2: A general decision tree with both continuous and categorical variable. The decision tree partitions the space into smaller rectangles and assigns a label (class 0 or class 1) for each rectangle. Image was taken from [76].

Decision trees can be utilized for classification tasks—to separate signal and background events; a decision tree is then just a graphical representation of a set of straight cuts. We have established a connection between decision tree classifier and cuts. It

is tempting to conclude that since the tree is not flexible, it can not be more effective and efficient compared to more flexible cuts (a diagonal cut like in Figure A.1). The opposite, however, is true. First, the deeper the decision tree can grow (more branches, more leaves), the better classification power it gains. For example, in Figure A.3 we show a fictitious example of two classes with the black region corresponding to background events and signal events in the white regions. The boundaries between the black and white regions are obviously irregular. The top plots in Figure A.4 show how a simple decision tree with only straight cuts can separate the two classes; the bottom plots illustrate that if the same tree continues to grow deeper and deeper, the tree can capture better the non-linear structure of the boundaries between the black and white regions. Second, so far we have illustrated using only a two dimensional space, but the decision tree's classification power becomes more significant when applied to high dimensional data; the algorithm to build a tree in higher dimensions is the same as in two dimension. We will address the question of how to build a decision tree in the next subsection.

Figure A.3: Plot of background (black) region and signal (white) regions. The task is to build a decision tree that can capture the boundaries between regions. Image was taken from [76].

A.2.1.1 Information Entropy and Information Gain

Each step in building a decision tree involves choosing one variable to be at a certain node and a value to place a cut on the chosen variable. For example, consider a set of *labeled* background and signal events (i.e., whether an event is signal or backgroud is known), each event has ten features (or ten variables), and we would like to build a decision tree to classify these events. One of the ten features is picked for the root of the tree. A cut is then placed on the chosen feature to split the data (create the first two branches). After that, the process repeats. Let us introduce how to pick a feature and its value for each node using *information entropy* [75], which measures the inhomogeneity of *training* data, i.e., the information entropy is largest if the

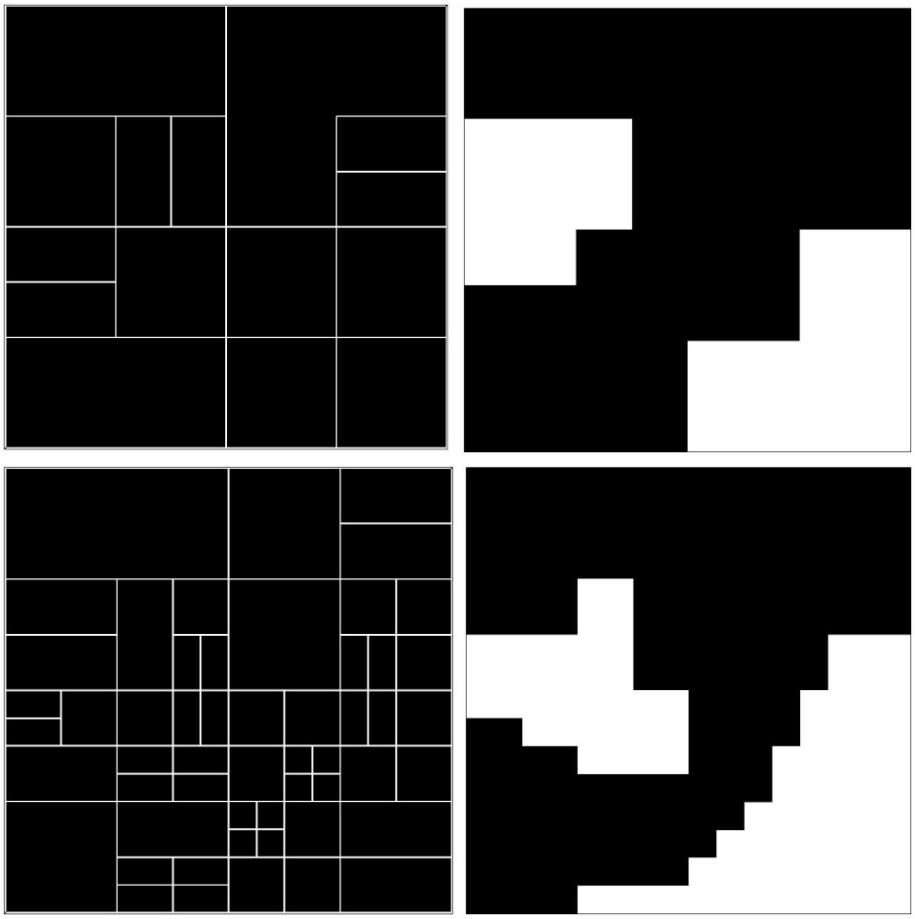

Figure A.4: Top: Classification result from a simple decision tree. Bottom: Classification result if the tree has more nodes. Image was taken from [76].

data consists of equal portions of background and signal events, while it is smallest if the data consists of only either background or signal events (information literally means computer bits), see Figure A.5. The mathematical formula for the information entropy is:

$$H(P(Y)) = \sum_{y=S,B} P(Y = y) \log_2 P(Y = y),$$

where Y is an categorical variable with two values: S means signal, B means background, $H(P(Y))$ is the information entropy (or measure of inhomogeneity) of the selected data sample (note that $H(P(Y = S)) = H(P(Y = B))$), and $P(Y = y)$ is the probability that a random label assignment for that particular event results in a correct labeling (in particular, if the weight of each event is $\frac{1}{N_S+N_B}$ where N_S, and N_B are the known number of background and signal events in the training data, respectively, then $P(Y = S) = \frac{N_S}{N_S+N_B}$).

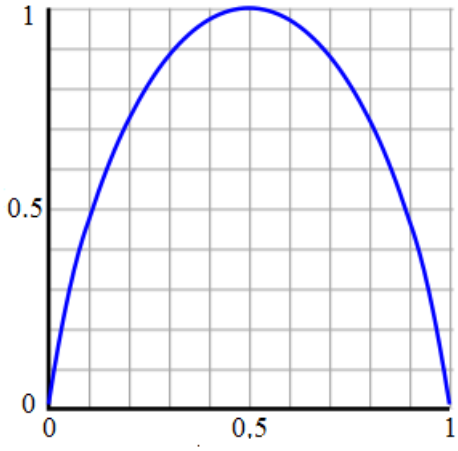

Figure A.5: The information entropy $H(P(Y = S))$ as a function of $P(Y = S)$.

Another entropy concept is the conditional information entropy $H(Y|X_i = x)$, which is the entropy of Y after selecting a cut at x on feature (variable) X_i:

$$H(P(Y|X_i = x)) = \sum_{X_i \gtrless x,} P(X_i \gtrless x) \sum_{Y=S,B} P(Y = y|X_i \gtrless x) \log_2 P(Y = y|X_i \gtrless x),$$

where $P(X_i \gtrless x)$ is the probability of $X_i < x$, and probability of $X_i \geq x$, respectively. Particularly, $P(X_i < x)$ is the ratio of the number of events *from both signal and background subsets* satisfied $X_i < x$ to the total number of events $N_S + N_B$. $P(Y = y|X_i \gtrless x)$ represents four disjoint conditional probabilities, which are $P(Y = S|X_i \geq x)$, $P(Y = S|X_i < x)$, $P(Y = B|X_i \geq x)$, and $P(Y = B|X_i < x)$. The idea is to pick a feature and a cut value such that the split data sets are purer than the original data sample and other split sub sets. Formally, in information theory this is referred to as maximizing *information gain (I)*, which measures the reduction in entropy [75]. This procedure includes two steps: first, for each feature i, one finds the cut value x such that the information gain is maximized; second, one picks the feature such that its maximized information gain is the largest among the features' maximized information gain. This procedure is summarized mathematically below:

$$arg\max_i \left[\max I(Y, X_i)\right] = arg\max_i \left[\max_x \left[H(P(Y)) - H(P(Y|X_i = x))\right]\right],$$

thus, a decision tree can be built recursively by the following procedure:

1. Computing the information entropy $H(P(Y))$ before splitting,
2. Iterating through all combination of features and their values to compute the conditional entropy $H(P(Y|X_i = x))$,

3. Selecting the the feature j and its cut value x, (X_j, x), that maximizes the information gain (I),

4. The construction for the current node is completed, split (to create two branches) the training data based on (X_j, x),

5. Traversing the tree and repeat step 1-4.

A.2.1.2 Overfitting by a Decision Tree

The decision tree method is popular for doing classification because it has a simple design thus is easy to implement. In addition, its interpretation is straightforward even with multidimensional data. However, it has one subtle issue. As mention earlier, if allowed to grow, a decision tree can perfectly classify the training data. In Figure A.6 we present the plots of the decision boundary constructed by a very large tree; comparing to Figure A.3 there is little difference. This is a desirable property when the data is noise-free and deterministic. In reality, such a situation is rare. Therefore, large decision trees tend to *overfit* and do not generalize well. As a result, usually the tree is only allowed to have up to certain depth which, of course, would reduce the overall classification performance. A solution for this problem is to construct a "forest" of *shallow*—to assure generalization—but *distinct* decision trees, and combine the trees to create a stronger classifier with better performance than any individual tree. The procedure is referred to as *boosting* [77], and we discuss this algorithm next.

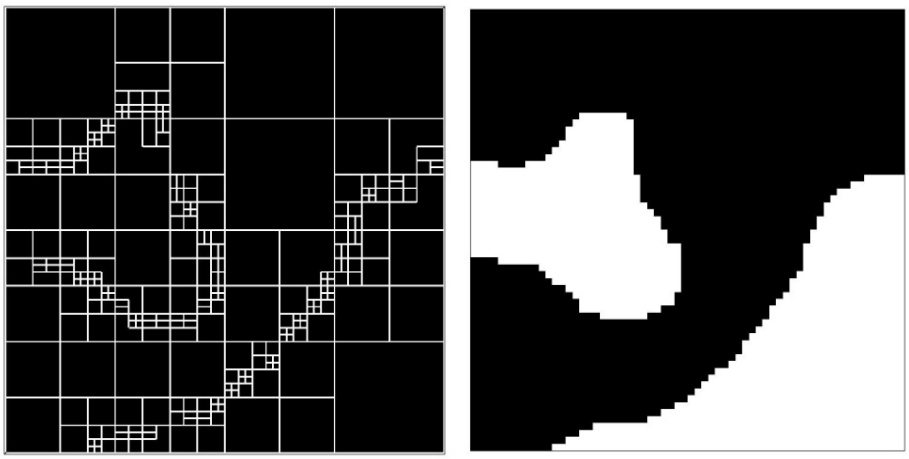

Figure A.6: Classification result from a large decision tree. The plot on the right is very smiliar to Figure A.3 indicating that a growing tree can construct a "perfect" decison boundary. Image was taken from [76].

A.2.2 Boosting

Boosting is a popular method to combine weak classifiers into a more powerful classifier (a typical weak classifier is a shallow decision tree). The boosting algorithm repeatedly calls this weak classifier, each time it feeds the classifier with the same training events but with a different weight distribution. Particularly, initially each event has a weight of $1/(N_S+N_B)$, and the first weak classifier is built based on this set of weights; the boosting algorithm then changes the weight distribution (the events now have a new set of weights), and the second weak classifier is constructed with this new set of weights. The process continues until the last weak classifier is finished. The rule for updating the weights is quite sensible: increase the weight on the events that were misclassified by the preceding weak classifier while reduce the weights for correctly classified events, so that the next classifier is "forced" to focus its attention on the "hardest" events. As for combining the weak classifiers, a natural and effective way is to simply take a (weighted) majority vote of their predictions. Below we present the Ada-Boost algorithm which has undergone intense theoretical study and empirical testing [77]:

Given training data represented by $(\mathbf{v}_1, y_1)$, $(\mathbf{v}_2, y_2)$, ..., $(\mathbf{v}_N, y_N)$, where $i \in \{1, 2, 3, ..., N\}$ (N is the total number of signal and background events),

$\mathbf{v}_i \in \mathbf{V} \rightarrow \mathbf{R^d}$, i.e., a d-dimension vector of real values for the input variables, and $y_i \in \{-1, +1\}$, i.e., a two-valued variable indicating the label of each event.

Initialize the weight distribution for the first weak classifier $D_1(i) = 1/N$, where i indicates the i^{th} event in the training data.

For $t = 1, ..., T$, where T is the number of weak classifiers (number of decision trees, for example):

- Train base learner using the weight distribution D_t. For example, $P(Y = S) = \sum_{i}^{N_S+N_B} D_t(i)\delta(Y_i = S)$, where $\delta(Y_i = S)$ equals one if the i^{th} event is signal event, and zero otherwise.

- Get classification decision for the i^{th} event from the t^{th} classifier $h_t(\mathbf{v}_i) \in \{-1, +1\}$, i.e, should i^{th} event be classified as background or signal event.

- Choose optimally $\alpha_t \in \mathbf{R}$ (we will discuss later).

- Update:

$$D_{t+1}(i) = \frac{D_t(i)\exp(-\alpha_t y_i h_t(\mathbf{v}_i))}{Z_t},$$

  where Z_t is a normalization factor (chosen so that sum of $D_{t+1}(i)$ of all N events is equal to one). In addition, note that if the event i^{th} is correctly classified by the h_t weak classifier, then $y_i h_t(\mathbf{v}_i) = +1$, while $y_i h_t(\mathbf{v}_i) = -1$ if the event is wrongly classified. As a result, the updated weights for wrongly classified

events are increased (i.e., $D_{t+1}(i) > D_t(i)$) while correctly predicted events have decreased weights (i.e., $D_{t+1}(i) < D_t(i)$).

Output the final classifier by combining the weighted prediction of the weak classifiers (if the weak classifier is the decision tree, then $H(\mathbf{v}_i)$ is the BDT output):

$$H(\mathbf{v}_i) = \sum_t^T \alpha_t h_t(\mathbf{v}_i).$$

For more detail, each training event is represented by a pair of $(\mathbf{v}_i, y_i)$ where y_i is the *true* label (identity) for the i^{th} event ($+1$ indicating signal and -1 indicating background) and $\mathbf{v}_i$ is a d-dimensional vector with the values of the d input features (variables). D_t is the set of event weights used by the h_t weak classifier, and $h_t(\mathbf{v}_i)$ is the prediction for i^{th} event from the h_t weak classifier.

A simple way to judge the performance of the final classifier $H(\mathbf{v}_i)$ is to count the number of events misclassifed (usually referred to as 0-1 training error). The training error of the final classifier is bounded from above as follows:

$$\frac{1}{N}\sum_i^N \delta(f(\mathbf{v}_i) \neq y_i) \leq \frac{1}{N}\sum_i \exp(-y_i H(\mathbf{v}_i)) = \prod_t \left[\sum_{i=1}^N D_t(i)\exp(-\alpha_t y_i h_t(\mathbf{v}_i))\right] = \prod_t Z_t,$$

where $f(\mathbf{v}_i) = +1$ if $H(\mathbf{v}_i)$ is positive and $f(\mathbf{v}_i) = -1$ otherwise, and $\delta(f(\mathbf{v}_i) \neq y_i)$ equals one if $f(\mathbf{v}_i) \neq y_i$ and zero otherwise. The resulting inequality is because $\exp(-y_i H(\mathbf{v}_i)) > 1$ if $f(\mathbf{v}_i) \neq y_i$ and $\exp(-y_i H(\mathbf{v}_i)) > 0$ if $f(\mathbf{v}_i) = y_i$, while the equality can be derived by invoking the definition of $D_t(i)$ recursively. The above equation shows that the training error is bounded above by $\prod_t Z_t$ and thus, can be reduced most rapidly by choosing α_t on each iteration to minimize Z_t:

$$Z_t = \sum_{i=1}^N D_t(i)\exp(-\alpha_t y_i h_t(\mathbf{v}_i)) = \sum_{i:\, y_i \neq h_t(\mathbf{v}_i)} D_t(i)e^{\alpha_t} + \sum_{i:\, y_i = h_t(\mathbf{v}_i)} D_t(i)e^{-\alpha_t}$$

$$Z_t = \epsilon_t e^{\alpha_t} + (1-\epsilon_t)e^{-\alpha_t},$$

where $\epsilon_t = \sum_i^N D_t(i)\delta(y_i \neq h_t(\mathbf{v}_i))$ is the training error from the h_t weak classifier. Taking partial derivative $\frac{\partial Z_t}{\partial \alpha_t}$ and setting it equal to zero yields:

$$\alpha_t = \frac{1}{2}\ln\left(\frac{1-\epsilon_t}{\epsilon_t}\right).$$

Subsituting α_t back into Z_t, we obtain an upper bound on the 0-1 training error, which is:

$$\frac{1}{N}\sum_{i}^{N}\delta(f(\mathbf{v}_i)\neq y_i)\leq\frac{1}{N}\sum_{i}\exp(-y_iH(\mathbf{v}_i))=\prod_{t}Z_t,=\prod_{t}\sqrt{1-(1-2\epsilon_t)^2},$$

while

$$\prod_{t}\sqrt{1-(1-2\epsilon_t)^2}\leq\exp\left(-2\sum_{t}^{T}\left(\frac{1}{2}-\epsilon_t\right)^2\right),$$

the proof for the exponential bound is in [77]. Notice that if the $\epsilon_t\neq\frac{1}{2}$, i.e., the weak classifier is not doing random guessing, the training error will achive zero exponenially fast. In conclusion, Ada-Boost provides an effective procedure to combine a set of weak classifiers into a very refined one at the end. Second, because the training error can theoretically go to zero, there might still be overfitting in such a situation (still the overtraining issue in BDT is less severe than the overtraining issue of a single decion tree); checking testing error is nessesary as always.

A.2.3 Why Use Boosted Desion Trees

First of all, the BDT is a powerful classifier because it can construct a non-linear, non-parametric boundary to separate signal and background subsets (only neural network and k-nearest neighbor methods can also construct non-linear, non-parametric boundaries). Secondly, the algorithm requires little tuning in order to obtain a reasonable result (on the other hand, neural networks require much more effort in tuning). Third, it is insensitive to the inclusion of poorly discriminating input variables (again, a neural network has difficulty when additional variables are introduced). And lastly, since the trees are binary, the processing speed is quite fast (while k-nearest neighbor processing time grows exponentially). In conclusion, the BDT selection method is an attractive alternative to the traditional cuts and requires just a small extra effort overall.

A.3 The TMVA Root Data Analysis Package

The Toolkit for Multivariate Data Analysis with ROOT (TMVA) provides a large variety of multivariate classification algorithms (including BDT). It has been integrated into the ROOT environment so that using the package should be straightforward for the nuclear and particle physics communities, who employ ROOT extensively for data analysis. Moreover, the TMVA Users Guide [56] is a very good reference for interested learners.

Here, we present, in detail, the steps to employ the BDT algorithm using the TMVA analysis package. First, a list of features (variables) is determined by the

user; different classification tasks require different sets of variables. A general recommendation is that the variables should not have strong correlation. We next instruct the TMVA training program how we want it to built the trees. In particular, the maximum depth of each tree is specified; this is crucial because there is a tradeoff between overfitting and performance (see previous discussion in section A.2.1.2). Also, the number of trees being built is important as well. Recall from section A.2.2 that training error approaches zero as the number of trees increases, but it only happens if the condition $\epsilon_t \neq \frac{1}{2}$ is true (ϵ_t is the 0-1 training error for t^{th} tree). Note that once the t^{th} tree has $\epsilon_t \approx \frac{1}{2}$, the next tree can not improve the performance further (boosting mechanism breaks down). After specifying all building options, the training data, which includes a signal or background label for each event, was input into the TMVA training program. The training program provides several useful diagnostics after it finishes running. For example, it reports variable ranking, i.e., how often the variables were used in building the trees, thus higher ranking means a better seperation power. In addition, a graphical user interface (GUI) like Figure A.7 provides an interface to view all the information that is necessary to determine the result of the training stage. Based on our experience, the following are important to check:

- Classifier Output Distributions of both training data and testing data (note that the TMVA program splits the training data (separately for signal and background) into test data and train data). Figure A.8 shows an example plot, the Kolmogorov–Smirnov test is employed to test for overtraining (overfitting). The test computes the probability that the BDT output distributions from the training and testing data could be drawn from one common parent distribution (the test is applied separately on signal data and background data). When the probability is low, reducing the maximum depth for the trees is necessary. Note that the maximum depth of the trees is unfortunately determined by brute force trial and error method—increasing the maximum allowed depth of the decision trees gradually if the final BDT is not overtrained.

- Classifier Cut Efficiencies suggest the value to place a cut on the BDT output (this is the only variable that we cut on). Given the initial estimation of signal to background ratio, this option suggests a cut value so that the misclassification cost is minimal (for example, see Figure A.9). If no initial signal to background ratio was provided by user, a default $1:1$ is assumed.

- Receiver Operating Characteristic (ROC) curve plots the background rejection efficiency as a function of signal efficiency, see Figure A.10. In short, it quantifies the performance of the BDT on a particular classification task. In Figure A.10, the closer a ROC curve comes to the top right corner, the more powerful the classifier is, while the diagonal line from top left to bottom right corners is the

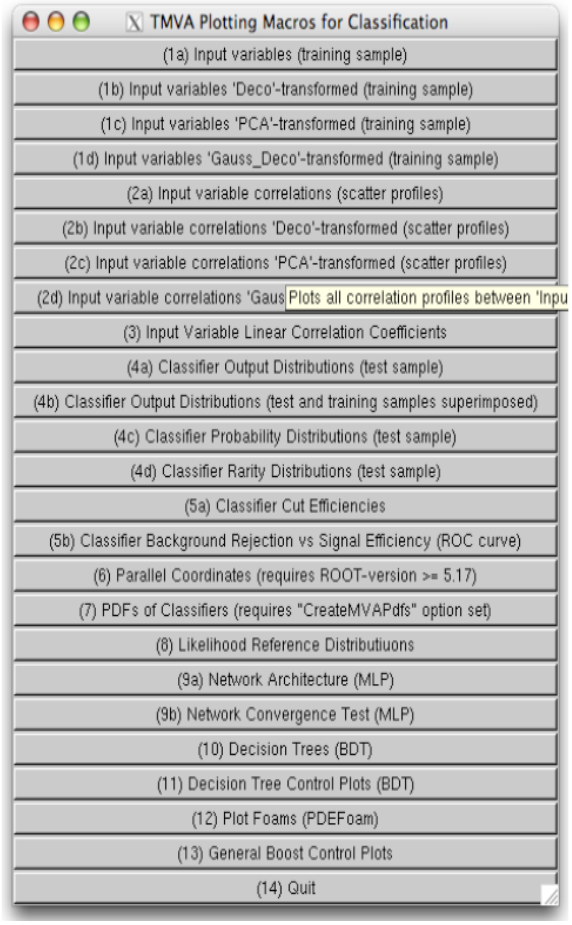

Figure A.7: Graphical user interface (GUI) provided after the training phase to help evaluating the training results. For more detail, see [56].

performance of a random-guessing classifier. Usually, ROC curves are used for comparing algorithms. In Chapter 6, it was shown that for the $K^0\Lambda$ analysis the ROC curves from the regular BDT and the categorical BDT suggest the categorical BDT has better performance.

After the training results have been evaluated, the BDT algorithm is applied to the real data to seperate signal and background events by applying a single cut on the BDT output. For systematics studies, we vary the cut to study the effect on our measurements (for example, the E asymmetry measurements).

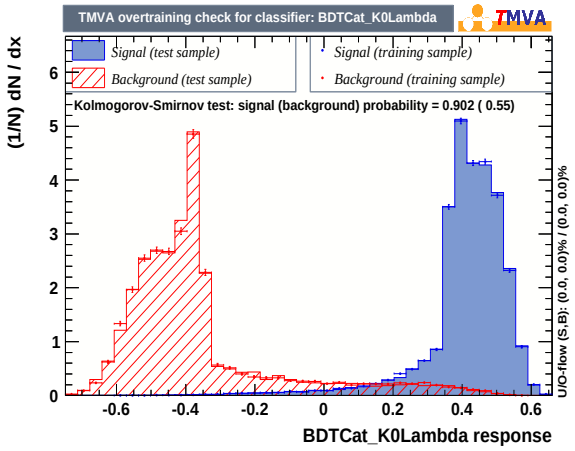

Figure A.8: Classifier Output Distributions of both training data (filled histograms) and testing data (pointed histograms). A high Kolmogorov-Smirnov probabilities for both signal (blue) and background (red) suggest no overtraining. This example is from the CLAS g14 $K^0\Lambda$ analysis.

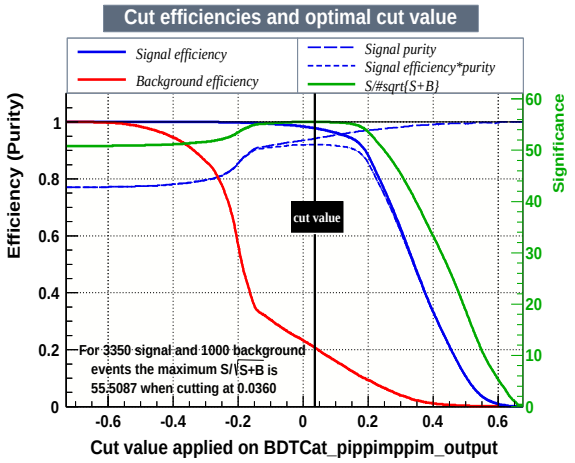

Figure A.9: Plots of cut efficiencies-shows the efficiencies as a function of cut value-and optimal cut value. This example is from the CLAS g14 $K^0\Lambda$ analysis. The cut is placed at +0.08.

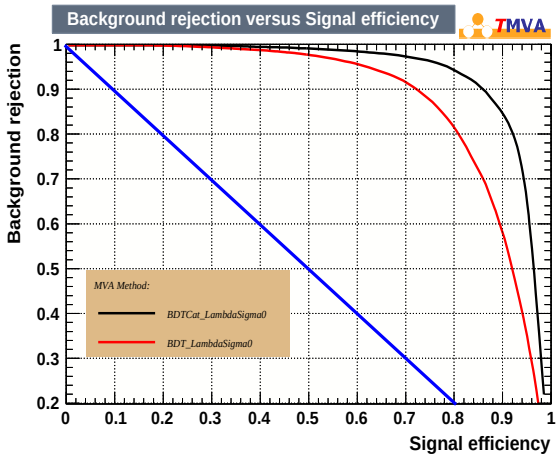

Figure A.10: Examples from the CLAS g14 $K^0\Lambda$ analysis for background rejection vs. signal efficiency (ROC curves).

Appendix B

E Measurements for Reaction $\gamma d \to \pi^- p(p_s)$

B.1 E Measurements as a Function of the Recoil Momentum

$\lvert p\rvert_{missing}$ (GeV/c)	E	σ_{stat}	σ_{sys}
0.005	-0.487134	0.0769727	0.0750187
0.015	-0.583526	0.030531	0.089863
0.025	-0.565306	0.0204594	0.0870571
0.035	-0.575039	0.0167727	0.088556
0.045	-0.574569	0.0153458	0.0884837
0.055	-0.587598	0.0150495	0.0904901
0.065	-0.570011	0.0153505	0.0877817
0.075	-0.548572	0.0161112	0.08448
0.085	-0.550319	0.0173109	0.0847491
0.095	-0.532784	0.0189121	0.0820487
0.105	-0.508126	0.0210035	0.0782514
0.115	-0.500882	0.0230725	0.0771359
0.125	-0.455396	0.02544	0.070131
0.135	-0.423265	0.028869	0.0651828
0.145	-0.457666	0.0333062	0.0704806
0.155	-0.34787	0.0370045	0.053572
0.165	-0.314668	0.0407769	0.0484589
0.175	-0.28822	0.0456238	0.0443859
0.185	-0.355769	0.0495343	0.0547884
0.195	-0.196886	0.054068	0.0303205

B.2 E Measurements as a Function of Cos$\theta^{\pi^-}_{CM}$[1]

W_{min} (MeV)	W_{max} (MeV)	cos$\theta^{\pi^-}_{CM}$	E	σ_{stat}	σ_{sys}
1480	1520	-0.75	0.406261	0.167858	0.0625641
1480	1520	-0.60	-0.0216592	0.0786597	0.00333551
1480	1520	-0.45	-0.343317	0.0745249	0.0528709
1480	1520	-0.30	-0.481451	0.0763039	0.0741434
1480	1520	-0.15	-0.658341	0.0727699	0.101385
1480	1520	0.00	-0.743052	0.0732445	0.11443
1480	1520	0.15	-0.732094	0.0687911	0.112742
1480	1520	0.30	-0.699644	0.0648639	0.107745
1480	1520	0.45	-0.484564	0.0663375	0.0746229
1480	1520	0.60	-0.323244	0.0819899	0.0497796
1480	1520	0.75	-0.082531	0.225398	0.0127098
1480	1520	0.90	-1.52972	2.36975	0.235576
1520	1560	-0.75	0.485651	0.179673	0.0747902
1520	1560	-0.60	-0.279189	0.0837906	0.0429952
1520	1560	-0.45	-0.410102	0.0793206	0.0631558
1520	1560	-0.30	-0.656394	0.0793337	0.101085
1520	1560	-0.15	-0.713395	0.0785531	0.109863
1520	1560	0.00	-0.821675	0.077045	0.126538
1520	1560	0.15	-0.813952	0.0734327	0.125349
1520	1560	0.30	-0.727743	0.0679686	0.112072
1520	1560	0.45	-0.574838	0.070444	0.088525
1520	1560	0.60	-0.327162	0.0784009	0.0503829
1520	1560	0.75	-0.236508	0.175342	0.0364223
1520	1560	0.90	2.66646	1.48938	0.410634
1560	1600	-0.75	0.0728968	0.195172	0.0112261
1560	1600	-0.60	-0.33152	0.0897521	0.0510541
1560	1600	-0.45	-0.693084	0.0796606	0.106735
1560	1600	-0.30	-0.651061	0.0717136	0.100263
1560	1600	-0.15	-0.655683	0.0748442	0.100975
1560	1600	0.00	-0.718012	0.0703443	0.110574
1560	1600	0.15	-0.552873	0.0671135	0.0851425
1560	1600	0.30	-0.462402	0.0575858	0.0712099
1560	1600	0.45	-0.437325	0.0611064	0.067348

[1]Global correction factor of 1.086 had been applied, see Section 4.3.4.1 for detail

W_{min} (MeV)	W_{max} (MeV)	$\cos\theta^{\pi^-}_{CM}$	E	σ_{stat}	σ_{sys}
1560	1600	0.60	-0.291281	0.0595739	0.0448572
1560	1600	0.75	-0.467245	0.114823	0.0719557
1560	1600	0.90	0.188378	0.755113	0.0290103
1600	1640	-0.75	-0.189463	0.182227	0.0291773
1600	1640	-0.60	-0.684609	0.0854119	0.10543
1600	1640	-0.45	-0.702872	0.0776243	0.108242
1600	1640	-0.30	-0.729026	0.0682844	0.11227
1600	1640	-0.15	-0.765152	0.07855	0.117833
1600	1640	0.00	-0.586752	0.0727952	0.0903598
1600	1640	0.15	-0.649449	0.067037	0.100015
1600	1640	0.30	-0.498151	0.0572943	0.0767152
1600	1640	0.45	-0.407131	0.0547405	0.0626982
1600	1640	0.60	-0.388219	0.0513476	0.0597858
1600	1640	0.75	-0.325098	0.0847155	0.0500651
1600	1640	0.90	-0.871585	0.567195	0.134224
1640	1680	-0.75	-0.45783	0.16789	0.0705059
1640	1680	-0.60	-0.663371	0.0839291	0.102159
1640	1680	-0.45	-0.705599	0.0788096	0.108662
1640	1680	-0.30	-0.64802	0.0673264	0.0997951
1640	1680	-0.15	-0.348022	0.0817373	0.0535954
1640	1680	0.00	-0.240315	0.0801798	0.0370085
1640	1680	0.15	-0.161014	0.07131	0.0247962
1640	1680	0.30	-0.385571	0.0622274	0.059378
1640	1680	0.45	-0.534553	0.0510491	0.0823212
1640	1680	0.60	-0.653125	0.0487816	0.100581
1640	1680	0.75	-0.674358	0.0658909	0.103851
1640	1680	0.90	-0.095026	0.45628	0.014634
1680	1720	-0.75	-0.0857446	0.155742	0.0132047
1680	1720	-0.60	-0.828244	0.087624	0.12755
1680	1720	-0.45	-0.519863	0.0803413	0.0800589
1680	1720	-0.30	-0.155556	0.0646964	0.0239556
1680	1720	-0.15	0.139672	0.0767192	0.0215094
1680	1720	0.00	0.236083	0.077013	0.0363569
1680	1720	0.15	0.0404959	0.0635336	0.00623636
1680	1720	0.30	-0.453288	0.0596253	0.0698063

W_{min} (MeV)	W_{max} (MeV)	$\cos\theta^{\pi^-}_{CM}$	E	σ_{stat}	σ_{sys}
1680	1720	0.45	-0.718247	0.044171	0.11061
1680	1720	0.60	-0.78328	0.0435952	0.120625
1680	1720	0.75	-0.746669	0.0504177	0.114987
1680	1720	0.90	-0.720969	0.347256	0.111029
1720	1760	-0.75	-0.207858	0.169973	0.0320101
1720	1760	-0.60	-0.602519	0.108174	0.0927879
1720	1760	-0.45	-0.271336	0.0994515	0.0417858
1720	1760	-0.30	0.228261	0.0799445	0.0351522
1720	1760	-0.15	0.683134	0.0857854	0.105203
1720	1760	0.00	0.626345	0.0815784	0.0964571
1720	1760	0.15	0.14752	0.0655838	0.0227181
1720	1760	0.30	-0.434327	0.0623895	0.0668864
1720	1760	0.45	-0.793644	0.0453259	0.122221
1720	1760	0.60	-0.819183	0.0447905	0.126154
1720	1760	0.75	-0.877694	0.0487175	0.135165
1720	1760	0.90	-1.22308	0.278836	0.188355
1760	1800	-0.75	-0.393418	0.178436	0.0605864
1760	1800	-0.60	-0.246945	0.130196	0.0380295
1760	1800	-0.45	0.0579503	0.120805	0.00892435
1760	1800	-0.30	0.465599	0.0998997	0.0717022
1760	1800	-0.15	0.469669	0.0929427	0.072329
1760	1800	0.00	0.466387	0.0833614	0.0718237
1760	1800	0.15	0.0423901	0.065643	0.00652808
1760	1800	0.30	-0.43939	0.0620077	0.0676661
1760	1800	0.45	-0.820637	0.0475485	0.126378
1760	1800	0.60	-0.983162	0.0451587	0.151407
1760	1800	0.75	-0.914435	0.0468158	0.140823
1760	1800	0.90	-0.450666	0.236274	0.0694025
1800	1840	-0.75	-0.501513	0.184713	0.0772331
1800	1840	-0.60	-0.100396	0.148344	0.015461
1800	1840	-0.45	0.180929	0.139059	0.0278631
1800	1840	-0.30	0.372702	0.118084	0.0573961
1800	1840	-0.15	0.408912	0.097748	0.0629725
1800	1840	0.00	0.34935	0.0842987	0.0538
1800	1840	0.15	-0.0312973	0.0676809	0.00481979

W_{min} (MeV)	W_{max} (MeV)	$\cos\theta^{\pi^-}_{CM}$	E	σ_{stat}	σ_{sys}
1800	1840	0.30	-0.483565	0.0625857	0.074469
1800	1840	0.45	-0.856031	0.0503471	0.131829
1800	1840	0.60	-0.927721	0.0458692	0.142869
1800	1840	0.75	-0.983349	0.0455784	0.151436
1800	1840	0.90	-0.810889	0.193607	0.124877
1840	1880	-0.75	-0.200017	0.172003	0.0308027
1840	1880	-0.60	-0.172904	0.14092	0.0266271
1840	1880	-0.45	0.081979	0.133739	0.0126248
1840	1880	-0.30	0.362788	0.118314	0.0558693
1840	1880	-0.15	0.0884012	0.0938631	0.0136138
1840	1880	0.00	-0.0518496	0.0846138	0.00798484
1840	1880	0.15	-0.239373	0.0686257	0.0368634
1840	1880	0.30	-0.696962	0.0623114	0.107332
1840	1880	0.45	-0.788202	0.0548299	0.121383
1840	1880	0.60	-1.03257	0.0476086	0.159015
1840	1880	0.75	-0.942213	0.0460726	0.145101
1840	1880	0.90	-0.869477	0.165754	0.133899
1880	1920	-0.75	-0.440201	0.177174	0.067791
1880	1920	-0.60	-0.089223	0.137388	0.0137403
1880	1920	-0.45	0.301322	0.122435	0.0464036
1880	1920	-0.30	0.394759	0.113695	0.0607929
1880	1920	-0.15	-0.291132	0.0924934	0.0448344
1880	1920	0.00	-0.531911	0.0812237	0.0819144
1880	1920	0.15	-0.513463	0.0705208	0.0790734
1880	1920	0.30	-0.768237	0.0624465	0.118308
1880	1920	0.45	-0.787213	0.0590329	0.121231
1880	1920	0.60	-0.897857	0.0513815	0.13827
1880	1920	0.75	-0.871049	0.047885	0.134142
1880	1920	0.90	-0.84122	0.152123	0.129548
1920	1960	-0.75	-0.471216	0.186777	0.0725672
1920	1960	-0.60	-0.079724	0.131837	0.0122775
1920	1960	-0.45	0.241671	0.109858	0.0372174
1920	1960	-0.30	-0.0204814	0.104445	0.00315414
1920	1960	-0.15	-0.319255	0.0893468	0.0491653
1920	1960	0.00	-0.495028	0.0754632	0.0762343

W_{min} (MeV)	W_{max} (MeV)	$\cos\theta^{\pi^-}_{CM}$	E	σ_{stat}	σ_{sys}
1920	1960	0.15	-0.700855	0.0704088	0.107932
1920	1960	0.30	-0.781482	0.0594399	0.120348
1920	1960	0.45	-0.804071	0.0614733	0.123827
1920	1960	0.60	-0.886406	0.052496	0.136506
1920	1960	0.75	-0.908015	0.0483925	0.139834
1920	1960	0.90	-0.73182	0.138675	0.1127
1960	2000	-0.75	-0.701515	0.218836	0.108033
1960	2000	-0.60	0.0531709	0.142295	0.00818831
1960	2000	-0.45	0.257676	0.11814	0.0396821
1960	2000	-0.30	-0.263695	0.112232	0.040609
1960	2000	-0.15	-0.442148	0.0941075	0.0680908
1960	2000	0.00	-0.558264	0.0805035	0.0859726
1960	2000	0.15	-0.753496	0.0783232	0.116038
1960	2000	0.30	-0.845836	0.0622951	0.130259
1960	2000	0.45	-0.927781	0.069881	0.142878
1960	2000	0.60	-0.933159	0.059276	0.143707
1960	2000	0.75	-0.824433	0.0561917	0.126963
1960	2000	0.90	-0.391164	0.141215	0.0602393
2000	2040	-0.75	-0.137448	0.247793	0.021167
2000	2040	-0.60	0.0562929	0.165355	0.00866911
2000	2040	-0.45	0.240555	0.123004	0.0370455
2000	2040	-0.30	-0.201632	0.113668	0.0310514
2000	2040	-0.15	-0.656445	0.0983558	0.101093
2000	2040	0.00	-0.868825	0.0825597	0.133799
2000	2040	0.15	-0.814742	0.0808296	0.12547
2000	2040	0.30	-0.746494	0.0647132	0.11496
2000	2040	0.45	-0.84577	0.0743234	0.130249
2000	2040	0.60	-0.815998	0.0655768	0.125664
2000	2040	0.75	-0.825113	0.0623679	0.127067
2000	2040	0.90	-0.47694	0.140924	0.0734487
2040	2080	-0.75	-0.387799	0.321465	0.0597211
2040	2080	-0.60	0.409752	0.205274	0.0631018
2040	2080	-0.45	0.286833	0.137183	0.0441723
2040	2080	-0.30	-0.470351	0.123902	0.072434
2040	2080	-0.15	-0.847347	0.110013	0.130492

W_{min} (MeV)	W_{max} (MeV)	$\cos\theta^{\pi^-}_{CM}$	E	σ_{stat}	σ_{sys}
2040	2080	0.00	-0.928148	0.0914391	0.142935
2040	2080	0.15	-0.773135	0.0888885	0.119063
2040	2080	0.30	-0.700785	0.0723175	0.107921
2040	2080	0.45	-0.826912	0.0868783	0.127345
2040	2080	0.60	-0.845435	0.0760632	0.130197
2040	2080	0.75	-0.91874	0.0702561	0.141486
2040	2080	0.90	-0.724978	0.150689	0.111647
2080	2120	-0.75	-0.818327	0.342715	0.126022
2080	2120	-0.60	0.348306	0.201983	0.0536391
2080	2120	-0.45	0.117933	0.142323	0.0181617
2080	2120	-0.30	-0.239914	0.122666	0.0369468
2080	2120	-0.15	-0.608971	0.111917	0.0937816
2080	2120	0.00	-0.996661	0.0945876	0.153486
2080	2120	0.15	-0.826831	0.0881574	0.127332
2080	2120	0.30	-0.638955	0.0803598	0.0983991
2080	2120	0.45	-0.670407	0.0921394	0.103243
2080	2120	0.60	-0.611134	0.0840042	0.0941147
2080	2120	0.75	-0.985745	0.0793942	0.151805
2080	2120	0.90	-0.640819	0.154374	0.0986861
2120	2160	-0.75	0.080259	0.367524	0.0123599
2120	2160	-0.60	0.626206	0.221473	0.0964357
2120	2160	-0.45	0.131864	0.158744	0.020307
2120	2160	-0.30	-0.701802	0.130991	0.108078
2120	2160	-0.15	-0.770667	0.124451	0.118683
2120	2160	0.00	-0.897329	0.107709	0.138189
2120	2160	0.15	-0.788329	0.102411	0.121403
2120	2160	0.30	-0.697803	0.0949481	0.107462
2120	2160	0.45	-0.525678	0.107135	0.0809544
2120	2160	0.60	-0.571588	0.10063	0.0880245
2120	2160	0.75	-0.801966	0.0938356	0.123503
2120	2160	0.90	-0.507158	0.179092	0.0781024
2160	2200	-0.75	0.733287	0.388133	0.112926
2160	2200	-0.60	0.237695	0.216656	0.0366051
2160	2200	-0.45	-0.147694	0.157626	0.0227449
2160	2200	-0.30	-0.581913	0.122368	0.0896146

W_{min} (MeV)	W_{max} (MeV)	$\cos\theta^{\pi^-}_{CM}$	E	σ_{stat}	σ_{sys}
2160	2200	-0.15	-0.892675	0.113872	0.137472
2160	2200	0.00	-0.931614	0.106285	0.143469
2160	2200	0.15	-0.858024	0.0991418	0.132136
2160	2200	0.30	-0.458656	0.0961305	0.070633
2160	2200	0.45	-0.170036	0.110739	0.0261856
2160	2200	0.60	-0.483471	0.10026	0.0744545
2160	2200	0.75	-0.955742	0.0878488	0.147184
2160	2200	0.90	-0.860275	0.154924	0.132482
2200	2240	-0.75	1.18851	0.426426	0.183031
2200	2240	-0.60	0.190145	0.225601	0.0292823
2200	2240	-0.45	-0.271587	0.175507	0.0418244
2200	2240	-0.30	-0.681088	0.138679	0.104888
2200	2240	-0.15	-0.75404	0.123954	0.116122
2200	2240	0.00	-0.892481	0.126403	0.137442
2200	2240	0.15	-0.836317	0.114987	0.128793
2200	2240	0.30	-0.396217	0.119902	0.0610175
2200	2240	0.45	-0.222632	0.127358	0.0342854
2200	2240	0.60	-0.353411	0.122923	0.0544253
2200	2240	0.75	-0.918678	0.0993565	0.141476
2200	2240	0.90	-0.913087	0.164901	0.140615
2240	2280	-0.75	0.439469	0.649139	0.0676782
2240	2280	-0.60	0.547263	0.329877	0.0842786
2240	2280	-0.45	-0.202071	0.27388	0.0311189
2240	2280	-0.30	-0.565996	0.210332	0.0871633
2240	2280	-0.15	-1.10338	0.167135	0.169921
2240	2280	0.00	-1.03311	0.212045	0.159098
2240	2280	0.15	-0.380215	0.170277	0.0585531
2240	2280	0.30	-0.0884788	0.197156	0.0136257
2240	2280	0.45	-0.0399517	0.19653	0.00615257
2240	2280	0.60	-0.277825	0.182935	0.0427851
2240	2280	0.75	-0.900345	0.127119	0.138653
2240	2280	0.90	-0.884624	0.204327	0.136232
2280	2320	-0.75	0.612957	0.759265	0.0943953
2280	2320	-0.60	0.663067	0.404526	0.102112
2280	2320	-0.45	-0.229859	0.331124	0.0353982

W_{min} (MeV)	W_{max} (MeV)	$\cos\theta^{\pi^-}_{CM}$	E	σ_{stat}	σ_{sys}
2280	2320	-0.30	-0.439801	0.259337	0.0677293
2280	2320	-0.15	-0.747322	0.20493	0.115088
2280	2320	0.00	-0.754905	0.270773	0.116255
2280	2320	0.15	-0.151619	0.219723	0.0233494
2280	2320	0.30	0.275831	0.270223	0.0424779
2280	2320	0.45	-0.204537	0.246996	0.0314988
2280	2320	0.60	-0.114379	0.233782	0.0176144
2280	2320	0.75	-0.694952	0.156378	0.107023
2280	2320	0.90	-0.611531	0.25566	0.0941758